Order Number 9304706

Photolithography of integrated optic devices in porous glasses

Mendoza, Edgar Alfredo, Ph.D.

City University of New York, 1992

U·M·I
300 N. Zeeb Rd.
Ann Arbor, MI 48106

PHOTOLITHOGRAPHY OF INTEGRATED OPTIC DEVICES IN POROUS GLASSES

BY

EDGAR A. MENDOZA

A dissertation submitted to the Graduate Faculty in Chemistry in partial fullfilment of the requirements for the degree of Doctor of Philosophy, from the City University of New York.

This manuscript has been read and accepted by the Graduate Faculty in Chemistry in satisfaction of the dissertation requirement for the degree of Doctor of Philosophy.

8/20/92

Date

Chairman of Examining Committee

8/20/92

Date

Executive Officer

Supervisory Committee

The City University of New York

Abstract

Photolithography of Integrated Optic Devices in Porous Glasses

Edgar A. Mendoza

Advisor : Professor Harry D. Gafney

Collaborative studies in our laboratories, and those of Corning Inc., have established that highly resolved patterns of refractive index gradients ranging from 0.01 to 0.001 can be produced by photolysis of organotin compounds physisorbed onto Corning's code 7930 porous Vycor glass (PVG) followed by thermal consolidation of the glass at 1200 °C. Photolysis binds the metal compound to the glass and thermal activation removes the unreacted adsorbate and converts the photoproduct to a transparent metal oxide. Deposition of the metal oxide changes the density of the glass and in turn, its refractive index. Although applications of gradient refractive index patterns within glass matrices in the field of integrated optics have been recognized for many years, full utilization of this technology requires a fundamental understanding of the chemistry involved during the photochemical and thermal reactions leading to metal oxide formation on the surface of PVG.

The research decribe in this thesis focuses on the study of the photochemistry of organotin compounds of the general formula R(4-n)SnXn where R = alkyl and aryl and X = halides and pseudohalides. Photochemical studies in solution are compared to those on PVG. The experiments take advantage of the transparency of PVG to characterize the

photochemical reactions of the adsorbed compounds using conventional spectroscopic techniques.

The goal of these studies is to develop a methodology capable of fabricating a wide range of integrated optical devices in a glass matrix. Examples of different optical components that have been produced by these photodeposition techniques are presented.

Acknowledgements

I would like to express my sincere appreciation to my thesis advisor. Professor Harry D. Gafney, for his supervision and guidance that produced the ideas to generate this thesis.

Thanks to Professor Arthur D. Baker and Professor Thomas C. Strekas whose discussions during the research group meetings helped to clarify ideas and organize thoughts.

Thanks to Steve Tysoe and Eugene Wolkow for their help in getting valuable data for this thesis. To Ottmar Safferling for his help in making the glassware used in most of the experiments, and to all my friends in the graduate program whose support and consultations made this years as happy as they were.

Most of all I give thanks to all my family for their love and help along these educational years. My dear wife Anna Patricia and my lovely son Maximilliano that had to endure the long years for this to happen. And my mother, father, and dear sisters that are always there when I need them.

Contents

Part I. Introduction.

Part II. Experimental Section.

Part III. Results.

Part IV. Discussion.

Figures.

Part I. Introduction.

Part II. Experimental Section.

Part III. Results.

Tables.

Part I. Introduction.

Part II. Experimental Section.

Part III. Results.

1. Introduction.

Application of gradient refractive index patterns within glass matrices in the field of integrated optics has been recognized for several years. [1] The shift of the fiber optic market from long-distance communications to short distance applications requires high performance, cost-effective passive optical components. Short-distance networks create a need for passive branching devices such as splitters or combiners, taps, star couplers and wavelength selective devices. Because of the components-intensive nature of applications such as data communications, sensors, instrumentation and distribution networks, cost effectiveness is an essential consideration.

The optical fiber remains an important element in a short distance communications link. However, the relative cost-and-performance of other passive and active components in the system becomes significant larger. As a result, the development of these devices is receiving a great deal of attention. Nevertheless, despite significant cost reductions and technological advancements in recent years, challenges remain in developing high performance, cost-effective devices.

An integration technology could achieve the required cost reductions for high performance passive optical components by eliminating the mass production limitations of piece-to-piece processes. Glass is an excellent, inexpensive material in which to form a passive component. It is moldable

and stable under a wide range of environmental conditions, and its properties can be chosen for compatibility with other system elements, and selected for specific optical properties.

The ability to produce changes in the refractive index of the glass of the order of 0.01 to 0.001 allows a laser beam to be guided through glass. To perform the functions required for passive elements, however, demands the formation of highly resolved gradient index patterns. Photolithographic techniques are currently evolving [2,3] for low frequency integrated circuit applications. Channel waveguides on the order of 10 μm in width are already attainable and those in the 2 to 5 μm width range may be achievable. The success of photonic switching, however, depends on the development of materials capable of both guiding light and processing the light signals without converting them to electronic forms. Porous glass impregnated with photosensitive organometallic compounds exhibits optical changes when exposed to light. Optical changes in both transmission and refractive index can be induced and are permanent after consolidation of the glass to a nonporous matrix.[4] Using combinations of elements similar to those described in the following sections offers a means of producing complicated optical circuits composed of both active and passive components.

The photochemical deposition of a metal oxide to achieve a gradient refractive index depends on several factors. First, the substrate must be photochemically active, specifically in the visible or near-UV regions. Since calcined PVG absorbs 50 % of the light at approximately 295 nm, visible or near-UV photosensitivity allows photolysis of the adsorbate through the bulk rather than that on the outer surface. It is important to note at this point, that optical conduction, unlike electrical conduction, occurs within

the bulk of the medium. Consequently, deposition within the bulk is essential. Of course, it is also desirable that the quantum yield of the reaction be high, 1.0 if possible, to have a reasonably efficient process. Second, the photochemical reaction must irreversibly bind the adsorbate to the PVG matrix. This is essential not only to the resolution of the resultant pattern, but also to prevent desorption during subsequent thermal consolidation. Third, the substrate must exhibit thermal stability, yet also retain volatility. Volatility is essential, since a key to obtaining a significant gradient is the ability to remove the unreacted material. If the unphotolyzed compound decomposes on the glass during the subsequent thermal consolidation to a nonporous glass, the gradient index generated photochemically will disappear.

Clearly, utilizing this chemistry to produce useful refractive index gradients requires a basic understanding of the primary photochemical events of the adsorbate, and the secondary photochemical and/or thermal reactions leading to metal oxide formation. Organometallic complexes satisfy these criteria, but transition metal organometallics generally formed colored oxides. Consequently, the experiments focused on organotin compounds of the general formula $R_{(4-n)}SnX_n$ (where R = methyl groups; X = halides). Organotin compounds produce transparent oxides in glass, in contrast to the well characterized transition metal compounds which form colored oxides. The compounds are sufficiently volatile to be introduced into the glass either by vapor deposition or by adsorption from solution. Exposure to light causes a change in color in the exposed region. However, the optical changes are of little use unless the sample could be subsequently " fixed ", i.e., have the optical change made permanent and insensitive to further light exposure. Fixing is accomplished by ultrahigh vacuum

vacuum removal of the unexposed material and subsequent gentle heating after exposure. In this case, heating converts the photoproduct to an oxide, and at 1200°C consolidates the glass, i.e., collapses the porous structure. Although the consolidation process produces a 30 % volume shrinkage, it occurs with no adverse effect on the photo-induced optical patterns. In each case, the induced optical changes are maintained.

Unfortunately, there is little precedent in the literature upon which to base these experiments. In contrast to the extensive literature regarding the photochemistry of transition metal organometallics, [5] few studies of the photochemistry of organotin compounds have been reported. The vast majority of these reports deals with the synthetic uses of this compounds in organic chemistry reactions. [6] The goal of this research is two fold: first, characterize the photochemistry of these organotin compounds on the glass; and second examine the use of the chemistry as a route to passive integrated optic devices in a glass matrix. The approach is to determine the mechanism and quantum efficiency of the primary and secondary photochemical events of organotin compounds adsorbed onto porous Vycor glass, characterize the distribution of the adsorbed reagent of the glass surface, and lastly, characterize the optimal parameters of the refractive index gradients produced by photolysis of these complexes in order to demonstrate the ability to generate passive integrated optic devices in porous Vycor glass.

2 . Integrated Optics.

2.1 Introduction.

The origin and evolution of the optoelectronics and integrated optics is associated with an effort to exploit optical radiation for the transfer, processing and storage of information. Optical radiation with frequency 10^{14}-10^{15} Hz. exceeds by many order of magnitude the usual radio frequencies. The transition from radio frequencies to microwaves and ultimately to the optical part of the electromagnetic spectrum by means of optoelectronics and integrated optics represents a very significant rise of the information density in space and time. Coherent optical sources, such as lasers, also enable transfer, processing and storage of information. Another positive aspect is an enormous compression of energy in space and time. From the point of view of the material scientist, the mutual interaction of the electromagnetic radiation with condense matter characterizes the optoelectronics and integrated optics. Scientist are interested in the effects of the absorption of radiation, generation of optical radiation by spontaneous and stimulated emission, and in propagation of optical radiation through different media. Of a great importance for basic research in applied optoelectronics is the interaction of light and matter

under an applied electric or magnetic fields. The study of all the aforementioned interactions reveals new basic information on the energy structure of solids, liquids and gases, and on the other hand, enables the construction of devices such as light modulators, nonthermal light sources, light waveguides, and other elements of optoelectronics.

The rapid growth of optoelectronics and integrated optics can be dated from the realization of the first lasers in the 1960's - the ruby laser [7] and several months later the He-Ne laser [8]. This was followed by many other types of lasers such as the coherent semiconductor laser [9] , the mode-locking Nd:YAG and ruby lasers which enable the generation of picosecond pulses. [10] In the same year, broad band tunable lasers were also built. [11] At present, the use and applications of lasers has grown tremendously because of their unique properties, such as, chromaticity, coherency, high intensity, and small divergence. Laser have found applications in alignment, metrology, inspection, welding, drilling and cutting, as well as in the areas of printing, information storage and retrieval. Interest is also high in the areas of monitoring equipment, medicine, laser induce chemical reactions, isotope separations and in nuclear fusion. The market of non-coherent light sources and displays is even more explosive, the most promising being LED's, liquid crystals, and plasma displays.

Compared to the tremendous development and use of light sources during the past two decades, the development of radiation detectors, sensors, optolelectronic devices has been rather slow. To date, the most important optoelectronic systems that have been developed are optical memories. Although optical storage technology has received considerable attention during the last decade, it has been overshadowed by the

continuous growth of magnetic storage media. Nevertheless, optical data storage presents many advantages, such as the high storage density and faster access time that are not attainable by conventional magnetic recording devices. Progress made in high performance semiconductors, lasers and integrated optics have made the optical erasable memory devices a reality. Yet, as noted in the recent review article by Di Chen, [12] the search for new materials for bit by bit and holographic recording continues. New materials are emerging; one of the most promising being a composite magnetooptic-photoconductive sandwich (MOPS). [13]

Optical waveguides, and waveguide devices and systems play an important role in these systems for both information transmission and processing. In principle, there are two different ways of processing optical signals. One is where coherent light is manipulated by classical optical means, such as, the laser beam passes through the discrete optical components secured to the common bench. Such systems, however, lack applicability since they depend on large bench layouts and are sensitive to fluctuations of the environment. Another approach to the manipulation of coherent light is based on the principles of microwave guidance. With microwaves, the electromagnetic waves are guided and manipulated in metallic waveguides with cross-sections comparable to the wavelength. Electromagnetic energy propagates in waveguides in the form of discrete modes with different phase and group velocities. In a similar manner waveguiding is possible at optical radiation frequencies.

Analogous to metallic waveguides as the basic component of microwave systems, the dielectric waveguide is the basic component of optical waveguides. The idea dates back to the beginning of the 20th century, and dielectric waveguides are described in microwave textbooks. [14] In 1969,

S. E. Miller [15] proposed the idea of the integration of optical systems into miniature optical guides and called it " integrated optics ". Miller discussed the dream of a new future of integrated circuits which would use photons instead of electrons. Since that time, research in this field has been growing, and a number of active and passive devices have evolved. Review articles [16] , as well as several books on optical waveguides [17] and integrated optics [18] summarize the exciting developments that are occurring in this field.

Integrated systems that guide light have many advantages in comparison with the classical ones. Integrated optical systems, composed of elements in a common substrate are compact and as a result not as sensitive to vibrations and changes in the environment. Nevertheless, usable integrated optical systems await the solution to a variety of problems. The original proposals for integrated optics components made by Miller in 1969 do not differ very much from today's designs. The question of why these components are still under development and not commercially available in large quantities is quite easy to answer: the technological processes required to produced integrated optical components are not yet economically feasible.

2.2 Waveguide Fundamentals.

As in optical fibers, light guiding in integrated optics is based on the phenomenon of total internal reflection. In an integrated device, this is accomplished by creating regions of higher refractive index than that of the

bulk medium. In its simplest form, the ratio of the index of refraction within these regions relative to that of the bulk defines the sine of the critical angle, i.e.,

$$\text{Sin}\,\theta_c = \frac{n_1}{n_2} \qquad 2.1$$

where n_1 and n_2 are the indices of refraction of the bulk medium and the guide, respectively. As a result, light that enters the region of higher refractive index within the critical angle is guided through the bulk medium. While any number of approaches might be taken to change the refractive index, it must be realized that the technique and/or materials used must have low losses at the working wavelength, and must offer a means of creating systems of high resolution.

2.2.1 Theoretical Fundamentals : The slab waveguide.

The theoretical approach to the description of integrated optics waveguide uses geometrical ray optics for multimode guides, and wave theory for single mode waveguides. Although the description of integrated optical waveguides is similar to that of optical fibers, complications arise because of the absence of circular geometry, and various theoretical methods have been developed, [19] to handle these complications.

As an aid to understanding the properties of planar waveguides, a brief description on the theory of a simple planar or slab waveguide follows. The description is divided into three parts: a description of the waveguide itself, a description of light, and a discussion of the transmission of light

through the waveguide.

The slab waveguide, shown in Figure 2.1, consist of a substrate coated with a thin waveguiding layer of thickness d. The index of refraction of the guiding layer, n_1, is greater than that of the substrate, n_2. It is assumed that the surrounding environment (superstrate) is air (n_3 = 1). The substrate and waveguide material are ideal (no loss) at the wavelength used, and it is assumed that the substrate-waveguide interface is a perfect plane.

Light as an electromagnetic wave is characterized by a combination of time varying electric $(\overrightarrow{E})$ and magnetic $(\overrightarrow{H})$ fields propagating through space. Maxwell showed that both these fields satisfy the same partial differential equation :

$$\nabla^2(\overrightarrow{E}, \overrightarrow{H}) = \frac{1}{c^2}\frac{\delta^2}{\delta t^2}(\overrightarrow{E}, \overrightarrow{H}) \qquad 2.2$$

where :

$$\nabla^2 = \left[\frac{\delta^2}{\delta x^2} + \frac{\delta^2}{\delta y^2} + \frac{\delta^2}{\delta z^2}\right]$$

This is called the time dependent *wave equation*, and is encountered in many different kinds of physical phenomena such as mechanical vibrations of a string or in a rod. The implication of equation 2.2 is that changes in the fields propagate through space with a speed c , the speed of light. The frequency of oscillation of the fields n, and their wavelength in vacuum, l_0 are related by :

Figure 2.1 - Schematic diagram for a slab waveguide.

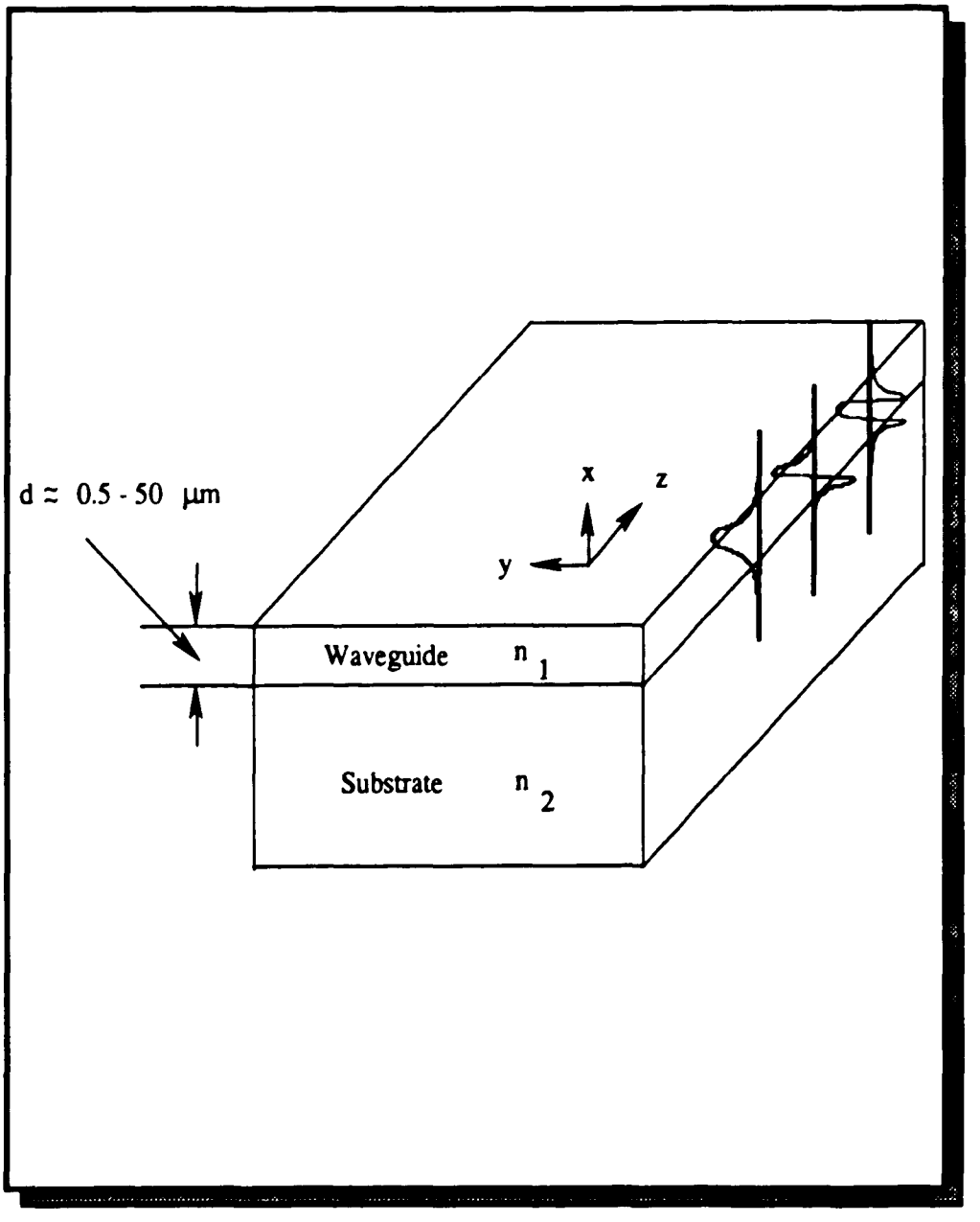

$$c = \nu \lambda_0 \qquad 2.3$$

and in any other medium the speed of propagation is given by

$$v = \frac{c}{n} = \nu\lambda \qquad 2.4$$

where n is the refractive index of the medium and λ is the wavelength in the medium.

The electric and magnetic fields vibrate perpendicular to one another and perpendicular to the direction of propagation, i.e., light waves are transverse waves. In describing optical phenomena, the magnetic field vector is often omitted. This simplifies mathematical descriptions, but it should always be remembered that there is also a magnetic field component which behaves in a similar way as the electric field component. The equation for a propagating wave along the z-axis is expressed mathematically as:

$$E_j(x, y, z) = e_j(x, y) \exp(i\beta_j z) \quad j = 0,1,2... \qquad 2.5$$

where β_j is called the propagation constant, or eigen value of the jth mode. Generally, each mode has a unique value of β_j.

The simplest example of a waveguide is the symmetric waveguide, Figure 2.1. For simplification, assume the light wave in the film to be infinitely wide in the y direction so that $d^2 / dy^2 = 0$. In this case, the electric and magnetic fields depend on x and z only, and :

$$\mathbf{E}_j(x, z) = \mathbf{e}_j(x) \exp(i\beta_j z)$$

$$\mathbf{H}_j(x, z) = \mathbf{h}_j(x) \exp(i\beta_j z) \qquad 2.6$$

If the waveguide has planar symmetry, i.e., it is uniform in both the *y*- and *z*- directions of Figure 2.1, and the principal axes of the material constituting the waveguide are parallel to the cartesian axes, then the structure supports TE (transverse electric) or TM (transverse magnetic) modes. On planar waveguides, TE and TM modes correspond to the two possible polarization states of the electromagnetic field. Thus, the origin of the difference between TE and TM modes in a planar waveguide is the polarization-dependent nature of plane wave reflection. The argument is easily generalized to include graded-index media using the notion of local plane waves. In this case, let z be the direction of the wave propagation parallel to the film. Using Maxwell's equations to solve for E_y for TE waves, or H_y for TM waves, the main equation for this special problem, after some mathematical manipulations, becomes [20]

$$\frac{\delta^2 E_y}{\delta x^2} + \left(n_i^2 k_0^2 - \beta^2\right) E_y = 0 \qquad 2.7$$

where E_y is the electric field in the *y* direction and n_i is the refractive index of the *i* th component of the medium *i* . The quantity *i* has integer values, *i* = 1, 2, 3,.., while k_0 is the propagation constant is given by $k_0 = 2\pi / \lambda_0$, where λ_0 is the wavelength in a vacuum. β is the propagation constant

of the wave in the guide. All the other components can be derived from E_y. The three different solutions for the three media, i.e., substrate, waveguide, and supersubstrate, can be calculated. By postulating continuity at the interfaces, the eigenvalue value equation for the planar slab waveguide is :

$$\frac{2\pi d\gamma}{\lambda_0} - \arctan\left(\frac{q_2\sigma}{\gamma}\right) - \arctan\left(\frac{q_3\alpha}{\gamma}\right) = m\pi \qquad 2.8$$

where :

$$\gamma = \left[n_1^2 - \left(\frac{\beta}{k_0}\right)^2 \right]^{1/2} \qquad 2.9$$

$$\sigma = \left[\left(\frac{\beta}{k_0}\right)^2 - n_2^2\right]^{1/2} \qquad 2.10$$

$$\alpha = \left[\left(\frac{\beta}{k_0}\right)^2 - n_3^2\right]^{1/2} \qquad 2.11$$

$$q_i = 1 \text{ for TE modes}$$
$$q_i = (n_1/n_i)^2 \text{ for TM modes; } i = 2 \text{ and } 3 \qquad 2.12$$

Obviously there are two different types of waves (or modes) that can propagate in the slab waveguide; transverse electric (TE) mode and the transverse magnetic (TM) mode. The TE modes are polarized parallel to the waveguide surface, while the TM modes are polarized perpendicular to

the waveguide surface, (Figure 2.2). Polarizations refer to the electric field vector, which is perpendicular to the propagation direction.

Although, the treatment is for the simplest form of a waveguide, the planar waveguide, equation 2.8 is a transcendental equation which cannot be solved analytically. However, some important information can be obtained from it, which is useful in the field of integrated optics sensors. The solution of equation 2.6 can only be real if equations 2.9, 2.10, and 2.11 are real, in which case

$$n_1 \geq \beta/k_0 \geq n_2, n_3 \qquad 2.13$$

Assuming TE modes, the minimum waveguide thickness d_{min} for the mth-order mode can be calculated as follows :

$$d_{min} = \frac{m\pi + \arctan\left[q_3 \left\{ \left(n_2^2 - n_3^2\right) / \left(n_1^2 - n_2^2\right)^{1/2} \right\} \right]}{k_0 \left(n_1^2 - n_2^2\right)^{1/2}} \qquad 2.14$$

where the parameter q_3 is define by equation 2.12, and $k_0 = 2\pi/\lambda$.

If the thickness d becomes smaller than d_{min} , then the light can no longer propagate. A very special case is when m = 0 (the fundamental mode) and $n_2 = n_3$ (the waveguide is covered with a material of the same refractive index as the substrate). Then d_{min} becomes zero and theoretically, the fundamental mode can propagate even if the waveguide

Figure 2.2 - Electromagnetic wave: TE (transverse electric), and TM (transverse magnetic) modes as they traveled through the slab waveguide in Figure 2.1.

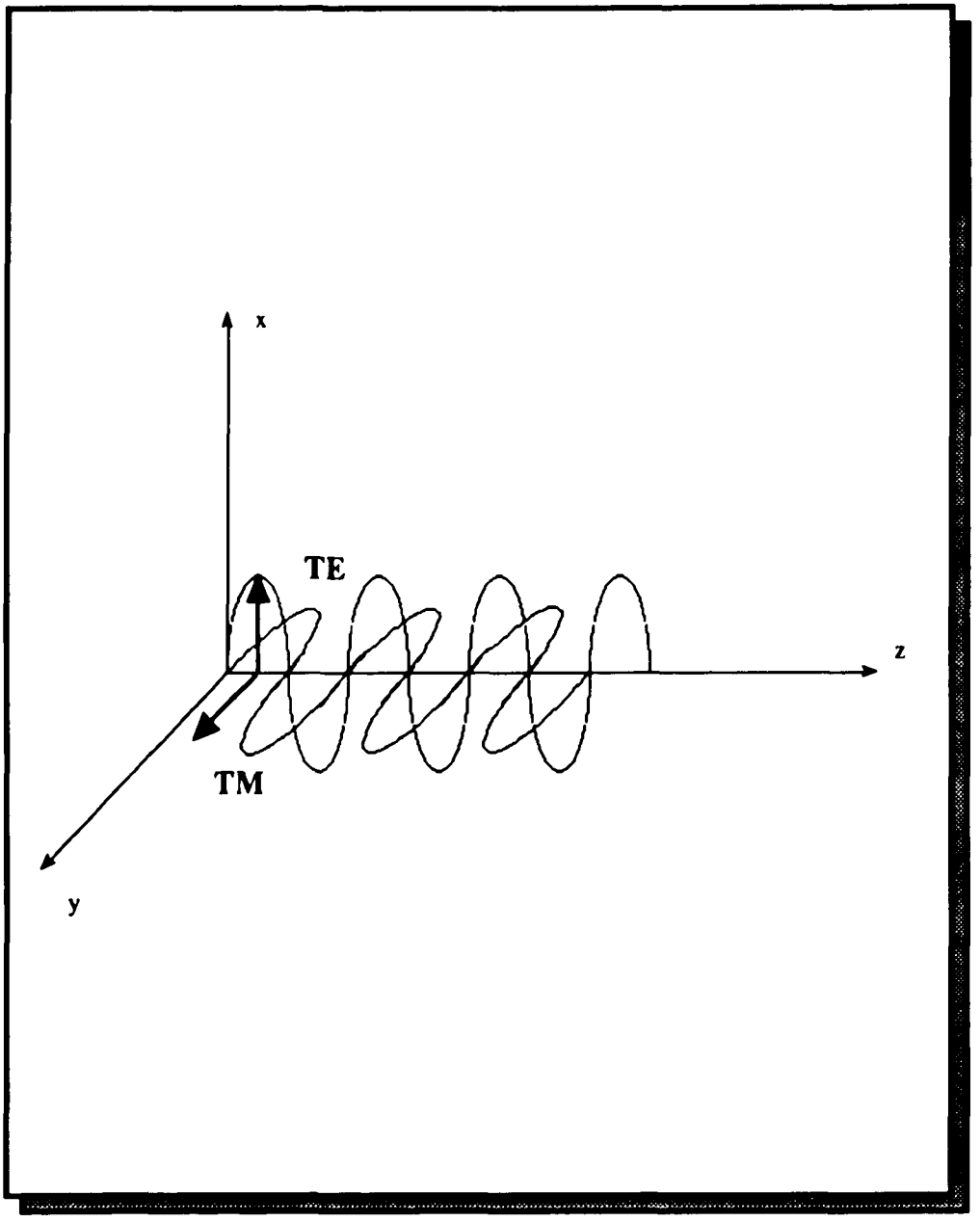

becomes infinitely thin. This behavior corresponds to an optical fiber in which the core is surrounded by one material only.

The eigenvalue equation 2.8 can be solved either numerically or geometrically. If the propagation constant β for all propagation modes is known, then the electromagnetic fields or, the intensity distribution for each mode can be evaluated. An example is shown in Figure 2.3 (note the coordinate system!). From this, the following important results are obtained :

a) The mode order, *m* , is equivalent to the number of intensity minima.

b) The light intensity is not restricted to the waveguide region only, but penetrates into the surroundings.

c) The smaller the difference between the refractive indices of the waveguide and the surroundings is, the further the light intensity penetrates into the surroundings.

d) The higher the mode order is, the higher the intensity of the light out side of the guide.

Assuming $n_2 > n_1$, the structural constant (V) for a slab waveguide is given by :

$$V = \frac{d\pi}{\lambda_0}\left(n_1^2 - n_2^2\right)^{1/2} \qquad 2.15$$

which can be used for a rough estimate of the total number of propagating modes (M) for a slab waveguide.

$$M = \frac{4V}{\pi} \qquad 2.16$$

2.3. Structures.

A number of different waveguiding structures have been proposed and realized. In addition to slab waveguides, which have been treated above, channel or strip waveguides are important. Unfortunately, the nomenclature is still inconsistent. Slab waveguides are sometimes called two dimensional waveguides since light is guided in two dimensions,such as transverse and longitudinal. Channel waveguides are known as three dimensional waveguides since guiding takes place in all three dimensions. Various guiding structures (Figure 2.4) have been investigated for channel waveguides. The simplest (Figure 2.4a) is a high index strip, which is generally a rectangular deposit on a low index substrate. The number of guided modes depends on the dimensions of the deposit, the refractive indices of the deposit and substrate, and the wavelength of light. Because the guide is not circularly symmetric, there is a distinction between transverse and lateral modes. The larger the dimensions of the guide and the larger the difference between the refractive indices of the guiding and surrounding materials, the larger the number of modes guided. An obvious disadvantage occurs when the whole waveguide is surrounded by air and the index difference is large.

To obtain a single mode waveguide, the dimensions of the waveguide have to be reduced to very small values, usually in the range of micrometers. However, this usually results in severe technological constrictions since the waveguide is surrounded by air.

Figure 2.3 - Intensity distribution of the TE mode of (a) zero, (b) first, and (c) second order for a slab waveguide. n_1= 1.515 (waveguide), n_2= 1.465 (substrate), n_3= 1 (superstrate).

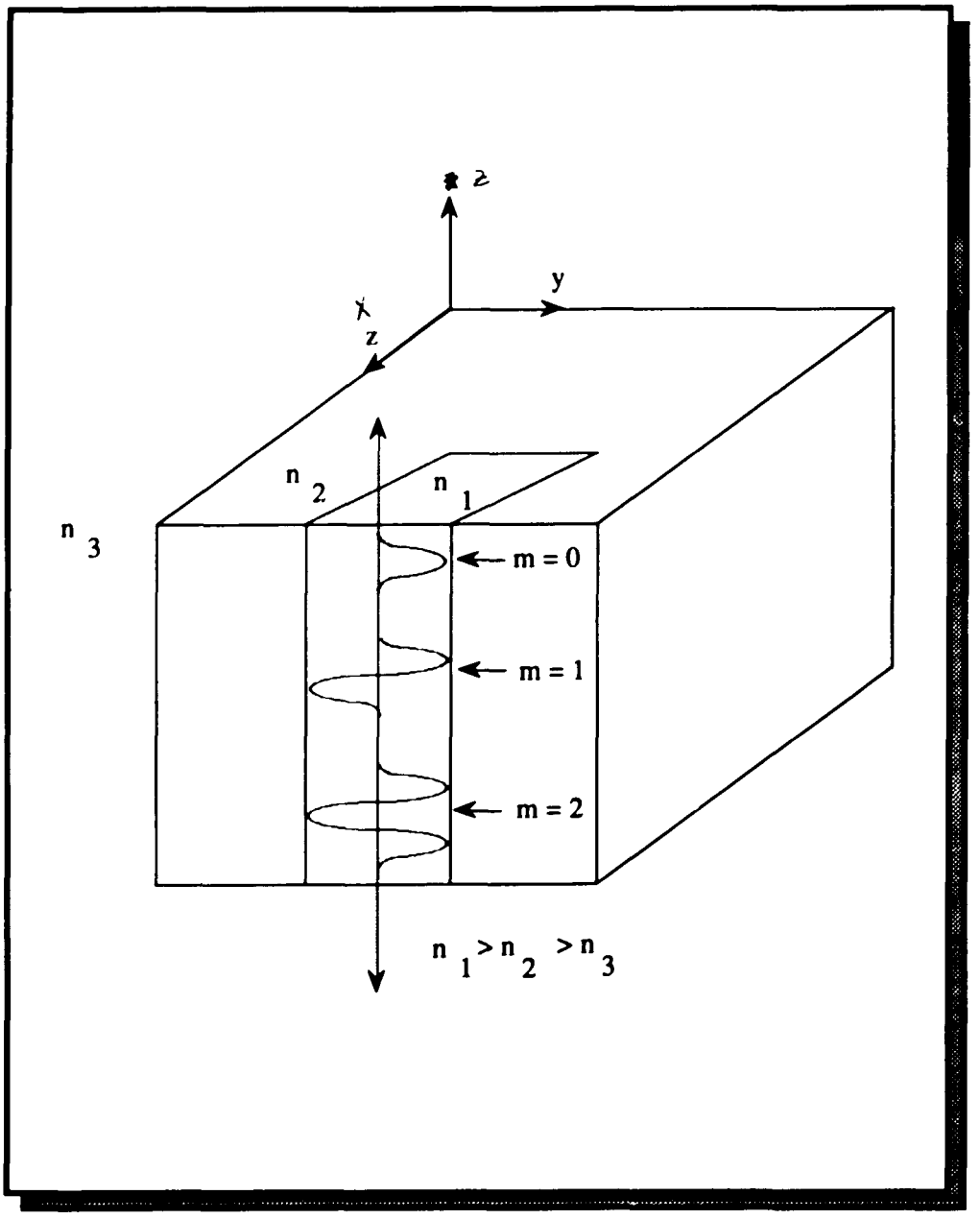

Figure 2.4 - Channel waveguides structures : (a) strip waveguide; (b) embedded waveguide; (c) buried waveguide; (d) ridge waveguide; (e) strip-loaded waveguide.

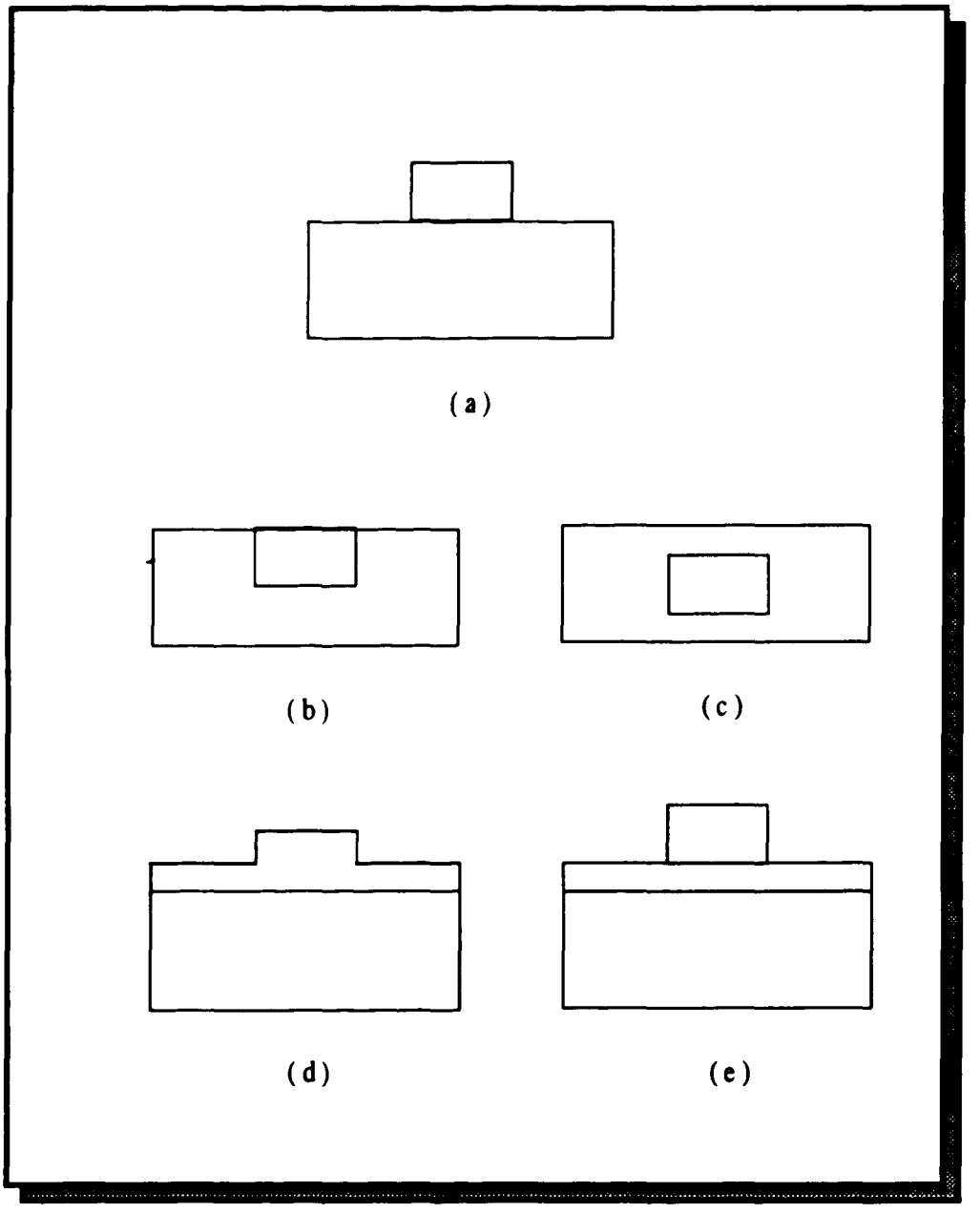

To avoid this problem, the guide can be embedded in the substrate (Figure 2.4b) so that only one face is adjacent to the surrounding air, but this approach suffers from the problem of losses in the intensity of the guided wave since the amount of scattered light depends on the surface roughness as well as the index difference. This problem can be avoid by burying the waveguide well below the substrate surface (Figure 2.4c). In this case, all waveguide-substrate interfaces have the same refractive index difference, which is usually small. The preparation of a low loss waveguide is much easier, but special techniques are required to prepare such buried waveguides.

Two other waveguide structures are important, particularly for integrated optics using semiconductor materials composed of groups III and V elements, Figure 2.4d shows one type called a ridge waveguide. A slab waveguide is deposited on the substrate, and then its thickness, d, outside the guide is reduced usually by chemical etching to below that needed for the fundamental mode intensity (m=0 in Figure 2.3). As a result, the light is confined to the thicker part of the slab waveguide. The second type is the strip-loaded channel waveguide (Figure 2.4e). In this case, a strip of high index material is placed over a slab structure, which is too thin to guide any mode, i.e., $d < d_{min}$,, so that together they formed a channel waveguide.

2.3.1 Principal Structures :

Table 2.1 classifies the different types of waveguides while Figure 2.5 illustrates some of the fundamental waveguide structures. The simplest element is a straight guide, Figure 2.5a, which connects one optical

Table 2.1 - Classification of integrated optics waveguides.

Passive	Waveguides with fix properties : beam splitters, curvatures, crossings etc.
Passive dynamic	Waveguides with variable components : modulators, switches, etc.
Active	Optically active waveguides : lasers, amplifiers, parametric oscillators etc.

elementto another. Its role is analogous to that of an electrical conductor, but unlike electrical conduction, curves are possible, but corners are not. The allowed radius of curvature depends very much on the refractive index difference and is usually large with respect to the wavelength of light. Figure 2.5b shows a branch or **Y** junction which is used to either split or to combine the light. A similar but more complicated structure is the 1:7 star coupler shown in Figure I.5c. Figure 2.5d is a typical directional coupler consisting of two adjacent parallel waveguides and four lead-down, lead-up waveguides. In this structure, light coupled to waveguide 1 will penetrate into the surroundings and will be collected by waveguide 2 in the parallel section of the two waveguides. Figure 2.5e is an integrated Mach-Zender interferometer consisting of two **Y** junctions. Here the two waves travel along the two arms of the interferometer and are combined at the second **Y** junction. Because the two waves arise from the same source, they are coherent and interfere if the lengths of the two arms differ by more or less than the coherence length of the light used.

2.3.2 Passive-dynamic structures :

Passive-dynamic structures respond to external influences. For example, the output of a Mach-Zender interferometer can be modulated by taking advantage of the electro-optic effect, acousto-optic, an thermo-optic effects. The efficiency of the effect depends on the material, and in the simplest structure (Figure 2.6) the guide is placed between two electrodes. If the waveguide material has a sufficiently high electro-optic coefficient, an external voltage will cause a phase change in the light wave. In the case of $LiNbO_3$, a few volts are sufficient. If such a phase shifter is introduce into

Figure 2.5 - Fundamental integrated optics waveguide structures: (a) Straight strip guide; (b) Y junctions; (c) 1-7 star coupler; (d) directional coupler; (e) Mach-Zehnder interferometer.

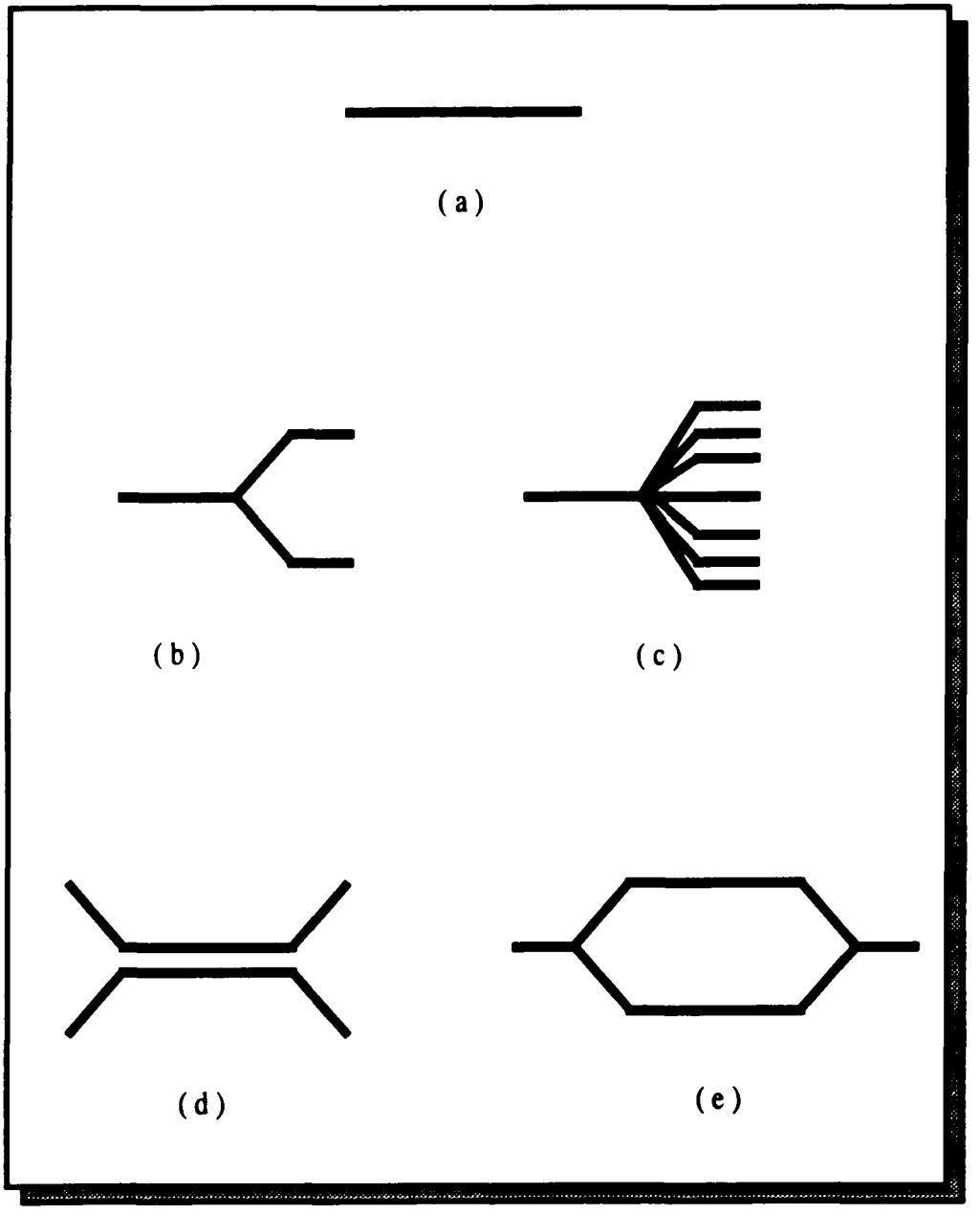

the two arms of a Mach-Zender interferometer, an on-off switch as well as an intensity modulator can be constructed. Figure 2.6 summarizes the passive dynamic waveguide configurations.

2.4 Materials.

Integrated optics creates a need for specific materials and techniques to modify these materials. For example, there is a need for a low loss material that allows specific modifications, such as structured areas with an increased refractive index. At present, three material systems are important to integrated optics technology : glass; dielectric crystals; and group III-V semiconductors. Table 2.2 summarizes these materials, the methods of modification and, the losses for a straight single-mode channel waveguide.

With glass, the most widely use modification technique is ion exchange, whereas Ti in-diffussion is the important for modifying $LiNbO_3$, a crystalline material with a high electro-optic constant. At present there is no preferred technology for InGaAsP, although it is likely that metal organic chemical vapor deposition (MOCVD) may be the most suitable because of its applicability for preparing large, relatively homogeneous substrates.

$LiNbO_3$ and InGaAsP can be used to build passive dynamic waveguides generally based on the electro-optic effect. For example, integrated optical elements in $LiNbO_3$ have been demonstrated in laboratories, and are now available commercially (Crystal Technology,

Figure 2.6 - Schematic diagram of a phase modulator as an example of a passive dynamic strip waveguide.

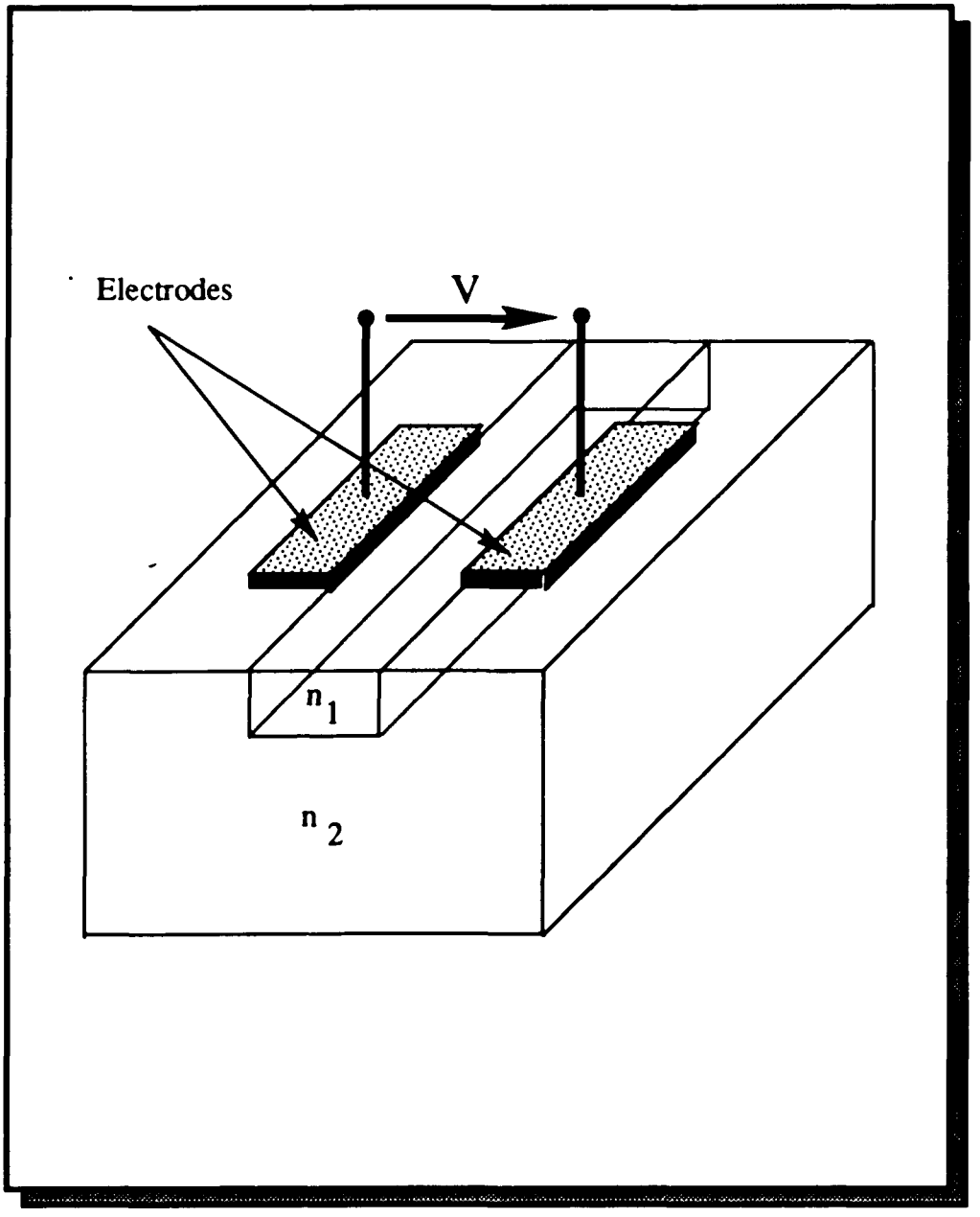

Figure 2.7 - Summary of the major passive dynamic waveguide configurations (a) Phase modulator; (b) directional coupler; (c) Mach-Zender interferometer.

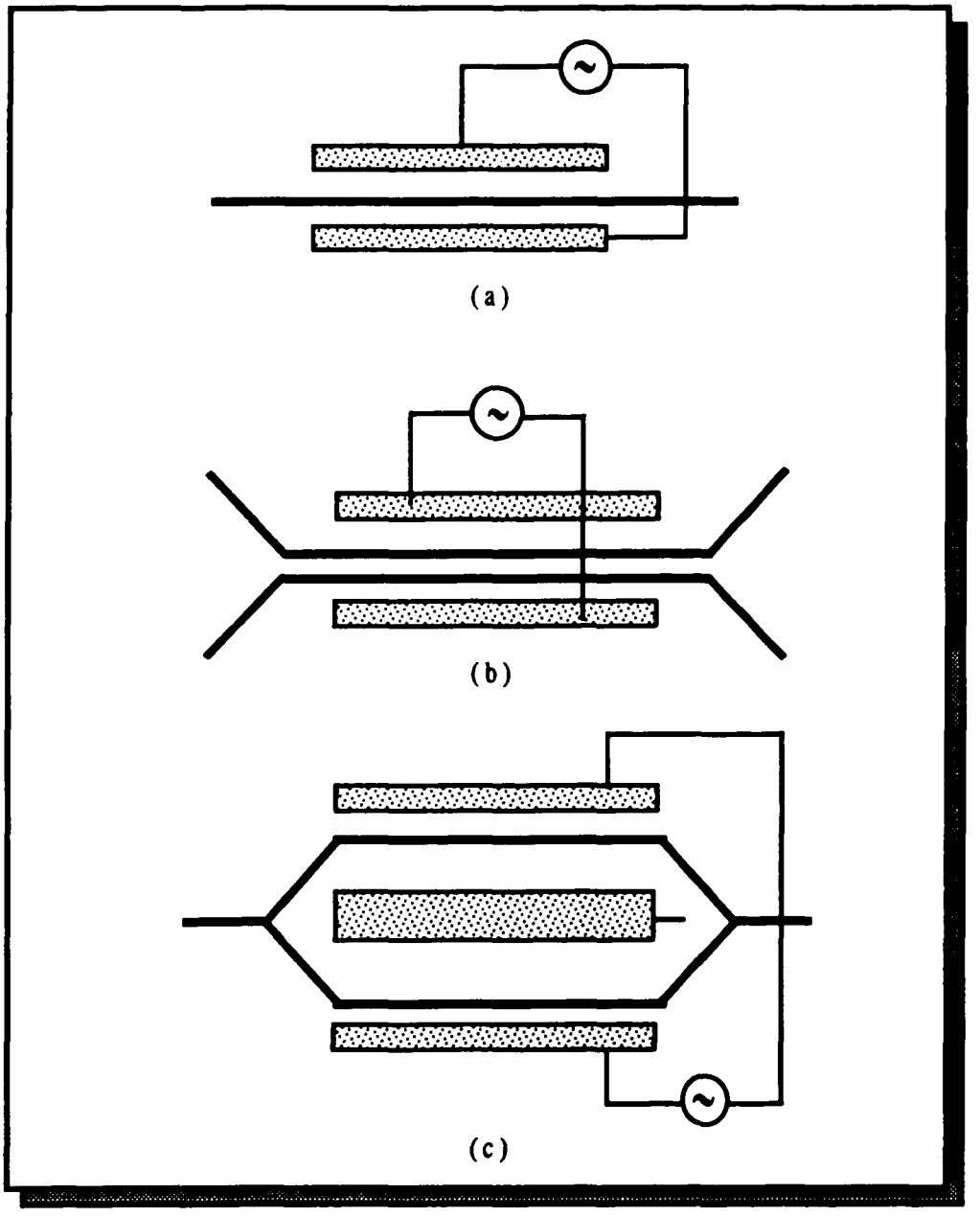

Table 2.2 - Materials for integrated optics

Material	Glass	Crystal ($LiNbO_3$)	Semiconductor (InGaAsP)
Technology	Ion Exchange Sputtering CVD	Ti in-diffussion Proton exchange	LPE MOCVD MBE
Loss (dB cm^{-1})	0.01	0.1	1.0

CVD, chemical vapor deposition; LPE, liquid phase epitaxy; MOCVD metallorganic chemical vapor deposition; MBE, molecular beam epitaxy.

USA; Barr and Stroud, UK). III-V semiconductor compounds can be used to fabricate active elements such as lasers or light amplifiers, but it is estimated that semiconductor integrated optics will not be commercially available to be used for another 5-10 years. Glass on the other hand, has been restricted to passive elements such as splitters and combiners. Nevertheless, the potential for both multimode and single mode technologies, new fiber optic connects for local networks, distributed sensors, and the possibility of dynamic elements based on the thermo-optic effect, has spurred an interest in glass integrated optics. A summary of the current technologies used to fabricate glass waveguides, such as the ion-exchange process and the silica on silicon (SOS) process, is presented in the next section.

2.5 Technology.

The problem is to increase the refractive index of a transparent substrate in the region of its surface. One has to intervene from the outside, through the surface. Two possible methods can be used : the ion exchange process, and the silica-on-silicon (SOS) technology.

2.5.1 The ion exchange process :

Figure 2.8 illustrates the two general approaches of the ion-exchange technique. The first approach (Figure 2.8a) is a straight forward ion-exchange process in which a glass containing ions M_1^+ is immersed in a

salt containing ions M_2^+. If the salt is heated above its melting point, ion exchange occurs in which the M_1^+ ions in the glass are exchanged with the ions M_2^+ in the melt. Thus, with appropriate ion combinations, the refractive index of the glass can be changed. For example, exchanging Na^+ ions in the glass with Ag^+ ions in the melt, will increase the refractive index of the glass. Alternatively, replacing a heavier ion within the glass matrix with a lighter ion decreases the refractive index of the glass. However, the ion exchange technique is usually very slow, and the fabrication of multimode waveguides usually takes weeks.

For this reason, the field-assisted ion exchange technique (Figure 2.8b) has been developed. The principle is the same, but the rate of exchange is accelerated by applying a voltage of about 50 V mm^{-1} between the front and back of the substrate. The front and back of the substrate are separated electrically, and the exchange of the cation is at the front only. Consequently, field ion exchange produces a larger index change at the surface, and a lower index change at the back of the substrate. The reduction of processing time achieved with field-assisted exchange is about an order of magnitude compared with thermal exchange, and it is the recommended technique for multimode waveguides.

2.5.2 Silica-on-silicon technology :

Silica on silicon (SOS) technology, developed by Kawachi and co-workers [21] , and Valette and co-workers [22] involves depositing a thin layer of pure silica on a silicon substrate using a flame hydrolysis technique (FHD). This layer acts as a buffer between the optical waveguide and the silicon (Figure 2.9), and is the substrate on which the waveguide is deposited. The

Figure 2.8 - Principle of ion exchange in glass: (a)Thermal; (b) Field assisted.

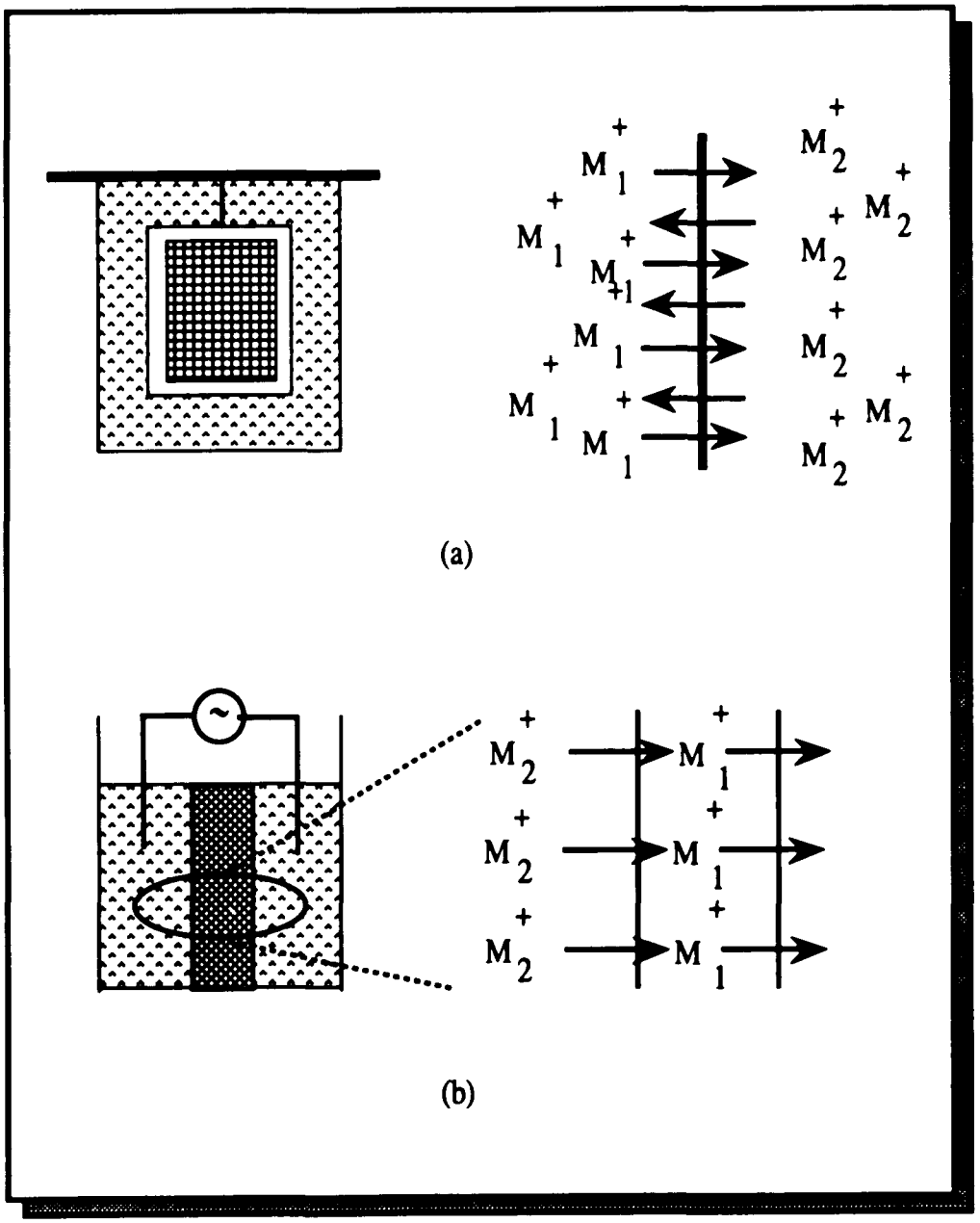

waveguide itself consist of titanium- doped SiO_2. Doping with titanium increases the refractive index of the guide relative to that of the substrate . Strip waveguides are formed by reactive ion etching and are then covered with pure FHD deposited SiO_2 as a superstrate. Both single and multimode waveguides have been obtained by this approach.

2.6 Integrated optical circuits :

To build integrated optical waveguides, it is not sufficient to simply create a region of high refractive index within a substrate of lower refractive index. Many different processing steps are necessary to fabricate complex integrated optical circuits. This is shown schematically in Figure 2.10. In addition to the fabrication of the waveguide, an etching process is required to interrupt the waveguides (groove with mirror), or to avoid an interaction between two adjacent waveguides (separating groove). Thin film technology is also necessary to provide antireflecting coatings, mirrors or buffer layers. Buffer layers are needed if the waveguide is not buried and metallic electrodes have to be deposited on top of the waveguides. These metallic electrodes can attenuate the guided light and therefore must be separated from the guide by a dielectric buffer layer with a low optical loss. Finally preparation of the edge of the waveguide is not a trivial problem because the edge between the front-end of the waveguide and the substrate surface has to be very sharp to prevent destruction of the waveguide end.

The fundamentals of integrated optics have been presented and considering the difficulties that have to be resolved to realize viable

integrated optics, a reasonable question to ask at this point is, what are the advantages of using integrated optics either in a circuit or as sensors? The main advantages are long term stability, miniaturization, the need for fewer adjustments, cost reduction and technical improvement. There is also the development of new optical structures such as the use of integrated optics in sensors.

2.6.1 Evanescent field sensor :

Evanescent field sensors play an important role in fiber optic sensors, and configurations using integrated optics have been proposed [23]. A typical arrangement makes use of the Mach-Zehnder interferometer shown in Figure 2.11a. One arm of the interferometer is protected from its surroundings while the other is exposed. Because the optical field is not totally restricted to the waveguide but some of the field is traveling as an evanescent wave at the guide-surface interface, any change in the surroundings medium will influence the guided mode. In this manner, chemicals can be identify through their interaction with the exposed arm. This method has been successfully used as a hydrogen sensor (Figure 2.11b) [24] . It consists of a single mode Y junction in which one arm acts as the reference and the second as the sensor. The sensor arm is coated with a thin layer of WO_3 (directly above the waveguide) on top of which is thin layer of palladium. The palladium layer acts as a discriminator through which only hydrogen can penetrate. The WO_3 and the hydrogen react and the colorless WO_3 is reduced to a colored $H_{2x}WO_3$ layer, which will absorb some of the light guided by the wave.

One of the main motivations for integrated optics comes from the

Figure 2.9 - Principle of the fabrication of a strip waveguide by SOS technology.

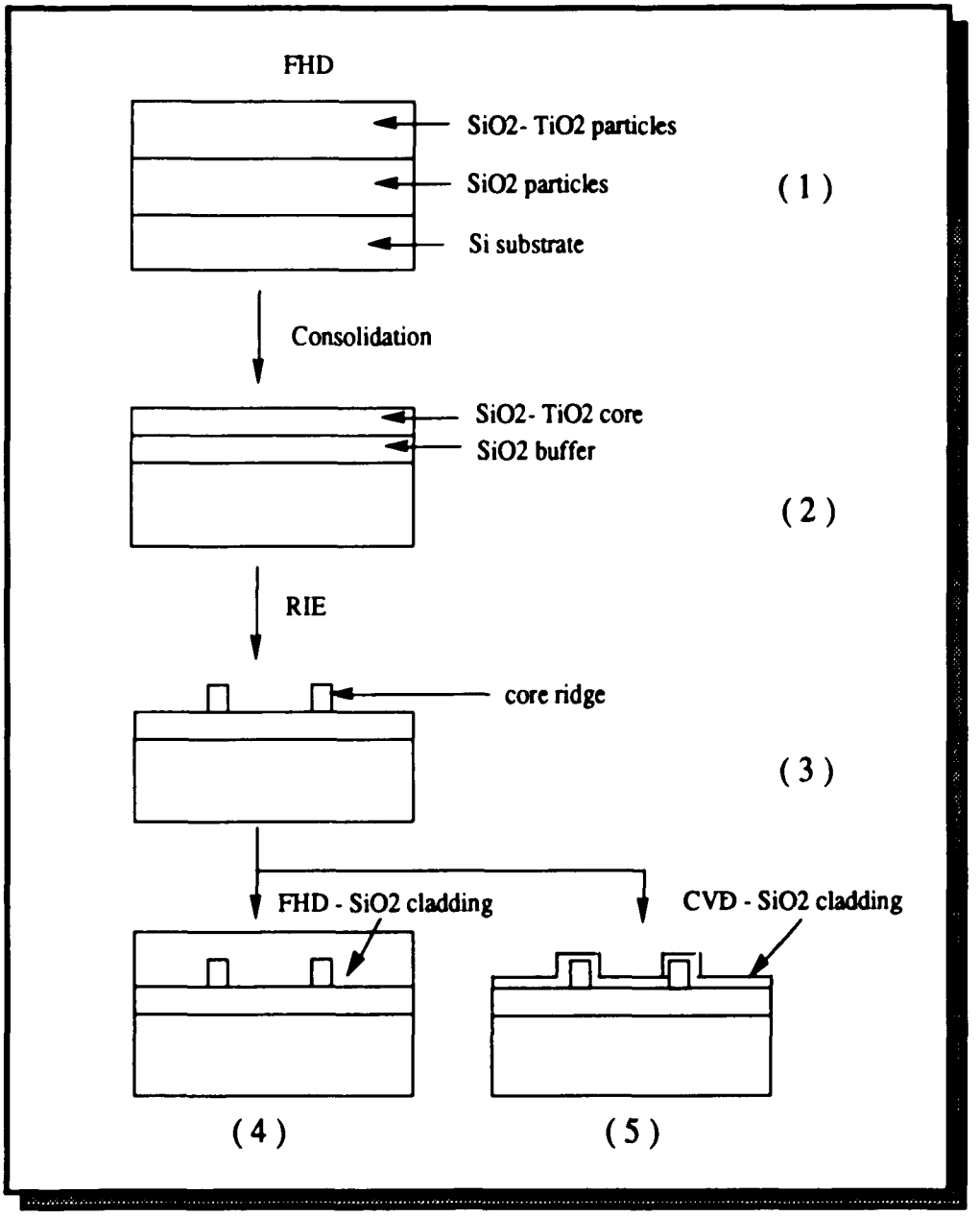

Figure 2.10 - Diagram of the various processing steps for the realization of integrated optics circuit.

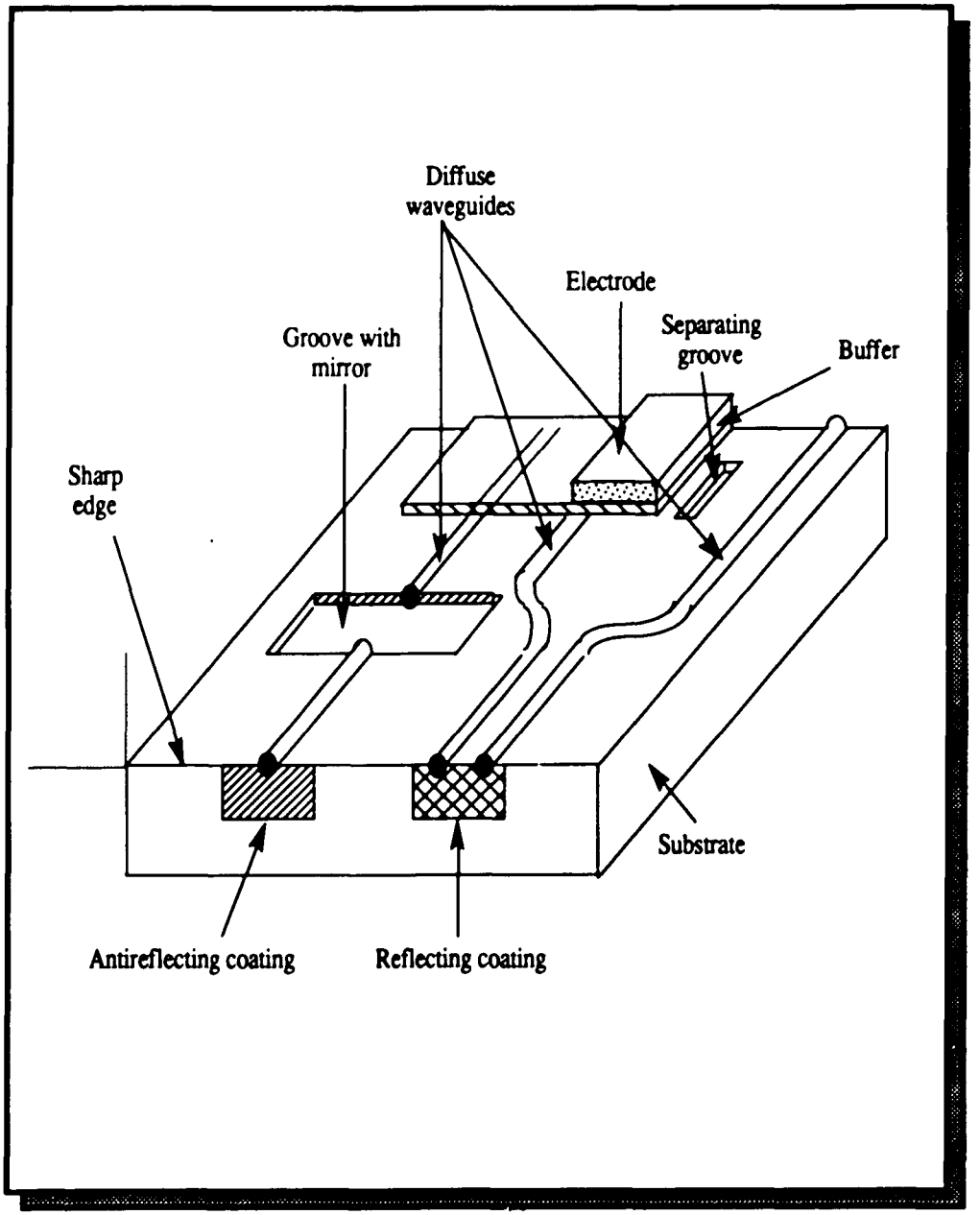

Figure 2.11 - Evanescent field sensors : (a) Chemical sensor; (b) Hydrogen sensor.

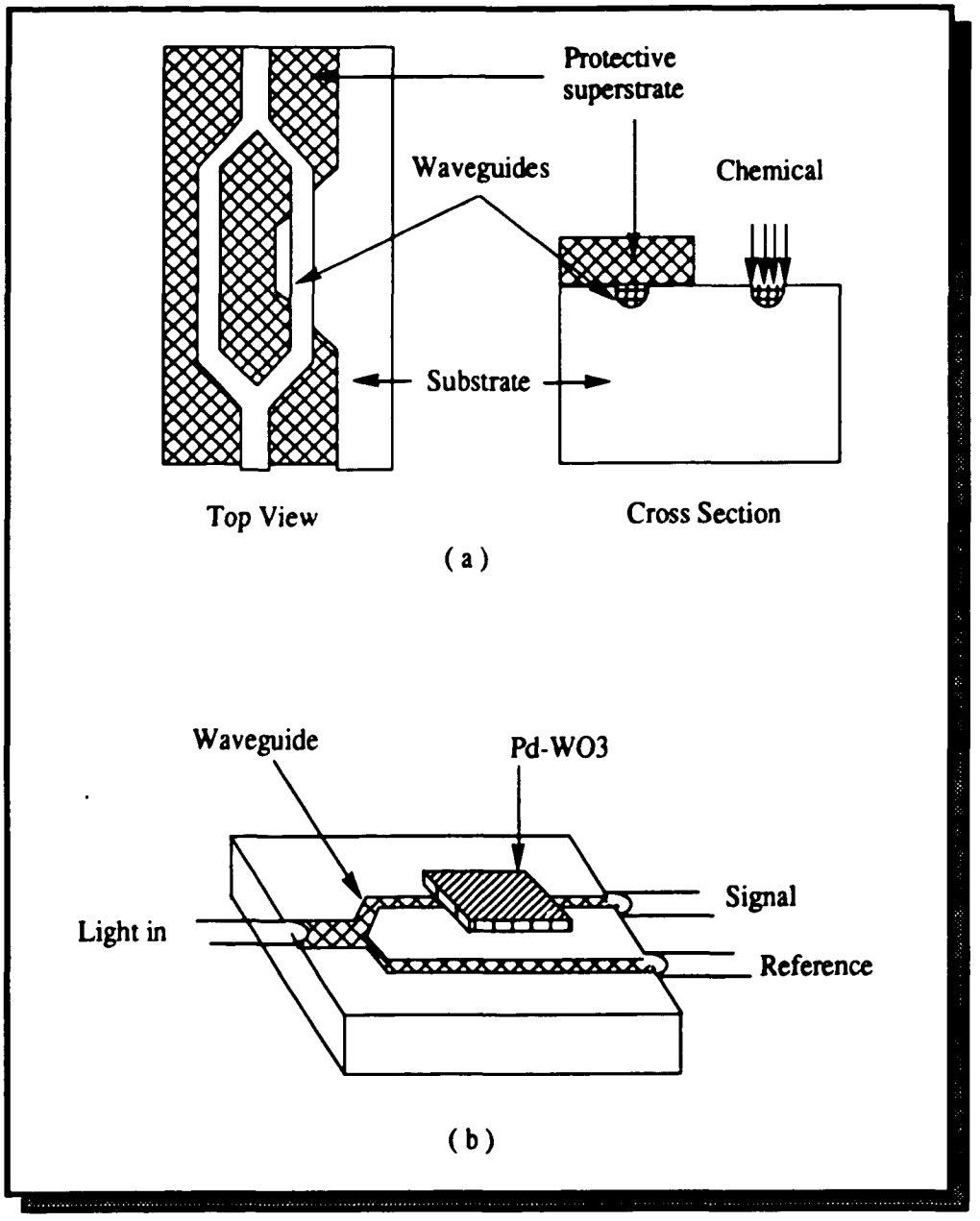

development of the optical gyroscope [25] (Figure 2.12). The upper diagram shows the main components of an optical gyroscope, while the lower one shows the integrated optics version. It must be emphasized that the integrated optics version is very small compared with the bulk optics version and that only the fibers have to be aligned to the integrated optics circuits, whereas in the bulk version each element has to be aligned, and the alignment maintained. Unfortunately, the integrated components have not yet achieved satisfactory performance. Two main problems involving the mode filter and the polarizer have yet to be resolved satisfactorily. Other applications have been suggested. For example, Kist and Sohler [26] have discussed the integrated optics Fabry-Perot resonator as a sensor. Valette and co-workers [15c] have proposed a planar design for a frequency multiplexing, and Nishihara and co-workers [27] have designed a laser doppler velocimetry LVD.

Although integrated optics have applications in the areas of optical sensors and fiber optic sensors and have been under development for some time, many fundamental problems remain to be solved. The most important of these are fiber coupling, the production of suitable masks, loss reduction, and appropriate packaging and housing.

Organotin compounds offer the means to generate changes in the index of refraction of the glass by photodeposition of tin oxide. Coupled with a photolithographic technique, high resolution optical waveguide patterns can be deposited on a glass substrate in a single step with the appropriate mask. Multiple step processes can be used to deposit different materials, at specific locations. Perhaps most important, the metal oxides are stable and can be deposited within the bulk of the glass which insures long term stability when the glass is consolidated. Glass is a perfect substrate for the

lithographic deposition of microscopic integrated optic devices, which are key components in the realization of optical computing.

Figure 2.12 - The fiber gyroscope. The upper diagram shows the bulk optics. In comparison only a small area is needed to realize the equivalent structure with integrated optics (lower diagram).

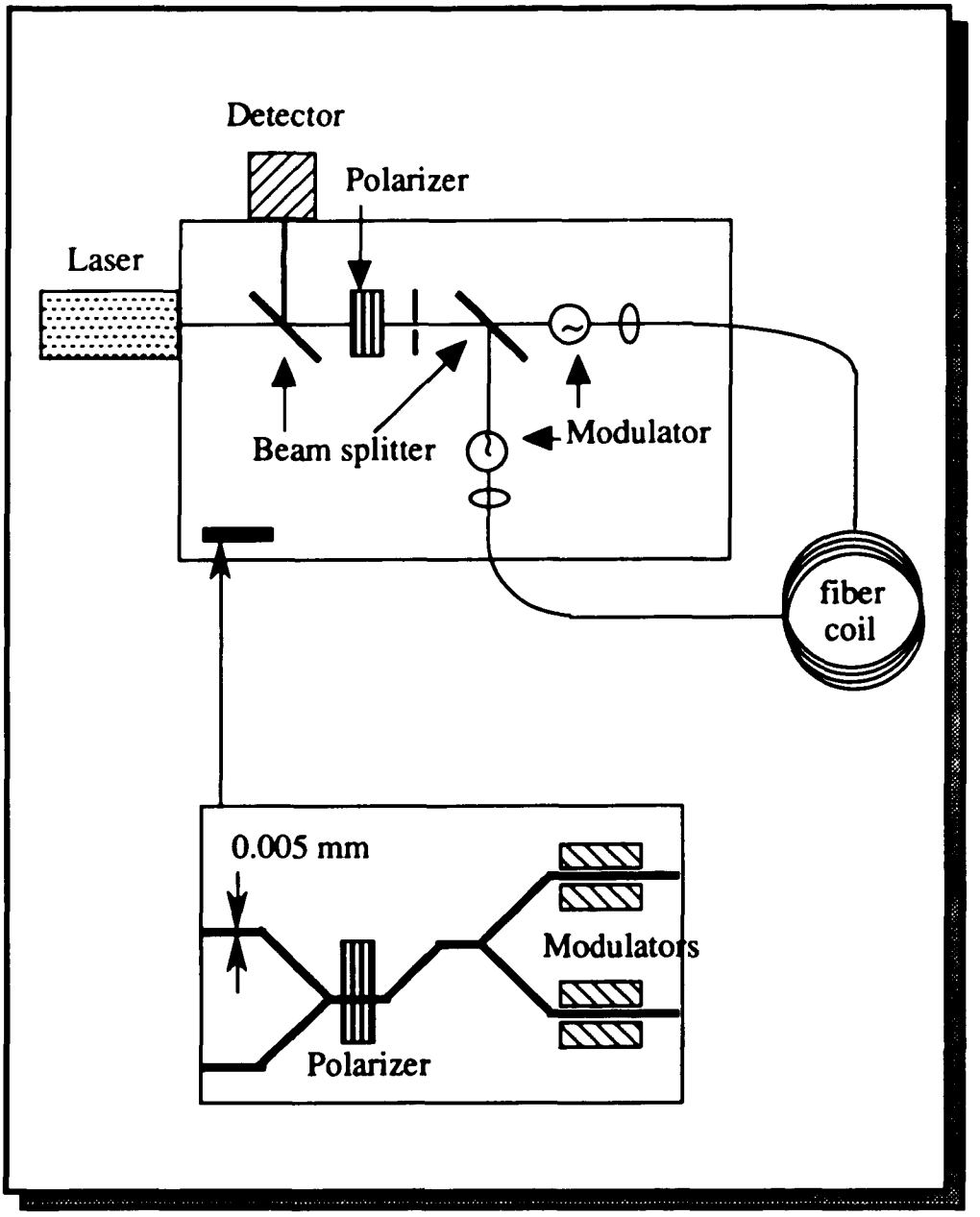

3. Organotin Compounds.

3.1 Introduction.

The first organotin compound was reported by E. Frankland in 1849. The report describes his fundamental work on ethyltin compounds. [28, 29] Organotin compounds are thus amongst the earliest known organometallic derivatives, but appear to have been neglected by most of his contemporaries. Frankland had a specimen of diethyltin diodide as early as 1849, and unambiguous characterization followed some years later. [30] Frankland's intuition and experimental technique, which he adapted with surprising skill to the characterization of organotin compounds , must be considered remarkable even by today standards. His primary interest was not organometallic compounds as such, but in testing the "Theory of Radicals ", an important link in the development of organic chemistry structure. This is also true of the work of his contemporaries, Cahours and Riche (1852) [31] and C. Lowig, who reported independent work on organotin compounds. [32] Until recently, this last publication was usually considered to represent the beginning of organotin chemistry. At the time of these studies, it was hoped that the investigation of organotin compounds would lead to further knowledge of the structure of organic molecules. It is not surprising, therefore, that even A. Kekule, the genius of organic structure

theory, concerned himself with tin alkyls. In 1861, he wrote the following : " I cannot resist the opportunity of once again drawing the attention of chemist to the analogy between tin compounds and carbon compounds... ". [33] After 1880, however, further investigations of organotin compounds faded as a result of the rapid progress of organic chemistry. It wasn't until 1931 that further reports in organotin chemistry appeared. Among the names associated with these newer developments are those of E. Krause and his co-workers in Germany [34] , C. A. Kraus in the United States, and K.A. Kozeshkov in Russia.

A renaissance of organotin chemistry occurred in 1950 with the discovery of commercial applications for the compounds as stabilizers against photodecomposition for polyvinylcholride and other polymers, and later as fungicides. By the end of 1970, an increasing number of groups working in many different countries had produced over 4000 publications . The rapid progress was made possible largely by a change in preparative methods, modern physicochemical methods of analysis, and an intense interest in bonding and structure. New methods for the preparation of the simple organotins R_4Sn, R_3SnX, R_2SnX_2, or $RSnX_3$, the synthetic uses of such compounds in reactions with complicated organic molecules, and the realization that stannyl compounds containing Sn --X (X = F, Cl, Br, I ,N, O, H) groups are capable of easier and more varied reactions than previously suspected further spurred the renasaince. Ingham, Rosenberg, and Gilman [35] summarized the field to 1959, and Dub [36] to 1964. Annual literature surveys from 1964 onwards are now available, [37] as well as, numerous specialized books on organotin chemistry. Two monographs in particular, [38, 39] and a multi-volume work [40] cover the field to 1970, while another review [41] deals with the period 1970-1980. Chapters on organotin

chemistry are now included in larger treatises, [42, 43, 44] and review articles summarize the use of the compounds in organic synthesis. [45] Finally, papers on organotin chemistry are now surveyed annually in reviews published in the *Journal of Organometallic Chemistry Library (Organometallic Chemistry Reviews)* , and in Specialist Reports published by the Royal Society of Chemistry (London).

In spite of this prodigious literature, an exhaustive library search of this literature from 1960 to the present failed to yield a publication dealing directly with the photochemistry of alkyltinhalides. A short communication by Lehn [46] in 1966, describing the mechanism of the photochemistry of triphenyltinazide, and a paper by Borrell and Platt [47] describing the photolysis of tetraalkyltin compounds in the vapor phase at different wavelengths were the only publications found dealing with the topic. During the 1980's a series of publications by Van der Kelen and Kochi and their groups dealt with the reactions of alkyltinhalides with photochemically generated iodine atoms and present mechanistic interpretations in terms of charge transfer interactions. [48 ,49] However, these papers are concerned primarily with the charge transfer properties of iodine and not the alkyltinhalides.

The original intent of this work was to use organotin compounds to change the refractive index of glass. However, the gap in the literature concerning the photochemistry of organotin halides was startling and required that the photochemical behavior of the compounds in fluid solution be established in order to understand the photochemical behavior of the compounds adsorbed onto a solid support.

3.2 Properties of Organotin Halides.

3.2.1 Physical :

The physical properties of a number of organotinhalide compounds are listed in Table 3.1. Tin atoms are 50 electron species, but possess a valence electron configuration, $5s^2\ 5p^2$, equivalent to that of carbon. Analogous to carbon compounds, the valence electrons are thought to be hybridized, and the tetravalent compounds are tetrahedral. However, unlike carbon compounds, tin atoms can readily change their coordination number.

With more electronegative substituents, the Lewis acidity of the metal increases, and coordination with electron rich Lewis bases leads to octahedral sp^3d^2 hybridization. Accordingly, acid-base complexes are obtained, and the compounds may show intramolecular coordination or autoassociation leading to dimers or polymers in both solution and in the solid state. Compounds of the general formula $R_{(4-n)}SnX_n$ (n= 1,2,3) are known, where R can be identical or different, substituted or unsubstituted, aliphatic or aromatic groups. X can be -OR, -SR, -OCOR, $-OSnR_3$, $-NR_2$, halogens, or some other acid radical, or neutral ligands, such as -H. The steric arrangement about the tin atom is tetrahedral, and there is no measurable change in the tetrahedral angle when more electronegative groups, such as, -OR, [50] or halogen [51] are present. Even the proximity of several such groups, as in R_2SnX_2 or $RSnX_3$, has no measurable influence on the angles. [52] In compounds like $R_3Sn\text{-}SnR_3$, the Sn-Sn angle also agrees with that of the tetrahedral model. [53]

The covalent radius of the tin atom, 1.40 Å, is surprisingly

Table 3.1 - Physical properties of organotin halides.

Compound	M.W. (gr./mol)	Melting Point (°C)	Boiling Point (°C)	Density (gr./ml)
$(CH_3)_3SnF$	182.81	37.5	decomp	----------
$(CH_3)_3SnCl$	199.25	37.5-39.5	154-156	----------
$(CH_3)_3SnBr$	243.70	26.0-27.0	163-165	----------
$(CH_3)_3SnI$	290.72	-5.0 to -3.0	160-170	2.1432
$(CH_3)_2SnCl_2$	219.59	107-108	185-190	----------
$(CH_3)SnCl_3$	240.04	45.0-46.0	----------	----------
$(C_6H_5)_3SnCl$	385.46	106.0	----------	----------
$(C_6H_5)_2SnCl_2$	343.81	42.0-44.0	180-185	----------
$(C_6H_5)SnCl_3$	302.16	----------	142-143	1.5871
$(CH_3)_3Sn(N_3)$	205.82	119-121	----------	----------
$(C_6H_5)_3Sn(N_3)$	392.01	117-120	----------	----------

independent of the nature of the ligands, and decreases only slightly when there is an accumulation of strong electron rich ligands around the tin atom (Table 3.2). Thus, the bonding of the substituents to tin appears to be entirely covalent , at least in crystalline solids, non-polar media, and the vapor phase. Even for tin-halogen bonds, changes in metal-ligand bond length that would be expected to follow from the difference in electronegativities (Table 3.3) are not observed, although this may be due to the relative large bond-lengths. Because of the small electrostatic interactions between the metal atom and the halogen atom, and the large Sn-X bond lengths, the bonds are easily polarizable, and in highly polar solvents, the compounds will undergo ionic dissociation, i.e.,

$$R_3Sn\text{-}X \text{ <-----> } R_3Sn^+ + X^- \qquad 3.1$$

The extent of dissociation is generally very slight even with strongly negative ligands, and in polar solvents. For example, the specific conductance of a 1.0 M solution of Et_3SnCl in nitrobenzene is 1.0×10^{-6} $ohm^{-1}\text{-}cm^{-1}$, and declines to 1.8×10^{-9} $ohm^{-1}\text{-}cm^{-1}$ in benzene. [54] Iodotrimethylstannane, $(CH_3)_3SnI$, shows very little conductance in benzene, and more in nitrobenzene. [55]

Radical reactions, on the other hand, are more common with organotin compounds. Because of the importance of bond-dissociation energies in understanding the radical reactions in organotin chemistry, the currently available bond energies are given in Table 3.4.

Table 3.2 - Bond Lengths and Covalent Radius in Tin Halides (Å) [11,12]

Bond Sn-X[a]	Length (Å)	Measured in	Covalent Radius Sn
Sn-C	2.18 ± 0.03	$MeSn_4$	1.41 ± 0.03
	2.19 ± 0.06	$MeSnCl_3$	1.42 ± 0.03
	2.19 ± 0.03	Me_3SnCl	1.42 ± 0.03
	2.17 ± 0.03	Me_3SnBr	1.40 ± 0.03
Sn-Cl	2.37 ± 0.03	Me_3SnCl	1.38 ± 0.03
	2.34 ± 0.03	Me_2SnCl_2	1.38 ± 0.03
	2.32 ± 0.03	$MeSnCl_3$	1.38 ± 0.03
	2.30 ± 0.03	$SnCl_4$	1.38 ± 0.03
Sn-Br	2.49 ± 0.03	Me_3SnBr	1.35 ± 0.03
	2.48 ± 0.03	Me_2SnBr_2	1.35 ± 0.03
	2.45 ± 0.03	$MeSnBr_3$	1.35 ± 0.03
	2.44 ± 0.03	$SnBr_4$	1.35 ± 0.03
Sn-I	2.72 ± 0.03	Me_3SnI	1.39 ± 0.03
	2.69 ± 0.03	Me_2SnI_2	1.39 ± 0.03
	2.68 ± 0.03	$MeSnI_3$	1.39 ± 0.03
	2.64 ± 0.03	SnI_4	1.39 ± 0.03
Sn-Sn	2.77 ± 0.03	$(Ph_2Sn)_6$	1.39 ± 0.03

[a] Accuracy and error limits are those found in the original literature.

Table 3.3 - Dipole Moments (Debye Units) of Organotin Halides in Hexane at 20 °C [56, 57,58,59]

Compound	μ, debye		
	(X = Cl)	(X = Br)	(X = I)
$(CH_3)_3SnX$	3.50	3.45	3.37
$(CH_3)_2SnX_2$	4.10	3.86	3.76
$(CH_3)SnX_3$	3.64	3.24	2.52
	(R = CH_3)	(R = C_2H_5)	(R = C_6H_5)
R_3SnCl	3.46	3.56	3.46
R_2SnCl_2	4.14	4.32	4.21
$RSnCl_3$	3.77	4.08	4.30

3.2.2 Solubility :

With the exception of fluoro compounds, the R_nSnX_{4-n} organotin halide are soluble in a variety of polar and nonpolar organic solvents. The insolubility of the R_nSnF_{4-n} compounds is believe to be due to their polymeric structure. In weak electron donor, low dielectric solvents, the chloro, bromo, and iodo compounds exist as undissociated monomeric species. In strong electron donor solvents, such as, dimethylsulfoxide (DMSO), dimethylformamide (DMF), dimethylamide (DMA), however, the solvent binds to the metal increasing its coordination number. In most cases, these solutions are nonconducting, but in some cases, specifically with high dielectric electron donor solvents, the Sn-X bond breakes, forming solvated organotin cations and halide anions. [60]

$$R_3SnX + Solvent \quad <\text{----}> \quad (R_3Sn\text{-}Solvent)^+ + X^- \qquad 3.2$$

Water would be expected to be an ideal solvent, but the organotin cations are strongly polarizing, i.e., behave like Lewis acids, and the aquo complex, $R_3SnOH_2^+$, becomes a fairly strong proton acid. Tobias has written an excellent review on the occurrence , structure and hydrolysis of the organotin-aquo cations, as well as their hydrolysis products. [61]

Donor-acceptor adducts, $R_3SnX{\cdot}B$, form between trialkyltin chlorides R_3SnCl (R= CH_3, C_2H_5) and Lewis bases such as pyridine, [62,63 ,64] TMSO, DMA, and DMF [65] . The solutions are not conductive, but NMR and UV spectra of $CH_3SnCl{\cdot}Py$ [66] yield evidence of some dissociation.

Table 3.4 - Dissociation Energies, D, and activation energies, Ea, for Sn-X Bonds in Organotin Halides R_3Sn-X. [67]

X	D	Ea [a]
	Kcal/mol	Kcal/mol
Cl	85.0 ± 5.0	89.0
Br	94.0 ± 4.0	74.0
I	80.0 ± 4.0	59.0
Me	73.0 ± 4.0	52.0
Ph	81.0 ± 5.0	61.0
Sn--Me	76.0 ± 6.0	35.0

[a] Lippincott, E. R.; Tobin, M. C., *J. Am. Chem. Soc.*, **75**, 4141, (1953)

Consequently, the molecular adduct is not ionic, but where the data can only be explained by assuming a coordination number of five around the tin atom, the donor-acceptor bond strength is rather weak. Based on NMR coupling constants J 119 $_{Sn\text{-}C\text{-}H}$, and formation enthalpies [68,69] of the complex, Bolles and Drago [70] suggested the following scheme :

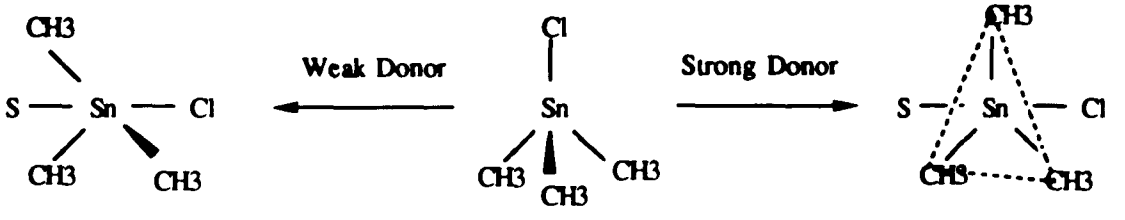

In both cases, the coordination number about tin increases to five. However, a strong donor causes a profound rehybridization of tin and the structure of the complex approaches a trigonal bypiramid with a CH_3-Sn-Cl angle of about 90 °. On the other hand, a weak donor forms an addition compound where the CH_3-Sn-Cl angle remains about the same as the tetrahedral angle of 109 °.

3.3 Reactions in solution.

While the chemistry of organotin halides in the gas phase often involves radical intermediates, formation of a solvent adduct, and in some cases, its dissociation raises the possibility of ionic intermediates in polar solvents.

As a result, homolytic cleavage of a bond and formation of free atoms and radicals is not necessarily favored over heterolytic cleavage and ion formation, particularly in solvents with high dielectric constants. Solvents such as water, alcohol, nitrobenzene, pyridine, acetone, may favor heterolytic cleavage and ion formation, whereas nonpolar solvents, such as ether, benzene, chloroform, carbon tetracholride, and n-alkanes favor homolytic cleavage and radical formation.

3.3.1 Ionic Mechanism :

Generally ionic reactions in solution, exhibit quite different characteristics from free-radical reactions. This arises from the fact that, with the exception of inorganic salts that are fully ionized in water, charge separation is usually not complete, and the ions are not actually free. Therefore, ionic reactions do not proceed by well defined reaction steps, but rather by smooth transitions accompanied by a shift of electrons.This is not always realized, however, and ionic reactions involving organic molecules are frequently envisioned as involving fully separated ions.

3.3.2 Free-radical Mechanism :

Free radicals can be produced in solution by the thermal, photolytic, and radiolytic methods. In the gas phase, free radicals produced by such methods usually migrate away from each other before they recombine. In solution, however, diffusion is much more difficult, and *primary recombination* more probable. This phenomenon, which is often referred to as the *Frank-Rabinowitch effect* or *cage effect* , tends to lower the actual

yield of radicals. [71]

Once a radical has succeeded in diffusing away from its partner, however, the cage of solvent molecules surrounding it will hinder its recombination with other radicals. On the other hand, there is now the possibility of displacement reactions with solvent molecules. Usually, the reactions occur readily. For example, radicals are found to dehydrogenate alcohols, hydrocarbons, and other molecules, and to dehalogenate solvents such as carbon tetrachloride. As a result, free radical reactions in solution are not necessarily characteristic of the primary radicals, but more characteristic solvent radicals. For example, free-radical reactions in aqueous solution are usually reactions involving the hydroxyl radical.

3.4 Spectroscopic characteristics.

A powerful array of spectroscopic techniques are available for the investigation of organotin compounds. The most important of these are UV-vis-, infrared-, nuclear magnetic resonance,- and Mossbauer spectroscopies. It is the practice of most laboratories to record UV-vis and infrared spectra routinely. All organotin halides absorbed light in the UV region, but in $R_{(4-n)}SnX_n$ complexes, the nature of X is the key determinant of the transition energy. With alkyl ligands, the compounds generally absorb at ≤ 230 nm, while with aryl ligands the compounds absorb at ≤ 260 nm, due to transitions localized in the aryl moiety. In polymeric complexes, the absorption shifts to longer wavelengths as the length of the chain increases. Consequently, complexes such as $(Et_2Sn)_6$ and $(Et_2Sn)_9$ exhibit

in each class of compounds, the intensity of the absorption increases in proportion to the number of ligands. [73]

The I.R. spectra of the complexes yield useful information, although almost all fundamental stretching vibrations involving the tin atom occur at frequencies below 650 cm^{-1}. It is costumary to complement I.R. spectra with Raman spectra to obtain the lower energy Sn-C stretching frequencies. [74] Monoalkyltin compounds exhibit only one Sn-C stretching band, whereas, the di- and tri-alkyltin compounds generally show two bands; one at 500-600 cm^{-1}, which is assigned to the asymmetric Sn-C stretch (ν_{as}), and one at 470-530 cm^{-1} which is assigned to the symmetric Sn-C stretch (ν_{s}). [75] The intensities of these bands vary considerably, and in some cases, are very weak. Unfortunately, the frequencies of the Sn-C stretching bands are not sensitive to changes in the coordination number of the tin atom, but the intensity and number of bands observed can be affected. [76] Although, knowledge of the factors affecting the position of the ν_{s} bands is limited, current data for the methyltin halides show that electronic effects are important.

In contrast to the Sn-C stretching frequencies, the tin-halogen stretching frequencies are very sensitive to changes in the coordination of the tin atom. More electronegative halogens and larger numbers of halogens, increase the the nuclear charge on the tin and shift the band to higher frequencies. [77] For example, in the R_3SnX (R= alkyl or aryl) series, the tin-halogen stretching frequencies are 385-318 cm^{-1} (ν Sn-Cl), 264-222 cm^{-1} (ν Sn-Br), and 207-170 cm^{-1} (ν Sn-I). A structural rearrangement from a 4 coordinate to six coordinate species shifts the Sn-X band 100 cm^{-1} to higher frequencies. [78] Similar shifts occur when an organotin monohalide is converted to a pentacoordinated complex $R_3SnX \bullet L$. The tin-halogen

stretch gives rise to an intense band in the 1880-1790 cm $^{-1}$ range.

In symmetrically substituted distannanes, $R_3Sn\text{-}SnR_3$, the Sn-Sn mode is infrared inactive but it can be observed in the Raman spectrum. In an unsymmetrically substituted compound, the band is IR active and occurs in the170-200 cm $^{-1}$ range.

Other vibrational frequencies have also been assigned, for example, the Sn-N_3 and Sn-NCO stretching frequencies, occur at 401 and 400 cm^{-1}, respectively.[79] Interpretation of the spectra containing tin-oxygen stretching frequencies has proven to be rather difficult. However, an empirical calculation [80] indicates that the tin-oxygen stretching frequency should occur at ~ 570 cm $^{-1}$, and experimentally, the frequencies appear to fall in the 575- to 550-cm^{-1} range. [81]

Organotin compounds have also been examined by NMR spectroscopy.[82] Although, some interest has centered on the factors affecting the chemical shift, most of the current data focuses on the tin-proton spin-spin coupling constants. The J (119 Sn- C-H) values are thought to be a measure of the percentage of *s* -character in the tin-carbon bond, but have also been shown to exhibit a strong dependence on the nature of the solvent. [83]

4. Porous Silica Glasses.

4.1 Surface chemistry.

The role of surfaces in chemical reactions has and continues to intrigue kineticists, colloid and polymer chemists, and material and surface scientists. The interaction of a molecule with a heterogeneous phase, such as gas-solid, liquid-solid, or liquid-liquid will not only change the local concentration of a reactant, but in some cases, its electronic structure as well. Both can affect fundamental changes in reactivity. The crux of the matter is whether adsorption onto a surface enhances a selected chemical change. The chemical change can be initiated by a number of means, but photoactivation has received considerable attention during the past few years. [84, 85, 86] In a photoactivated system, the support may directly participate in the reaction by either absorbing the incident photons and/or transferring charge carriers (holes or electrons) to the substrate. Alternatively, it may act in a more passive, although no less important, manner by affecting local concentrations, rates of diffusion, or imposing an interface. A molecule adsorbed on a surface may react with another molecule also adsorbed on the surface, or with a molecule that visits the surface from an external phase. The kinetics may be as simple as those found in homogeneous solution, or more complex in that the rate constant

may be time dependent, specific adsorption sites may give rise to a Poisson type kinetics, or the kinetics may be "static" in nature. [87]

The evolution of new physical techniques during the past twenty years have truly revolutionized the photophysics and photochemistry of adsorbed species. Computerization of electronic spectrometers and fourier transform infrared spectrometers [88] have allowed signals due to the adsorbate to be separated from those of the support. Diffuse reflectance techniques offer a means of obtaining infrared spectra of an adsorbate on an opaque support. New and more reliable CW and pulse laser have made the measurement of emission quantum yield, lifetime, and polarization ratio much simpler, and as a result, more applicable to examining photophysical and photochemical process of an adsorbate on a surface. [89] In fact, transient adsorption spectroscopy such as flash photolysis is now being employed to directly detect and characterize photochemical reaction intermediates on a support.

In spite of the variety of techniques that can be applied, the complex nature of a reaction occurring on a solid surface usually impedes the development of a mechanistic interpretation. The reaction is not only governed by a series of chemical and physical steps that are encountered in fluid solution, but further complicated by adsorption and desorption, diffusion on or within the support, and the chemical nature of the adsorbate, which may be quite different from that in solution or the gas phase. As in fluid solution, the occurrence of the species involved in a processes is inferred by the kinetics of formation and depletion. Several spectroscopic techniques [90] have been applied to the study of the mechanism of the reaction including ex situ methods for static characterization and in situ techniques for real-time analysis. Nevertheless, the researcher

attempting to acquire a fundamental understanding of the nature of the reactive intermediates is face with several problems. Assuming that the spectroscopic technique is sensitive enough to extract relevant chemical and physical information, which is not always the case, the observed spectral features must be sorted out and assigned to a distinct molecular species. Suitable models must be located in the literature, prepared by independent means, deduced from chemical principles, or derived from appropriate calculations. Highly reactive, short lived intermediates must be postulated. Although not directly observed, these species are essential to a comprehensive understanding of the system under consideration.

4.2 Photochemistry.

The aim of these studies is the understanding of photochemical reactions at glass surfaces. Therefore, a brief description of the basics of photochemistry, along with an introduction into surface photochemistry will be presented.

Photochemistry deals with a unique type of chemical reaction; the absorption of a photon by a molecule and the subsequent chemical and physical changes that result from this interaction. The absorption of the photon leads to the formation of a electronically excited molecule. The lifetime of these states can range from picosecond (10^{-12} seconds) to millisecond (10^{-3} seconds), with the electronic energy being dissipated physically, i.e., equations 4.3, 4.4, or chemically eq. 4.2.

$$A + h\nu \quad \text{---}> \quad A^* \qquad 4.1$$

$$A^* \quad \text{---}> \quad \text{primary products} \quad \text{---}> \quad \text{final products} \qquad 4.2$$

$$A^* \quad \text{---}> \quad A + h\nu' \qquad 4.3$$

$$A^* \quad \text{---}> \quad A + \text{heat} \qquad 4.4$$

In any photochemical reaction, two questions interest the photochemist. First, what is the nature of the reactive state, which may or may not be the state populated on absorption, and second what pathways dissipate the excitation energy.

In any photochemical reaction, a chemical change occurs while the reactant species is in the excited state. The reactive species may be in the same state as was initially populated by the excitation, or some other state reached by a rapid intramolecular conversions. To understand the detailed mechanism by which a photochemical reaction occurs, the identity of the excited state, as well as the nature and yield of the products must be established. Information about the excited states of a molecule derive from : a) absorption spectroscopy, b) photochemistry, c) absorption and emission spectra of the excited species, and d) intermolecular quenching and sensitization. If possible, explorations of excited states must be also complimented by detailed studies of the decay mechanisms.

One of the most useful and fundamental quantities is the quantum yield, Φ. Its size and the influence of the experimental variables upon it give important information as to the nature of the reaction. Quantum yields of

primary photochemical events are of great importance, but are often difficult to measure. One usually measures overall quantum yields of product formation, and from these infer information regarding the primary quantum yield, and the mechanism of the reaction. The quantum yield measures the number of molecules which undergo a specific event per unit of light absorbed. The first law of photochemistry states that *" Only the light which is absorbed by a molecule can be effective in producing photochemical change in the molecule "*. Therefore, the quantum yield is, in effect, an efficiency factor. The quantum yield of the photodecomposition of a reactant is defined as

$$\Phi = \frac{d[A]/dt}{I_a} \qquad 4.5$$

where d[A]/dt is the rate of disappearance of A and I_a is the light intensity adsorbed by A. Ia is related to the incident intensity, I_0, by the equation :

$$I_a = I_0\left(1 - 10^{-\varepsilon lc}\right) \qquad 4.6$$

where ε is the molar extinction coefficient of A at the excitation wavelength, l is the pathlength, and c is the concentration of A. The incident intensity, I_0, can be measured by a number of different techniques, although the most frequently used is chemical actinometry. In this case, the incident light intensity is measured by the reaction of a compound with

a well known quantum yield.

4.2.1 Photochemistry of molecules adsorbed onto solid supports :

Historically, the solid state has been of interest to inorganic chemists as the birthplace of crystal-field-theory. Nevertheless, the study of photochemistry in the solid state has progressed at a much slower rate than that of solutions. This was not the result of a lack of interest in solids and solid supports, but the difficulties encountered in measuring parameters as simple as the quantum yield. As noted previously, the experimental techniques of adequate sensitivity needed to probe a molecule on a surface have only recently become available. In fact, considering the current use of photochemical techniques in making solid state electronic components, photography, and photolitography, its applications have outpaced the understanding of the fundamental chemical and physical events.

The changes in the emission and absorption spectra of adsorbed molecules during photochemical reactions are fundamentally the same as the ones observed in reaction in solution. The excited states of compounds adsorbed into solid surfaces, at least those observable by means of spectroscopic means, are similar to those in fluid solution. Metal complexes adsorbed into solid supports have discrete molecular energy states with internal *d-d* or ligand-field and charge-transfer-transitions. However, the rigidity and periodicity of solids, can modify the reactions. Excitation at one site can induce electron migration to another site several lattice sites away. Photocurrents and photovoltages, for example, are produced upon irradiation in charge-transfer absorptions of ionic complexes. Many light induced chemical reactions are also related to

crystal defects, such as vacancies or impurity centers, or are a consequence of interfacial (solid-solution or solid-gas) phenomena.

These differences in behavior, as well as the evolution of new analytical techniques capable of probing solids surface phenomena, and adsorbates on a support, have led to a renaissance in solid state photochemistry. New concepts have emerged, previous concepts elaborated, and applications extended in the fields of electronics, semiconductors, and material science.

4.3 Porous Vycor Glass.

The importance of phase separations in the manufacture of glass has been recognized for the past 25 years. Phase separation during the making of glass melts is a viable approach to changing the properties of glass and achieving uniform crystallization of glass ceramics. The chemical durability of Pyrex borosilicate glass, for example, arises from the phase evaporization that occurs during thermal treatment of sodalime-silicate glass. Similarly, the Vycor process for the manufacture of 96% silica is based on the separation of the boron and silica-rich phases during the cooling of a 96% SiO_2, 3% B_2O_3, and 1% Na_2O and Al_2O_3 melt. The extent of separation is controlled by the time the melt is maintained at a specific temperature. When the melt is quenched, such as, converted to the glass phase by more rapid cooling, the result is a transparent, biphasic glass in which an interconnected boron rich phase is randomly dispersed throughout the silica matrix. The boron rich phase is then acid leached giving a porous material that is consolidated at ca. 1000 °C to a nonporous Vycor glass. The advantage of the procedure is that a nonporous glass,

which contains ≥ 96 % SiO_2, can be obtained at temperatures considerably lower than the ≥ 1800 °C needed to prepared fused silica.

Porous Vycor glass (PVG), nicknamed " thirsty glass ", is the acid leached, porous intermediate in the Vycor process. Acid leaching of the boron-oxide phase yields a myriad of precisely controlled pores interconnected throughout the glass in a random three dimensional array. Pore size is determined by the extent to which phase separation is allowed to occur and acid leaching. Pore sizes ranging from 20 Å to 2500 Å in diameter are currently available. However, our interest in this material stems from its transparency and porosity. Transparency offers amenability to spectroscopy and photochemistry while porosity offers chemical access. However, transparency in general declines as cavity size increases. PVG samples, where the cavities are ≥ 100 Å in diameter, appear opalescent white, while samples with cavities ≤ 100 Å in diameter are transparent. The difference is due to light scattering, which in turn, limits transmittance. Transparency is essential to this research since the idea is to utilize photoactive organotin compounds to change the refractive index of the glass. Consequently, the experiments described here are limited to PVG containing 70 ± 21 Å diameter cavities.

4.3.1 Properties of Porous Vycor glass :

4.3.1.1 Structure :

Small angle X-ray scattering (SAXS) confirms a microporous material that can be modeled by a bicontinuous spinodal structure. Scanning electron micrographs of the polished PVG (Figure 4.1) reveal a surface composed of

Figure 4.1 - Scanning Electron Micrograph of Porous Vycor Glass. Magnification: 100,000 X.

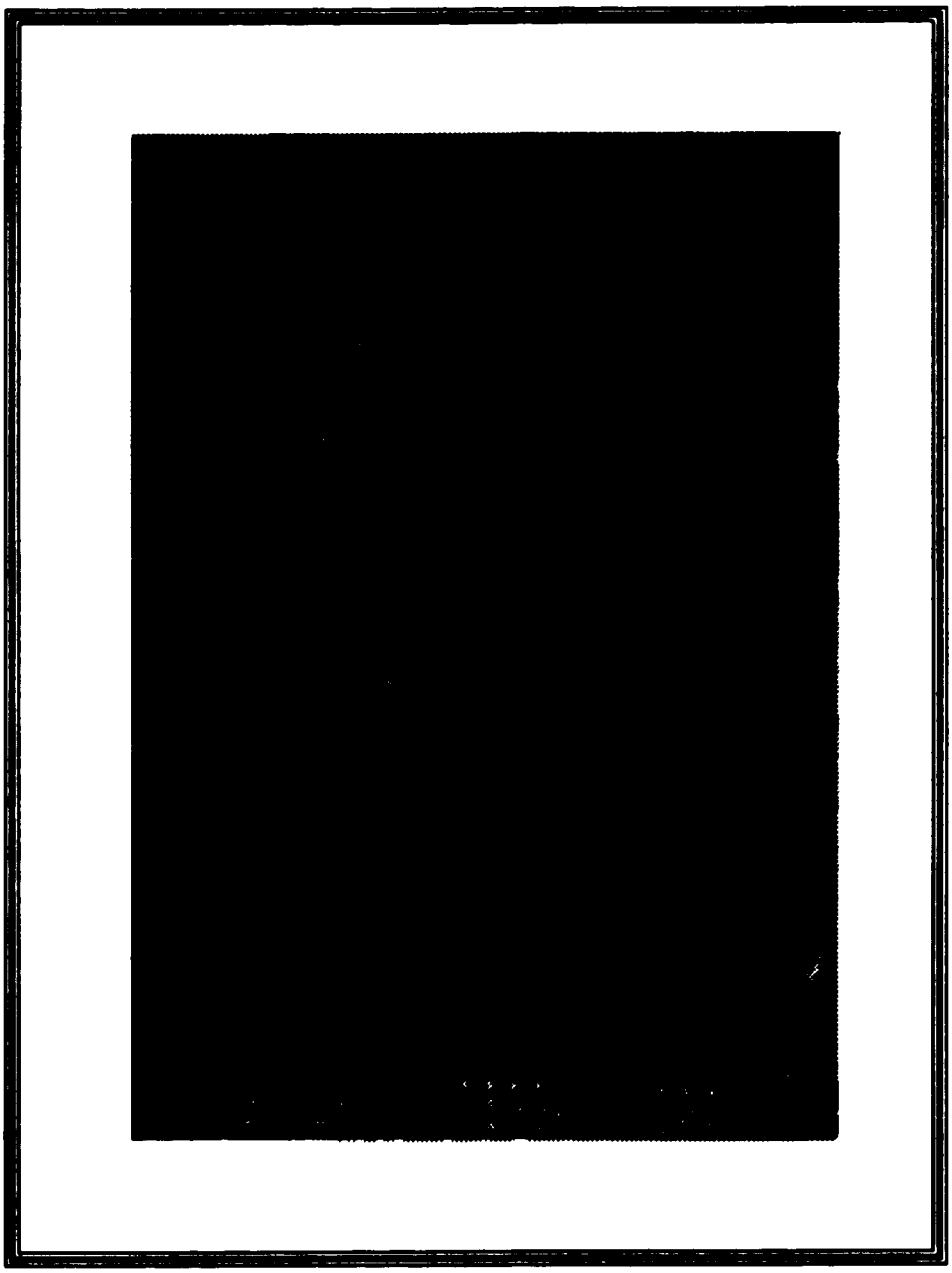

interconnected glass nodules with intervening crevices. Some of the latter, but certainly not all, contain the openings into the interior pore structure. SEM analysis of ground samples indicates that the interior structure of the glass is similar to that shown in Figure 4.1, i.e., an array of glass nodules with an intervening porous network.

4.3.3.2 Surface chemistry of porous Vycor glass :

It is now well established that physisorption, chemisorption, surface chemistry and surface conductivity depend on the structure and chemical nature of the surface. At the molecular level the chemistry of an adsorbate on a glass surface, certainly its initial events, also reflects the chemical nature of the surface. The wide spread use of silica gel as a catalyst, catalyst support, and adsorbent, has lead to extensive studies of the silica SiO_2 surface. As noted by Ernsberger [91] in an excellent review of the properties of the glass surface, the surface structure of oxide glasses depends on the reactions of "dangling" oxide bonds. These bonds, as well as coordinatively unsaturated Si generated in the melt at the glass surface rapidly react with atmospheric water to form surface Si-OH groups. These groups hydrogen bond to additional water molecules to form a hydrated surface. Therefore, the surface of an oxide glass is composed of Si-OH groups, and hydrogen bonded water. The thickness and structure of the latter depends on its thermal history and the humidity of its environment .

The hydroxyl groups on silica surfaces have been examined by infrared spectroscopy. [92,93,94] Figures 4.2a, 4.2b illustrates the spectral changes that occur upon heating at room temperature in air, and in vacuum. The broad band centered at 3400 cm^{-1}, and another band at 1250

Figure 4.2 - Infrared Spectra of Si-OH Groups on Carbosil Silica. [95]

A) temperature dependence in air; B) temperature dependence in vacuum.

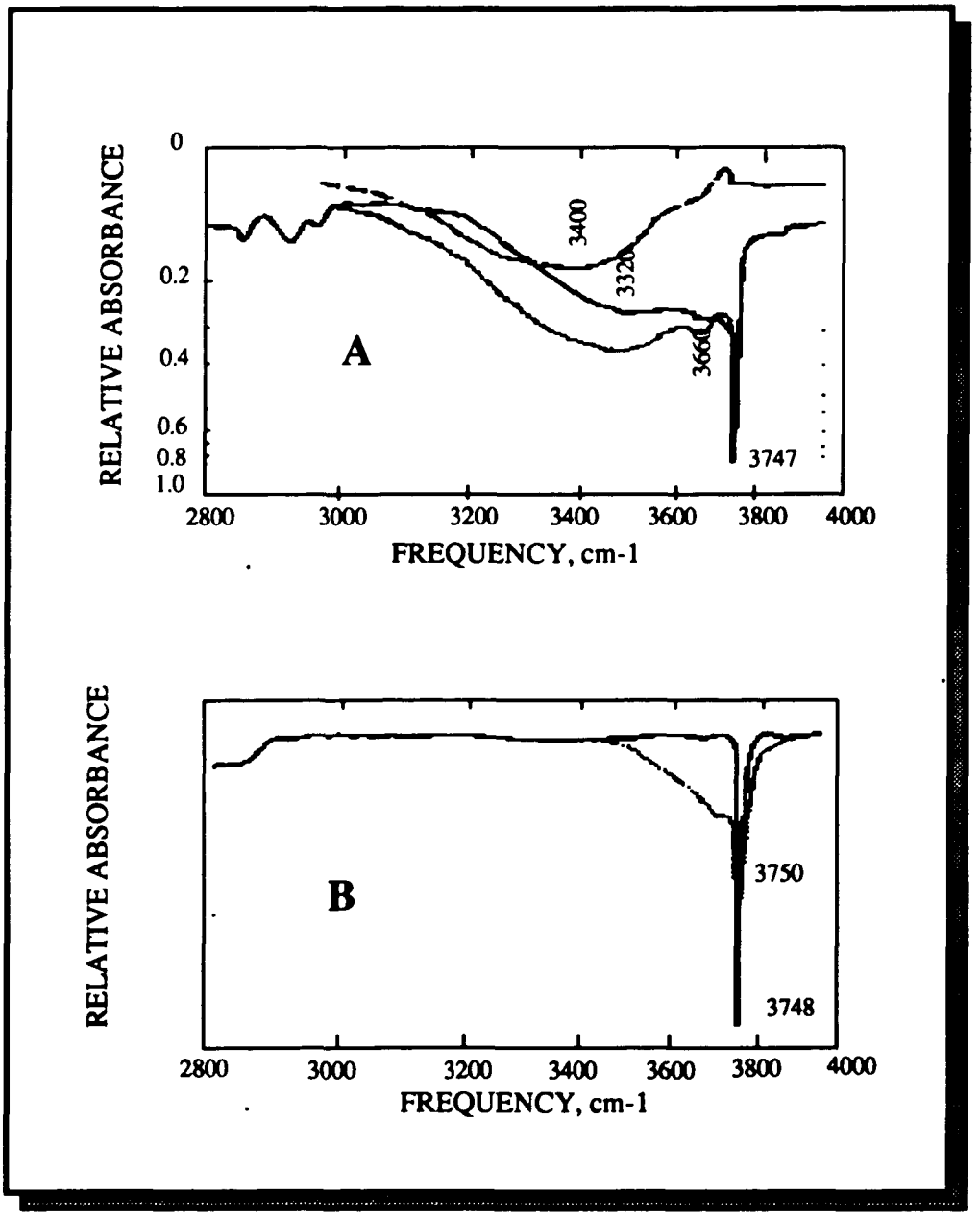

cm^{-1} are assigned to OH vibrations of physisorbed water. Similar bands occur in the spectrum of water, and both bands disappear after pumping at room temperature, or heating to 150 °C for a short time. As the temperature is raised, a broad band at 3660 cm^{-1}, and a band at 3748 cm^{-1} become more prominent. Above 150 °C, the 3660 cm^{-1} band slowly disappears, and at high temperatures, only the band at 3748 cm^{-1} remains. The latter band is attributed to isolated SiOH groups, whereas the 3660 cm^{-1} band is assigned to associated silanol groups, i.e., closely spaced surface hydroxyl groups that are associated via hydrogen bonds. Another type of silanol groups is postulated to exist near the silica surface. namely, an internal Si-OH groups, [96,97,98,99] An internal SiOH group results from the diffusion of water molecules into silica and their subsequent reactions with the silica lattice to form two SiOH groups. The presence of this type of groups was inferred from deuterium exchange reactions on PVG, and water adsorption studies suggest that its formation becomes important at a temperature above 100 °C. [100]

Figure 4.3 illustrates the different types of hydroxyl groups that exist on silica surfaces. Isolated SiOH groups are referred as silanol groups, hydrogen-bonded SiOH groups are referred to as associated silanols, internal SiOH groups, and molecular adsorbed water. The relative amounts of these different groups on silica depend on its thermal history and the temperature and humidity of its surroundings at the time of observation.

The transparency of PVG (50 % at 295 nm vs. air) is ideal for the study of photoinduced reactions of adsorbed compounds. Determination of quantum yields for the photoprocesses is possible since the scattering and absorption of the incident radiation by PVG is almost negligible. Furthermore, the transparency enables the characterization of surface

Figure 4.3 - Schematic Diagrams of Hydroxyl Groups on Silica Surface. (a) Isolated group; (b) Hydrogen-bonded groups with isolated water molecule; (c) Two hydroxyls in one silicon atom.

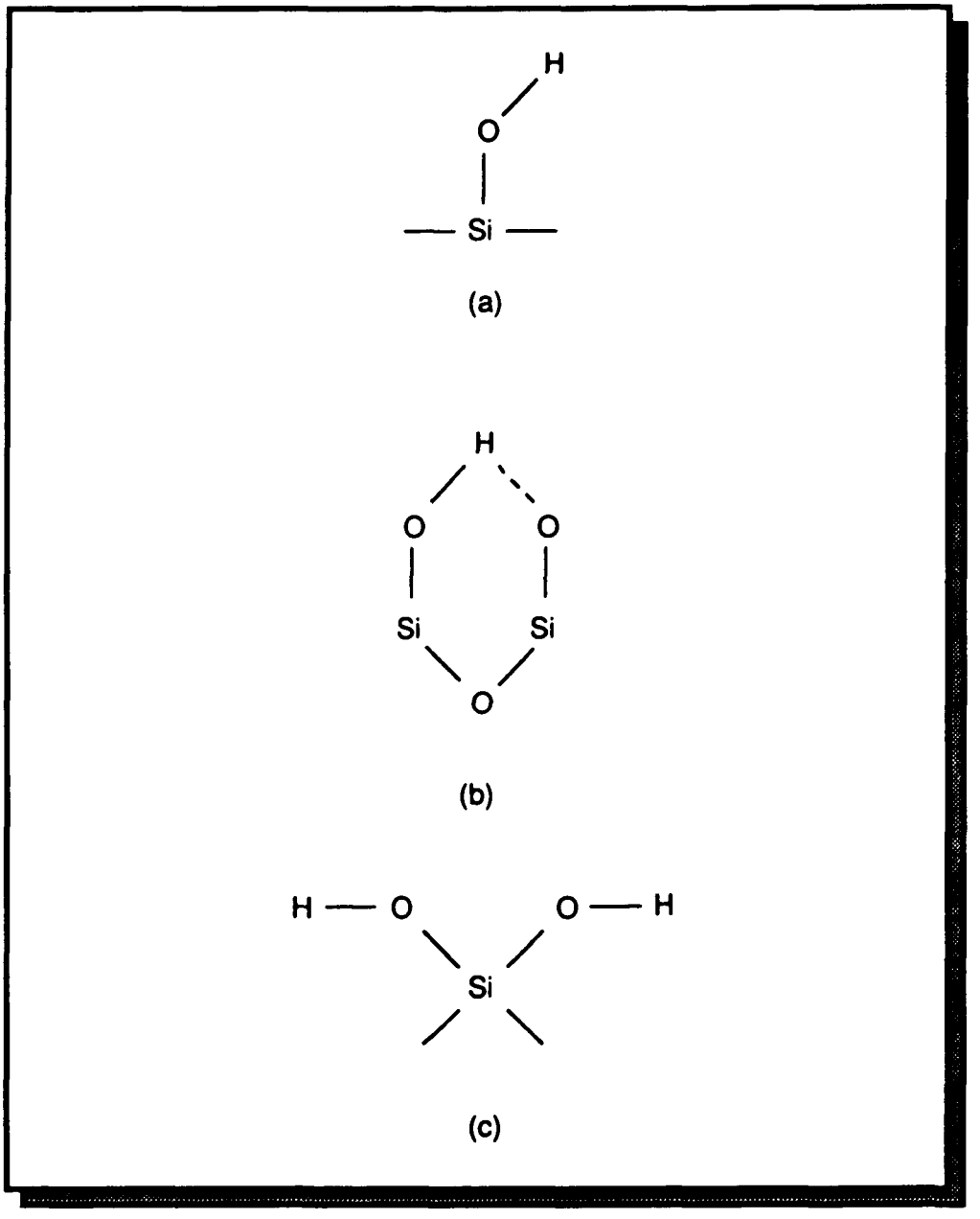

reactions by absorption spectroscopic techniques which is difficult with more opaque supports.

4.4 Sol-gels.

The conventional way of producing pure silica glass is to heat quartz powder far above its melting point of 1723 °C and then quench it. Because of its high viscosity at the melting point, refining the glass and forming shapes tends to be difficult, but crystallization is rarely a problem. The purity of the glass formed depends on the purity of the raw materials and the melting conditions.

Since the early 1900's pure silica has been formed by what is now called the Sol-Gel process. Using this process, a solution of metal alkoxides, water, alcohol and a catalyst are reacted to form a gel, which is then dried to form a porous hydrated glass. Glasses produced using alkoxides are reported to be of higher purity and require lower processing temperatures than comparable glasses produced by conventional melting. The higher purity of these glasses results from higher purity reagents. Also, less contamination occurs during firing because of the lower temperatures required and less contact with the firing container. The higher purity of gel glasses, as compared to melted glasses, refers to metallic impurities and does not consider residual water. When the sol-gel process is to used to duplicate fused silica, the dried gel is heated to a temperature to collapse the gel microstructure and convert the porous material to a nonporous glass.

4.4.1 Processing :

The sol-gel process for silica involves mixing a silicon alkoxide [$Si(OR)_4$], water and alcohol. On mixing, this is a true solution so the term "sol", which means a dispersion of colloidal particles, is not correct. Nevertheless, the term is used, and acid or base is added to catalyze the reaction.

$$Si(OR)_4 + n\ H_20 \text{ -----> } Si(OR)_{4-n}(OH)_n + n\ ROH \qquad 4.7$$

R represents either a proton or other ligand, and ROH is an alcohol. Depending on the amount of water and catalyst present, this reaction may not go to completion and therefore silicic acid, $Si(OH)_4$, is only partially formed. Soon after hydrolysis starts condensation polymerization begins. This is represented by the reactions:

$$Si(OR)_{4-n}(OH)_n + Si(OR)_4 \text{ -----> } Si(OR)_{4-n}(OH)_{x-1}\text{-O-}Si(OR)_3 + ROH$$

and

$$2\ Si(OR)_3(OH) \text{ -----> } (RO)_3Si\text{-O-}Si(OR)_3 + H_20 \qquad 4.8$$

Under acidic conditions, polymerization leads to the formation of highly branched chains,. whereas adding a base leads to more condensed clusters. After some period of time, depending on concentrations and reaction temperature, the sol-gel transition is reached. This is when the

reaction temperature, the sol-gel transition is reached. This is when the viscosity of the solution rises rapidly and a gel is formed. This gel can be dried to a microporous solid having interconnected porosity.

4.4.2 Dried and heat treated Gels :

Dry gels have been characterized in terms of bulk density, apparent density, pore volume, surface area and refractive index. From these physical measurements, the microstructure has been inferred. The generally accepted microstructure is an oxide skeleton covered with silanol groups surrounding interconnected pores. The scale of the microstructure depends on the preparation of the solution before gelling, and the sharpest difference in scale is between acid-catalyzed and base-catalyzed solutions. In general, small amounts of acid give a fine-textured gel with a microstructure that cannot be resolved easily with electron microscopy, while small amounts of base gives a coarse-textured gel with a somewhat particulate appearance.

Although many studies on the densification of gels have been reported,[101] it is very difficult to compare the results, because different preparations are made. For example, a given glass composition can be produced by using either tetraethylorthosilicate (TEOS), $(C_2H_5O)_4Si$, and tetramethylorthosilicate (TMOS), $(CH_3O)_4Si$, or produced using hydroxides and colloidal particles. For silica, the water to alkoxide molar ratio varies from about 1:1 to 32:1. Also both acid and base catalysis are used for gel preparation. The amount of catalyst used is defined by the pH or molarity of the total solution. Because nonaqueous solutions are used, molarity [or MV as opposed to pH] may be a more descriptive quantity. Reaction temperatures vary from -78.6 to about 80°C and reaction times vary from

seconds to days. Qualitative differences in the resulting gels have been reported, [102] but the differences in the densification characteristics are not understood.Even the qualitative effects of these variations are not understood.

Gelation and drying conditions also affect the densification of gels. Gelation occurs from room temperature to 70°C in open or closed containers. Gels produced under these conditions are called xerogels. When hypercritical conditions, i.e., critical temperature and pressure in phase transformation diagrams, are used the resultant gels are called aerogels.

The chemical and physical changes that occur during the heat treatment of xerogels are : 1) physical desorption of water and solvent from micropore walls; 2) carbonization and combustion of residual organic groups; 3) condensation polymerization; 4) volume relaxation; and 5) viscous sintering.

Water desorption occurs from 120- to 150°C at atmospheric pressure, but at lower temperatures under reduced pressure. According to Iler, all hydrogen bonded water is gone by 180°C. [103]

In the combustion of residual organics, Klein and Garvey [104] report an exothermic peak and corresponding weight loss centered at about 400 °C and ending by 425 °C. This occurs with a heating rate of 10°C per minute, but slower heating rates yield lower temperatures. According to Susa and co-workers, [105] residual organics remain in the silica gel up to about 700°C, while Kamiya and co-workers, [106] report a large weight loss below 250°C during thermal gravimetric analysis (TGA) that corresponds to the loss of water and organics. A slight weight loss that continues at higher temperatures is attributed to the vaporization or decomposition of organic

materials of higher molecular weight. Henning and Svensson [107] report that gels heated to 500°C still contain 0.3 wt.% carbon. Analysis of a borosilicate gel densified at 750°C by Brinker and co-workers, [108] reveal 0.25 wt.% residual carbon.

The temperature at which the combustion of residual organics is completed depends on heating rate, soak times and firing atmosphere. For pure silica gels densified at a heating rate of 5°C/min in an oxidizing atmosphere to a temperature of 800°C, residual carbon does not affect densification. The possible effects of residual carbon on post-densification bloating will be discussed later.

4.4.3 Hydroxyl Groups :

The chemical and physical changes that occur during the heat treatment of a gel are a third phase in the process. During this phase, further condensation polymerization occurs, i.e.,

$$\text{Si-OH} + \text{HO-Si} \dashrightarrow \text{Si-O-Si} + H_2O \qquad 4.9$$

The removal of water formed in this reaction is important because it changes the gel. In colloidal silica composed of 1-10nm particles, the interfacial Si-OH---H_2O energy is around 50 to 100 erg/cm^2, and water removal requires surpassing an activation energy barrier of 42 kJ/mole. As a result, complete removal of the hydrogen bonded water requires temperatures of at least 180°C.

Condensation (reaction 4.9) produces four important effects. First, it dehydrates a glass and is a compositional change. Second, it is a

polymerization reaction which densifies and strengthens a gel. Third, it converts a lower energy silanol surface to a higher energy siloxane (Si-O-Si) surface. Fourth, dehydration may cause the formation of highly strained, and therefore highly energetic bonds.

The compositional changes arise from the loss of water. The theoretical hydroxyl concentration for a pure silanol surface is 4.5 OH/nm^2. [109] If a gel has 500 m^2/gr. of surface area, each gram of gel contains 0.036g of water in the form of hydroxyls, consequently pure silica gel is 97% silica and 3% water. At room temperature the experimental value is about 8 OH/nm^2, therefore a sample of pure silica gel contains 6% water. At 400°C, there are about 2.8 OH/nm^2 and the number slowly decreases to 0.06 OH/nm^2 as the temperature rises to 1100°C. [110] These are generally accepted values, but Carturan [111] reports that no weight loss occurs above 450°C for a pure silica gel. Kiselev, [112] who used Et_3N adsorption to determine the number of OH's on silica surfaces, found that at 1000°C in vacuo, 0.5 OH/nm^2 remain. On the other hand, Boer [113] found no residual OH at 900°C at atmospheric pressure, and Gonzalez-Oliver [114] report that the water content of a silica gel was less than 0.1 wt.% at 800°C. Zarzycki [115] found that a TEOS gel that dehydrated at 950°C had 0.8 wt.% water, whereas a precipitated colloidal silica, Ludox, gel had 2.1 wt.% water.

Part of the problem of obtaining reproducible silanol numbers is that the number appears to depend on surface curvature. Pores with small negative radii of curvature tend to have more hydrogen bonded OH and are harder to dehydrate. Also, the range of the values may be due to impurities. Sodium [116] and boron, [117] in particular, tend to segregate to the surface. Thus, small bulk concentrations can lead to large surface concentrations, which will affect the surface OH number.

The condensation reaction, 4.9, has been studied in some detail. Yamane [118] reports that the monotonic decrease in hydrogen content and concurrent increase in density with temperature corresponds to the progress of dehydration polymerization. Iler [119] reports that isothermal dehydration occurs with a relatively rapid loss of water for the first 6 to 10 hours after the temperature is raised. Nogami and Moriya [120] suggest that the water removal is diffusion controlled because the water content in glasses prepared by the gel process decreases in proportion to the square root of heating time. Brinker and Scherer [121] interprete the weight loss versus time curves differently. At low temperatures, ≤ 500°C, condensation occurs predominantly in the bulk and water removal is diffusion limited. At temperatures, ≥ 500°C, the hydroxyls are primarily on surfaces [122] and the weight loss follows first order kinetics. The weight loss, DW, is proportional to $\exp^{(Kt)}$, where K is a rate constant and t is time. The reversibility of these condensation reactions appear to depend on temperature. Hair [123] reports that at temperatures below 400°C, the reactions are reversible, but not at higher temperatures.

In general, attempts to elucidate the rates and mechanisms of dehydration have been unsuccessful. In part, this is due to the fact that the number of OH's/unit area depends on parameters such as surface curvature and impurity levels. Also, the nature of the surface hydroxyls varies with temperature. At ≤ 500 °C, associated hydroxyls are present, and are more easily removed than the single or vicinal OH. On the other hand, at 800°C, [124] only the single or vicinal hydroxyls remain.

In addition to the above effects, dehydration polymerization also changes the surface energy. Brunauer's. [125] measurements of the surface energies of hydrous and anhydrous amorphous silica, by measuring the

heats of solution of samples having different specific surface areas and bound water contents, yields 129± 8 ergs/cm^2 hydroxylated silica based on 8 OH/nm^2, and surface energy to be 259±3 ergs/cm^2 at 23°C. The surface energy above about 400°C is of interest in sintering experiments. At 400°C, there are about 3 OH/nm^2, which leads to a surface energy of about 200 erg/cm. Thus, the surface energy changes by 130 ergs/cm or 100% on going from a gel at ambient temperature to a glass at high temperature. For sintering experiments, the surface energy changes by less than 60 ergs/cm^2 or ≤ 30%.

Brinker and co-workers, [126] report that dehydration polymerization also results in the formation of strained bonds. This is suggested by an increase in the intensities of the D_2 defect band in Raman spectra of silica gels. They also report that the concentration of these defects increases up to at least 700°C.

For colloidal silica gels, bulk water/OH removal begins at 200°C and is completed by 1000 °C. [127] However, Krol and van Lierop [128] find that this may not be applicable to TEOS gels. Their Raman studies of hydroxyl type and concentration versus temperature of a TEOS derived gel shows that, between 400 and 700°C, only surface silanols, characterized by peaks at 3750 and 980 cm^{-1}, are present. As the temperature was raised from 700- to 900°C, however, the 3750 cm^{-1} band disappears accompanied by the appearance of a broad band center at 3680 cm^{-1}. The 980 cm^{-1} peak shifts to 970 cm^{-1} corresponding to a change from surface silanols to bulk silanols.

4.4.4 Volume relaxation and skeletal density :

Because glasses are not in an equilibrium state, but are quenched in,

Brinker [129] describes the next step in the heat treatment as a volume relaxation. Three relaxation regions in a synthetic (high OH content) silica glass having a fictive temperature of 1300°C. [130] In one region, 800-1000 °C, the sample contracts to reach the metastable equilibrium volume. In the, 500-700 °C region, contraction occurs due to the healing of "open bonds", such as the linkage of Si-O units by regrouping the $Si-O_4$ tetrahedra. In the third region, 200-300 °C, the sample expands. The volume expansion in the synthetic silica glasses is attributed to the looseness and openness of the structure, and the higher mobility of the tetrahedra because of the water content.

These relaxation regions probably also occur in gel glasses, but at slightly lower temperatures because of their higher water, and non-bridging water content. The low temperature expansion may help to explain high coefficients of thermal expansion observed in gel glasses from ambient temperature to 250-300 °C. [131] On the other hand, contributions from the first region are lost in viscous sintering, while those from the second region are overshadowed by the condensation polymerization reaction. However, one exception has been reported by Brinker and co-workers. [132] In this case, a marked shrinkage in a TEOS gel occurs at 650°C with little corresponding weight loss. Contributions from the first region are overwhelmed by viscous sintering.

The skeletal density of a gel is of interest because small changes in skeletal density correspond to large changes in glass structure. Although, the generally accepted value for the density of fused silica is 2.20 g/cm^3, the actual values vary widely. Brunauer [133] reports the density of a precipitated silica gel to be 2.29± 0.01 g/cm^3, while Yamane [134] reports that the true or skeletal density of a TMOS gel is 1.98 g/cm^3 . Although, the skeletal density

is supposed to be independent of how a gel is formed and equal to 2.05 g/cm^3, in fact for silica produced at ambient temperature, the density depends on the heat treatment. Iler, [135] for example, reports that the density for colloidal silica is 2.18 g/cm^3 after heating to 100°C in helium and 2.22 g/cm^3 after heating to 1000 °C. Brinker and co-workers [136] find a minimum density of 1.72 g/cm^3 after heating to 300 °C and a maximum of 2.38 g/cm^3 after heating to 700 °C, although the latter value is attributed to experimental error. Small angle X-ray scattering (SAXS) porosity plots [137] for TEOS gels after heating to 650°C reveal excess free volume, or density fluctuations on the molecular scale. BET measurements also revealed an unaccounted volume of 0.005 cm^3/g after heating to 650°C. However, all fluctuations disappear after heating to 900°C.

As a sample of fused silica is heated to 1000°C it expands slightly, and its density decreases. Between 1000 and 1500 °C, it contracts slightly, and its density increases. Above 1800 °C, fused silica expands rapidly such that at 2300 °C it has a density of 1.92 g/cm^3.[138]

4.4.5 Densification :

The final stage in the heat treatment of a gel is a reduction of surface area and pore volume by viscous sintering. Surface area and pore size of a gel is usually determined by nitrogen adsorption. This is referred to as the BET method and involves adsorbing and desorbing nitrogen from nitrogen helium mixtures at liquid nitrogen temperatures. The method is independent of whether the surface is hydrated, and is accurate if there are no pores smaller than about angstrom in diameter. [139] Gels with pore radii less than 3 Å irreversibly absorb nitrogen. [140]

Although it might be expected that viscous sintering decreases the average pore size , BET measurements [141] on TEOS gels and colloidal silica gels [142] show that the average pore size does not change. On the other hand, control heating leads to a step wise loss of surface area. [143]

TEOS gels are reported to lose about 10 to 25% of their surface area at temperatures that are too low for viscous sintering. This decrease in surface area without a corresponding decline in the average pore size may be due to collapsing micropores or surface diffusion, since micropores having a diameter less than 12 Å appear as surface area in a BET measurement. Since silica gels start to densify above 200 to 300 °C, dehydration polymerization may collapse these pores and prevent their rehydration.

Nogami and Moriya [144] report that the lowest temperature for producing a dense silica glass from an acid catalyzed TEOS gel is 700 °C. However, gels densify over a wide temperature range and constant rate of heating (CRH) sintering equations have been applied to understand the densification process. At intermediated temperatures, shrinkage is independent of the heating rate. [145] Whereas in the higher temperature viscous sintering range, plots of $\Delta L/L$, where L is the dimension of the sample before heating, and ΔL is the amount that the sample shrinks while heating, versus heating rate exhibit a minima at 9.36°C/min., and 2.5 °C/min. [146] However, Nogami and Moriya [147] claim that no equation could satisfactorily model the shrinkage of acid catalyzed gels.

The failure of CRH sintering equations is thought to be due to the fact that weight loss decreases as heating rate increases. [148] This means that a faster heating rate leads to a gel with a higher water content gel and lower viscosity. Although a faster heating rate gives a gel less time to shrink, the

lower viscosity implies that the gel will need less time to shrink. The increased heating rate may also lead to increased structural relaxation, which seems to be consistent with the lower viscosity, but inconsistent with the statement that decreasing the heating rate increases skeletal densification.

Part II

Experimental Section

1. Materials.

Iodotrimethylstannane, $(CH_3)_3SnI$, (Organometallics Inc., 97-99%.), bromotrimethylstannane, $(CH_3)_3SnBr$, (Aldrich Co., 95%), and chlorotrimethylstannane, $(CH_3)_3SnCl$, (Aldrich Co., 95%), were used without further purification since their absorption and infrared spectra agree with published spectra. [1] Chlorotriphenylstannane, $(C_6H_5)_3SnCl$, (Aldrich Co., 95.0 %), dichlorodiphenylstannane, $(C_6H_5)_2SnCl_2$, (J. T. Baker Chemical Co., 98.0 %), and trichlorophenylstannane, $(C_6H_5)SnCl_3$, (City Chemical Corporation, 97.0 %), were also used without further purification since their infrared and electronic spectra also agreed with published spectra. [2, 3] All the organotin compounds were stored in the dark at cool temperatures to avoid degradation. Ironpentacarbonyl, $Fe(CO)_5$, (Pressure Chemical Co. 98.0%) was vacuum distilled and stored in a freezer under an inert atmosphere. UV-visible and IR spectra of the distilled complex agreed with published spectra.

Sodium azide, NaN_3 (Fisher Scientific., 95%), crystalline iodine (Aldrich Co., 99.9%), silver acetate, $AgCH_3CO_2$, (Aldrich Co., 99.9%), silver nitrate, $AgNO_3$, (Aldrich Co., 99.9%), Tetramethylorthosilicate, TMOS, $Si(OCH_3)_4$, (Aldrich Co., 95.0%), and reagent grade soluble starch, (Fisher Scientific, 95.0%), were used without further purification. All solvents were spectroscopic quality, (Aldrich Co., gold label > 99%), and

were distilled and dried over molecular sieves prior to use.

Phenyltinazides, $(C_6H_5)_{(4-n)}Sn(N_3)_n$, were synthesized according to the procedure of Thayer and West, [4] i.e.,

$$(C_6H_5)_{(4-n)}SnCl_n \xrightarrow{NaN_3} (C_6H_5)_{(4-n)}Sn(N_3)_n \qquad 1.1$$

A volume of a 0.08M aqueous solution of NaN_3 was added to an ethanol solution 0.1M in $(C_6H_5)_3SnCl$, and the mixture refluxed for two hours. The volumes of reagent solutions were varied depending on the stoichiometry of the reaction, and the amount of product desired. After refluxing, the solution was cooled in an ice bath (0°C) until white crystals precipitated from solution. The product was filtered off and twice recrystallized in hexane. The melting point of the compounds are listed along with other physical data in Table 3.1 Part I. The IR and NMR spectra of the compounds agreed with the published data and spectral data is sumarized in Table 2.5 Part III.

Potassium ferrioxalate, $K_3Fe(C_2O_4)$, was synthesized according to the procedure of Hatchard and Parker [5] and recrystallized three times from hot water. The 0.2% 1,10 phenantroline monohydrate (Aldrich Co., 97%) solution was prepared when needed to avoid degradation problems. [6] The buffer solution was prepared by diluting 600 ml of 1.0 N sodium acetate and 360 ml of 1.0 N sulfuric acid, to 1.0 liter. Excitation intensities were determined with a 0.006M aqueous solution of $K3[Fe(C2O4)3]$ according to the procedure of Calvert and Pitts. [7]

Samples of code 7930 porous Vycor glass, in the form of 25mm x 25mm x 2mm plates, containing ~ 70 ± 21 Å cavities were obtained from the

Corning Glass Works. The glass plates were cleaned by first extracting them in a soxlytic extractor with a 50:50 acetone : distilled water mixture for 12 hours, and then twice with distilled water for an equivalent period of time. The extracted samples were dried under vacuum at 70 °C, and then calcined at 650 °C for ≥ 72 hours. The calcined samples were stored in a muffle furnace at 650°C until needed. Prior to use, they were transferred to a vacuum desiccator and cooled to room temperature under vacuum ($p \leq 10^{-3}$ torr).

Silica gels were prepared by the method of Zarsycky [8] using TMOS-methanol-water mixtures (Table 1.1). The TMOS, water and methanol were mixed for about 10 minutes, then a catalyst, ammonia, was added to facilitate the polymerization process. After adding the catalyst, the solution was transferred to different sized glass containers to achieve glass gels of the desired size and shape. For large samples, ~ 2 inches in diameter, the geling solution was poured onto liquid mercury. Casting the gel on mercury minimized the stresses that arise between the glass container and the gel during the drying process. The sample containers were then covered with polyethylene film and maintained at 60°C. Under these conditions, gelation occurred in approximately 2 hours. The gels were then cooled to room temperature (23°C) and allowed to dry for about 2-3 weeks. After drying at room temperature, the gels were heated to 60 °C under vacuum ($p \leq 1.0 \times 10^{-6}$ *torr*) for 12 hours. This additional drying was found to be necessary to prevent cracking during subsequent high temperature treatment. The gels were then heated to 650 °C at a heating rate of 20 °C/hour, followed by a dwelling time of 24 hours at 650 °C, and cooling to room temperature at a rate of 100 °C/hour.

Table 1.1 - Composition of silica xerogels by volume.

Sample #	TMOS (ml)	MeOH (ml)	H_2O(ml)	NH_4OH (ml)
1	6.00	4.00	3.0	1.0
2	6.00	10.00	3.0	1.0
3	6.00	15.00	3.0	1.0
4	6.00	20.00	3.0	1.0
5	6.00	25.00	3.0	1.0
6	6.00	35.00	3.0	1.0

2. Impregnation Procedures.

The problem is to diffuse and organometallic compound through the cavities of a porous glass and obtained a homogeneous distribution. Since the goal is to increase the refractive index of the glass at selected areas, the diffusion process must be controlled. Impregnation of PVG plates, glass gels, or crushed PVG (50 to 400 mesh), was accomplished by either solution adsorption or vapor deposition.

2.1 Solution adsorption.

A weighed, calcined PVG plate was mounted upright in an Eastman Kodak chromatography tank (catalog # 13265). An aliquot of a solution of known concentration and sufficient volume, usually 50.0 ml, to completely immerse the glass plate was added to the tank. The tank was covered and kept in the dark at room temperature, ~ 25 °C. Samples containing from 10^{-9} to 10^{-4} mol of adsorbate/gr. of PVG were prepared by varying the molarity of the impregnating solution, the exposure time, or both. The number of moles adsorbed on the glass was determined by measuring the decrease in absorbance of the impregnated solution via the relation :

$$\frac{A_{Initial}^{Solution}}{A_{Final}^{Solution}} = \frac{M_{Initial}^{Solution}}{M_{Final}^{Solution}} \qquad 2.1$$

where

$$\text{moles adsorbed} = M_{Initial}^{Solution} - M_{Final}^{Solution}$$

The impregnated glass sample was removed from the tank and attached to a Teflon sample holder. The sample was then mounted vertically in a 30mm x 15mm x 75mm rectangular quartz cell, and attached to an upper section equipped with a 60 mm O-ring, a side arm and a high vacuum valve, (Figure 2.1). The unit was then attached to a vacuum line, and the solvent incorporated during impregnation was removed under a vacuum of 1.0×10^{-3} torr at room temperature for a period of 1.0 hour.

Absorption spectra of the dried samples were recorded from 700-185 nm, and corrected by subtracting the spectrum of a freshly calcined PVG sample recorded under identical conditions. A calibration curve, similar to that in Figure 2.2, was constructed by plotting the absorbance of the glass at specific wavelength vs. the number of moles adsorbed. The plots were used in the quantum yield measurements to determine the number of moled that underwent reaction. The error in the procedure was calculated to be ~ 10.0 - 15.0 %, with the largest error at the high concentration loadings. Relative extinction coefficients of compounds adsorbed in the glass were obtained from slopes of the plots.

Figure 2.1 - Photochemical degassing cell.

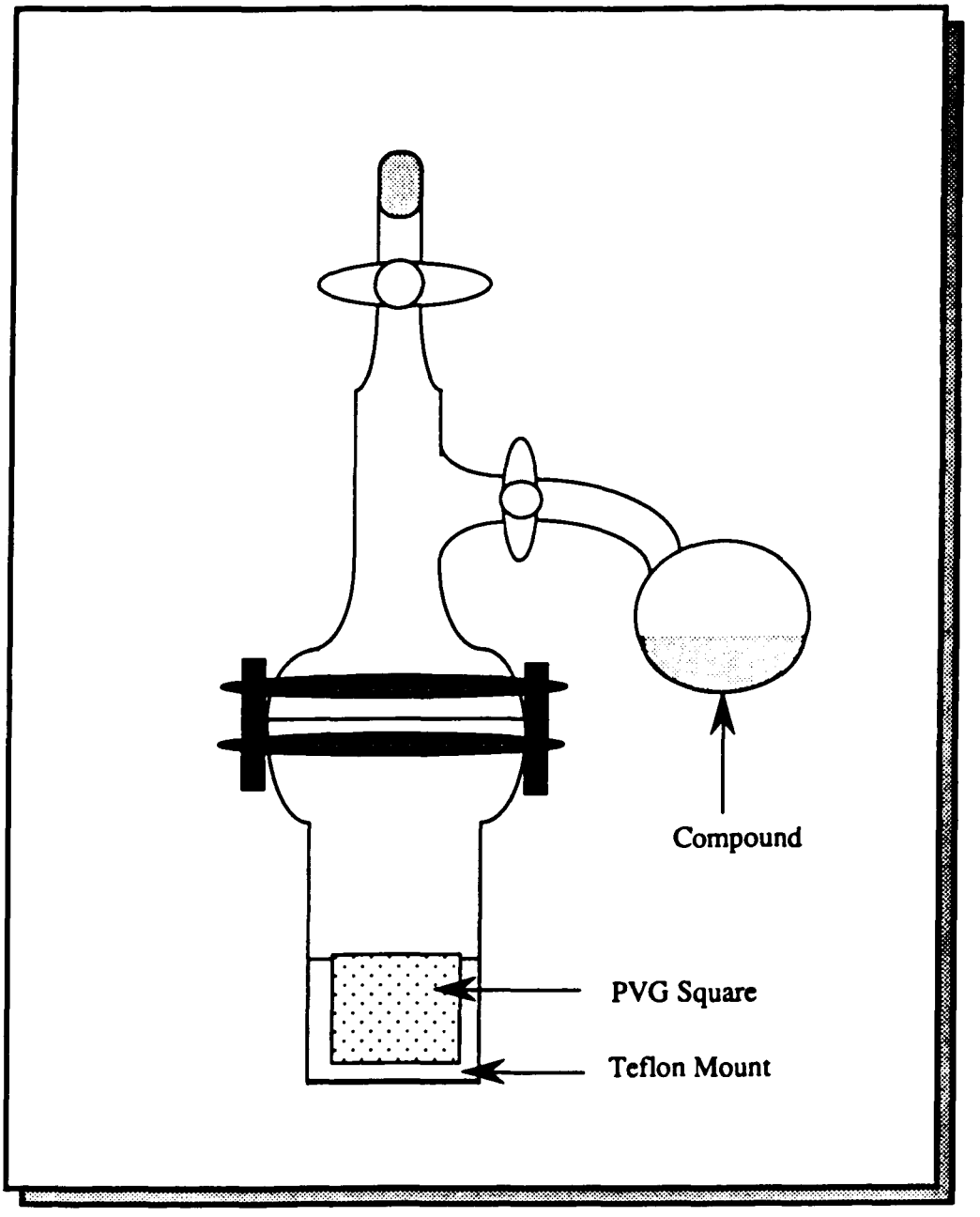

Figure 2.2 - Absorption calibration curb : Moles adsorbed of $(CH_3)_3SnI$/ g. of PVG vs. Absorption intensity at 230 nm.

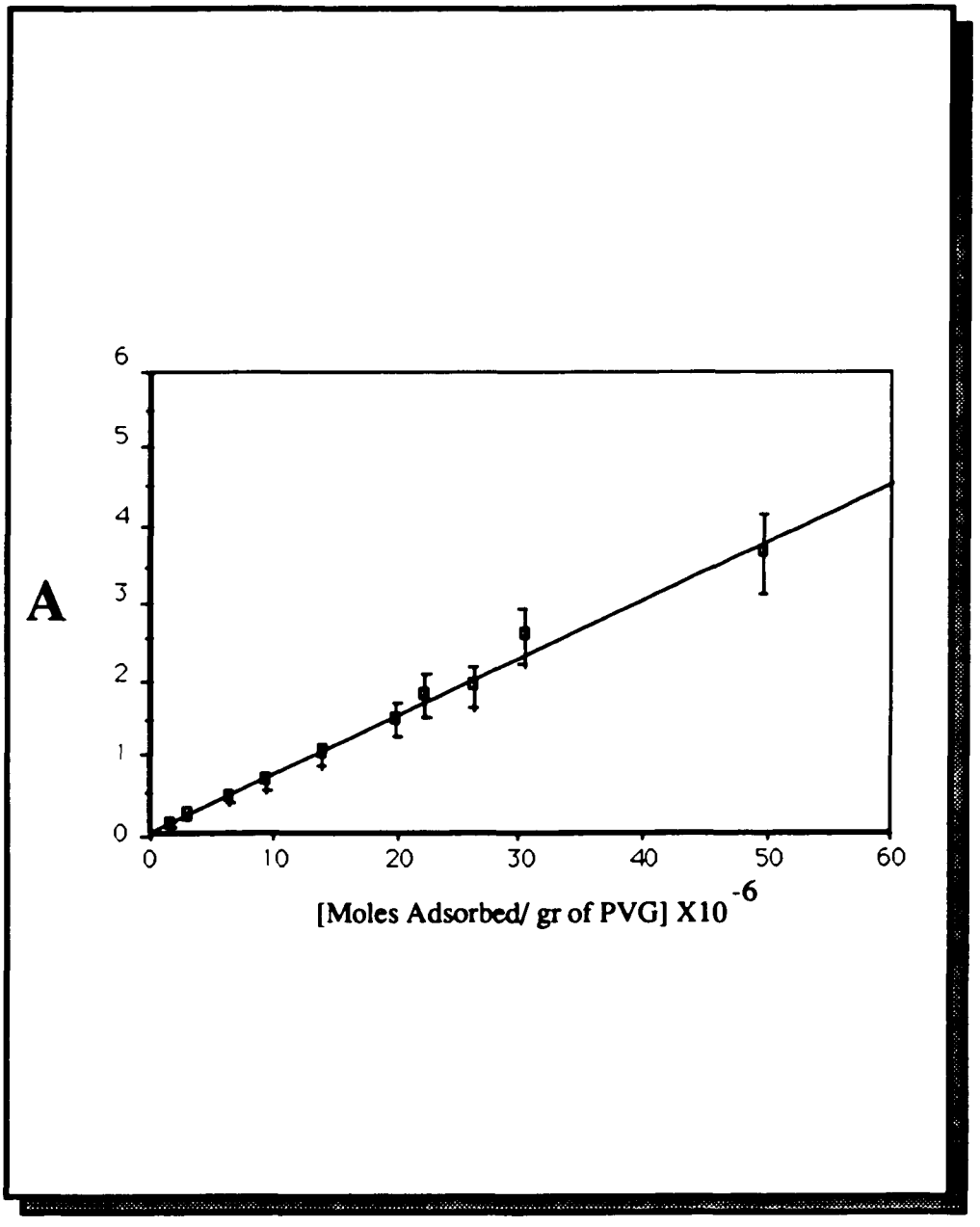

2.2 Vapor deposition.

Vapor deposition was used to impregnate PVG with $(CH_3)_3SnI$, $(CH_3)_3SnBr$, $(CH_3)_3SnCl$, $(C_6H_5)SnCl_3$, and $Fe(CO)_5$, since these reagents exhibit sufficient volatility at room temperature, ~ 25 °C. Different sublimation apparati were used to impregnate the solid and powder samples. To impregnate PVG plates and the solid glass gels, the samples were mounted vertically in a Teflon sample holder, which was mounted on top of a weighing dish that contained a 10 ml glass petrie dish (Figure 2.3). The weighing dish was covered by a metal grid with a mesh size of $1mm^2$. Between 100 to 200 µl of the pure compound were placed in the petrie dish along with a micro magnetic stirring bar, and the entire apparatus was placed in a bell jar. The bell jar was covered with aluminum foil to prevent photodecomposition during impregnation, and the entire apparatus was placed on a hot plate stirrer, evacuated to a pressure of 10^{-3} torr, and if necessary, warmed to increase volatility of the reagent. The rate of adsorption and the number of moles adsorbed was followed by measuring the absorption spectra of the glass as a function of exposure time.

In another sublimation apparatus, (Figure 2.4), a weighed sample of powder glass, usually about 300 mg, was place in the glass cup and suspended in the middle of the apparatus. 100 to 200 µl of the pure compound was placed in the bottom of the flask, and the cell and its contents were degassed by freeze-pump-thaw cycles. The evacuated cell was then closed off and allowed to equilibrate at room temperature to sublime the compound onto the glass powder. All impregnations, whether by sublimation or solution impregnation, were carried out in the dark to avoid

Figure 2.3 - Glass sublimation apparatus.

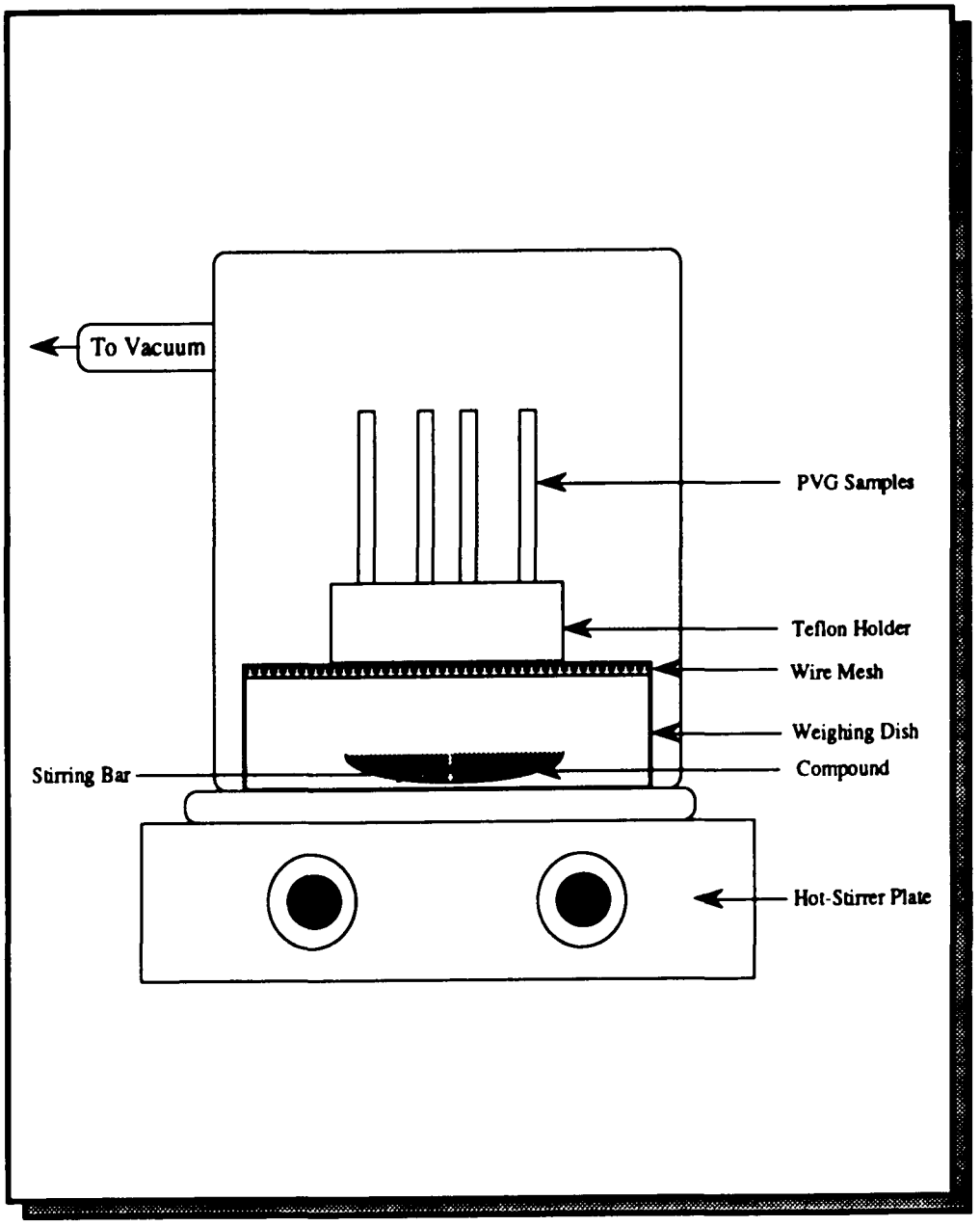

Figure 2.4 - Powder sublimation cell.

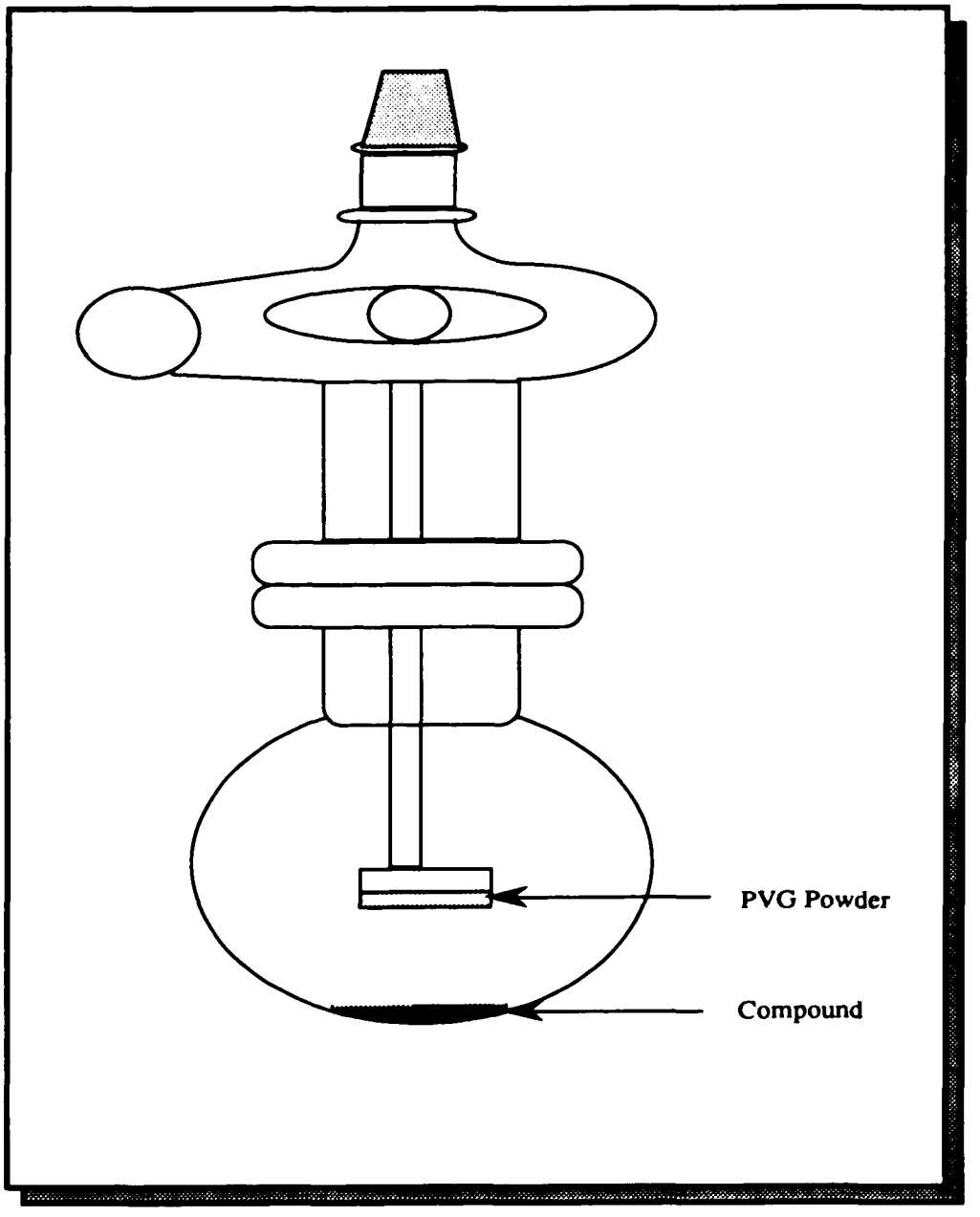

possible degradations from photolytic events.

3. Photochemical Techniques.

3.1 Solution.

In preparative experiments, 250.0 mls. of a solution ranging from $1.0x10^{-4}$ - $1.0x10^{-9}$ M in the reagent were placed in a tubular quartz cell. The solution was deaerated by nitrogen or helium bubbling, and mounted upright (Figure 3.1a) in a Rayonet Reactor (Southern New England Ultraviolet Corp.) equipped with either 254-, 310-, or 355 nm bulbs. The cell was either closed off after deaeration, or bubbling was continued as a means to stir the solution during photolysis. The solution was sampled periodically and the extent of reaction was analyzed spectrophotometrically.

Following photolysis, the solvent volume was reduced by vacuum distillation at temperatures ≤ 60 °C. Precipitates were removed by filtration and analyzed by means of the physical techniques described below. The volume of the filtrate was reduced further by vacuum distillation and also examined by these techniques.

In a kinetic experiment, a 5.0 ml aliquot of a solution of known concentration was placed in the side arm of a cell (Figure 3.1b) and degassed, ($p \leq 5.0x10^{-5}$ torr), by three freeze-pump-thaw cycles. After degassing, the cell was closed off, removed from the vacuum line, and the tipped to flow the degassed solution into a 1.0 cm pathlength fused quartz

Figure 3.1 - Arrangement and cells for preparative and kinetic experiments.

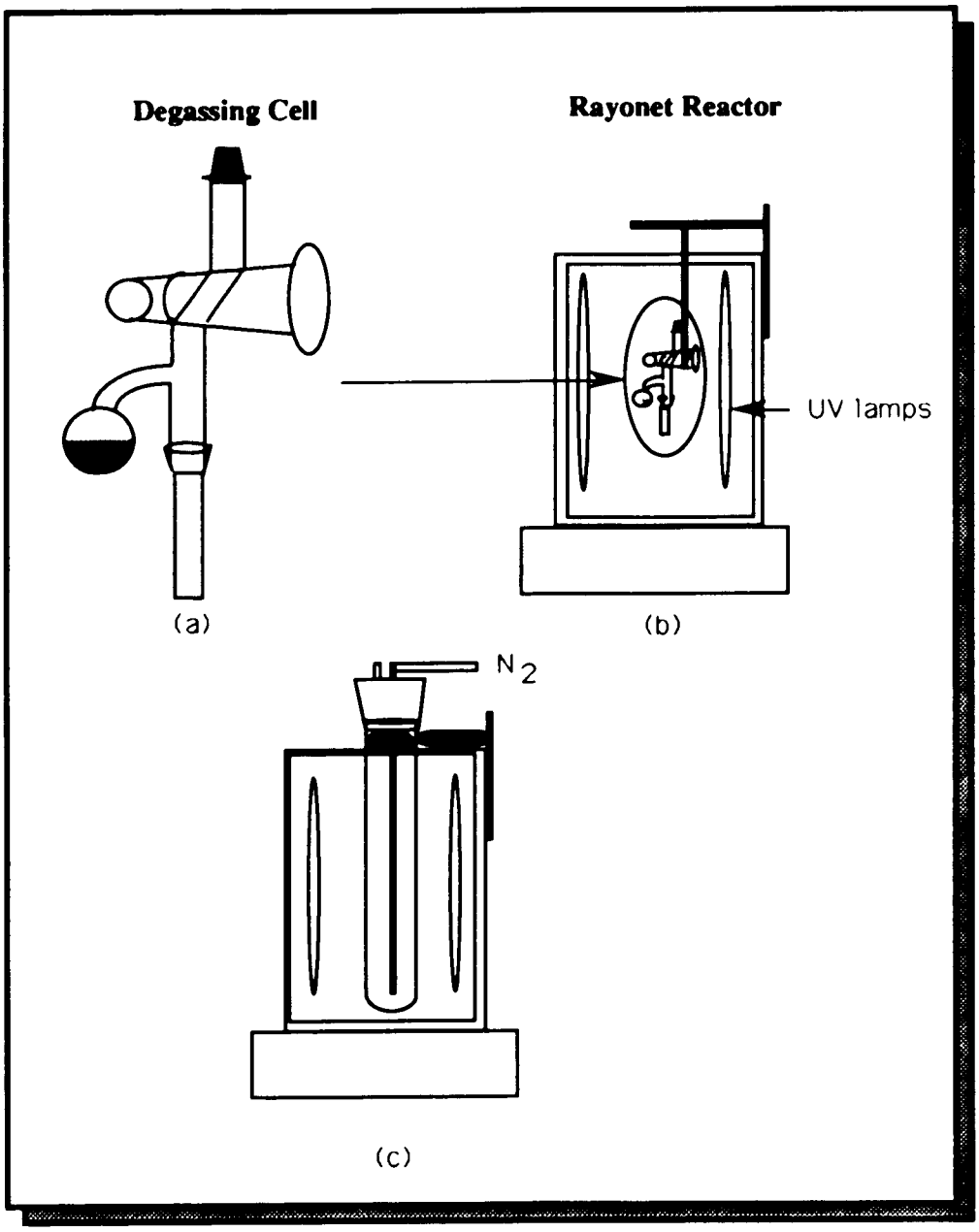

cell. The cell was then suspended in the Rayonet Reactor, (Figure 3.1c).

The degassed samples were irradiated with either 254-, 310-, 355- nm light. Electronic spectra were recorded periodically to determine the rates of starting material disappearance and product appearance. The light intensity incident on the cell, I_0, was determine by ferrioxalate actinometry. Typical intensities at 254-, 310-, and 355- nm were 1.22×10^{-7}, 3.76×10^{-8}, and 2.0×10^{-9} (eisntein/ cm^2- sec.), respectively.

Quantum yields of disappearance or product appearance, Φ, were calculated from the initial rates of change, d[A]/dt, and the adsorbed intensities, I_a, i.e.

$$\Phi = \frac{d[A]/dt}{I_a} \qquad 2.3$$

Rates were determine spectroscopically, and the adsorbed intensity, I_a, was calculated from the initial intensity, I_0, by the relationship in equation II.4:

$$I_a = I_0 (1 - 10^{-A_\lambda}) \qquad 2.4$$

where A_λ is the absorbance of the starting material at the excitation wavelength. Since A_λ changes during photolysis, in general, the reactions were limited to $\leq$ 15% conversion, and A_λ was taken to be equivalent to its initial value. With larger percent conversions, A_λ was taken as the average of the initial and final absorbances at the excitation wavelength.

3.2 Glass.

As in the solution experiments, both preparative and kinetic experiments were carried out with the glass samples. However, since the photoproducts could not be desorbed intact from the glass, preparative refers to the generation of sufficient product for spectroscopic characterization. In the preparative experiments, a square glass sample was mounted upright in a Teflon mount and placed inside a quartz photolysis cell (Figure 2.1). Approximately 200 μl of pure $(CH_3)_3SnI$ was pipeted into the side arm of the cell, and degassed by three freeze-pump-thaw cycles. After degassing, the compound was flowed onto the glass and allowed to impregnate the glass. Periodically, the cell was tipped to flow the compound back into the side arm. The side arm valve was closed and the cell evacuated ($p \leq 10^{-6}$ torr). Absorption spectra of the glass were then recorded to determine the number of moles adsorbed. Once the desired number was obtained, the cell was attached to the vacuum line and evacuated for about 5 min to remove any residual unimpregnated compound. The absorption spectrum of the glass was again recorded to established the number of moles prior to photolysis. The cell was then mounted upright in the Rayonet reactor and the sample photolyzed with either 254-, 310-, or 355 nm light. Absorption spectra were recorded periodically during photolysis to determined the extent of the reaction.

Preparative experiments with impregnated powdered samples were also carried out in the diffuse reflectance cell of the FTIR. The glass powder samples were impregnated by sublimation (Figure 2.3), and transferred to

the sample cup of the diffuse reflectance cell equipped with a quartz window. The samples were either evacuated ($p \leq 10^{-6}$ torr) or irradiated in air with an Analamp Model #6254 Hg lamp FTIR. The photochemical reaction was followed by periodic recording of diffuse reflectance FTIR spectra.

In the kinetic experiments, an impregnated square glass sample was mounted in a quartz photolysis cell (Figure 2.1) and irradiated with either 254-, 310-, or 355-nm light in the Rayonet reactor. Absorption spectra were recorded periodically, typically every 10 seconds, to measure the rates of starting material disappearance and of product appearance. The light intensity incident on the glass sample was measured by ferrioxalate actinometry. To approximate the area of the glass sample exposed to the exciting light, a volume of the actinometric solution, usually 10 ml, that had a surface area very close to that of the glass was irradiated. Under these conditions, typical excitation intensities were 1.0×10^{-8} (Einstein/sec-cm^2). Nevertheless, there is an error in measuring the light incident onto a solid sample with a liquid phase actinometer. However, based on the geometries of the different samples the error is estimated to be $\leq 5\%$.

4. Photolithographic Techniques.

4.1 Image generation.

Most of the photolithographic experiments were carried out with porous Vycor glass or base catalyzed glass-gel samples impregnated with either $(CH_3)_3SnI$, or $Fe(CO)_5$. However, other organotinhalide compounds, such as $(CH_3)_3SnBr$ and $(CH_3)_3SnCl$, were also examined.

In most experiments, the initial impregnation levels were 1.0×10^{-4} mol adsorbed of each compound/grof glass. The impregnated samples were mounted in a photolithographic optical bench (Figure 4.1), where the excitation was focused through the mask and then onto the impregnated sample. All irradiations were carried out in air, and in most cases, with near UV light, since the masks transmitted light greater than 300 nm. The light sources were either an Illumination Industries 400 W Xe or a 150W Tungsten halogen lamp. Photolysis times were varied depending on the transmission of the mask and the desired depth of photodeposition in the glass. In general, the longer the exposure time, the deeper into the glass the photoproduct was deposited. With $(CH_3)_3SnI$ or $Fe(CO)_5$ impregnated samples, photolysis time range between 5 minutes to 4 hours.

After photolysis, the sample was transferred to a vacuum chamber and degassed at a pressure of 5.5×10^{-5} torr for 24 hours to remove the

Figure 4.1 - Photolithographic bench layout.

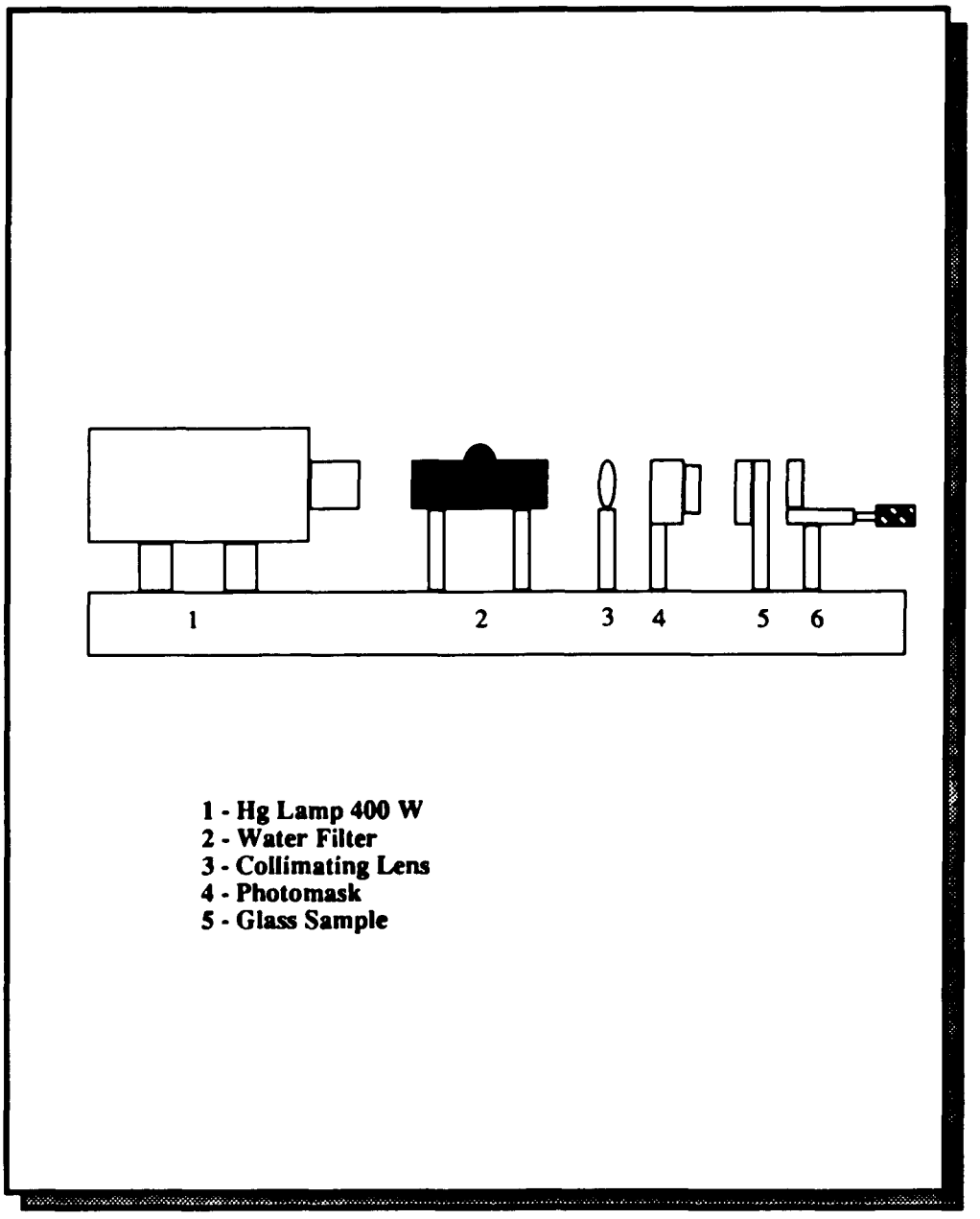

unphotolyzed compound. The samples were then heat treated according to the heating scheme given in Figure 4.2. Heating removes any unphotolysed adsorbate, and converts the photoproduct to a metal oxide. The startling result was that the porous glass could be heated to 1200 °C, which collapses the pore structure and produces a consolidated glass, without loss of image resolution. Consolidation occurred with a 30 % reduction in sample volume, but has no adverse effect on the photodeposited image.

4.2 Microlithography.

Microlithography experiments were carried out with the optical arrangement shown in Figure 4.3. The light source was either a pulsed Nd:YAG laser (Quanta Ray Model # 500) with either the 266-, or 355-nm excitation, or a Xe (Model #) 150 W lamp. The mask was mounted on a 1.5 cm diameter x 2mm thick 50:50 quartz beam splitter in the light path of a Zeiss Model MC368 microscope. The microscope was equipped with a 10x-, and 30x (DPlan 4) objectives. Quatrz optics in the objectives were used in order to withstand the full amplified power of the Nd:YAG laser, ~ 60 mJ/pulse.

In a routine experiment, the image of the mask was focused to a desire magnification with either of the two objectives onto an impregnated sample on the microscope sample stage. A 535 nm filter was used to prevent preexposure of the sample during the focusing operation. Once focusing was achieved, the sample was exposed. Exposure times varied depending on the source. With the Nd:YAG laser, exposure times were

Figure 4.2 - Thermal processing sintering cycle for PVG and sol-gel samples.

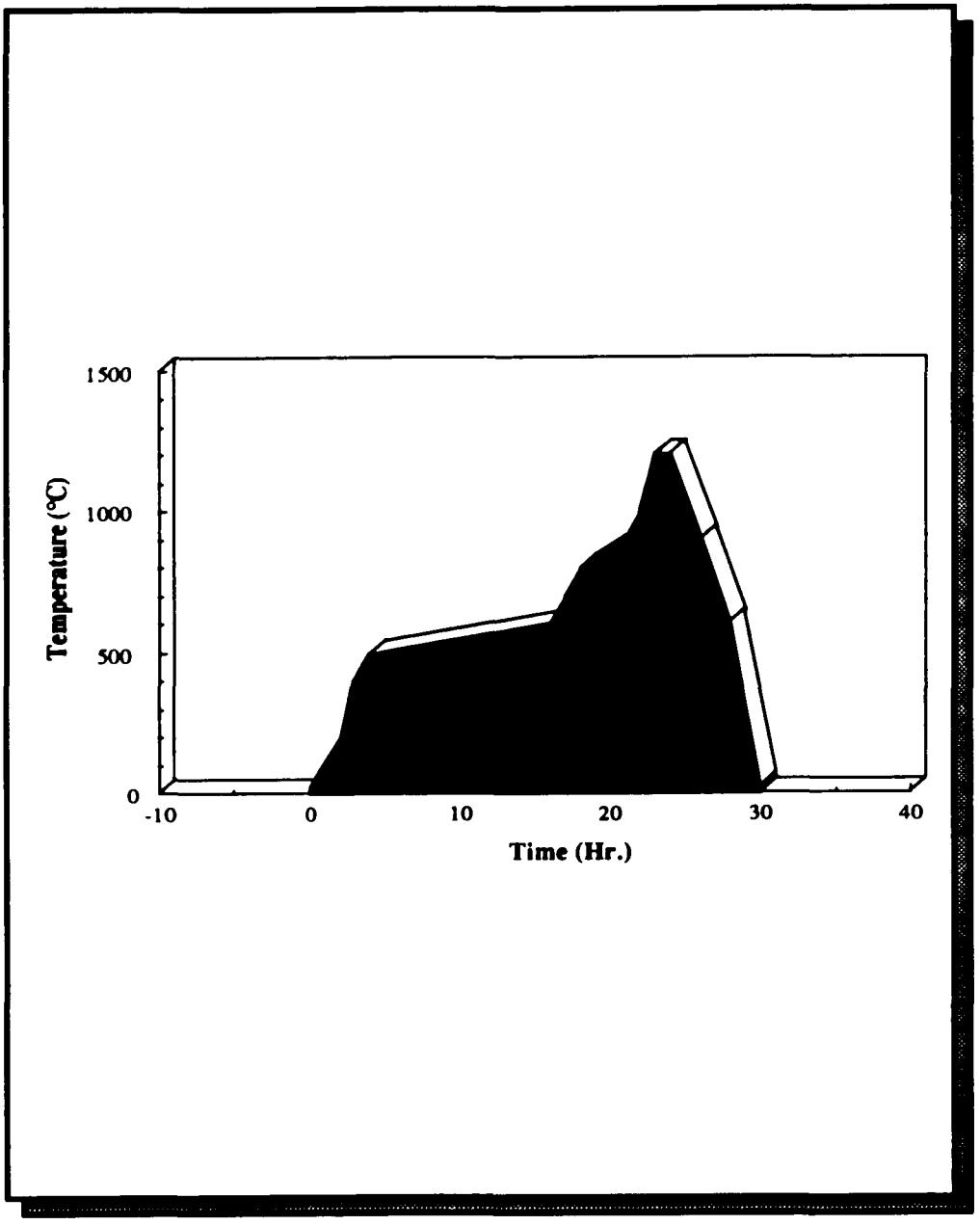

Figure 4.3 - Microlithography optical bench layout.

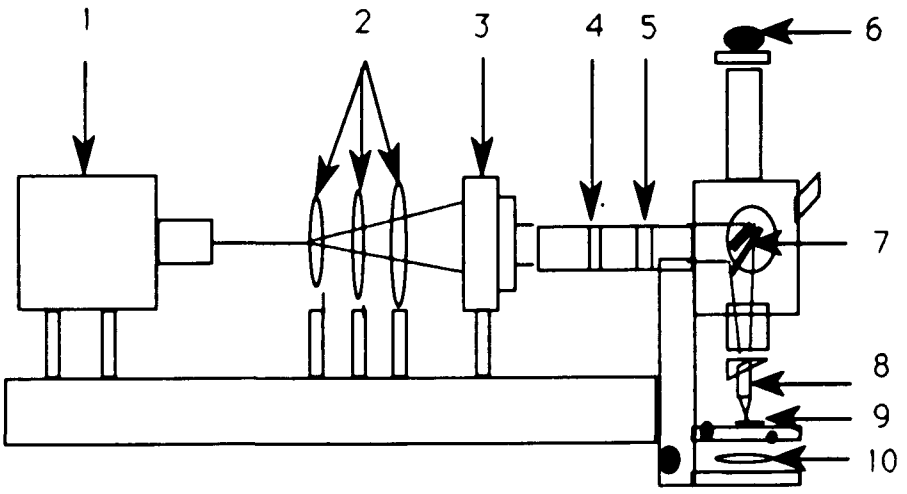

1- Nd:YAG Laser, or Hg Lamp 400 W

2- Beam expander, series of three lenses

3- Shuter

4- 500 nm Filter

5- Lens

6- 35 mm Camera

7- Photolitographic mask

8- 10x or 30x Objectives

9- Glass sample

10- 500 nm Filter.

usually one minute at a pulse rate of 60 pulses/minute, and an average power of 30 mJ/pulse. With the xenon lamp, exposures of 30 min were common.

4.3 Photomask design.

One of the biggest problems encountered in these studies was obtaining masks of appropriate resolution. Commercially available chrome masks are very expensive, the number of designs are limited, and of those available, few are applicable to the generation of integrated optics. Consequently, it was decided to design and fabricate our own masks.

Mask layouts were designed with a graphics program from the Macintosh computer and an 8.5x11 inch copy of the layout was printed. Figure 4.4 illustrates a mask design for photodepositing an optical waveguide pattern The hard copy was then reduced photographically by a factor of 200. This image was then photographed using a 300 x magnification zoom lens to obtain a 35mm slide. Although the resolution of the computer generated image was limited by the printer output (300 dpi), the mask obtained by means of this photolithographic procedure had a maximum resolution of 1.0 μm. The resolution of the computer generated mask was measured under the microscope, and compared to the resolution of a standard resolution mask (Air Force Standard Target Mask). A large variety of both positive and negatives mask designs were made in this way, to generate optical waveguides and integrated optical devices. The results obtained from the chrome mask and the computer generated mask gave the

Figure 4.4 - Computer generated photomask.

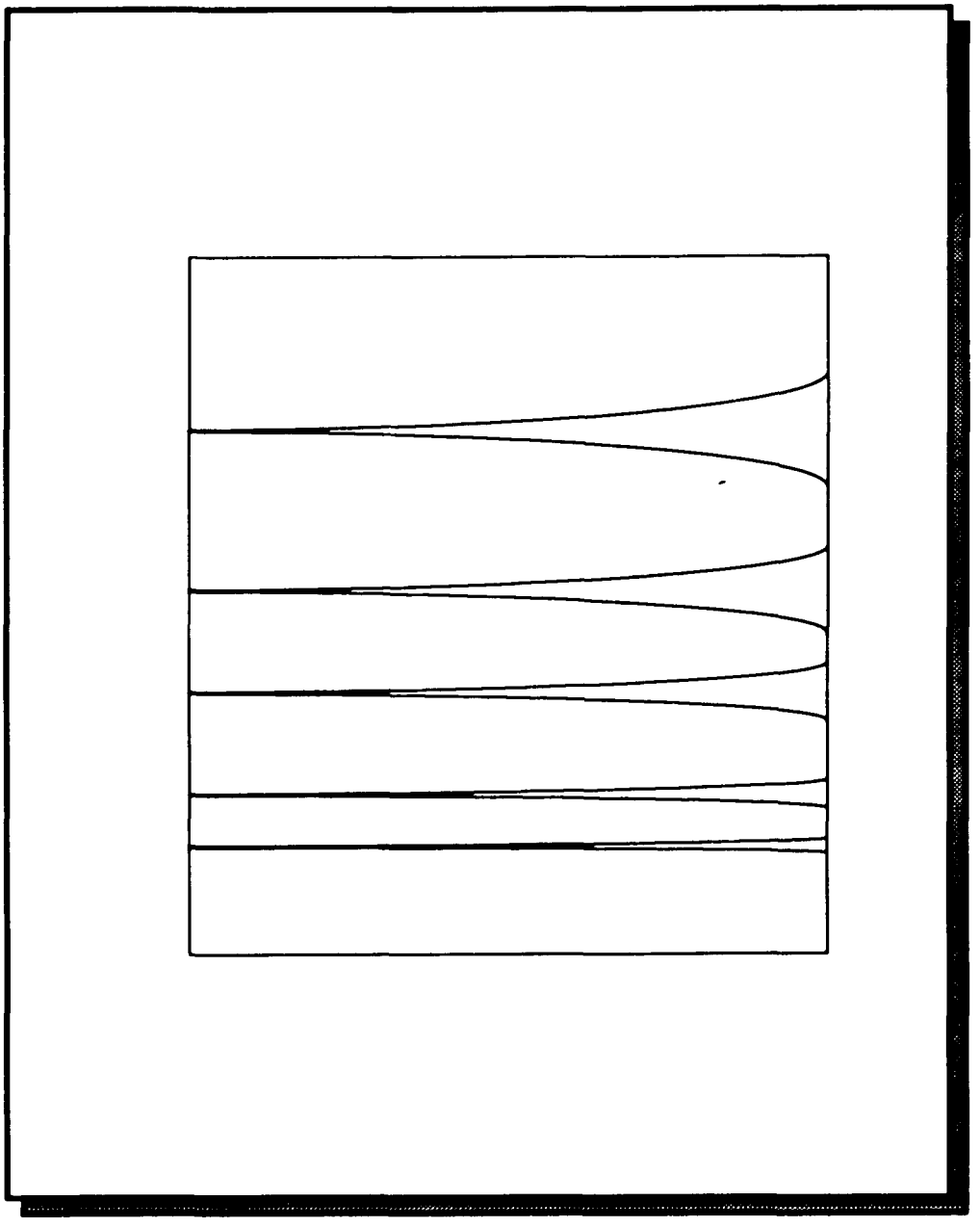

same resolution. The maximum resolution obtained, measured by optical microscopy, was 0.1 μm.

Other masks that were used included the U. S. Air Force standard chrome resolution mask, Ronchi Rulings (Edmund Scientific) of 150-, 300-, and 5000 lines/inch, and electron microscopy dispersive micro grids, (SPI Microscopy Supplies), of different shapes and size. The Air Force mask (Figure 4.5) has sets of lines ranging from a maximum line thickness of 50 μm, and a minimum line thickness of 0.01 μm with a decrease of 10 μm from set to set.

Figure 4.5 - Schematic diagram of the Air Force standard target mask. Basic element (50 μm - 0.001 μm series).

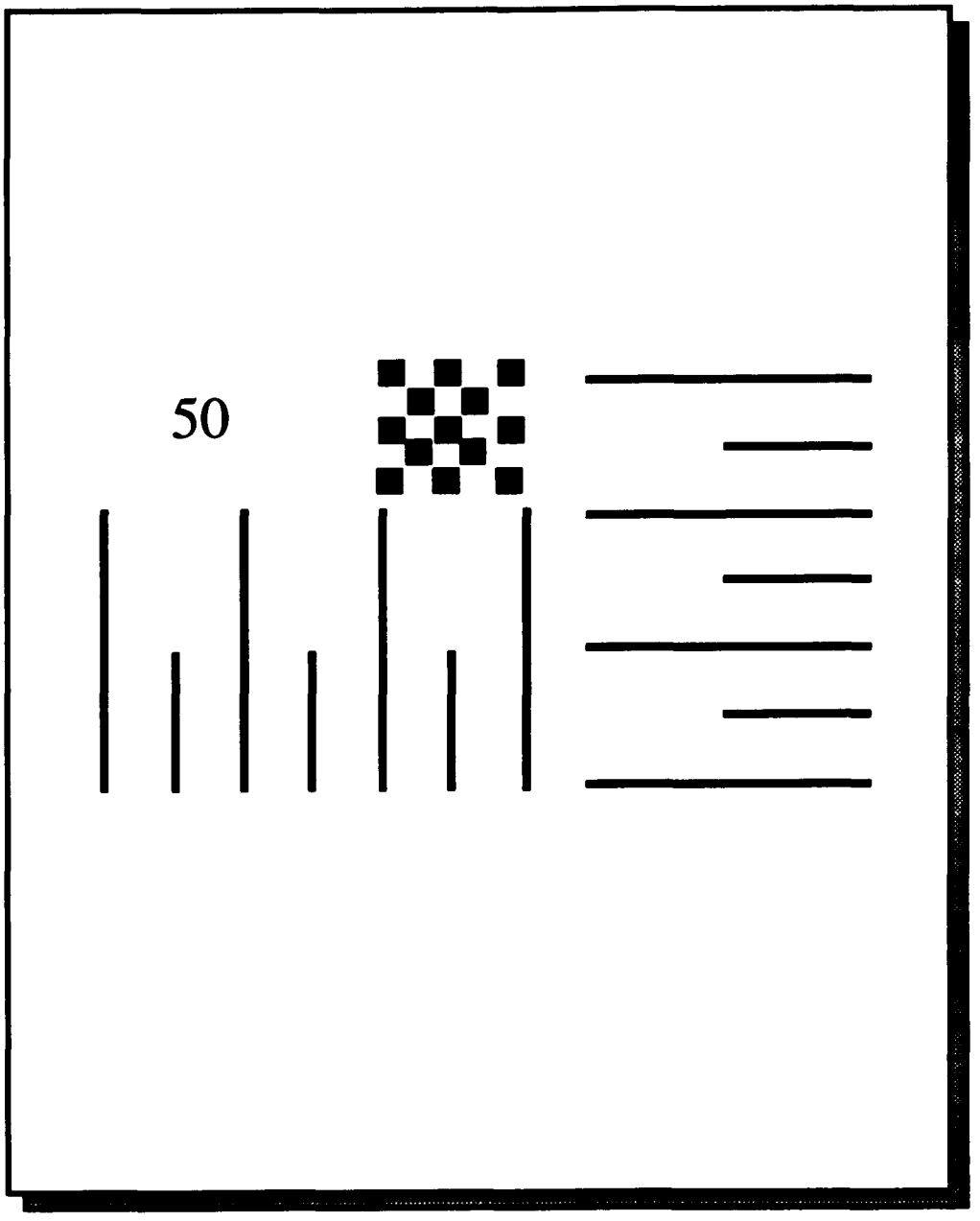

5. Physical Measurements.

Gaseous photoproducts were collected by expanding the gas in the photolysis cell into a Toepler pump and then transfer the gas to the sample loop (Figure 5.1). Generally, three cycles were needed to quantitatively transfer the gas to the loop. The loop was then closed off and attached to Gow Mac Model 69-100 gas chromatograph equipped with a Re-W thermal conductivity detector, and a 6' x 0.25" stainless steel column packed with 5Å (80 / 100 mesh) molecular sieve (Supelco). The conditions for N_2 analyses were an oven temperature of 100 °C, a flow rate of 40 ml/min, and a detector current of 150 mA. Helium (CP grade, Matheson Gas Products) was used as the carrier gas, and Nitrogen (HP grade, Matheson Gas Products) as a calibration standard. The detector response was calibrated by injecting a known pressure and volume of N_2, and recording the response (Figure 5.2) on a Shimadzu R-111 millivolt recorder A calibration plot (Figure 5.3), was constructed by plotting peak height vs. the number of moles of gas injected.

UV-visible spectra were recorded on a computerized AVIV model 14DS UV-VIS spectrophotometer. The wavelength range used in all measurements was from 700 to 185 nm with a scanning rate of 1.0nm / sec. The computer is equipped with a data manipulation software package that includes spectral subtraction, peak area integration, peak picking, and kinetics routines. Spectral subtractions were carried out by subtracting the spectra of the unphotolysed sample from that of the photolyzed sample.

Figure 5.1 - Diagram of Toepler pump set up.

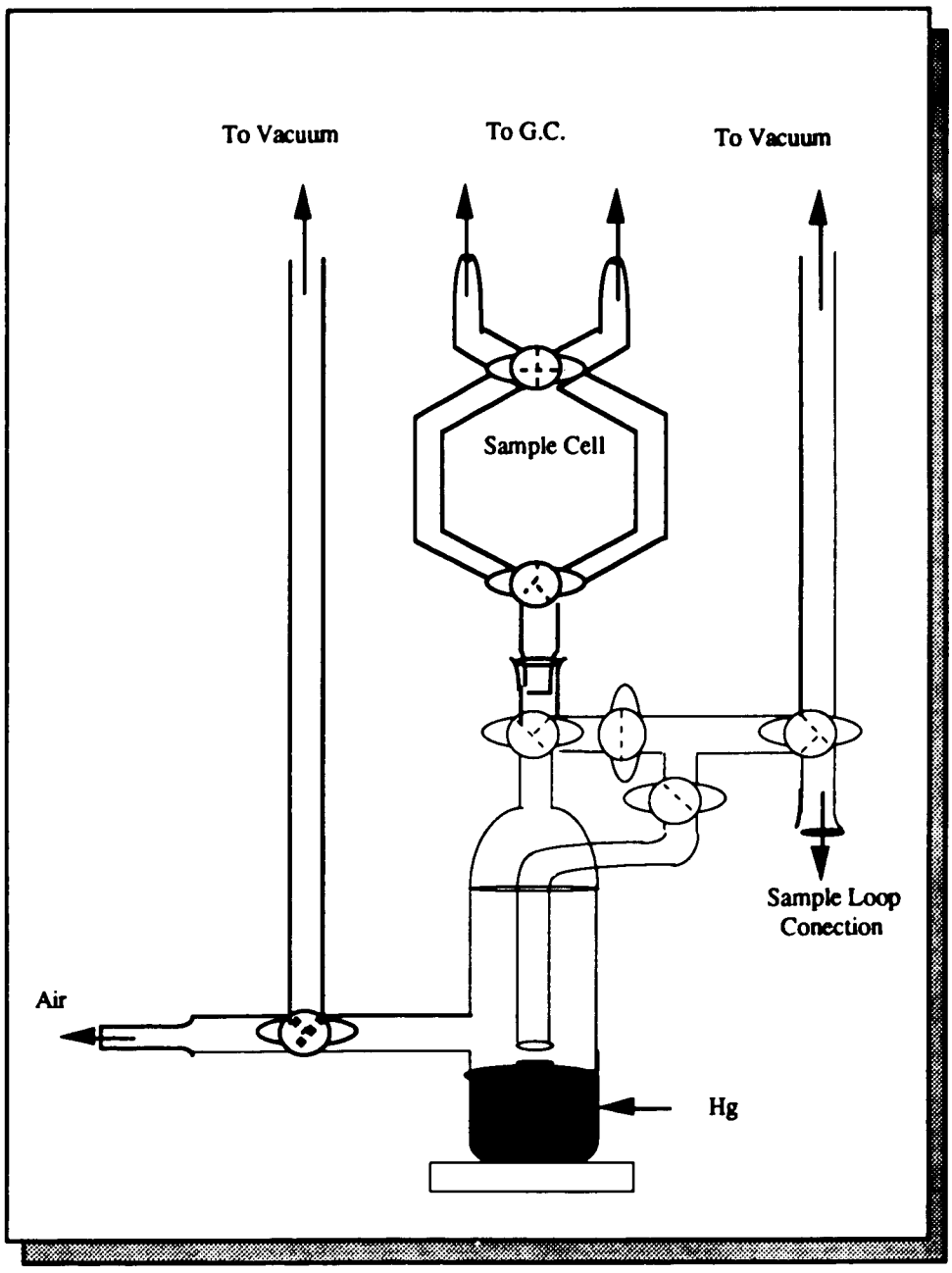

Figure 5.2 - Nitrogen gas chromatograph

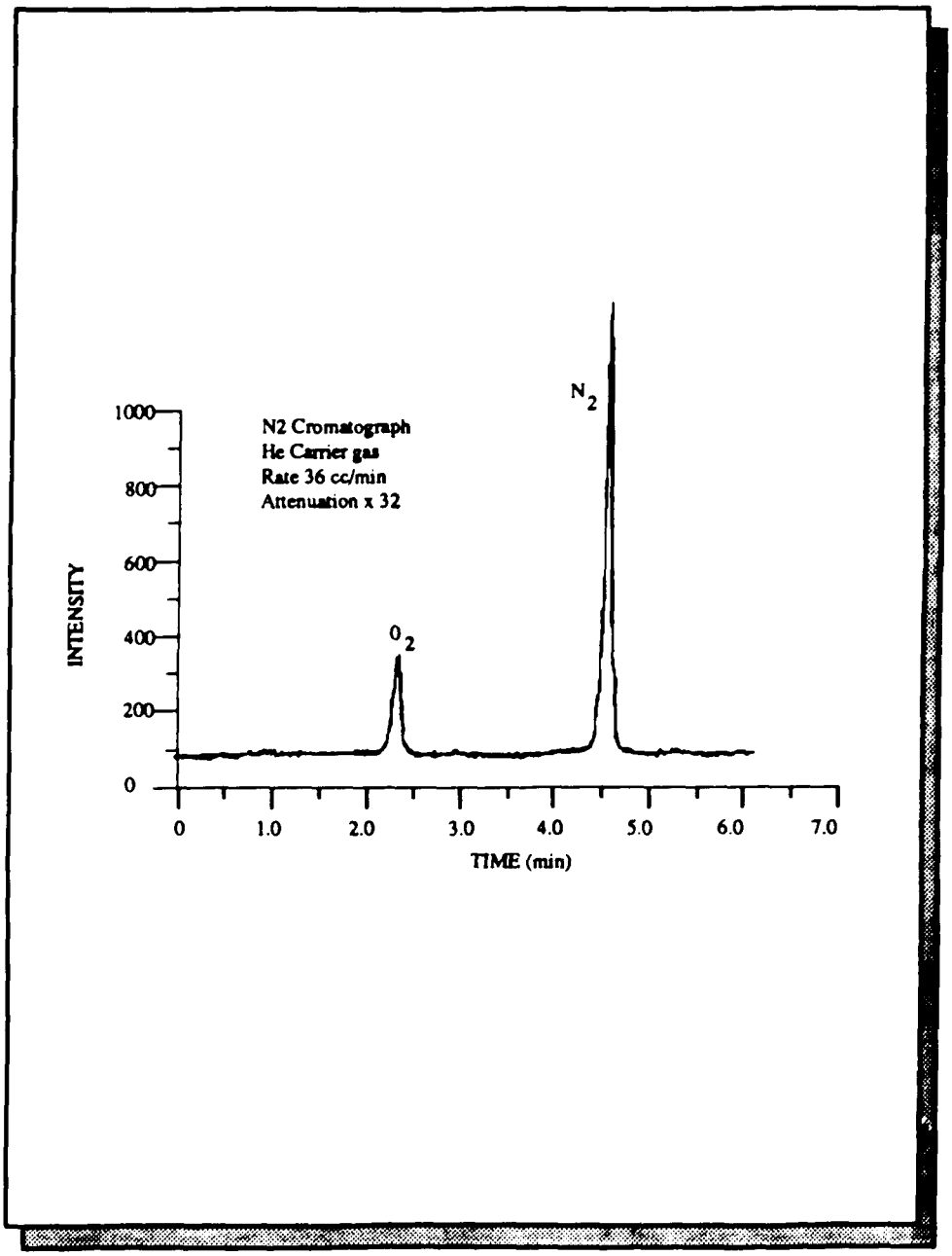

Figure 5.3 - Nitrogen calibration curve. Peak height vs. number of moles

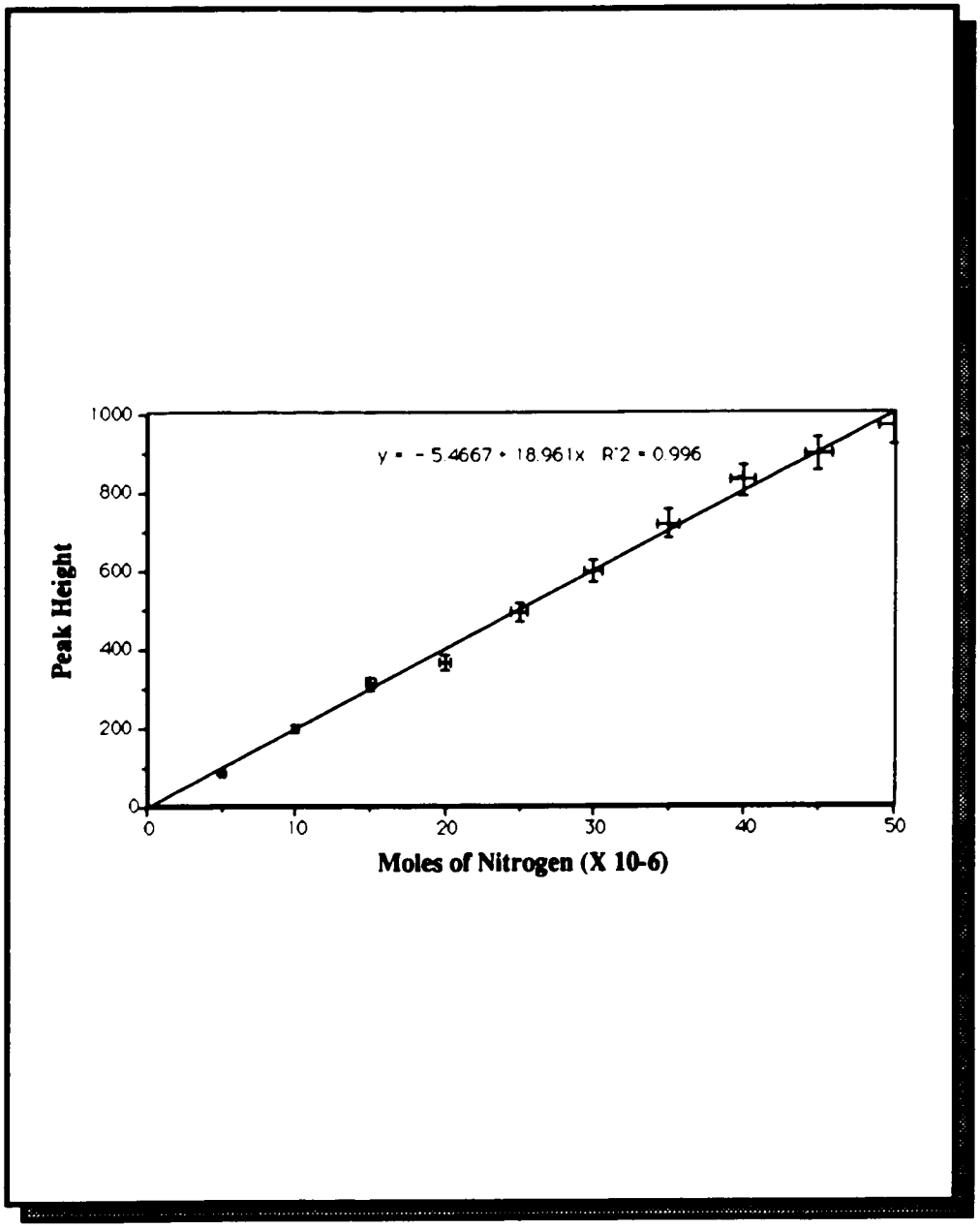

All samples were contained in 1 cm x 1cm x 4cm fused quartz cell (NSG Precision Cells, Inc.) equipped with a 10:30 quartz joint. The cells were attached to an upper section with a vacuum stopcock and a side arm for degassing solutions by freeze-pump-thaw cycles. In the latter procedure, the frozen samples (77 K) were evacuated to a pressure of $\leq 5.0 \times 10^{-5}$ torr. Solution spectra were recorded relative to the solvent, while spectra of the glass samples were recorded relative to air, or a sample of unimpregnated, calcined glass. When recorded relative to air, the absorption due to the glass was removed by spectral subtraction.

Emission spectra were recorded on a Perkin-Elmer Hitachi MPF-2A emission spectrophotometer equipped with a red sensitive Hamamatsu R818 photomultiplier. At ambient temperatures, solutions contained in a 1 cm x 1 cm quartz cells were deaerated by N_2 or He bubbling, or degassed by repetitive freeze-pump-thaw cycles. For low temperature (77K) emission spectra, the solutions were placed in a 2 mm diameter quartz tubes and mounted in a quartz Dewar filled with liquid N_2.

Raman spectra were obtained with a Spectra Physics 164-08 Ar^+ laser, and a SPEX 14018 1.0 meter double monochromator equipped with holographic ruled gratings. A 514.5 nm rejection filter was mounted before the entrance slit of the monochromator to remove the scattered laser radiation. The detector was a Princeton Instruments IRY-700G with an optical multichannel analyzer (OMA) self scanning photodiode (SPD) array detector of 1024 photodiodes and 700 channels. The detector was mounted on the first half of the monochromator to obtain maximum spectral coverage. All spectra were collected and processed by using OSMA (Optical Spectrophotometric Multichannel Analyzer) operating system and software package.

In a typical Raman experiment, a solution of $(CH_3)_3SnI$, $7.37x10^{-1}$ M, was placed in a 100 µl disposable Borosilicate micropipettes and the spectra recorded with 90° transverse excitation. To minimize the time between photolysis and spectral analysis, the sample mounted in the spectrometer was irradiated with an Analamp Model HG254 mercury lamp. Excitation was limited to wavelengths ≥ 300 nm by the transmittance of the micropipette sample holder. The excitation intensity, typically $1.0x10^{-8}$ einstein / cm^3-sec, was determined by ferrioxalate actinometry. In a typical run, the sample was irradiated for 5 sec, the lamp was shut off, and the Raman spectra recorded. The procedure was repeated using a new sample after each exposure to obtain the time dependence of the spectral changes.

Fourier transform infrared (FTIR) spectra were recorded on a Nicolet Model 5/20 DX FTIR spectrometer equipped with a narrow band MCT detector. The FTIR computer software provided all the setups, controls, and advanced analysis functions.

In the solution experiments, 10^{-2} to 10^{-1} M solutions of $(CH_3)_3SnI$ were irradiated in the Rayonet reactor. The solution was irradiated for 5 seconds and then sampled by means of the arrangement shown in Figure 5.4. A portion of the photolyte was pumped into a demountable 0.2 mm path length cell (Harrick Inc. Model # N930) equipped with NaCl, or KBr windows. The FTIR spectrum of the photolyte was recorded and the solution was then flushed into a 1.0 cm quartz cell. The photolyte was diluted with 5.0 ml of solvent and its absorption spectrum recorded to quantitate the extent of reaction. The FTIR scanning time was 10 seconds with a resolution of 4.0 cm^{-1}.

Time resolved, diffuse reflectance FTIR (DRIFT) spectra were recorded with a Harrick Scientific Inc. Model DRA-PMN diffuse reflectance

Figure 5.4 - FTIR Photolysis Set Up.

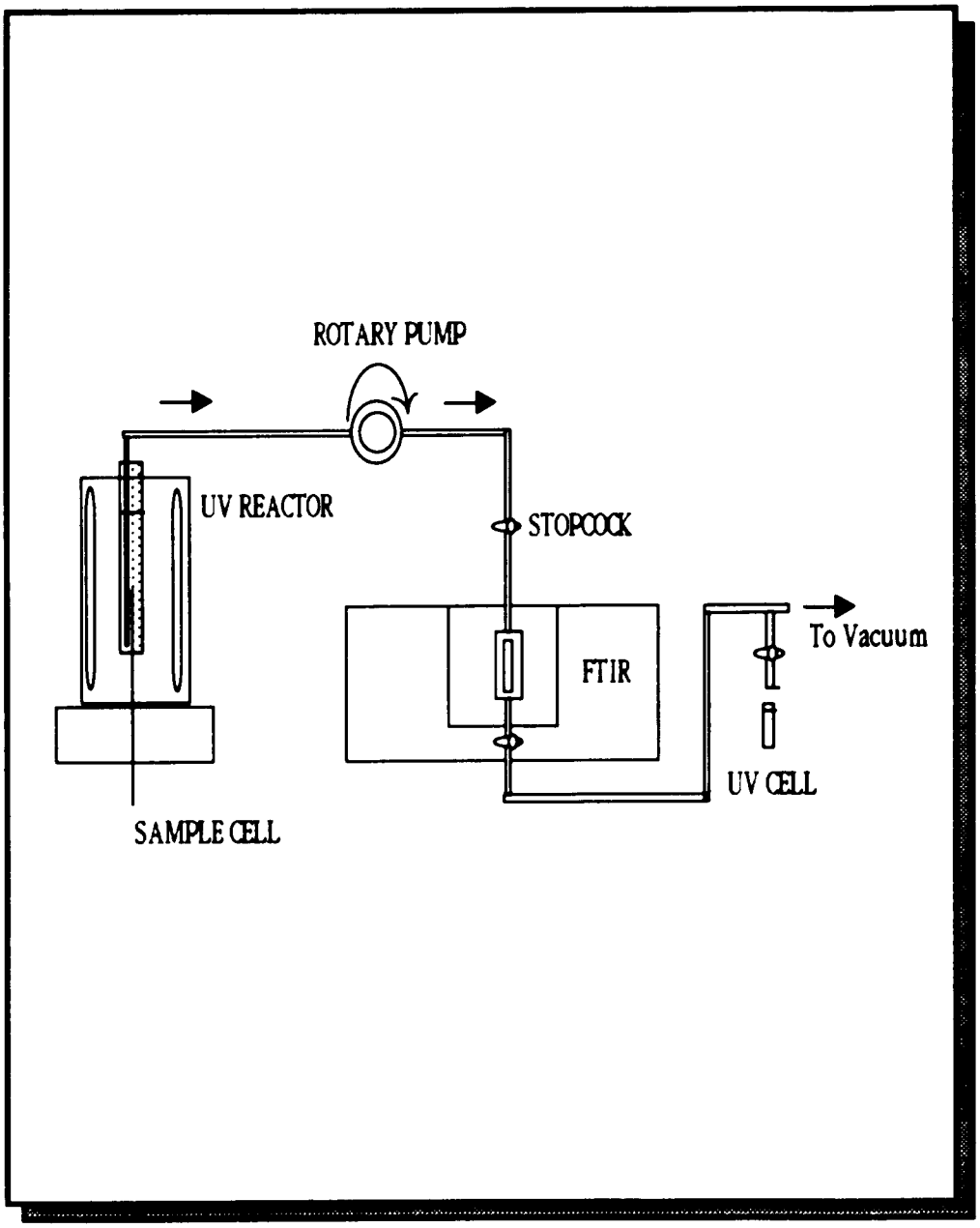

Figure 5.5 - High vacuum diffuse reflectance cell attachment for FTIR.

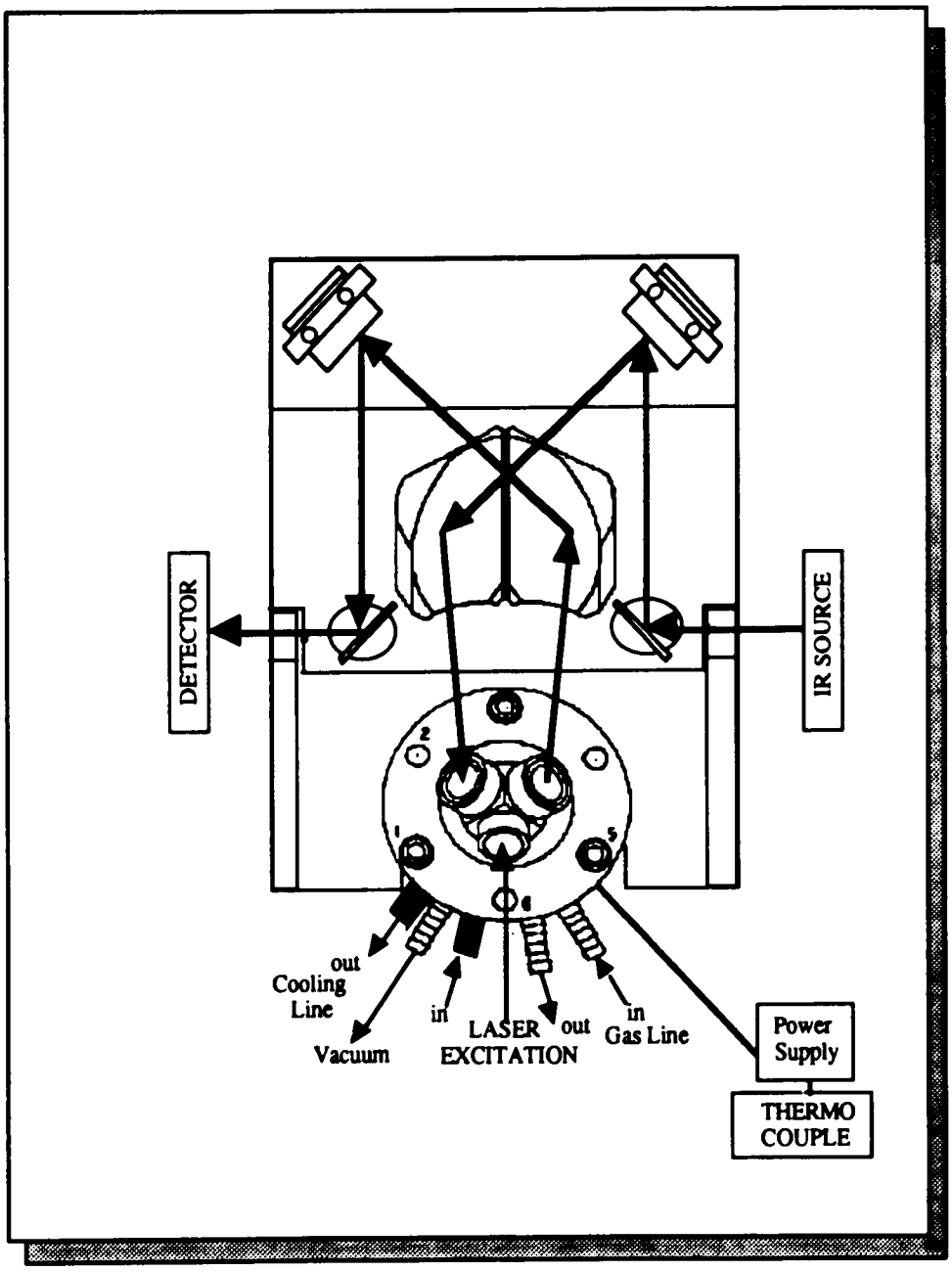

accessory (Figure 5.5). The sample compartment has two, 10 mm diameter CsI windows for transmission of the infrared radiation and a 10 mm quartz window for in situ photolysis. Ports are provided for evacuating the sample compartment, or passing a gaseous reagent through the powdered sample. In addition, ports for passing a coolant through the base of the sample holder and a 7.0 W heater, driven by an external temperature controller (Spectra-Tech) allows samples to be examined at temperatures ranging from ambient to 800 °C. A thermocouple in the sample holder monitors the temperature. The microreactor was attached to a vacuum manifold with an Edwards Model E2M5 forepump, and a CVC Model E01 oil-diffusion pump.

In a typical DRIFT experiment, 300 mg of a mixture composed of 30 mg of freshly calcined, crushed (200 mesh) PVG, and 270 mg of dry IR grade KBr, were placed in the 11.5 mm diameter x 5.0 mm deep sample holder. The FTIR spectrum of the crushed PVG-KBr mixture was recorded and saved on disk as the reference spectra. The mixture was then impregnated by expanding 200 µl of $(CH_3)_3SnI$ that had been degassed by repeated freeze-pump-thaw cycles through the PVG-KBr mixture. The extent of impregnation was monitored by measuring the growth of the C-H stretch peaks of $(CH_3)_3SnI$ at 2992, and 2926 cm^{-1}. The measured band intensity was compared to a calibration plot of concentration of $(CH_3)_3SnI$ in solution (Figure 5.6). In the calibration curve, the intensities of the 2992 cm^{-1} peak vs. the molar concentration of $(CH_3)_3SnI$ in ethanol were plotted. To justify the comparison of the 2992 cm^{-1} band on PVG and in solution, ethanol was chosen as the solvent, since both ethanol and the surface of PVG posses hydroxyl groups, and the relative intensities in each medium are similar. From this comparison, the loadings used in the DRIFT were generally $1.0 \pm 0.2 \times 10^{-4}$ moles/ g. of PVG.

Figure 5.6 - (CH3)3SnI FTIR concentration calibration Curve in ethanol

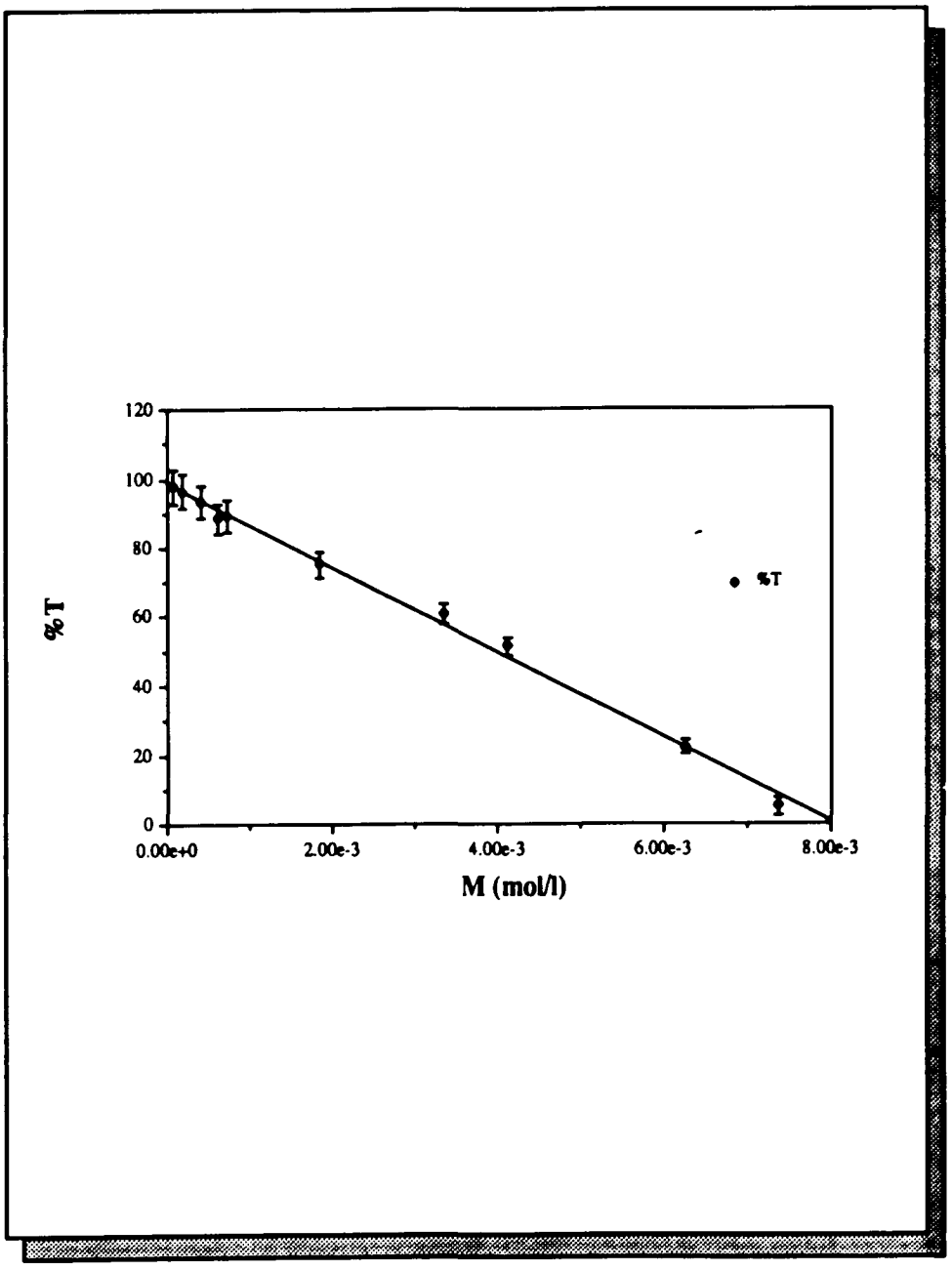

In a photochemical experiment, the initial spectrum of the unimpregnated sample was recorded and saved. The sample was then irradiated and spectra are recorded periodically during photolysis. A kinetics macro program, Appendix 3, was written to control the FTIR during data acquisition. The program directed the spectrometer to acquire and save an interferogram at predetermined intervals over a specific length of time, usually 60 to 180 seconds. The program was most useful during those kinetic experiments that required photolysis times of less than 30 seconds. Since operator manipulation of the FTIR takes about 30 sec per spectra, only one spectra could be obtained in such a short time. With the aid of the program, however, 30 successive interferograms could be recorded at one second intervals.

After photolysis, the interferometric data were Fourier transformed, and the photolyzed spectra were substrated from the reference spectrum recorded before photolysis. In this way, difference spectra were obtained in which disappearing peaks appear as negative absorptions, while developing peaks appear as a positive absorptions.

Cyclic voltametry measurements were recorded on a PAR electrochemistry system consisting of a PAR Model 273 (EG&G Princeton Applied Research) potentiostat analyzer driven by a PAR Model 175 universal programmer. The output was displayed on a Houston Instruments Model VP- 6424S Omnigraphic X-Y recorder. Voltammograms were recorded with a glassy carbon electrode (Fisher Scientific Model # 13-620-274), a Ag/AgCl combination reference electrode (Orion Model 9512), and a Pt wire auxiliary electrode at sweep rates varying from 20 to 500 mV/sec.

In a typical experiment, 100 µl of $(CH_3)_3SnI$ was dissolved in 100 ml

of an electrolyte solution composed of 0.1 M tetramethylammonium tetrafluoroborate in either hexane, acetonitrile, or ethanol. Immediately after the solution was prepared, a 5.0 μl aliquot was photolyzed for 60 sec with 254 nm light in the Rayonet reactor, 1.0 x 10^{-7} (einstein/cm^2-sec), and then analyzed electrochemically.

Thermal analyses were performed with a Perkin-Elmer 7 Series Thermal Analysis System equipped with thermal gravimetric analysis (TGA), thermo mechanical analysis (TMA), and differential scanning calorimetry (DSC) attachments. Instrument control and data manipulations were performed with a Perkin-Elmer 7700 Data Station. In a TGA experiment, for example, a 30-40 mg sample of PVG or a sol-gel glass was placed in a Pt sample cup. The samples were heated under 1 atm of dry nitrogen from 30 °C to 1400 °C at a rate of 5 °C/min.

Differential thermal analyses (DTA) were carried out on a Perkin-Elmer 1700 DTA System driven by a Perkin-Elmer System 4 microprocessor, and a Perkin-Elmer 3700 Thermal Analysis Data Station. The system was calibrated from 30 °C to 1200 °C with a gold standard, which indicated a 0.001% error for the gold transition temperature. DTA experiments were performed by weighing out ca. 15 mg samples of PVG or the gel glass in alumina sample cups. The samples were analyzed relative to a high purity alumina standard (Ferro Inc. Alumina A-310) under a N_2 atmosphere at a rate of 5 °C/min from 30 °C to 1450 °C.

Multipoint adsorption-desorption isotherms were measured using the continuous nitrogen sorption method. [9] Adsorption and desorption isotherms for PVG and TMOS gels were measured with a Omnisorp 360 BET Analyzer. The adsorption isotherms were analyzed following the well-known BET model

$$\frac{x}{V(1-x)} = \frac{1}{V_m C} + \frac{C-1}{V_m C} \qquad 5.1$$

where x is the partial pressure of nitrogen, V the volume of gas adsorbed, V_m the monolayer volume and C the heat adsorption constant. The monolayer volume (V_m) is related to the surface area A in $m^2 \cdot g^{-1}$ by

$$A = 10^{-18}\left(\frac{V_m}{22414}\right)\frac{a_m L}{W} \qquad 5.2$$

where a_m is the area of a nitrogen molecule (0.162 nm^2), L is Avogadro's number, and W the sample weight in grams.

The desorption isotherm was analyzed to obtain information on the pore size distribution using the Kelvin equation : [10]

$$\ln x = -\frac{2\sigma V_l}{RTr_p} \qquad 5.3$$

where x is the partial pressure of nitrogen, V_l is the molar volume of the liquid, r_p the pore radius, R the gas constant, and T the nitrogen temperature (77 °K).

Samples of ~ 20 mg for BET measurements were ground with an alumina mortar and pestle. Samples were weighed in the sample cell, and

then attached to the outgassing station of the BET analyzer. The samples were outgassed at $p \leq 10^{-5}$ torr at 200 °C for several hours to remove water as well as organic species that may be physically adsorbed to the pore surfaces. After cooling to room temperature, the holder was transferred to a liquid nitrogen bath for the adsorption and desorption measurements. N_2 was the adsorbate and the amount adsorbed was calculated from the gas flow multiplied by the time passed. The adsorption isotherm was measured with a nitrogen pressure ranging from 1.33×10^3 Pa (10 mm Hg) to 2.66×10^4 Pa (200 mm Hg). The reference pressure or the saturation pressure of N_2 was also recorded and remained in the vicinity of 775 mm Hg. The desorption isotherm experiment followed the adsorption, but took a much longer period of time. Desorption isotherms were measured with a N_2 pressure ranging from 1 atmosphere to 1.79×10^4 Pa (135 mm Hg).

To obtain an indication of the shape and scale of the microstructure, i.e., surface area and pore size distributions, samples were heated in flowing nitrogen at a rate of 1°C/min from 200 °C to 1200°C. The volume of pores with radius less than 50 Å was determined by first adsorbing pure nitrogen then switching to a mixture of nitrogen and helium. Isotherms were obtained with ten prepared mixtures of nitrogen and helium, and their surface area was measured from the isotherms.

Small angle x-ray scattering (SAXS) experiments were performed on the X-23A3 Microprobe beam line of the National Synchrotron Light Source at Brookhaven National Laboratory. Samples were exposed to 7.0 KeV x-rays and the scattered radiation was analyzed with a double-crystal Bonse-Hart type diffractometer, [11] using single crystal Ge (111) optics. SAXS intensities were placed in absolute units by correcting for background, sample thickness, source luminosity, and detector solid angle. Slit length

collimation effects were removed by Lake's method. [12]

In the SAXS experiments, PVG or gel glass plates were ground to a thickness of 50.0 μm in a Buehler Mininet polisher prior to impregnation, photolysis and heat treatment. Although it took approximately one day to reduce the thickness from 2mm to 50 μm, grinding was necessary to ensure adequate x-ray transmission through the sample. Transmission through the sample is given by Bragg's Law,

$$\left(\frac{dE}{dx}\right)_{S\rho_2 S_n O_2} = \frac{1}{M_{S_i O_2 S_n O_2}}\left[28\left(\frac{dE}{dx}\right)_{S_i} + 32\left(\frac{dE}{dx}\right)_O\right] + \left[119\left(\frac{dE}{dx}\right)_{S_n} + 32\left(\frac{dE}{dx}\right)_O\right] \qquad 5.4$$

where $\left(\frac{dE}{dx}\right)$ is the stopping potential of a particular atom, and M is its molecular weight. Using the stopping potential for Fe and Sn, the maximum thickness of the impregnated samples was calculated to be 50 μm.

Samples containing high and low loadings were examined by the SAXS technique, which correspond to initial loadings of 10^{-4} mol/gr. and 10^{-6} mol/gr., respectively. To examine metal diffusion within the glasses, the thermal histories of the samples were also varied. In this case, some of the samples containing the different loadings were heated to 650°C while others were heated to 1200°C, which is sufficient to consolidate the glass. In order to monitor diffusion within the glass matrix, however, impregnation was limited through one face of the glass plates. Samples were

impregnated by the previously described procedures except that, to achieve asymmetric impregnation, two glass plates were placed face to face and held together with teflon tape. In this way, only one surface of each glass plate was exposed to the compound during sublimation. The number of moles adsorbed onto each plate was determine by the previously described spectral techniques, and these data showed that the number of moles adsorbed onto each plate differed by < 15%. With each pair of asymmetrically impregnated samples, one was photolyzed (I_a = 1.00 x 10^{-5} einstein/sec- cm^2) to 75% consumption of the starting adsorbate, while the other, which was not photolyzed, was used as a reference. Once the photolysis was completed, the photolyzed and reference samples were placed in vacuum cells and kept under vacuum (p ~ 5.5≥10^{-5} torr) for 48 hours to remove the unphotolyzed material. The samples were then transferred to a Lindbergh heavy duty tube furnace and heated at an approximate rate of 2°C / min. to either 650°C or 1200°C.

Rutherford Backscattering experiments were carried out using 2.0 MeV alpha particles from the Van der Graaf generator at Brookhaven National Laboratories. PVG or sol-gel glass samples, typically impregnated with 10^{-4} mol/g, were cut into a 1.0 cm x 1.0 cm x 2.0 mm pieces. The samples were photolyzed and heated as previously described, and the energies of the alpha particles scattered from these samples were measured and converted into a mass vs. depth scale of atoms in the sample. During transportation to Brookhaven, the samples were stored in a vacuum dessicator.

X-ray microprobe analyses (XRF), were carried out at Brookhaven National Laboratory using the Synchrotron Accelerator. The accelerator produces protons that release an x-ray beam. The beam size was varied by

means of an arrangement of slits producing beam sizes ranging from 50 to 100 μm in diameter. The detector was a silica doped lithium detector filtered with a bellirium window. In the XRF experiments, samples were 2.5 cm x 2.5 cm x 0.2 cm PVG plates or glass gel plates impregnated with ~ 1.0×10^{-4} moles/g of PVG. After photolysis and heat treatment, the samples were cut in half with a diamond saw, and the cross-sectional distribution of the deposited metal determined. Plots of the metal fluorescence intensity vs. depth (μm) were obtained. To examine the resolution of the photolithographic images, fluorescence intensities were measured across a photodeposited image of a 100 μm Ronchi Ruling.

Secondary ion mass spectroscopy (SIMS) experiments were carried out at Bellcore Materials Analysis Research Laboratory, Red Bank, N.J. An oxygen ion beam with an ion current of 15 KeV, a scan width of 0.75 mm, and a beam size of 1.0 μm width was used. The penetration depth was varied by varying the exposure time, which for these glass samples was typically 6 hours.

Impregnated PVG samples were cut into 1.0 cm^2 pieces and mounted in the sample compartment of the instrument under vacuum ($\leq 1.0 \times 10^{-6}$) to avoid sample charging effects . An optical microscope with a magnification of a 100x was used to position the ion beam on the glass. The sample was then bombarded for a period of six hours with a scan speed of 5 frames per second. As the ion beam penetrated the glass surface to a depth of ca. 3000 Å, metal atoms scattered from the glass were analyzed with a mass spectrometer.

Scanning Electron Microscopy (SEM) analyses were conducted on a Hitachi S-570 SEM equipped with a PGT System IV analyzer and an EDX elemental analysis attachment with a silica doped lithium detector, filtered

with a bellirium optical window. Photolyzed samples that had been heated to various temperatures were cut into $5mm^2$ pieces. These pieces were pasted onto a microsample stub with a silver slurry mix to avoid charging effects. The samples were then coated with a 300 Å layer of gold-palladium in a Film-Vac Inc. mini-coater at a pressure of $1.0x10^{-6}$ torr and a current of 30 mA .

Transmission electron microscopy was carried out in a JEOL USA 100 CX electron microscope operating in the bright field mode with an electron energy of 100 Kv. All samples were prepared by the dispersive method, where the glass sample was pellitized in a Gatan Dual Model 1400 ion miller to ca. 1.0 μm diameter quasi-spheres at an accelerating voltage of 7 Kv. A supporting film was prepared using a 1.0 % colloidal dispersion of the pellitize glass powder in methanol. The dilution ratio was chosen to ensure that the particles would not form clusters, but at the same time, there would be an adequate number of particles to be observed in the field of view. A carbon coated 400 mesh slim grid was immersed in the colloid solution for a few seconds to incorporate some of the glass particles into the holes of the grid. The grid samples were then dried in a vacuum dessicator for a period of 24 hours.

A Zeiss Model MC368 microscope equipped with 10x and 30x objectives was used for optical microscopy. As previously described in the section on the microlithography procedures, an external light beam could be introduced into the optical path of the microscope by simply moving a beam splitter, or a high reflectance stainless steel plate into position. The microscope was also equipped with an automatic exposure 35mm camera.

Index of refraction measurements were accomplished by using the optical bench layouts shown in Figures 5.7 and 5.8. In the far-field method

Figure 5.7 - Experimental set up for Far Field refractive index measurement

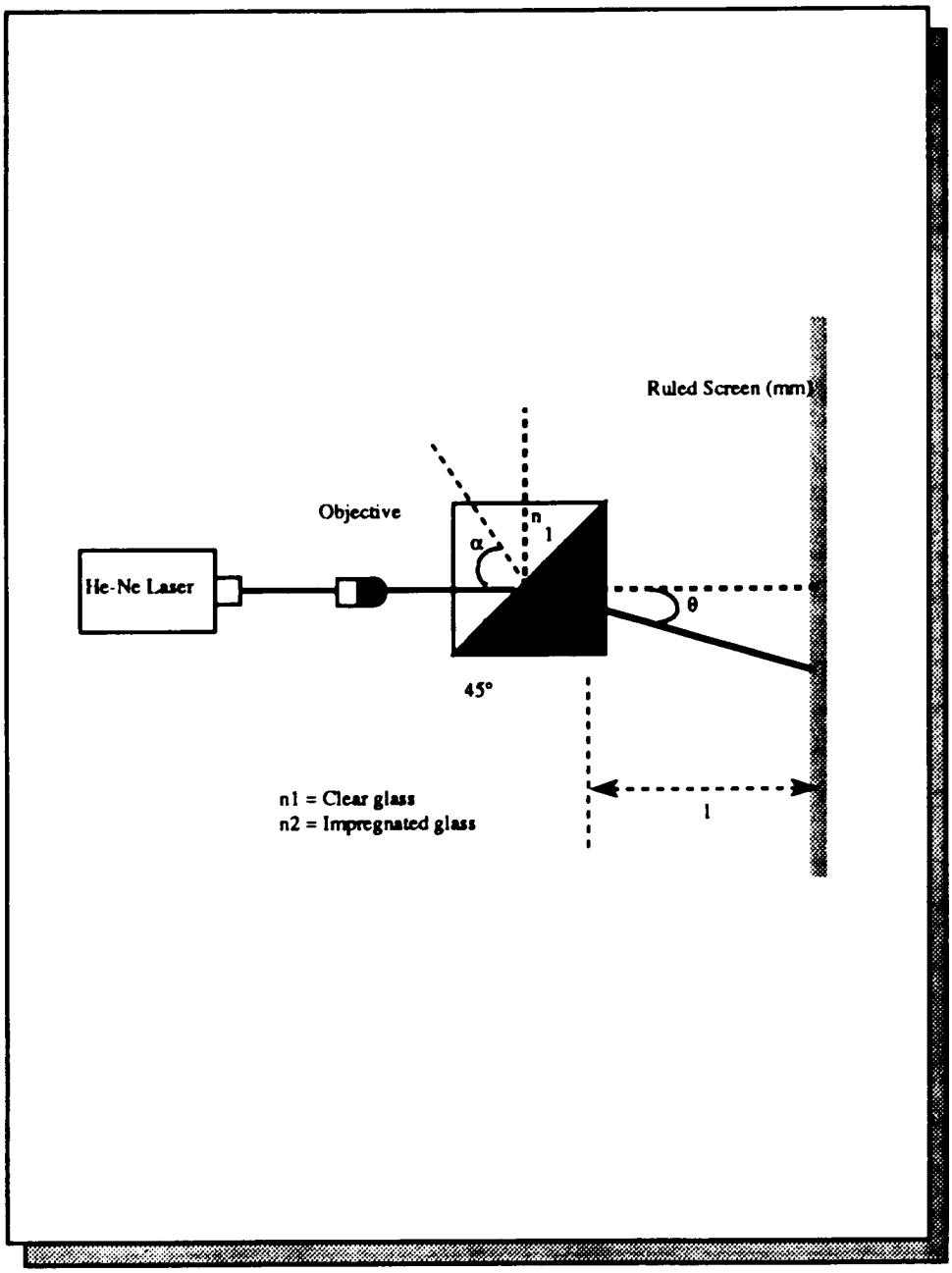

Figure 5.8 - Experimental set up for the Total Internal reflection measurements

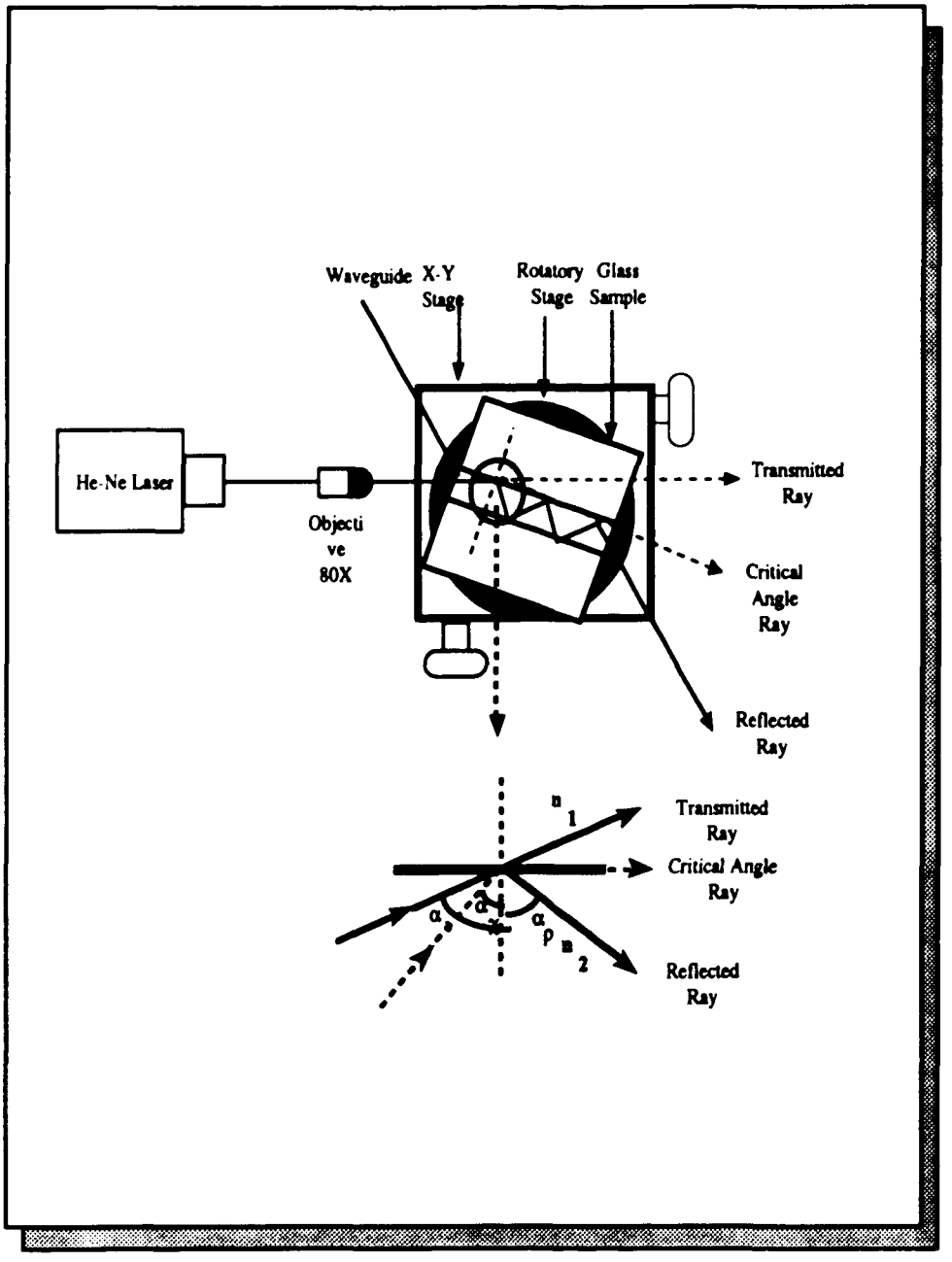

(Figure 5.7), a 30 μm in diameter He-Ne laser beam was passed orthogonally through a reference glass sample onto a ruled screen 3.0 m beyond the sample. The position of the laser beam was marked on the ruled screen and the reference sample was replaced with an impregnated sample. The laser beam was passed through the impregnated sample and the displacement of the beam from that of the reference sample was measured. The angle of refraction, θ, was calculated from the measured displacement and the experimental geometry. The index of refraction of the impregnated sample was calculated from Snell's relation :

$$\frac{\sin \alpha}{\sin \theta} = \frac{n_1}{n_2} \qquad 5.5$$

where α is the angle of incidence, (45°), n_1 is the refractive index of the reference (unimpregnated) glass (n_1=1.5), and n_2 is the refractive index of the impregnated glass. The change in the refractive index induced by photodeposition, Δn, was taken to be n_2-n_1.

The samples examined by the far field method were prepared by the previously described vapor impregnation techniques and were generally of the order of 1.0×10^{-4} mol / g of PVG. The glass samples were photolyzed by using a 45° angle photomask. This mask allowed half the sample to be exposed at a 45° angle as shown in Figure 5.7. By using this procedure the impregnated sample could be placed at exactly the same position as the reference glass sample.

With deposited optical waveguides, refractive index measurements,

were obtained by measuring the angle of total internal reflection as shown in Figure 5.8. The impregnated samples were placed on a miniature 2-inch diameter rotatory translation stage (Edmund Scientific). This stage allows quick, continuous rotation over 360° plus a precise angular adjustment at any selected position. The accuracy of the stage was 0.5°. The laser beam was first allowed to fall orthogonally onto the 100 μm optical waveguide. Then, the stage was rotated periodically until the beam was guided through the optical guide. This was the point at which total internal reflection occurs. The index of refraction was calculated from the following equation :

$$\alpha_c = \sin^{-1} \frac{n_2}{n_1} \qquad 5.6$$

where α_c is the critical angle, or the angle at which total internal reflection occurs.

Waveguide loss measurements were made by introducing a known optical power in one end of the waveguide and measure the power emerging from the other end. The method use to measure the waveguide loss was to focus a Sectra Physics Model 2000 Ar^+ laser (514 nm) directly onto a polished input face of the waveguide as shown in Figure 5.9, and then measure the total power transmitted. The waveguides were made by the photodeposition of SnO_2 (1.0×10^{-4} mol adsorbed/gr. of PVG) onto PVG followed by lithography of the waveguide (10 μm width, 100 μm deep), and consolidation of the porous glass. The input and output faces of the waveguide were then polished in a Buehler polisher with diamond paste to

a finished polished of 1.0 μm. Power measurements were made with a Spectra Physics Model 175-C power meater, in the range of 10-100 mW. Care was taken to align the laser beam for optimum coupling, by maximizing the observed output power, before each measurement.

Figure 5.9 - Experimental set up forattenuation measurements in planar waveguides

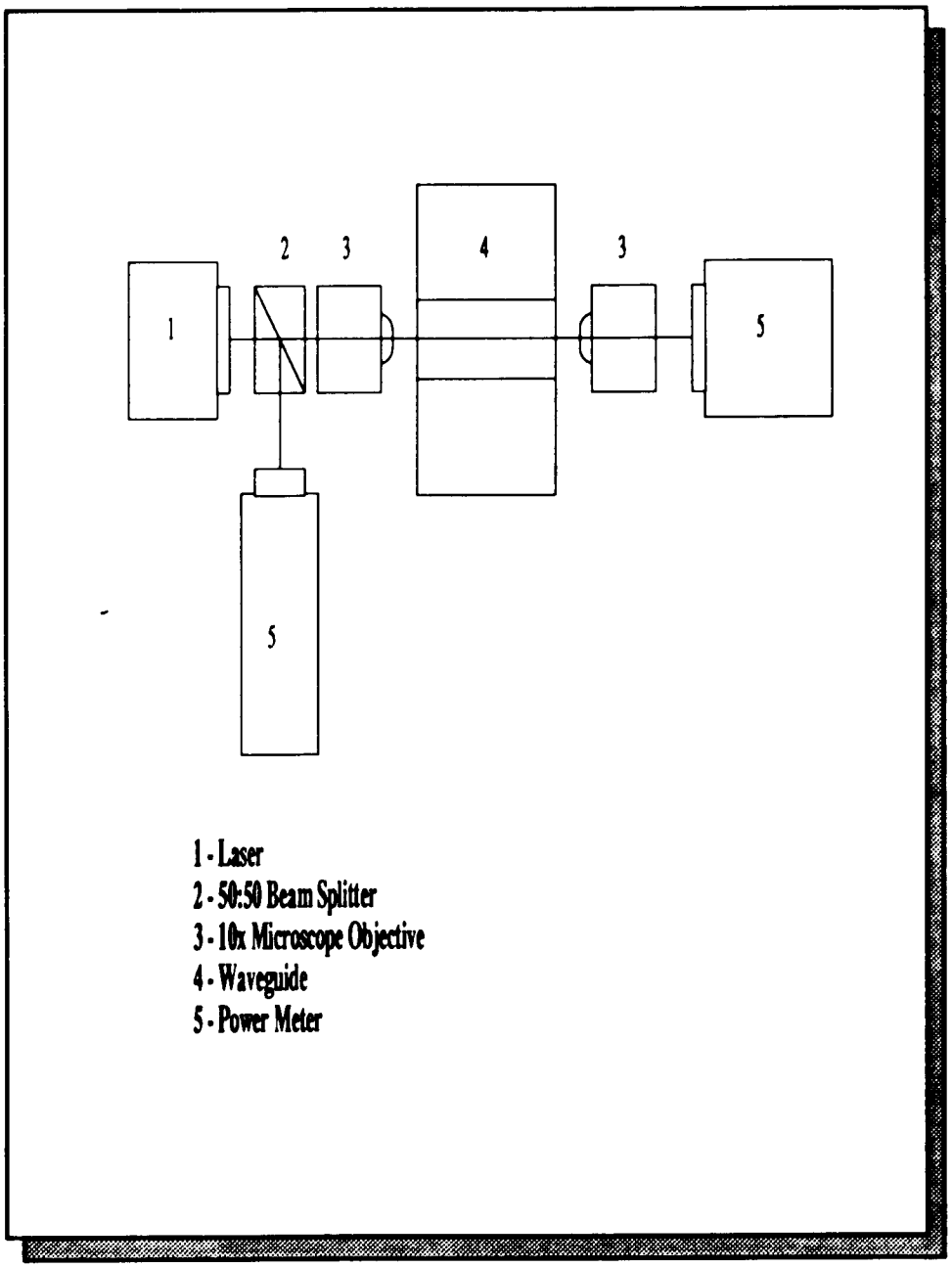

Part III

Results

1. Characterization of Porous Glasses.

1.1 Thermal Analysis.

1.1.1 Porous Vycor Glass.

The most obvious physical change that occurs when a porous glass is heated above room temperature is its weight loss. DRIFT and thermogravimetric analysis indicate that the majority of the change is due to water desorption. The thermogravimetric curve (TGA) for PVG (Figure 1.1) from 50°C to 900°C at a heating rate of 5 °C/min in a controlled atmosphere is clearly divided into two regions. Region I, which runs from 25 °C to 200 °C with an onset at 100 °C, is assigned to the desorption of physisorbed water. Region II, which runs from 200 °C to 900 °C with an onset at 380 °C, is assigned to the desorption of chemisorbed water. In general, the amount of physisorbed water in a calcined PVG sample (650°C) exposed to the atmosphere at room temperature for 24 hours is approximately 5 % by weight, while the amount of chemisorbed water is approximately 3% by weight. The adsorption desorption of water is reversible, and DRIFT spectra (see below) comfirm that the majority of the weight change is due to the reversible adsorption-desorption of water.

Differential thermal analysis (DTA) (Figure 1.2) shows an

Figure 1.1 - Thermogravimetric curve of PVG.

Straight line - TGA curve; doted line - 1st derivative of TGA curve.

Sample Wt.= 22.5 mg; Rate 5 °C/min; Temperature range = 30-900°C.

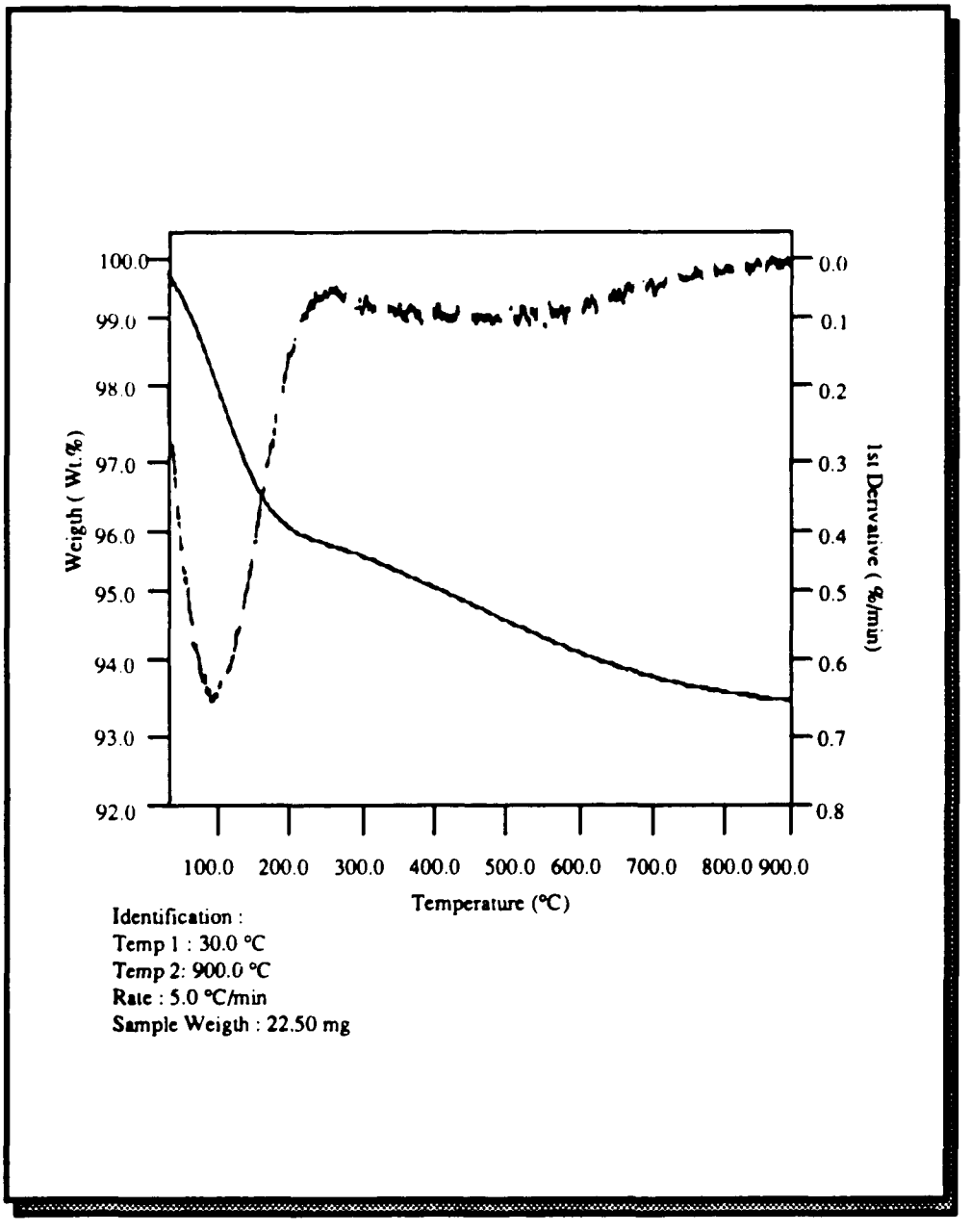

Figure 1.2 - Differential thermal analysis curve of PVG.

Sample weight=19.35 mg; Scan Rate= 5°C/min.

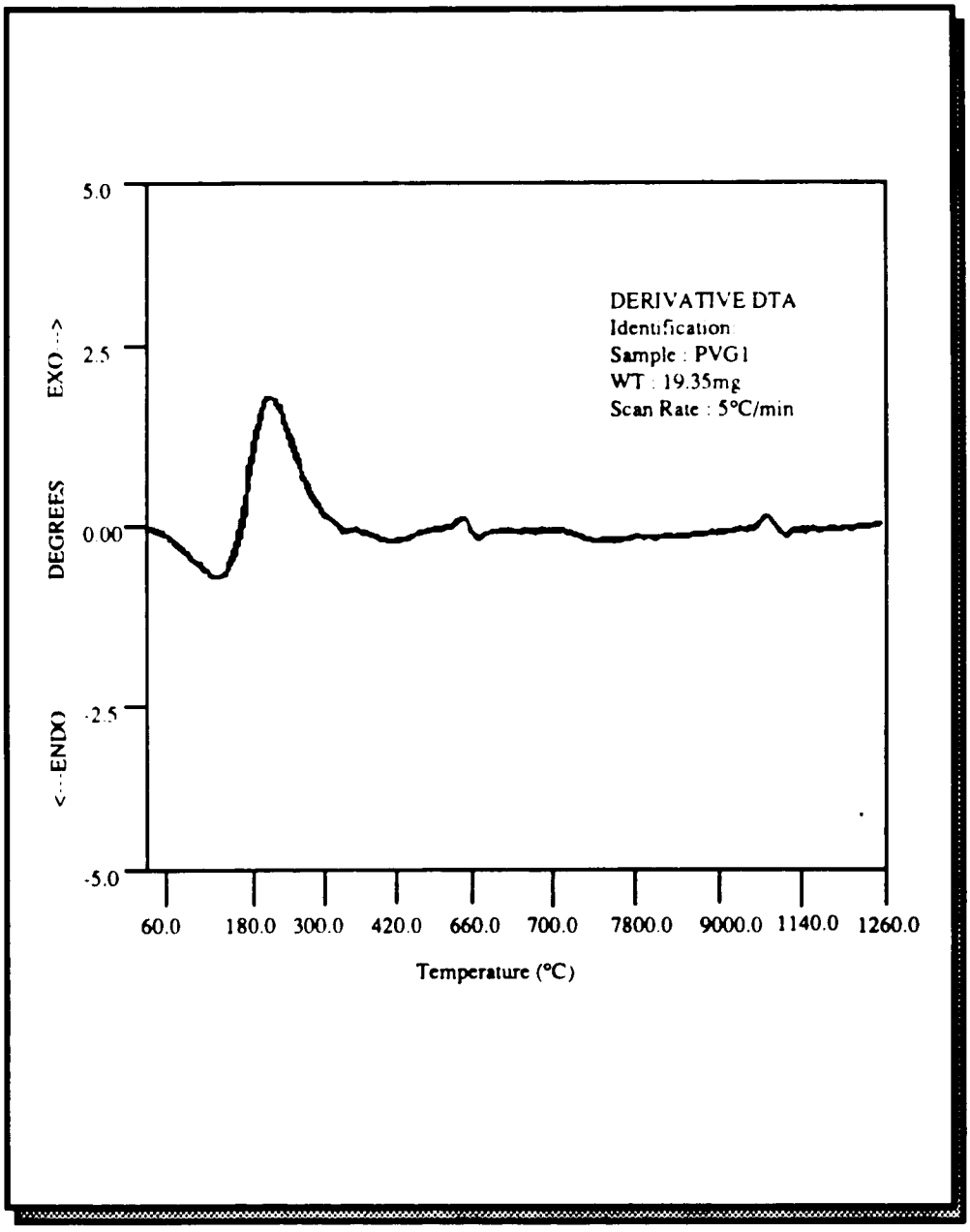

endothermic peak from 25 °C to 180 °C with a maximum at 100 °C corresponding to loss of physisorbed water. The exothermic peak, which occurs at 550 °C, is assigned to the glass transition temperature (Tg) of PVG. The exothermic peak at 1150 °C is assigned to the sintering temperature, where PVG consolidates to a nonporous glass matrix.

DRIFT spectra of uncalcined PVG (Figure 1.3) exhibits a broad adsorption between 3800 and 3000 cm^{-1} which corresponds to the stretching vibrations of different hydroxyl groups. This band has been shown to be composed of a superposition of the following stretching modes: [1]

3744 cm^{-1} - free silanol groups on the surface of the glass.

3660 cm^{-1} - hydrogen bonded silanol groups.

3550 cm^{-1} - silanol groups linked to molecular water through hydrogen bonds.

3500 cm^{-1} - adsorbed water.

The 2000 to 1350 cm^{-1} region exhibits combinations of the SiO_2 vibrational modes. The most prominent of these occur at 1960-, 1870-, and 1640 cm^{-1}, although in most cases the 1960 cm^{-1} band often appears as a shoulder on the 1870 cm^{-1}band. The latter is always well resolved, but not very intense. The 1640 cm^{-1} band is often obscured by the band due to the deformation of adsorbed water at 1620 cm^{-1}.

Bands due to the silica network [2] occur between 1100- and 700 cm^{-1}. The asymmetric Si-O-Si stretch appears at 1080 cm^{-1}, while the symmetric Si-OH or $Si-O^-$ stretchs occur at 950 cm^{-1}, and the symmetric Si-O-Si stretch at 800 cm^{-1}. On heating a PVG sample in a nitrogen atmosphere from 25 °C to 650 °C (Figure 1.4), the broad band at 3500 cm^{-1} due to adsorbed water as well as the 3550- and the 3660 cm^{-1} bands disappear leaving the 3744 cm^{-1} Si-OH band well resolved. The lower frequency bands

Figure 1.3 - DRIFT spectra of uncalcined PVG.

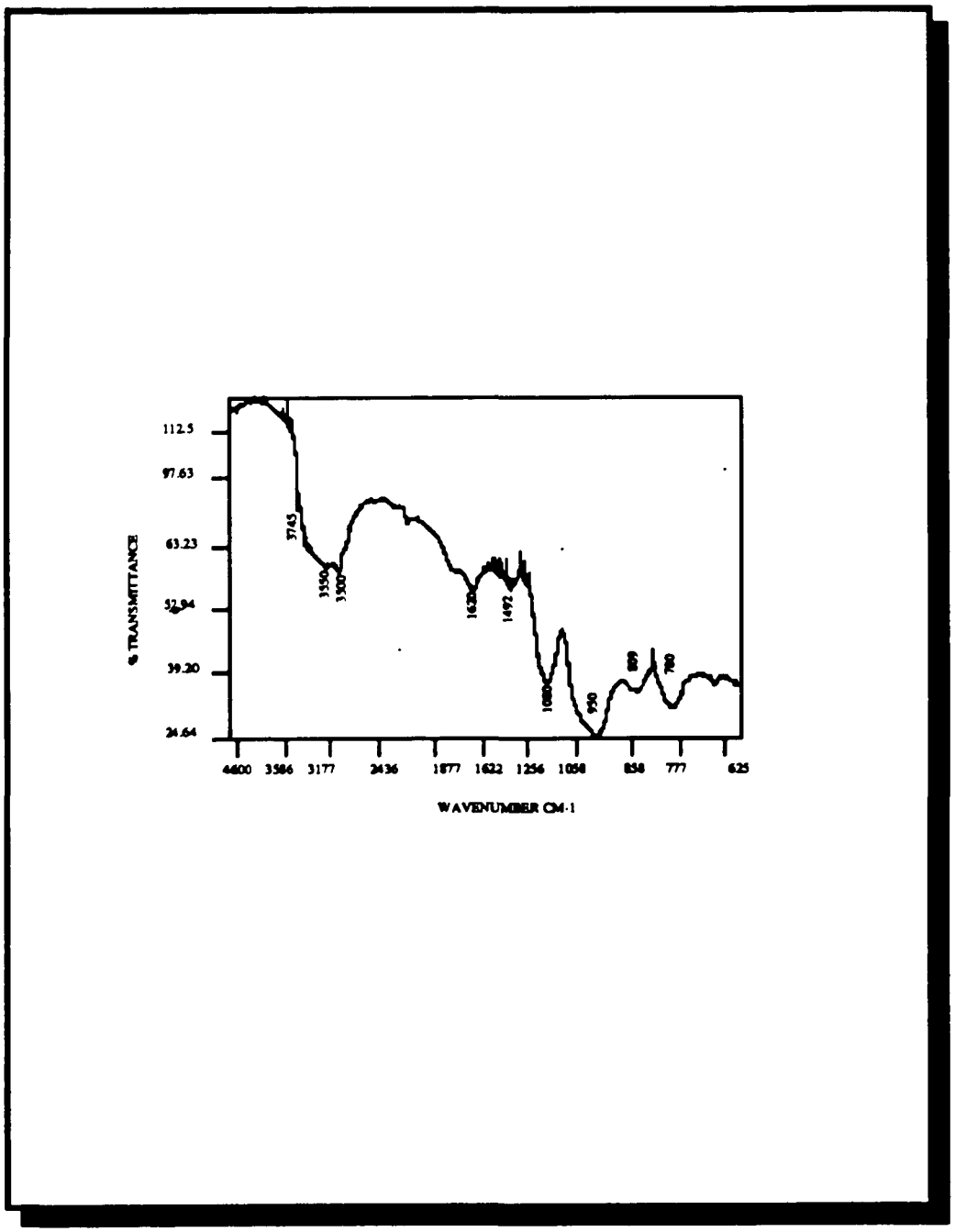

characteristic of the SiO_2 matrix are essentially independent of temperature.

1.1.2 TMOS Xerogels.

Like PVG, the surface topology of TMOS xerogels possess silanol groups. Consequently, their thermal behavior is simmilar to that of PVG. Thermogravimetric analysis (Figure 1.5) exhibits three regions. Region I, which run from 25 °C to 250 °C with an onset at 100 °C, is assigned to the desorption of physisorbed water and perhaps residual methanol. Region II, which runs from 250 °C to 510 °C with an onset at 341 °C, is assigned to the desorption of unpolymerized organics, and some chemisorbed water, while region III, which runs from approximately 500 °C to 900 °C, is assigned principally to the desorption of chemisorbed water.

Differential thermal analysis (Figure 1.6) agrees with the TGA results. The endothermic peak from 50 °C to 180 °C is assigned to desorption of water, while that at 220 °C is assigned to the desorption of organics. An exothermic glass transition (Tg) peak appears at 790 °C, and a sintering peak at 1120 °C. Table 1.1 summarizes the results of the thermal analyses of PVG and TMOS xerogels.

At room temperature (25 °C), DRIFT spectra of dry TMOS xerogels (Figure 1.7) are very similar to those of uncalcined PVG (Figure 1.3). The broad adsorption at 3500 cm^{-1} is assigned to physisorbed water, while the free silanol occurs at 3744 cm^{-1}. The two small peaks at 2959 cm^{-1} and 2852 cm^{-1} are assigned to the C-H stretch modes of unhydrolyzed methyl groups from either the solvent or TMOS. [3] TMOS xerogels prepared under the exact same conditions, but using deuterated methanol (CD_3OH) do not

Figure 1.4 - DRIFT spectra of calcined PVG at 650 °C.

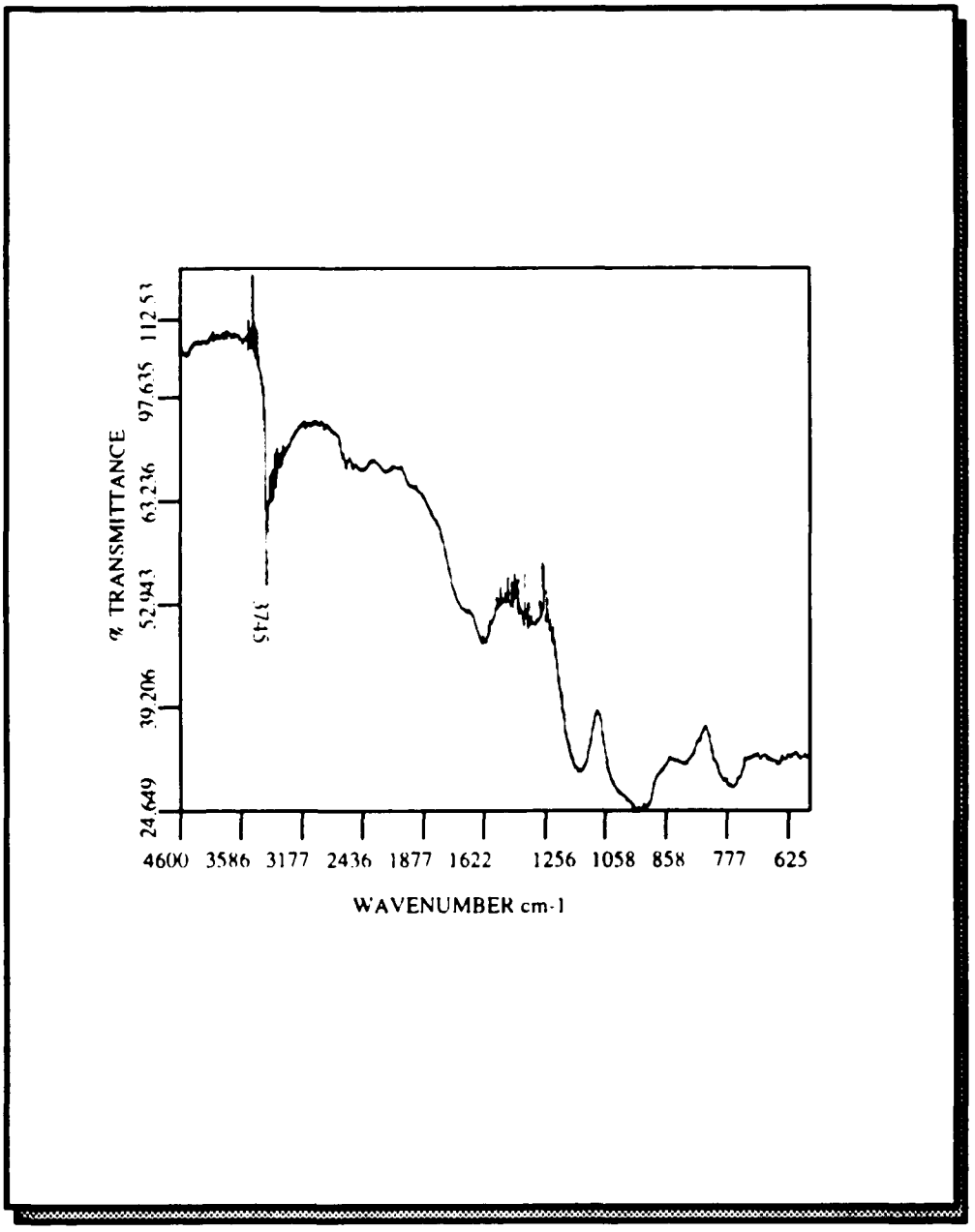

Figure 1.5 - Thermogravimetric curve of TMOS xerogel.

Straight line - TGA curve; doted line - 1st derivative of TGA curve.

Sample Wt.= 18.75 mg; Rate 5 °C/min; Temperature range = 30-900°C.

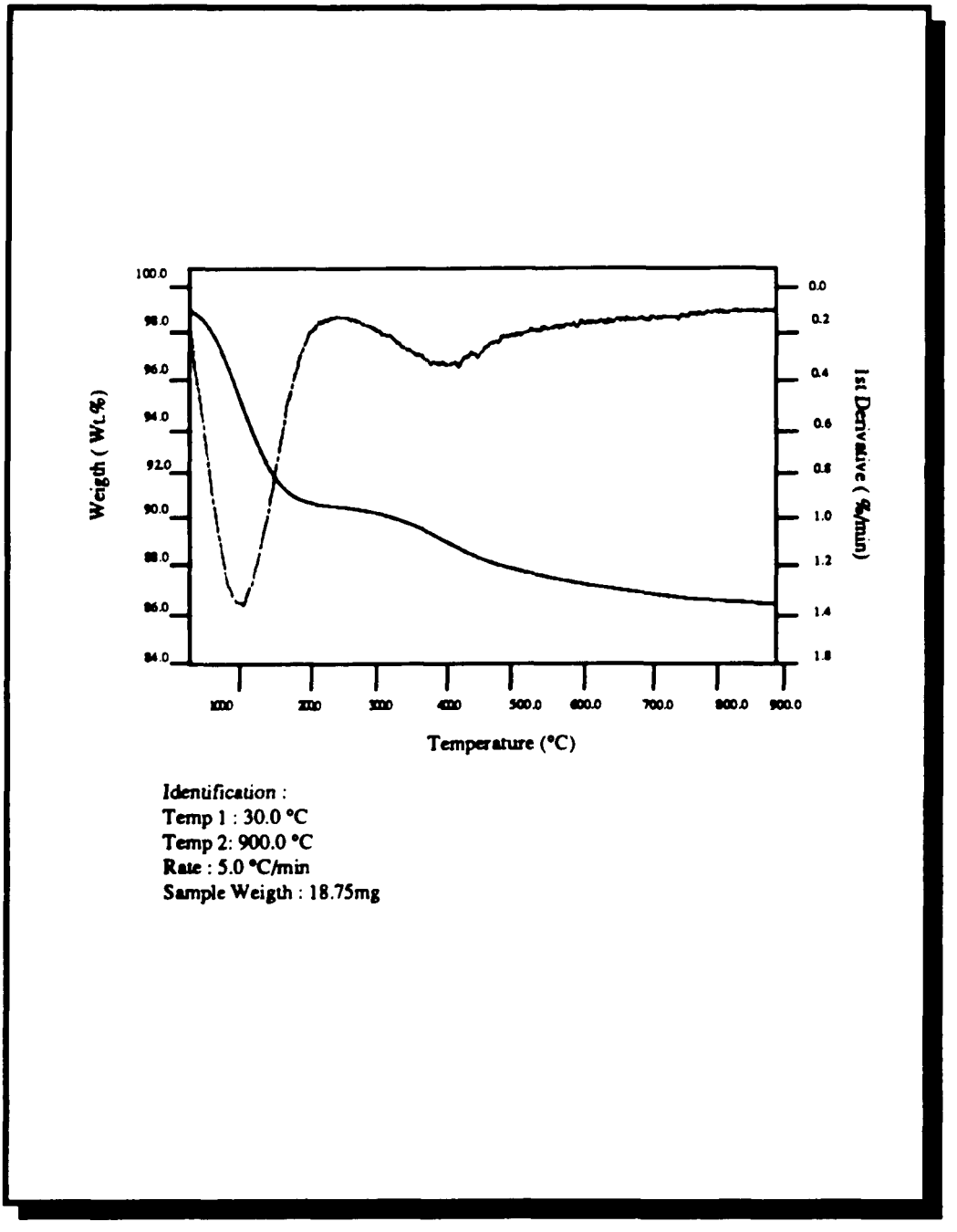

Figure 1.6 - Differential thermal analysis curve of TMOS xerogel.

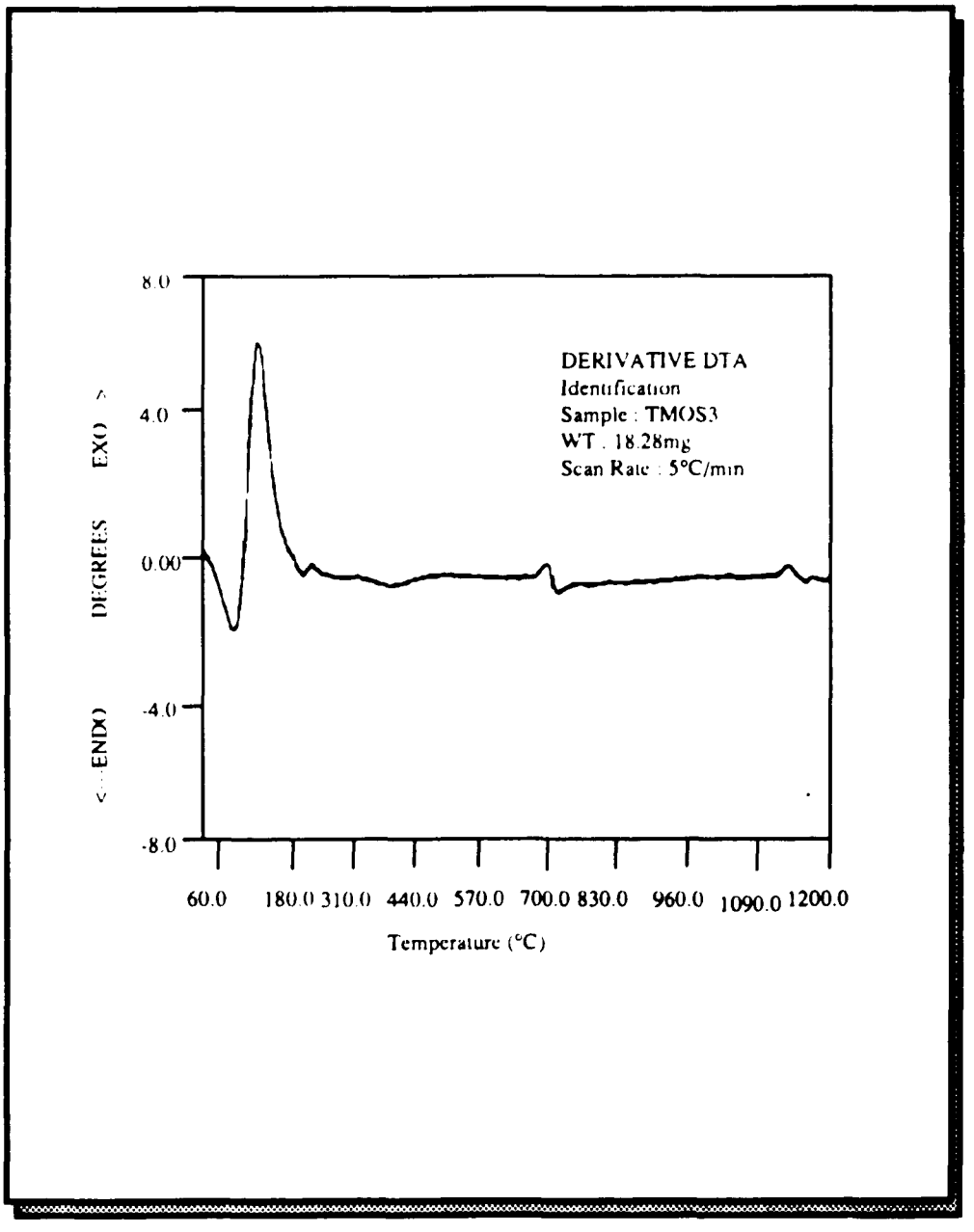

exhibit peaks in the C-H stretch region (Figure 1.8). However, an unambiguous determination of the source of these C-H bands was not possible. The intense vibrations of the silica network prevented monitoring the intense 1050 cm-1 and 1100 cm-1 bands of methanol and TMOS respectively.

Table 1.2 summarizes the infrared absorption frequencies for PVG and TMOS systems. On heating a gel from 50 °C to 650 °C (Figure 1.9), the peak at 3500 cm^{-1} due to adsorbed water disappears, and the peaks at 3744 cm^{-1}, 2959 cm^{-1} and 2852 cm^{-1} become more resolved. Suprisingly, even after heating to 650 °C, the gel contains Si-O-CH_3 functionalities. These are thought to arise from incomplete hydrolysis of the solvent at room temperature, or from esterification of Si-OH groups during the later stages of the heat treatment.

UV-vis spectra of PVG and TMOS xerogels (Figures 1.10 and 1.11 respectively), show that both materials are transparent in the visible, but absorb in the UV. However, transparency in the UV region is very dependent on the thermal history of the glass. Controlled heating to 650 °C in a moisture free atmosphere lowers the absorption of PVG to about 230 nm, while the TMOS xerogels become transparent to 200 nm. The transparency of these glasses in the UV region makes them ideal surfaces for the study of reaction mechanisms by electronic spectroscopic techniques.

Table 1.1 - Thermogravimetric results for PVG and TMOS obtained from Figures 1.1-2, and 1.5-6.

Results	PVG	TMOS
T_1	46.10 °C	39.43 °C
T_2	244.4 °C	246.71 °C
ΔY	4.738 Wt.%	9.164 Wt.%
Onset	65.97 °C	69.34 °C
Rate	6.52×10^{-3} mg/°C	1.23×10^{-2} mg/°C
Peak	110.41 °C	109.77 °C
Peak Area	0.734 mg	2.185 mg
T_3	277.43 °C	240.90 °C
T_4	877.76 °C	892.30 °C
ΔY	2.732 Wt.%	4.603 Wt.%
Onset	392.51 °C	341.96 °C
Rate	1.24×10^{-3} mg/°C	1.97×10^{-3} mg/°C
Peak	557.35 °C	432.46 °C
Peak Area	0.241mg	0.917 mg
$T_{water\ desorption}^{(DTA)}$	100 °C	101 °C
$T_{glass\ transition}^{(DTA)}$	550 °C	790 °C
$T_{sintering\ transition}^{(DTA)}$	1050 °C	1120 °C

Figure 1.7 - DRIFT spectra of uncalcined TMOS xerogel.

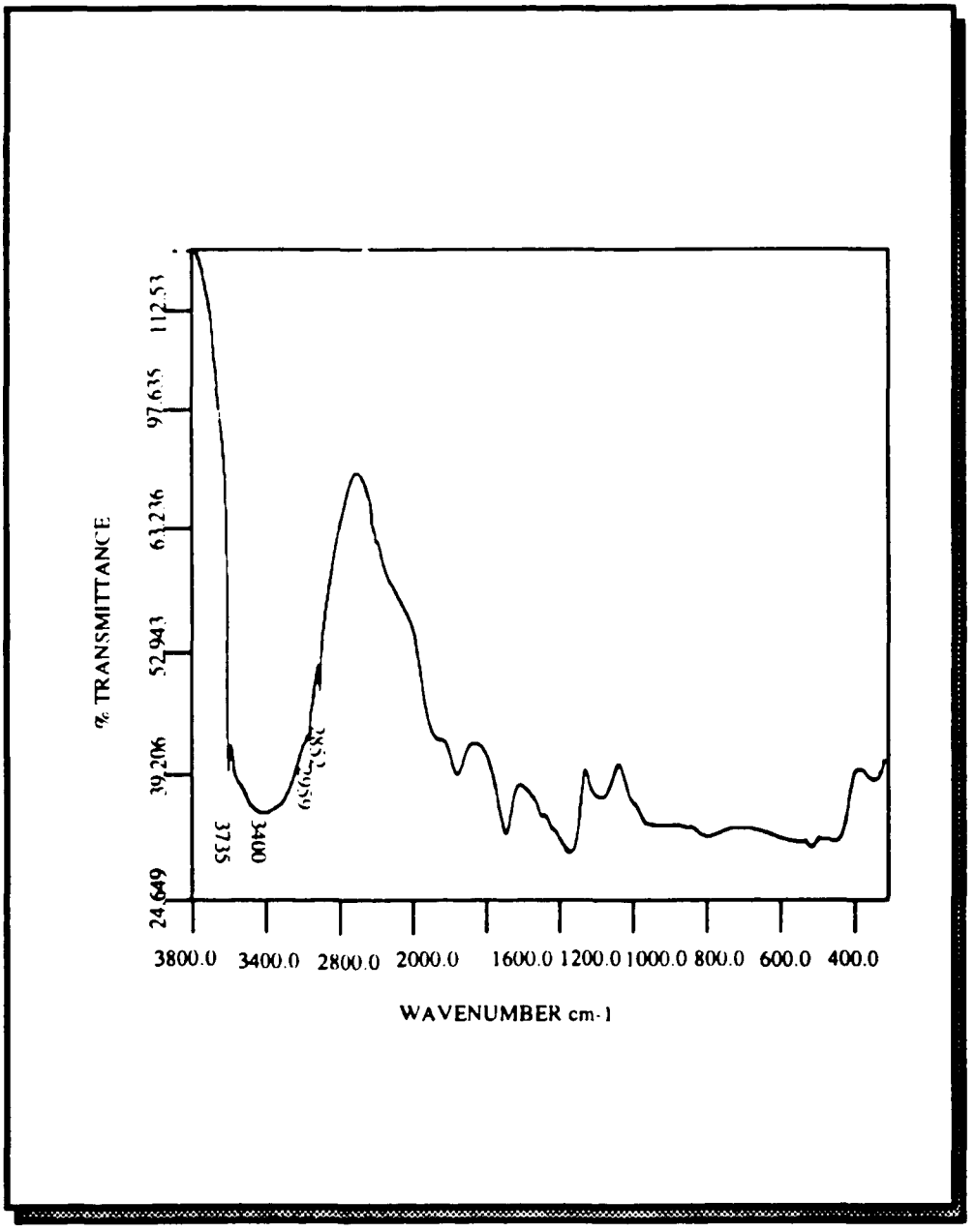

Figure 1.8 - DRIFT spectra of deuterated TMOS xerogel.

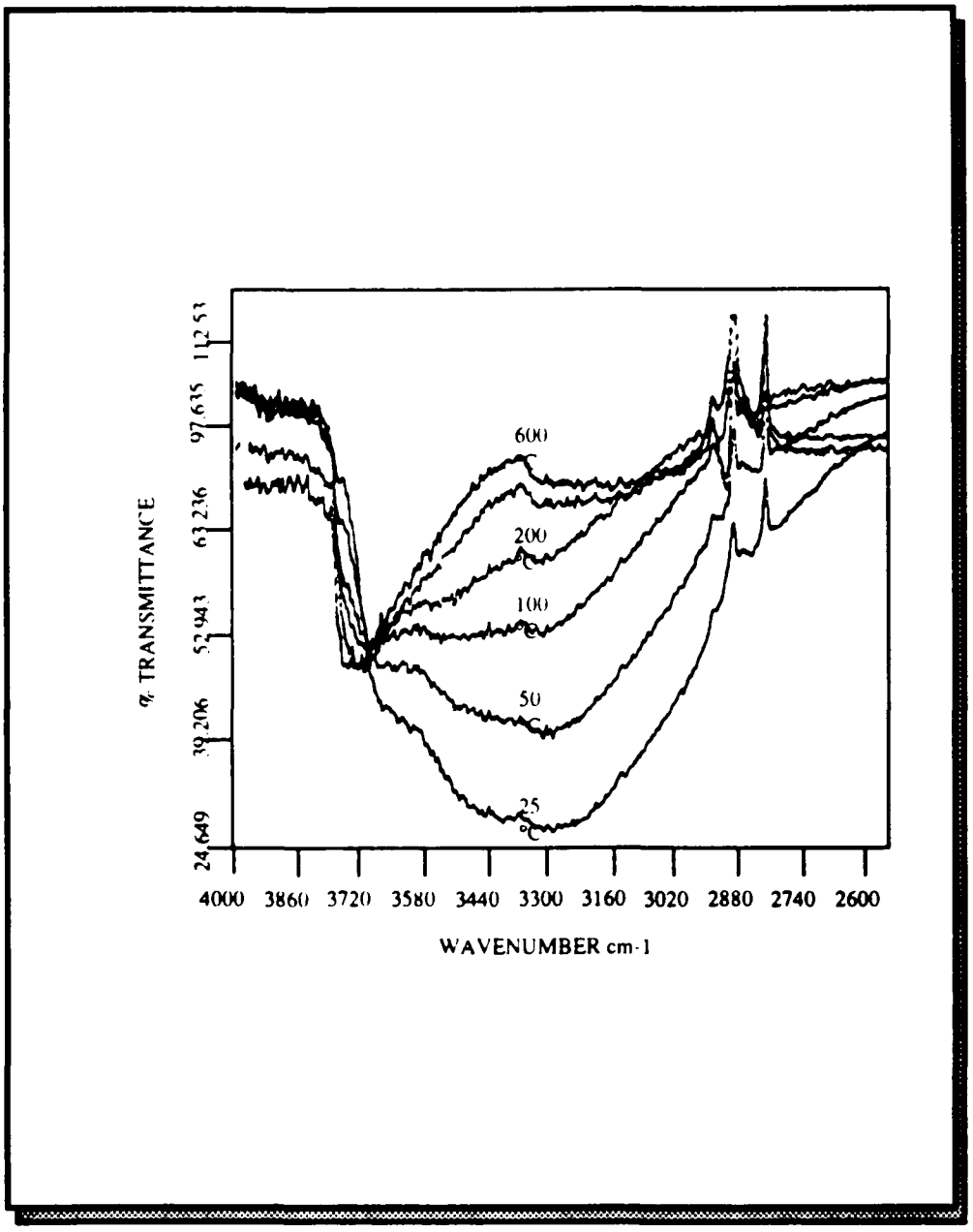

Figure 1.9 - DRIFT spectra during heat treatment from 50 °C to 650 °C of TMOS xerogel.1) 50 °C; 2) 200 °C; 3) 300 °C; 4) 650 °C.

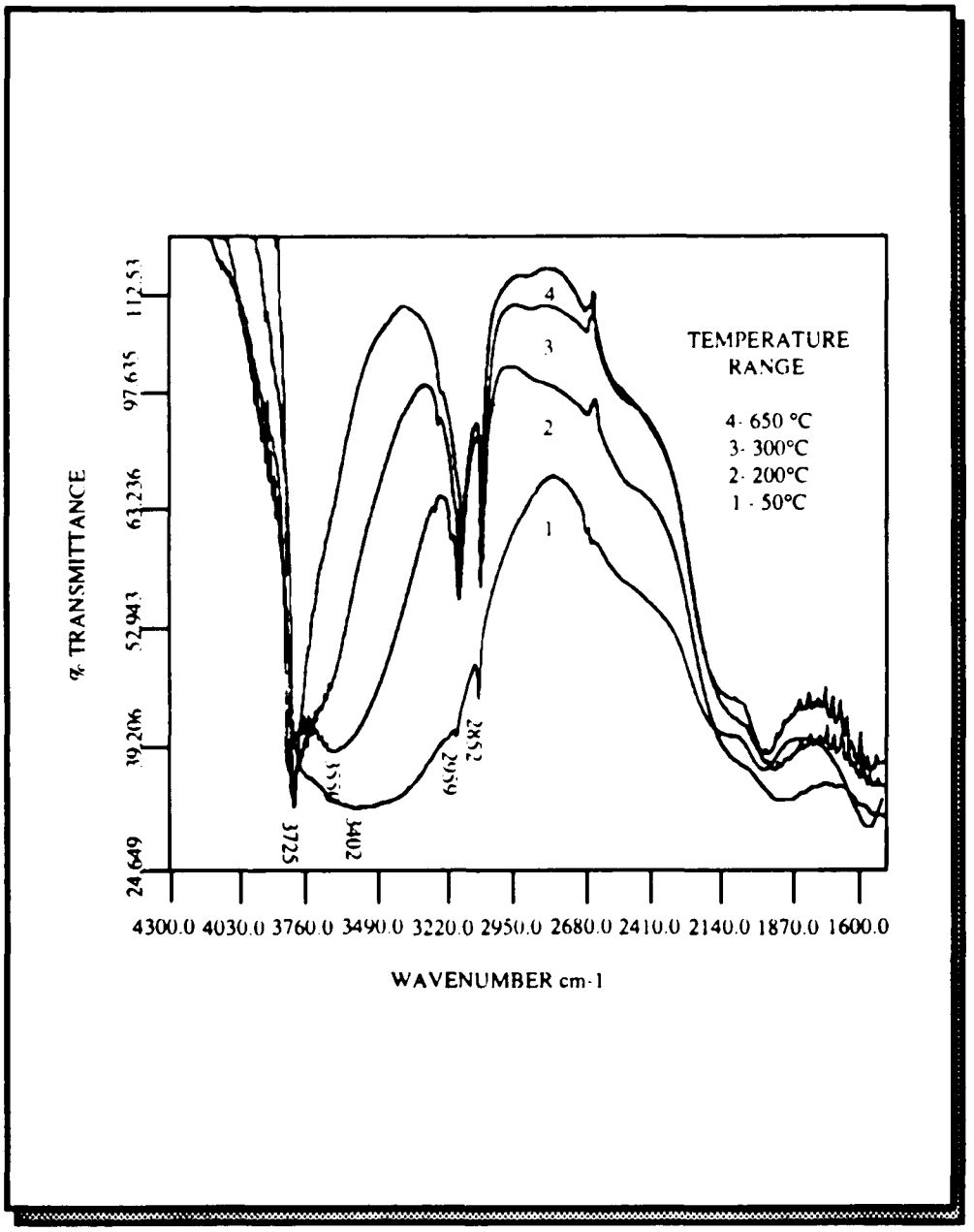

Table 1.2 - Infrared absorption bands for the PVG and TMOS systems.

Wavenumber (cm^{-1})	**Assigment** [4]
4600-4300	stretching + deformation C-H
4557	stretching + deformation free Si-OH
3750	stretching free surface Si-OH
3660	stretching Si-OH···OH-Si
3540	stretching Si-OH···H_2O
3400-3500	stretching adsorbed H_2O
3000-2750	symmetric and assymetric stretching CH_3
2990	stretching C-H (H_2-C=O)
2858	symmetric stretching Si-O-CH_3
	stretching C-H (CH_3-OH)
2857	stretching C-H (CH_3-OH, CH_3-CHO, CH_3-O-Si)
1960	combination Si-O
1867	combination Si-O
1700	stretching C=O 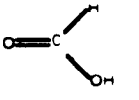
1685	stretching C=O 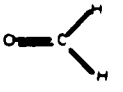
1640	overtone Si-O
1620	bending molecular H_2O
1599	assymetric stretching 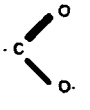
1492	deformation OH 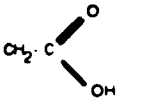

Wavenumber (cm^{-1})	Assigment
1472	bending C-H (CH_3-O-Si)
1390	deformation C-H (CH_3-OH)
1375	symmetric stretching 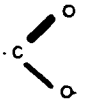
1080	stretching <-- SiO--> <--Si
950	stretching Si-OH, Si-O^-
800	stretching <-- Si-O-Si -->
455	deformation

1.2 Morphology and Surface Topology.

SEM analyses of calcined (650 °C) PVG or TMOS xerogels reveal similar surfaces consisting of glass nodules with interveaning, interconnected crevices that are ramdomly dispersed throughout the interior of the glass structure. The resulting cavity sizes range from a few microns to about 100 μm. Although Vycor glass and the TMOS xerogel exhibit similar surface characteristics, differences in the morphology exist and these can be of importance during the adsorption and chemistry of organometallic compounds.

TEM studies of calcined PVG powder (Figure 1.12), reveal an assemble of interconected clusters, with pore sizes ranging from 40- to 100 Å. The pore size distribution was determined by measuring the BET desorption isotherms as a fuction of densification temperature (Figure 1.13). The BET measurements show that the total pore volume decreases as the temperature increases. However, the average volume of the pores remains approximately constant at 100 μm upto 600 °C. Further heating causes the pore volume to decline to baseline level indicating the consolidation of the pore structure. These results are correlated by BET surface area measurements as a function of temperature (Figure 1.14). The initial surface area of PVG at room temperature is ca. 160 (m^2/g) ± 20, and remains constant upto about 600 °C. Above 600 °C, surface area declines with increasing temperature, and reaches a minimum value at the consolidation temperature, about 1100 °C.

Analyses of the TMOS xerogels, however, reveal suprising differences from the structure of PVG. SEM and TEM analyses show a

Figure 1.10 - UV-VIS Spectra of PVG vs. air.

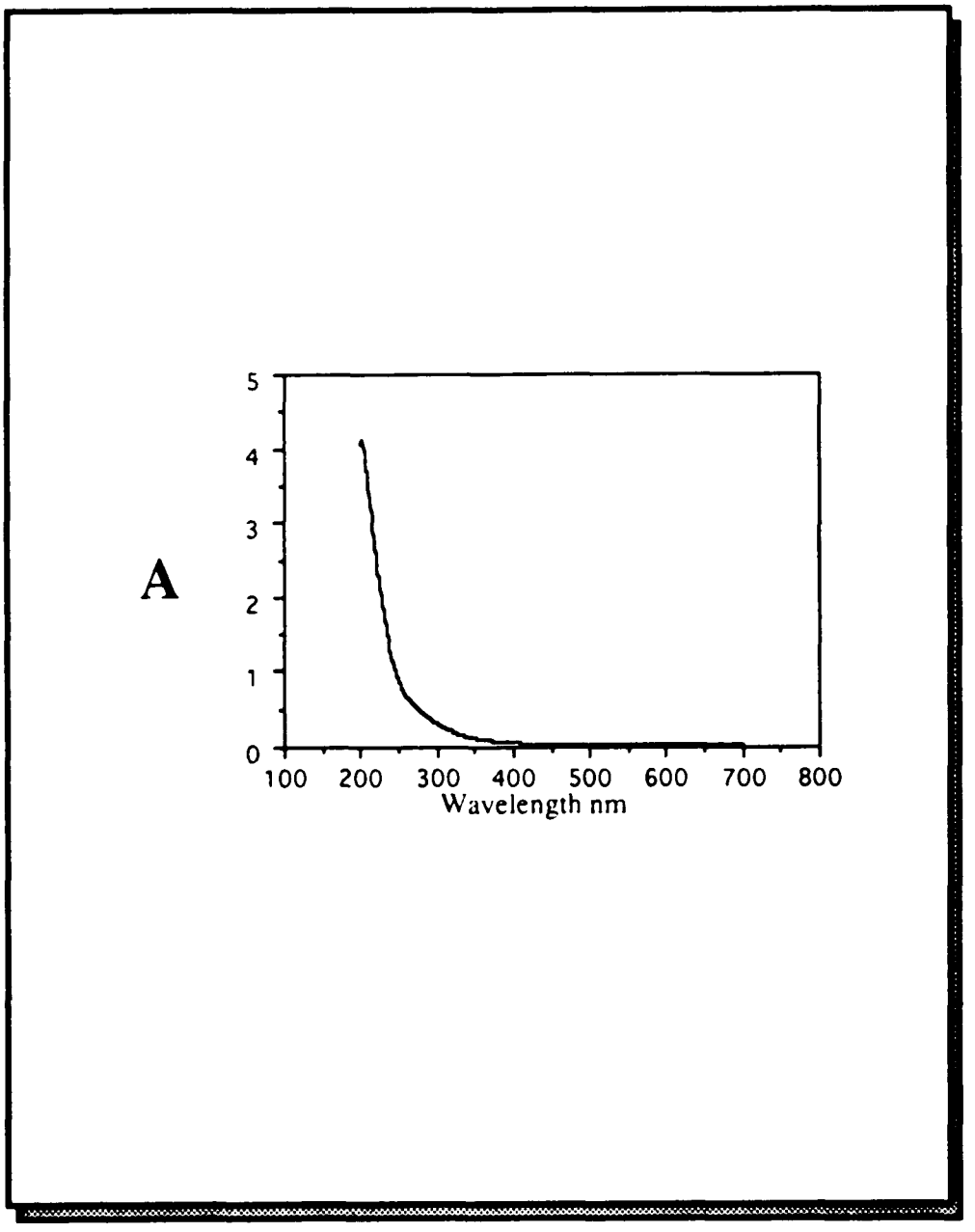

Figure 1.11 - UV-VIS Spectra of TMOS Xerogel vs. air.

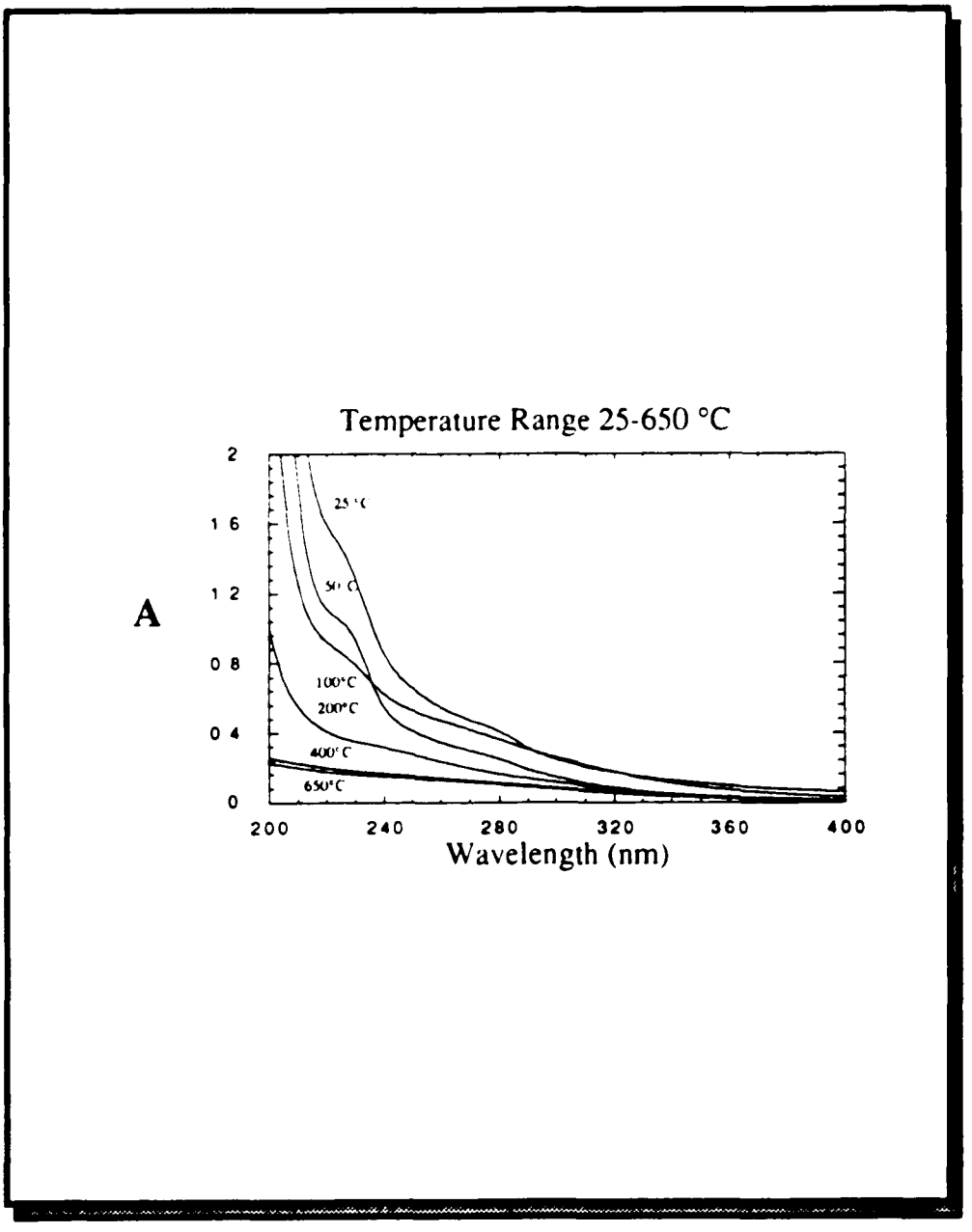

Figure 1.12 - TEM micrograph of calcined PVG powder at 550 °C. Magnification 120.000 X.

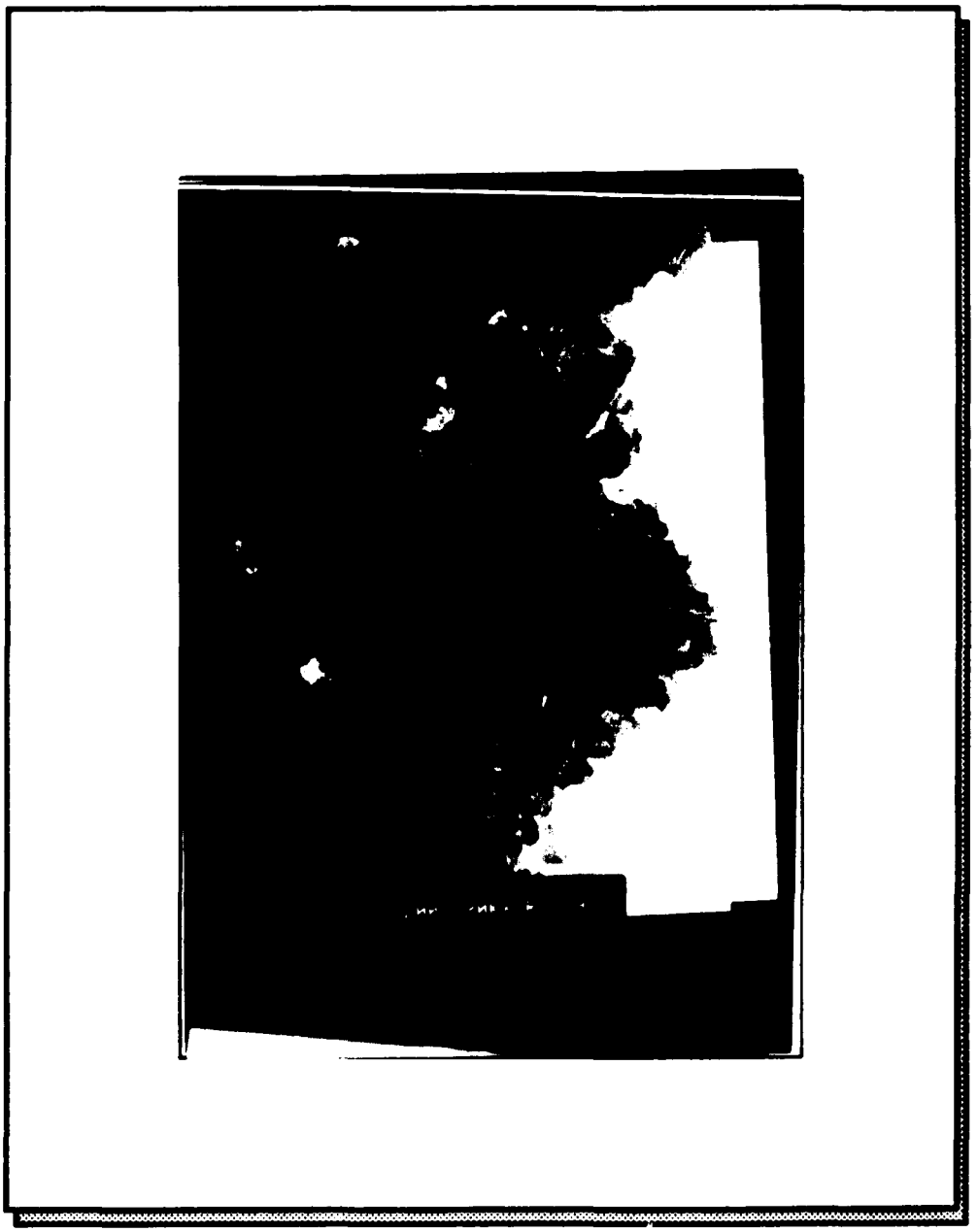

Figure 1.13 - Pore size distribution from BET measurements for PVG at temperatures ranging from 200 to 1200 °C.

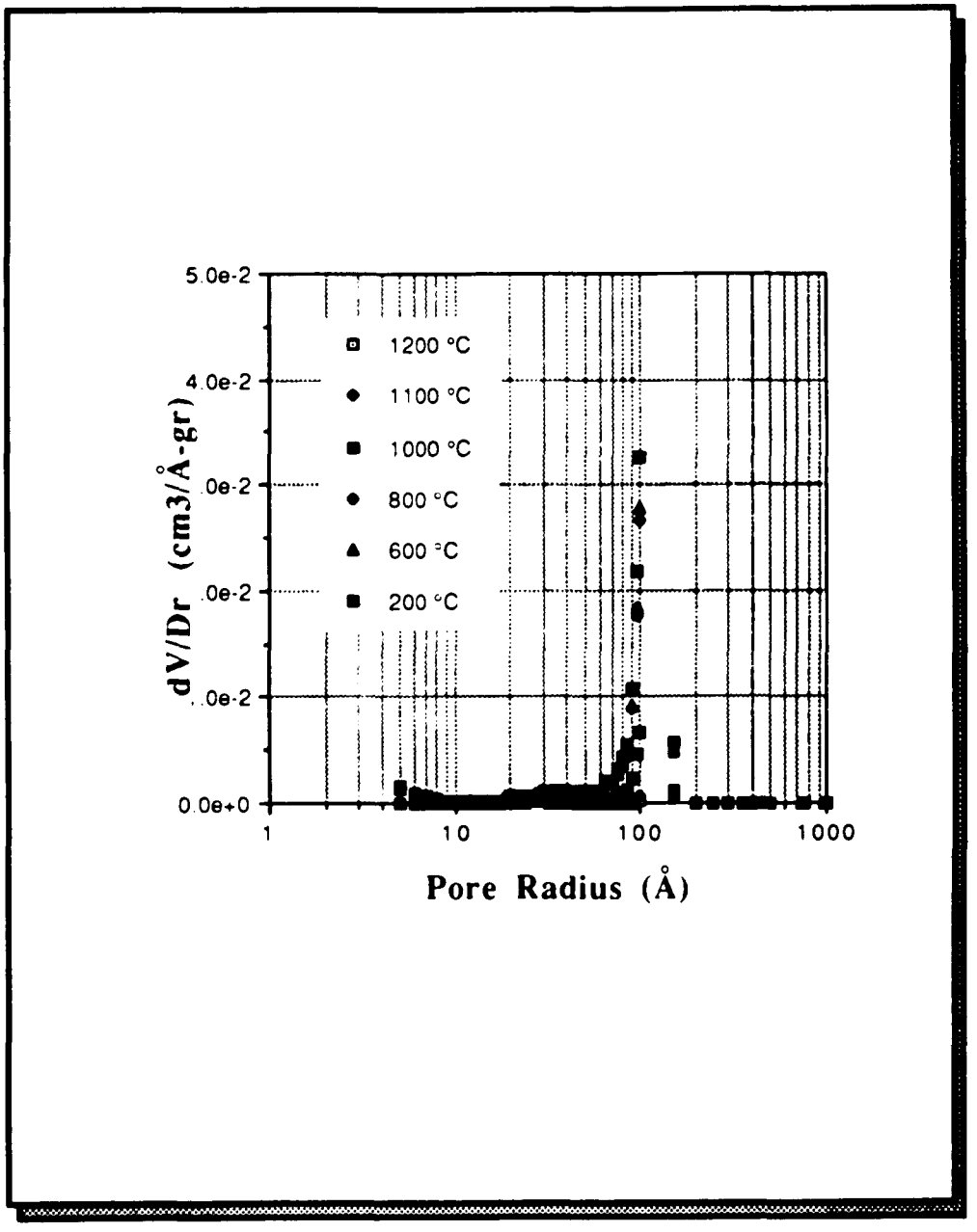

Figure 1.14 - BET surface area for PVG as a function of densification temperature from 50 to 1200°C.

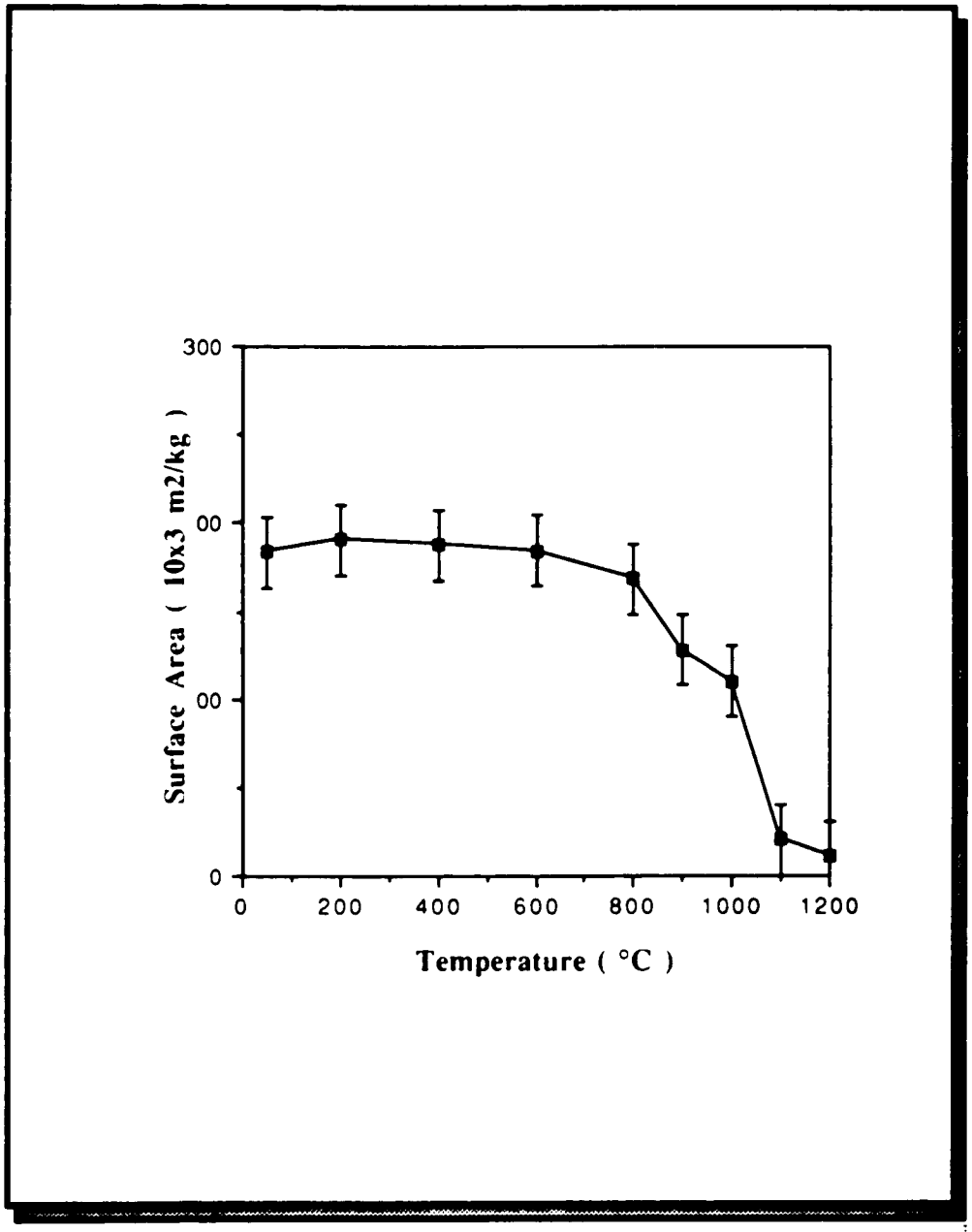

morphology similar to that of PVG, i.e., interconnected glass nodules with intervening creavices distributed ramdomly throught the matrix. Electron microscopy indicates that the cavities between the nodules range from 50 Å to micron in size, Figure 1.15. In addition to this macroporosity, which is similar to that found in PVG, BET measurements (Figure 1.16) reveal a microporosity within the glass nodules, where pore size range from 5 to 30Å. Consequently, two realms of porosity exist within the TMOS xerogels : a microporostiy which exists within the clusters, where the pore diameter is about 10 Å, and a macroporosity which exist between the clusters with pores size ranging from 50 Å to micron.

Like PVG as the temperature increases, the pore volume decreases. The BET data (Figure 1.17) yield a surface area of ~ 600±50 (m^2/g) for room temperature xerogel samples, which is significantly larger than that obtained for PVG. The surface area is independent of temperature upto about 600 °C, and then decline to a minimum at the consolidation temperature, ca. 1100 °C.

Figure 1.15 - TEM micrograph of calcined TMOS xerogel powder at 550 °C. Magnification 120.000X

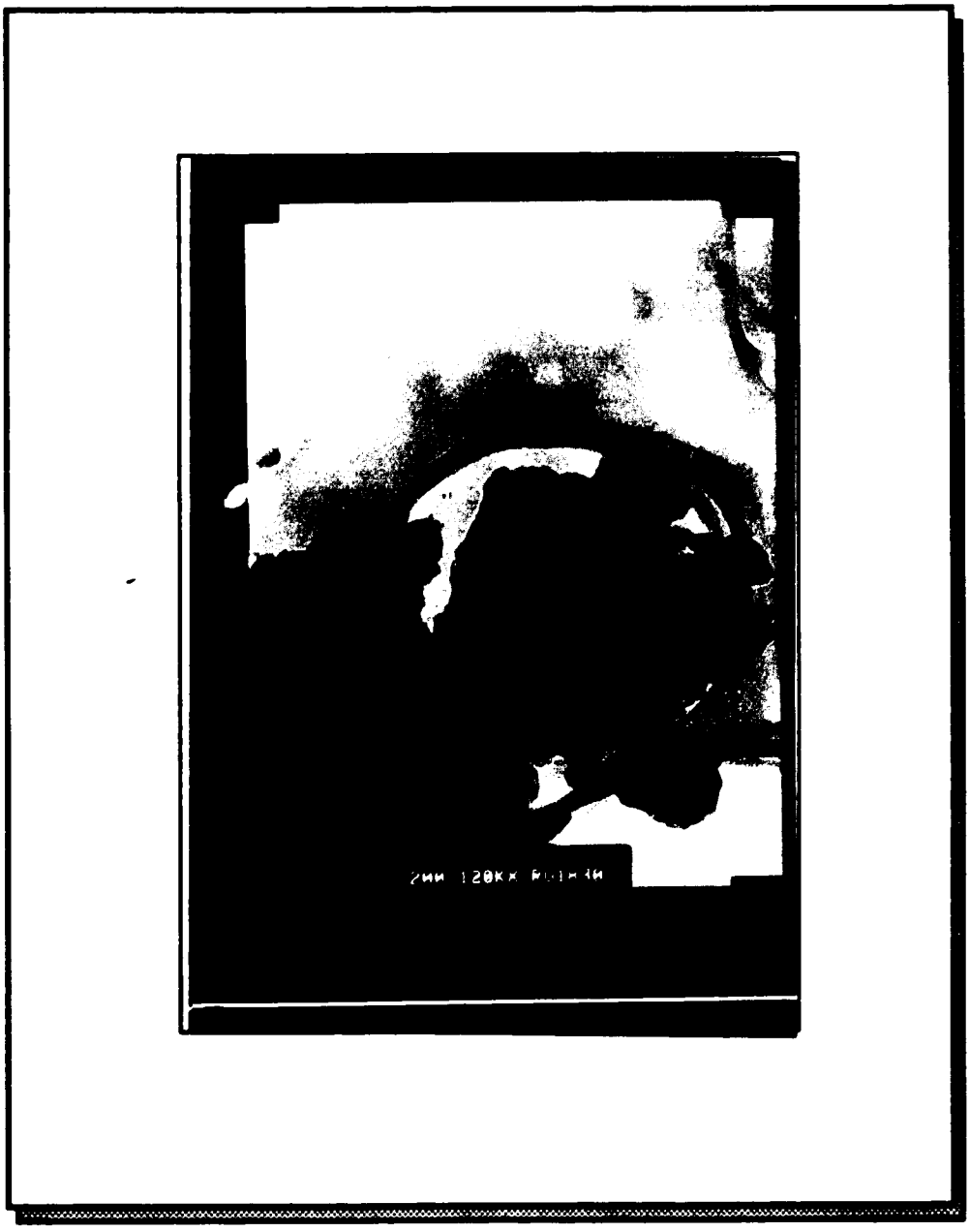

Figure 1.16 - Pore size distribution from BET measurements for TMOS xerogel at temperatures ranging from 200 to 1200 °C.

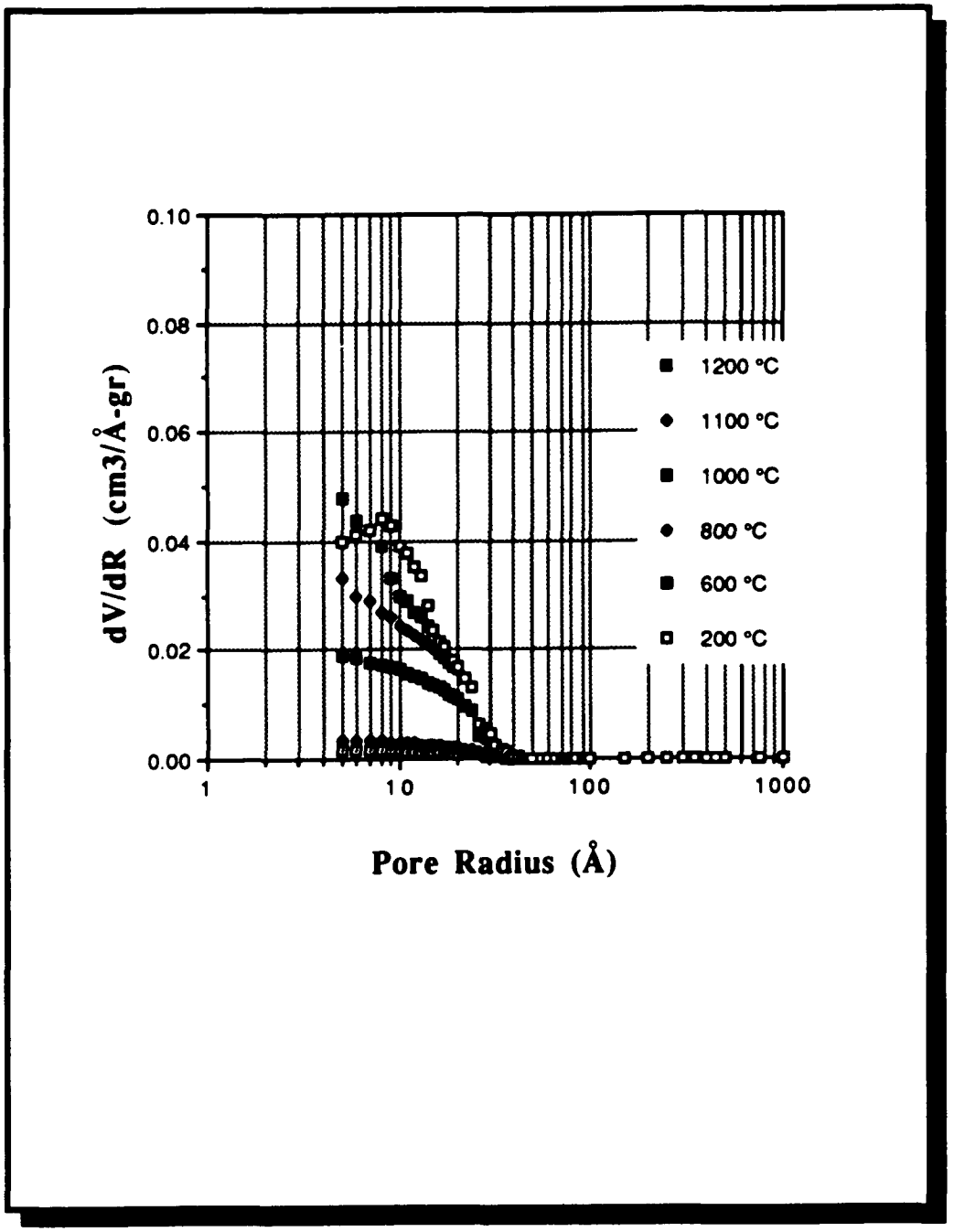

Figure 1.17 - BET surface area for TMOS xerogel as a function of densification temperature from 50 to 1200°C.

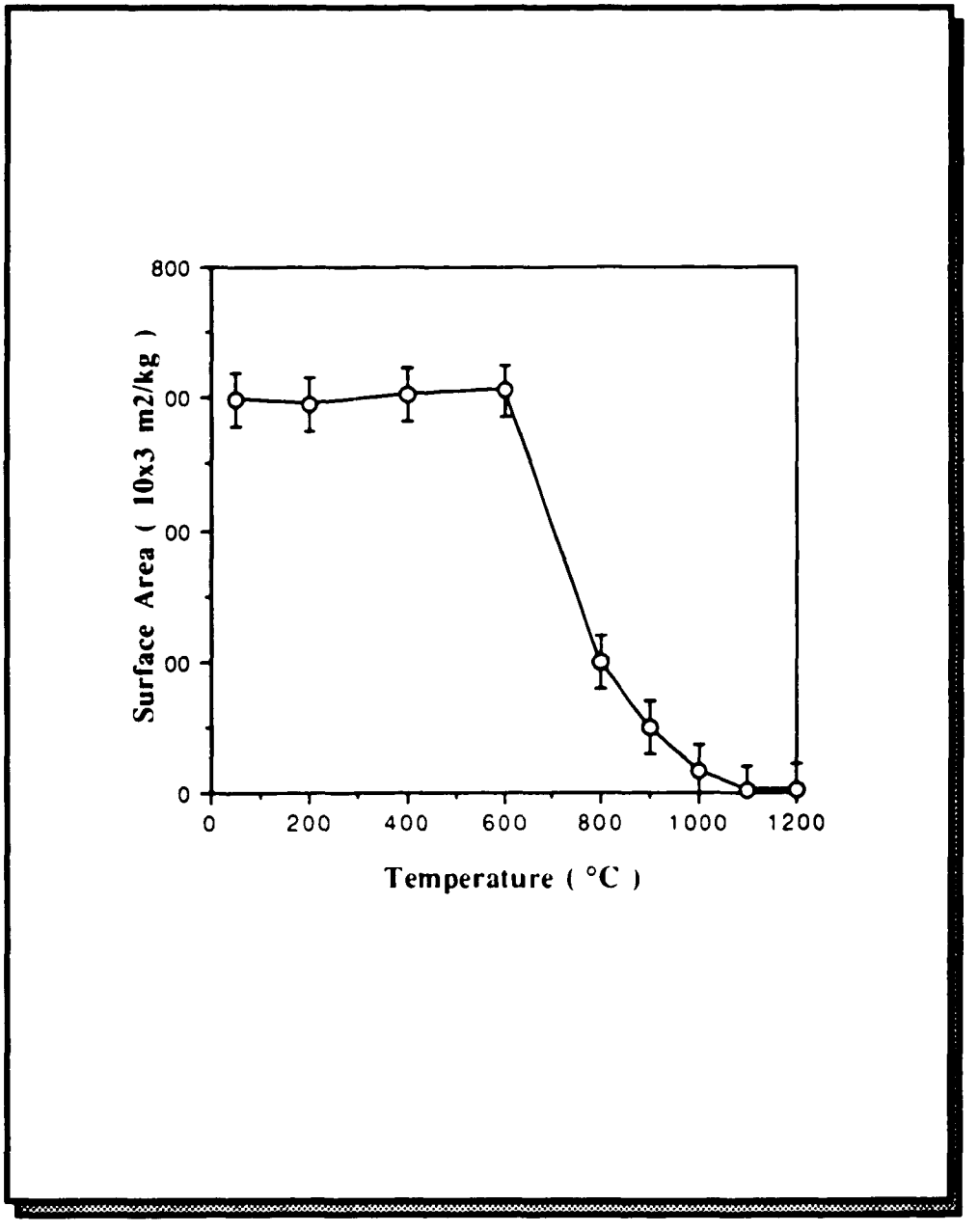

2. Photochemistry of Methyltinhalide Compounds in Solution.

Because of the difficulties encountered in studying photochemistry on a support, particularly characterizing the photoproducts, the approach has been to study the photochemistry in solution and then compare these results to those obtained on the glass surface. When this study was begun, however, we were surprised by the lack of quantitative data in the literature on the solution photochemistry of $(CH_3)_3SnX$ compounds. Consequently, initial experiments focused on characterizing the photochemistry of these compounds in solution.

One of the reasons for the absence of quantitative data is the difficulty of studying the solution photochemistry. The principal difficulty is that the compounds electronic absorption occurs in the far UV, $\leq$ 250nm. Consequently, excitation with conventional light sources, $\geq$ 254nm, is limited to the low energy side of the absorptions, and the number of solvents that can be used is limited to those that are transparent to ca. 200nm. Since the nature of the species in solution and its electronic spectrum depend on solvent polarity, solution studies were carried out in hexane and cyclohexane (nonpolar), and acetonitrile, hexanol, and ethanol (polar).

2.1 Spectral Characteristics of Trimethyltinhalide Compounds in Solution.

2.1.1 UV-visible spectroscopy.

The electronic spectrum of each trimethyltinhalide in solution (Figure 2.1) exhibits an absorption band located in the 250- to 200nm region. The lower energy transition is dependent on the nature of the halide, and in solution and on the glass, shifts to lower energy as the atomic number of the halide increases (Tables 2.1 and 2.2). Although the extensive delocalization that occurs in these covalent compounds clouds the assigment of their electronic spectra, the lower energy transition is thought to posses charge transfer character because of the shift to lower energy with increasing atomic number. [5, 6, 7] The $\sigma - \sigma^*$ transition locallyzed within the CH_3 groups as well as interligand and Sn-CH_3 charge transfer transitions occur at higher energy, ≤ 180 nm, and are not observed under the conditions of these experiments.

The UV spectra of trimethyltinhalides in solution depend on the polarity and nature of the solvent. As the polarizability constant of the solvent increases, the lower energy absorption exhibits a bathochromic shift, and an increase in the extinction coefficient (Table 2.3). In solvents capable of acting as a Lewis base, this shift is assigned to the formation of a charge transfer complex. [8] $(CH_3)_3SnX$ (X= Cl, Br, I), for example, forms 1:1 and 1:2 adducts with mono- and bidantate Lewis bases. Formation of the 1:1 adduct converts the tetrahedral $(CH_3)_3SnX$ to a trigonal bipyramidal molecule (Figure 2.2) in which the donor atom of the Lewis base occupies

Figure 2.1 - UV-vis absorption spectra of trimethyltinhalides in hexane.

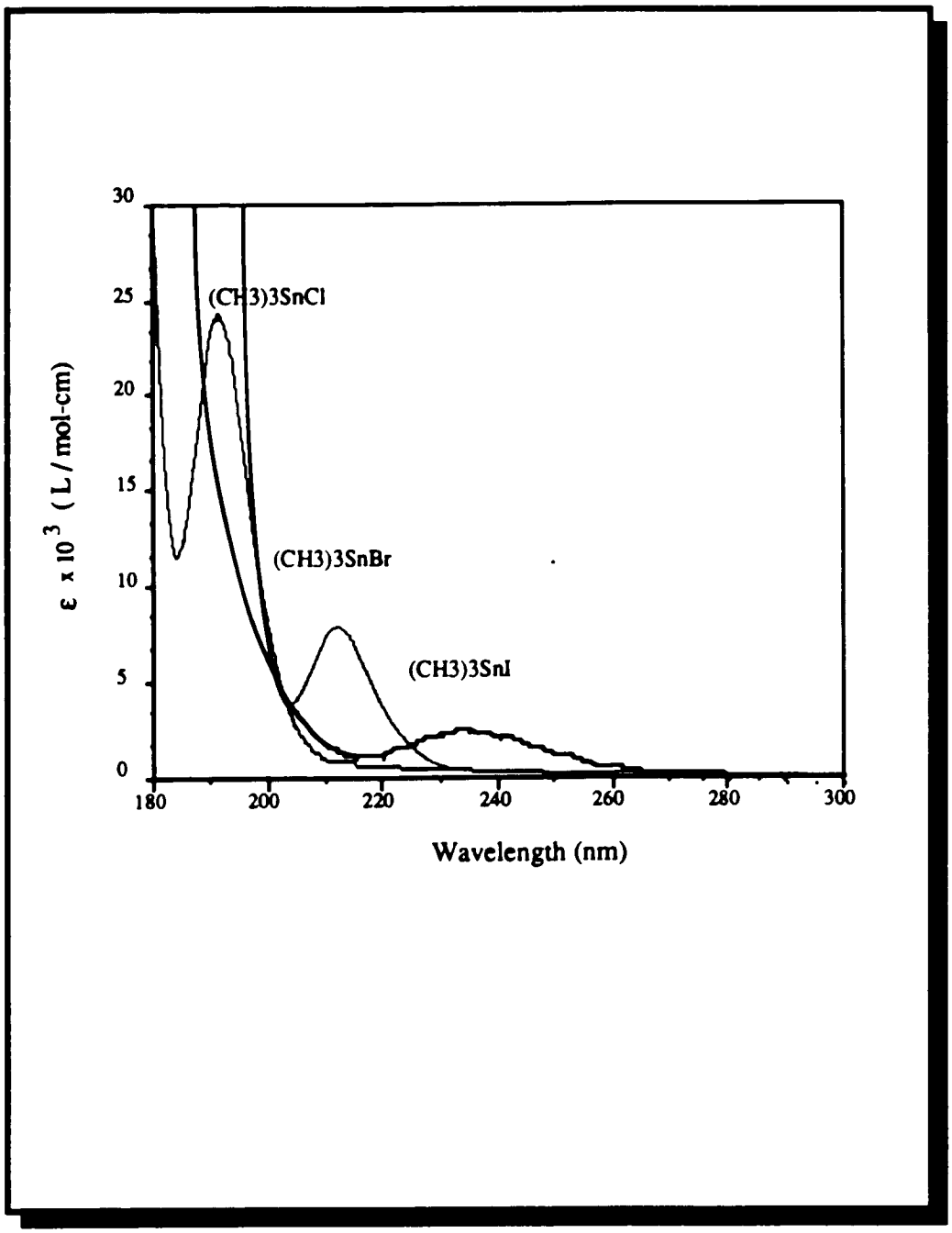

Table 2.1 - Absorption wavelengths and relative absorption coefficients of trimethyltinhalides adsorbed onto PVG and dissolved in Hexane.

	PVG		Hexane	
$(CH_3)_3Sn$-X	Wavelength	Epsilon (mol	Wavelength	Epsilon
X=	(nm)	ads./gr. PVG)	(nm)	(l/mol-cm)
Iodine	230.0	7.38×10^4	234.0	3.43×10^3
Bromine	230.0*	5.33×10^4	212.0	7.33×10^3
Chlorine	230.0*	2.46×10^4	195.0	2.46×10^4

*The maximum absorption of this compounds, which occurs below 220nm, could not be measured since PVG absorbs strongly (e ≥ 1.0e5) below 220nm.

Table 2.2 - Absorption wavelengths and absorption coefficients of Trimethyltinhalides, Alkylhalides, and molecular halides in carbontetrachloride solution.

$(CH_3)_3Sn$-X	Wavelength (nm)	Epsilon (l/mol-cm)
Iodine	234.0	3.43×10^3
Bromine	212.0	7.33×10^3
Chlorine	195.0	2.46×10^4

$(CH_3)_3$-X *	Wavelength (nm)	Epsilon (l/mol-cm)
Iodine	257.0	1.20×10^3
Bromine	204.0	1.80×10^3
Chlorine	172.0	....

X_2 **	Wavelength (nm)	Epsilon (l/mol-cm)
Iodine	515.0	900
Bromine	420.0	160
Chlorine	335.0	60

* Calvert, J. G.; Pitts, J. N., *Photochemistry*, Wiley & Sons, New York, 1966, pp 265

** Calvert, J. G.; Pitts, J. N., *Photochemistry*, Wiley & Sons, New York, 1966, pp 184

Table 2.3 - Absorption wavelengths and epsilon values of Trimethyltiniodide in polar and nonpolar solvents.

Solvent	Wavelength (nm)	Epsilon (l/mol-cm)	Dielectric Constant* (e)
1- Hexane	234.0	3.45×10^3	1.89
2- Cyclohexane	234.0	3.87×10^3	2.22
3- CCl_4	234.0	3.43×10^3	2.23
4- Acetonitrile	226.0	5.27×10^3	37.5
5- Hexanol	221.0	8.85×10^3	13.3
6- Ethanol	218.0	1.54×10^4	24.3

* CCR Handbook of Chemistry and Physics, 67th Ed., pp E-50

Figure 2.2 - Trimethyltinhalide molecular complexes.

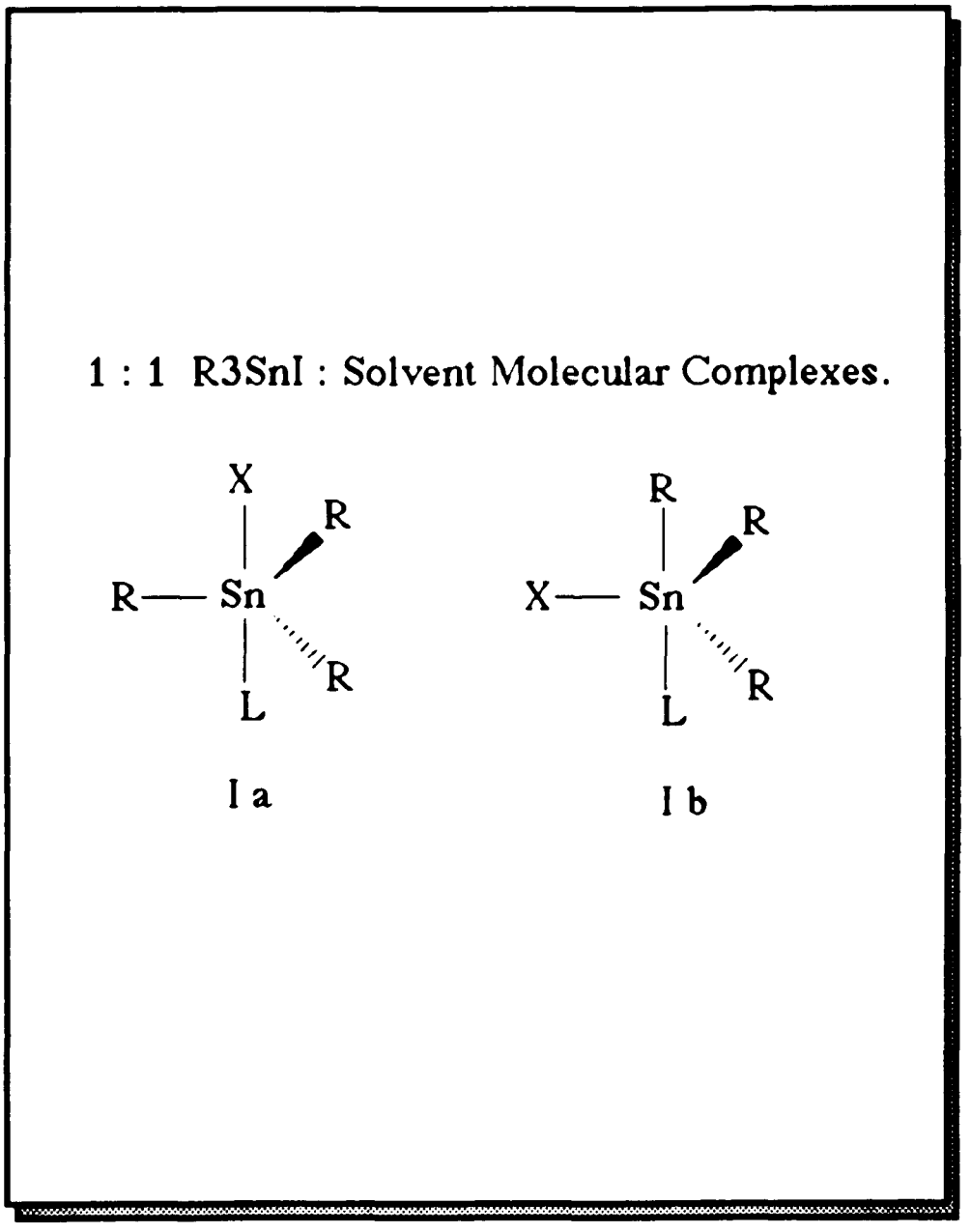

an axial position opposite to the hydrogen, and the methyl groups are in the trigonal plane. The Sn-X bond becomes more polar, and it has been suggested that this is due to an increase in the S orbital electron density in the Sn-C bond and the Sn-X bond. The amount of S orbital electron density increases with electron donor ability of the Lewis base.

Formation of a $(CH_3)_3SnI$-solvent adduct was confirmed by titration of $(CH_3)_3SnI$ in hexane with hexanol. Hexanol was used used for two reasons. First, it posses a hydroxyl function similar to the Si-OH functionality on the glass surface, and second, it is sufficiently soluble in nonpolar hydrocarbons, such as hexane, to allow spectroscopic examination.

As the amount of hexanol increases, the 234 nm band undergoes a bathochromic shift to 221nm (Figure 2.3) with an isosbestic point at 237 nm, as well as an increase in the value of the extinction coefficient. The occurrence of an isosbestic point suggest the appearance of a new species, and plots of the difference in absorbance between $(CH_3)_3SnI$/hexane and $(CH_3)_3SnI$/hexanol at 221 nm, against the mole fraction of hexanol (Figure 2.4) shows an initial linear dependence. The maximum occurs when the mole fraction of hexanol equals the mole fraction of $(CH_3)_3SnI$, which corresponds to the formation of a 1:1 $(CH_3)_3SnI$- hexanol adduct.

It was not possible to carry out equivalent titrations of $(CH_3)_3SnBr$ and $(CH_3)_3SnCl$ since the spectral changes, $\leq$ 200 nm, occur beyond the range of the spectrometer. Nevertheless, the occurrence of a bathochromic shift on addition of hexanol suggest that these compounds also form solvent adducts. In view of the similarity of the $(CH_3)_3SnX$ compounds, it is assumed that $(CH_3)_3SnBr$ and $(CH_3)_3SnCl$ also form 1:1 adducts. Thus, $(CH_3)_3SnX$ (X= I, Br, Cl) are tetrahedral complexes in nonpolar solvents,

but in solvents capable of acting as Lewis bases form trigonal bypiramidal solvent adducts. Formation of the adduct and its accompanying comformational and electronic changes are thought to be the principal reason for the change in photochemical behaviour.

2.1.2 Emission spectroscopy.

Hexane solutions of $(CH_3)_3SnI$ exhibit an emission with a maximum at 372nm when excited with 255nm light (Figure 2.5). Changing the halogen from I to Br and then to Cl causes a bathocromic shift in the emission maximum (Table 2.4). The shift, which is similar to that observe in tha absorption spectra of (CH3)3Sn-X, occurs with a pronounced decline in intensity. In fact, with (CH3)3SnCl, only a small shoulder at 300nm is observed upon excitation with 255nm light.

2.1.3 FTIR spectroscopy.

In the 4000- to 400 cm^{-1} region, the FTIR spectra of $(CH_3)_3SnX$ (X= I, Br, Cl) (Figure 2.6) are identical, and exhibit bands characteristic of the CH_3 and Sn-CH_3 vibrations, (Table 2.5). The bands associated with the Sn-X vibrations occur beyond the low frequency detection limit of the spectrometer, but are readily detected by Raman spectroscopy. Their frequencies as well as the assignments of the IR bands are summarized in Table 2.5.

Figure 2.3 - UV-vis spectra of the titration of 7.37×10^{-4} M trimethyltiniodide in the hexane:hexanol system.

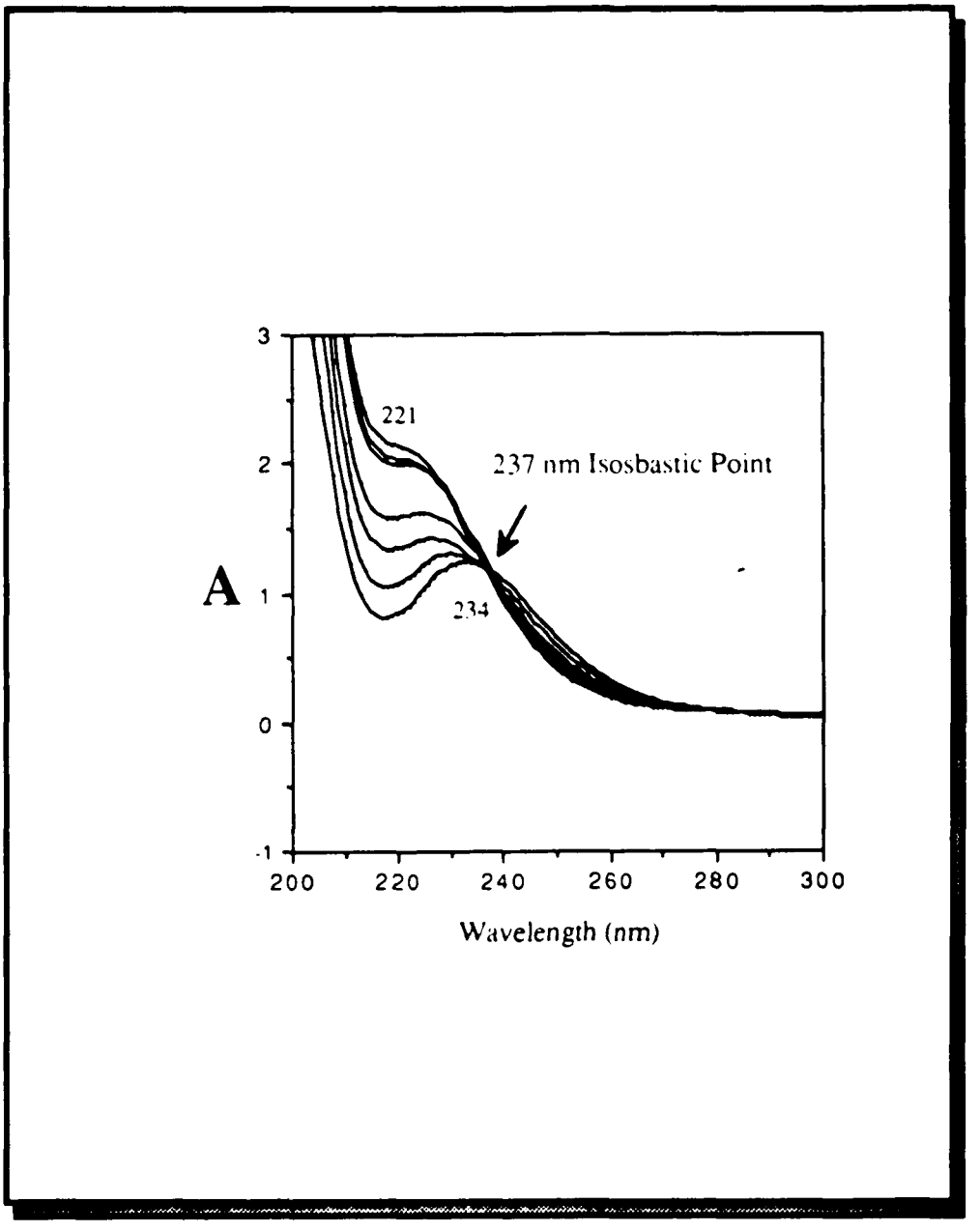

Figure 2.4 - Plot of the titration of trimethyltiniodide in the hexane:hexanol system.

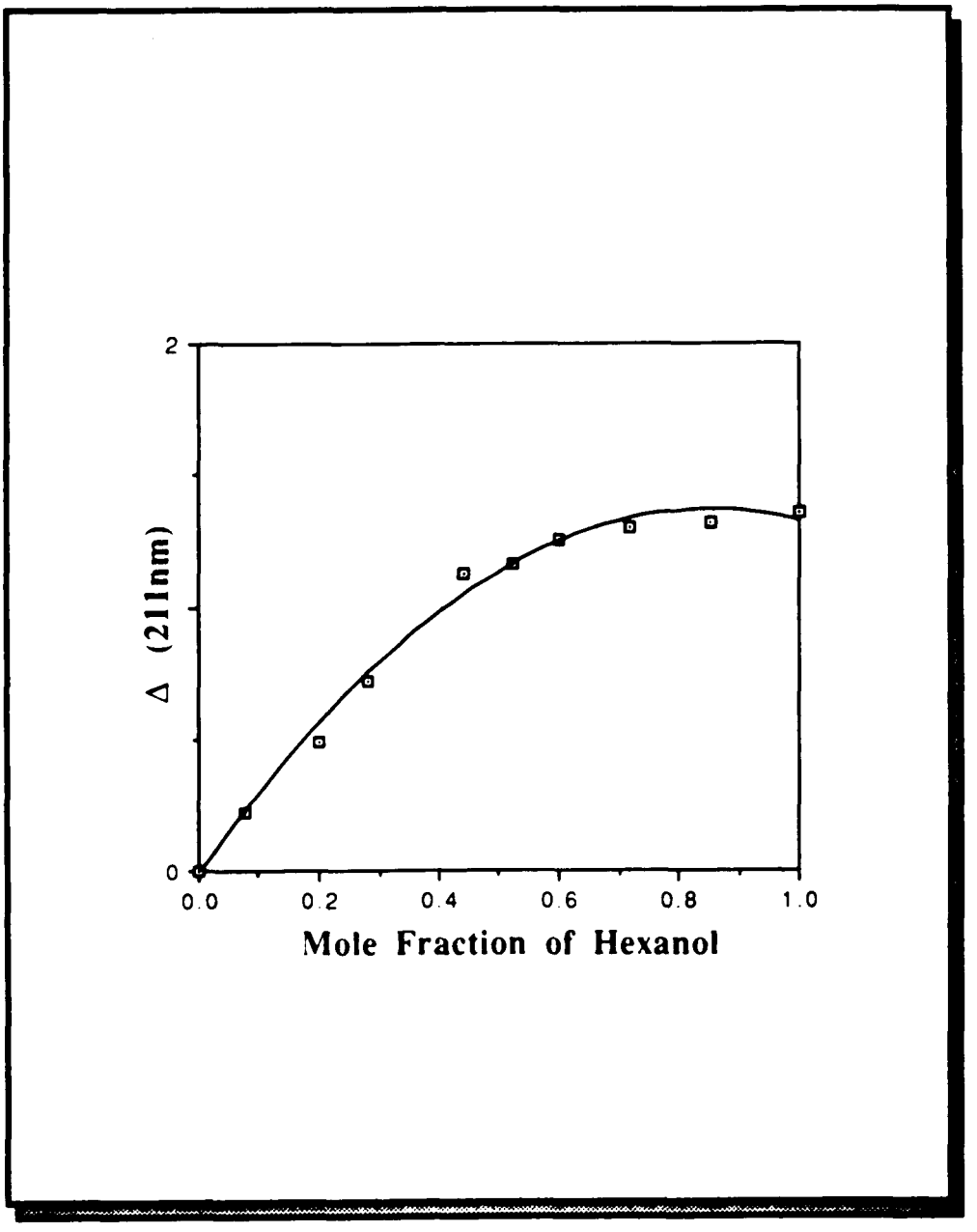

Figure 2.5 - Emission spectra of $1.0x10^{-4}$M solution of trimethyltiniodide in hexane upon excitation with 250nm light.

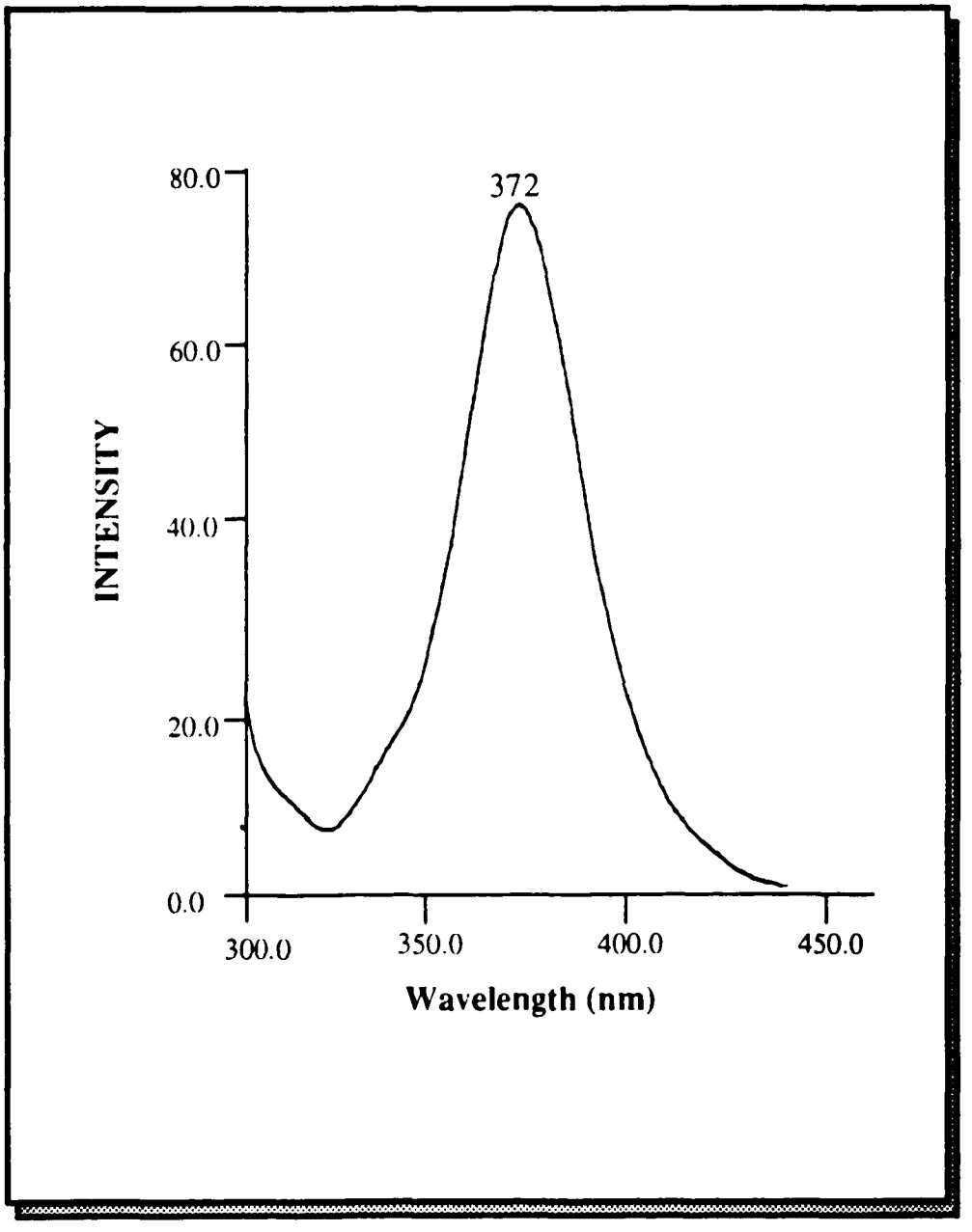

2.2 Photochemical Studies.

Because of the lack of quantitative data in the literature, the photochemistries of the $(CH_3)_3SnX$ compounds, principally $(CH_3)_3SnI$, were first examine in nonpolar solvents, and then, to more closely mimic the glass surface, in polar solvents. The latter data was then compared to that obtained with the compounds adsorbed onto PVG.

2.2.1 Nonpolar Solvents.

2.2.1.1 Photochemistry of Trimethyltiniodide in Hexane.

Solutions of trimethyltiniodide in hexane exhibit no spectral change when stored in the dark at 25 °C for prolonged periods of time (≥ 6 months). Consequently,the compound is thermally stable, but reacts immediately on exposure to UV light. As previously described, the electronic spectrum of $(CH_3)_3SnI$ in hexane consists of a single absorption with a maximum at 234nm and the edge of a high energy absorption with a maximum at < 200nm. Excitation of a degassed 7.37×10^{-4} M hexane solution of $(CH_3)_3SnI$ with 254 nm light causes an immediate decline in the 234-nm absorption (Figure 2.7), and the simultaneous growth of bands at 211-, 290-, 365-, and 520-nm. Isosbestic points, which occur at 224nm and 252nm are maintained through > 50% of the reaction. Nevertheless, all photolysis were limited to ≤ 50% conversion of the starting material. Comparison of the photolyte spectra with those of pure $(CH_3)_3Sn\text{-}Sn(CH_3)_3$ shows that the 211 nm band is characteristic of the $[(CH_3)_6Sn]_2$ dimer. Raman and FTIR

Table 2.4 - Peak assignment of the emission spectra of trimethyltinhalides in hexane upon excitation with 255nm light.Excitation slit:Emission slit = 30:4.

$(CH_3)_3Sn$-X X=	Peak Maxima (nm)	Intensity (%)
I	372	90
Br	320	30
Cl	300 (shoulder)	5

Table 2.5 - Infrared vibrational frequency assignments for the Sn-CH3 vibrational modes in the region 4000- to 400 cm-1, [9] and Infrared and Raman frequency assignments for the Sn-X (X= halide or Sn atoms) vibrational modes in $(CH_3)_3SnX$ and $(CH_3)_3Sn\text{-}Sn(CH_3)_3$.[10]

Assignment	Wavenumber cm^{-1}
C-H asymmetric stretch	2992
C-H symmetric stretch	2918
C-H bend	1400
C-H symmetric distortion	1187
C-Sn-C symmetric stretch	785
Sn-C asymmetric stretch	547
Sn-C symmetric stretch	527

Sn-X	**Wavenumber cm^{-1}**	
X=	**IR**	**Raman**
Cl	382	331
Br	264	235
I	207	167
Sn	190	187

Figure 2.6 - FTIR spectra of trimethyltinhalides in hexane.

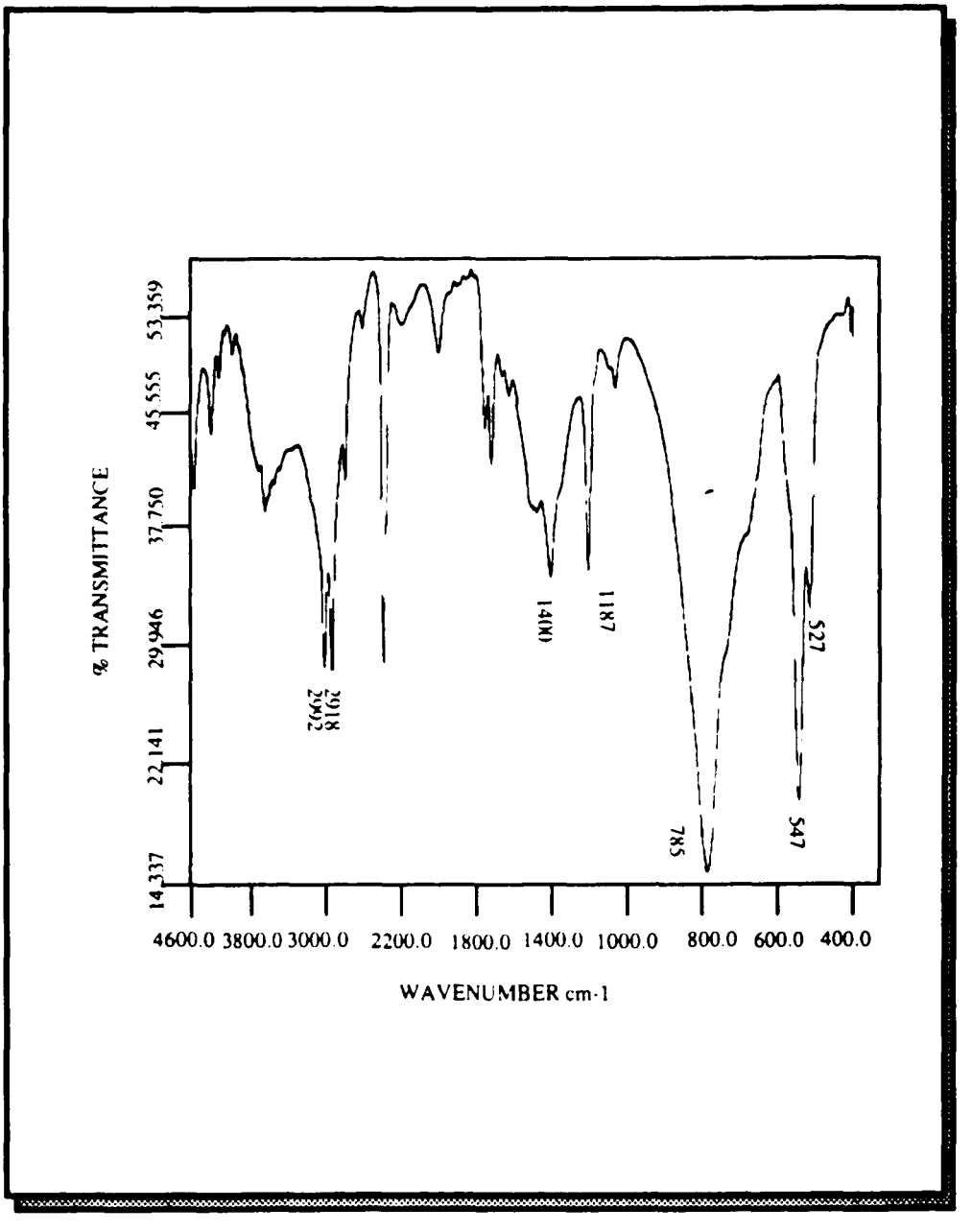

spectra confirmed its formation.

Raman spectra recorded during photolysis (Figure 2.8) shows that the intensity of the 186 cm^{-1} Sn-Sn vibration of $[(CH_3)_6Sn]_2$ increases concurrent with the disappearance of the 167-, 512-, and 546 cm^{-1} bands of $(CH_3)_3SnI$. In the alkyl and metal-alkyl regions, the FTIR of $(CH_3)_3SnI$ and $[(CH_3)_3\ Sn]_2$ are similar except that the intensity of the Sn-CH_3 stretch at 508 cm^{-1} in $[(CH_3)_3\ Sn]_2$ is ca. twice that in $(CH_3)_3SnI$. Consistent with $[(CH_3)_6Sn]_2$ formation, FTIR recorded during photolysis (Figure 2.9) show an increase in the 508 cm^{-1} band.

The 520 nm peak that develops during photolysis (Figure 2.7) agrees with that of I_2 dissolved in hexane, and is assigned to its formation. The peaks at 290-,and 365-nm are assigned to the formation of small amounts of I_3^-. Although the latter absorptions are more intense, the amount of I_3^- formed never exceeds more than 2% of the total I_2 yield. Consequently, I_3^- appears to be a secondary product arising from photolysis of I_2.

The intensity of the 370 nm emission from (CH3)3SnI also declines during 254 nm photolysis, (Figure 2.10). The decline in the emission intensity corresponds to the disappearance of the 234nm peak in the UV-visible spectra. It should be mentioned that neither I_2 or I_3^- in hexane exhibit an emission spectra upon excitation with 254 nm light.

2.1.1.2 Kinetics of the Photochemical Reaction of Trimethyltiniodide.

Because of the high efficiency of the photochemical reaction, and the fact that the product I_2 is itself photochemically active, kinetic measurements to elucidate the kinetic process were limited to ≤ 40% conversion of $(CH_3)_3SnI$. In general, photolysis times were ≤ 30 seconds, and the $(CH_3)_3SnI$

Figure 2.7 - UV-visible spectra of the 254 nm photolysis of 7.37×10^{-4} M solution of trimethyltiniodide in hexane.

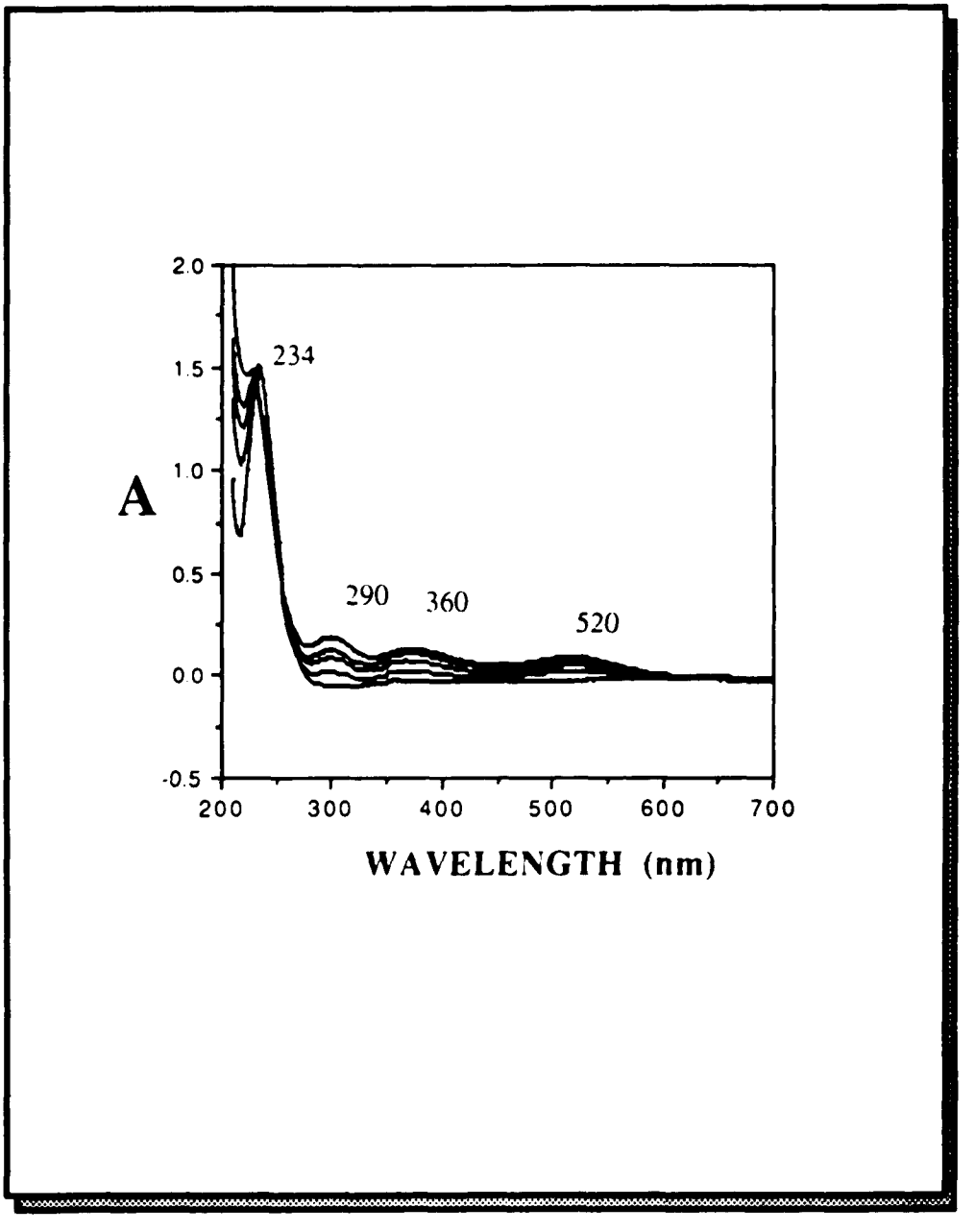

Figure 2.8 - Raman spectra of the 254nm photolysis of 7.37×10^{-3} M solution of trimethyltiniodide in hexane.

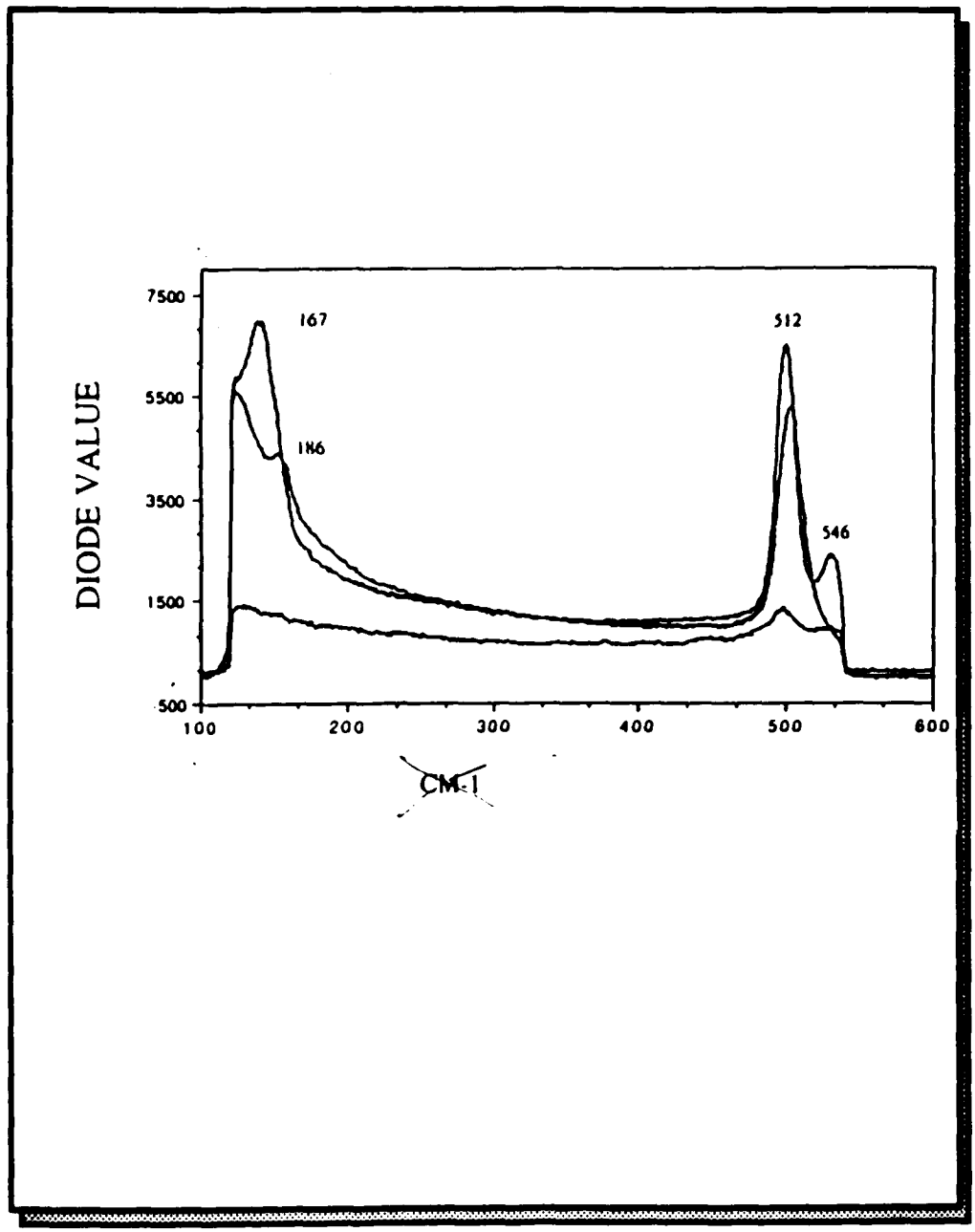

Figure 2.9 - FTIR spectra of the 254nm photolysis of 7.37×10^{-3} M solution of trimethyltiniodide in hexane.

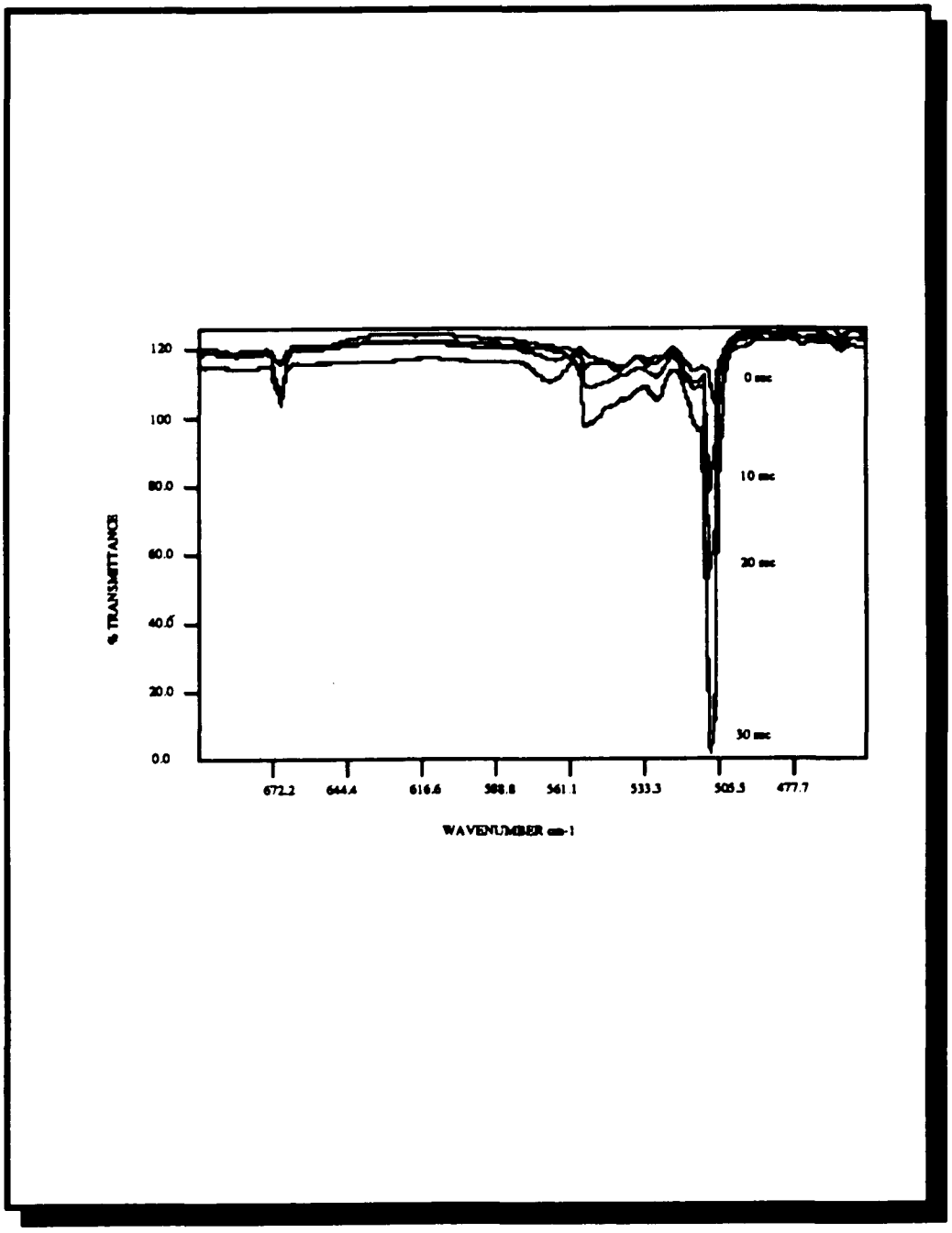

Figure 2.10 - Emission spectra of the 254nm photolysis of 1.00×10^{-4} M solution of trimethyltiniodide in hexane at room temperature (25°C).

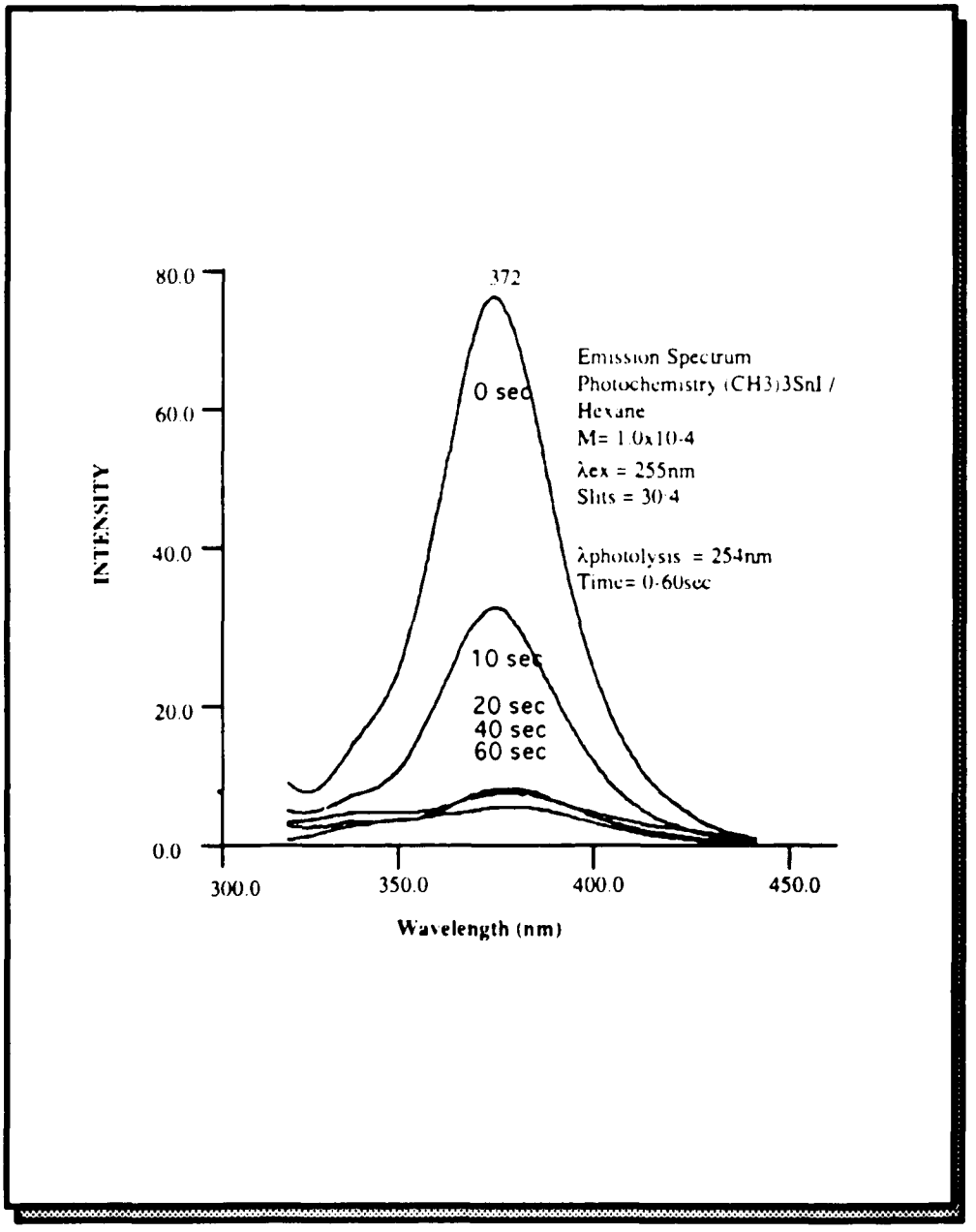

concentrations were 10^{-5} to 10^{-4} M in order to follow the reaction by UV-visible spectroscopy. In these experiments both the quantum yield of $(CH_3)_3SnI$ disappearance, Φ_d, and product appearance, Φ_a, were measured to elucidate the primary photochemical process. Typically, the sample and the $Fe(C_2O_4)^{-3}$ actinometer were irradiated simultaneously. The intensity incident on the sample, I_o, was calculated according to the procedure of Calvert and Pitts, [11] while the rate of the reaction of the tin compounds was determined by periodic spectral analysis. Difference spectra (Figure 2.11) were obtained by subtracting the spectrum before photolysis from those recorded periodically during photolysis. Optical densities of the resulting maxima and minima were obtained by a "peak-picker" program, an the values obtained at different times are summarized in Table 2.6.

Since, the total absorbance of the solution, particularly in the UV region, is the sum of the absorbances of the individual components present at a given time, the measured optical densities at 234nm (Table 2.6) were corrected by means of the following equation :

$$A^{234}_{correct} = A^{234}_{measured} - \left[[(CH_3)_6Sn_2]\, \varepsilon^{234}_{(CH_3)_6Sn_2}\, l \right] - \left[[I_2]\, \varepsilon^{234}_{I_2}\, l \right] \qquad 2.1$$

$[(CH_3)_3\,SnI]$ and $[I_2]$ refer to the molar concentration of the species, and the ε^{234}'s are the molar extinction coefficients at 234 nm of trimethyltiniodide, and iodine, respectively, (Table 2.7). The quantity l is the path length of the photocell (l= 1.0 cm). The concentration of I_2 present was calculated from the change in absorbance at 520 nm, while the concentration of $(CH_3)_6Sn_2$ was calculated from the change in absorbance at 211 nm, (Figure 2.11).

Figure 2.11 - Spectral subtraction of the one minute photolysis of trimethyltiniodide in hexane.

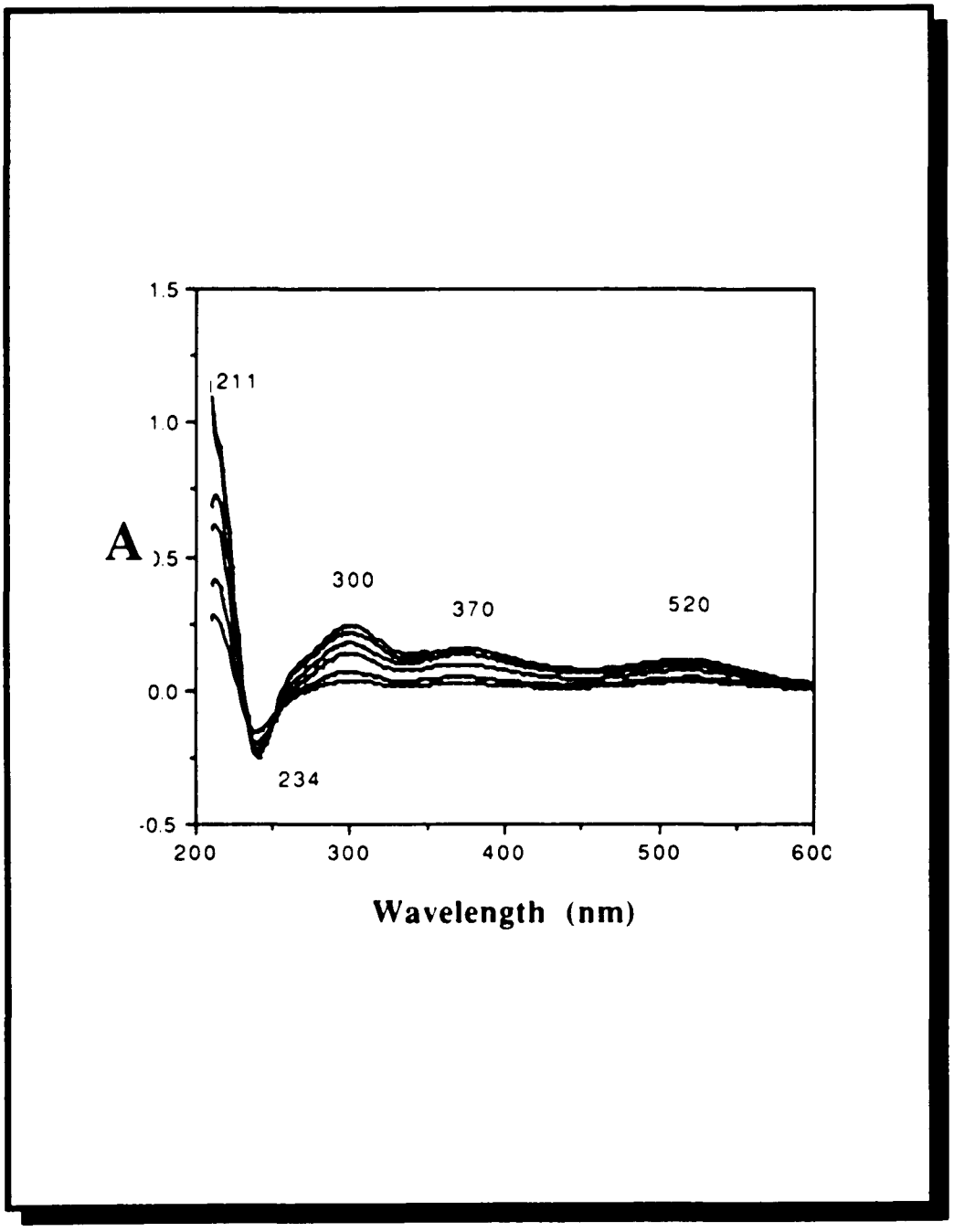

Table 2.6 - Spectral Subtraction data during photolysis of 2.211×10^{-6} mol of trimethyltiniodide in hexane.

Time	Absorption Peak (nm.)				
(sec.)	211	234	300	370	520
0.00	0.000	0.000	0.000	0.000	0.000
5.00	0.143	-0.101	0.015	0.007	0.017
10.00	0.278	-0.157	0.034	0.034	0.030
15.00	0.356	-0.175	0.050	0.047	0.037
20.00	0.417	-0.199	0.070	0.062	0.045
25.00	0.524	-0.214	0.107	0.096	0.061
30.00	0.614	-0.240	0.137	0.087	0.073
35.00	0.557	-0.270	0.123	0.113	0.075
40.00	0.734	-0.226	0.176	0.156	0.091
45.00	0.765	-0.249	0.184	0.133	0.999
50.00	0.812	-0.247	0.215	0.133	0.102
55.00	0.833	-0.244	0.022	0.138	0.106
60.00	0.856	-0.257	0.241	0.112	0.112

The reaction products also absorb at the excitation wavelength, 254nm. Consequently, the intensity absorbed by $(CH_3)_3SnI$ was corrected for inner filter effects according to :

$$I_a = I_0\left[1 - 10^{-Abs_{254}^{Corrected}}\right] \qquad 2.2$$

where $Abs_{254}^{Corrected}$ is given by :

$$Abs_{254}^{Corrected} = Abs_{254}^{Measured} - \left[\left[(CH_3)_6Sn_2\right] \varepsilon_{(CH_3)_6Sn_2}^{254} l\right] - \left[\left[I_2\right] \varepsilon_{I_2}^{254} l\right] \qquad 2.3$$

The programs used to analyze the measure absorbance changes according to equations 2.1 and 2.2, and in turn the quantum yields are described in Appendices 1 and 2.

Plots of the calculated quantum yields vs. irradiation time, Figure 2.12, show that the the quantum yield of $(CH_3)_3SnI$ disappearance is independent of the O_2 concentration. Within experimental error, the quantum yield of trimethyltiniodide dissapearance in hexane (Table 2.8) is independent of whether the solution was saturated with O_2, N_2, or Ar, or degassed by repeated freeze-pump-thaw. Also, the quantum yield of $(CH_3)_3SnI$ disappearance with 254 nm excitation is independent of initial $(CH_3)_3SnI$ concentration, (Figure 2.13). However, the quantum yield is very dependent on the excitation wavelength, and declines rapidly as the excitation wavelength shifts from 254nm to 355nm (Table 2.9).

The ratio of the limiting quantum yields of $(CH_3)_3SnI$ disappearance

Table 2.7 - Extinction coefficient values of $(CH_3)_3SnI$, $(CH_3)_6Sn_2$, and I_2 at different absorption wavelengths in hexane.

	ε ($M^{-1} \cdot cm^{-1}$)		
Wavelength	**$(CH_3)_3SnI$**	**$(CH_3)_6Sn_2$**	**I_2**
211 nm	5.91×10^3	2.11×10^4	1.02×10^4
234 nm	3.45×10^3	4.48×10^3	3.78×10^3
254nm	1.43×10^3	1.39×10^3	2.75×10^3
520 nm	0.00	0.00	920

Figure 2.12 - Initial quantum yield of the photochemical reaction of 7.37 x 10^{-4} M solution of trimethyltiniodide in hexane.

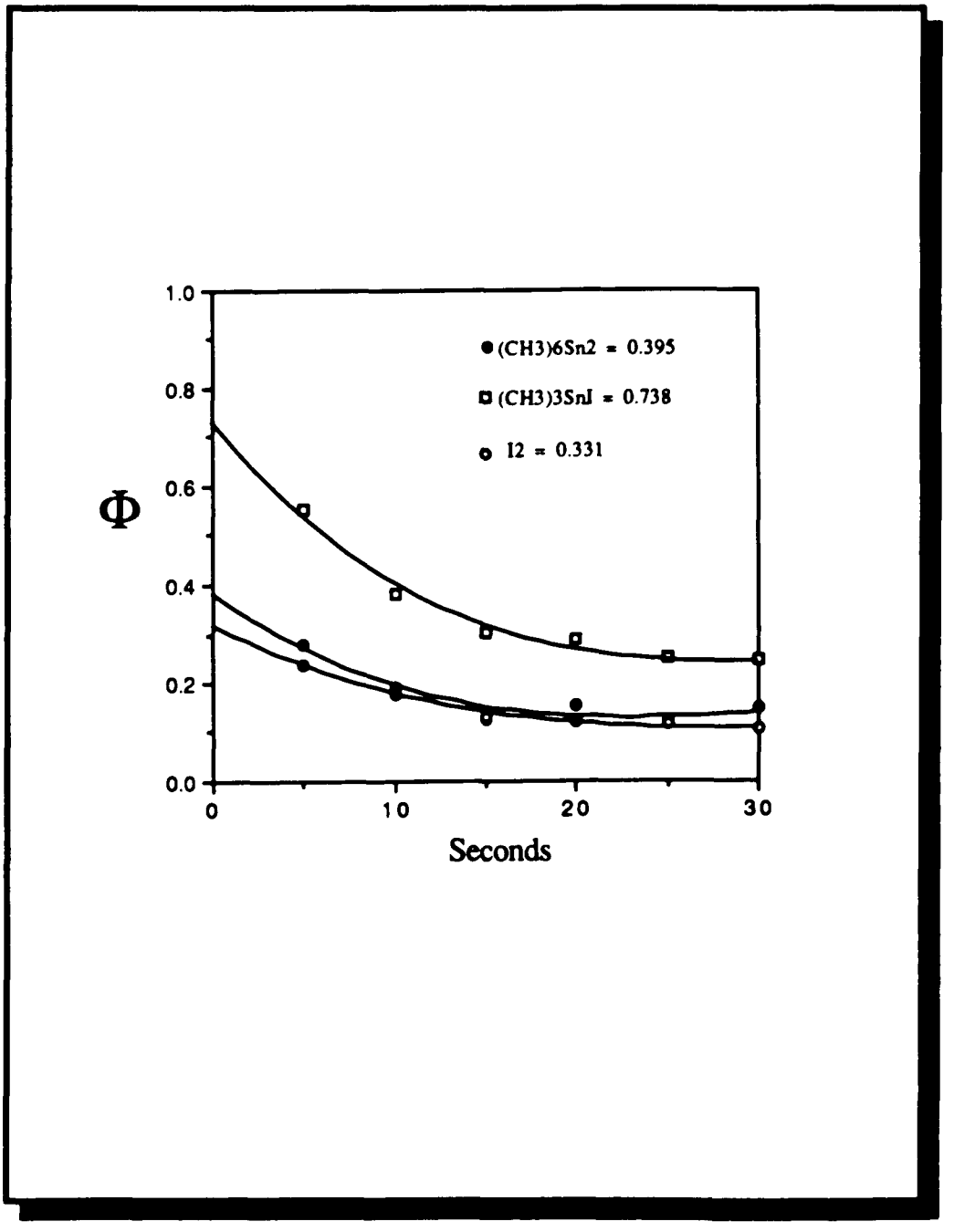

Table 2.8 - Effect of oxygen, nitrogen , and air free atmospheres on the quantum yield of the photochemical reaction of 7.37 x 10^{-4} M solution of trimethyltiniodide in hexane at a constant light intensity of 1.22×10^{-7} einstein/L-sec.

	Φ_1	Φ_2	
Environment	$(CH_3)_3SnI$	I_2	Φ_1/Φ_2
Air	0.323 ± 0.05	0.170 ±0.06	1.90
Oxygen	0.338 ± 0.05	0.169 ±0.06	2.00
Nitrogen	0.320 ± 0.05	0.171 ±0.06	1.87
Argon	0.328 ± 0.05	0.169 ±0.06	1.93

Table 2.9 Quantum yield of the photochemical reaction of 7.37 x 10^{-4} M solution of trimethyltiniodide in hexane as a function of the light source wavelength, and a a constant light intensity of 1.22x10^{-7} einstein/L-sec.

	Φ		
Wavelength (nm)	$(CH_3)_3SnI$	$(CH_3)_6Sn_2$	I_2
254	0.323 ± 0.05	0.165 ± 0.06	0.170 ± 0.06
310	0.109 ± 0.06	0.060 ± 0.01	0.065 ± 0.01
355	no reaction	no reaction	no reaction

and $(CH_3)_6Sn_2$ and I_2 appearance, 2.06 ± 0.17, are consistent with an overall reaction stoichiometry of :

$$2\,(CH_3)_3SnI \xrightarrow{h\nu} (CH_3)_6Sn_2 + I_2 \qquad 2.4$$

The ratio of the quantum yield of the reactant to products is constant (~2), as well as the ratio of the quantum yields of the products are independent of the initial $(CH_3)_3SnI$ concentration. However, at high initial $(CH_3)_3SnI$ concentration, ≥ $1.0x10^{-3}$ M, the quantum yield of $(CH_3)_3SnI$ dissapearance increase to approximately twice that of the lower concentrations.

The variables of light intensity and excitation wavelength are unique to photochemical reactions. Since, as noted above, the quantum efficiency declines with increasing wavelength, studies of the intensity dependency were limited to 254nm excitation. Since $\Phi = \frac{dA}{dt} / I_a^n$ for any process, plots of log Φ vs. log I (Figure 2.14) show that the quantum yield of $(CH_3)_3SnI$ disappearance as well as I_2 appearance exhibit, within experimental error, first order dependences, n=0.83, on the excitation intensity.

The effect of I_2 and $(CH_3)_6Sn_2$ were also examined not only to probe the details of the photochemistry in hexane, but at the time, it seem essential to understanding the differences that occur in the photochemistry of $(CH_3)_3SnI$ in nonpolar and polar solvents, and on the glass surface. The amount of I_2 added was always less than the maximum amount of I_2 formed in the photolysis, but within this range of I_2 concentrations, the quantum yield of $(CH_3)_3SnI$ disappearance and product formation (Figure 2.15) are independent of added I_2.

Figure 2.13 - Quantum yield dependence on the trimethyltiniodide concentration at a light intensity of 5.562 x 10^{-8} einstein - L^{-1}- sec^{-1}.

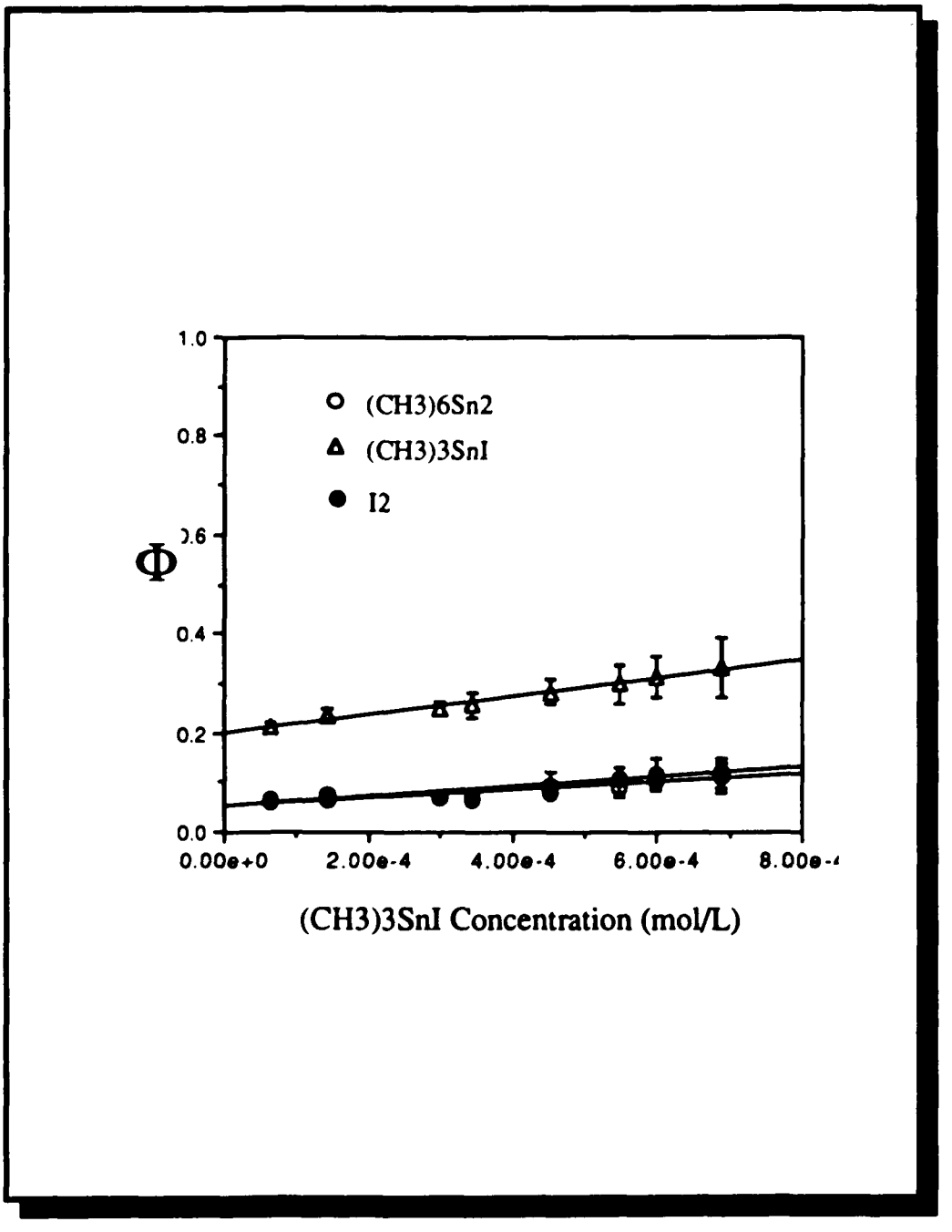

With added $(CH_3)_6Sn_2$, the results are more complex. With $\leq 2.0x10^{-6}$ M $(CH_3)_6Sn_2$, the quantum yield of $(CH_3)_3SnI$ disappearance is independent of the added dimer. However, with a concentration of $(CH_3)_6Sn_2 \geq 2.0x10^{-6}$ M the quantum yield of $(CH_3)_3SnI$ disappearance increases rapidly and becomes surprisingly large, i.e., $\Phi > 1.0$.

During the course of these photochemical experiments, it was discovered that the photoproducts, I_2 or $(CH_3)_6Sn_2$, thermally react to reform the starting material, i.e.,

$$I_2 + (CH_3)_6Sn_2 \xrightarrow{K_t} 2(CH_3)_3SnI \qquad 2.5$$

Since this would affect the measured quantum yield of $(CH_3)_3SnI$ dissapearance, the rate of the thermal back reaction was determined spectrophotometrically. The rates of I_2 disappearance and $(CH_3)_3SnI$ appearance were measured using the kinetic program of the Aviv UV-visible spectrometer. The program measures the absorbance at specific wavelengths with an acquisition time of 10 scans / sec.

Figure 2.17 is a typical plot obtained by the spectroscopic method. The initial concentrations of I_2 and $(CH_3)_6Sn_2$ were usually in the range 10^{-5} to 10^{-4} M, depending upon the rate of the reaction. In all runs the I_2 concentration was kept constant while the $(CH_3)_6Sn_2$ was changed. In a typical experiment, 1 to 10 ml aliquots of a $4.59x10^{-5}$ M $(CH3)6Sn2$ solution were injected into 10 ml of a degassed $1.66x10^{-4}$ M hexane solution of I2. The kinetics program was initiated and rates of I2 dissapearance and $(CH_3)_3SnI$ appearance measured. All experiments were carried out at 25

Figure 2.30 - Quantum yield dependence of the 254 nm photochemical reaction of 2.93×10^{-4} M solution of trimethyltiniodide on the light intensity.

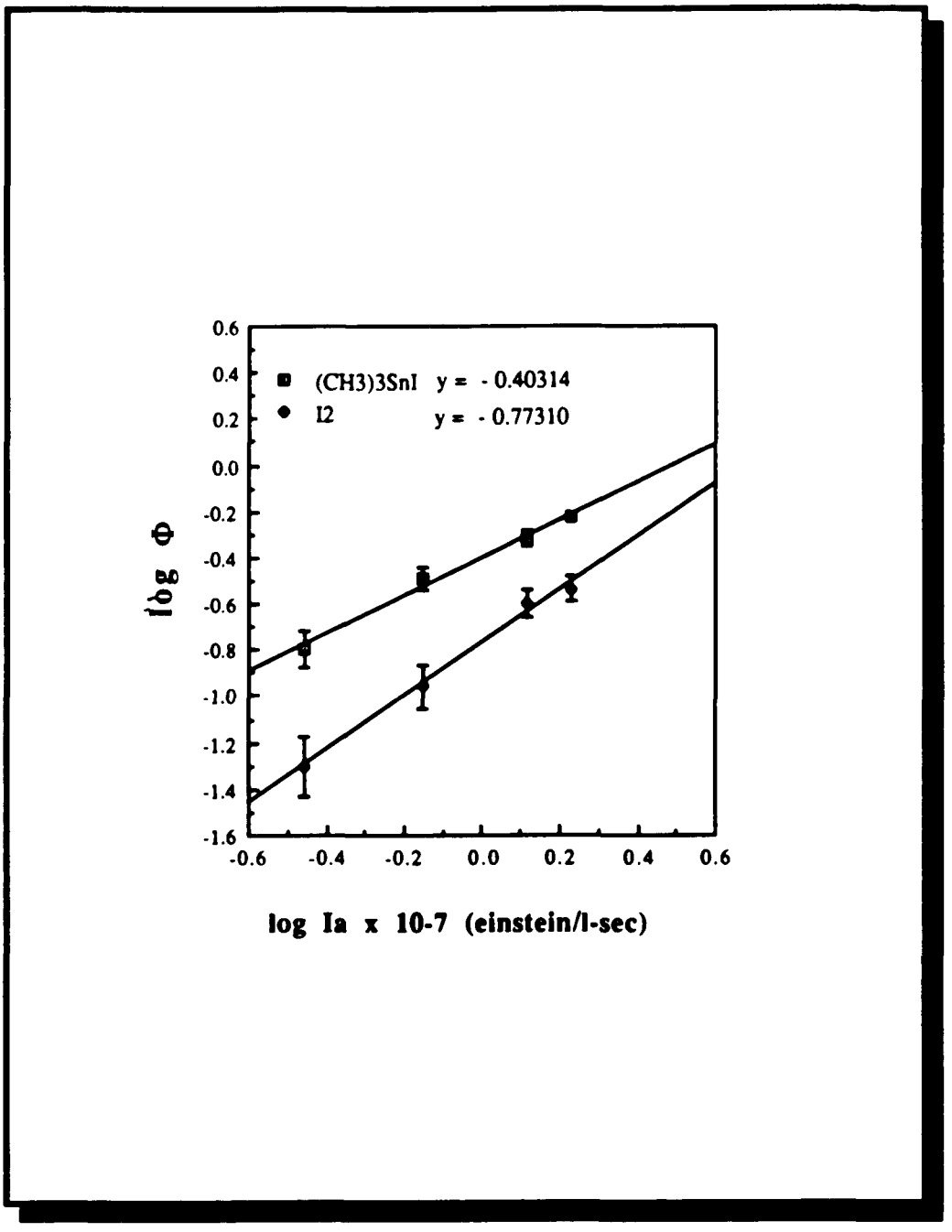

Figure 2.15 - Quantum yield as a function of the I_2 concentration at a constant $(CH_3)_3SnI$ concentration of $2.93x10^{-4}$ M solution and a constant light intensity of 1.22×10^{-7} (einstein/l-sec).

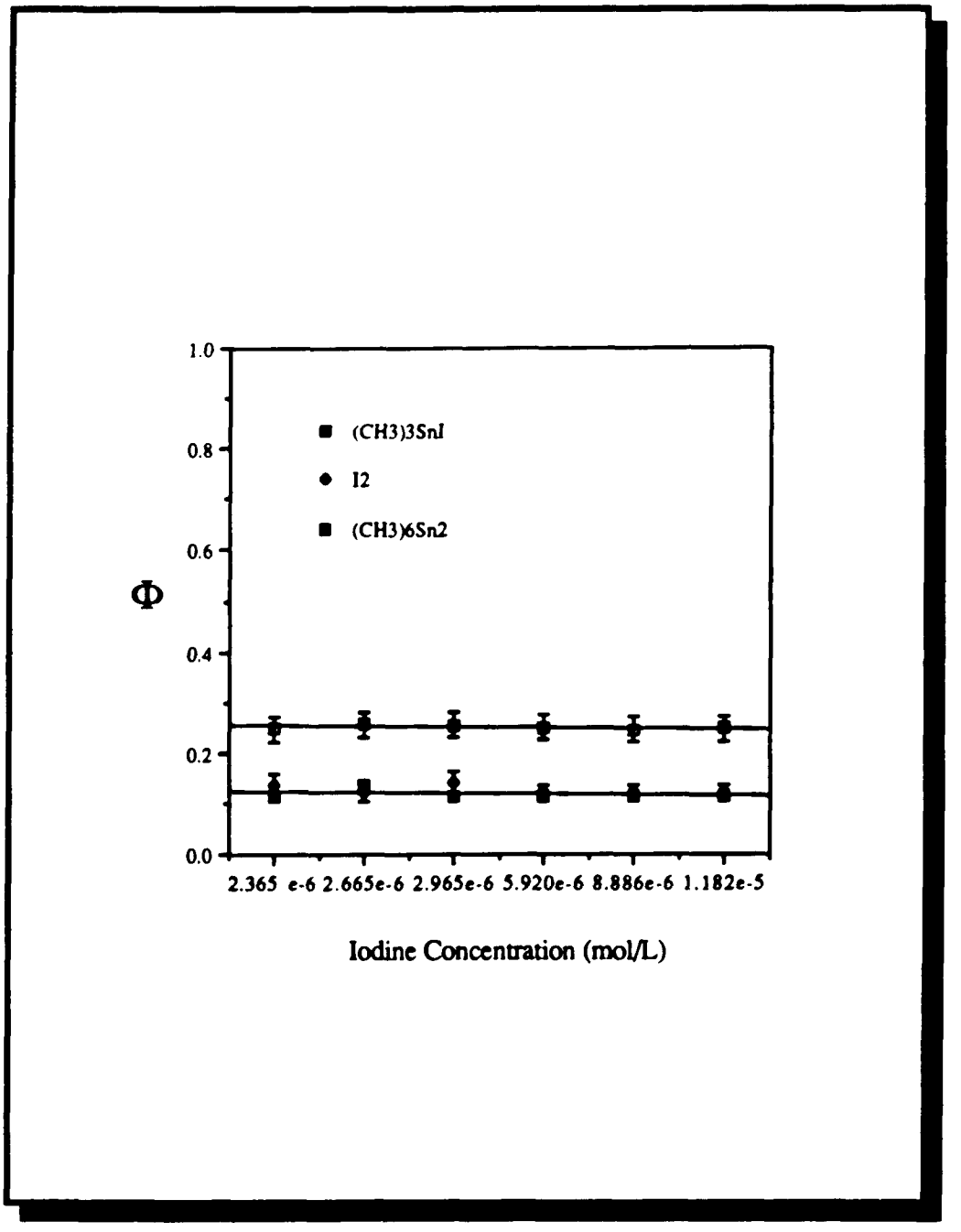

Figure 2.16 Quantum yield as a function of the $(CH_3)_6Sn_2$ concentration at a constant $(CH_3)_3SnI$ concentration of $2.93x10^{-4}$ M solution and a constant light intensity of 1.22×10^{-7} (einstein/l-sec).

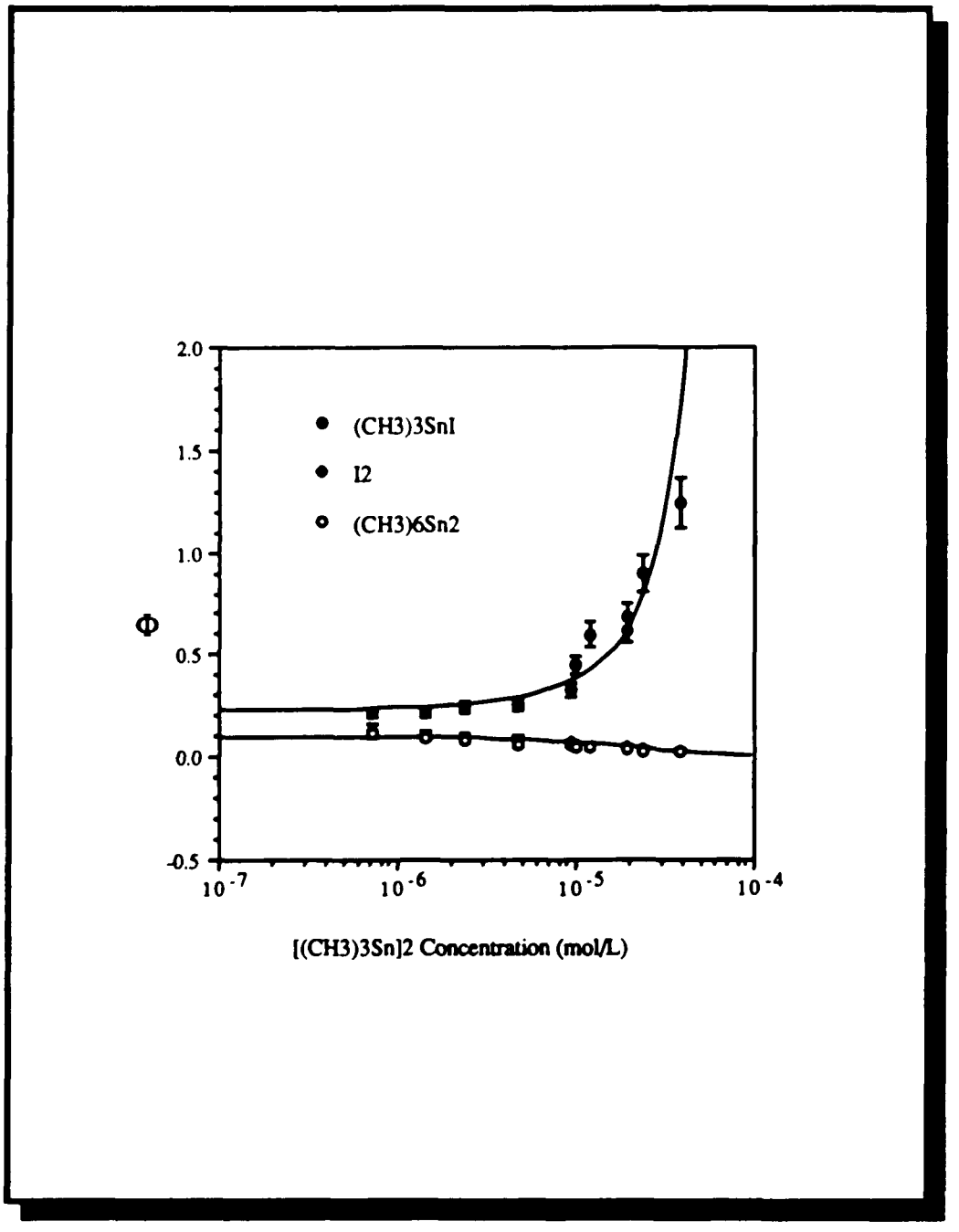

°C. The experimental data (Figure 2.17) was fitted to the general rate expression :

$$\frac{d[(CH_3)_3SnI]}{dt} = K_t [I_2]^n [(CH_3)_6Sn_2]^m \qquad 2.6$$

and the values of n and m , $n = m = 1$, was determined by the method of integration and by the differential method. [12] The values of K_t (Table 2.10) were calculated from the integrated second-order equation:

$$K_t = \frac{2.303}{t\,(a - b)} \log \frac{b\,(a - x)}{a\,(b - x)} \qquad 2.7$$

where a = $[(CH_3)_6Sn_2]_0$, b = $[I_2]_0$, and x = the decrease in the I_2 concentration, and yield an average value 226.4±0.5 M^{-1}-sec^{-1}.

The data gathered to this point suggests that the primary photochemical event in a nonpolar solvent is the homolytic cleavage of the $(CH_3)_3Sn$--I bond leading to $(CH_3)_3Sn\bullet$ and I• radicals. Consequently, the addition of a radical scavenger would be expected to reduce the product yields, but not the rate of disappearance of $(CH_3)_3SnI$. Indeed, as shown in Figure 2.18, the addition of isoamylnitrite [13] (1.0×10^{-4}M) has no effect on the quantum yield of $(CH_3)_3SnI$ disappearance, but reduces the quantum yield of I_2 from 0.35 to 0.05 in hexane containing 1.0×10^{-4} M isoamylnitrite.

Figure 2.17 - Example of a spectroscopic kinetic plot as obtained for the reaction of 10 ml of 1.66 x 10^{-4} M I_2 and 2 ml of 4.59 x 10^{-5} M $(CH_3)_6Sn_2$ in hexane at 25 °C.

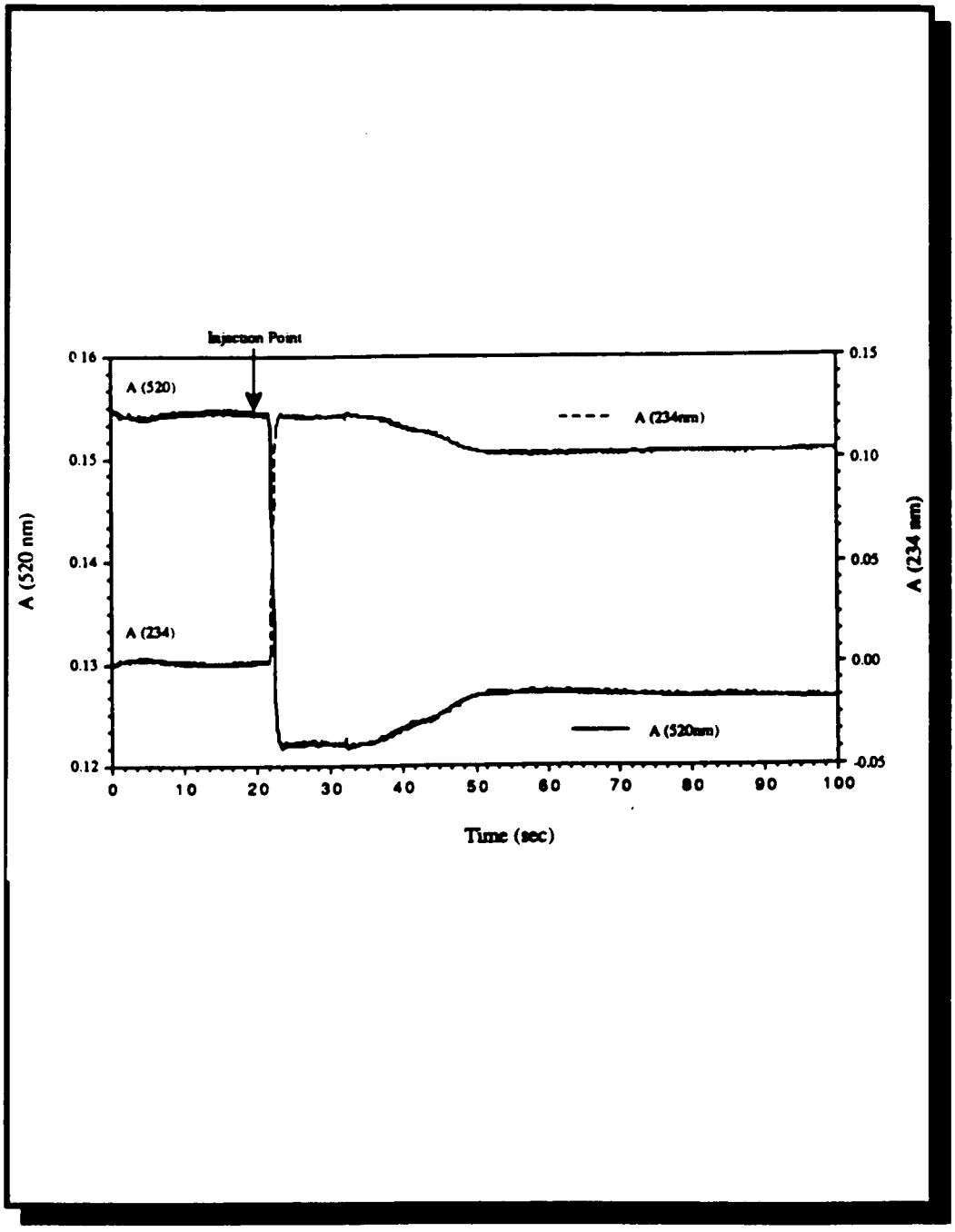

2.2.1.3 Photochemistry of Trimethyltinbromide in Hexane.

Our main interest in the study of the photochemical reaction of $(CH3)3SnBr$ in solution was to compare it with the results obtained for trimethyltiniodide in order to decide which of the two compounds was more suitable for the photochemical studies on the glass matrices. The same conditions used during the photochemical studies of trimethyltiniodide were applied in this case. However, the photochemical reaction could only be studied in nonpolar, hexane, solvents since the UV-visible absorption maximum of $(CH_3)_3SnBr$ in polar solvents, ethanol and\or acetonitrile, is not resolved due to the proximity of the absorption cutoff point of the solvents, ~ 200nm.

Prolonged photolysis with 254 nm light of 7.88 x 10^{-5} M solution of $(CH_3)_3SnBr$ in hexane causes a decline of the 212 nm band and the simultaneous growth of a broad band centered at 420 nm (Figure 2.19), and a nondescript increase in absorbance at ≤ 210nm. The absorption at 420 nm is assigned to Br_2 formation since molecular bromine in hexane exhibits an equivalent absorption, while the nondescript increase below 210 nm is assigned to $(CH_3)_6Sn_2$ formation. An isosbestic point occurs at 240nm and is maintained to 40% conversion of $(CH_3)_3SnBr$.

Stoichiometric data calculated from UV-visible difference spectra yield a 2:1 ratio for the quantum yields of $(CH_3)_3SnBr$ disappearance and Br_2 appearance. The quantum yield was calculated by the method described for $(CH_3)_3SnI$, with appropriate corrections for the contribution in absorbance of $(CH_3)_3SnBr$ and Br_2 at 254 nm.

The quantum yield of $(CH_3)_3SnBr$ disappearance in hexane is independent of the O_2 content. Within experimental error, the values

Table 2.10 - Reaction of 10 ml of 1.66 x 10^{-4} M I_2 and 2 ml of 4.59 x 10^{-5} M $(CH_3)_6Sn_2$ in hexane at 25 °C.

Time t (sec)	$\frac{2.303}{t\,(a-b)}$ (x 10^2)	(b - x) (x 10^{-4})	x (x 10^{-5})	(a - x) (x 10^{-5})	K_t* ($M^{-1}sec^{-1}$)
21.8	±0.000	1.663	0.00	4.593	0.00
21.9	-3.813	1.618	0.455	4.134	225.9
22.0	-3.605	1.578	0.846	3.743	225.3
22.1	-3.424	1.539	1.238	3.351	226.7
22.2	-3.210	1.499	1.641	2.948	226.7
22.3	-2.981	1.457	2.065	2.524	226.9
22.4	-2.774	1.420	2.434	2.155	227.1

* Average value 226.4 ± 0.5

Figure 2.18 -Effect of inhibittor, $1.0x10^{-4}$ M isoalmylnitrite, on the quantum yield during 254 nm photolysis of $(CH_3)_3SnI$, $2.93x10^{-4}$ M, in hexane, and a constant light intensity of 1.22×10^{-7} (einstein/l-sec). a) effect on $(CH_3)_3SnI$, b) effect on I_2.

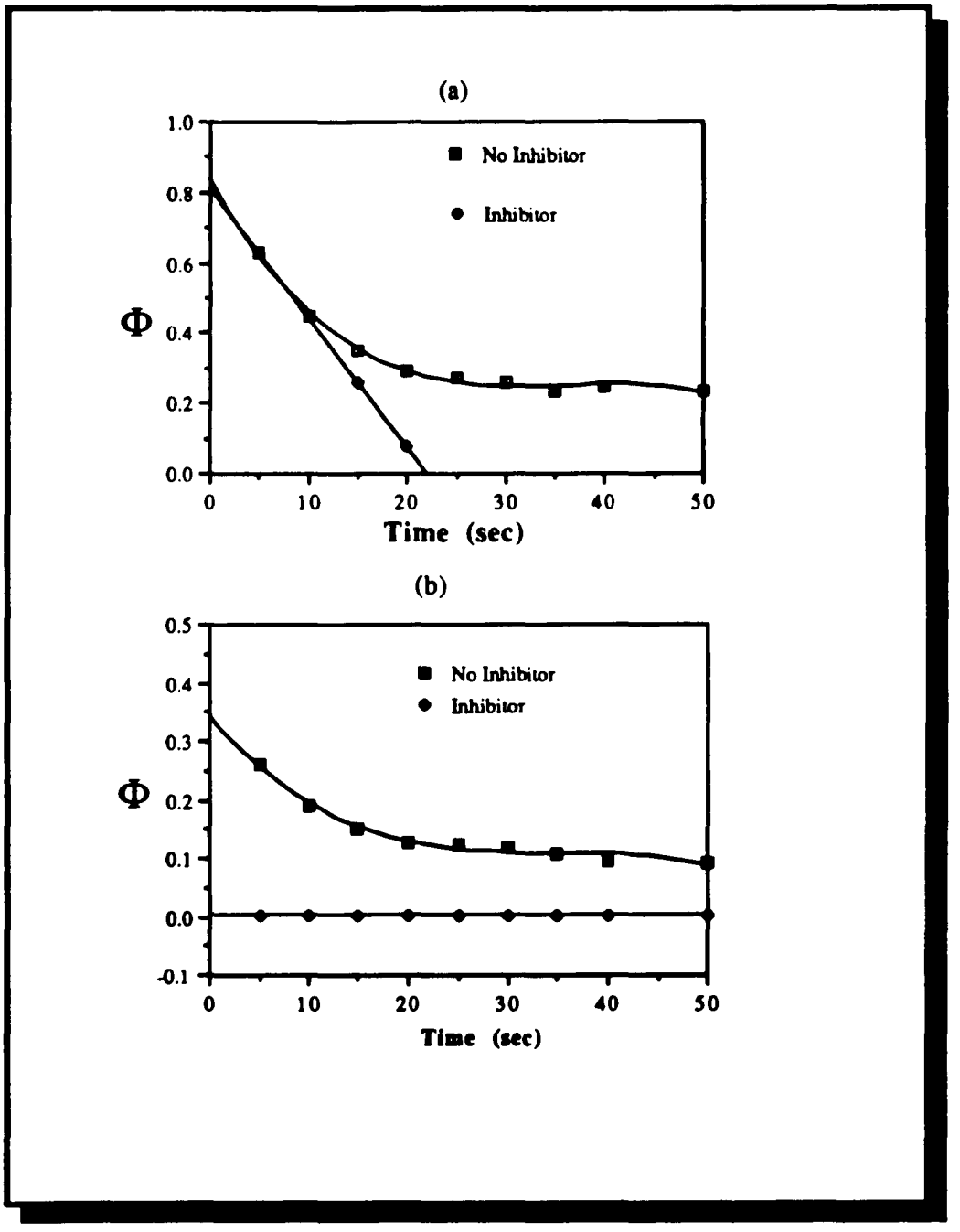

Figure 2.19 - UV-vis of the photochemical reaction of 7.88 x 10^{-5} M of trimethyltinbromide in hexane irradiated with a 254nm light source.

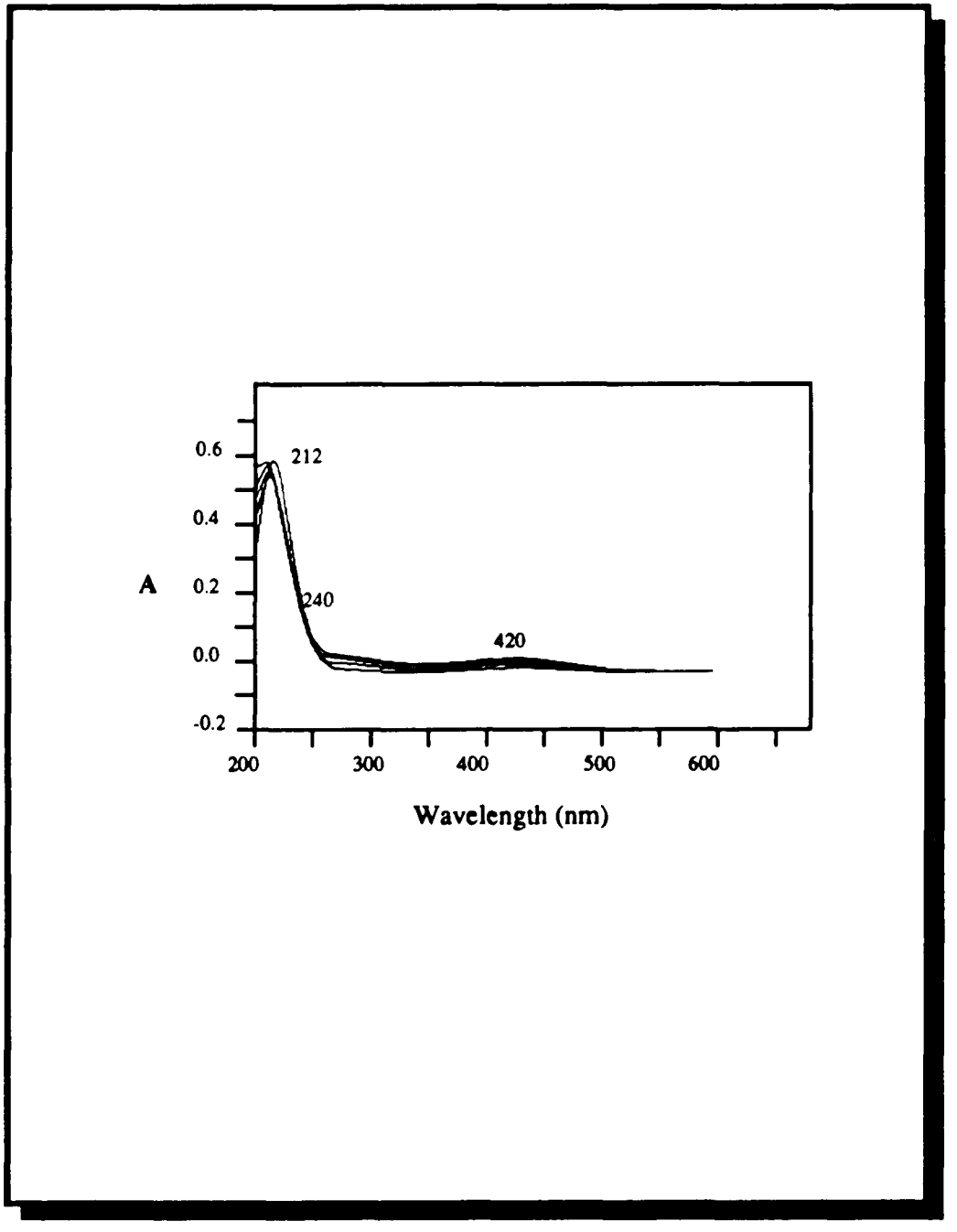

obtained in O_2 saturated solutions are equivalent to those obtained in N_2 saturated and degassed solutions, (Table 2.11).

As found with $(CH_3)_3SnI$, the quantum yield of $(CH_3)_3SnBr$ dissapearance is independent of initial concentration (Figure 2.20) and exhibits a first order dependence on the excitation intensity (Table 2.14). However, the dependence on excitation wavelength is more pronounced. In fact, there is no evidence of reaction with 310- and 355-nm excitation regardless of intensity and exposure time.

A number of attempts were made to follow the reaction via FTIR and Raman spectroscopy, but even with a 0.1 M solution of $(CH_3)_3SnBr$ and prolonged photolysis, no reproducible spectral change could be detected due to the low efficiency of the reaction with 254 nm excitation. Nevertheless, the stoichiometry of the reaction and the similarity of the UV-visible spectral changes with those of $(CH_3)_3SnI$ indicates an equivalent photochemical reaction, i.e.,

$$2(CH_3)_3SnBr \xrightarrow{h\nu} (CH_3)_6Sn_2 + Br_2 \qquad 2.9$$

2.2.1.4 Photochemistry of trimethyltinchloride in hexane.

Photolysis of $(CH_3)_3SnCl$ in hexane with 254-,310-,or 350nm did not produce any spectral changes regardless of solution concentration, excitation intensity, or exposure time.

Table 2.11 - Effect of oxygen, nitrogen , and air free atmospheres on the quantum yield of the photochemical reaction of 7.88×10^{-5} M solution of trimethyltinbromide in hexane at a constant light intensity of 7.49×10^{-7} einstein/L-sec.

Environment	Φ_1 $(CH_3)_3SnBr$	Φ_2 Br_2	Φ_1/Φ_2
Air	0.013 ± 0.005	0.005 ±0.005	2.60
Oxygen	0.018 ± 0.005	0.009 ±0.005	2.00
Nitrogen	0.016 ± 0.005	0.010 ±0.005	1.60
Argon	0.188 ± 0.005	0.009 ±0.005	2.00

Table 2.12 - Quantum yield of the photochemical reaction of 7.88×10^{-5} M solution of trimethyltinbromide in hexane as a function of the light intensity at 254 nm.

Intensity (I_o) [einstein-L^{-1}. sec^{-1}]	Φ_1 $(CH_3)_3SnBr$	Φ_2 Br_2	Φ_1/Φ_2
5.56×10^{-8}	No reaction	No reaction	----------
1.22×10^{-7}	No reaction	No reaction	----------
2.14×10^{-7}	0.006	0.003	2.0
2.82×10^{-7}	0.009	0.004	2.2
3.76×10^{-7}	0.010	0.004	2.5
7.49×10^{-7}	0.013	0.005	2.6

Figure 2.20 - Quantum yield dependence on the trimethyltinbromide concentration at a light intensity of 7.49 x 10^{-7} einstein - L^{-1}- sec^{-1}.

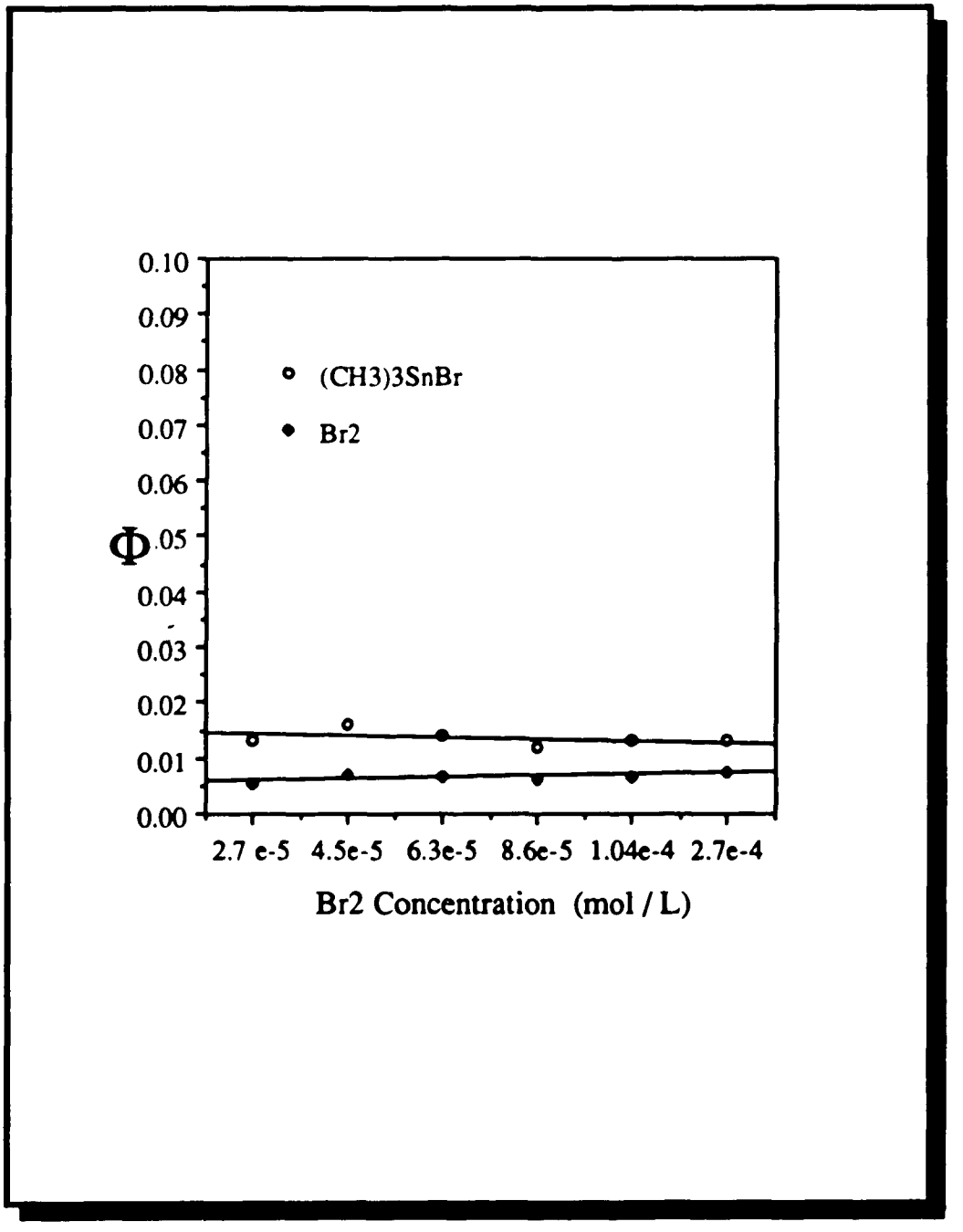

2.2.2 Polar Solvents.

The above results are consistent with previous investigations and confirm that photolysis of $(CH_3)_3SnX$ (X= Br, I) in nonpolar solvents leads to homolytic cleavage of $(CH_3)_3Sn–X$ bond. However, it was immediately apparent that this was not the case when the complex was adsorbed onto PVG. To resolve this discrepancy and to understand the photochemistry on the glass surface, the experiments were extended to polar solvents, as a way to mimic in fluid solution, the behavior that may occur on the polar, hydroxylated surface of porous glass, or glass gels.

2.2.2.1 Photochemistry of Trimethyltiniodide in Ethanol and Acetonitrile.

As previously described, the absorption maximum of $(CH_3)_3SnI$ shift from 234 nm in hexane to 219 nm in ethanol and acetonitrile due to the formation of a five coordinate solvent adduct (Figure 2.2). Nevertheless, 254nm photolysis of the adduct in both solvents results in the appearance of bands at 290- and 360nm concurrent with the disappearance of the adduct absorption (Figure 2.21). There is no indication during photolysis in these polar solvents of either a high energy absorption characteristic of $(CH_3)_6Sn_2$ or the visible absorption of I_2. An isosbestic point at 260nm is maintained through ≥ 100% conversion, and comparison with the spectra of the known compounds indicates that the 290- and 360nm bands are indicative of I^- and/or HI formation. Also, no emission occurs in the 260-850-nm region when room- and low temperature (77K) solutions of $(CH_3)_3SnI$ are excited with 254 nm light.

The stoichiometry of the reaction was calculated from the ratio of the rate of disappearance of the reactant vs. the rate of appearance of the products. In nonpolar solvents, the ratio of the disappearance of $(CH_3)_3SnI$ vs. the appearance of I_2 is 2.0±0.2. However, in these polar solvents, the ratio of the disappearance of $(CH_3)_3SnI$ vs. the appearance of HI is 1.0±0.2.

The apparent stoichiometric formation of ionic species was rather surprising in view of the results obtained in nonpolar solvents. In that case, homolytic cleavage of the Sn-I occurs, whereas in the polar solvents, heterolytic cleavage appears to occur. Consequently, further physical and chemical analysis were carried out to established the nature of the photoproduct formed.

To probe the formation of the ionic species, cyclic voltammograms were recorded periodically during 254 nm photolysis. Comparison of typical voltammograms obtained during photolysis of $7.37x10^{-4}$ M ethanol solution of $(CH_3)_3SnI$ (Figure 2.22) with those of a $1.0x10^{-3}$ M iodic acid solution (Figure 2.23) show that both exhibit equivalent half reduction potential ($E°_{1/2}$). The photolytes obtained by 254nm photolysis of $(CH_3)_3SnI$ in hexane or cyclohexane were examined in an equivalent manner, but no wave indicative of either I^- or HI formation occurs. Thus, the electrochemical and spectral data are consistent with the inmediate formation of I^- and/or HI, as opposed to I_2.

The photolytes were titrated with starch and $AgNO_3$ solutions. [14] Starch forms an intense blue-colored complex in the presence of I_3^-, and is sufficiently sensitive to detect very low concentrations ≤ $1 x10^{-5}$ M of I^{-3}. However, titrations of 5 ml aliquots after 1.0 minute 254 nm photolyses of $7.37x10^{-3}$ M $(CH_3)_3SnI$ in ethanol and acetonitrile showed no absorbance at 435 nm, which is the absorption maximum of the starch-I^{-3} complex. On

Figure 2.21 - UV-vis of the photochemical reaction of trimethyltiniodide in ethanol.

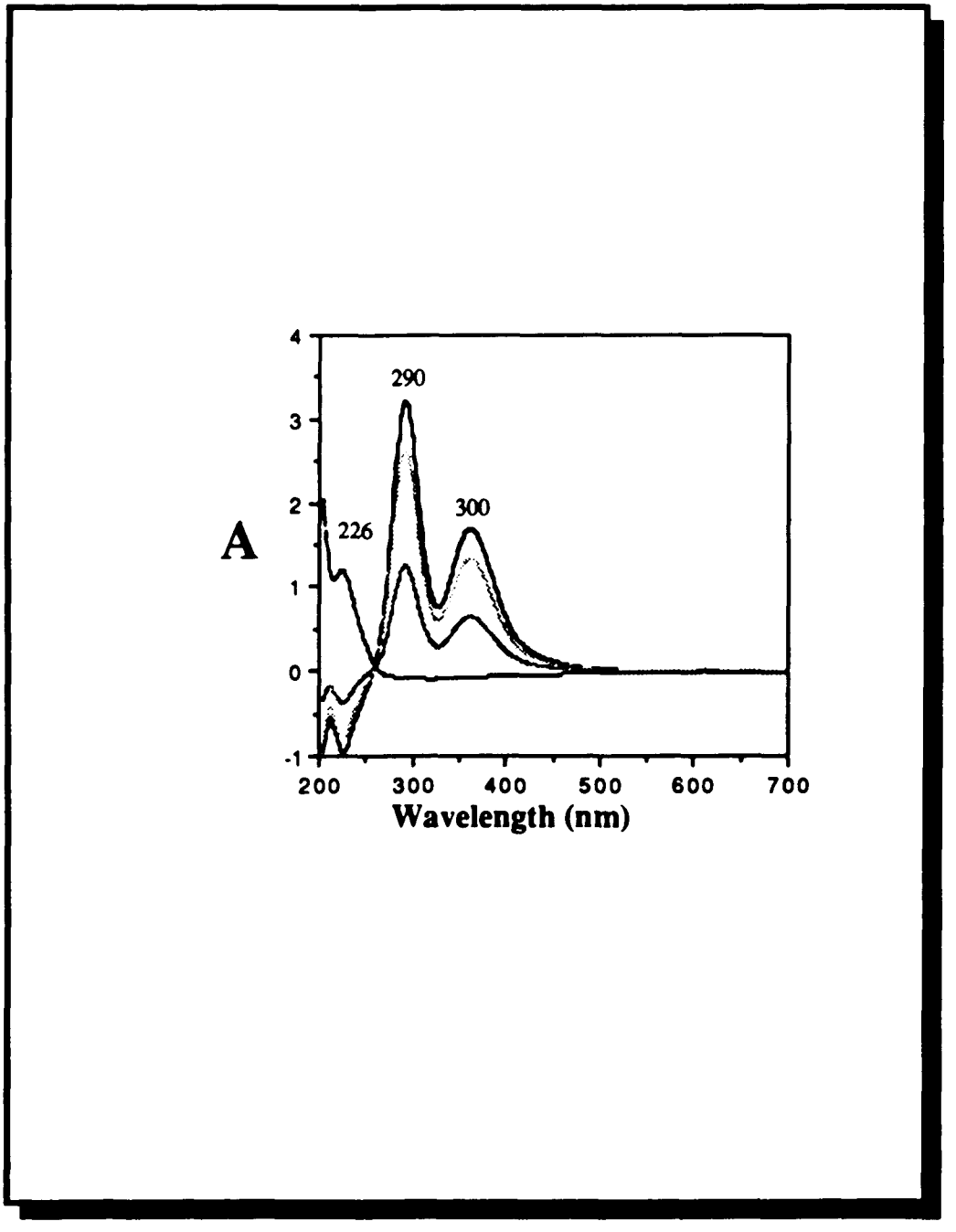

Figure 2.22 - Voltammogram of the photolysis of trimethyltiniodide in ethanol.

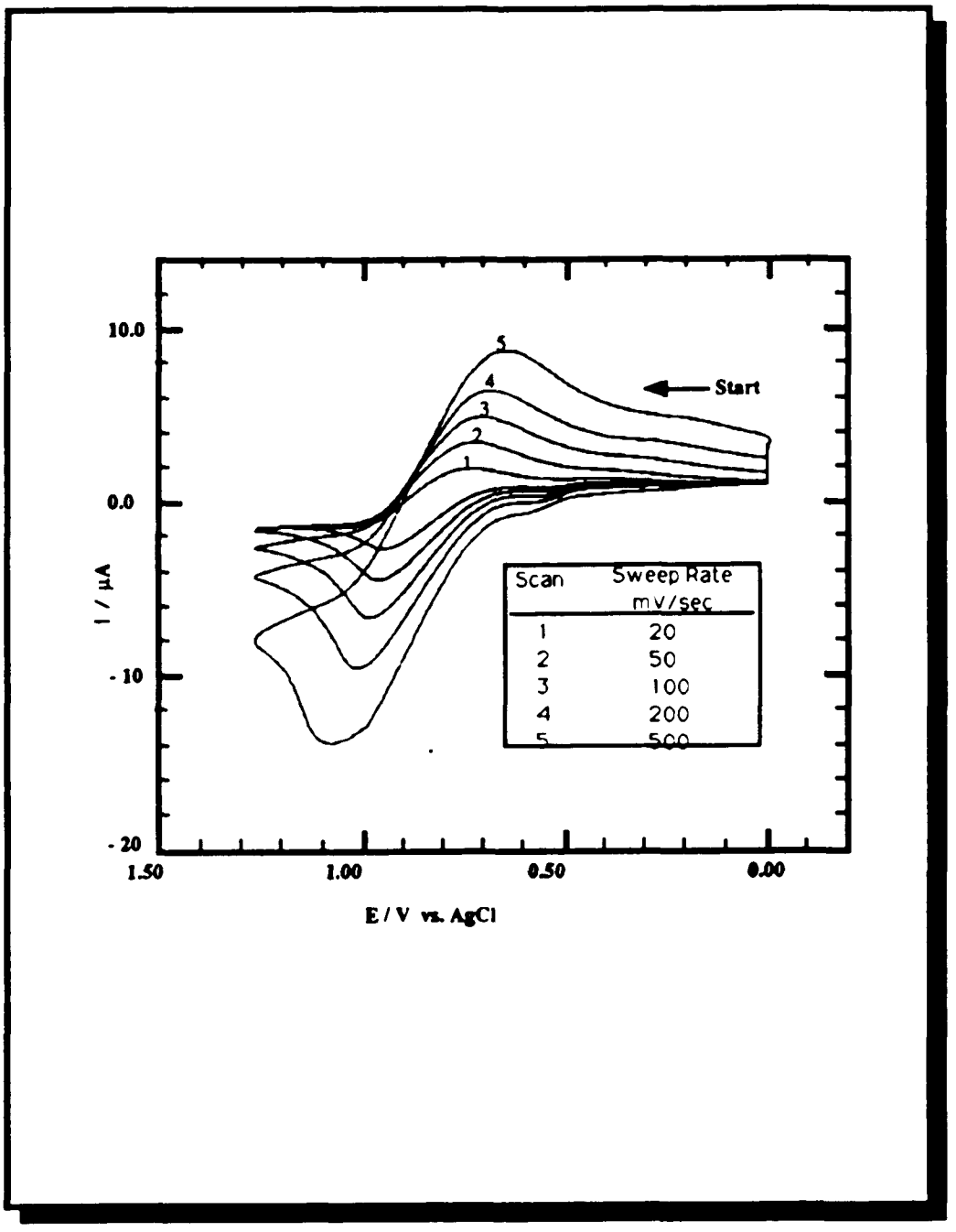

Figure 2.23 - Voltammogram of iodic acid in ethanol.

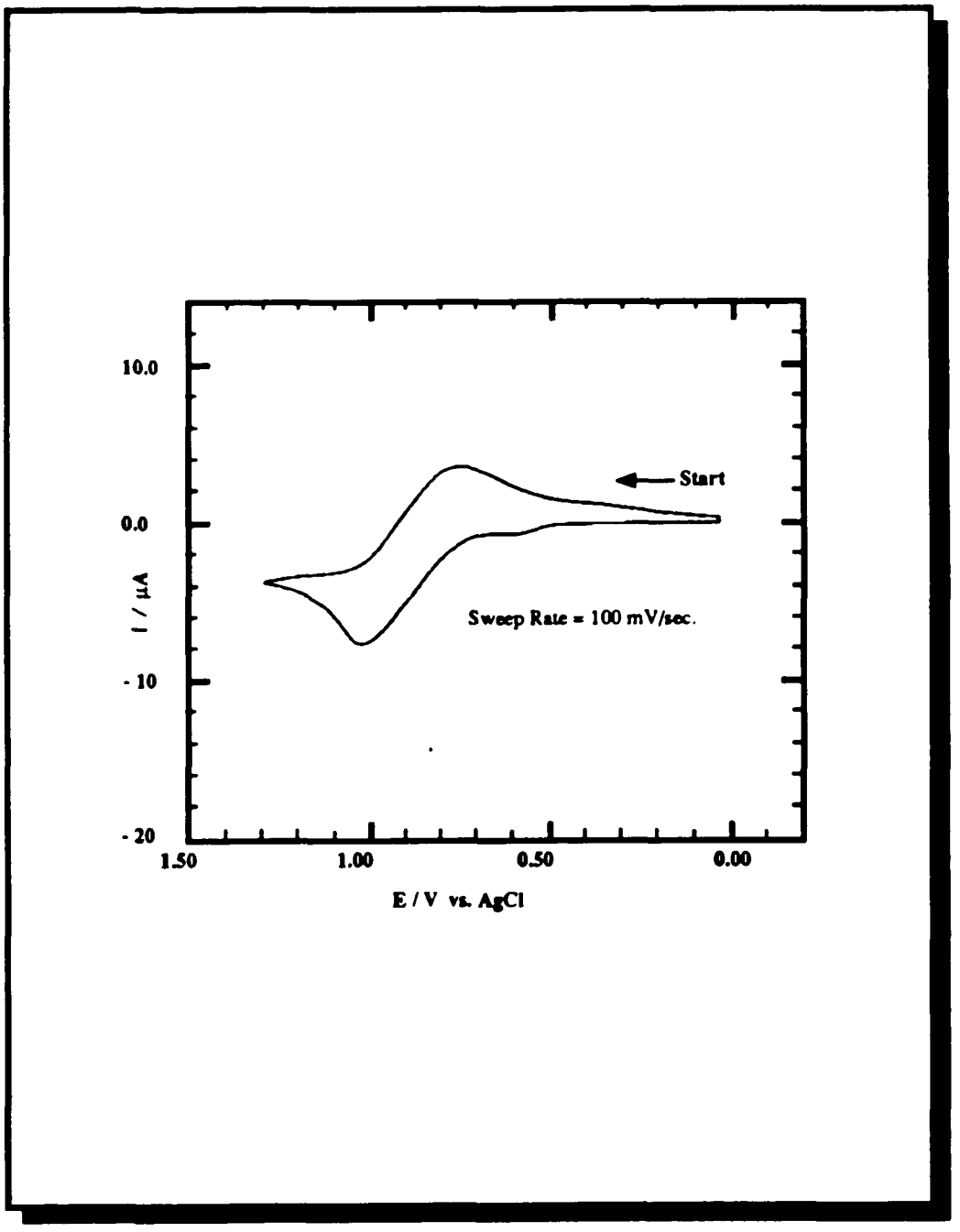

the other hand, titrating equivalent aliquots with $AgNO_3$ resulted in the inmediate dissapearance of the 290- and 360-nm bands of HI and the appearance of a pale yellow AgI precipitate. Unfortunately, the amount of precipitate formed was to small to quantitate. Nevertheless, the absence of a positive starch test, but the inmediate appearance of AgI precipitate indicates the inmediate formation of I^- without concurrent I_2 formation. Furthermore, the ratio of absorbance at 290 nm relative to that at 360 nm is 1.78 for I^{-3} in either ethanol or acetonitrile. On the other hand, HI yields a ratio of 1.9, which in excellent agreement with the ratio of absorbances formed in the photolyzed solution.

The electrochemical, spectral, and chemical analyses point to the inmediate formation I^- rather than I_2. Consequently, 254 nm photolysis of $(CH_3)_3SnI$ in polar solvents, i.e., photolysis of the five coordinate solvent adduct leads to heterolytic bond cleavage of the Sn–I bond. In ethanol the primary photoprocess is :

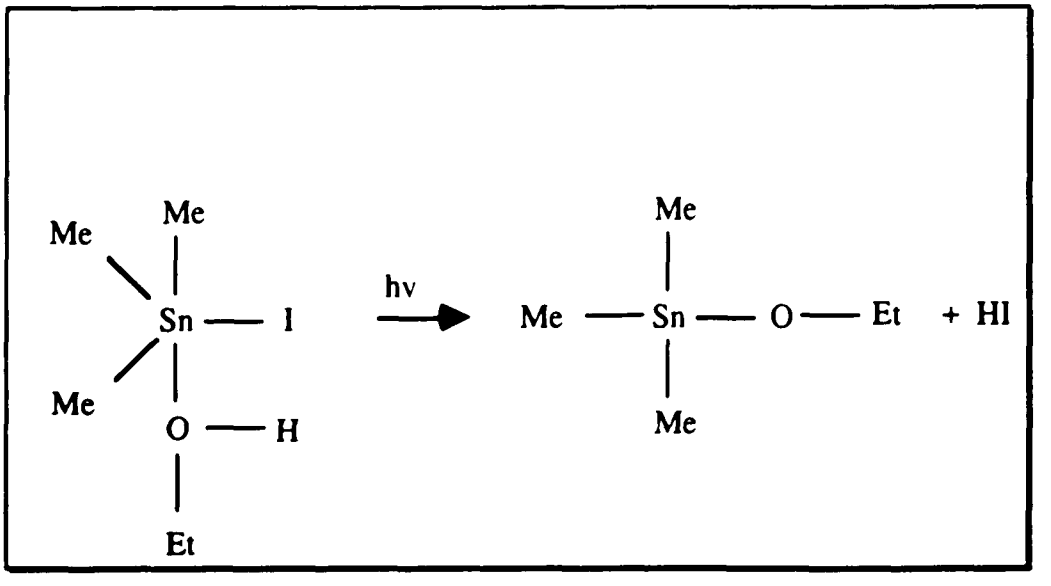

2.2.2.2 Kinetics of the Photochemical Reaction of Trimethyltiniodide in Ethanol and Acetonitrile.

With 254 nm excitation,the quantum yield of $(CH_3)_3SnI$ disappearance is equal to the quantum yield of HI appearance (Table 2.13). Although I_2 absorbs strongly in the UV region ($\epsilon = 2.75 \times 10^3\ M^{-1}\ cm^{-1}$ at 254nm), HI does not derive from secondary photolysis of I_2. There is no indication of an induction period preceeding HI formation. Rather, the 290- and 360-nm bands characteristic of HI appear immediately and increase in intensity with the maintenance of an isosbestic point at 260 nm through 100% conversion. Furthermore, the quantum yield is independent of added I_2 (Figure 2.40). In the presence of 1.0×10^{-5} to 5.0×10^{-5} M I_2, the quantum yield of HI appearance during 254 nm photolysis, 0.65 ± 0.09, is within experimental error of that measured in the absence of I_2.

As in nonpolar (hexane) solvents, the quantum yield of $(CH_3)_3SnI$ disappearance in polar (ethanol and acetonitrile) solvents is independent of the presence of O_2 (Table 2.17), and the (CH3)3SnI concentration (Figure 2.41). In all of the quantum yield experiments the ratio of the quantum yield of (CH3)3SnI disappearance and the quantum yield of appearance of HI remain constant, 0.98, this results is consistent with a 1:1 stoichiometric net reaction :

$$(CH_3)_3SnI \xrightarrow{h\nu} (CH3)3Sn^+ + I^- \qquad 2.11$$

These results as well as the wavelength dependence of the quantum yield , suggest that the reaction initiates in the high energy state populated

Table 2.16 - Quantum yields of 7.37 x 10^{-4} M of trimethyltiniodide at a constant light intensity of 1.22 x 10^{-7} (einstein/L-sec) as a function of the dielectric constant of the solvent and the wavelength of the excitation source.

	Solvent		
	Hexane	**Acetonitrile**	**Ethanol**
Dielectric Constant*	**1.890**	**37.50**	**24.30**
Φ 254 nm	0.323 ± 0.05	0.653 ± 0.05	0.457 ± 0.05
Φ 310 nm	0.190 ± 0.05	0.011 ± 0.005	0.008±0.005
Φ 355 nm	≤ 0.001	≤ 0.001	≤ 0.001

*CCR Handbook of chemistry and physics, 90th ed., pp-E-161

on absorption. Nevertheless, in nonpolar solvents, the primary photochemical event is homolytic cleavage, whereas, in polar solvents the data indicate that the primary photochemical event is heterolytic cleavage of the Sn-I bond.

Figure 224 - Quantum yield as a function of the iodine concentration at a constant trimethyltiniodide concentration of 7.37 x 10^{-4} M and a constant light intensity of 1.22 x 10^{-7} einstein/ L-sec

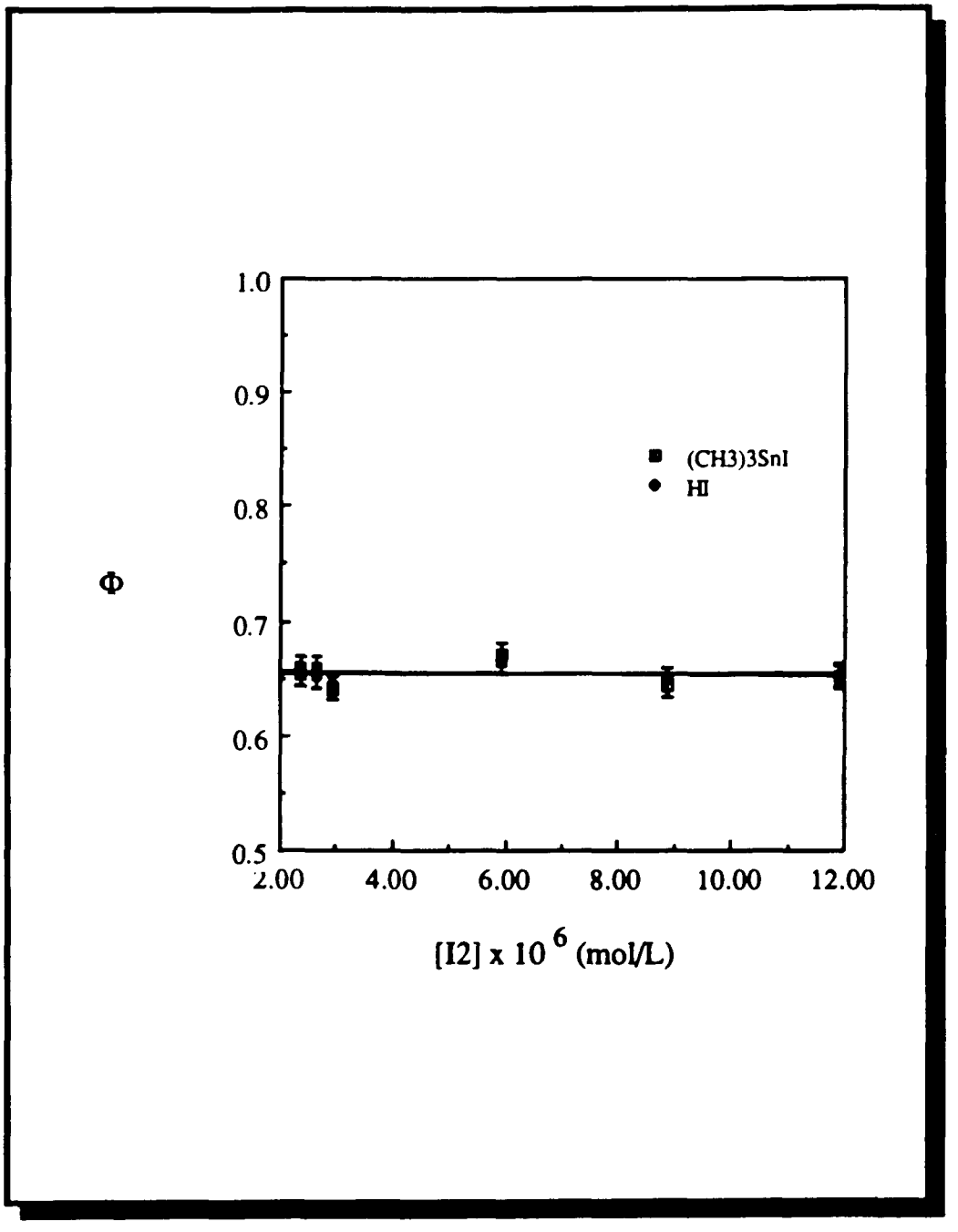

Table 2.17 - Effect of oxygen, nitrogen , and air free atmospheres on the quantum yield of the photochemical reaction of 7.37×10^{-4} M solution of trimethyltiniodide in ethanol at a constant light intensity of 1.22×10^{-7} einstein/L-sec.

	Φ_1	Φ_2	
Environment	$(CH_3)_3SnI$	**HI**	Φ_1/Φ_2
Air	0.653 ± 0.05	0.659 ± 0.05	0.99
Oxygen	0.658 ± 0.05	0.652 ±0.06	1.00
Nitrogen	0.650 ± 0.05	0.654 ±0.06	0.99
Argon	0.653 ± 0.05	0.721 ±0.06	0.90

Figure 2.25 - Quantum yield as a function of the $(CH_3)_3SnI$ concentration in ethanol at a constant light intensity of 1.22×10^{-7} einstein/ L-sec

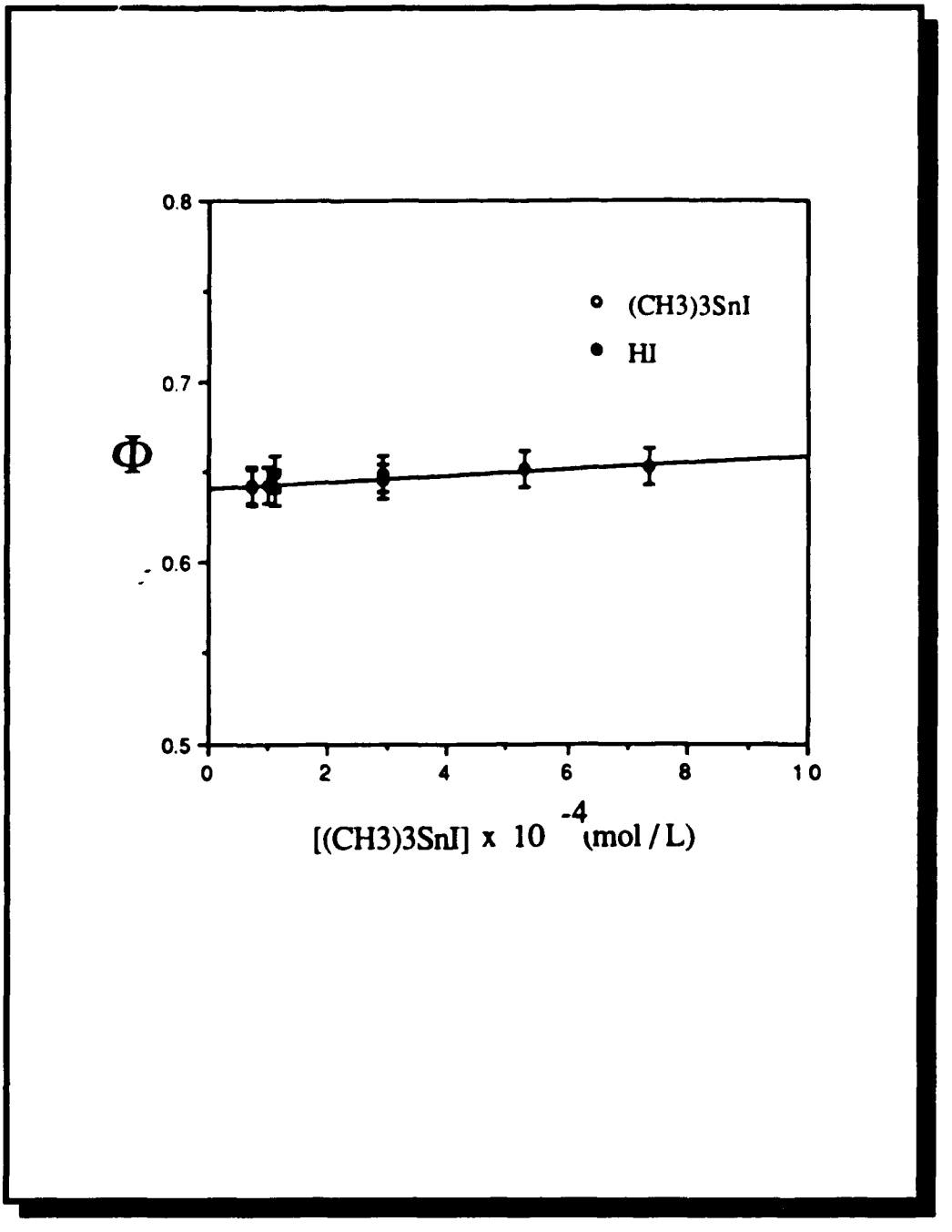

3. Photochemistry of Phenyltin Halides and Phenyltin Azides in Solution.

The purpose of this study was to established the photochemistry of relatively volatile organotin compounds so that they could be used to photochemically modified the refractive index of the glass. In such an application, however, a major concern is the absorption spectrum of the compound relative to the UV transmittance of the glass. A major drawback of the $(CH_3)_3SnX$ compounds is that their optical absorption occur in the UV ≤ 250-nm beyond the transmittance of the glass. Consequently, photolysis is limited to the molecules on the outer most surfaces of the glass. It may not be possible to completely eliminate this problem with simpler organotin compounds since those with adequate volatility generally absorb in the UV. Nevertheless, the experiments were extended to $(C_6H_5)_{(4-n)}SnCl_n$, and $(C_6H_5)_{(4-n)}Sn(N_3)_n$ (n=1, 2 , 3) compounds, since these complexes exhibit intense phenyl centered absorptions in the 250- to 280-nm region.

3.1 Spectroscopic Properties of Phenyltin Halides and Phenyltin Azides in Solution.

Absorption spectra of the $(C_6H_5)_{(4-n)}SnCl_n$, and $(C_6H_5)_{(4-n)}Sn(N_3)_n$

(n=1, 2 , 3) compounds in solution consist of a series of bands from 275- to 250nm, while Figure 3.1 is representative of the spectra, the band maxima and molar extinction coefficients of the different compounds are listed in Table 3.1. [15] It is immediately apparent from Table 3.1 that the intensity of the absorptions decrease as the number of phenyl rings decreases from three to one. Furthermore, these bands are simmilar to those of C_6H_6, and as a result have been assigned to a phenyl localyzed p –> p* transition with a superimposed vibrational progression.

Unlike the $(CH_3)_3SnX$ compounds, the absorption maxima of the $(C_6H_6)_3SnX$ (X= Cl, N_3) compounds is independent of the solvent polarity and Lewis basicity. Consequently, there is no indication that these compounds react to form a solvent adduct. However, spectroscopic and photochemical studies were limited to polar solvents (ethanol) due to the poor solubility, ≤ 1.0 x 10^{-6} M, of the $(C_6H_5)_{(4-n)}SnCl_n$, and $(C_6H_5)_{(4-n)}Sn(N_3)_n$ (n=1, 2 , 3) compounds in nonpolar solvents (hexane, and cyclohexane). Even in ethanol, typical concentrations range from 5.0 x 10^{-5} - to 5.0 x 10^{-4} M solutions.

$(C_6H_6)_3SnCl$ exhibits an emission at ca. 320 nm when excited with 254 nm light (Figure 3.2). The energy of the emission peak, and its intensity are independent of the solvent polarity, as observed in the UV-visible spectra. Each $(C_6H_6)_{(4-n)}SnCl_n$ and $(C_6H_6)_{(4-n)}Sn(N_3)_n$ (n= 1, 2, 3) compounds exhibits an emission of simmilar energy, but the emission intensity declines as the number of phenyl groups decline. With each, the emission intensity is independent of whether the solution is air saturated or degassed. Similar emission ca. 300nm is observed for benzene when excited with 254nm light. [16]

Figure 3.1 - Absorption spectra of $(C_6H_5)_3SnCl$ in ethanol.

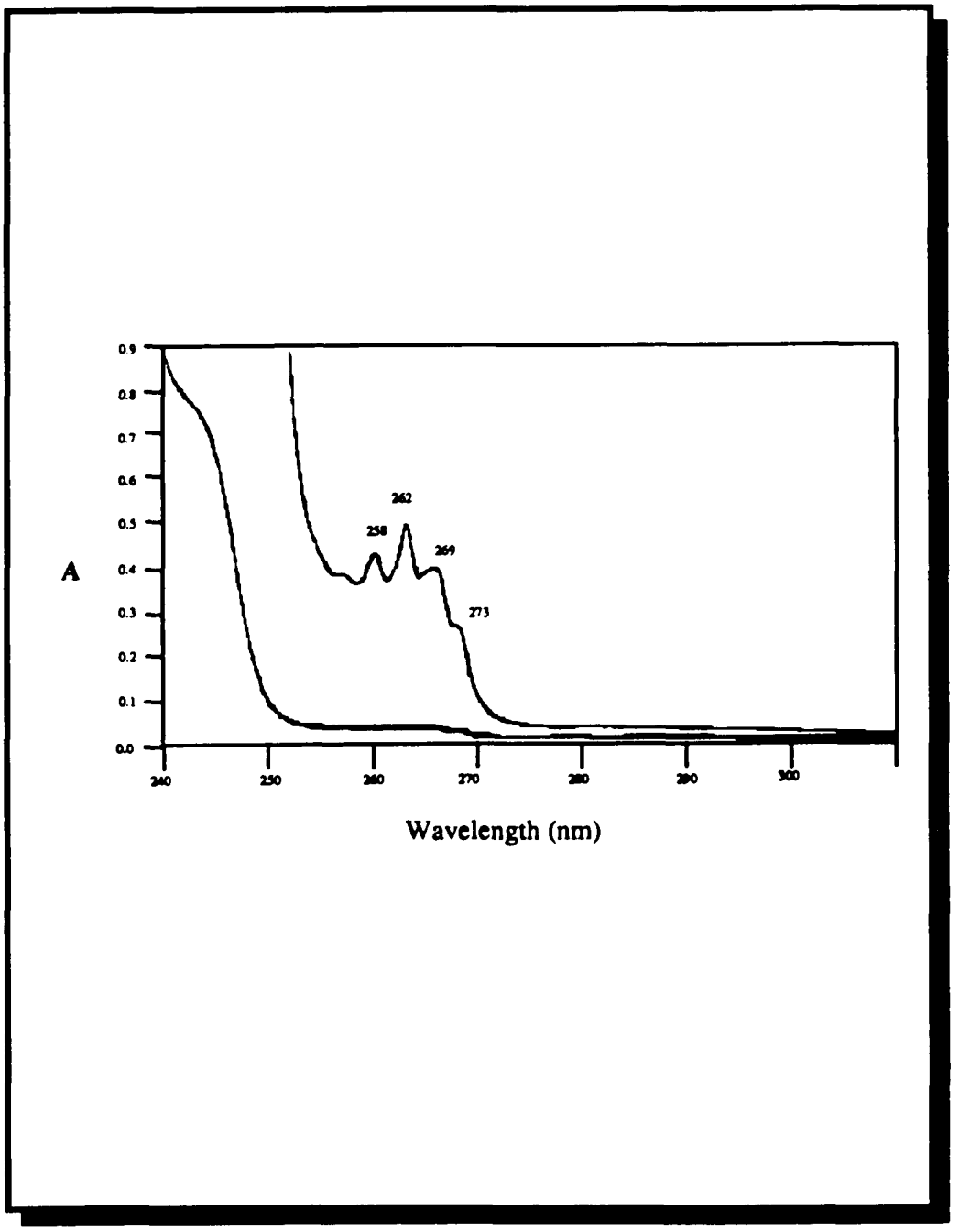

Table 3.1 - Absorption coefficients and band maxima of $(C_6H_5)_{(4-n)}SnCl_n$, and $(C_6H_5)_{(4-n)}Sn(N_3)_n$ (n=1, 2 , 3) compounds in ethanol.

Compound	A	B	C	D
$(C_6H_5)_3SnCl$	267nm	263nm	257nm	251nm
ε(l/mol-cm)	535	835	1070	918
$(C_6H_5)_2SnCl_2$	269nm	265nm	260nm	254nm
ε(l/mol-cm)	347	542	695	596
$(C_6H_5)SnCl_3$	272nm	268nm	264nm	258nm
ε(l/mol-cm)	294	460	590	506
$[(C_6H_5)_3SnCl]_2$	267nm	263nm	257nm	251nm
ε(l/mol-cm)	600	930	1200	1050
$(C_6H_5)_3SnN_3$	267nm	263nm	257nm	251nm
ε(l/mol-cm)	561	841	1080	939
$(C_6H_5)_2Sn(N_3)_2$	270nm	266nm	262nm	255nm
ε(l/mol-cm)	349	557	705	601
$(C_6H_5)Sn(N_3)_3$	273nm	270nm	266nm	260nm
ε(l/mol-cm)	299	465	595	513
$[(C_6H_5)_3Sn(N_3)]_2$	267nm	263nm	257nm	251nm
ε(l/mol-cm)	609	936	1192	1065

Figure 3.2 - Emission spectra of 3.75×10^{-4} M solution of $(C_6H_5)_3SnCl$ in ethanol; $l_{Excitation}$= 254 nm; Slits Ex:Em = 20:6 .

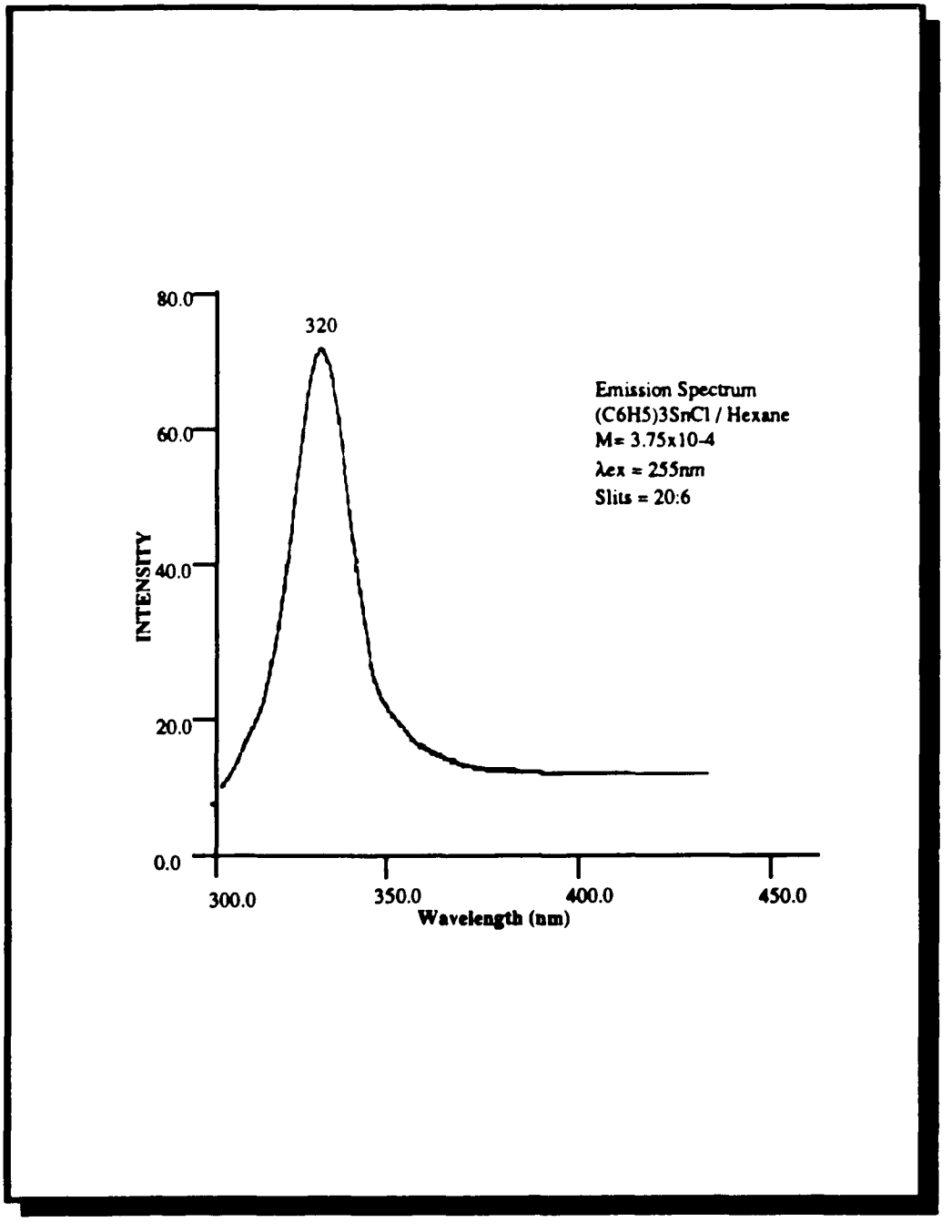

The FTIR spectra of $(C_6H_6)_{(4-n)}SnCl_n$ and $(C_6H_6)_{(4-n)}Sn(N_3)_n$ (n= 1, 2, 3) compounds is very similar, Figures 3.3, and 3.4 respectively. Most of the vibrational bands observed are associated with the phenyl vibrational modes. The phenyl bands in the 1660- to 2000 cm^{-1} region have a typical pattern which can be correlated to the mode of substitution of the phenyl ring. [17] The Sn-phenyl band is observed in all the compounds, it occurs in the 1070 cm^{-1} region of the spectrum. The Sn-Cl stretching mode occurs at about 330 cm^{-1}, however, it is not observed with conventional KBr optics spectrometers. Consequently, the Sn-Cl vibration is not observed with our FTIR spectrometer. The Sn-N_3 asymmetric stretch occurs at 2100 cm^{-1}. A complete vibrational frequency assignment for the $(C_6H_6)_{(4-n)}SnCl_n$ and $(C_6H_6)_{(4-n)}Sn(N_3)_n$ (n= 1, 2, 3) compounds in carbontetrachloride is given in Table 3.2.

The proton NMR spectra for the $(C_6H_6)_{(4-n)}SnCl_n$ and $(C_6H_6)_{(4-n)}Sn(N_3)_n$ (n= 1, 2, 3) compounds in a carbon tetrachloride solution is identical (Figure 3.5). It consist of two peaks centered at 7.4 and 7.7 ppm respectively. This peaks are assigned to the protons in the phenyl rings. As the number of phenyl ring decreases from three to one the intensity of the bands decreases proportionally.

3.2 Photochemistry of $(C_6H_6)_{(4-n)}SnCl_n$ (n= 1, 2, 3) Compounds in Solution.

As already mentioned, the photochemical studies were limited to ethanol due to the poor solubility of the compounds in nonpolar solvents. The

Figure 3.3 - FTIR spectra of $(C_6H_5)_3SnCl$ in CCl_4.

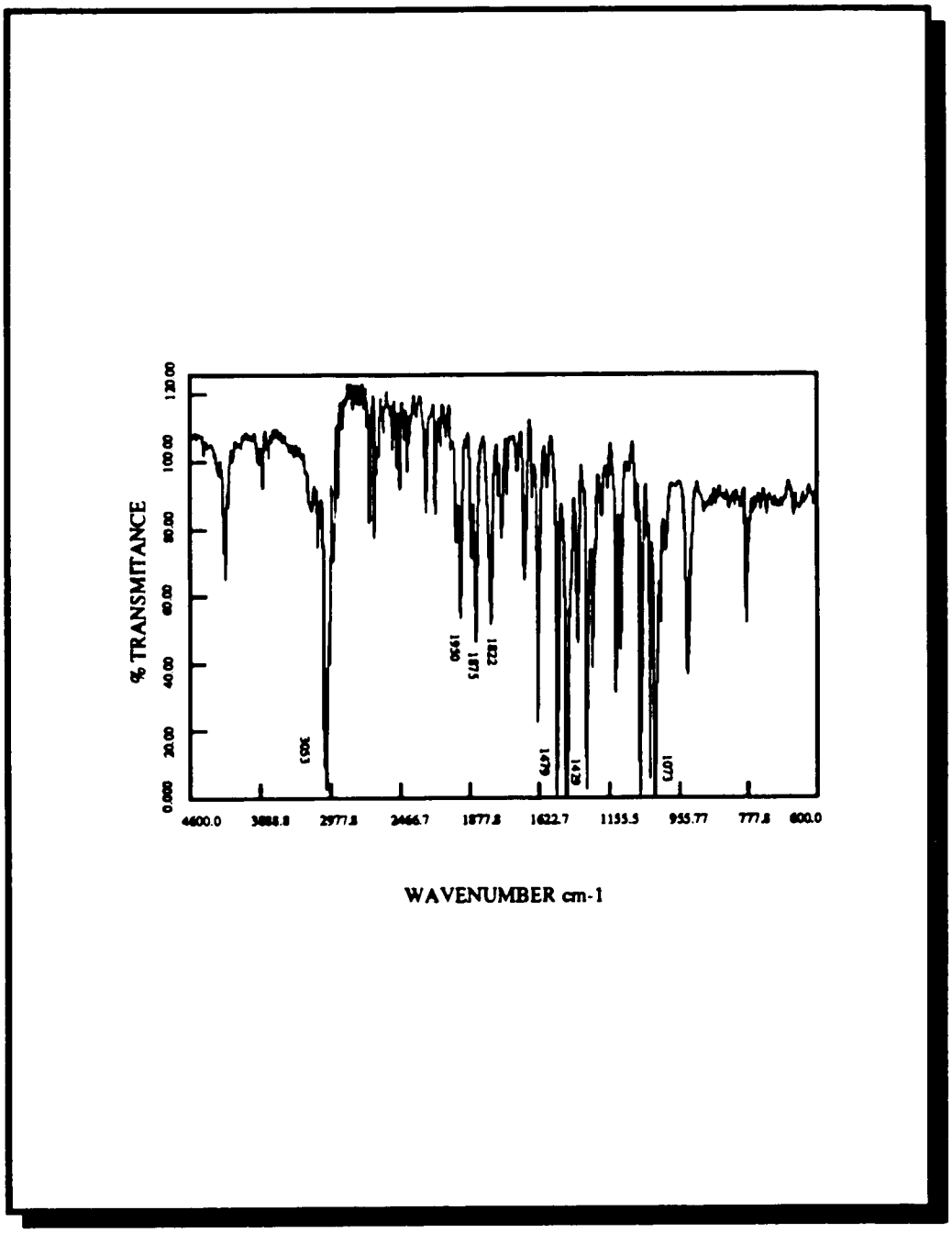

Figure 3.4 - FTIR spectra of $(C_6H_5)_3Sn(N_3)$ in CCl_4.

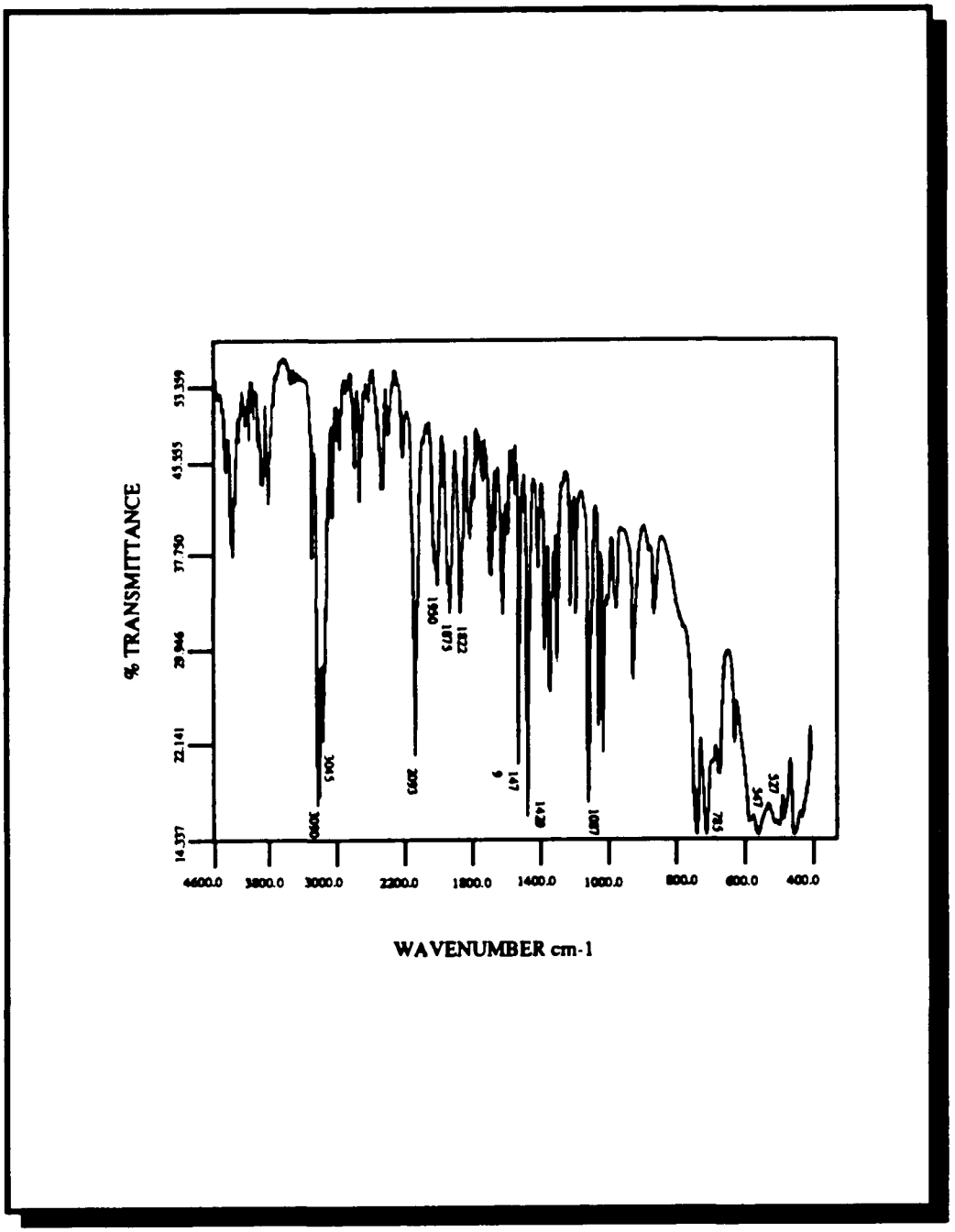

Table 3.2 - Infrared band assignment for the vibrational modes of $(C_6H_6)_{(4-n)}SnCl_n$ and $(C_6H_6)_{(4-n)}Sn(N_3)_n$ (n= 1, 2, 3) compounds in a carbontetrachloride solution.[18]

Frequency (cm^{-1})	Assignment
3090 s	C-H symmetric stretch
3045 s	C-H symmetric stretch
2093 vs	N-N-N asymmetric stretch
1950 w	phenyl ring modes
1875 w	phenyl ring modes
1822 w	phenyl ring modes
1479 s	C-C stretch
1429 s	C-C stretch
1073 s	Sn-phenyl stretch
335 w	Sn-Cl stretch

Figure 3.5 - Proton NMR spectra of $(C_6H_6)_3SnCl$ in CCl_4

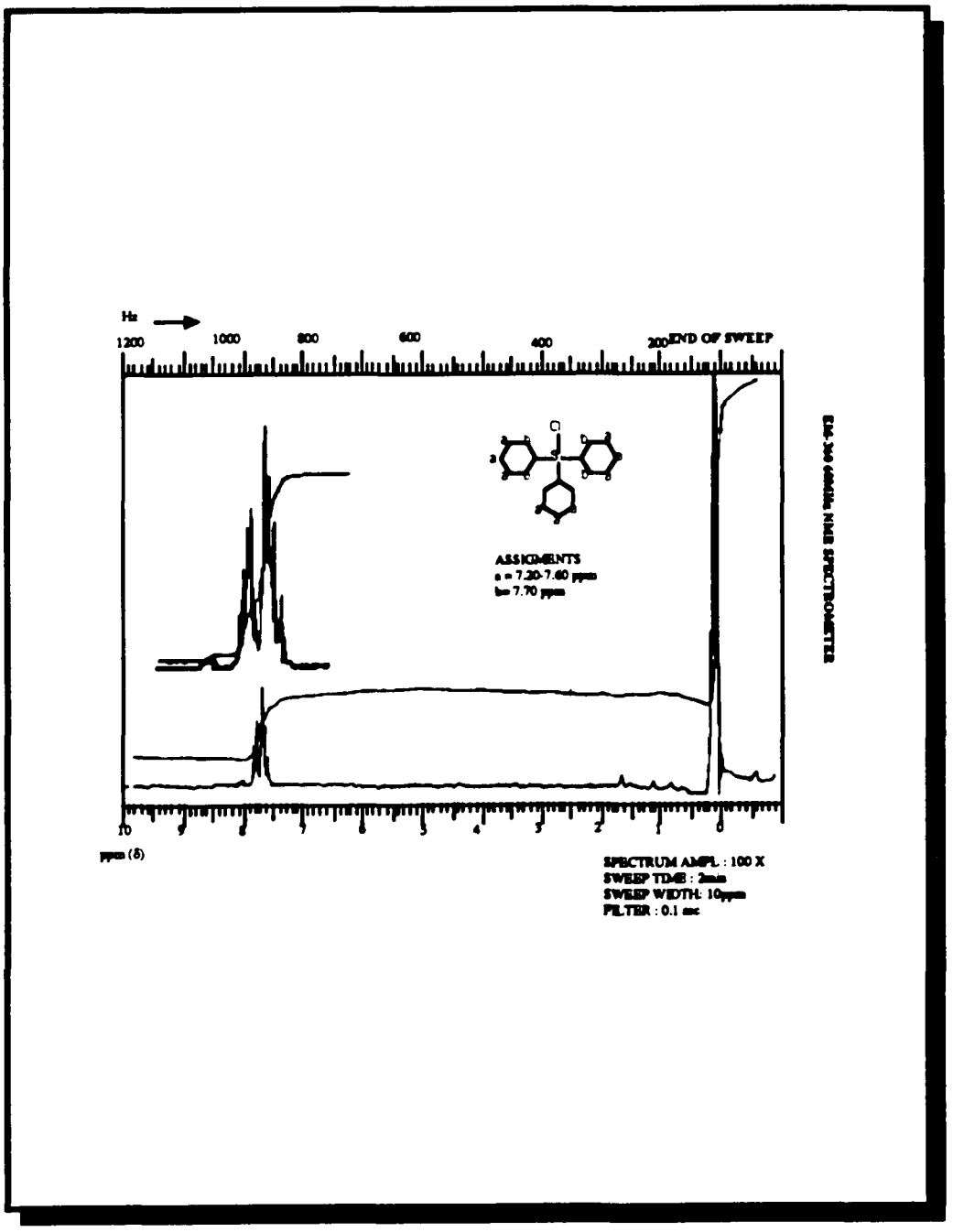

photochemical reaction of $(C_6H_6)_{(4-n)}SnCl_n$ (n= 1, 2, 3) compounds in solution was followed in situ by UV-vis, Fluorescence, and FTIR spectroscopies. Excitation of a degassed 1.0 x 10^{-4} M ethanol solution of $(C_6H_5)_3SnCl$ with 254-nm light causes a decline in the intensity of the 263-nm absorption band (Figure 3.6), and the simultaneous growth of a band at 330-nm. An isosbestic point at 290nm occurs during the first minutes of the reaction, but then disappears on further photolysis concurrent with the reappearance of the 260-nm band. The 330nm band that develops during photolysis agrees with that of Cl_2 dissolved in ethanol, and its assigned to its formation. The reappearance of the 260nm band is assigned to the formation of the $(C_6H_5)_3Sn\text{-}Sn(C_6H_5)_3$ dimmer, since comparison with the spectra of pure $(C_6H_5)_3Sn\text{-}Sn(C_6H_5)_3$ in ethanol shows similar spectra.

The emission spectra peak at 320 nm of a degassed 3.75 x 10^{-4} M solution of $(C_6H_5)_3SnCl$ in ethanol disappears as a function of photolysis time (Figure 3.7), when photolyzed with 254-nm light. The disappearance of the emission peak occurs simultaneously with the disappearance of the 263 nm peak in the UV-visible spectra.

FTIR spectra recorded during photolysis of $1.0x10^{-3}$M solution of $(C_6H_5)_3SnCl$ in ethanol with 254 nm light for two hours (Figure 3.8), shows the formation of two new bands at 1658-, and 1579 cm^{-1} which are assigned to the formation of $(C_6H_5)_3Sn\text{-}O\text{-}CH_2CH_3$, since the C-O stretching vibrations of tin acetonate compounds often occur as two bands in the 1600 cm^{-1} region of the spectrum. [19] The same photochemical experiment was repeated in hexane under the same conditions, however there is no indication for the formation of this bands. Also, from the spectra is observed that no disruption of the phenyl-tin matrix occurs during photolysis, since there are no changes in the intensity, or position of the

Figure 3.6 - UV-vis spectra during photolysis with 254 nm light of 3.75×10^{-4} M solution of triphenyltinchloride in hexane.

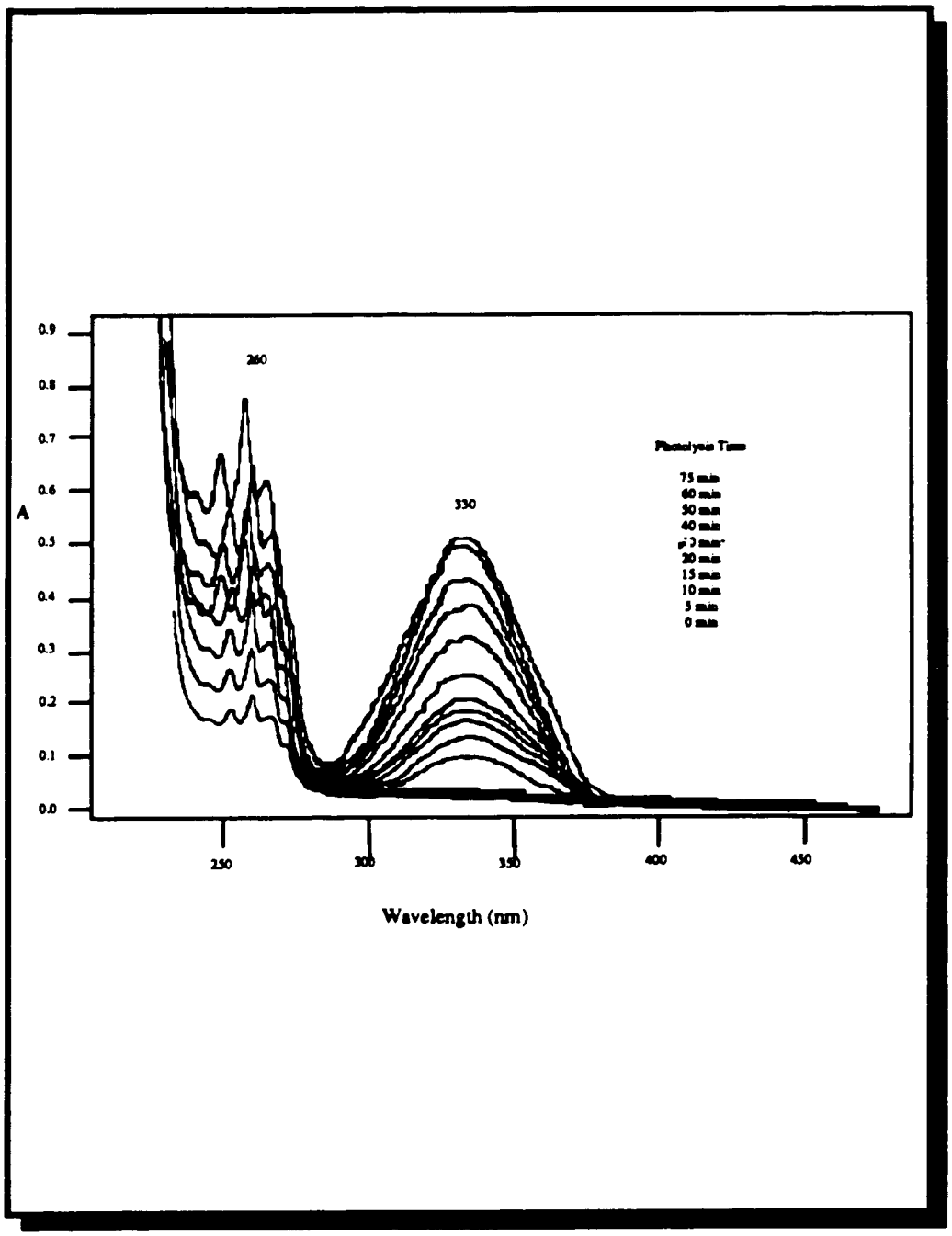

Figure 3.7 - Emission spectra during photolysis with 254 nm light of 3.75×10^{-4} M solution of $(C_6H_5)_3SnCl$ in ethanol.

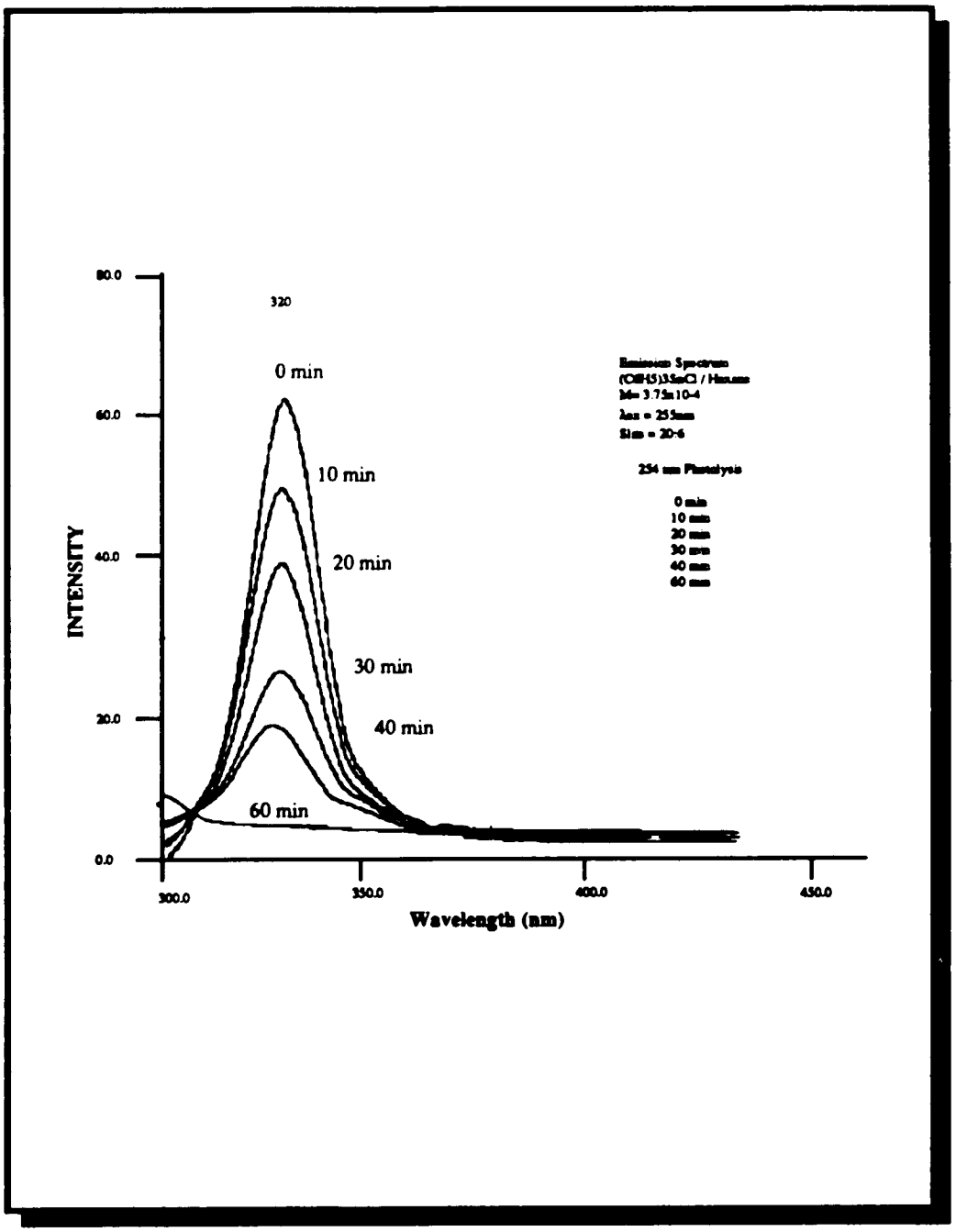

Figure 3.8 - FTIR spectra of the 254-nm photolysis of 1.0 x 10^{-3} M solution of $(C_6H_5)_3SnCl$ in ethanol.

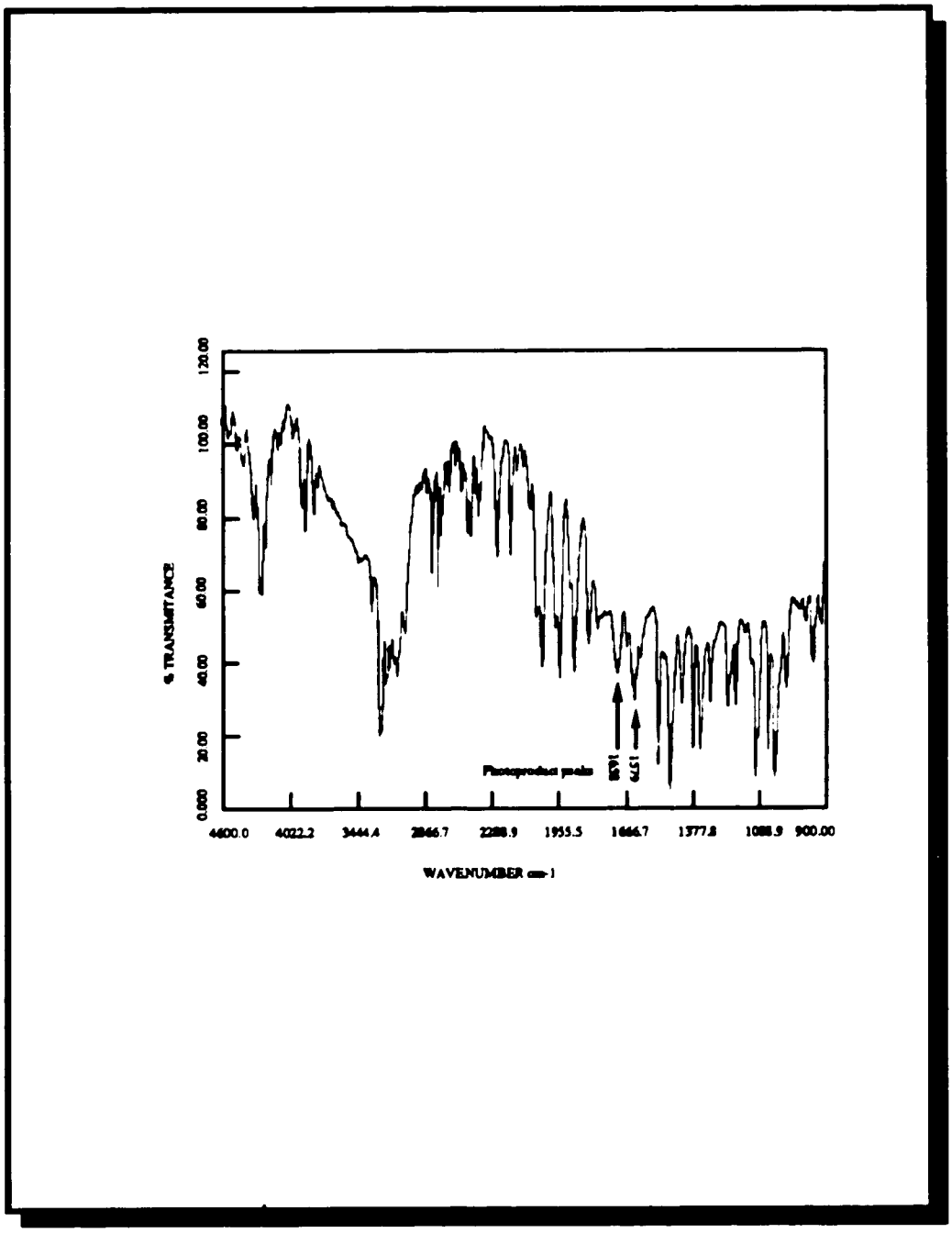

Figure 3.9 - UV-visible spectra recorded during photolysis of 3.6 x 10^{-4}M degassed solution of $(C_6H_5)_2SnCl_2$ in ethanol at a constant light intensity of 7.49 x 10^{-7} (einstein/l-sec) at 254 nm.

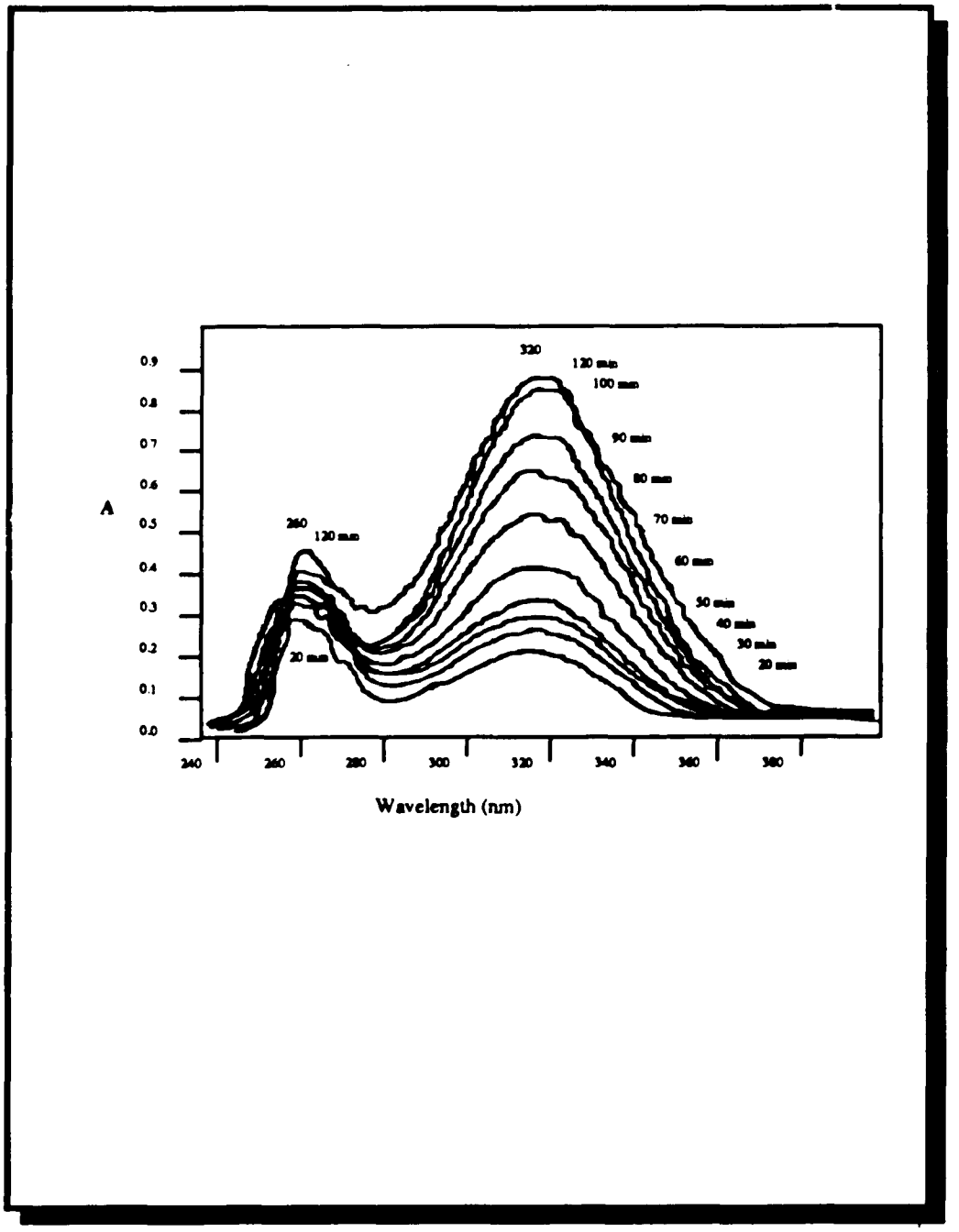

1073 cm^{-1} band, which corresponds to the phenyl-tin stretch. From the NMR spectra a small shift, Dd = 0.29 ppm, of the proton signals of the phenyl group are seen to occur with photolysis. However, the intensities and the shape of the signal do not change.

As in the case of $(C_6H_6)_3SnCl$, photolysis with 254-nm light of 1.0 x 10^{-4} M solution of $(C_6H_6)_2SnCl_2$ and/or $(C_6H_6)SnCl_3$ in ethanol shows the disappearance of the 265nm peak (Figure 3.9), followed by the appearance of a peak at 320-nm which is assigned to the appearance of Cl_2. However, from the spectra there is no indication of the formation of a tin derivative, since the 263nm peak is not seen to reappeared. Similarly, the emission spectra shows the decrease of the 320nm peak upon excitation with 254nm light.

The FTIR and NMR of $(C_6H_6)_2SnCl_2$ and/or $(C_6H_6)SnCl_3$ in ethanol when excited with 254-nm light show no changes on the spectra regardless of the photolysis time.

3.2.1 Kinetics of the Photochemistry of $(C_6H_6)_{(4-n)}SnCl_n$ (n= 1, 2, 3) Compounds in Solution.

To further understand the mechanism of the photochemical reaction of $(C_6H_5)_{(4-n)}SnCl_n$ (n= 1,2,3) compounds, quantum yield calculations were made in 1.0 x 10^{-4} M solutions in ethanol at a constant light intensity of $7.49x10^{-7}$ (einstein/l-sec) with 254nm light under a variety of conditions. The quantum yield of disappearance of the $(C_6H_5)_{(4-n)}SnCl_n$ (n= 1,2,3) compounds is independent of the O_2 concentration (Table 3.3), and decreases drastically as the excitation wavelength shifts from 254- to 355-nm (Table 3.4). There is no evidence of a photochemical reaction at the low

Table 3.3 - Effect of oxygen, nitrogen, and air free atmospheres on the quantum yield of the photochemical reaction of 3.65 x 10^{-4} M solution of $(C_6H_5)_{(4-n)}SnCl_n$ (n= 1,2,3) in ethanol with a constant light intensity of 7.49 x 10^{-7} (einstein/l-sec) at 254 nm.

Enviroment	n =	Φ_1 $(C_6H_5)_{(4-n)}SnCl_n$	Φ_2 Cl_2
Air	1	0.009±0.003	0.005±0.003
	2	0.015±0.003	0.012±0.003
	3	0.021±0.003	0.030±0.003
Nitrogen	1	0.011±0.003	0.006±0.003
	2	0.015±0.003	0.011±0.003
	3	0.025±0.003	0.033±0.003
Degassed	1	0.009±0.003	0.006±0.003
	2	0.017±0.003	0.012±0.003
	3	0.020±0.003	0.031±0.003

Table 3.4 - Quantum yield of the photochemical reaction of 3.65 x 10^{-4} M solution of $(C_6H_5)_{(4-n)}SnCl_n$ (n= 1,2,3) in ethanol as a function of the light source wavelength with a constant light intensity of 7.49 x 10^{-7} (einstein/l-sec).

Wavelength	n =	Φ_1 $(C_6H_5)_{(4-n)}SnCl_n$	Φ_2 Cl_2
254nm	1	0.009±0.003	0.005±0.003
	2	0.015±0.003	0.012±0.003
	3	0.021±0.003	0.030±0.003
310 nm	1	N.R	N.R
	2	N.R	N.R
	3	N.R	N.R
355 nm	1	N.R	N.R
	2	N.R	N.R
	3	N.R	N.R

Figure 3.10 - Quantum yield dependence of the $(C_6H_5)_{(4-n)}SnCl_n$ (n= 1,2,3) concentration in ethanol at a constant light intensity of 7.49 x 10^{-7} (einstein/l-sec).

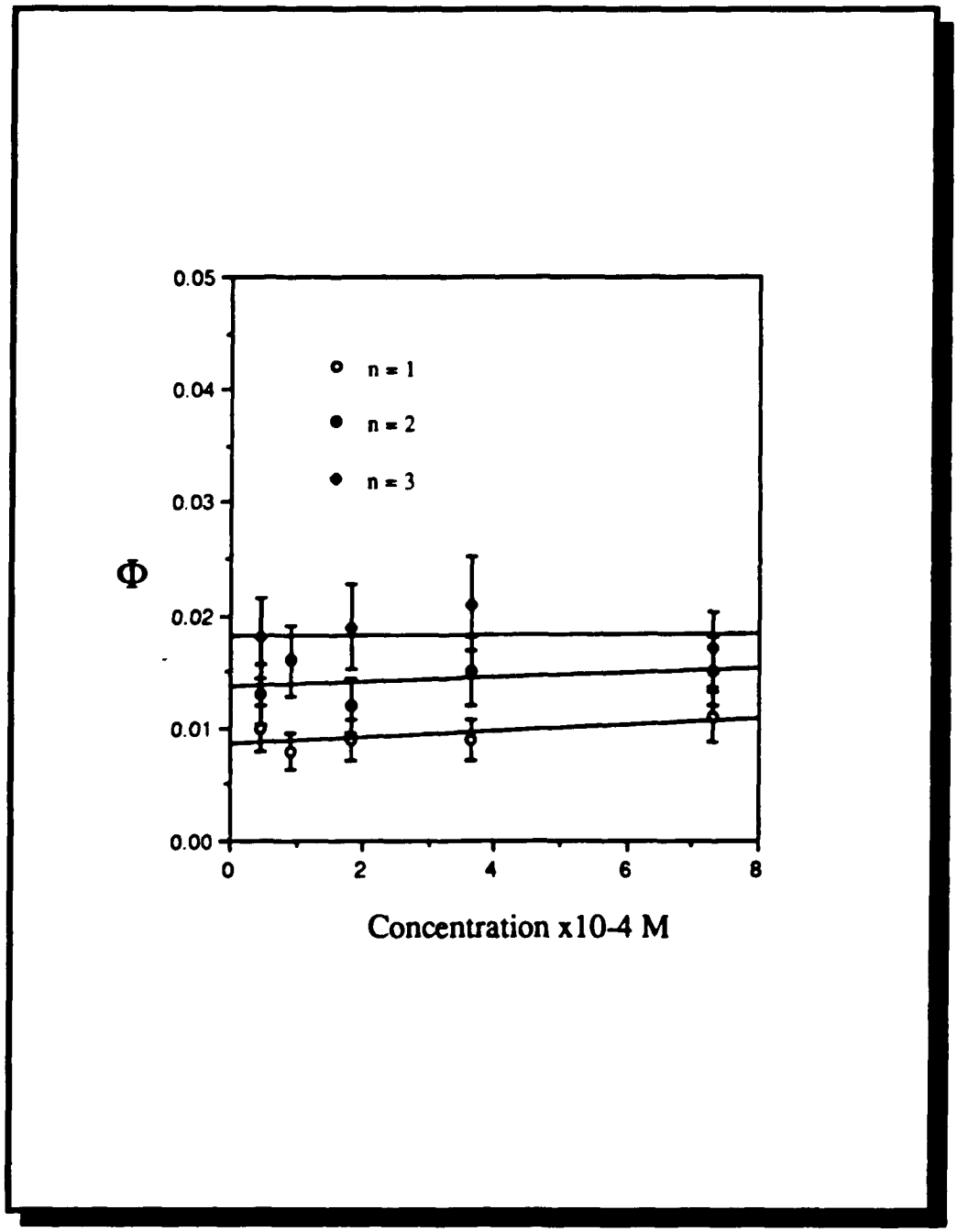

Figure 3.11 - UV-vis spectra recorded during photolysis with 254nm light of $1.0x10^{-4}$ M degassed solution of $(C_6H_5)_3SnN_3$ in ethanol at a constant light intensity of $7.49x10^{-7}$ Einstein/l-sec.

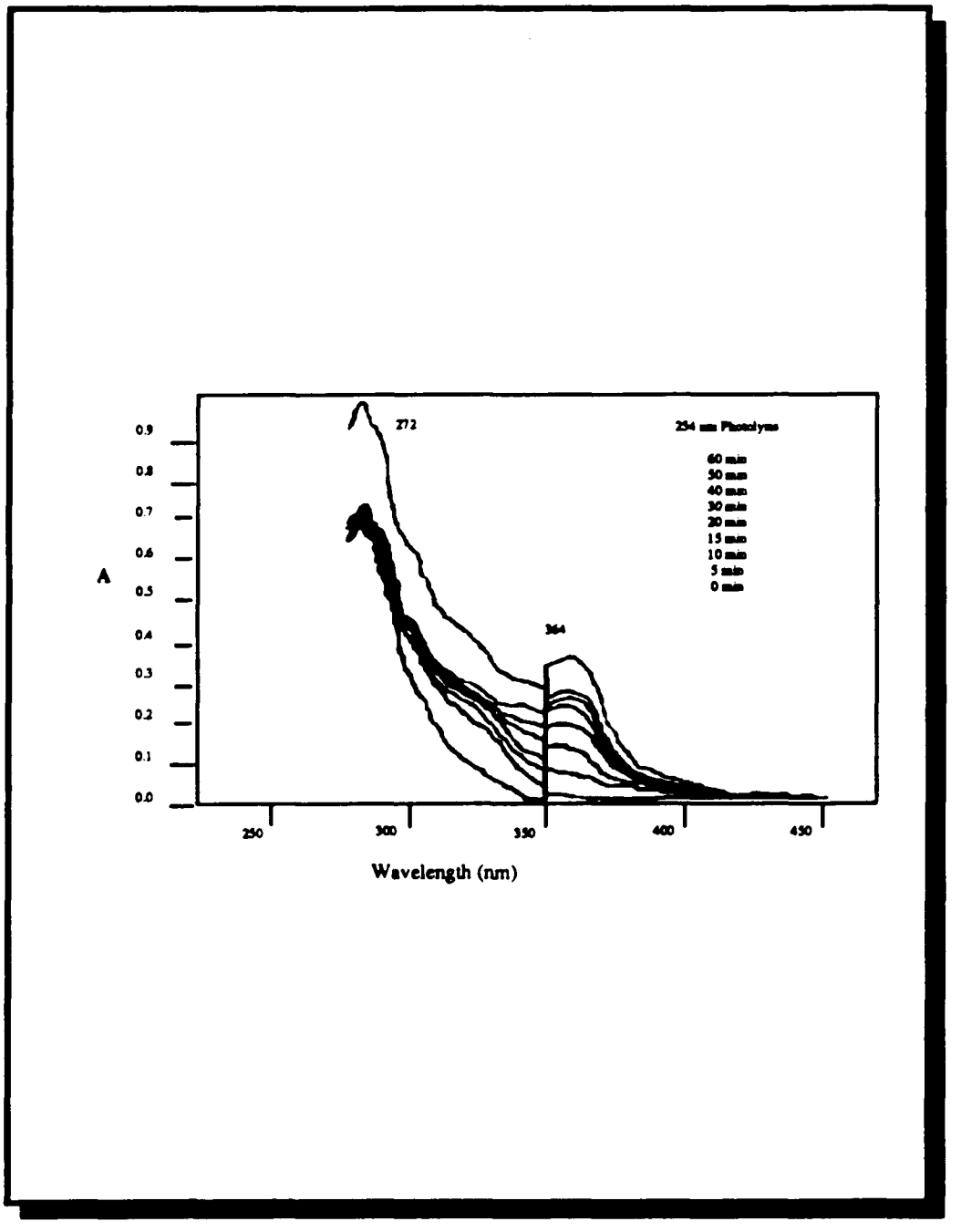

energy excitation wavelengths. Nor, there is evidence of a photochemical reaction at lower excitation intensities.

The ratio of the limiting yields of $(C_6H_5)_{(4-n)}SnCl_n$ (n= 1,2,3)disappearance and Cl_2 appearance, (Table 3.4), is consistent with the following reaction :

$$(C_6H_5)_{(4-n)}SnCl_n \xrightarrow{hv} (n/2)\,Cl_2 + \text{other products} \qquad 3.1$$

Also, the quantum yield of $(C_6H_5)_{(4-n)}SnCl_n$ (n= 1,2,3) disappearance, and Cl_2 appearance are independent of the $(C_6H_5)_{(4-n)}SnCl_n$ (n= 1,2,3) concentration (Figure 3.10).

The results obtained indicate that photolysis of $(C_6H_5)_{(4-n)}SnCl_n$ (n= 1,2,3) compounds with 254nm light leads to the homolytic cleavage of the Sn-Cl bond, followed by Cl• radical recombination to form Cl_2.

3.3 Photochemistry of $(C_6H_5)_{(4-n)}Sn(N_3)_n$ (n= 1,2,3) Compounds in Solution.

The photochemical reaction of the $(C_6H_5)_{(4-n)}Sn(N_3)_n$ (n= 1,2,3) compounds shows similar spectroscopic changes to those observed for the $(C_6H_5)_{(4-n)}SnCl_n$ (n= 1,2,3) compounds. Photolysis of a $1.0x10^{-4}$ M solution of $(C_6H_5)_3Sn(N_3)$ in ethanol with 254 nm light causes a decline in the intensity of the 263 nm absorption band (Figure 3.11), and the simultaneous growth of a band at 364-nm. An isosbestic point at 285 nm appears during the first minutes of photolysis, but then disappears on further photolysis

concurrent with the reappearance of the 263 nm band.The photoproduct peak at 364nm, as well as the reappearance of the 263 nm band, have been assigned to the formation of $(C_6H_5)_3Sn\text{-}N{=}N\text{-}Sn(C_6H_5)_3$, since azo compounds i.e. $(C_6H_5)\text{-}N{=}N\text{-}(C_6H_5)$, have similar absorptions in this region (ca. 360 nm) of the spectrum.[20] Furthermore, photolysis with 355-nm light of the photoproduct formed induces the disappearance of the 364nm peak, and the disappearance of the 263nm peak.

As in the case of $(C_6H_5)_{(4-n)}SnCl_n$ (n= 1,2,3) compounds, the emission peak at 320 nm of a degassed 1.0×10^{-4} M solution of $(C_6H_5)_3SnN_3$ in ethanol disappears as a function of photolysis time when excited with 254 nm light.

The FTIR spectra of the 254nm photochemical reaction of $1.0x10^{-3}$M solution of triphenyltinazide in ethanol (Figure 3.12) shows the disappearance of the N_3 asymmetric stretching band (2073 cm^{-1}), followed by the simultaneous growth of two new bands at 1723- and 1665 cm^{-1}. This bands are assigned to the formation of $(C_6H_6)_3Sn\text{-}N\text{-}O\text{-}(C_2H_5)$, from the reaction between a nitrogen radical and the adventitious solvent, since the (-N-O-R) functionality has a characteristic vibrational frequency in this region. [21] The strong infrared band, at about 2200 cm^{-1}, characteristic of the azo, (-N=N-), group is only observed after prolonged (≥ 2 hours.) photolysis. There is no evidence of a photochemical reaction of the phenyl groups, or the dissociation of the Sn-phenyl bond, since the IR bands associated with this groups do not change. Similarly, there are no changes in the NMR spectra during photolysis of $1.0x10^{-3}$M solution of triphenyltinazide in ethanol.

Nitrogen gas evolution was observed during the photolysis of 250 ml of a $1.0x10^{-3}$M solution of triphenyltinazide in ethanol with 254nm light by

Figure 3.12 - FTIR spectra during photolysis of $1.0x10^{-4}$M solution of triphenyltinazide in carbontetrachloride with 254 nm light source.

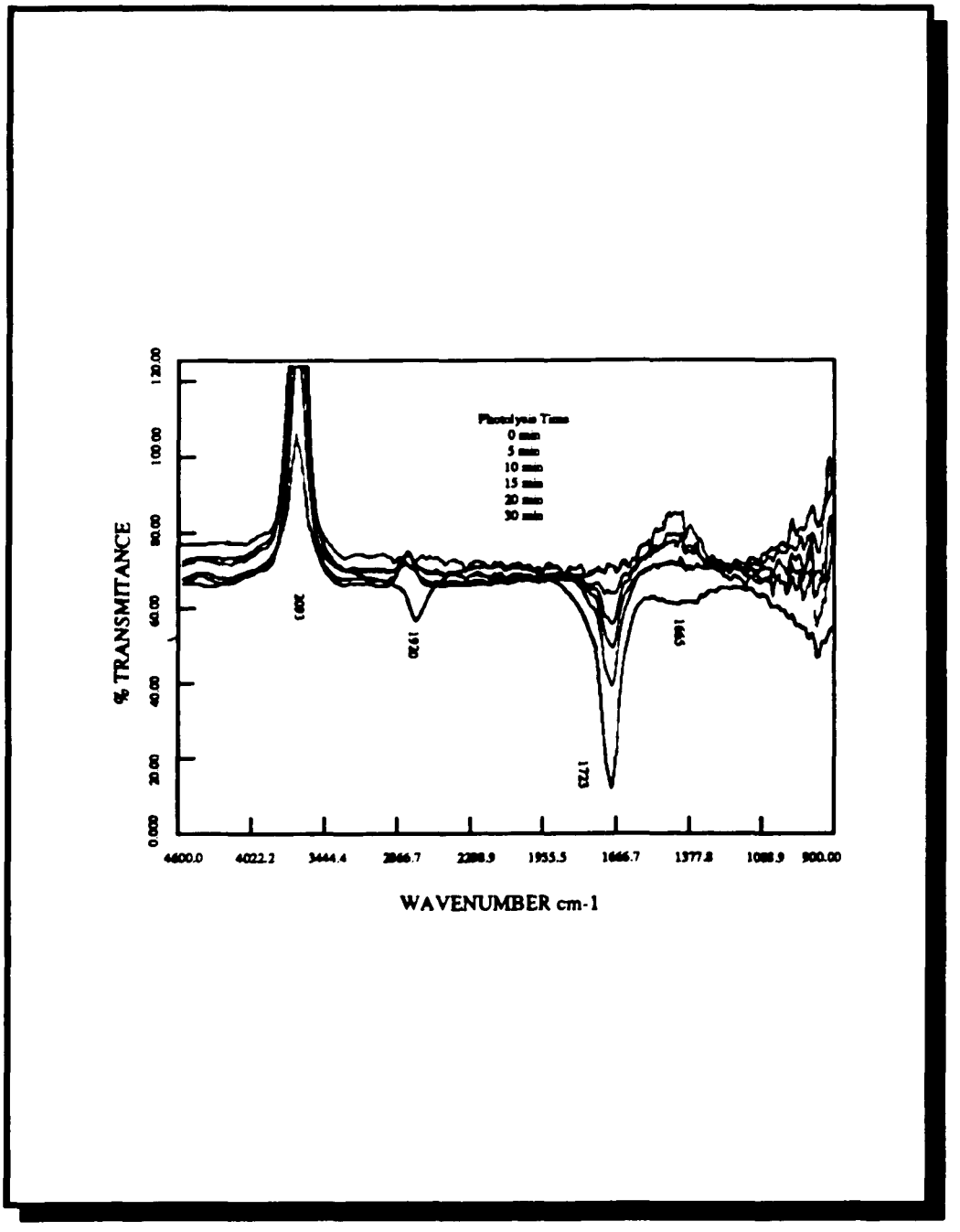

gas chromatography (Figure 3.13). The amount of nitrogen gas produced never exceeded more than 5% from the total amount of $(C_6H_6)_3SnN_3$ photolyzed. Furthermore, the amount of nitrogen gas produced was found to be independent of the concentration of $(C_6H_6)_3SnN_3$.

As in the case of $(C_6H_6)_3Sn(N_3)$, photolysis of a 1.2 x 10^{-4}M solution of $(C_6H_6)_2SnN_3$ and/or $(C_6H_6)Sn(N_3)_3$ in ethanol with 254 nm light shows the disappearance of the 263 nm peak, followed by the appearance of a peak at 340 nm which is tentatively assigned to the formation of an azo (-N=N-) compound. Similarly, the emission spectra shows the disappearance of the 320nm peak upon excitation with 254 nm light. The disappearance of the emission peak occurs simultaneously with the disappearance of the 263 nm peak in the UV-visible spectra.

The FTIR of the photochemical reaction of 1.0 x 10^{-3}M solution of $(C_6H_6)_2SnN_3$ and/or $(C_6H_6)Sn(N_3)_3$ in ethanol with 254 nm light shows the disappearance of the N_3 asymmetric stretch band at 2070 cm^{-1}. However, there are no other changes in the spectra indicative of the formation of a photoproduct. Also, there are no changes in the NMR spectra.

Detail quantum yield calculations of the photochemical reaction of the $(C_6H_6)_{(4-n)}SnCl_n$ (n = 1, 2, 3,) compounds were not performed, since there was not a conclusive evidence of the different photoproducts formed. Nevertheless, calculations of the quantum yield of disappearance of $(C_6H_6)_{(4-n)}Sn(N_3)_n$ (n = 1, 2, 3,) compounds gave simmilar results to the results obtained for the $(C_6H_6)_{(4-n)}SnCl_n$ (n = 1, 2, 3,) compounds, from 0.01 to 0.001 when excited with 254 nm at a light intensity of 7.49 x 10^{-7} (einstein/ l-sec).

The results obtained indicate that the photolysis of $(C_6H_6)_{(4-n)}Sn(N_3)_n$ (n = 1, 2, 3,) compounds with 254 nm light induces the breaking

Figure 3.13 - Gas chromatograph the photolysis of 250 ml of a $1.0x10^{-3}M$ solution of $(C_6H_6)_3Sn(N_3)$ in ethanol with 254nm light at a constant light intensity of 7.49×10^{-7} (einstein/ l-sec); He carrier gas, Rate 36cc/min, Attn =128x.

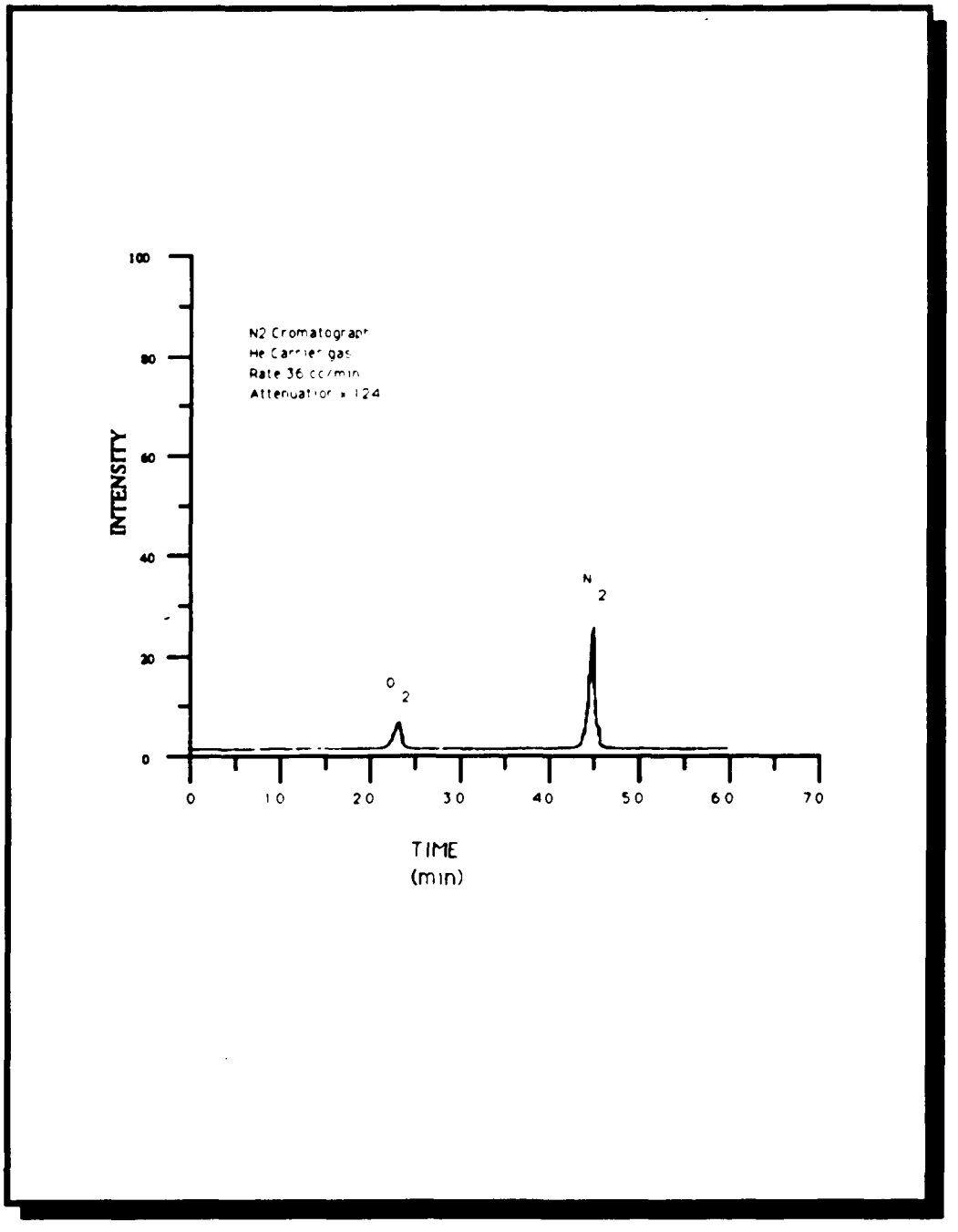

of the nitrogen bond in the azide functionality forming a nitrene reactive intermediate accordingly with the following reaction:

$$(C_6H_6)_3SnN_3 \xrightarrow{hv} (C_6H_6)_3SnN: + N_2 \qquad 3.2$$

The nitrene intermediate then reacts either with another nitrene radical to form the azo dimmer, or with the adventitious solvent to produce a quinoxime compound accordingly to the following reactions :

$$(C_6H_6)_3SnN: + (C_6H_6)_3SnN: \longrightarrow (C_6H_6)_3SnN{=}NSn(C_6H_6)_3 \qquad 3.3$$

$$(C_6H_6)_3SnN: + (C_2H_5)OH \longrightarrow (C_6H_6)_3SnN\text{-}O\text{-}(C_2H_5) \qquad 3.4$$

4. Summary of Solution Photochemical Studies.

The photochemical studies of $(CH_3)_3SnX$ (X= I, Br, Cl) compounds in solution show that the mechanism of the photochemical reaction is solvent dependent. In the nonpolar solvents hexane and cyclohexane, the primary photochemical event is the homolytic cleavage of the Sn-X bond, followed by the rapid recombination of the halide (X•) and trimethyltin ($(CH_3)_3Sn$•) radicals to form X_2 and $[(CH_3)_3Sn]_2$ as photoproducts.

Quantum yield calculations of the photochemical reaction in hexane show that the ratio of the limiting yield of $(CH_3)_3SnX$ disappearance, and X_2 appearance (X= I, Br) is consistent with the net reaction:

$$2\,(CH_3)_3SnX \xrightarrow{h\nu} (CH_3)_6Sn_2 + X_2 \qquad 4.1$$

On the other hand, 254 nm photolysis of $(CH_3)_3SnI$ in polar solvents such as ethanol and acetonitrile, induces a heterolytic cleavage of the Sn-X bond, and the formation of HI as a photoproduct. The quantum yield calculations yield 0.97 ± 0.07 mol of HI formed / mol of $(CH_3)_3SnI$ consumed, consistent with the net reaction :

$$(CH_3)_3SnX \xrightarrow{hv} X^- + (CH_3)_3Sn^+ \qquad 4.2$$

The change in behavior of the photochemical reaction is attributed to formation of a solvent adduct between $(CH_3)_3SnX$ compounds and solvents capable of acting as Lewis bases. Formation of a solvent-adduct increases the coordination number of tin in $(CH_3)_3SnI$ from 4 to 5 and the structure changes from tetrahedral to a distorted trigonal bypiramidal. This causes a change in the electronic structure of the compound. [22,23]

In both polar and nonpolar solvents the quantum yield is independent of the O_2 concentration, and the concentration of the starting $(CH_3)_3SnX$ (X= I, Br, Cl) compound. However, the quantum yield is dependent on the halide susbstituent, and decreases as the absorption energy of the $(CH_3)_3SnX$ (X= I, Br, Cl) compound shifts from 234 nm to 212-, and 190-nm for the respective halide. The quantum yield of the photochemical reaction is high, $\Phi \geq 0.8 \pm 0.5$ if excited with with 254 nm light, and is linear as a function of the light intensity, However, the yield decreases rapidly as the excitation wavelength shifts from 254nm to 310- and 355-nm.

Similarly, the photochemical reactions of $(C_6H_5)_{(4-n)}SnX_n$ (X= Cl, N_3; and n= 1,2,3) compounds were investigated, since these complexes exhibit higher energy absorptions, 250- to 280-nm, than the $(CH_3)_3SnX$ (X= I, Br, Cl) compounds, 190- to 240-nm. The electronic absorption of the $(C_6H_5)_{(4-n)}SnX_n$ (X= Cl, N_3; and n= 1,2,3) compounds shows no solvent

dependence, and similar absorption energies are observed in polar and nonpolar solvents. The solubility of the compounds in nonpolar solvents is low, $\leq 10^{-5}$ M. Consequently, all the experiments were done in polar solvents such as ethanol.

The photochemical reactions of $(C_6H_5)_{(4-n)}SnCl_n$ (n= 1,2,3) are similar to the reaction of the $(CH_3)_3SnX$ (X= I, Br, Cl) compounds in nonpolar solvents, since photolysis with 254 nm light induces the homolytic cleavage of the Sn-X bond followed by X_2 formation.

The quantum yield of $(C_6H_5)_{(4-n)}SnCl_n$ (n= 1,2,3) compounds is relatively low, Φ = 0.01 ±0.005, when excited with 254 nm light, and no photochemical event is observed when excited with 310-, and 355-nm light. Also, the quantum yield is independent of the O_2 concentration, and the concentration of the starting $(C_6H_5)_{(4-n)}SnCl_n$ (n= 1,2,3) compound.

A different mechanism occurs in the photochemical reaction of $(C_6H_5)_{(4-n)}Sn(N_3)_n$ (n= 1,2,3) compounds. The results indicate that 254 nm photolysis of $(C_6H_5)_{(4-n)}Sn(N_3)_n$ (n= 1,2,3) compounds induces the homolytic cleavage of the nitrogen bond in the azide functionality (N=N—N) to form a nitrene intermediate, accordingly to the reaction:

$$(C_6H_5)_{(4-n)}Sn(N_3)_n \xrightarrow{h\nu} (C_6H_5)_{(4-n)}Sn\text{-}N: + N_2 \qquad 4.3$$

that later reacts to form tin-azo (-Sn-N=N-Sn-) compounds by recombination with another nitrene radical, or by a reaction with an adventitious solvent.

In depth quantum yield calculations were not performed due to the inconclusive nature of the photoproducts formed. Nevertheless,

calculations of the quantum yield of disappearance of the starting $(C_6H_5)_{(4-n)}Sn(N_3)_n$ (n= 1,2,3) compound show that the yield is similar to the one observed in the $(C_6H_5)_{(4-n)}SnCl_n$ (n= 1,2,3) compounds, Φ = 0.01 to 0.001.

From the results obtained in the photochemical studies of the different organotin compounds is clear that the $(CH_3)_3SnX$ (X= I, Br, Cl) compounds are the most suitable for the photochemical studies on the glass matrices, since the mechanism of the photochemical reaction is better understood, and the quantum yield of the reaction is high.

5. Photochemistry of Trimethyltin Halides Adsorbed onto Porous Glass Matrices.

The goal of the photochemical studies describe here is to understand the photochemical reaction mechanism of organotin compounds adsorbed onto porous glasses. The organotin compounds are used as precursors to the photodeposition of a metal oxide onto the glass matrix, and in turn to generate a gradient refractive index in the glass. The photochemical deposition of a metal oxide to achieve a gradient refractive index depends on several factors. First the organometallic precursor should be photochemically active in the visible or near-UV, since calcined PVG exhibits 50% at 295 nm. Second, the quantum yield of the reaction must be high, 1.0 if possible, to have an efficient process. And third, volatility and stability are essential, since a key to create a gradient refractive index depends in the ability to remove the unreacted compound. Consequently, if the unphotolyzed compound decomposes during the subsequent thermal treatment of the glass, the gradient index generated photochemically will disappear.

The results of the photochemical studies in solution indicate that $(CH_3)_3SnX$ (X= I, Br, Cl) compounds are the most suitable for the photochemical deposition of a tin oxide compound on the glass, since the quantum yield of the photochemical reaction ($\Phi \sim 0.8$) is high as compared to the low yield ($\Phi \sim 0.01$) of the $(C_6H_5)_{(4-n)}SnX_n$ (X= Cl, N_3 ; and n= 1,2,3)

compounds. Also, the trimethyltin halides are all volatile at 25 °C, in contrast to the phenyltin compounds which are solids at 25 °C. However, a major drawback of the $(CH_3)_3SnX$ compounds is that their optical absorption occurs at ≤ 250 nm below the transmittance of the glass.

5.1 Spectroscopic Properties of Methyltin Halide Compounds Adsorbed onto Porous Glasses.

Electronic spectra of $(CH_3)_3SnX$ (X= I, Br, Cl) compounds adsorbed onto PVG, or TMOS xerogels in the region of 180- to 800 nm resemble fluid solution spectra. Each $(CH_3)_3SnX$ (X= I, Br, Cl) compound exhibits an absorption band located in the 250- to 180 nm (Figure 5.1) region. However, due to the high absorption of the glass in this region, only the $(CH_3)_3SnI$ absorption maxima is observed. For the other two $(CH_3)_3SnX$ (X= Br, Cl) compounds, only the long wavelength edge of the absorption band is observed. Table 5.1 summarize the adsorption maxima and relative extinction coefficient of the compounds adsorbed onto PVG and TMOS. Furthermore, there is no indication of an emission spectra when 1.12×10^{-4} (mol/gr. PVG) of $(CH_3)_3SnI$ adsorbed onto PVG are excited with 254 nm light.

A spectral change similar to that which occurs when hexanol is added to a hexane solution of $(CH_3)_3SnI$ also occurs when the compound is adsorbed onto PVG. On adsorption, the absorption maximum shifts from 234nm in hexane to 230nm in PVG. The shift is not as large as that which occurs when hexanol is added to a hexane solution of $(CH_3)_3SnI$. However,

Figure 5.1 - UV-visible absorption spectra of (CH3)3SnX (X= Br, I) compounds adsorbed onto PVG.

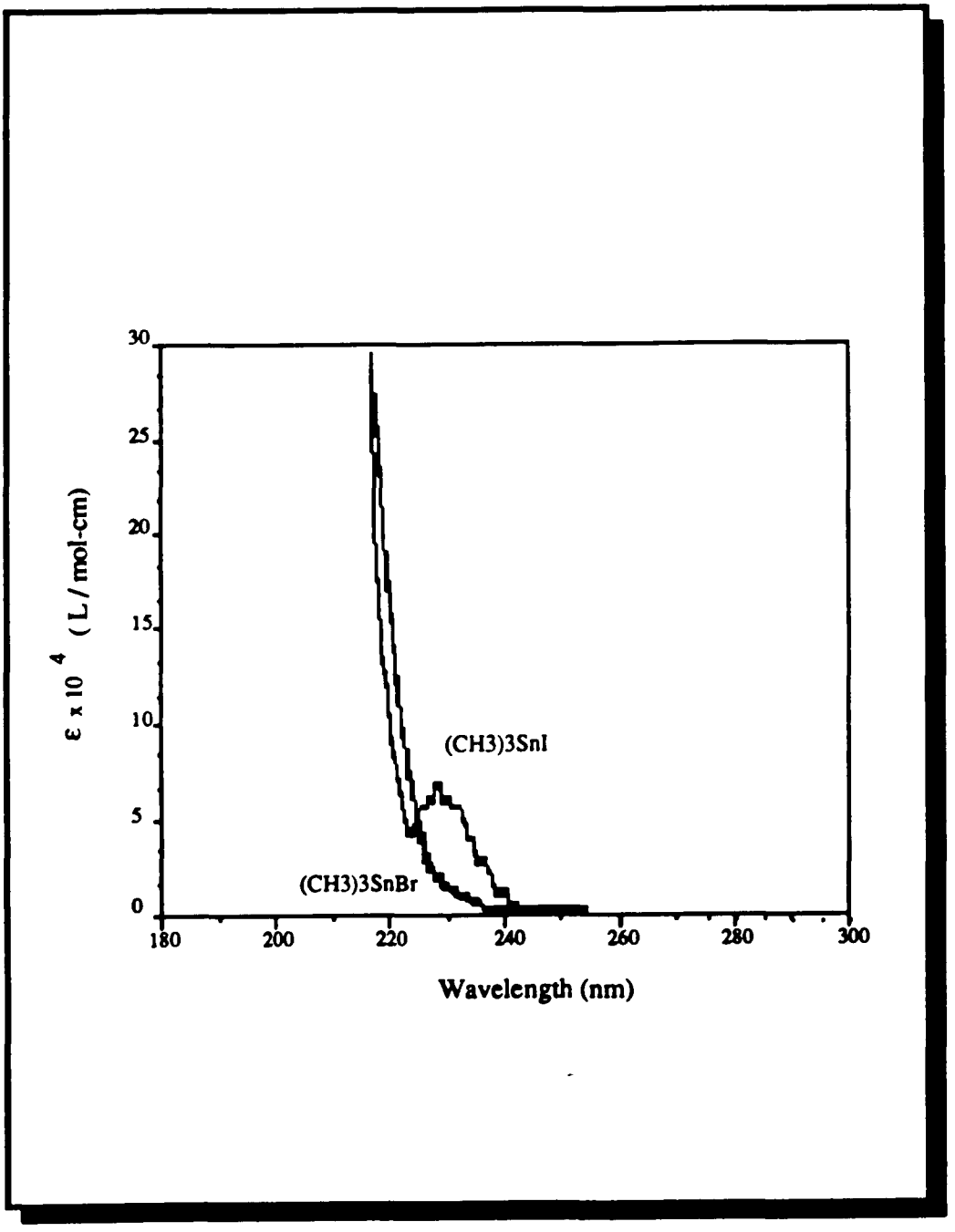

Table 5.1 - Absorption wavelengths and relative absorption coefficients of trimethyltinhalides adsorbed onto PVG.

	PVG		TMOS	
$(CH_3)_3Sn$-X X=	Wavelength (nm)	Epsilon (mol ads./gr PVG)	Wavelength (nm)	Epsilon (l/mol-cm)
Iodine	230.0	7.38×10^4	230.0	7.38×10^4
Bromine	230.0*	5.33×10^4	230.0*	5.33×10^4
Chlorine	230.0*	2.46×10^4	230.0*	2.46×10^4

*The maximum absorption of this compounds, which occurs below 230nm, could not be measured since PVG absorbs strongly (e ≥ 1.0e5) below 230nm.

the shift is in the same direction as that found in ethanol (218nm) and acetonitrile (226nm). Since the surface of PVG possesses Si-OH functionalities, the bathochromic shift suggests that the adsorption involves the formation of an $(CH_3)_3SnI$--OH-Si adduct. Further evidence that this is indeed the case arise from DRIFT and desorption experiments.

DRIFT spectra recorded during the adsorption of trimethyltiniodide onto PVG (Figure 5.2) show a decline in the intensity of the 3744 cm^{-1} silanol band. The decline in the intensity is proportional to the amount of $(CH_3)_3SnI$ adsorbed, and is accompanied by the simultaneous growth of a broad band centered at 3550 cm^{-1}. The two other bands which appear at 2993-, 2917-cm^{-1} are due to the C-H stretch of the methyl groups of $(CH_3)_3SnI$. Since adsorption of $(CH_3)_3SnI$ does not result in water formation, the appearance of the broad band at 3550 cm^{-1} is attributed to the formation of a $(CH_3)_3SnI$--OH-Si adduct. By coordinating to the lone pair on oxygen, $(CH_3)_3SnI$ reduces the SiO-H bond order and, in turn, shifts the band to lower frequency.

Although the term coordination has been used to designate the $(CH_3)_3SnI$--OH-Si interaction, it should be realized that this appears to be a relatively weak interaction and does not occur with a net chemical change in either the complex or the glass. Desorption of the compound under vacuum at room temperature occurs with a decline of the intensity of the broad 3550 cm^{-1} band and concurrent reappearance of the 3744 cm^{-1} silanol band. Furthermore, UV and FTIR spectra of the adsorbed compound trapped in CCl_4 upon desorption are exactly equivalent to the spectra of $(CH_3)_3SnI$ dissolved in CCl_4.

Consequently, adsorption of $(CH_3)_3SnX$ compounds onto PVG involves the reversible formation of a $(CH_3)_3SnI$--OH-Si adduct.

Figure 5.2 - DRIFT spectra of adsorption process of $(CH_3)_3SnI$ onto PVG.

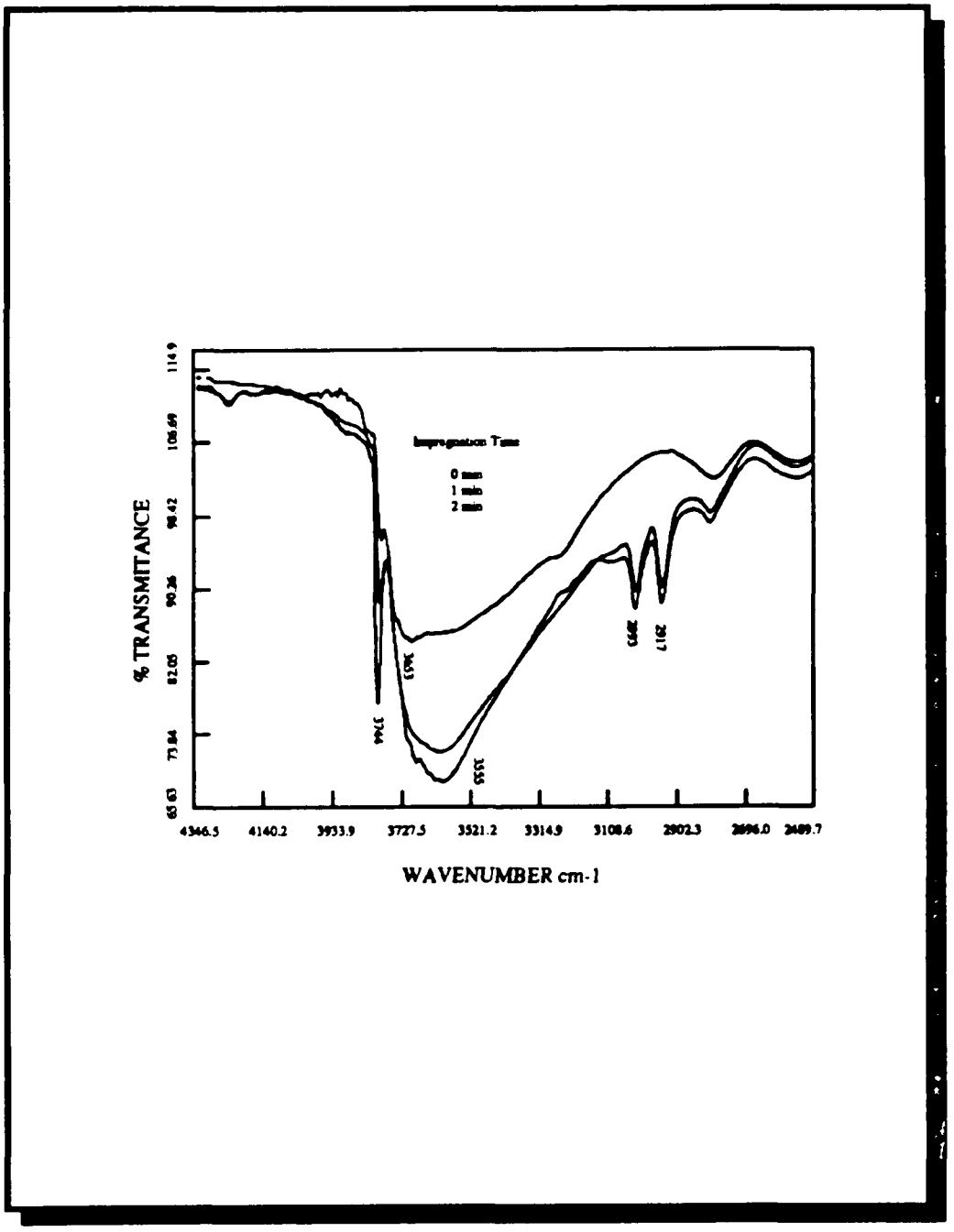

5.2 Adsorption of Trimethyltinhalide Compounds onto Porous Glass.

Adsorption of $(CH_3)_3SnX$ (X= I, Br, Cl) compounds onto the surface of porous Vycor glass were measured by UV-visible spectroscopy, where the number of moles adsorbed/unit time was determined from the increase in absorbance at 230 nm. All measurements were carried out under a constant pressure of 10^{-6} torr of each $(CH_3)_3SnX$ (X= I, Br, Cl) compound.

Plots of moles adsorbed vs. time (Figure 5.3) show three distinct rates of adsorption. The initial rate of adsorption is relatively slow, but as the number of moles adsorbed increases, the rate increases. Further increases in the moles adsorbed appear to result in saturation, where the number of moles adsorbed becomes independent of exposure time. Each $(CH_3)_3SnX$ (X= I, Br, Cl) compound exhibits a similar adsorption curve, except in the case of $(CH_3)_3SnCl$, where the saturation region is not observed. Table 5.2 summarizes the slower initial, and faster secondary rates of adsorption for each of the $(CH_3)_3SnX$ (X= I, Br, Cl) compounds.

In our studies, we were also concerned with the desorption process, since an equally important process is the removal of the unphotolyzed compound from the PVG surface. Very little desorption occurs when the impregnated sample remains under 1 atm. of air (Figure 5.4). However, under a dynamic vacuum ($p \leq 10^{-6}$ torr), essentially complete desorption occurs within approximately 10 minutes. DRIFT experiments yield similar results. After impregnation, if the microreactor is maintained under vacuum ($p \leq 10^{-6}$ torr), desorption from the powdered glass occurs in a matter of minutes. The faster rate of desorption from the powder glass

Figure 5.3 - (a) Fractional surface coverage and (b) Rate of adsorption of $(CH_3)_3SnX$ (X= I, Br, Cl) compounds adsorbed onto PVG.

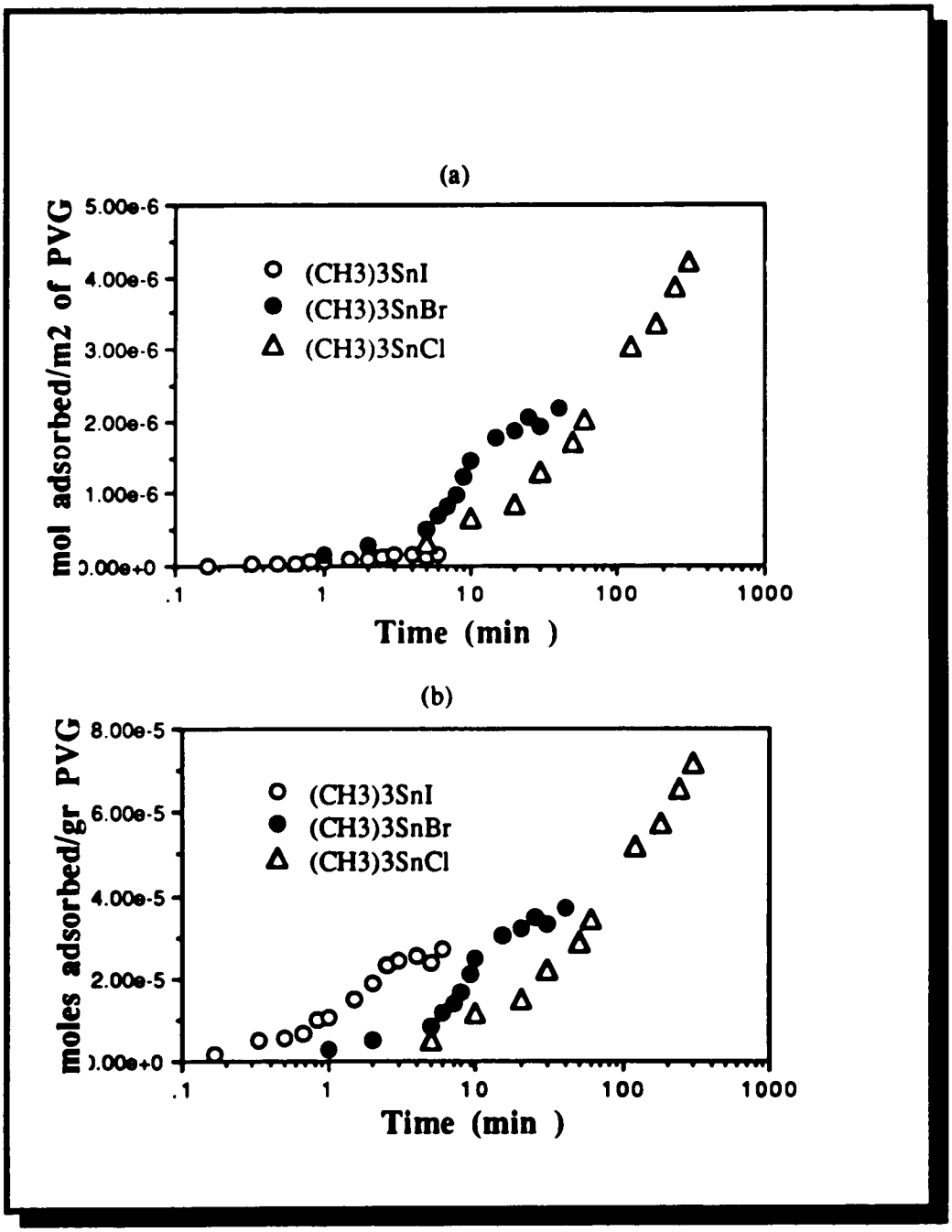

Table 5.2 - Rates of adsorption of $(CH_3)_3SnX$ (X= I, Br, Cl) compounds onto PVG.

$(CH_3)_3Sn$-X X=	Region I (mol ads/gr PVG-min)	RegionII (mol ads/gr PVG-min)
Iodine	1.150×10^{-5}	8.632×10^{-6}
Bromine	2.590×10^{-6}	2.115×10^{-6}
Chlorine	5.743×10^{-7}	3.671×10^{-7}

relative to that from the plate samples of glass appears to be a consequence of the larger surface area of the powder. Also, since the IR bands of the compound, principally the methyl bands, decline at the same rate, desorption occurs without decomposition, at room temperature.

5.3 Photochemical Studies on PVG.

5.3.1 Photochemistry of $(CH_3)_3SnI$ adsorbed onto PVG.

The photochemical reaction of $(CH_3)_3SnI$ adsorbed onto PVG was studied under different conditions in order to understand the mechanism of the reaction. It is expected that the photochemical reaction may proceed by a similar mechanism as the one observed in polar solvents, since the surface of the glass is polar in nature, and the peak position in the UV-vis spectra shifts to lower wavelengths as observed in the case of ethanol.

The molar concentration of $(CH_3)_3SnI$ adsorbed onto the glass surface in these photochemical studies range from about 1.0×10^{-6} to 5.0×10^{-5} (moles/gram) of glass sample. These concentrations were used in order to obtained UV-vis absorption spectra at 230 nm with absorption intensities between 0.5 and 2.0 absorption units. The observations made during the 254nm photolysis of 1.76×10^{-5} (moles/gr of PVG) of $(CH_3)_3SnI$ adsorbed onto PVG were the decrease of the 230 nm, followed by the simultaneous growth of two bands at 290 and 360 nm. (Figure 5.5). The product bands have been assigned to the formation of HI, since the position of the product bands, and the ratio of the 290nm:360nm intensities is equal

Figure 5.4 - Rate of desorption of $(CH_3)_3SnI$ adsorbed onto PVG.

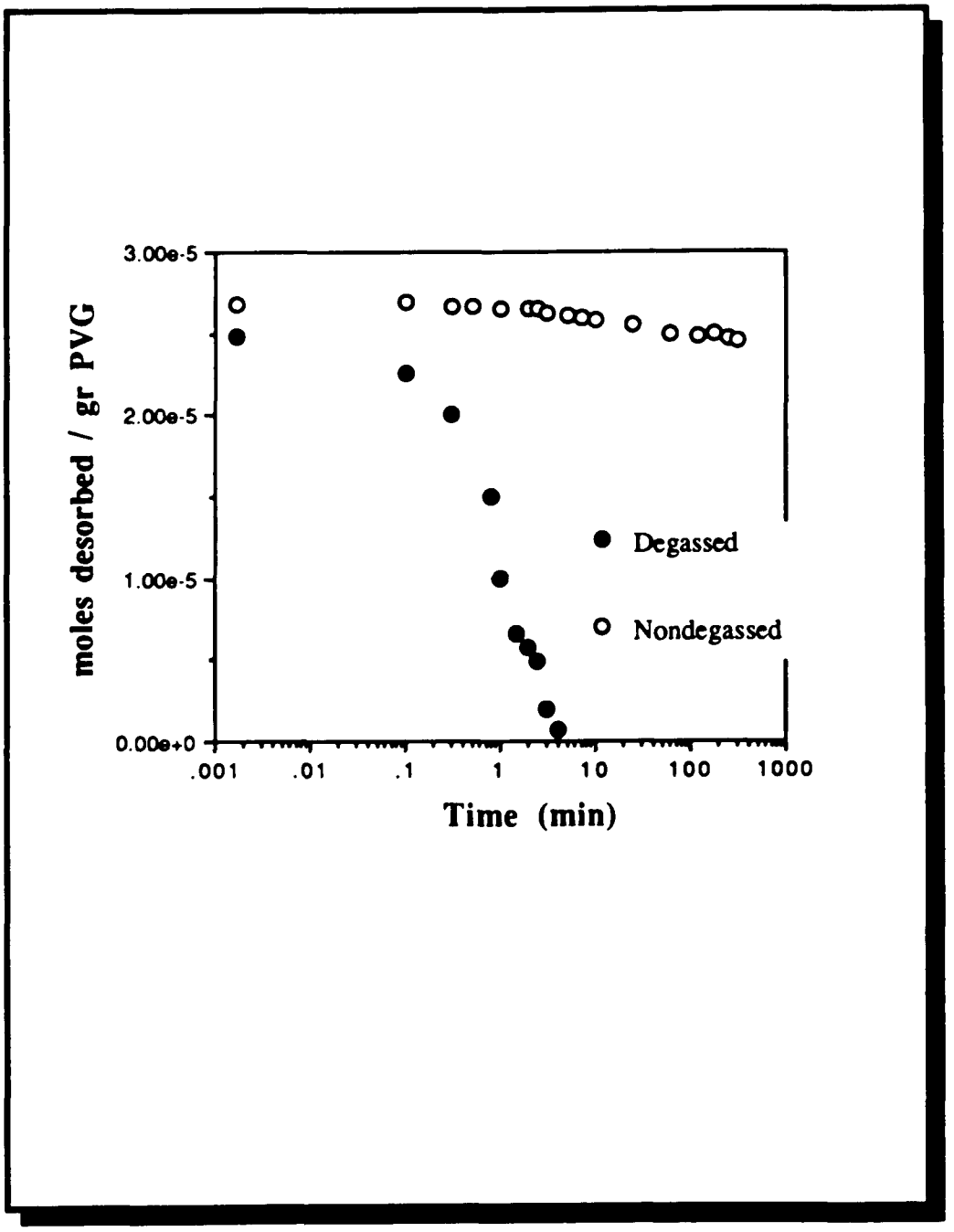

to those observed in the absorption spectra of HI adsorbed onto PVG, $A_{290nm} : A_{360nm} \sim 1.90$. Furthermore, the UV-vis spectra of $5.0x10^{-5}$ (moles/gr of PVG) of I_2 sublimed onto the PVG surface was recorded (Figure 5.6), in order to insure that the product peaks belong to HI and not to I_2. The I_2 spectra shows three peaks at 290-, 360-, and 500 nm. Similar spectra is observed when I_2 is dissolved in polar solvents. The characteristic I_2 bands in a polar solvent such as ethanol are: a) the blue shifted peak at 500 nm, which occurs at 520nm in the vapor phase, and b) charge transfer peaks at 290- and 360 nm, which suggest that I_2 undergoes a charge transfer interaction with the OH groups of the PVG surface. Similar results are observed upon adsorption of $(CH_3)_3SnI$ onto the PVG surface.

The photochemical reaction of $(CH_3)_3SnI$ adsorbed onto PVG was followed in situ by FTIR. The photochemically induced changes in the spectra were recorded by taking sixty, one second, consecutive interferograms while the sample was being photolyzed. Since the 254-nm photolysis source was at a 90 ° angle to the analyzing beam and radically different in wavelength, there was no interference between the two. From the DRIFT spectra (Figure 5.7) it was observed that upon photolysis the surface undergoes a structural change opposite to the one found during the $(CH_3)_3SnI$ absorption process. The hydroxyl band at 3550 cm^{-1} that appeared during the adsorption process disappears upon photolysis followed by the simultaneous increase in the intensity of the free silanol band at 3744 cm^{-1}. At the same time the C-H stretch bands of the methyl groups of the adsorbed $(CH_3)_3SnI$ at 2992-, and 2916 cm^{-1} increased simultaneously indicating that the this transition has become more allowed. Attempts to obtained the Raman spectra of the photoreaction in

Figure 5.5 - UV-visible spectra of the 254nm photolysis of $1.76x10^{-5}$ (moles/gr of PVG) of $(CH_3)_3SnI$ adsorbed onto calcined PVG at a constant light intensity of 1.22x10-7 (einstein/l-sec)

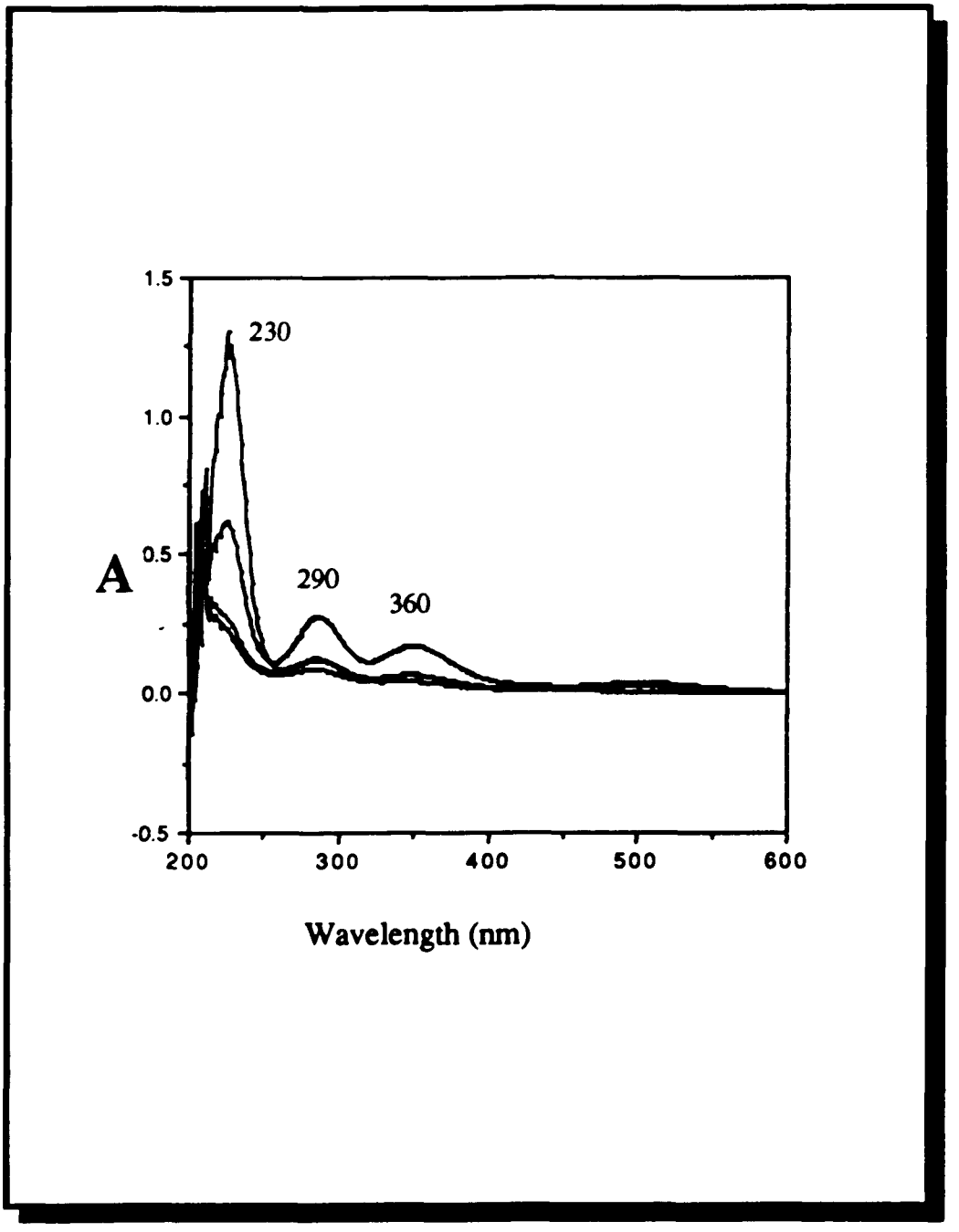

Figure 5.6 - UV-vis of 5.0×10^{-5} (moles/gr of PVG) of I_2 adsorbed onto calcined PVG.

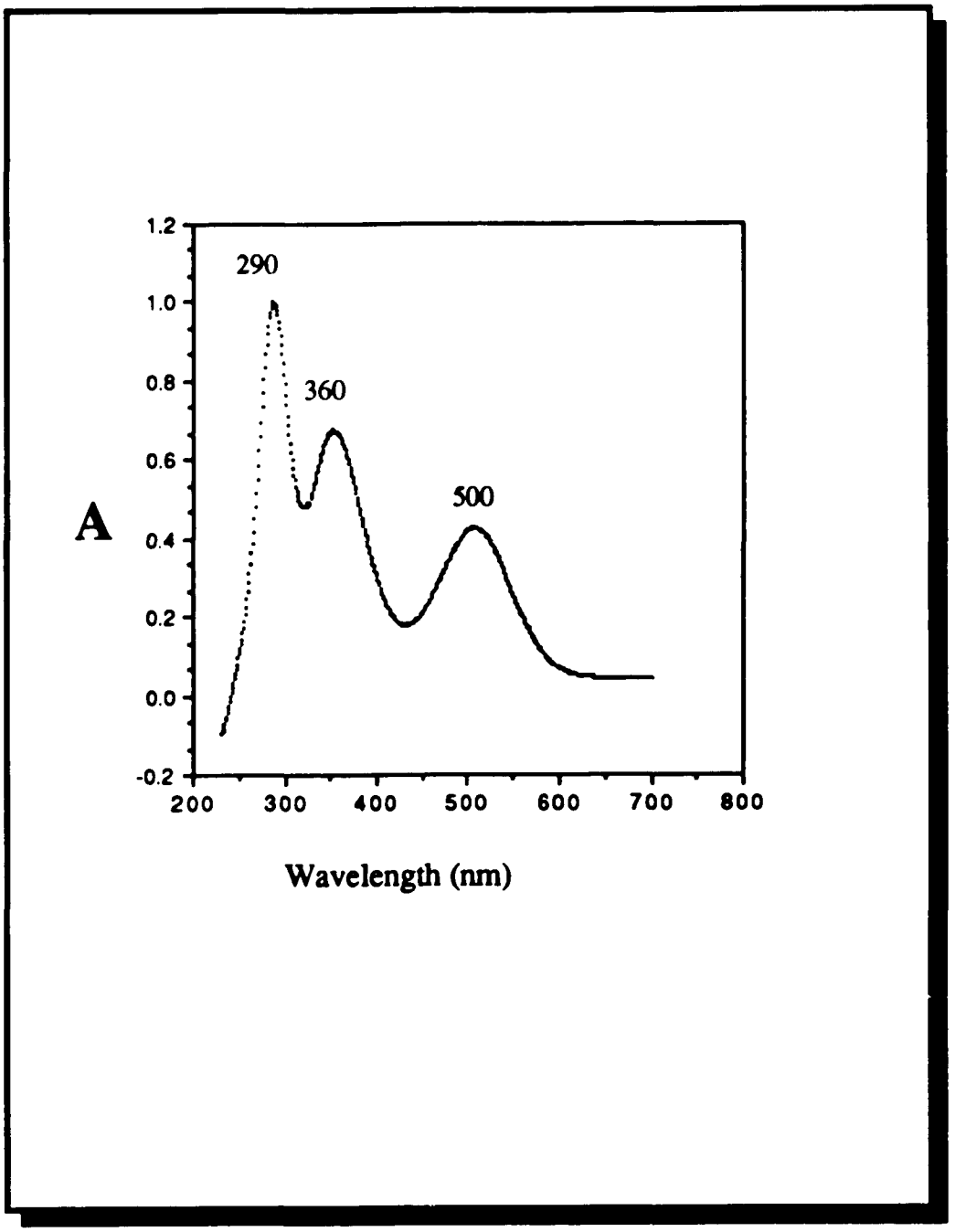

Figure 5.7 -FTIR of the photolysis of $(CH_3)_3SnI$ adsorbed onto calcined PVG.

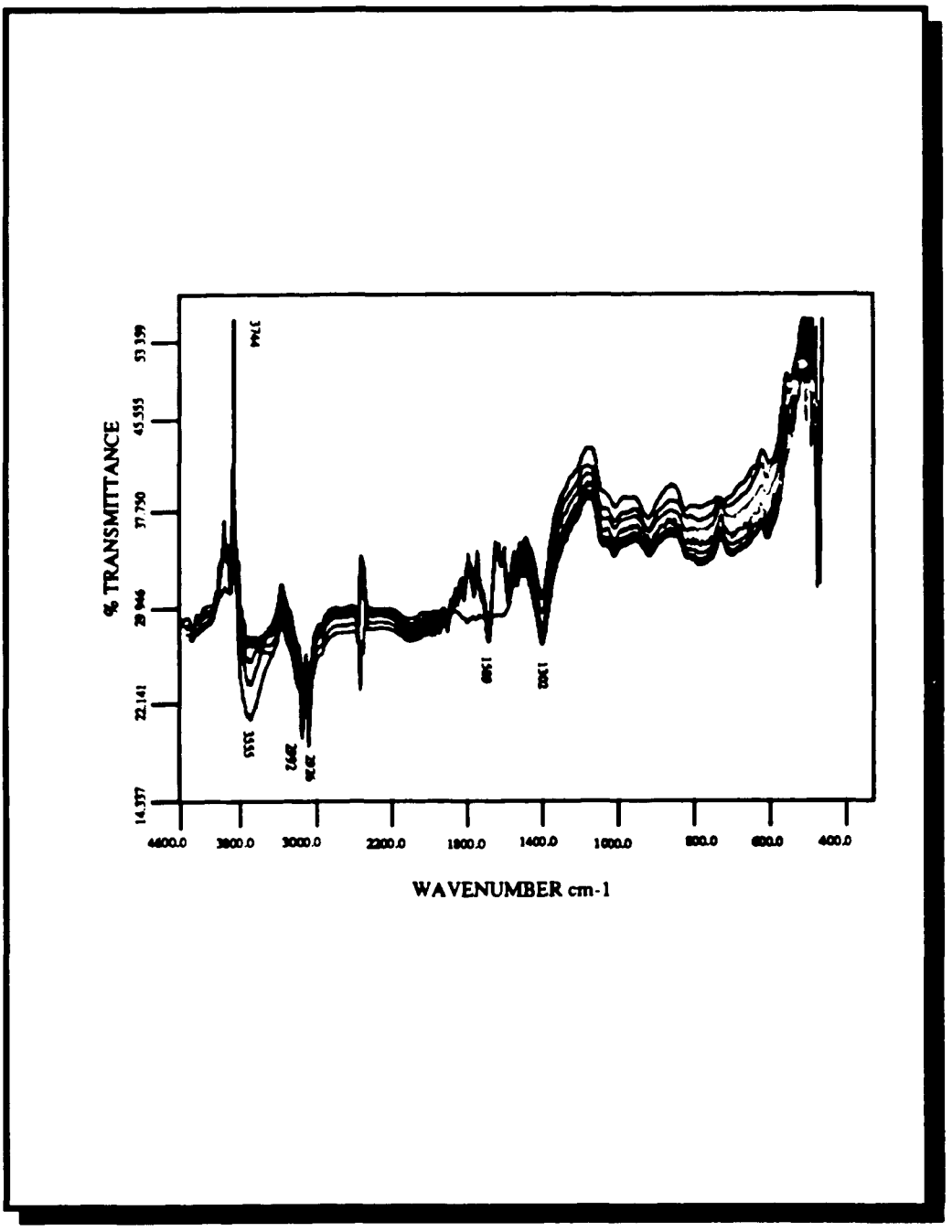

order to identify the dissociation of the Sn-I bond were taken. However, due to the large scattering of the analyzing beam from the porous surface of PVG a well resolved spectra was not possible to be obtained.

In order to established the efficiency of the photochemical reaction of $(CH_3)_3SnI$ adsorbed onto PVG, the quantum yield of the disappearance of $(CH_3)_3SnI$ and the quantum yield of appearance of iodic acid were followed under a variety of experimental conditions by UV-vis spectroscopy. The same procedure followed during the kinetic measurements in solution was followed here with one exception. In the solution experiments, a new aliquot was used at each time interval during the rate measurements. On the other hand, on PVG, only one impregnated sample was used for a complete set of time measurements, since the exact same concentration cannot be duplicated on PVG. Average values of approximately 10 runs were used to compute the quantum yield, (Figure 5.8).

First, as in the case of solution, the quantum yield of disappearance of 1.62×10^{-5} (moles/gr of PVG) of $(CH_3)_3SnI$ adsorbed onto PVG at a constant light intensity of 1.22×10^{-7}(einstein/l-sec) is independent of the O_2 concentration. The results obtained indicated that there is no difference within experimental error between the quantum yield values obtained under nitrogen and those obtained in air, oxygen, and completely degassed atmospheres (Table 5.3) .

Second the quantum yield of 1.62×10^{-5} (moles adsorbed/gram of PVG) of $(CH_3)_3SnI$ adsorbed onto PVG shows a linear dependence on the light intensity (Figure 5.9), since the slope of the log Ia vs log F is approximately equal to one. Similarly, the quantum yield of appearance of HI also shows a first order linear dependence on the light intensity. Moreover, the quantum yield decreases rapidly as the excitation wavelength shifts from 254-nm to

Figure 5.8 - Quantum yield of the 254nm photolysis of 1.62×10^{-5} (moles/gr of PVG) of $(CH_3)_3SnI$ adsorbed onto PVG at a constant light intensity of 1.22×10^{-7} Einstein/l-sec.

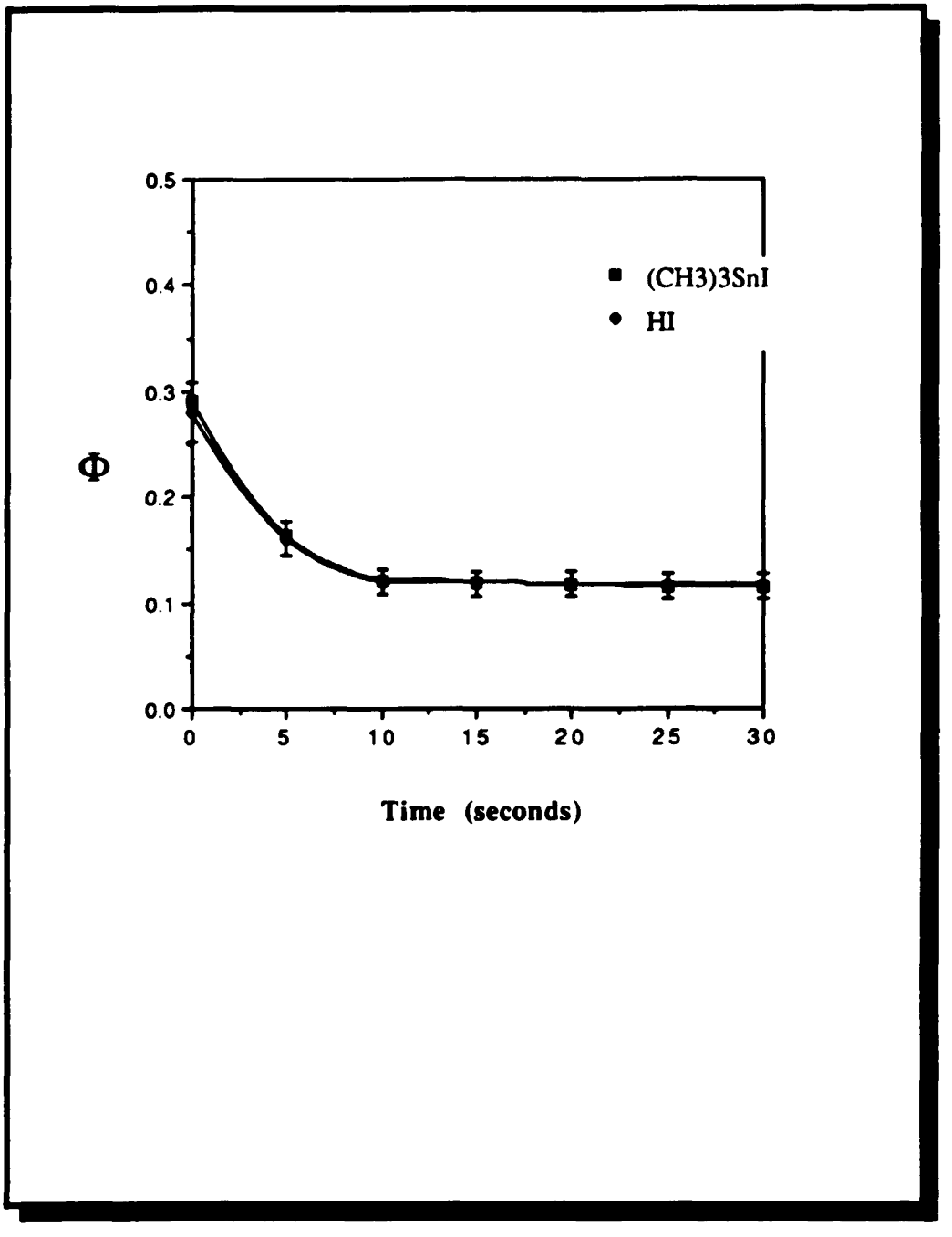

Table 5.3 - Effect of oxygen, nitrogen, and air free atmospheres on the quantum yield of the 254nm photolysis of 1.62×10^{-5} (moles/gr of PVG) of $(CH_3)_3SnI$ adsorbed onto PVG at a constant light intensity of 1.22×10^{-7}(einstein/l-sec).

	F_1	F_2	
Environment	$(CH_3)_3SnI$	**HI**	F_1/F_2
Air	0.287 ± 0.05	0.286 ± 0.05	1.00
Oxygen	0.301 ± 0.05	0.296 ± 0.05	1.01
Nitrogen	0.292 ± 0.05	0.281± 0.05	1.03
Vacuum	0.296 ± 0.05	0.296 ± 0.05	1.00

Figure 5.9 - Quantum yield of the 254nm photolysis of $1.62x10^{-5}$ (moles/gr of PVG) of $(CH_3)_3SnI$ adsorbed onto PVG as a function of the light intensity.

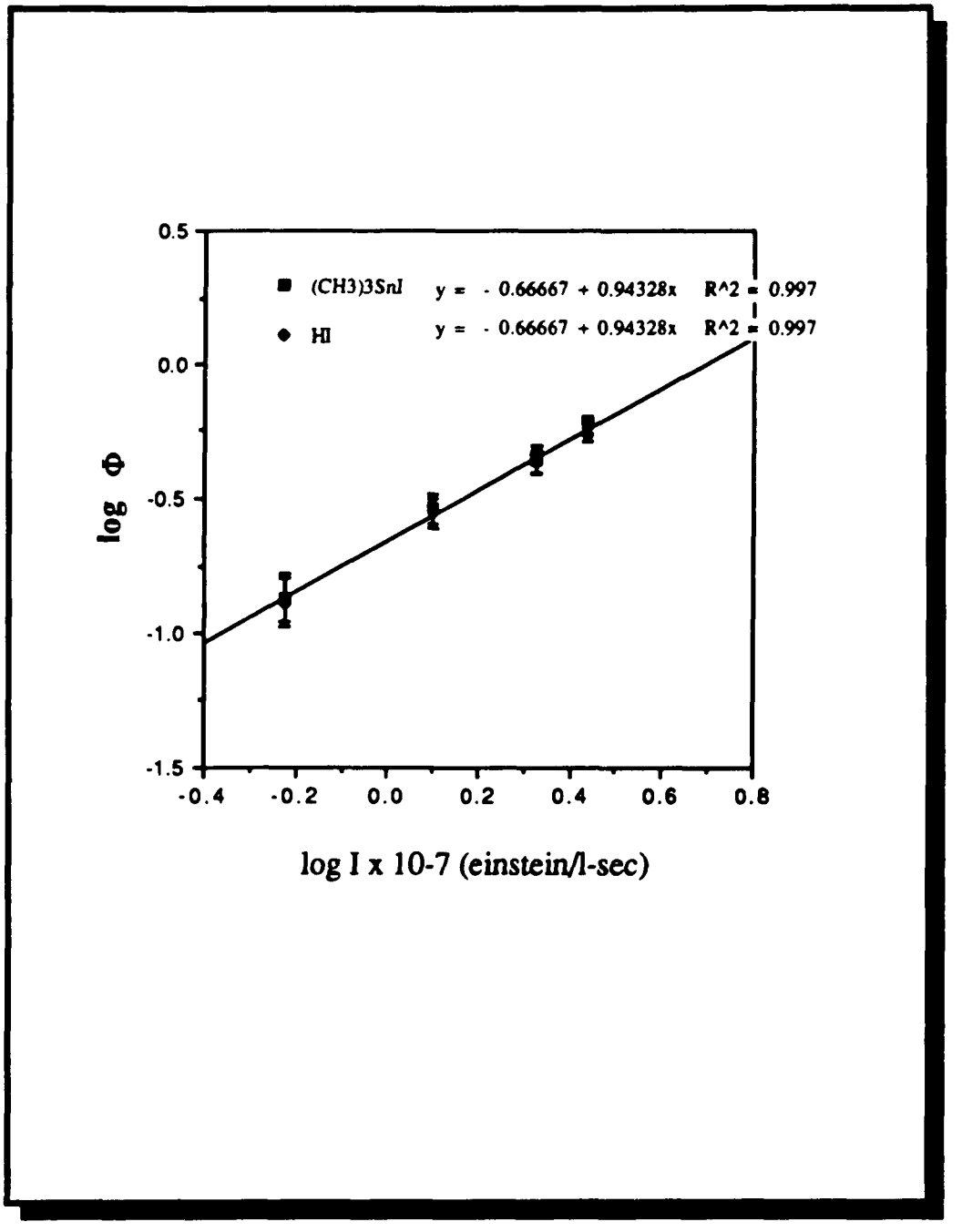

Table 5.4 - Quantum yield of the 254nm photolysis of 1.62×10^{-5} (moles/gr of PVG) of $(CH_3)_3SnI$ adsorbed onto PVG as a function of the light source wavelength.

Wavelength (nm)	F $(CH_3)_3SnI$	F HI
254	0.292 ± 0.05	0.281 ± 0.05
310	0.010 ± 0.05	0.006 ± 0.05
355	N.R.	N.R.

310- and 355-nm (Table 5.4). Third, the ratio of the limiting yields of $(CH_3)_3SnI$ disappearance and HI appearance, 1.0 ± 0.3, is consistent with the net reaction

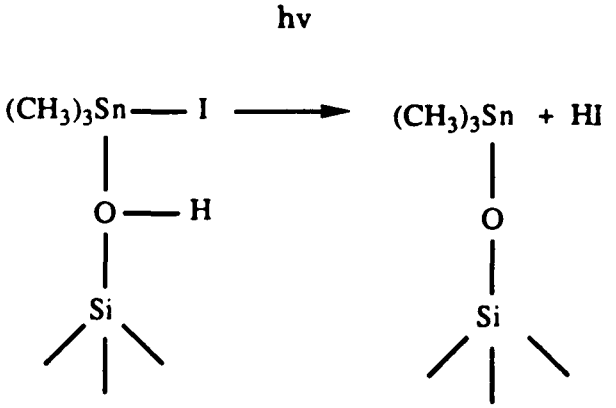

5.1

The quantum yield is independent of the $(CH_3)_3SnI$ concentration (Figure 5.10), and the ratio of the quantum yield of disappearance of $(CH_3)_3SnI$ relative to the quantum yield of appearance of HI (~1.0) remains constant.

The results gathered to this point suggest that the primary photochemical event during the 254 nm photolysis of $(CH_3)_3SnI$ adsorbed onto PVG is the heterolytic cleavage of the Sn-I bond, followed by the ionic recombination of I^- with adventitious H^+ from the glass surface to produce HI, and similarly the formation of $(CH_3)_3Sn$-O-Si by the reaction between $(CH_3)_3Sn^+$ and the silanol groups on the glass.

5.3.2 Photochemistry of $(CH_3)_3SnBr$ and $(CH_3)_3SnCl$ adsorbed onto PVG.

Photolysis with 254 nm light of 3.5×10^{-4} (mol/gram of PVG) of $(CH_3)_3SnBr$

Figure 5.10 - Quantum yield of the 254 nm photochemical reaction of $(CH_3)_3SnI$ as a function of the $(CH_3)_3SnI$ concentration at a constant light of 1.22×10^{-7} (einstein/l-sec)

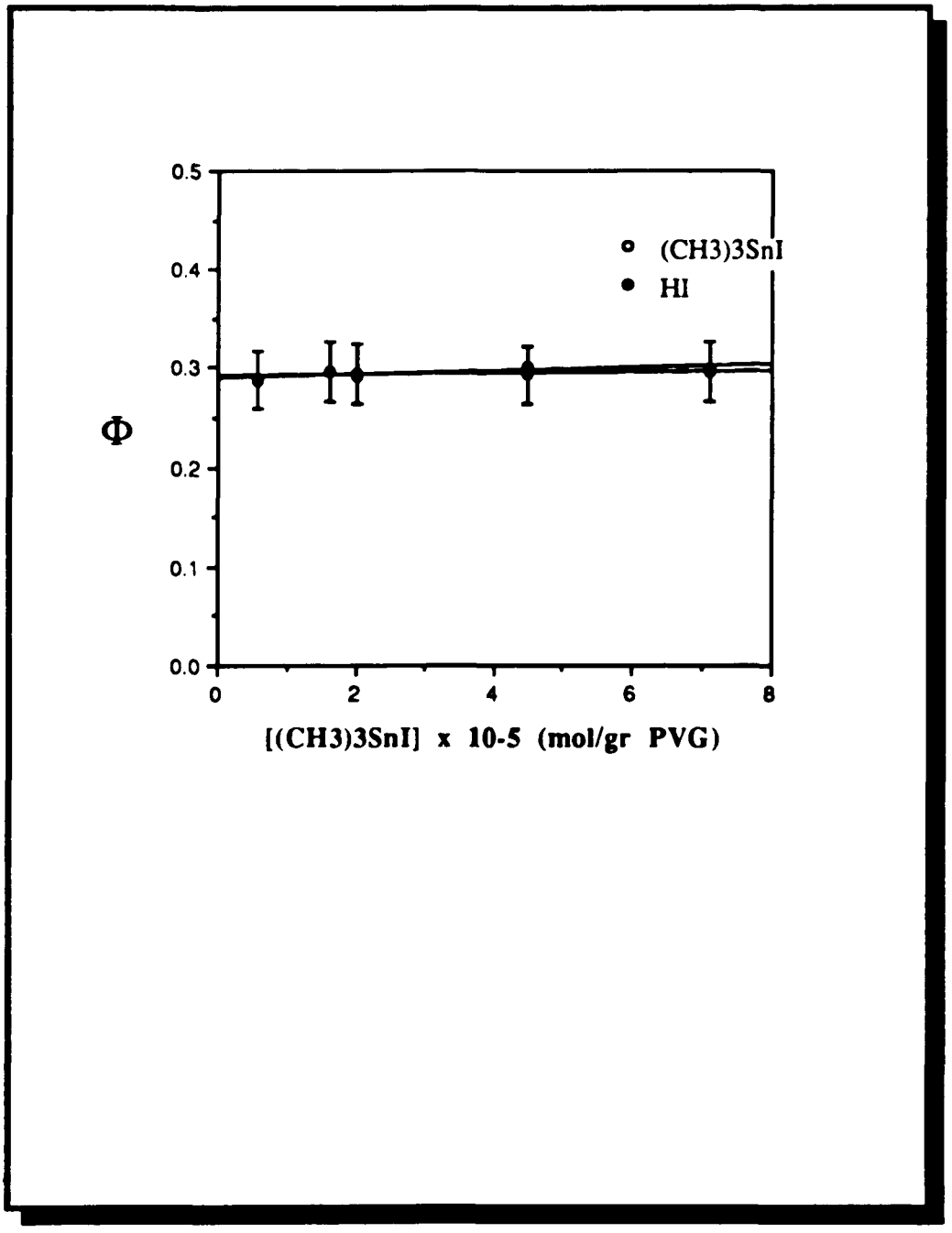

Figure 5.11 - UV-visible during the 254nm photolysis of 4.5 x 10^{-4} (mol/gr. of PVG) of $(CH_3)_3SnBr$ adsorbed onto calcined PVG at a constant light intensity of 1.22x10^{-7} (einstein/l-sec)

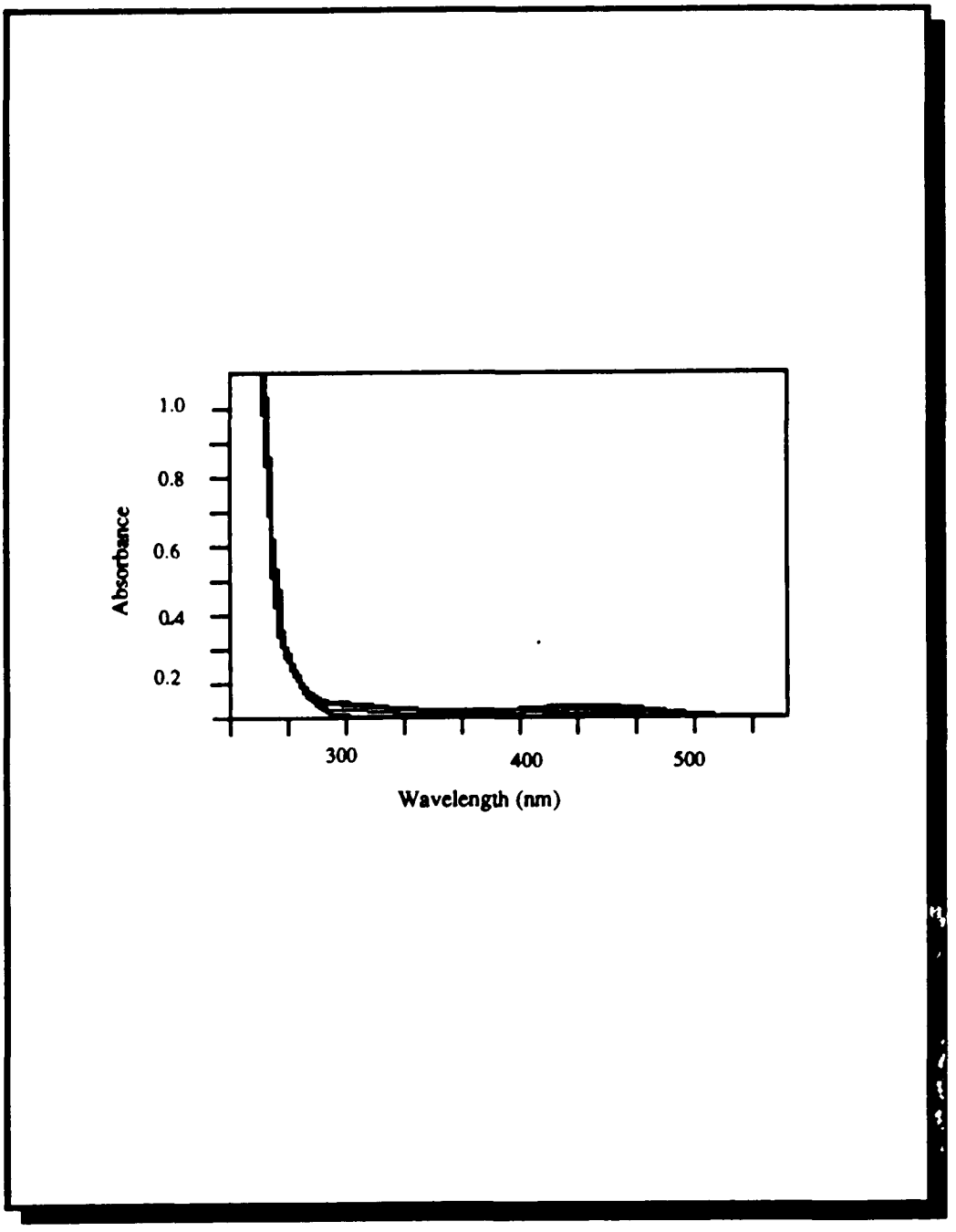

adsorbed onto PVG shows very little changes in the UV-visible spectra except for the appearance of a small band at 420 nm after prolonged photolysis ≥ 72 hours (Figure 5.11). The 420 nm peak is tentatively assigned to the formation of Br_2, however there is very little grounds for this assignment, except that Br_2 adsorbed onto PVG shows a similar absorption in this region ca. 450 nm.

Similarly, FTIR recorded during 254-nm photolysis of $(CH_3)_3SnBr$ adsorbed onto PVG show no change on prolonged photolysis ≥ 72 hours. From the information obtained there is no conclusive evidence to assign a mechanism for the 254 nm photolysis of $(CH_3)_3SnBr$ adsorbed onto PVG. Similarly, 254 nm photolysis of $(CH_3)_3SnCl$ adsorbed onto PVG shows no indication of a photochemical process, since there are no changes in the UV-visble, or FTIR spectra upon photolysis.

5.4 Photochemical Studies on TMOS Xerogel.

5.4.1 Photochemistry of $(CH_3)_3SnI$ adsorbed onto TMOS xerogel:

The photochemical studies in porous glasses were extended to TMOS xerogels in order assure that a similar reaction mechanism occurs as the one observed in PVG. This is expected, since the chemical structure of the TMOS xerogel consist of silanol groups, as in PVG. Consequently, the same photochemical reaction should occur.

Photolysis with 254 nm light of 5.06 x 10^{-4} (mol/gr. of PVG) of $(CH_3)_3SnI$ adsorbed onto a 1 mm xerogel plate (Figure 5.12), causes the

Figure 5.12 -UV-visible of the 254nm photolysis of 5.06 x 10^{-5} (mol/gr of PVG) of $(CH_3)_3SnI$ adsorbed onto calcined TMOS xerogel at a constant light intensity of 1.22x10-7 (einstein/l-sec).

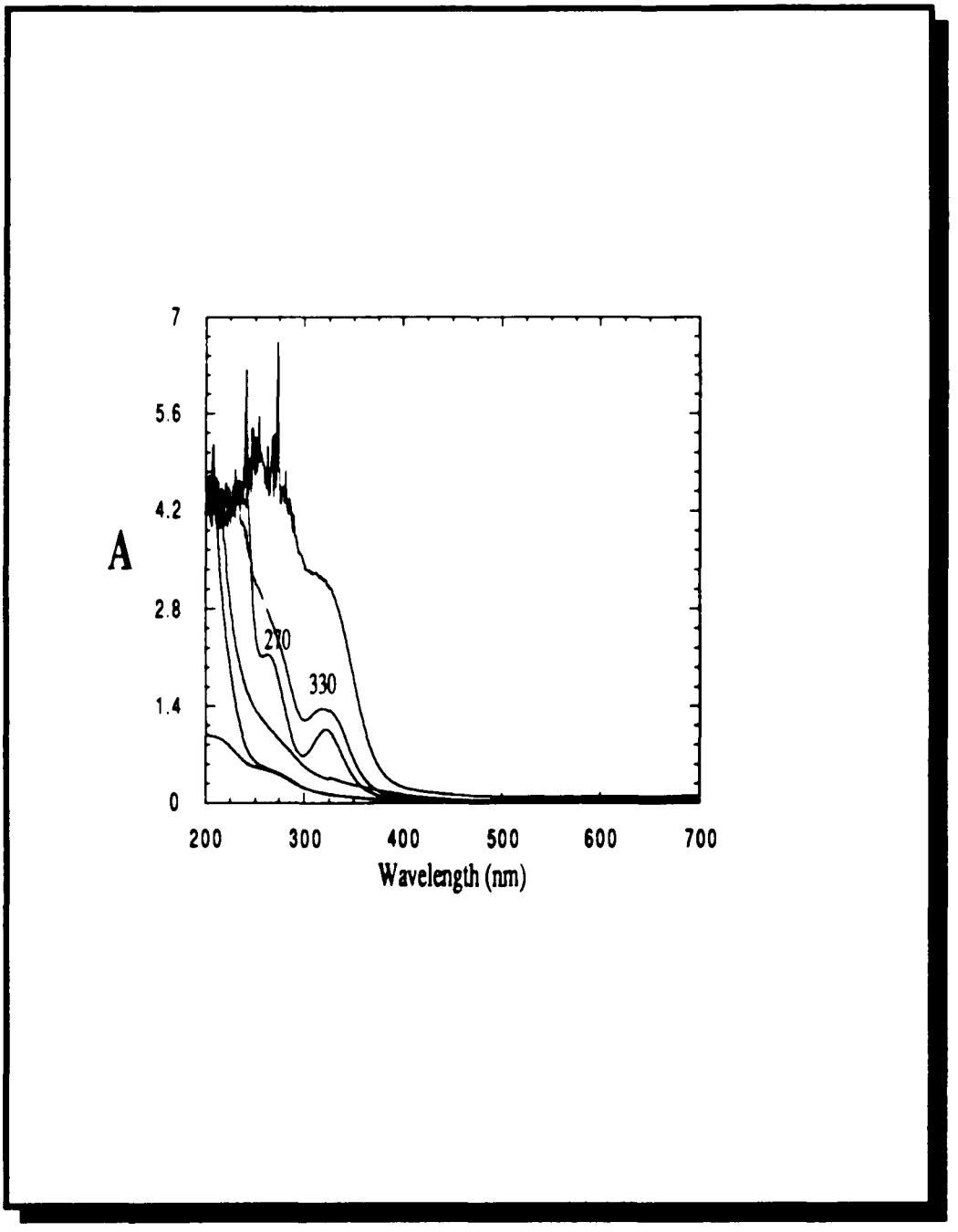

Figure 5.13 - Quantum yield of the 254 nm photolysis of $(CH_3)_3SnI$ adsorbed onto PVG, and TMOS xerogel at a constant light intensity of 1.22×10^{-7} (einstein/l-sec) as a function of the $(CH_3)_3SnI$ concentration.

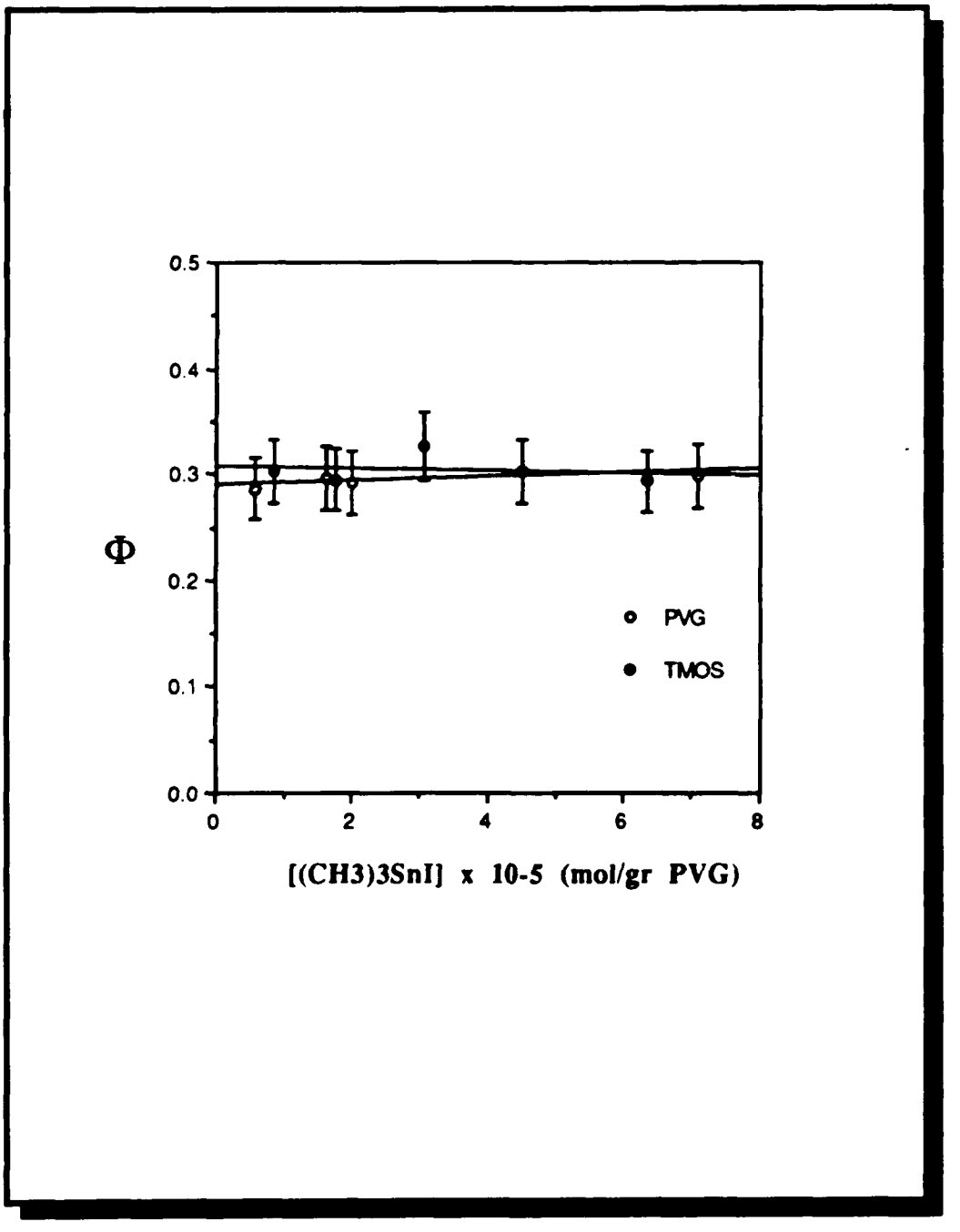

immediate decline of the 230 nm band and the simultaneous growth of two new bands at 270- and 330 nm. As in the case of PVG, the 270- and 330 nm bands are assigned to the formation of HI. However, the higher energy band of HI appears to shift from 290 nm in PVG to 270nm in the xerogel.

The quantum yield of the photochemical reaction was measured in order to compare it with the quantum yield results obtained for PVG. Figure 5.13 shows the quantum yield of the 254 nm photolysis of $(CH_3)_3SnI$ at a constant light intensity of 1.22×10^{-7} (einstein/l-sec) as a function of the $(CH_3)_3SnI$ concentration in PVG and the xerogel. From Figure 5.13 is clear that, within experimental error, there is no difference between the quantum yield in PVG and the quantum yield in the xerogel.

From the UV-visible and quantum yield experiments, it is clear that the same photochemical reaction that occurs in PVG also occurs in the TMOS xerogel. Consequently, more detailed studies were not persuded. Experiments with $(CH_3)_3SnBr$ and $(CH_3)_3SnCl$ compounds were not performed, since the photochemical results obtained in PVG were not satisfactory, and similar results were expected in the TMOS glass gel.

From the photochemical results obtained on both PVG and the TMOS xerogels, the mechanism of the photochemical reaction of $(CH_3)_3SnI$ on the glass is similar to that occuring in polar solvents. Moreover, the quantum yield results show that the photochemical reaction of $(CH_3)_3SnI$ is most efficient when excited with 254 nm light, and is linearly proportional to the light intensity.

6. Photoinduced Metal Oxide Deposition onto Porous Glass Matrices.

Experiments in our laboratory have shown that highly resolved (≤ 1 μm) patterns can be produce by the photochemical deposition of tin and iron oxides in porous Vycor glass (PVG) and TMOS silica glass gels. [24, 25] Photolysis binds the organometallic compound to the glass surface, and prevents migration during thermal consolidation of the glass matrix to a nonporous glass. Thermal consolidation, which requires temperatures ≥ 1000 °C, volatilizes the unreacted adsorbate from the glass and converts the photoproduct to a metal oxide. The details of the latter reaction remain to be established.

Photodeposition of a metal oxide on the glass yields a level of image resolution that cannot be achieved by a thermal process alone. Pattern resolution appears to be a consequence of the photoinduced binding of the reagent to the glass substrate. However, the temperatures require for the glass consolidation are ≥ 1000 °C, and it is not clear, under this conditions, that the pattern resolution depends solely on the chemical binding of the metal to the glass surface. [26] Even if it is assumed the formation of a M-O bond (-O- being a silanol oxygen), typical M-O bond energies (≤ 150 Kcal/mol) [27] are less than the Si-O bond energy (185 Kcal/mol). Consequently, at the consolidation temperature, ~1200 °C, where there is

sufficient energy to either break or weaken the Si-O bond so that the porous structure of the glass collapses to a nonporous glass, it would be expected that there is also sufficient energy to break the M-O bond. Yet, surprisingly, consolidation, which causes a 30 % shrinkage of sample volume, occurs with no detectable loss of pattern resolution.

The results discussed in this section focus on the effects produced by the photo deposition of tin and iron oxides in the glass matrix. The latter species was obtained by photolysis of $Fe(CO)_5$ and was chosen because its photochemistry and its use as a photoimaging reagent in PVG had been previously investigated. [28] This work concentrates on two aspects; the nature of the metal oxide species formed during consolidation, and the role of the topology of the glass matrix. The latter arises from the fact that, regardless of the metal oxide deposited, the chemistry occurs within the crevices and interior pores of the matrix where translational mobility is severely restricted. [29] In order to understand the mechanism by which the metallic oxides either diffuse within the matrix, or are bound to the glass surface, studies of the photodeposited metal oxides in PVG and the TMOS xerogel were performed by various complementary surface analysis techniques. Since PVG and TMOS xerogels were used because the surface properties and topology of the porous glasses are similar. [30]

6.1 Photodeposition of Tin and Iron Oxides onto PVG.

Experimentally, tin and iron oxides were photodeposited onto PVG by previously described methods, [31] and examined before and after consolidation of the porous structure. Secondary-Backscatter electron

microscopy analyses of the fracture surface of a consolidated Vycor glass rod (5 mm diameter) impregnated with tin oxide (~ 10^{-4} moles/gr. of PVG) and heat tretaed to 650 °C shows a homogeneous film over the entire glass surface. The film is made up of microscopic tin oxide particles, ranging from 10- to 50 nm in diameter, with voids of glass between the particles ranging from 50 to 300 nm (Figure 6.1). From the micrograph, it is also observed that the size of the tin oxide particle decreases from the surface down into the bulk glass. Since photolysis occurs initially at the surface, a large fraction of the adsorbed precursor undergoes photolysis than that in the bulk. Consequently, the surface particles grow larger than the particles in the bulk of the glass.

Similarly, Figure 6.2 shows the SEM-Backscatter micrograph of iron oxide (~1.0 x 10^{-4} moles adsorbed/gr. of PVG) impregnated onto consolidated PVG. The observed iron oxide particles, which range from about 5 to 10 nm in diameter, form large clusters of aggregate particles that can extent to a few microns in diameter depending on the extent of photolysis. The longer the photolysis time, the larger the diameter of the clusters formed.

To understand if the iron oxide particle agglomeration takes place during the impregnation process, or during the photolysis process, a PVG plate impregnated with $Fe(CO)_5$ was photolyzed in such a way that half the glass plate was masked with Al foil to prevent light exposure in this region, while the other half was exposed to the light. The glass plate was examined immediately after photolysis under an optical microscope (Figure 6.3). From the micrograph it is observed that only in the region exposed to the light did particle agglomeration occur. The other half, even though it

contains unexposed $Fe(CO)_5$ does not show any indications of particle formation or agglomeration.

In order to complement the SEM results the same impregnated PVG samples were analyzed by small angle x-ray scattering (SAXS), and Rutherford backscatter (RBS) surface analyses techniques. In the SAXS experiments, a plot of x-ray intensity vs. transfer momentum $q = 4\pi / l \sin \theta$, is independent of the presence of the photodeposited metal.

Figure 6.4a shows a plot of the scattered intensity vs. the transfer momentum of a dry unimpregnated PVG sample heated to 650 °C. The dominant feature observed in the SAXS spectra is a broad peak centered at $q = 0.018$ $Å^{-1}$, which corresponds to a correlation length of 23.2 nm. [32] This result agrees with a previous examination of PVG by small angle neutron scattering (SANS) which exhibits a scattering peak at $q = 0.023$ $Å^{-1}$. [33] This is reminiscent of a microporous network of a spinodally decomposed material. This structure arises when the original borosilicate melt is cooled below its phase transition temperature. The boron-oxide-alkali-oxide phase separates, and on acid leaching, yields a microporous network where pore size is determined by the time the melt is allowed to decompose. The scattering intensity for a bicontinuous spinodally decomposed material has been given by Cahn [34] to be :

$$I(q) = \frac{I_0}{(1+q^2)\, e\left[\frac{-2q^2 t}{(q^2-1)}\right]} \qquad \text{eq 6.1}$$

Figure 6.1 - SEM-Backscatter micrograph of tin oxide photodeposited onto the surface of consolidated PVG. Magnification 50K.

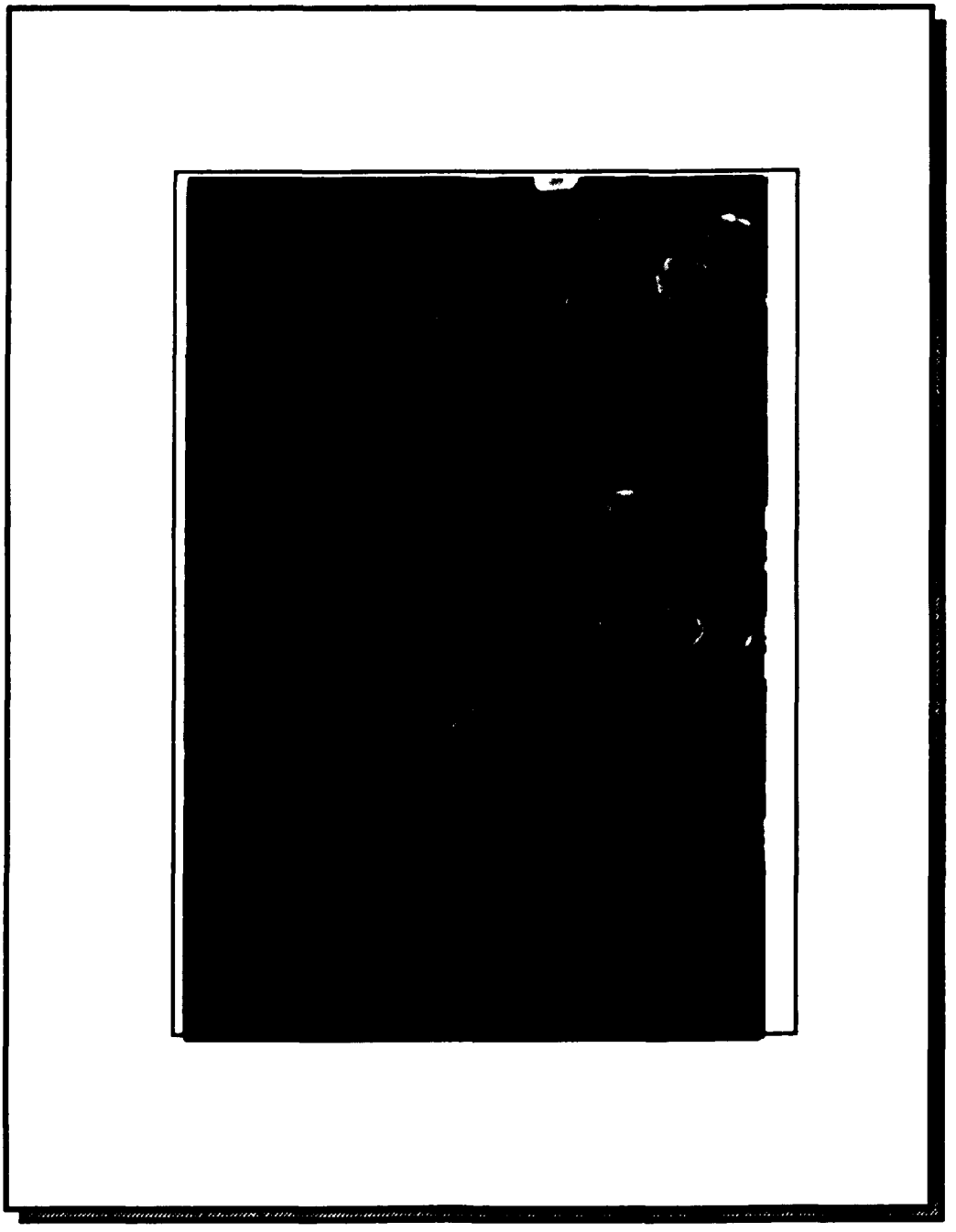

Figure 6.2 - SEM-Backscatter micrograph of iron oxide photodeposited onto the surface of consolidated PVG. Magnification 50K.

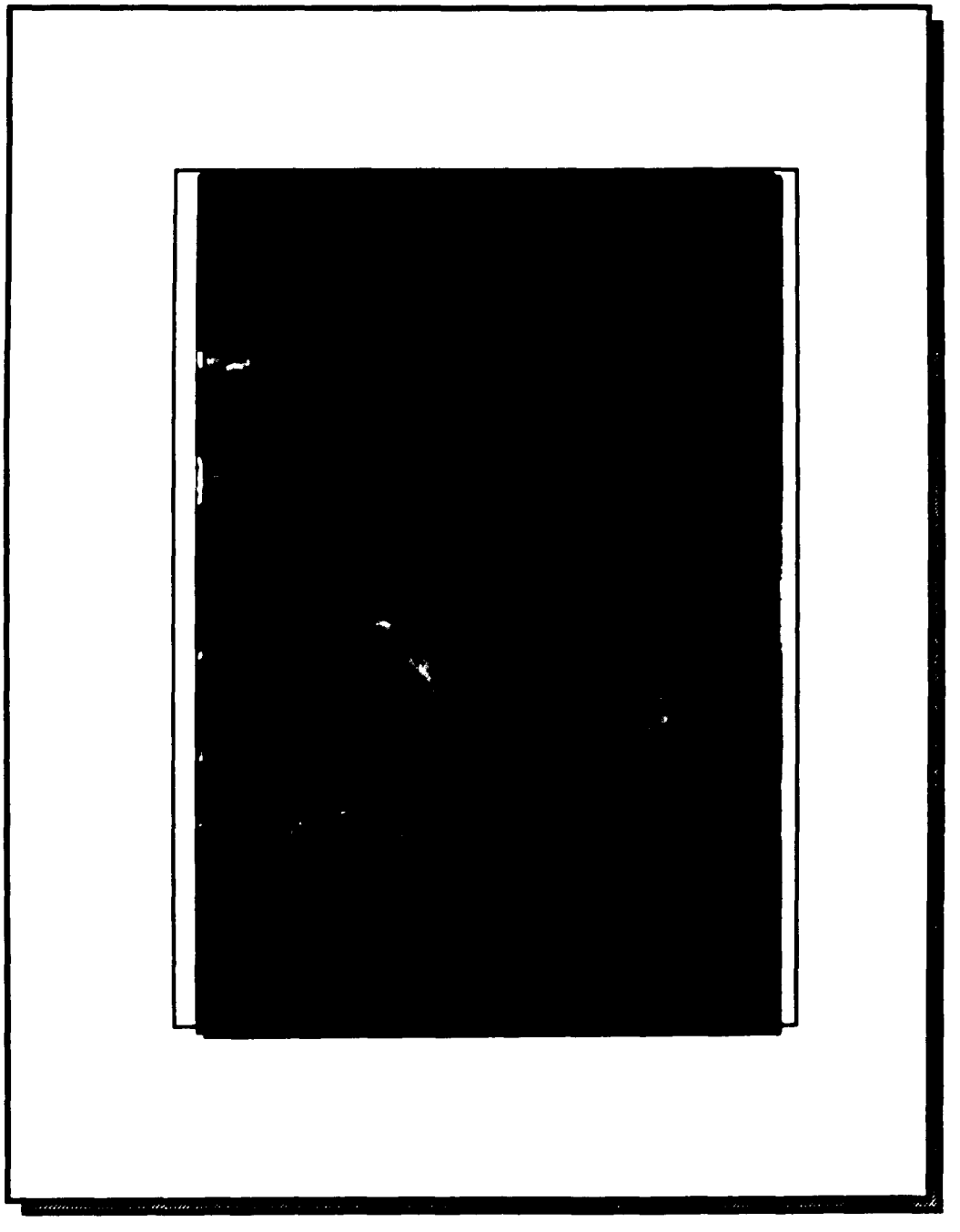

Figure 6.3 - Optical micrograph of iron oxide adsorbed onto consolidated PVG. Magnification 100X.

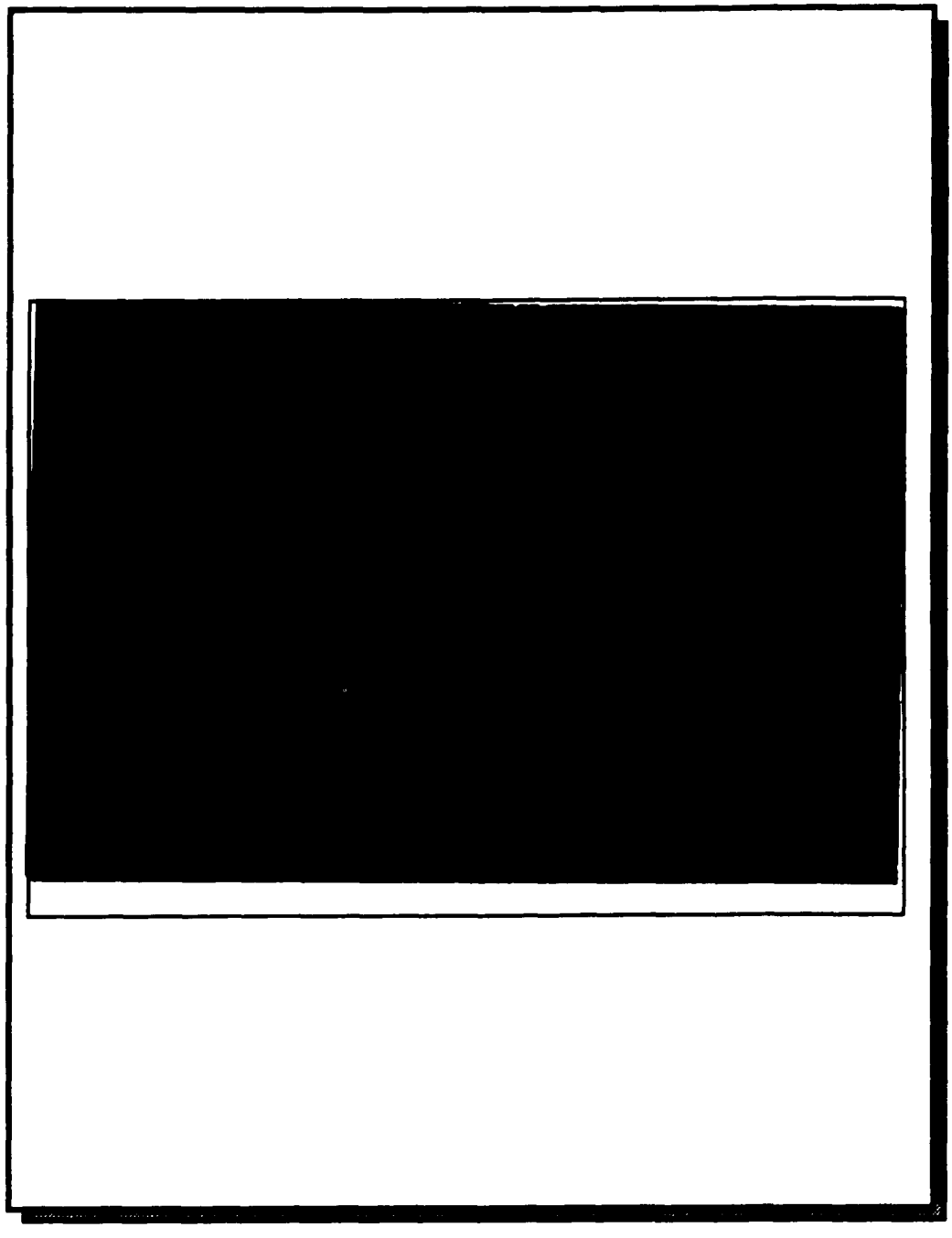

Figure 6.4 - Small angle x-ray scattering (SAXS) of (a) porous Vycor glass. (Tcalcined = 650°C); (b) consolidated PVG (Tconsolidation = 1200°C).

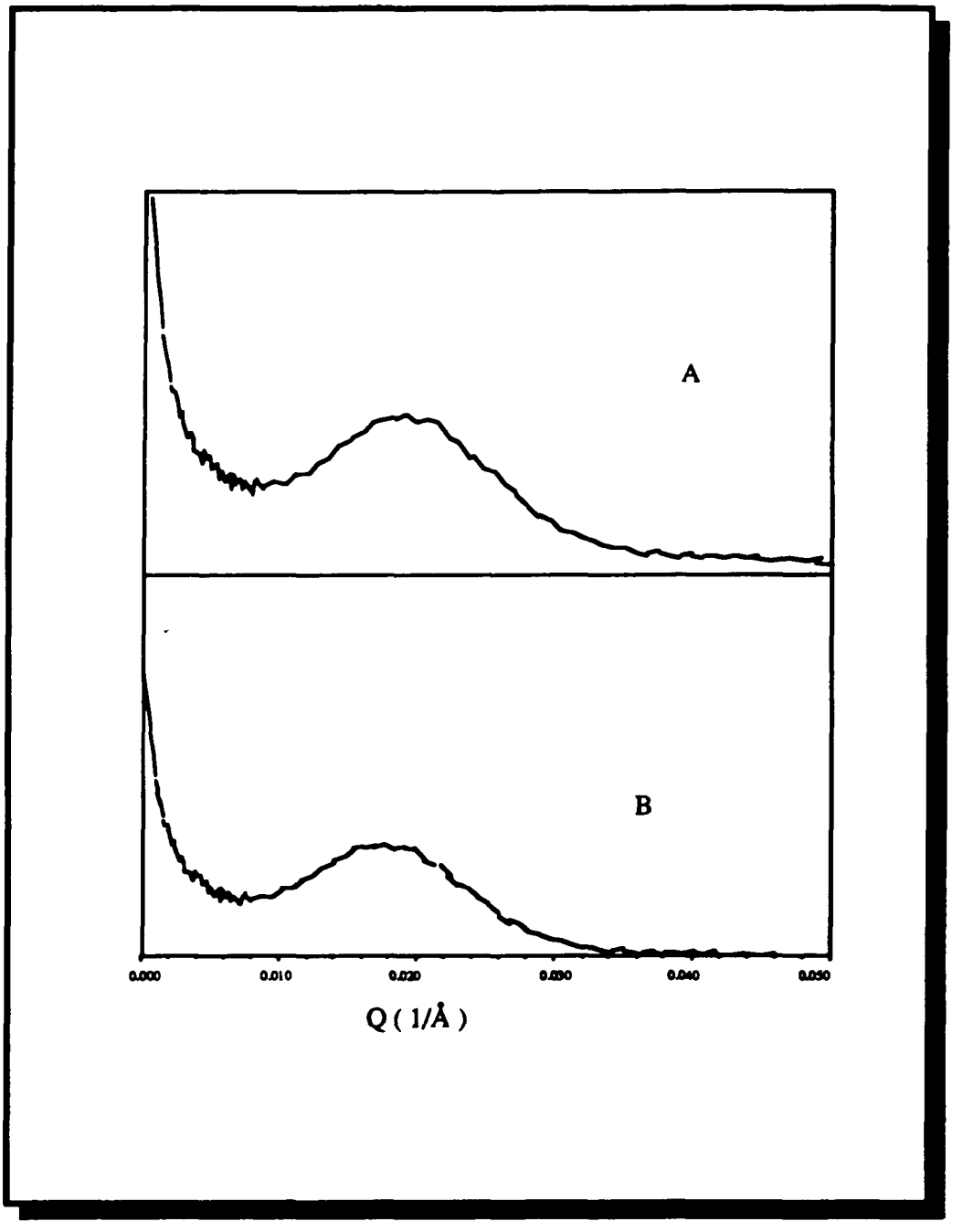

where I_0 is the incident flux, q is the scattering vector, l is the experimental x-ray wavelength, 1.76 Å, and q is the scattering angle. The analysis yields the average distance between regions of different density, which in PVG is most likely the average distance between the pores, and is valid for $q \leq 0.02$ $Å^{-1}$. Similar results are obtained when iron oxide is photodeposited onto calcined PVG (Figure 6.4b). In this case, least squares fitting of the SAXS data yields the correlation lengths given in Table 6.1.

Heating the unimpregnated sample to 1200 °C causes the loss of the scattering peak indicating that the pores collapse and the glass consolidates to a nonporous, uniform material. Similarly, the sacttering peak from the iron oxide impregnated sample (Figure 6.5a) also dissapears when heated to 1200°C . The absence of scattering from the consolidated sample suggest that the iron oxide is distributed uniformly over the entire glass matrix.

Quite different results are obtained with the samples containing tin oxide. Heating these samples to 1200 °C, under identical conditions to those used to consolidated the iron oxide impregnated samples, does not lead to the loss of the scattering peak (Figure 6.5b). The SAXS data continue to exhibit a broad peak at $q = 0.018$ $Å^{-1}$, and a least squares fitting of the data yields a correlation length of 188.0 Å. The latter, which is essentially equivalent to the original porous sample, indicates that even though the tin oxide sample was heated to 1200 °C, the glass still retains a porous structure.

The lack of consolidation of the porous structure exhibited in PVG samples containing tin oxide was further confirmed by Rutherford Backscattering. Comparing the scattering data obtained from samples heated to 1200 °C with the calculated spectrum from a smooth, uniform glass of composition $SiO_2M_{0.001}$, where M = Fe or Sn, shows that iron oxide

impregnated samples agree well with the model (Figure 6.6). The tin oxide samples, on the other hand, show a non-stoichiometric excess of oxygen, and deviations from the sharp, calculated step like profile (Figure 6.7). The latter indicates that the tin oxide exists in a nonuniform, granular, or porous material. The excess oxygen found in the RBS spectra is believed to be due either by the adsorption of oxygen or water from the atmosphere, since the consolidated samples where handled in the open atmosphere during the measurements. It is known that tin oxides glasses have being developed as sensor devices for the detection of small traces of oxygen and water. [34]

The results obtained from the SAXS and RBS measurements indicate the presence of porosity in consolidated (1200 °C) PVG samples impregnated with tin oxide, but not in the samples impregnated with iron oxide, or in the unimpregnated glass samples. To further confirm the presence of porosity in a consolidated PVG samples impregnated with tin oxide, an experiment was done in which three consolidated PVG samples, a plain one, one impregnated with tin oxide, and one impregnated with iron oxide, were soaked on a 1.0 x 10^{-5} M solution of tris(2,2'-bipyridine)ruthenium (II), $[Ru(bpy)_3]^{2+}$ (ε = 1.5x10^{-4} M^{-1}-cm^{-1}), in acetonitrile for a period of 2 weeks, and absorption spectra of the samples at 450 nm were recorded at regular intervals. The sample containing the tin oxide exhibited an increase in the absorption spectra of 0.15 absorbance units at 452-nm, whereas the other two samples show no change in absorption during the given time. This experiment establishes that the photodeposition of tin oxide prevents glass consolidation even after heating to 1200 °C, and perhaps more important, the porous regions can be impregnated with other reagents.

Figure 6.5 - Small angle x-ray scattering (SAXS) of (a) iron oxide photodeposited onto consolidated PVG; (b) tin oxide photodeposited onto consolidated PVG. (Tconsolidation 1200°C).

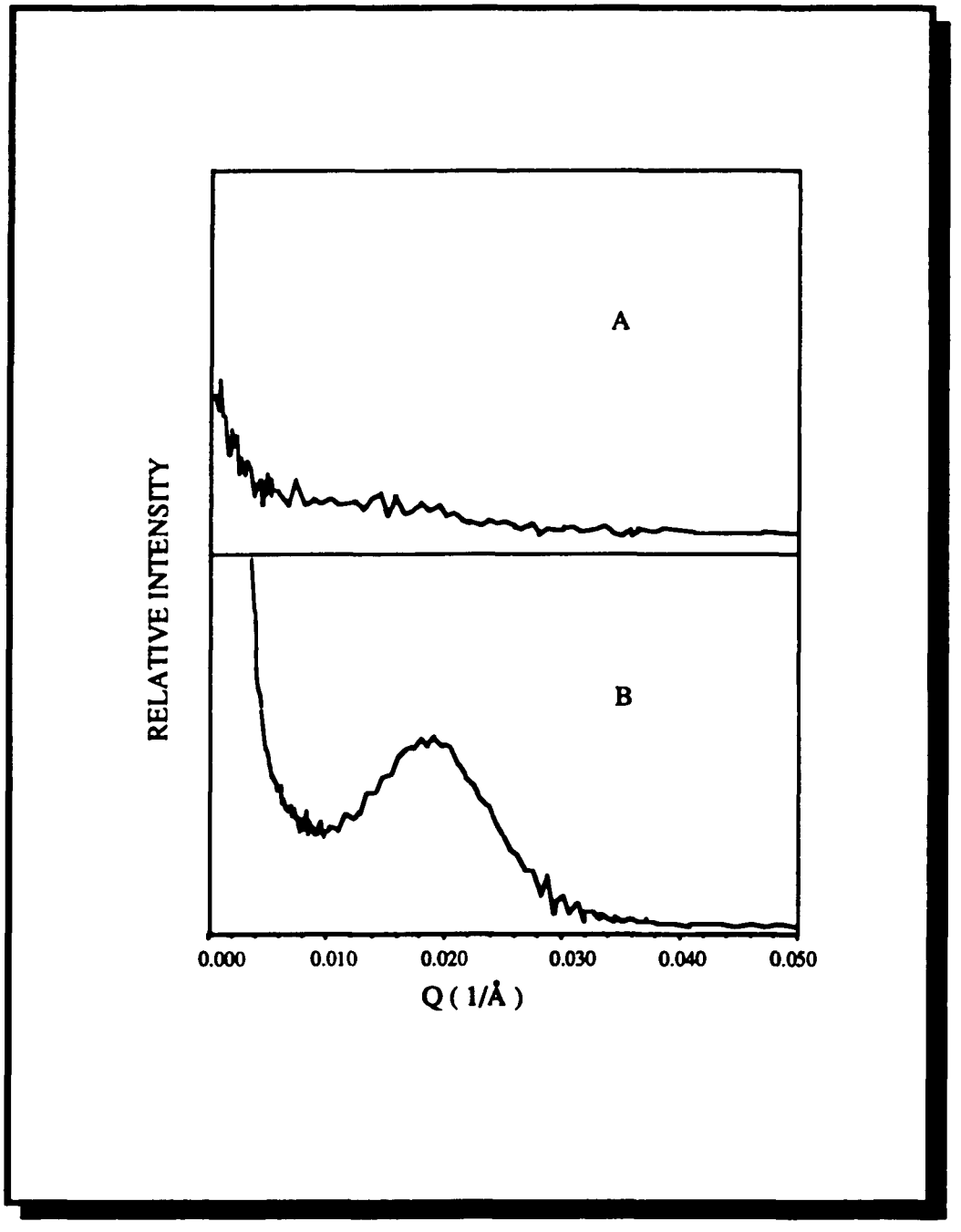

Table 6.1 - Correlation lengths for the unimpregnated and the tin and iron oxide impregnated PVG.

SAMPLE	CORRELATION LENGTH (Å)
Plain	179.0
Tin Oxide	188.0
Iron Oxide	182.0

Figure 6.6 - Rutherford bakscatter plot of iron oxide adsorbed onto consolidated PVG.

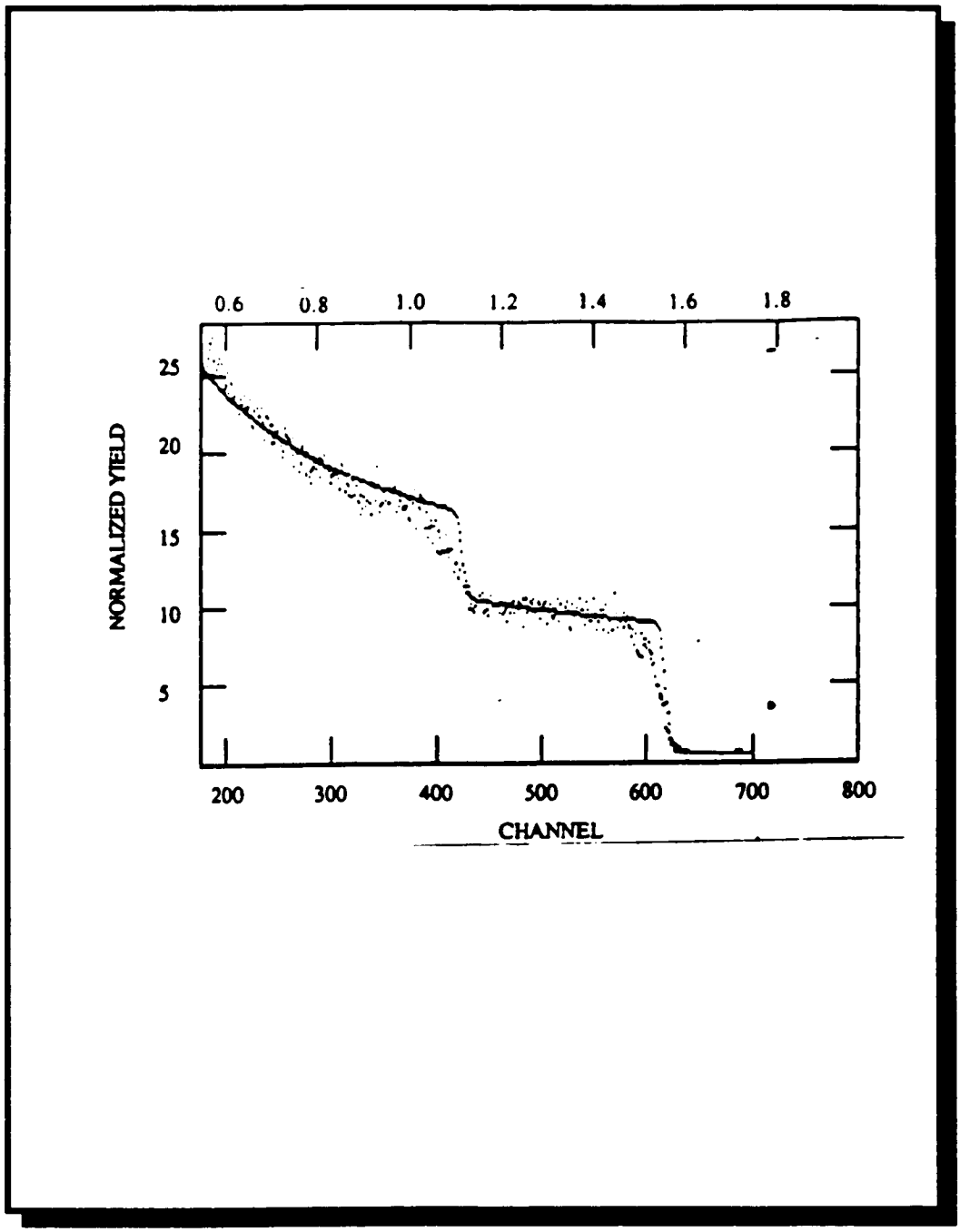

Figure 6.7 - Rutherford bakscatter plot of tin oxide adsorbed onto consolidated PVG.

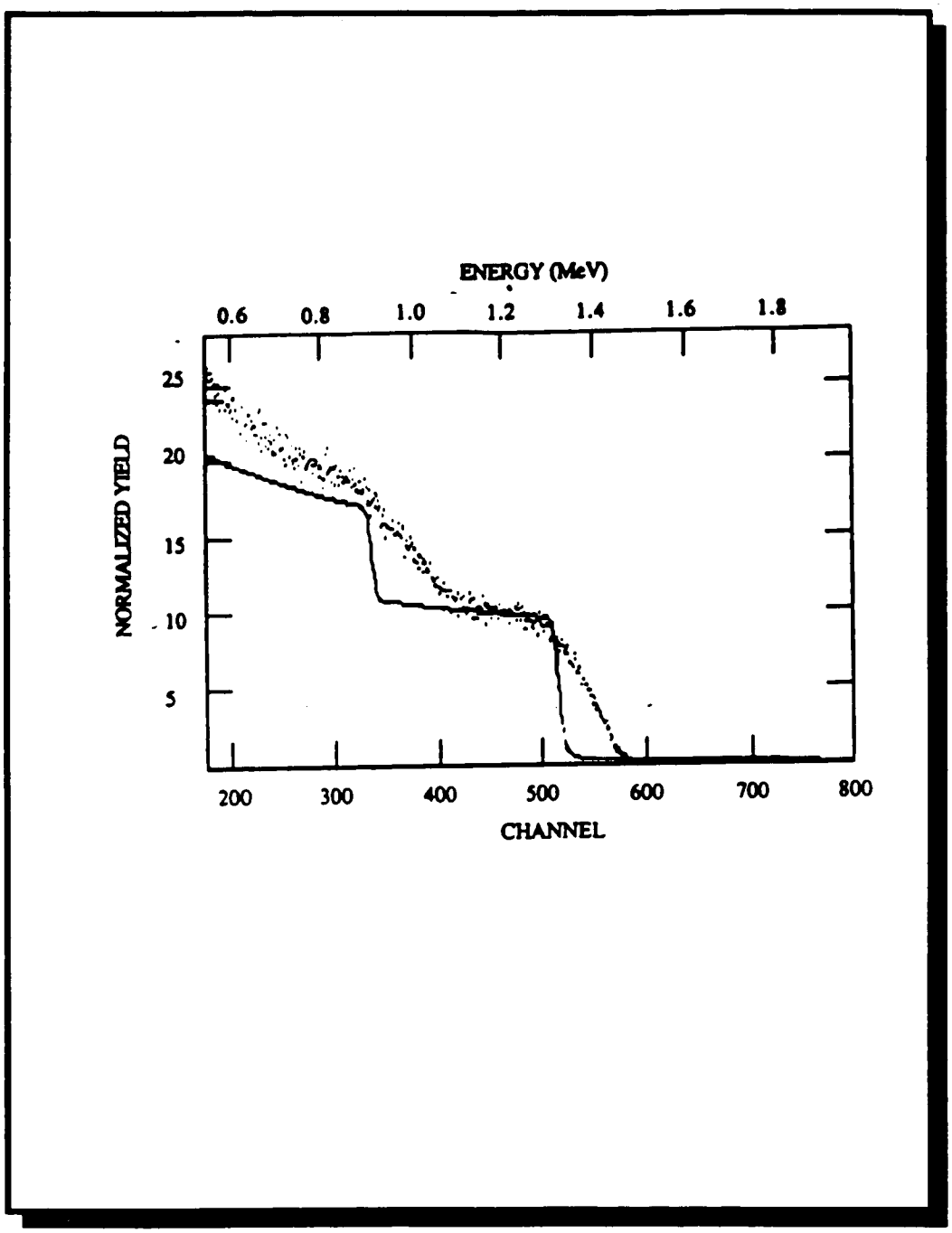

Further experiments to elucidate the nature of the metal and metal oxides at the different stages of the reaction are in progress. Maintaining levels of porosity in an otherwise, consolidated glass, removes the limitations imposed by the consolidated glass. These regions offer the possibility of incorporating a large variety of reagents into a glass matrix that were previously excluded because of an inability to withstand the consolidation temperatures. Consequently, this may open the door for the impregnation of nonlinear optical materials in the consolidated glass, and the fabrication of optical sensors in planar glass substrates.

6.2 Diffusion studies of metal oxides into porous glass matrices.

A study of the diffusion of photodeposited metals and/or metal oxides in porous glass matrices is fundamental to the understanding of the mechanism of image resolution. The diffusion profile of tin and iron oxides in porous and consolidated PVG was obtained by secondary ion mass spectroscopy (SIMS), and total x-ray fluorescence (TXRF). The samples were analyzed by measuring the amount of metal present in a cross-sectional cut of the glass from the surface into the bulk. The cross-section of the glass was scanned with a 50μm probe beam in both experiments. The samples analyzed and the analysis conditions are listed in Table 6.2. From these experiments, it was found that the initial adsorption and diffusion of the organometallic vapors through the glass porous surface is relatively fast. Exposing the impregnated samples to UV light binds the metal to the glass surface and prevents diffusion into the unexposed regions. No further

Table 6.2 - Impregnated tin oxide and iron oxides onto porous and consolidated PVG.

Sample	Concentration (moles/gr. PVG)	Porous (Tmax=650°C)	Non-Porous (Tmax=1200°C)
Sn	High (1.0×10^{-4})	hv; and no hv	hv; and no hv
Sn	Low (1.0×10^{-6})	hv; and no hv	hv; and no hv
Fe	High (1.0×10^{-4})	hv; and no hv	hv; and no hv
Fe	Low (1.0×10^{-6})	hv; and no hv	hv; and no hv

migration occurs even during the heat treatment of the glass from 25-1200°C.

SIMS experiments show that the tin concentration in a consolidated PVG sample has a maximum at the surface and decreases exponentially to a depth of 1000 Å were it reaches a steady plateau (Figure 6.8). X-ray fluorescence measurements of the tin oxide distribution in consolidated PVG (Figure 6.9) shows that tin oxide is uniformly distributed in the unphotolyzed region, while the photolyzed region has a distribution consistent with the absorption of light. Nevertheless, a significant amount of tin remains in the unphotolyzed region due to the thermally activated decomposition of the precursor $(CH_3)_3SnI$-(ads). The latter reduces both image contrast and resolution. The diffusion profiles are independent of the tin oxide concentration (Figure 6.10), the only difference observed, as expected, is in the intensity of the signal.

The diffusion profiles of the iron oxide samples are quite different from those observed in the tin oxide samples. SIMS experiments show that relatively little iron oxide is on the outermost surface of the consolidated glass (Figure 6.11). Instead it shows an overlying layer of glass ~ 50 Å thick that contains no iron. At a depth of 50 Å, there is a sharp rise in iron content, then it decreases linearly to a depth of about 500 Å where the iron counts remain essentially constant to a depth of at least 4000 Å.

Figure 6.12 shows a TXRF plot of high and low concentration loadings of photodeposited iron oxide on consolidated PVG. The concentration of iron is low at the surface of the glass, increases rapidly to a maximum at approximately 50 μm, and then decreases exponentially to base line level at 1000 μm deep in the high concentration samples and about 500 μm deep in the low concentration samples. A distinction between

Figure 6.8 - Secondary ion mass spectra (SIMS) of tin oxide adsorbed onto consolidated PVG.

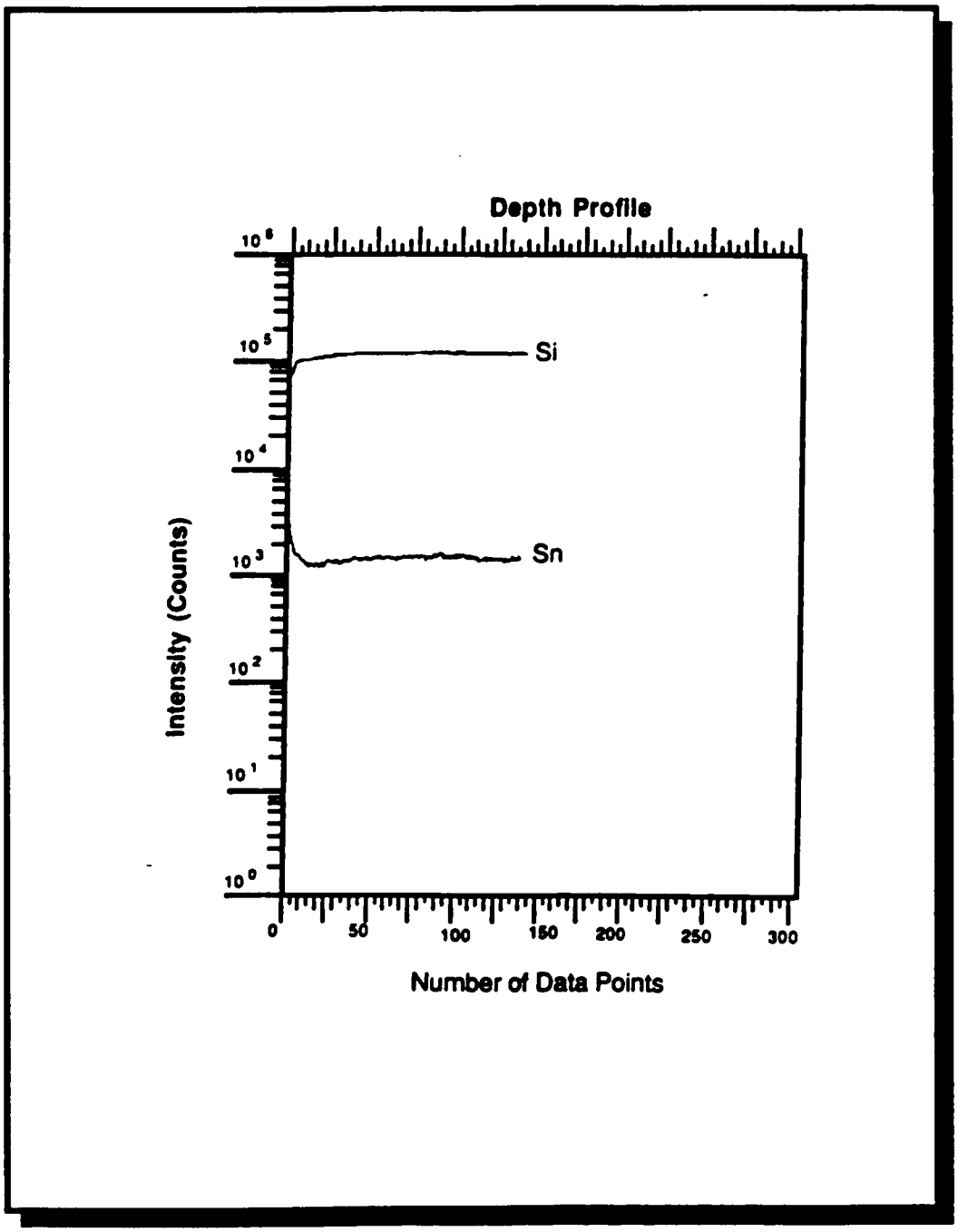

Figure 6.9 - X-ray fluorescence of the cross sectional distribution of tin in the photolyzed and unphotolyzed regions of a calcined PVG sample heated to 1200°C.

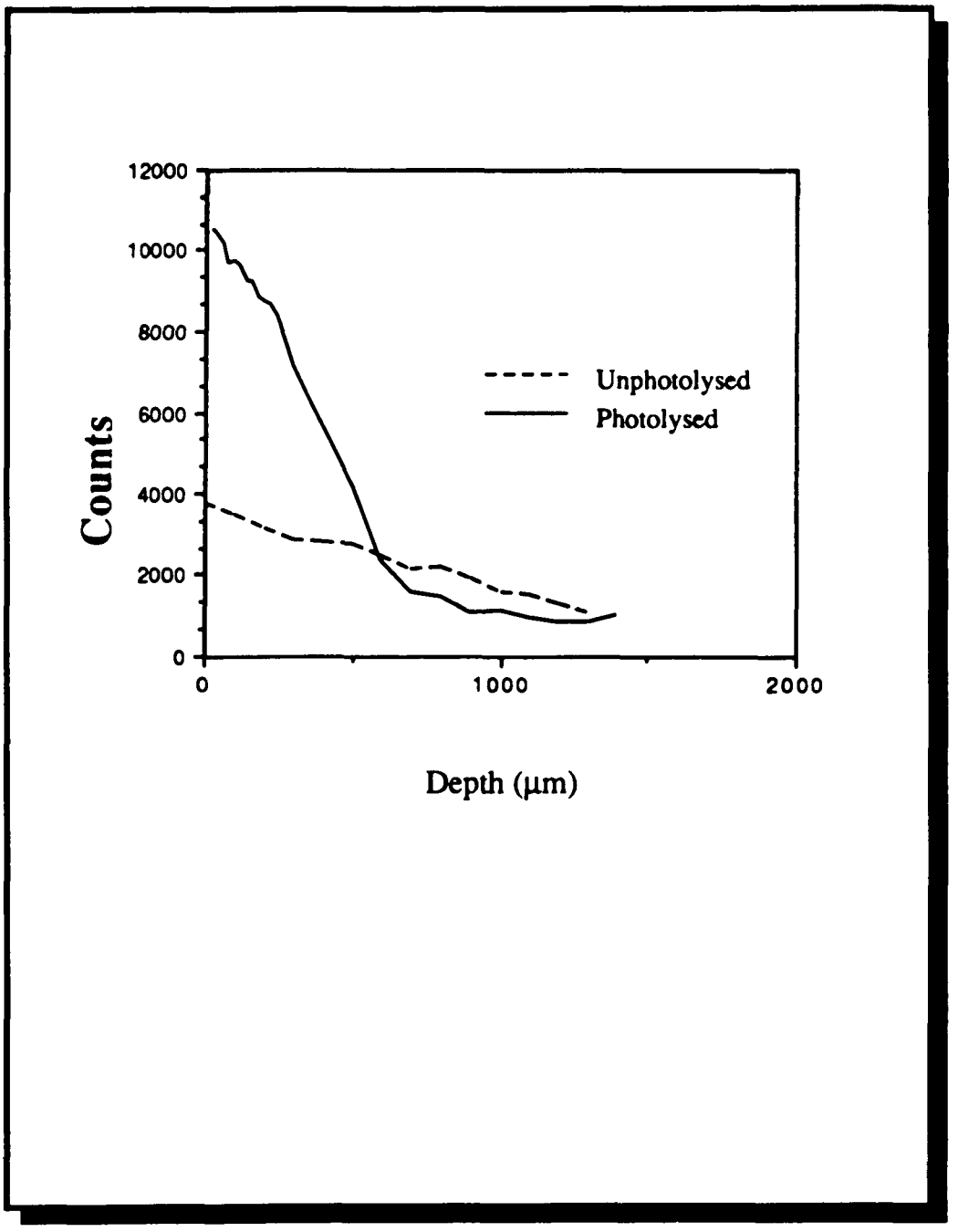

Figure 6.10 - X-ray fluorescence of the cross sectional distribution of tin at high ($1.0x10^{-4}$ mol ads./gr. of PVG), and low ($1.0x10^{-6}$ mol ads./gr. of PVG) tin concentrations in a consolidated PVG sample heated to 1200°C.

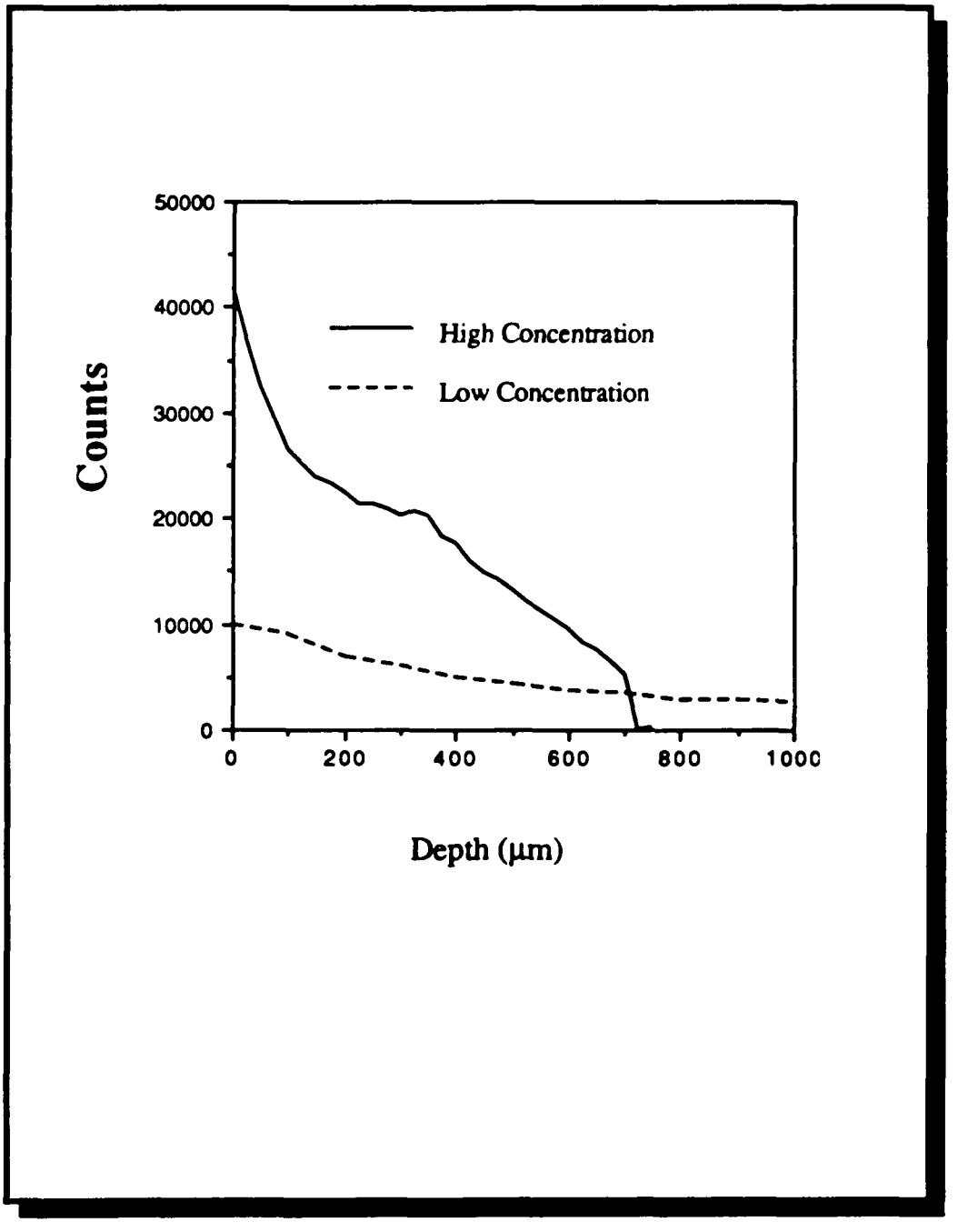

Figure 6.11 - Secondary ion mass spectra (SIMS) of iron oxide adsorbed onto consolidated PVG.

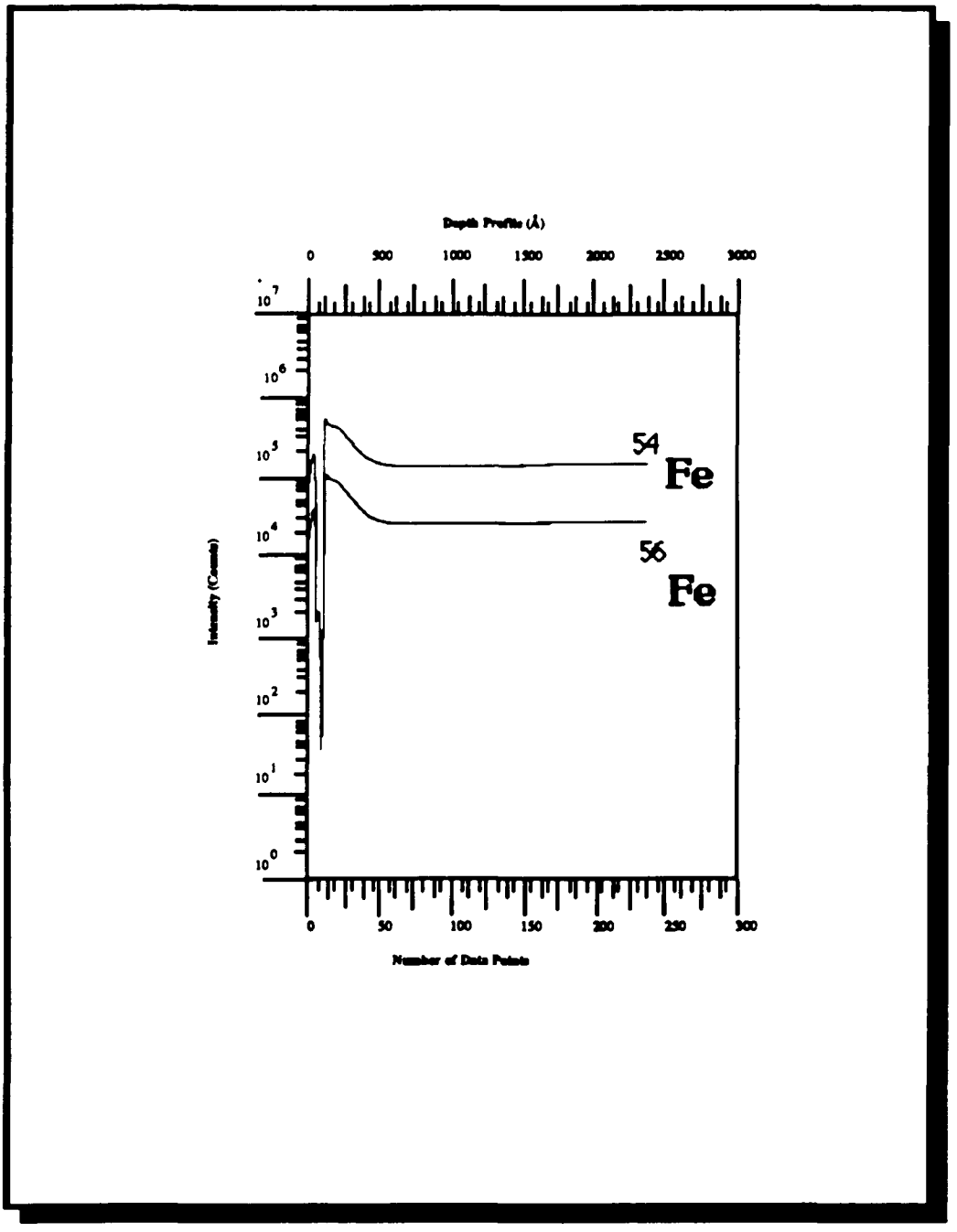

Figure 6.12 - X-ray fluorescence of the cross sectional distribution of iron at high ($1.0x10^{-4}$ mol ads./gr. of PVG), and low ($1.0x10^{-6}$ mol ads./gr. of PVG) iron concentrations in a consolidated PVG sample heated to 1200°C.

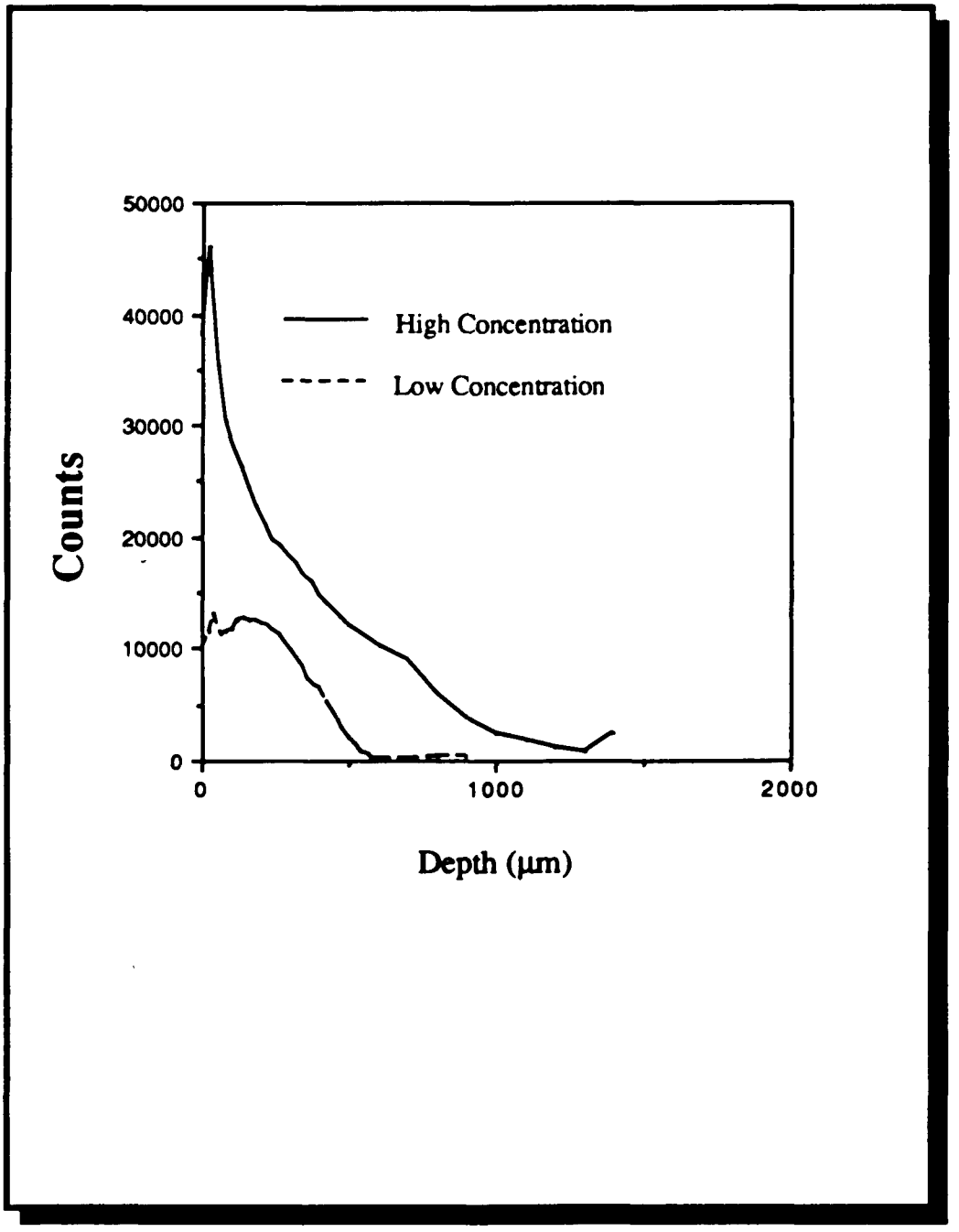

the high and low concentration samples is in the shape of the distribution peak. In the high concentration sample a sharp peak with a maximum at 50 μm is observed. In contrast the low concentration sample exhibits a broad peak with a maximum at 100 μm. The difference may be due to a diffusion effect in which, at high concentration, the iron oxide diffuses rapidly on the glass, and reaches the saturation point at shorter distance from the surface. At lower concentrations, the diffusion effect is not as pronounced and as a consequence, the maximum is broader and found deeper in the sample bulk.

Pattern resolution depends on the ability to remove the unphotolyzed reagent. A comparison between photolyzed and unphotolyzed iron oxide impregnated samples (Figure 6.13) shows that very little iron is found in the unphotolyzed region when the sample is heated to 1200 °C. The relative low intensity in the unphotolyzed product indicates that the unreacted organometallic precursor, in this case $Fe(CO)_5$, desorbs during the consolidation process with relatively little decomposition.

In summary, there are significant differences in the diffusion parameters of iron and tin oxides photodeposited in PVG. The main difference is that the highest tin oxide concentration is found right at the surface of the glass, whereas the highest concentration of iron oxide occurs 50 Å below the glass surface. This changes, along with the proposed adsorption properties of iron and tin compounds could have a significant effect on the differences found during the consolidation studies. Further experiments are being conducted to determine the diffusion of the precursors in the glass, and the diffusion of polymers of different molecular weights into the glass under different conditions.

Figure 6.13 - X-ray fluorescence of the cross sectional distribution of iron in the photolyzed and unphotolyzed regions of a calcined PVG sample heated to 1200°C.

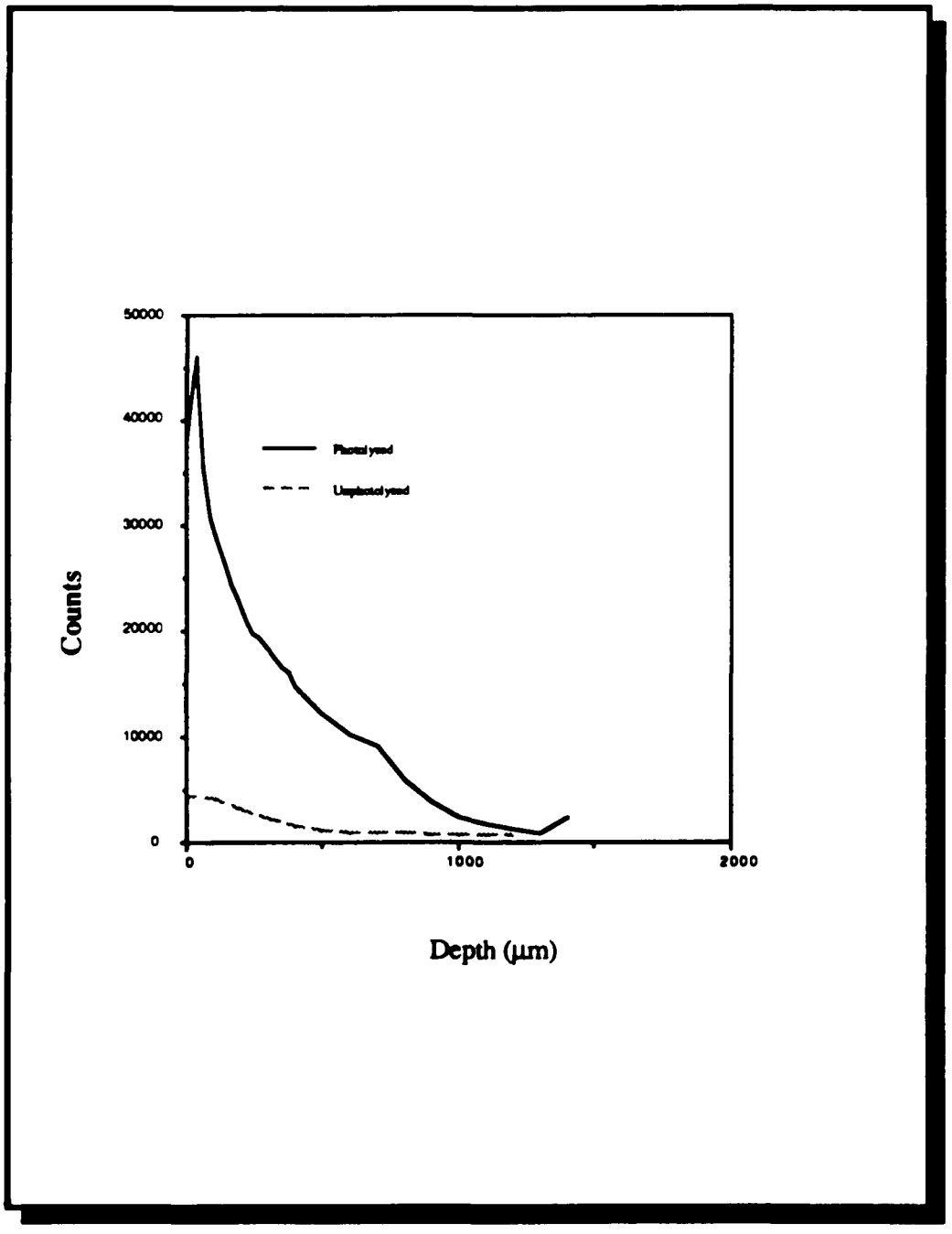

6.3 Photodeposition of tin and iron oxides onto TMOS xerogels.

Tin and iron oxides were photodeposited onto TMOS xerogels by the same method as on PVG. The previous two sections have concentrated on the characterization of the diffusion of tin and iron oxides onto PVG, and their effects on its sintering behavior. In this section, the results obtained with PVG will be compared with those obtained with the morphologically similar TMOS xerogel. Tin and iron oxides physisorb into both materials, and photodeposition followed by thermal consolidation yields images of equivalent resolution in both substrates (Figure 6.14).

The photodeposition of tin and iron oxide onto TMOS xerogel is similar to that observed in PVG (Figure 6.15). However, Mossbauer spectra recorded after photolysis of PVG samples containing 10^{-4} mol of $Fe(CO)_5$ /g exhibit two quadrapole doublets with splittings of 0.98 and 0.93 mm/s (Figure 6.16).[35] The appearance of two doublets implies that iron exists in two sites in the PVG matrix, although in both sites, the isomer shift, 0.40 ± 0.05 mm/s, are consistent with Fe^{3+}, and similar to those compounds possessing octahedrally coordinated Fe^{3+}.[36] It was not possible to record Mossbauer spectra of the tin containing samples since the instrument did not have a Sn source.

EXAFS spectra of iron oxide samples is consistent with the Mossbauer analysis. Figure 6.17 shows the Fourier transform of the EXAFS spectra of iron oxide impregnated PVG. The near edge fine structure indicates that the predominant species is Fe^{3+}, while the major peak in the oscillatory part of the spectrum indicates that Fe^{3+} is surrounded by an octahedral array of oxygen atoms at a distance of 1.5 ± 0.15 Å. This relatively short

distance is similar to the Fe–O distance, 1.33 A, in Fe_2SiO_4 formed in SiO_2 glasses, [37] rather than the approximately 2.0 Å distances in iron oxides. [38]

Under equivalent loading and photolysis conditions, similar results occur in the TMOS xerogel. Mossbauer spectra (Figure 6.16) consist of a single quadrupole doublet with a splitting of 0.91 mm/s. Apparently, the majority of the iron in the xerogel exists in a unique site. Nevertheless, the isomer shift is again consistent with Fe^{3+}, and similar to those compounds with octahedrally coordinated Fe^{3+}.

Heating the samples to 1200 °C consolidate the glass matrices. Consolidation reduces the volume of both substrates by as much as 40 %, and as a result, reduces image size. However, it occurs with no detectable loss of image resolution in either medium. Consolidation entraps the iron species, but it occurs without further chemical change. Although some asymmetry appears, in general, Mossbauer spectra of the iron in the consolidated xerogel (Figure 6.18) remain equivalent to those recorded after heating the sample to 650 °C (Figure 6.16). Consolidation of PVG samples prepared with initial $Fe(CO)_5$ loading of $\leq 10^{-5}$ mol/g yield equivalent results. In both glasses, consolidation entraps a nonmagnetic, octahedrally coordinated Fe^{3+} species.

Consolidation of PVG samples prepared with an initial $Fe(CO)_5$ loading of 10^{-4} mol/g, however, results in a loss of the quadrupole doublets and the appearance of two six-line spectra (Figure 6.19) characteristic of two magnetic hyperfine fields. These fields 370 and 425 kG, respectively, differ from the fields found in Fe_2O_3 (515 kG) and Fe_3O_4 (450, 500 kG). [39, 40] The isomer shifts correspond to Fe^{3+}, and the Fourier transform of the EXAFS of samples exhibiting magnetic hyperfine fields (Figure 6.20) yields an Fe nearest neighbor distance of 1.5 ± 0.15 Å.

Figure 6.14 - Optical micrograph of a grid pattern in consolidated a) PVG and b) TMOS xerogel. Magnification 50X.

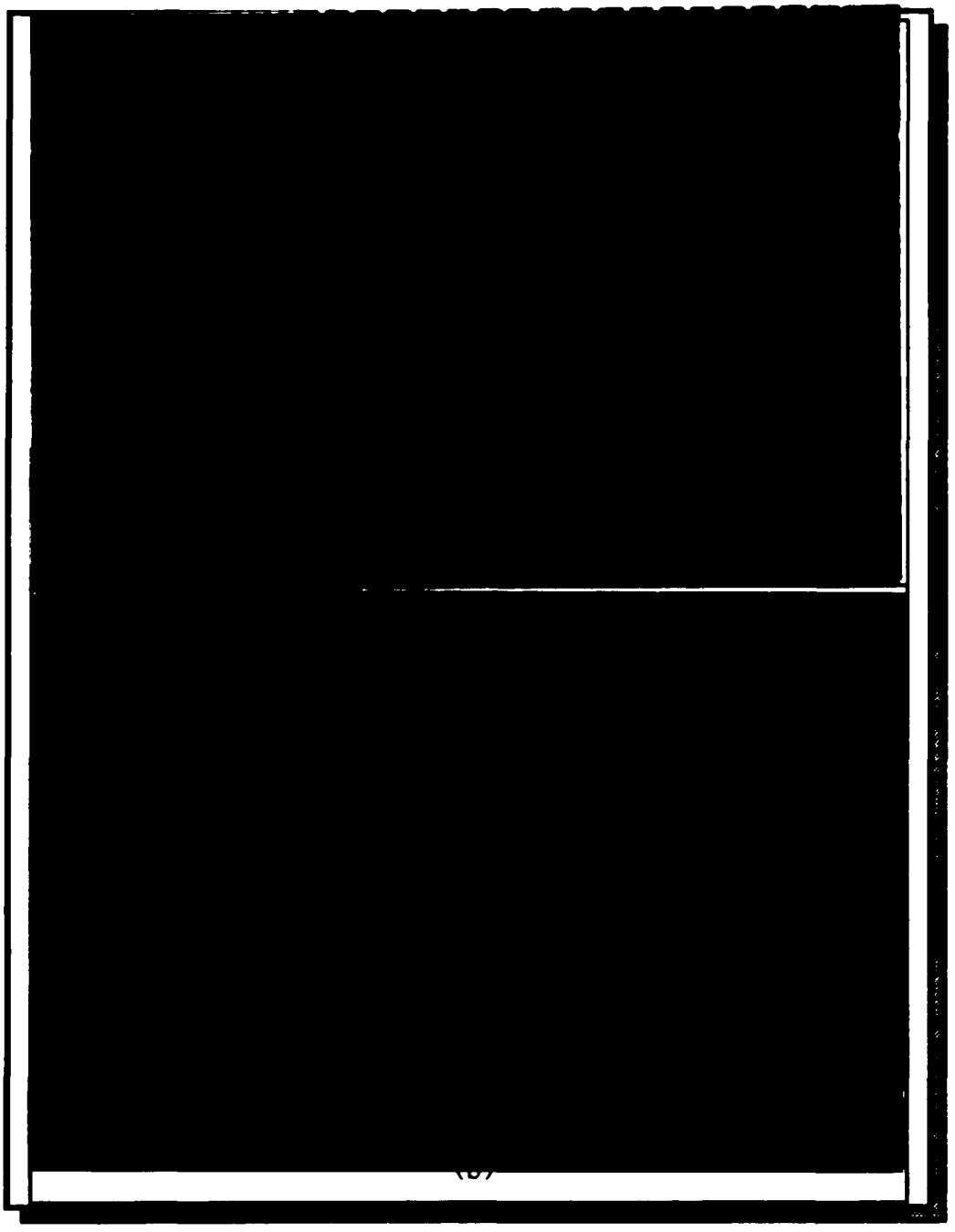

Figure 6.15 - X-ray fluorescence of the tin and iron oxide distribution in consolidated TMOS xerogel.

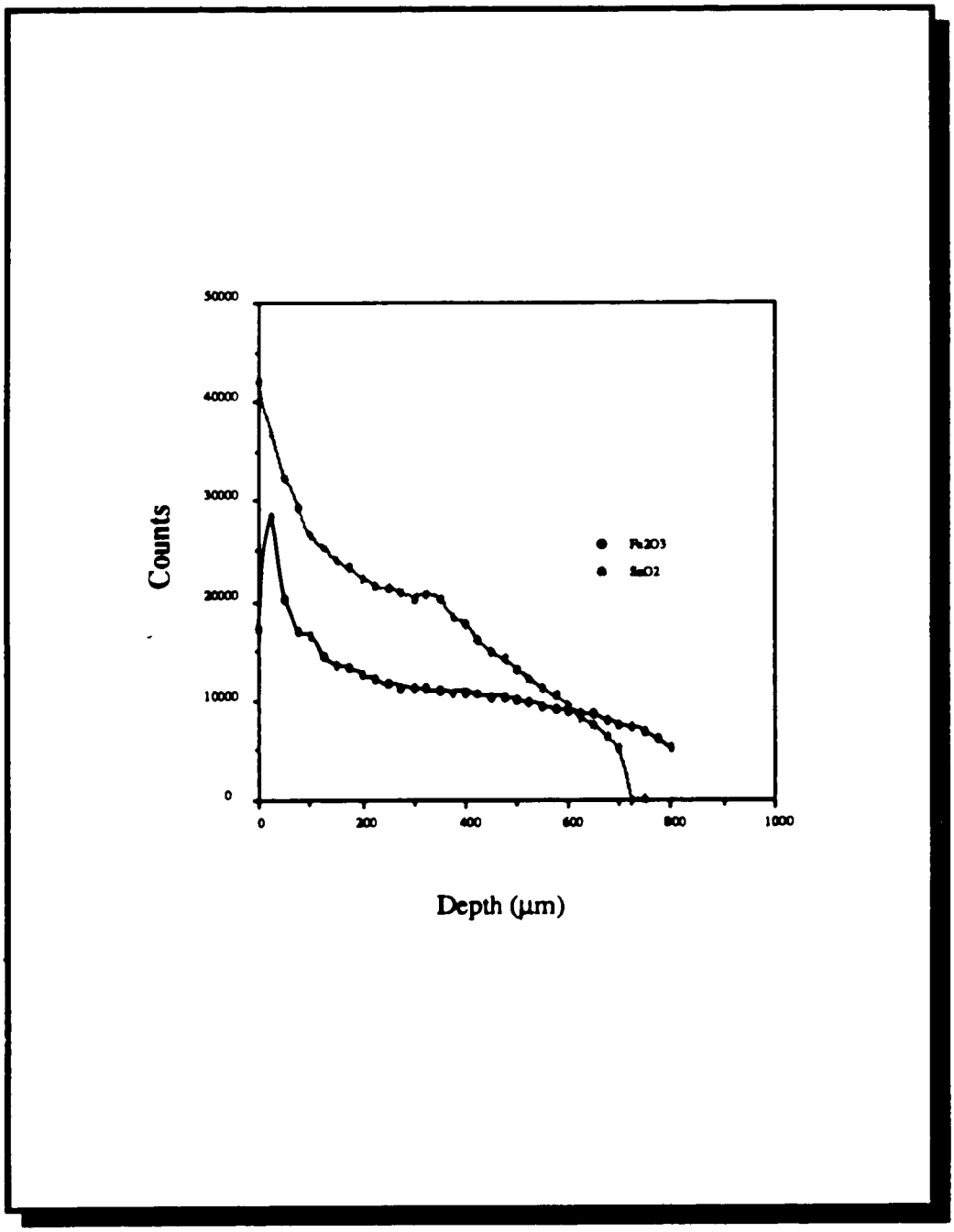

The equivalence of these data with that obtained for the porous and nonmagnetic, consolidated samples suggests that essentially the same species is formed in all samples, i.e., an octahedrally coordinated Fe^{3+} species. Yet. magnetic hyperfine fields appear only in the consolidated PVG samples prepare with high loadings of $Fe(CO)_5$. Apparently, if the number of Fe^{3+} species is sufficient, consolidation of PVG yields a magnetically ordered material in which either the magnetic moments of the individual ions or relatively small clusters of the ion align to give a relatively large magnetic moment.

In these glasses, pattern resolution and formation of magnetically ordered impregnates appear to be a length dependent phenomena. The data gathered up to now suggest that the occurrence of magnetic coupling depends on the average spacing between the adsorbates. Further experiments to test these ideas, and to determine whether the hyperfine fields in the consolidated PVG samples correspond to nonequivalent magnetic phases, are in progress.

Figure 6.16 - Mossbauer spectra of photodeposited Fe after heating samples (a) PVG and (b) TMOS xerogel to 650°C.

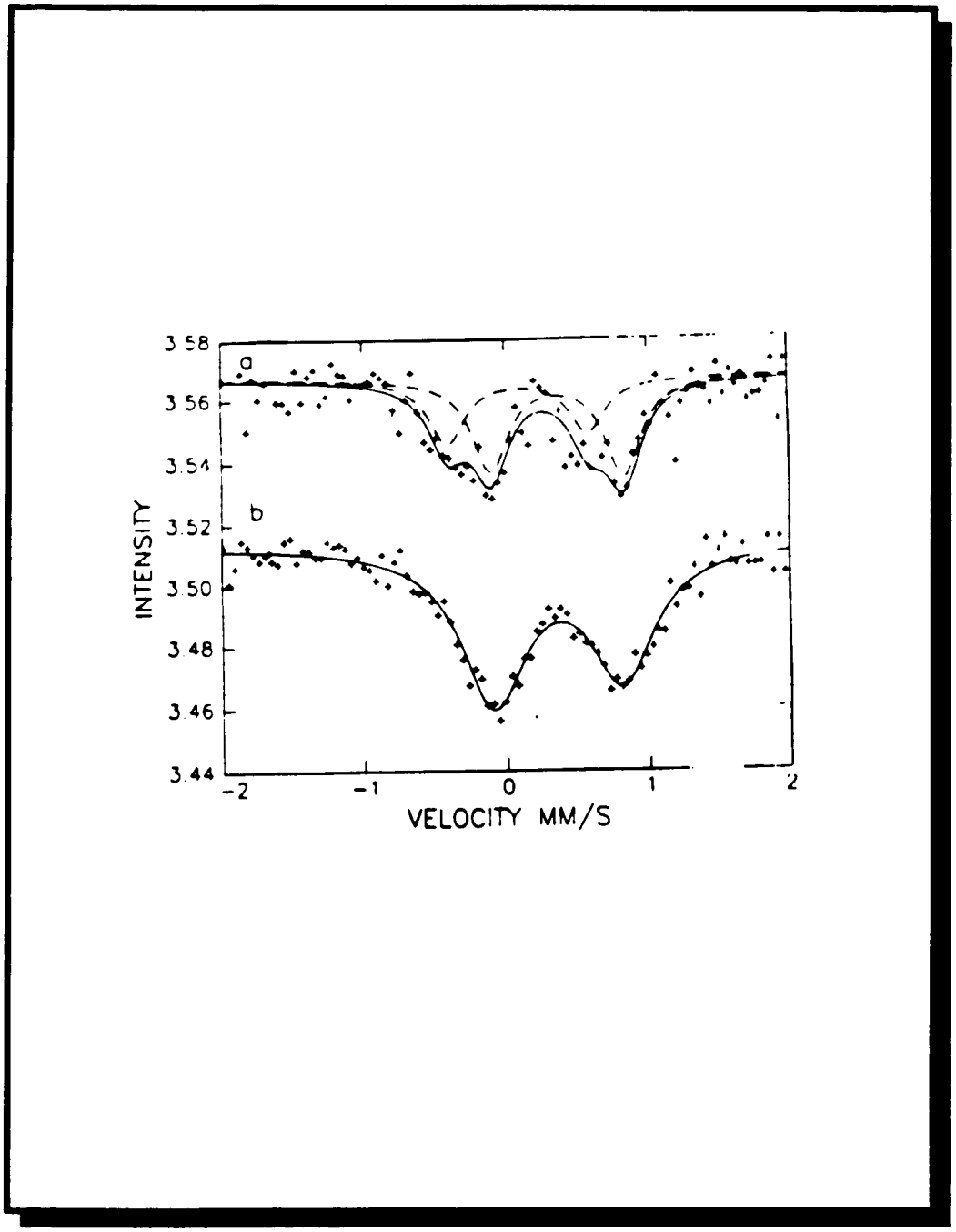

Figure 6.17 - Fourier transform of the EXAFS spectrum of a photolyzed iron-impregnated PVG sample after heating to 650°C.

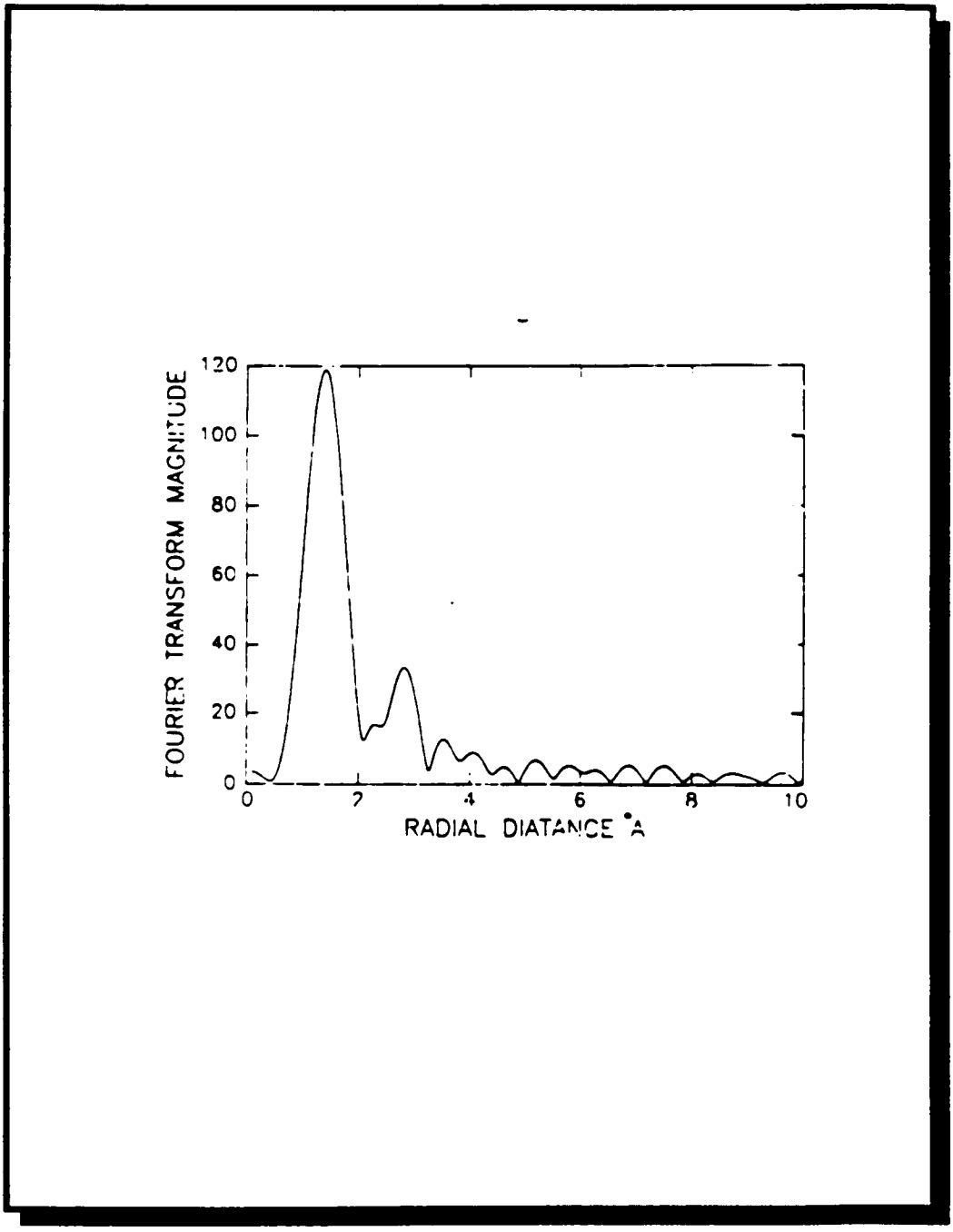

Figure 6.18 - Mossbauer spectrum of Fe in consolidated TMOS xerogel.

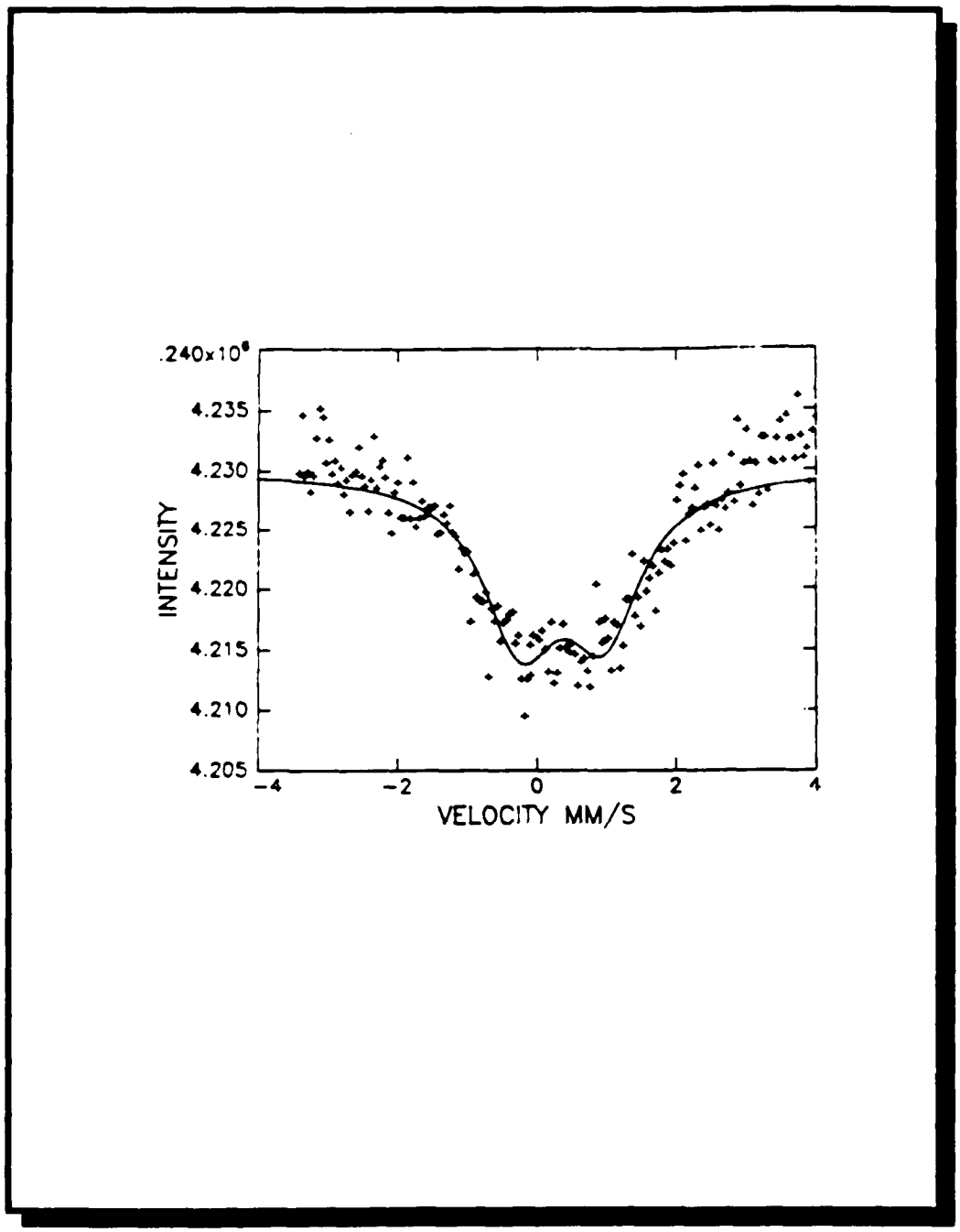

Figure 6.19 - Mossbauer spectrum of Fe in a consolidated PVG sample.

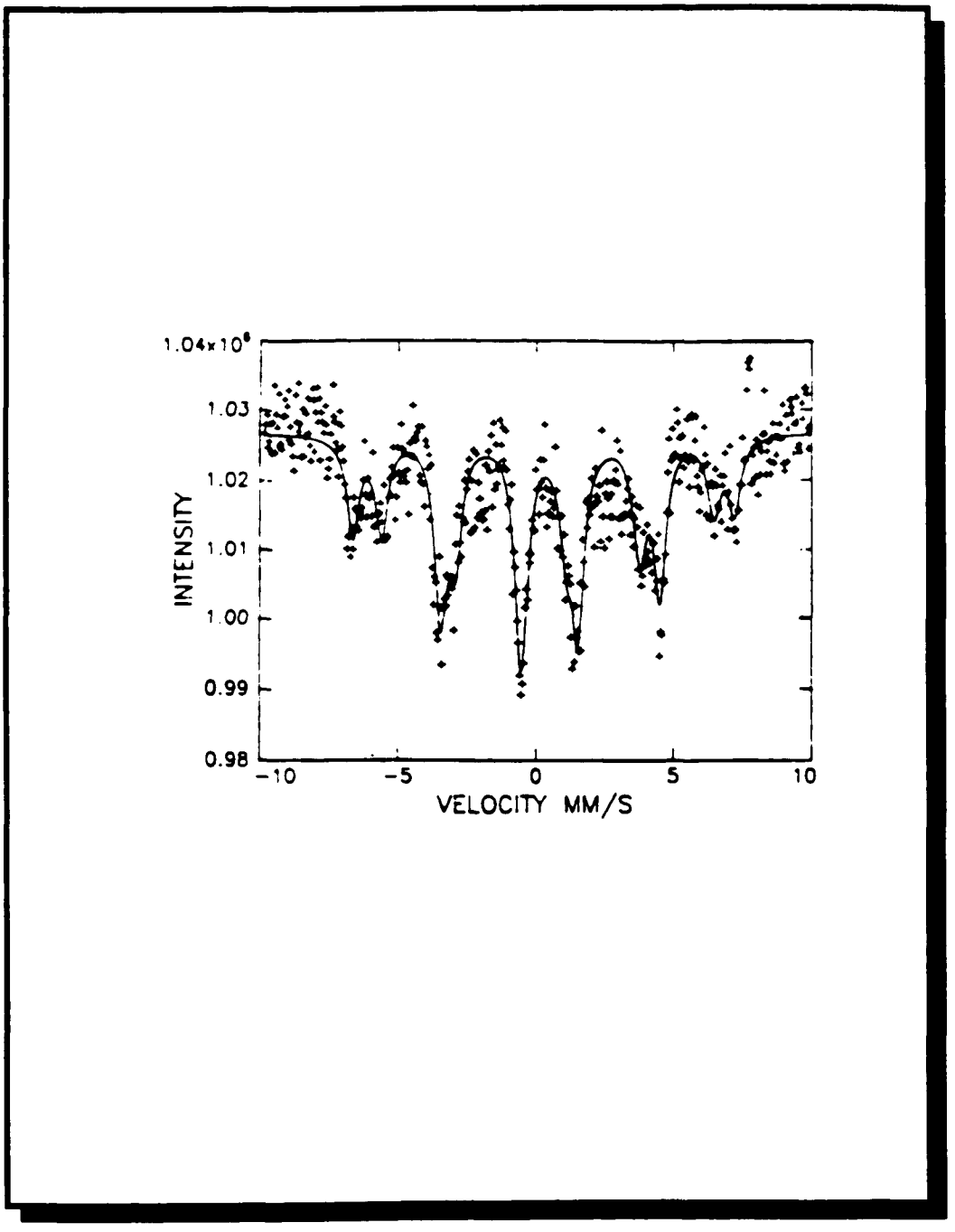

Figure 6.20 - Fourier transform of the EXAFS spectrum of a photolyzed Fe impregnated PVG sample after consolidation at 1200 °C.

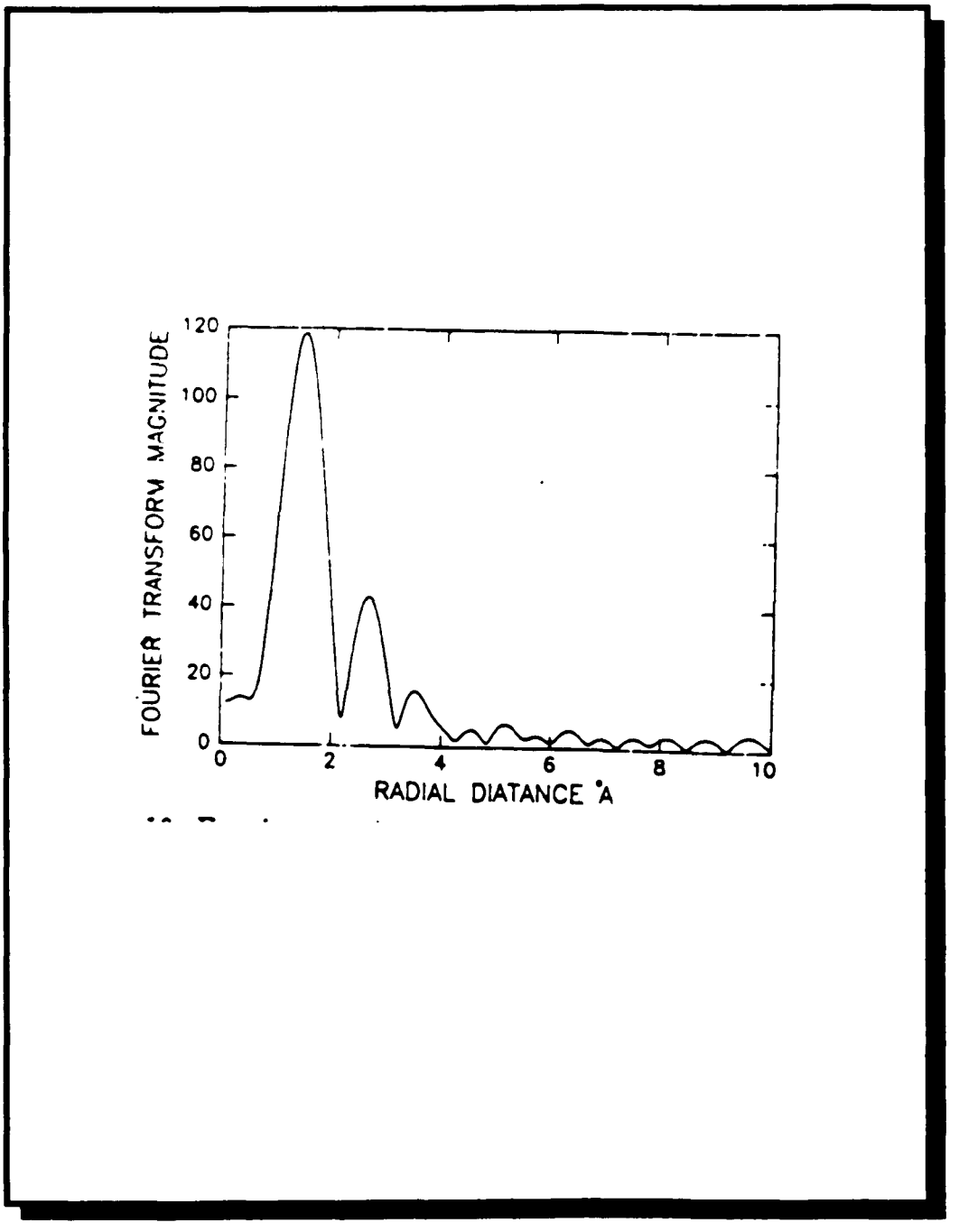

7. Photolithographic Generation of Refractive Index Gradients in Porous Glasses.

Porous glasses impregnated with photosensitive organometallic compounds exhibit optical changes when exposed to light. Optical changes in transmission and refractive index can be induced and are permanent after consolidation of the glass to a nonporous matrix. [42] For example, highly resolved patterns of gradient indices are obtained by photochemically binding $(CH_3)_3SnI$ to the glass matrix followed by thermal consolidation. [43] Similarly, photolysis of $Fe(CO)_5$ followed by thermal consolidation leads to equally well resolved patterns of iron oxide. [44] With both compounds, photolysis binds the reagent to the glass matrix. Binding prevents migration and maintains pattern resolution during thermal consolidation. Thermal consolidation, which requires temperatures ≥ 1000 °C, volatalizes the unreacted adsorbate from the glass and converts the photoproduct to a metal oxide.

The photolithographic deposition of metal oxides in porous glasses followed by consolidation of the porous matrix to a nonporous, nonscattering, glass was used to produced changes in the index of refraction of the glass of the order of 0.1 to 0.001. Changes in the index of

refraction allows the deposition of multimode planar waveguides, ~ 10 μm in width and 1.0 in radius of curvature, capable of guiding a He-Ne laser beam through the glass with low optical losses (~ 0.6 dB/cm). [45] The results presented here describe the methodology involved in the processing of high resolution planar waveguides in porous glasses. Examples of the different guiding structures realizable from this method are provided.

7.1 Photoinduce metal oxide imaging onto porous Vycor glass.

Figure 7.1 shows the photograph of an image of a periodic table made by the photodeposition of iron oxide on the surface of a square PVG plate. A similar image, but more transparent can be produced by the deposition of tin oxide. The periodic table image was photolithographed by contact printing using a 35 mm negative as photomask, followed by exposure with UV light, and heat treatment to 1200 °C. Surprisingly, consolidation of the PVG sample, which produces a 40 % volume shrinkage, occurs without the loss of image resolution.

Visually or under low magnification, the metal oxide images of the periodic table in the consolidated glass, whether produced by photolysis of samples containing 10^{-4} mol $(CH_3)_3SnI$ (ads.)/g or 10^{-4} mol $Fe(CO)_5$ (ads.)/g, appear equivalent. However, more detailed analysis reveals startling differences. The iron oxide images (Figure 7.2a) are grainy with small whiskers along the edges, whereas the tin oxide image (Figure 7.2b) appears more dense and uniform, almost cloudlike, with sharp, well-define edges. SEM of the photodeposited metal oxides images shows a uniform

Figure 7.1 - Photolitographic image of a periodic table made by photoinduced iron oxide on consolidated PVG. Actual sample dimensions 21.4 x 21.0 x 1.4 mm^3.

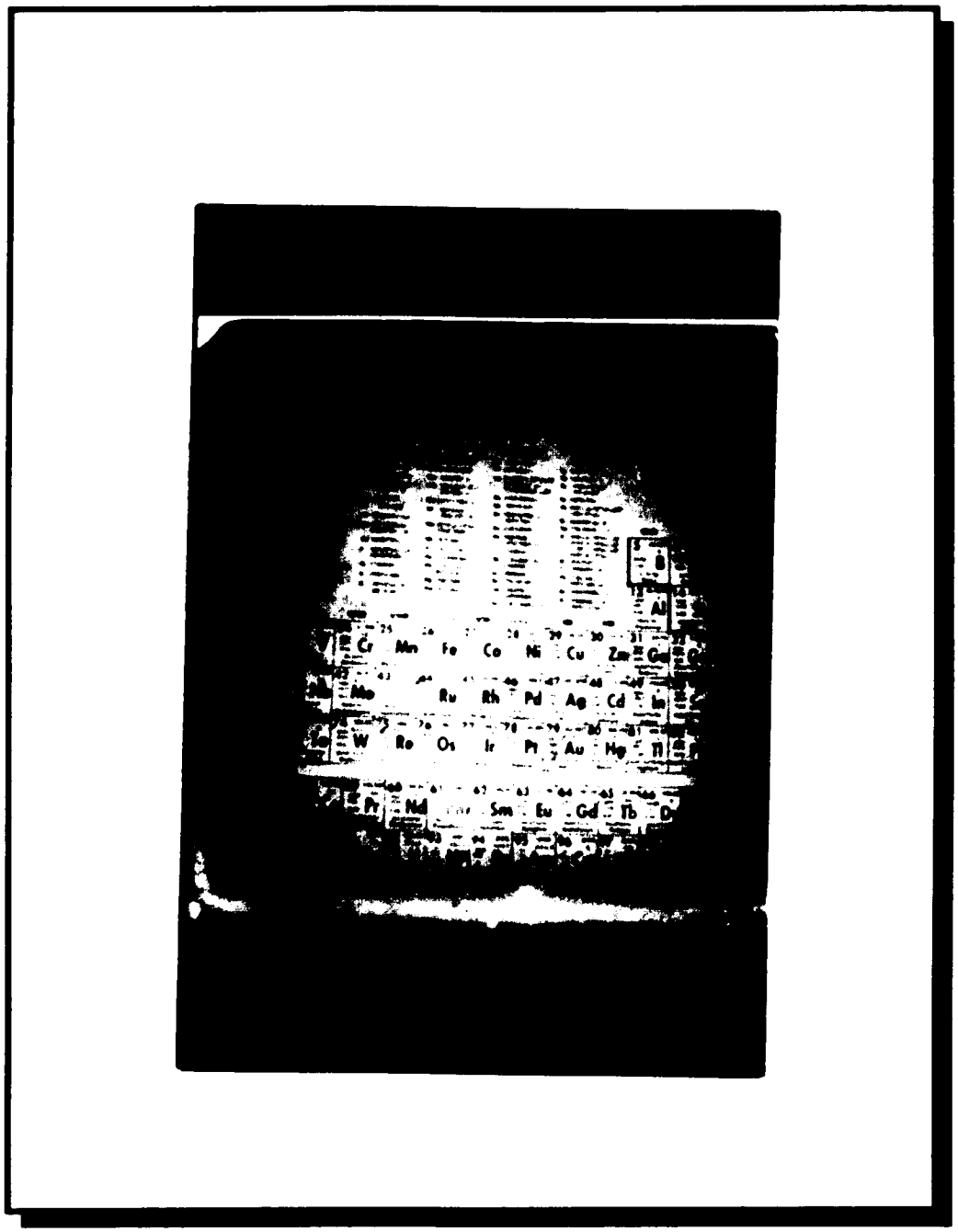

Figure 7.2 - Optical micrograph images of a photoinduced image of an element in a periodic table (a) iron oxide and (b) tin oxide onto consolidated PVG. Magnification 50X.

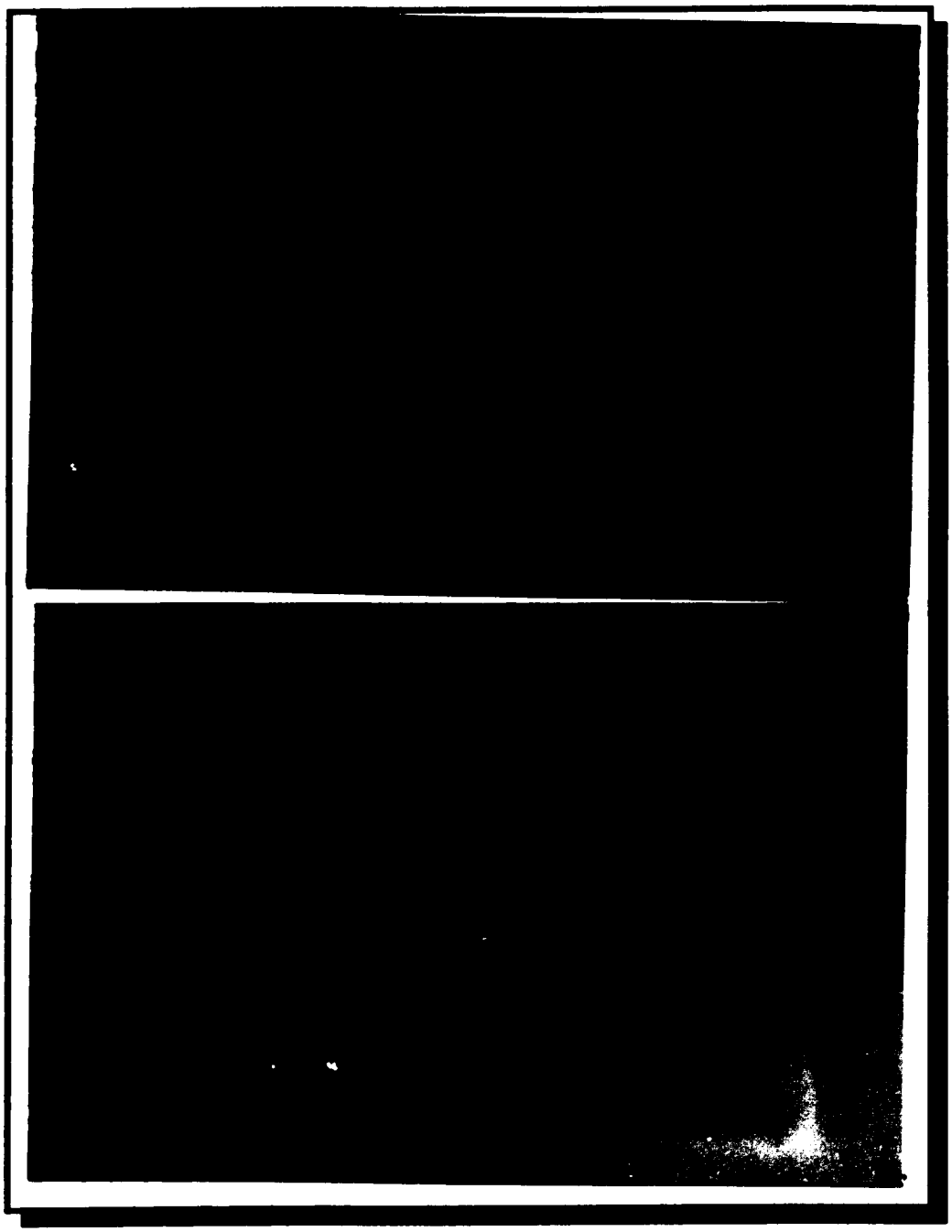

distribution of relatively small tin oxide particles (Figure 6.1), whereas the iron oxide appears as distinct, relatively large clusters of aggregated particles (Figure 6.2).

Figure 7.3 shows the SEM Backscatter micrograph of the same iron oxide image in the periodic table sample. The backscatter image gives more detailed information since contrast depends on difference in the scattering atoms. As a result, a high contrast image is observed. From the micrograph is clearly seen that the whiskers at the edges of the image that appear in Figure 7.2a are not present. This indicates that the optical micrographs are subject to diffraction effects cause by the elongated clusters of the iron oxide image. The resolution of the element letters in the periodic table (Figure 7.2) , as measured from the backscatter micrograph, is ~ 120 μm in width, and that of the atomic numbers is ~ 20 μm in width.

From this simple photolithographic test, it is observed that high resolution patterns, in the micrometer range, have been produced using the photodeposition of metal oxides onto PVG. However, to fully utilized the photolitographic technique, an understanding of all the parameters involved in the image resolution must be accomplished. For example, Figure 7.4 is a micrograph of a tin oxide sample before consolidation. A difference in the grain size of tin oxide is observed before and after consolidation. Before consolidation the grains are spherical (~ 50 nm diameter) and well defined, with observable spatial separations between grains of the order of 50-300 nm. While in the consolidated sample the grains collapse together into plate like facets, which indicate the formation of high density tin oxide regions, due to the shrinkage process that occurs upon consolidation. Preliminary experiments indicate that the tin oxide density (contrast) of the image depends in the initial concentration of

Figure 7.3 - Backscatter SEM micrograph of a letter from a periodic table photoinduced iron oxide onto consolidated PVG. Magnification 50X.

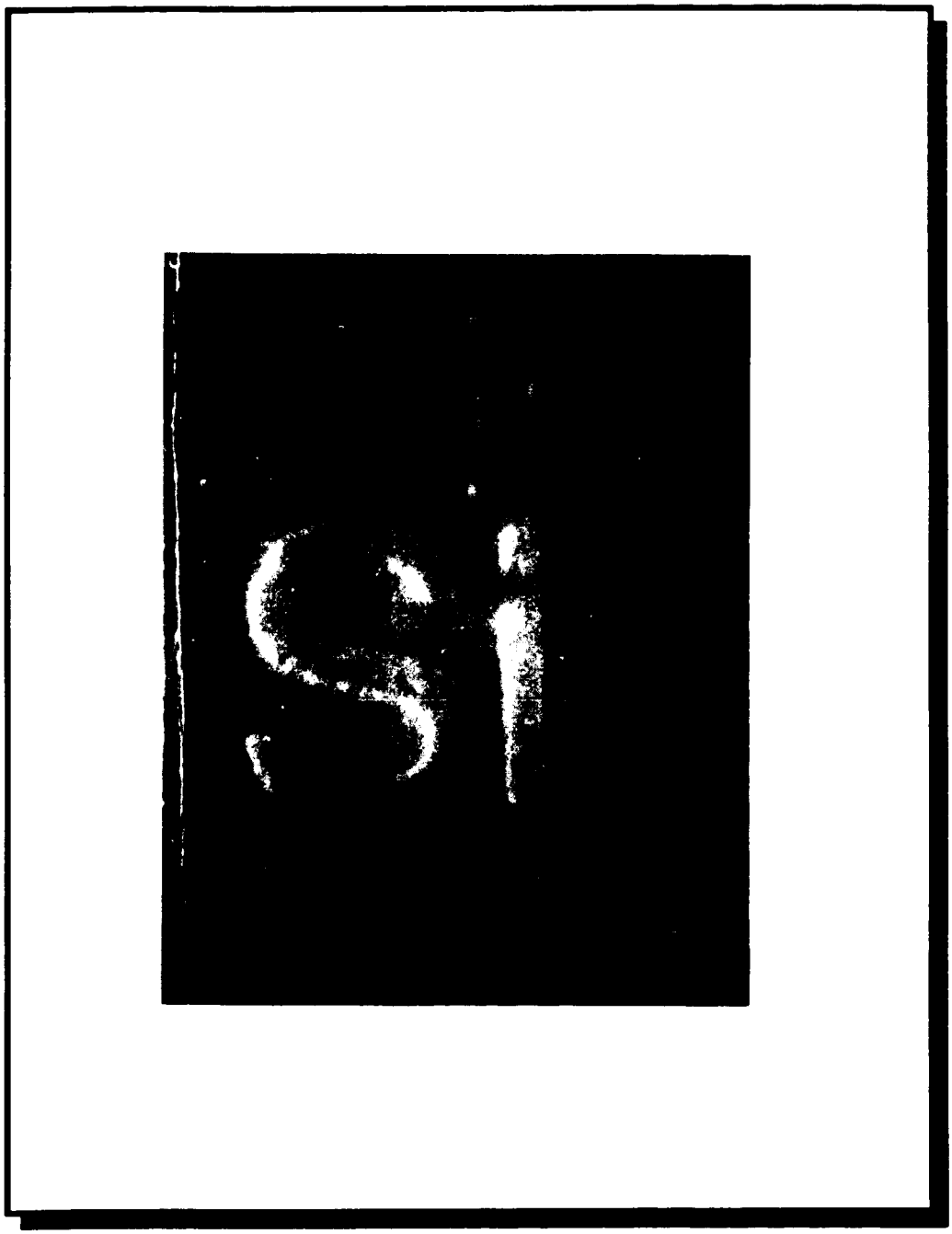

Figure 7.4 - Micrograph image of a letter from a periodic table photoinduced tin oxide onto calcined PVG.

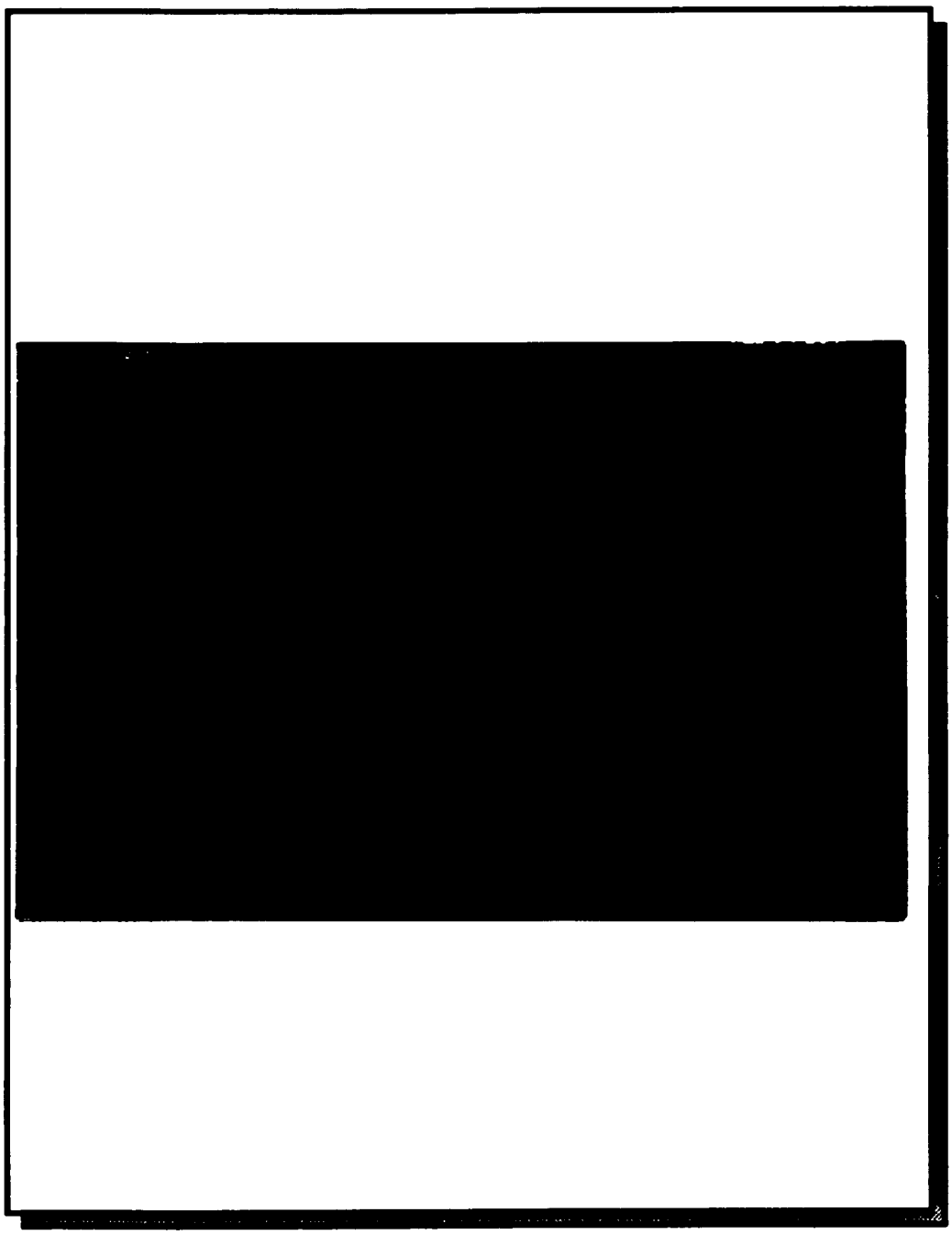

Figure 7.5 - Micrograph image of a letter from a periodic table photoinduced tin oxide (1.0×10^{-7} mol ads./gr.) onto calcined PVG.

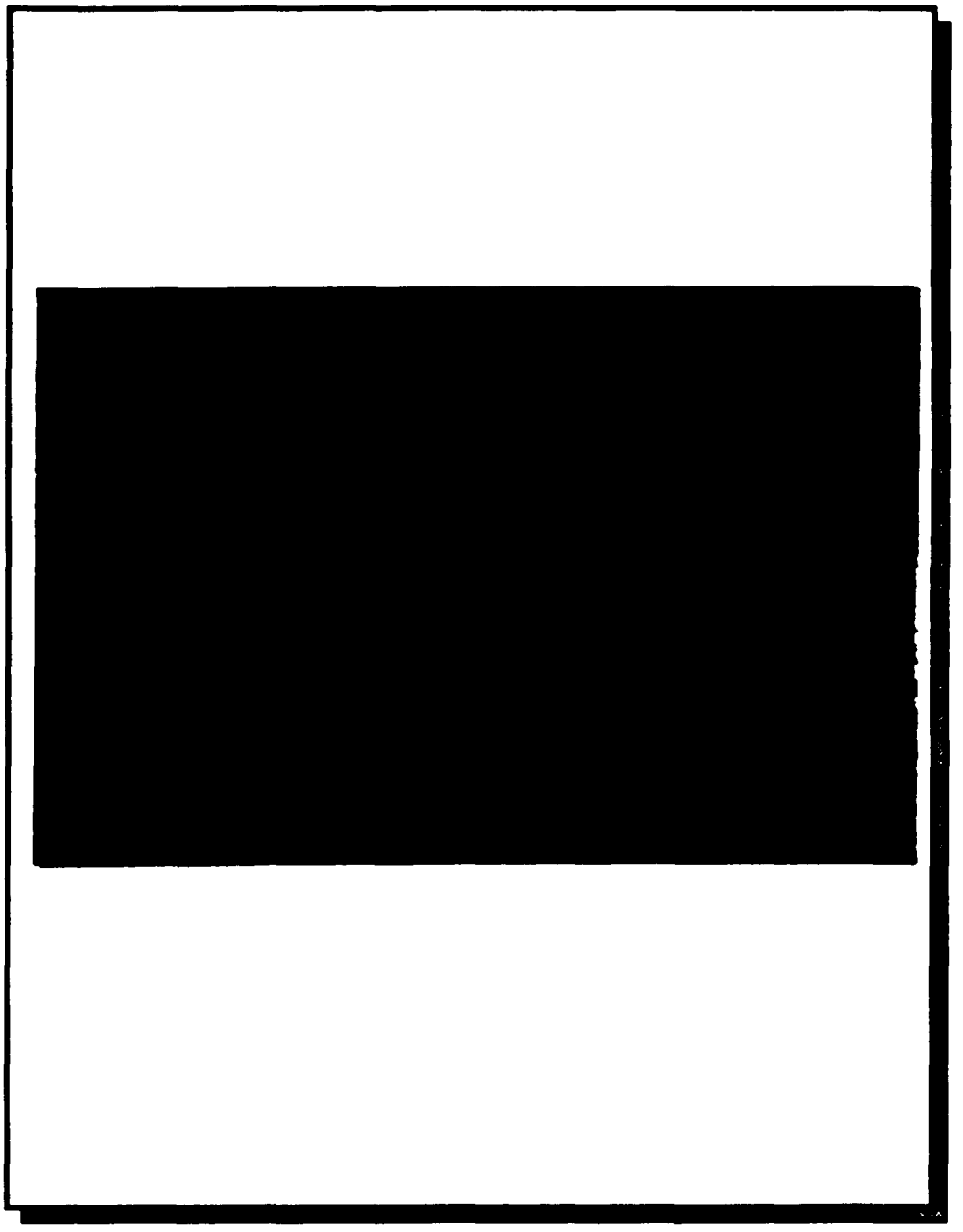

$(CH_3)_3SnI$ (ads.)/g, and the length of exposure to the light source. Figure 7.5 shows a similar image of a letter in the periodic table of a sample containing 10^{-7} mol $(CH_3)_3SnI$ (ads.)/g and were photolyzed with 254-nm light for 1.0 minute.

In the tin oxide samples, there is no loss of image resolution as the exposure time is increased, on the contrary, the resolution of the image increases with exposure time since more contrast is exhibited between the exposed and the unexposed areas. The observation is that instead of the tin oxide particles loosing lateral resolution, as observed in the iron oxide images, the resolution declines vertically into the glass bulk. The loss of resolution can be observed in Figures 7.6 and 7.7, where a 30 μm^2 square grid pattern was photolithographed onto the front surface of a (4.00 mm diameter by 2 cm length), PVG rod. The separation between the squares was measured under the microscope to be 20 μm. The rod was fracture along the long axis, and the cross-sectional distribution of tin oxide was observed with an optical microscope. Photolysis creates a conical distribution of tin oxide in the glass to a depth of ~ 600 μm. Therefore, from the micrograph, it is observed that resolution is lost inwards with depth and photolysis time. Lateral and cross-sectional distribution depend directly on the number of molecules adsorbed, and their distribution decreases exponentially with depth as previously described (see section Part III-6.2). The conical shape of the image is caused by the bending of the light, due to the induced change in the index of refraction as the concentration of the photolysed molecules increases at the surface. This optical effect is shown graphically in Figure 7.8, and experimentally by a 100 μm grating in Figure 7.9. These observations suggest that the resolution of the tin oxide patterns is best maintained at high

Figure 7.6 - Optical micrograph (x 30 magnification) of tin oxide microgrid (side ways) photoinduced pattern onto the surface of a consolidated PVG rod. Rod dimensions 3.0 x 0.25 cm.

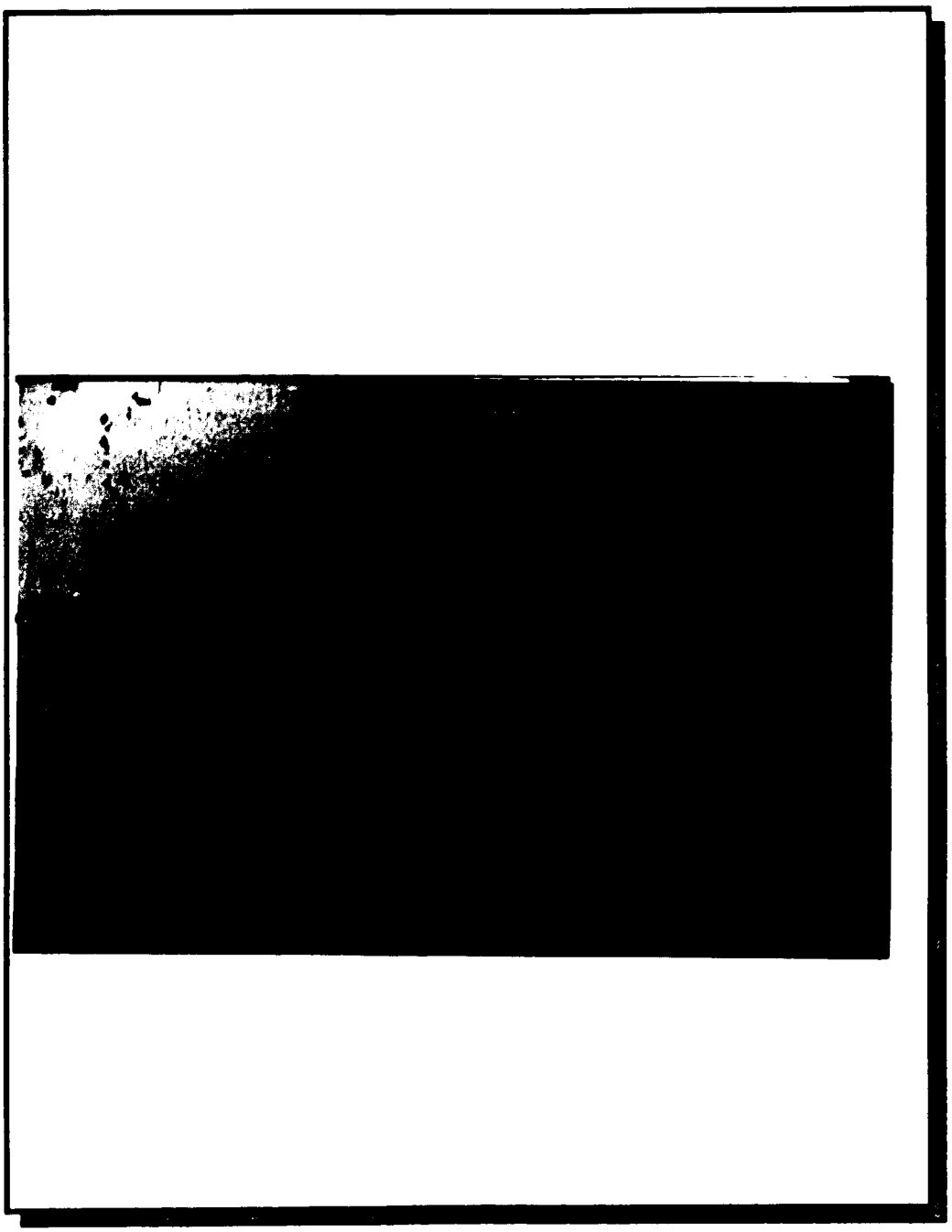

Figure 7.7 - Optical micrograph (x 30 magnification) of tin oxide microgrid (front surface) photoinduced pattern onto the surface of a consolidated PVG rod. Rod dimensions 3.0 x 0.25 cm.

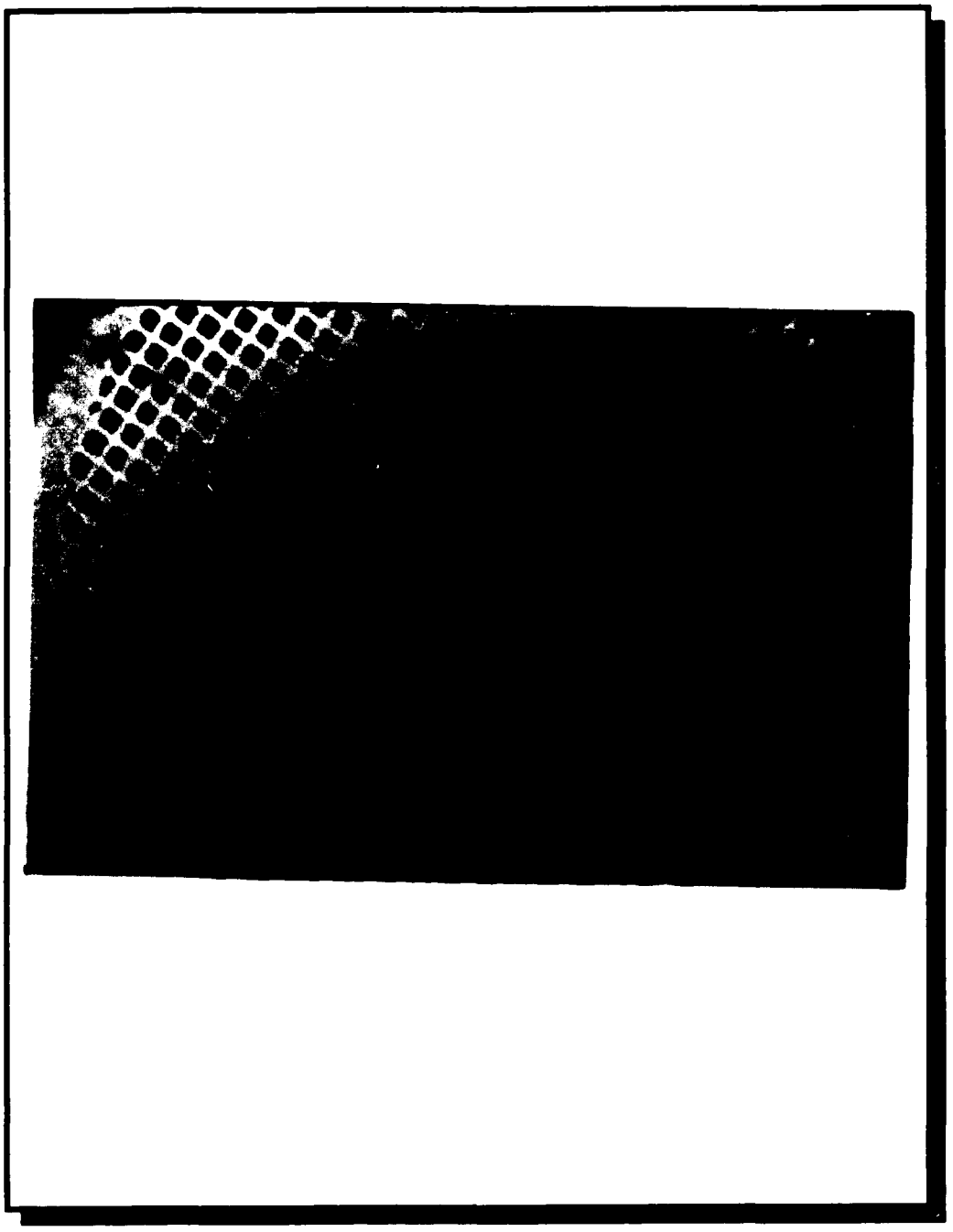

Figure 7.8 - Schematic diagram of the bending of light of a microgrid with a different index of refraction than the support.

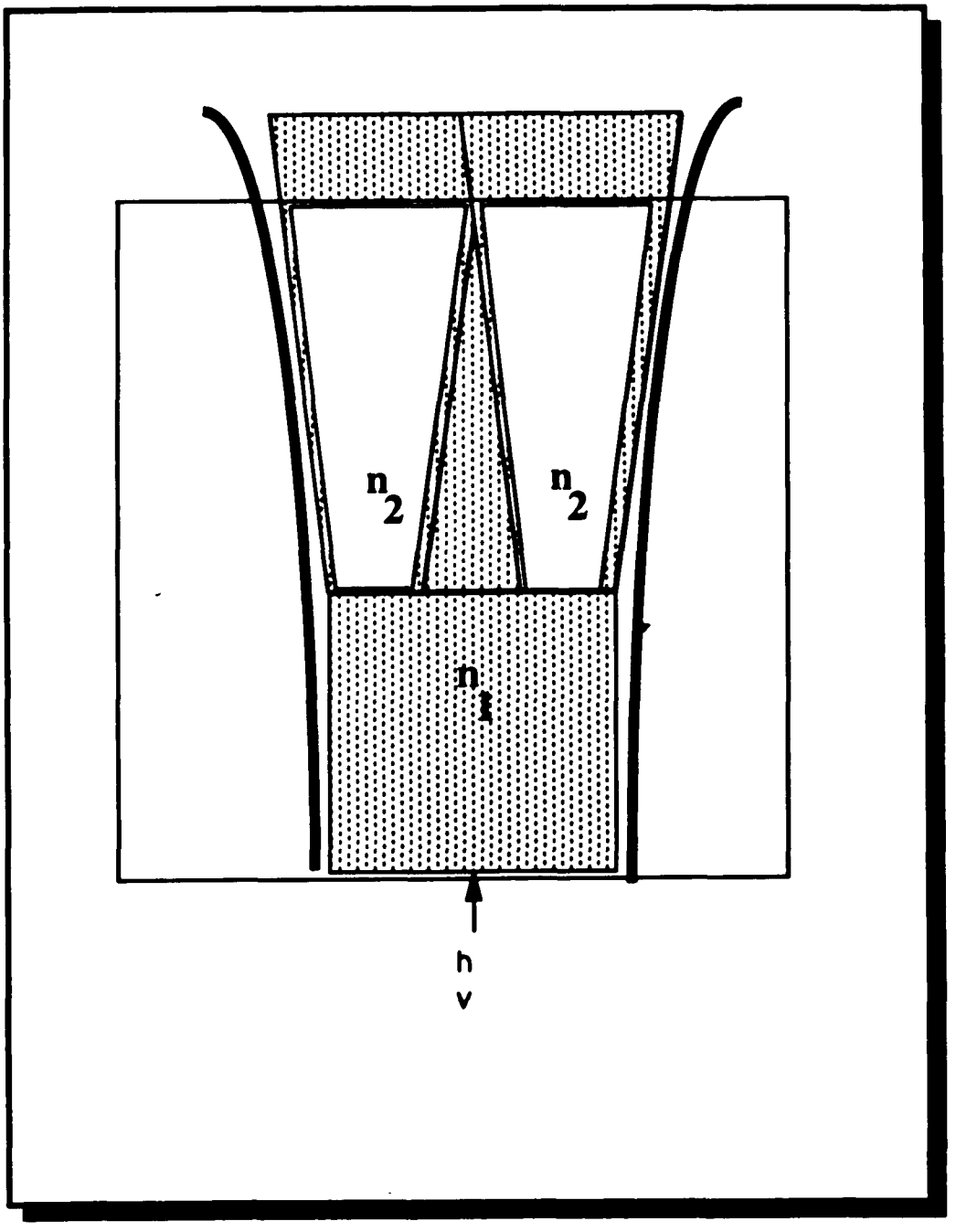

Figure 7.9 - Lens effect by a 100 μm line gradient photoinduce tin oxide on consolidated PVG.

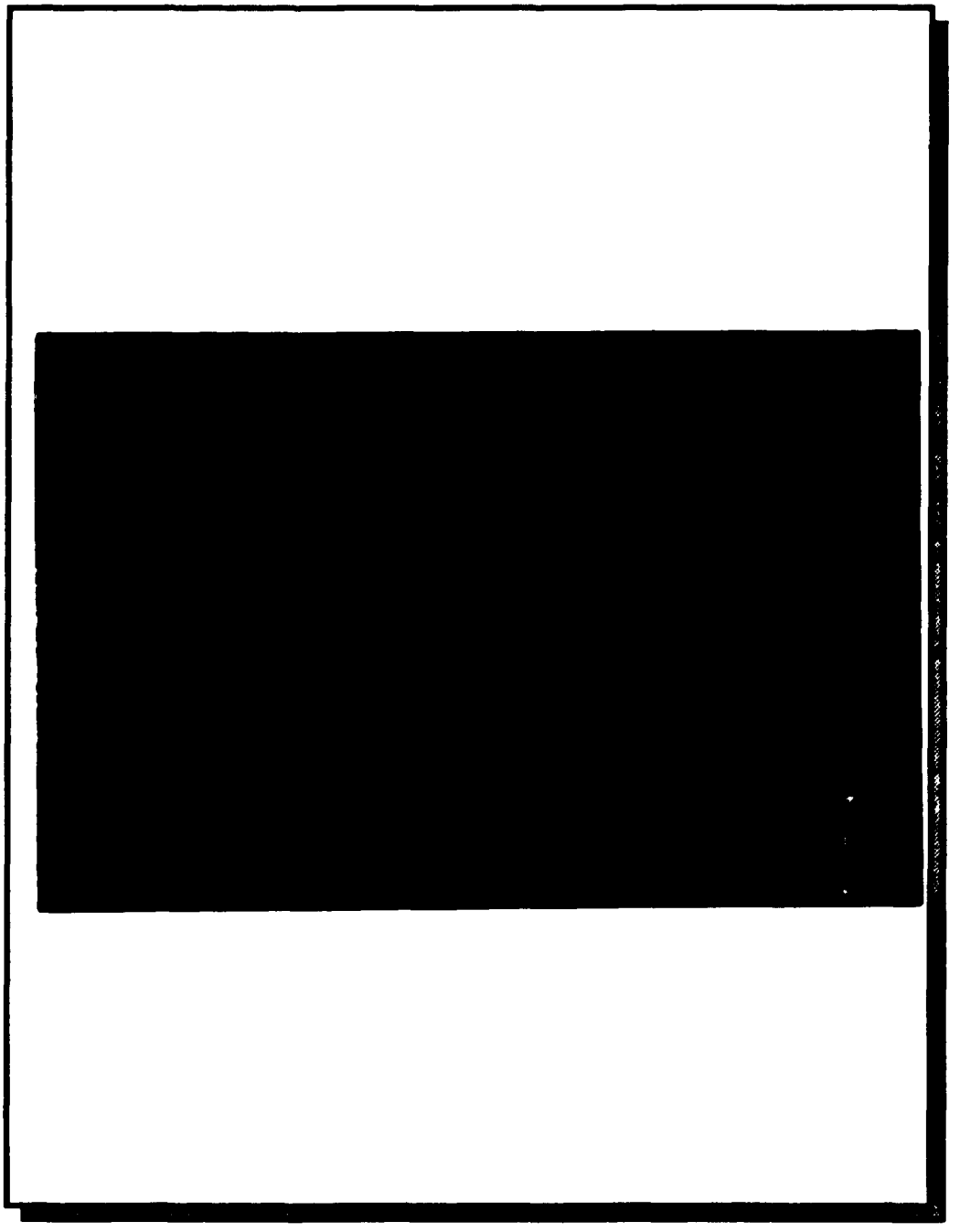

concentrations, high source intensities, and short exposure times.

In the case of iron oxide samples the resolution of the images, which are also controlled by the initial concentration of $Fe(CO)_5$, and exposure times, deteriorates as either the concentration of $Fe(CO)_5$, or the time of exposure increases. Longer exposure times yield longer agglomerated clusters. In some instances, for example, the particle clusters grow out of the exposed region into the unexposed region. This reduces the resolution of the pattern, as shown in the optical micrograph of a 100 μm line grating formed by the photolysis of 1.0×10^{-4} mol/g of $Fe(CO)_5$ under light exposure for 2 hrs, Figure 7.9.

In imaging science, resolution is measured by using standard chrome resolution photo masks, Figure 7.10. Both positive and negative masks are made of a progressive series of elements at right angles to each other. Each element consist of a series of lines and spaces of equal width and length. The element size decreases geometrically as the sixth root of two, or conversely, the number of lines per milliliter doubles with every sixth element. These groups of sixth elements are referred to as a Group, and are assigned a group number which tells the power at which the element had been reduced.

The resolution mask used in this experiments was the Air Force standard target mask with a maximum line thickness of 50 μm and a minimum line thickness of 0.001 μm. The mask was used to evaluate the maximum resolution obtainable, in both positive and negative grids, by the photodeposition of tin and iron oxide onto PVG (Figures 7.11-13).

A comparison of the resolution obtained by using a positive or negative mask to produced a tin oxide image clearly shows that the negative mask gives a better resolution. In the positive image (Figure 7.11), the lines

Figure 7.10 - Schematic diagram of the Air Force standard target photolithographic mask. Basic element (50 μm - 0.01 μm series).

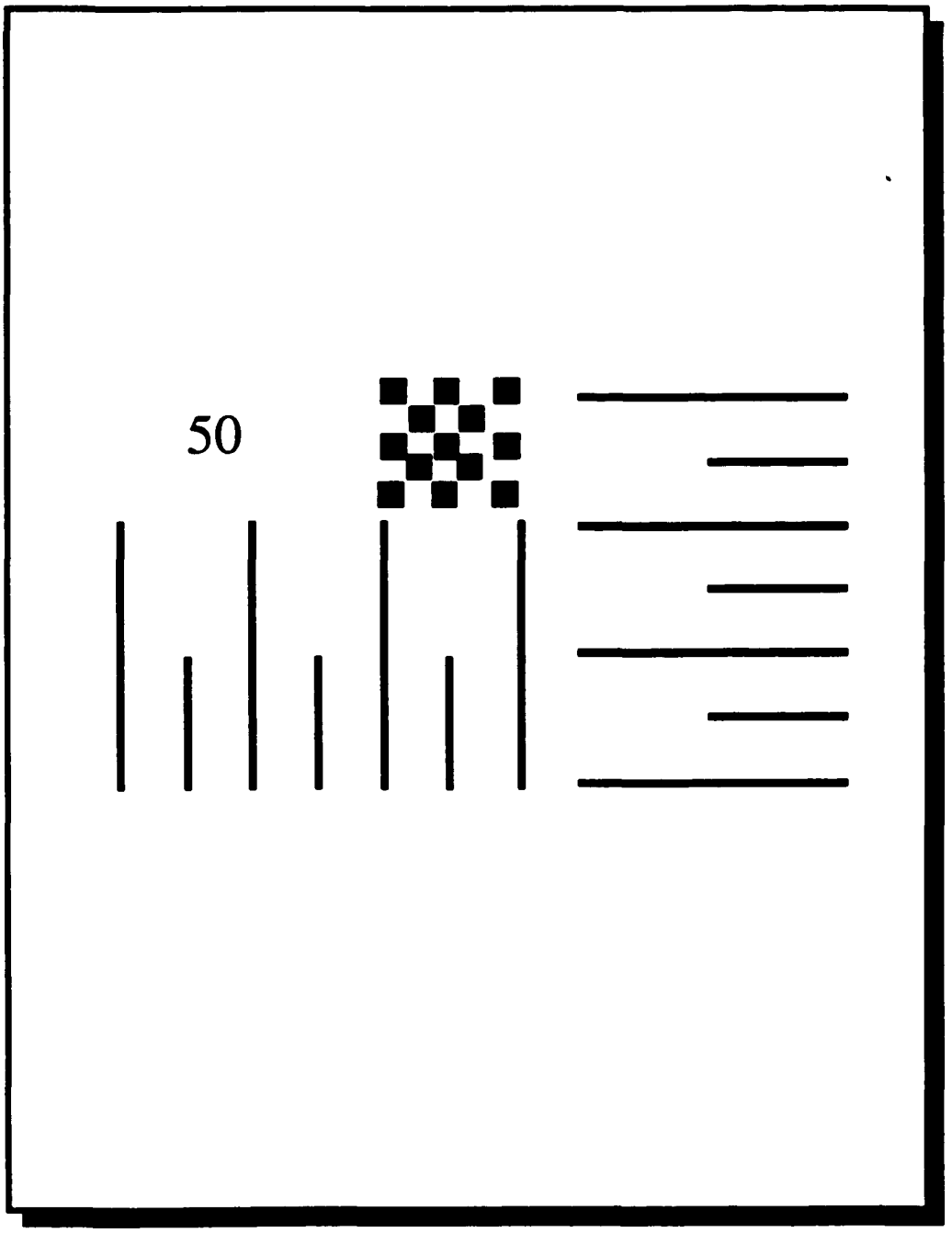

Figure 7.11 - Air Force standard target positive mask photoinduced with tin oxide onto the surface of PVG. Magnification 100X

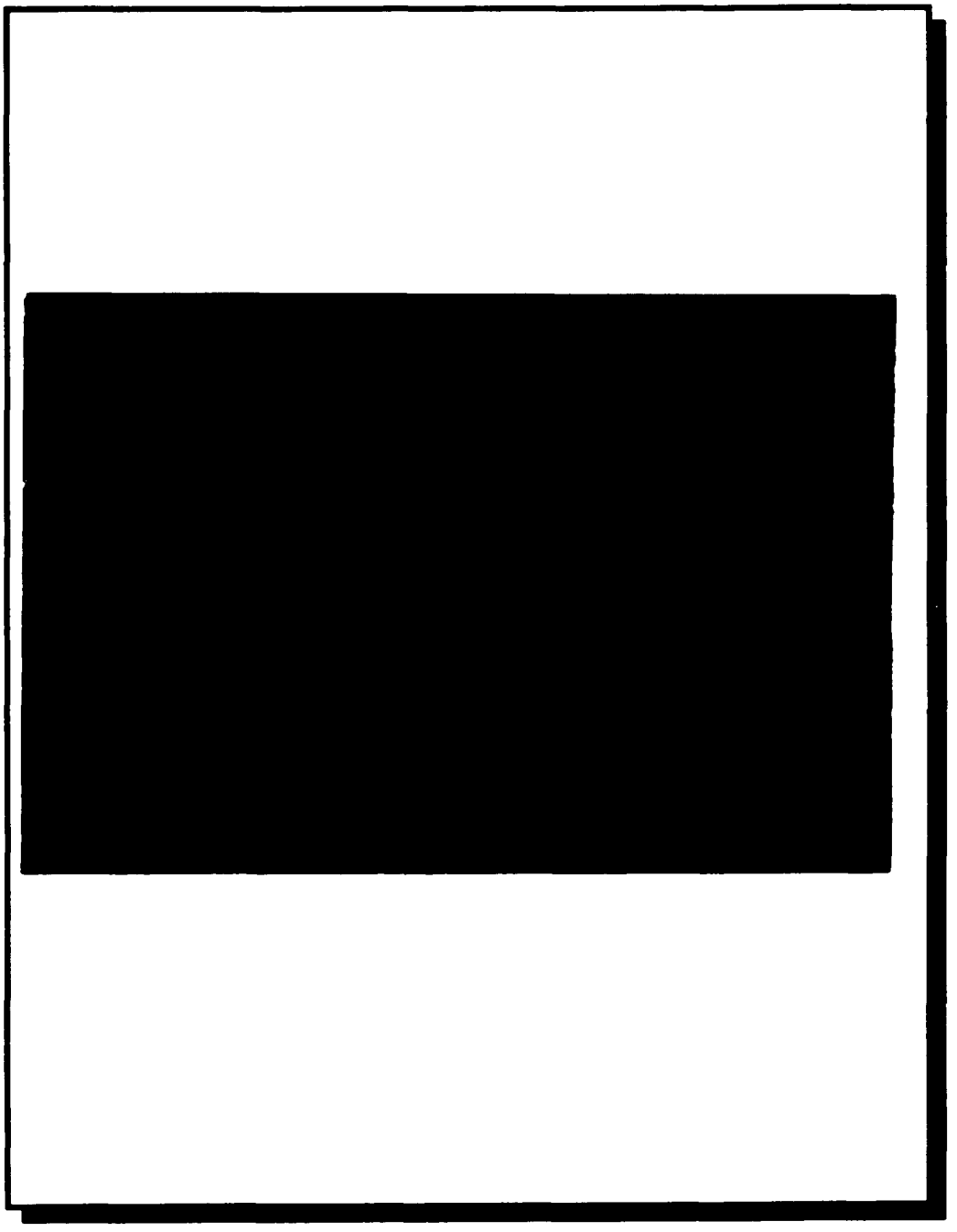

Figure 7.12 - Air Force standard target negative mask photoinduced with tin oxide onto the surface of PVG. Magnification 100X

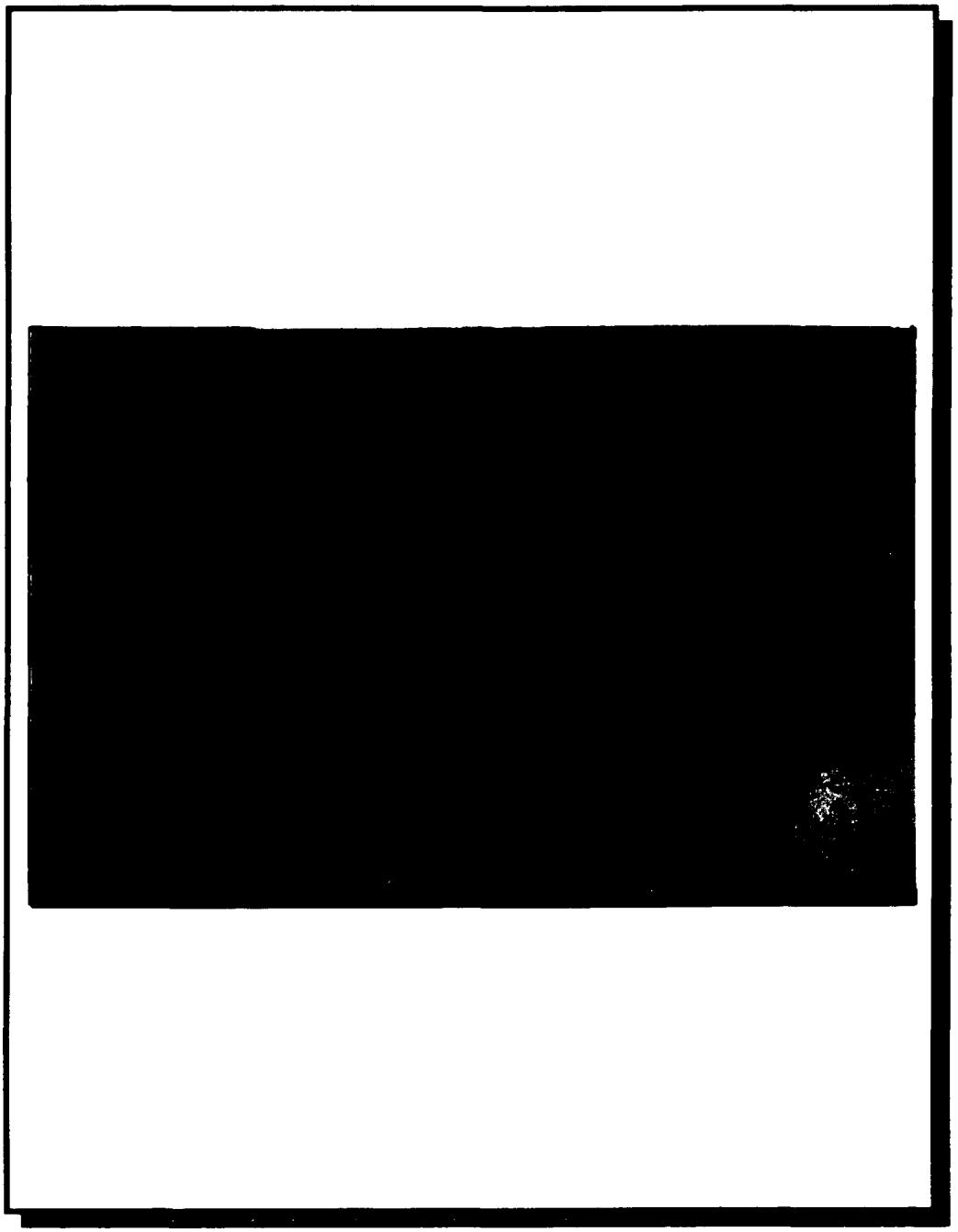

Figure 7.13 - Air Force standard target negative mask photoinduced with iron oxide onto the surface of PVG. Magnification 100X

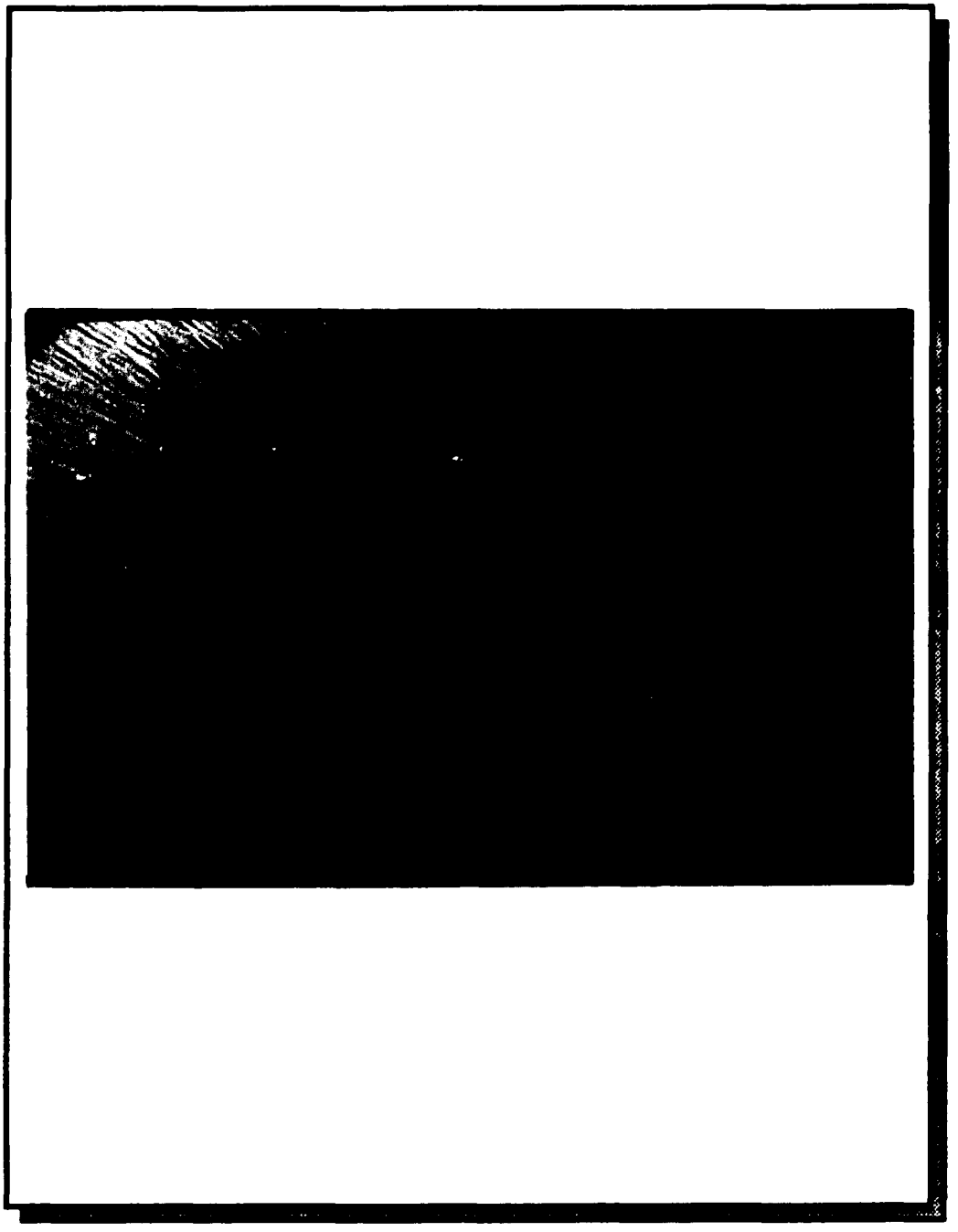

are jagged and the dots are not well-resolved. With the negative mask (Figure 7.12) the image lines are clear with sharp edges, and the dots are circular. The maximum resolution observable under an optical microscope with 100X magnification is 0.1 μm. However, it appears that under higher magnifications, possibly with an SEM, submicron resolutions could be observed.

The resolution of the iron oxide images is similar to those of tin oxide. Images of ~ 1.0 μm have been made, however it can not be critically analyzed under the optical microscope because the light is diffracted by the edges of the lines. Only under the SEM could an accurate resolution be totally defined, as already discuss.

Images of equivalent resolution to those obtained in PVG have been made in the TMOS xerogels (Figure 6.14). Although there is no difference at the microscopic level between the two, there are differences at the atomic level as mention in chapter 6. The iron oxide species formed in consolidated PVG shows hyperfine magnetic splitting, while that in the TMOS xerogel doe not. The difference in the Mossbauer spectrum indicates the formation of different metal oxides in consolidated PVG and the xerogel. Consequently, it is expected that their optical behavior would differ also since the optical properties depend in the index of refraction of the particular metal oxide deposited.

In summary, it has been demonstrated that images of ≤ 1.0 μm resolution have been made by the photolithographic deposition of metal oxides onto PVG. Image resolution is dependent upon the concentration of the precursor and the exposure times. The resolution is maintained even after the glass is collapsed to a nonporous state at ~ 1200°C.

7.2 Generation of diffraction gratings in porous glass.

When the cross section of a beam of light is limited by allowing the light to pass through one or more openings on an opaque screen, the distribution of the intensity in the transmitted beam observed on another screen is called a diffraction pattern. When the wave front from a source passes one or more obstacles and then proceeds directly to the point of observation without modifications by lenses or mirrors, the resulting phenomenon is known as Fresnel diffraction. If the diffracted wave is focused by a mirror or a lens, the result is known as Fraunhofer diffraction. Fundamentally, both types of diffraction are of the same nature and are explained by the Huygen's diffraction principle. [46]

The Fraunhofer diffraction grating is typically a series of clear slits and opaque bars of equal width. The energy from the source passes through the slits and it is diffracted into the various orders in accordance with the Young's diffraction equations. [47] In this type of grating, 50% of the energy is reflected and absorbed by the opaque part of the grating. The diffraction patterns obtained in our experiments by passing of a He-Ne laser beam through the glass, Figure 7.14, are due exclusively to the difference in the index of refraction between the glass and the photodeposited metal oxide. This type of diffraction grating is refered to as phase grating. The diffraction of the incident energy of a phase grating, relative to the source wavelength, is a function of the index of refraction of the substrate, the grating period, and depth of the grating. Up to 90% of the input energy can be effectively utilized in a phase diffraction grating since there are no opaque bars to block the energy.

As previously mentioned, the photolithographic technique can be used to impregnate any periodic pattern on the glass down to submicron resolutions. Consequently, the applications of this technique in the fields of Fourier optics and integrated optics has a tremendous future. In our laboratory, simply to demonstrate the possibility of its applications, we have been able to make crude diffraction phase gratings, binary phase gratings, and microscopic lenses.

7.2.3 Diffraction gratings.

Whenever a light wave encounters an obstruction with dimensions similar to the wavelength of the light wave, some energy in the wave is scattered. If the obstruction is periodic, or if there is a periodic variation of any parameter which affects the propagation of the wave, the energy will be scattered into discrete directions or " diffracted orders ", as shown in Figure 7.14. Any structure that acts in this way may be referred as a " diffraction grating ". For a wave in a diffracted order, the effect of the grating is to change the direction of propagation, and the amount by which it does depends upon the relationship between the wavelength and the period. In principle, by interacting with a suitable electromagnetic wave, any periodic structure may generate diffracted orders. Similarly, any wave motion may be split up into a spectrum provided that it interacts with a suitable grating.

Although any periodic structure can act as a grating, we will consider only a one dimensional array of equally spaced parallel lines in a plane. There are two basic types of commercially available diffraction gratings: a) Ruled gratings, and b) Interference Holographic gratings.

Figure 7.14 - Intensity of a He-Ne laser beam diffracted from a 10 μm SnO_2 slit on PVG and falling on a screen 1 m beyond.

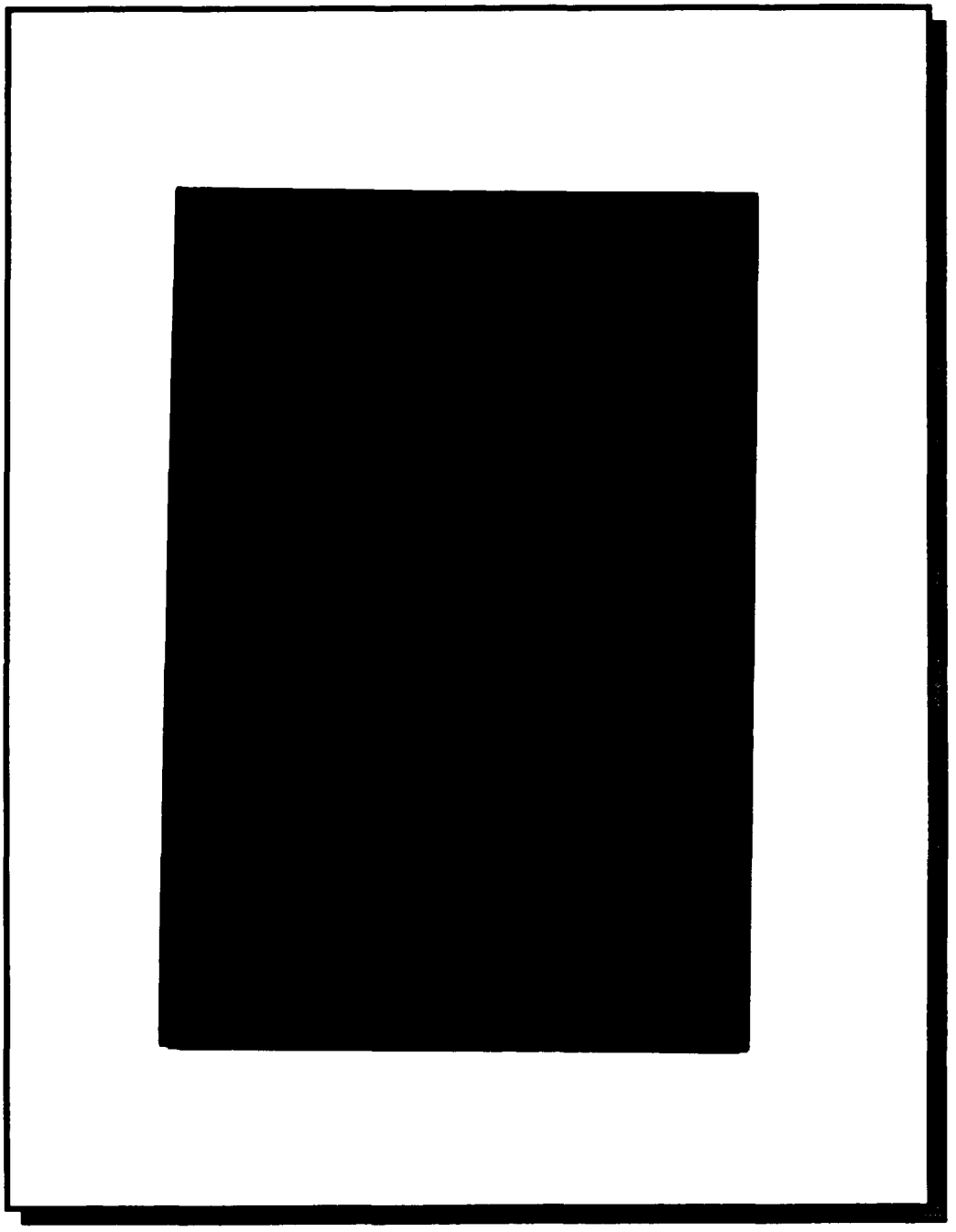

Ruled gratings present a problem in their manufacture because expensive diamond ruling tools have to be replaced often due to wearing and fracturing. Holographic gratings also present a problem in the deterioration with time of the photoactive polymeric material upon which the interference grating is generated.

The photo imaging technique previously demonstrated was used to fabricate diffraction gratings by photodepositing tin or iron oxide onto the surface of PVG, and TMOS gels. Gratings with line spacing of 160-, 80-, 20-, and 1-μm were made by contact printing using chrome Ronchi Rulings (Edmund Scientific) of equal line width and space width as the photomask. Figure 7.15 shows a tin oxide 20 μm line width grating as observed in an optical microscope before and after heat treatment to 1200 °C. Similarly, Figure 7.16 shows a 1 μm grating, although the resolution in this grating is difficult to observe by optical microscopy because of the diffraction of the light. As previously mentioned, the resolution of the gratings is maintained after the glass is consolidated at 1200 °C. Also, the resolution of the grating increases as the glass collapses, since the consolidation occurs with a 40% reduction in the glass volume. The photolithographic lines generated also experienced a proportional decrease in the line width. Consequently, a 1 μm line width in the grating before consolidation reduces to a 0.6 μm line width after consolidation. The grating spacings in commercially available grading range from 1.0 to 0.1 μm.

Further experiments are needed to characterize the optical properties of these photodeposited gratings. However, initial experiments show that the photolithographic gratings can be used to separate white light into different wavelengths. The optical bench used to establish this property is shown in Figure 7.17. With this set up, it was observed that the

Figure 7.15 - - 20.0 μm line width grating of photodeposited tin oxide onto PVG. (a) right after photolysis, (b) after consolidation.

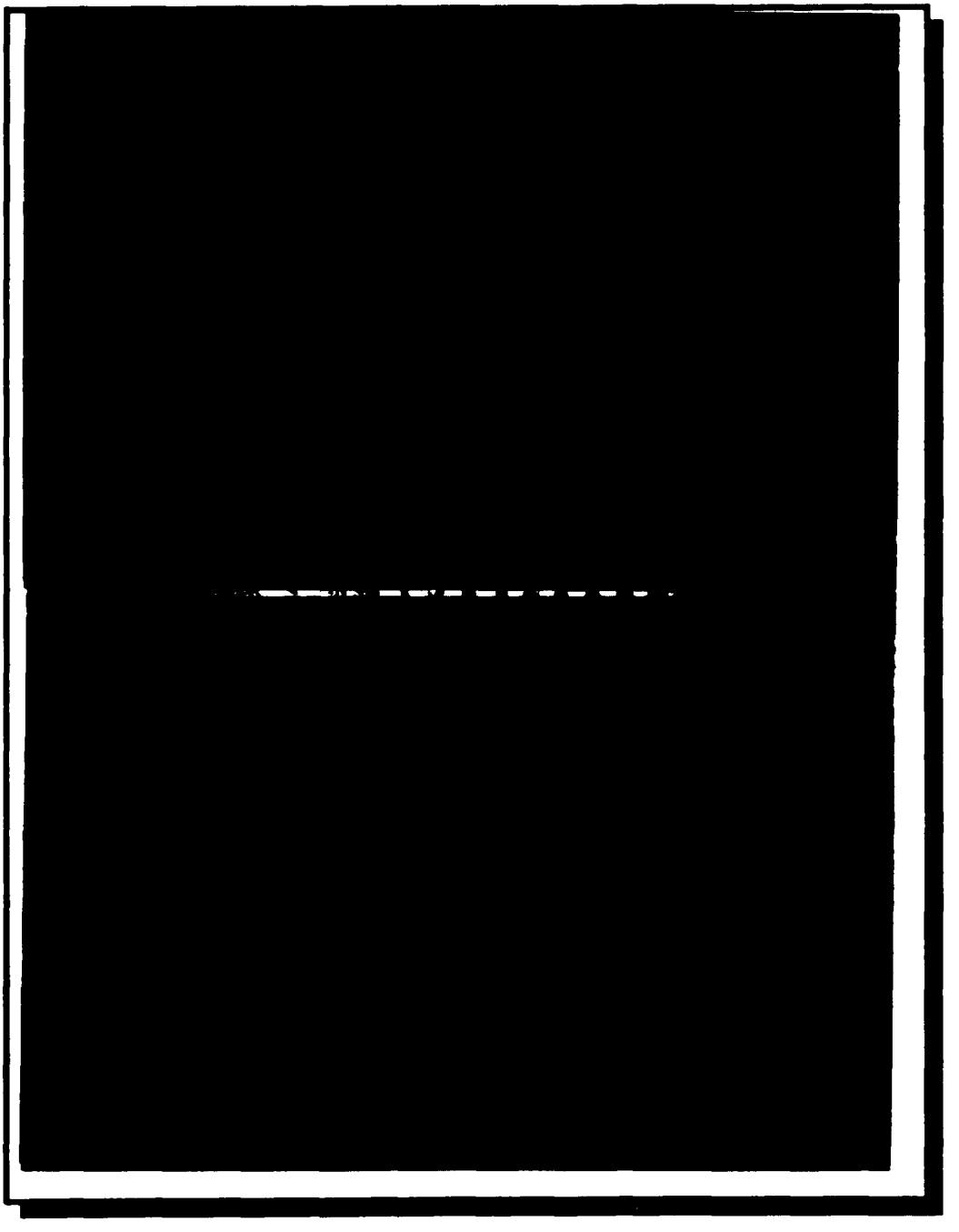

Figure 7.16 - 1.0 μm line grating of photodeposited tin oxide onto PVG after consolidation.

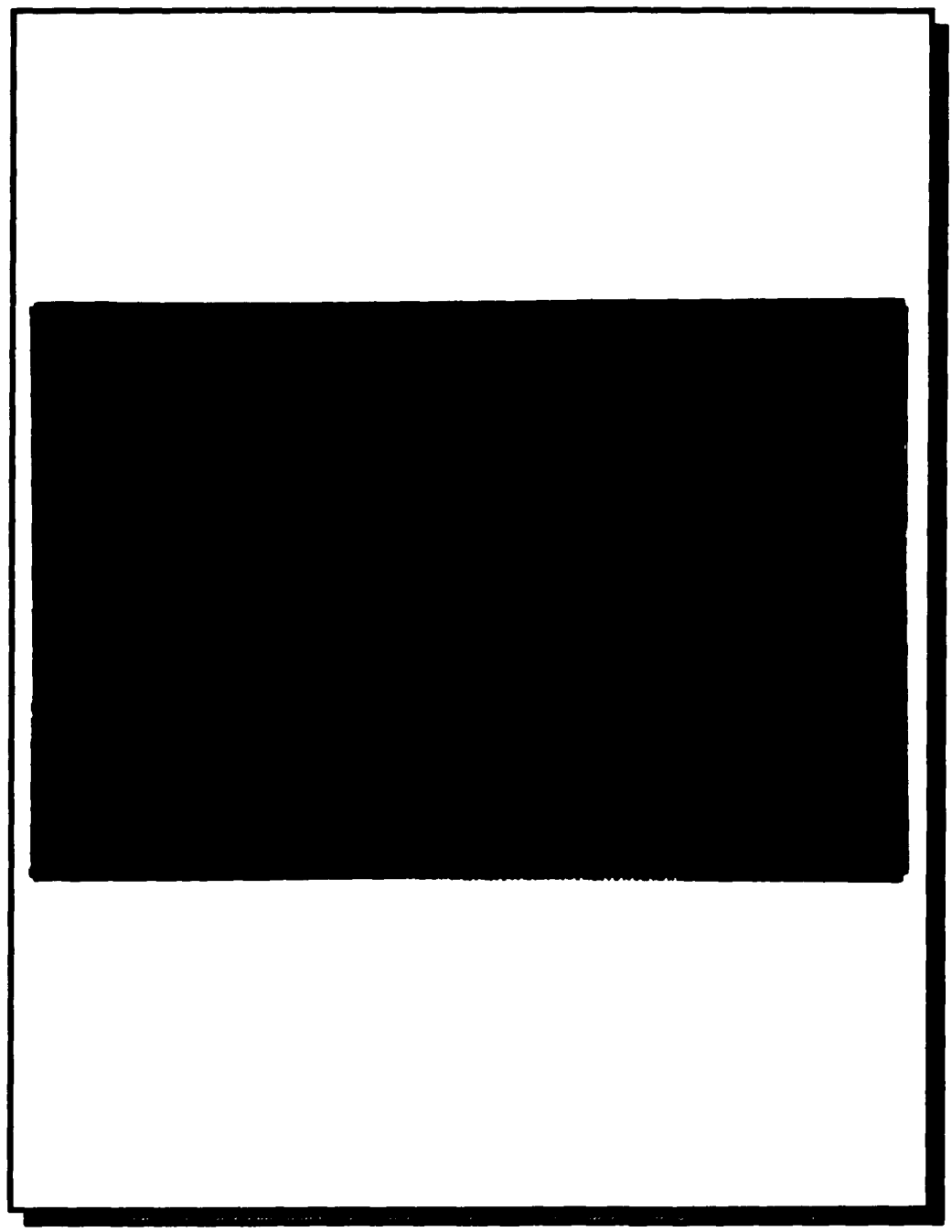

Figure 7.17 - Experimental bench set up for the observation of the diffracted orders of photodeposited phase gratings onto PVG and TMOS xerogels.

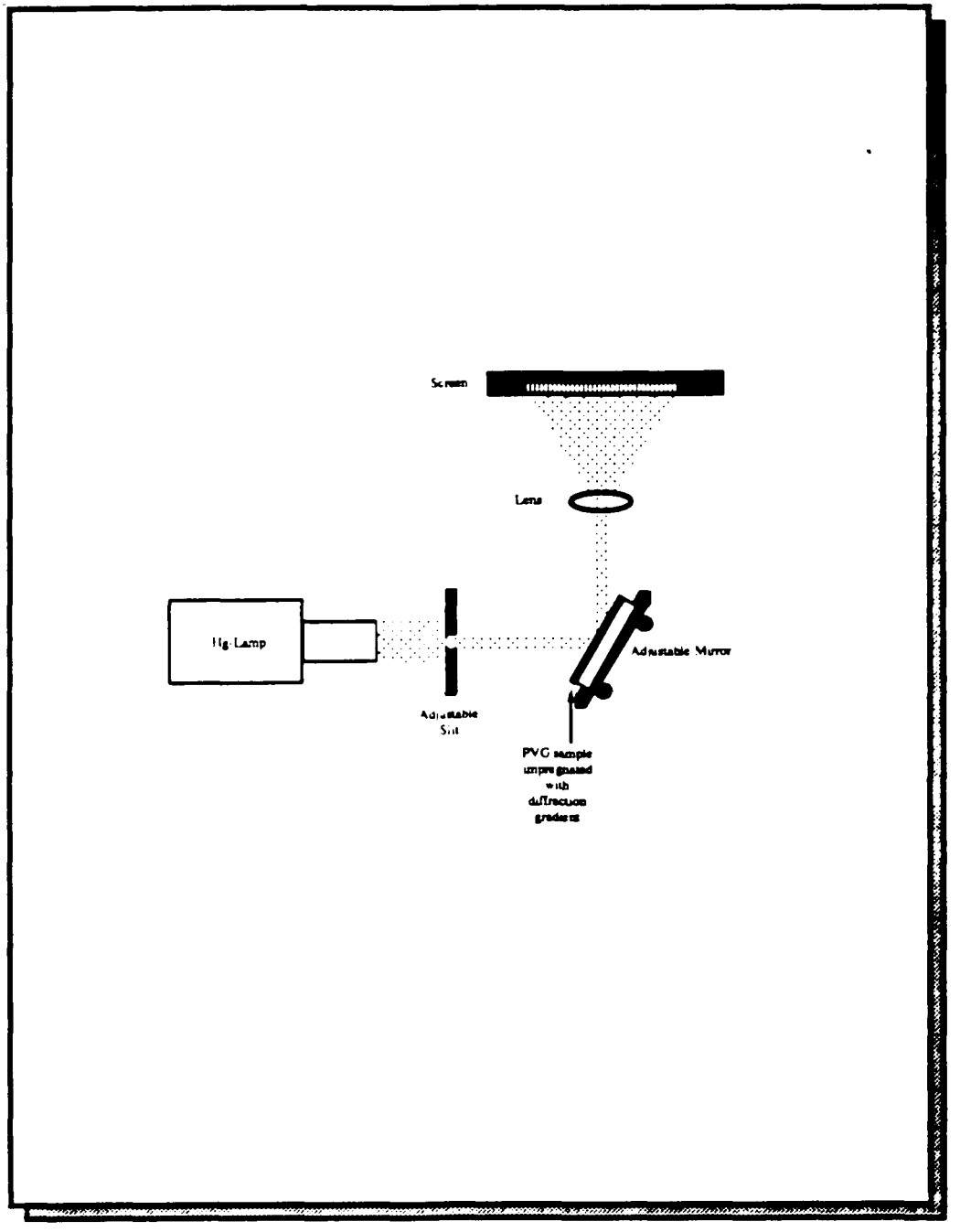

Figure 7.18 - Spectrum from a white light source after being reflected from 300 lines/mm SnO_2 photodeposited grating onto PVG.

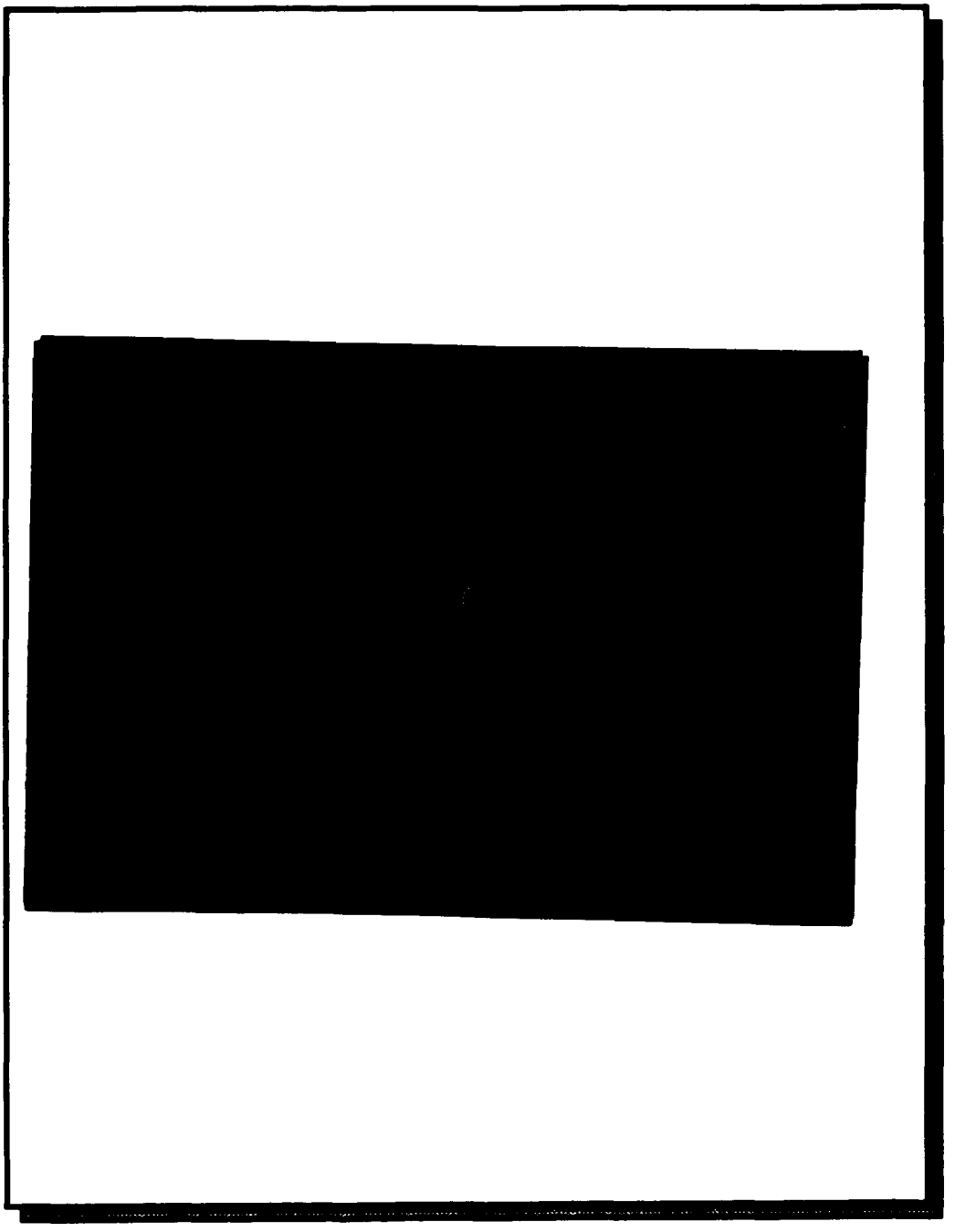

Figure 7.19 - Experimental bench set up for the generation of holographic gratings in PVG and TMOS xerogels.

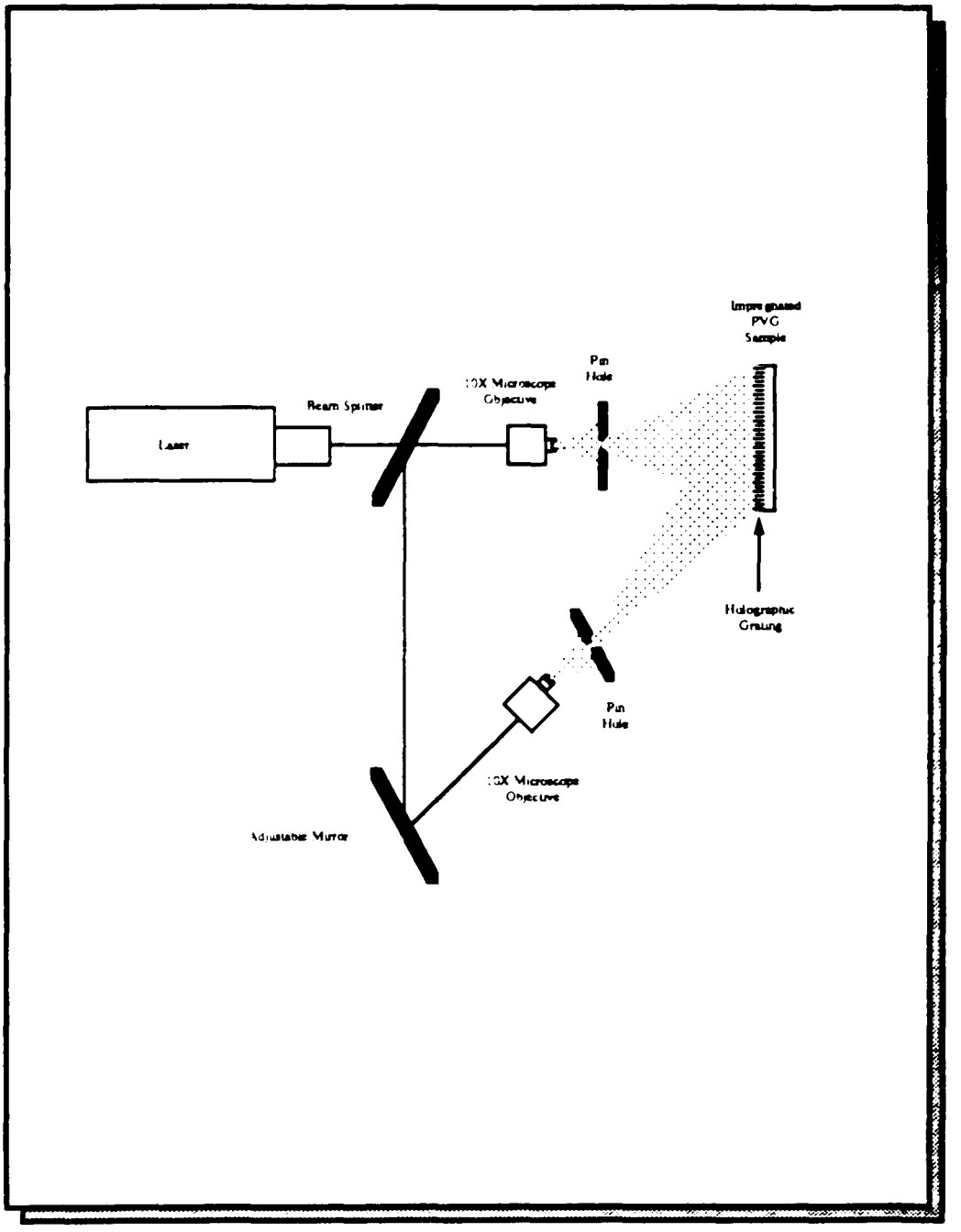

Figure 7.20 - Schematic diagram of microlens formation.

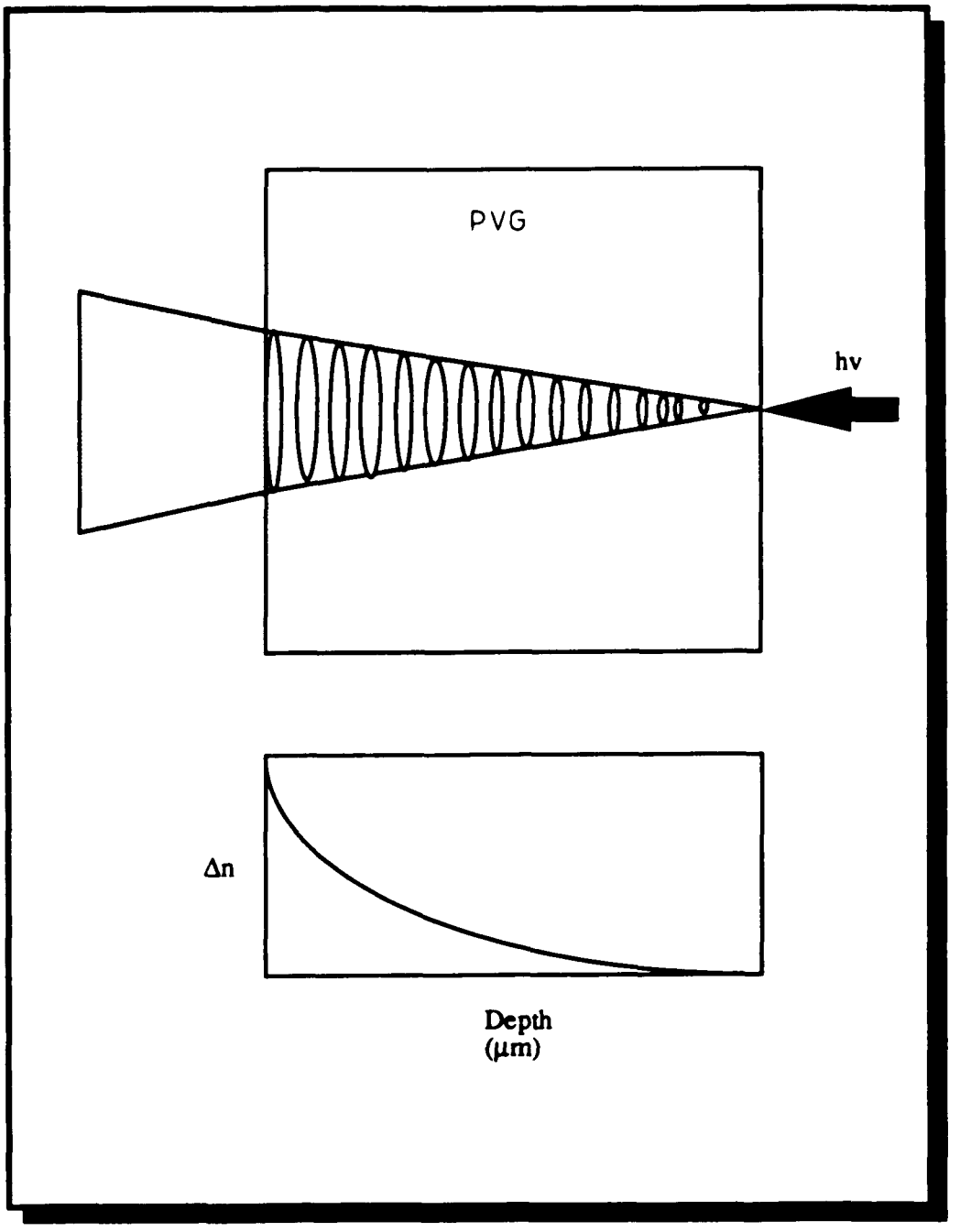

best separation of white light occurs at a 125 ° angle between the light path and the grating. The spectral separation obtained under these conditions is shown in Figure 7.18.

Further experiments are being conducted to characterize the efficiency, the spectral purity, and the resolving power of these gratings. Also, a holographic set up, Figure 7.19, is being build to generate holographic gratings onto PVG or xerogels. This optical set up has the potential to generate gratings of 3600 lines/mm.

7.2.2 Micro-lenses.

The basic components for digital optics have been identified as modulators and detector arrays, which in many cases, require two dimensional microlens arrays for imaging. The basic unit of the array is the individual microlens, which is a region with an index gradient embedded in a glass substrate as a result of selecting doping (Figure 7.20). The actual manufacture of this type of lens is difficult and often leads to optical aberrations, limiting the number of components that can be stacked together. Yet, they are ideal for many applications including beam splitting, and beam profile shaping commonly used in optical computing. [48]

Microlens arrays were made by the photodeposition of tin and iron oxide onto PVG and TMOS xerogels using the already described microlithography technique. Cupper grids of 200 to 1000 mesh size (SPI Supplies) were used as photomasks. Figure 7.21 shows a backscatter micrograph of 50 μm^2 square lens made by the photodeposition of SnO_2. The micrograph shows contrast as a function of differences in atomic masses. The micrograph shows a spherical contrast distribution in the

region where SnO_2 was deposited. The contrast profile, which is a function of concentration, is proportional to the index change.

The microlenses produced take advantage of the change in the index of refraction in the exposed region to change the direction of the incident light. Since the index change is relatively constant within the lens profile, the optical characteristics of the microlens depend only on the value of Δn (n=index of refraction) and the lens shape. Therefore, by varying the mask design parameters, such as the shape of the basic pattern, spacing between each element, exposure time, and concentration of the metal oxide, different types of microlenses have been made. The basic structure of the photodeposited microlens is shown in Figure 7.8. The microlens has a conical depth distribution, and the index profile follows the same distribution. In order to avoid optical aberration due to the depth profile distribution, high metal oxide concentrations, high exposure intensities, and relatively short exposure times are required.

Figure 7.22 shows an enlarge view of a Fresnel lens photodeposited on a PVG plate. The same image has been reduced by a factor of 10^4 and microlithographed onto PVG with comparable resolution. This generates 10^4 arrays of microlenses (2.54 μm in diameter) onto a PVG plate. These types of arrays are shown in Figures 7.23 and 7.24 where square and hexagonal arrays have been photodeposited to be used for the fabrication of binary phase gratings.

7.2.1 Binary phase gratings.

Binary phase gratings (BPG's) are key components as interconnects in decision-making planes in an optical computing system, [49,50] since they

Figure 7.21 - Backscatter SEM micrograph of a 50 μm^2 square array of photodeposited SnO_2 microlens.

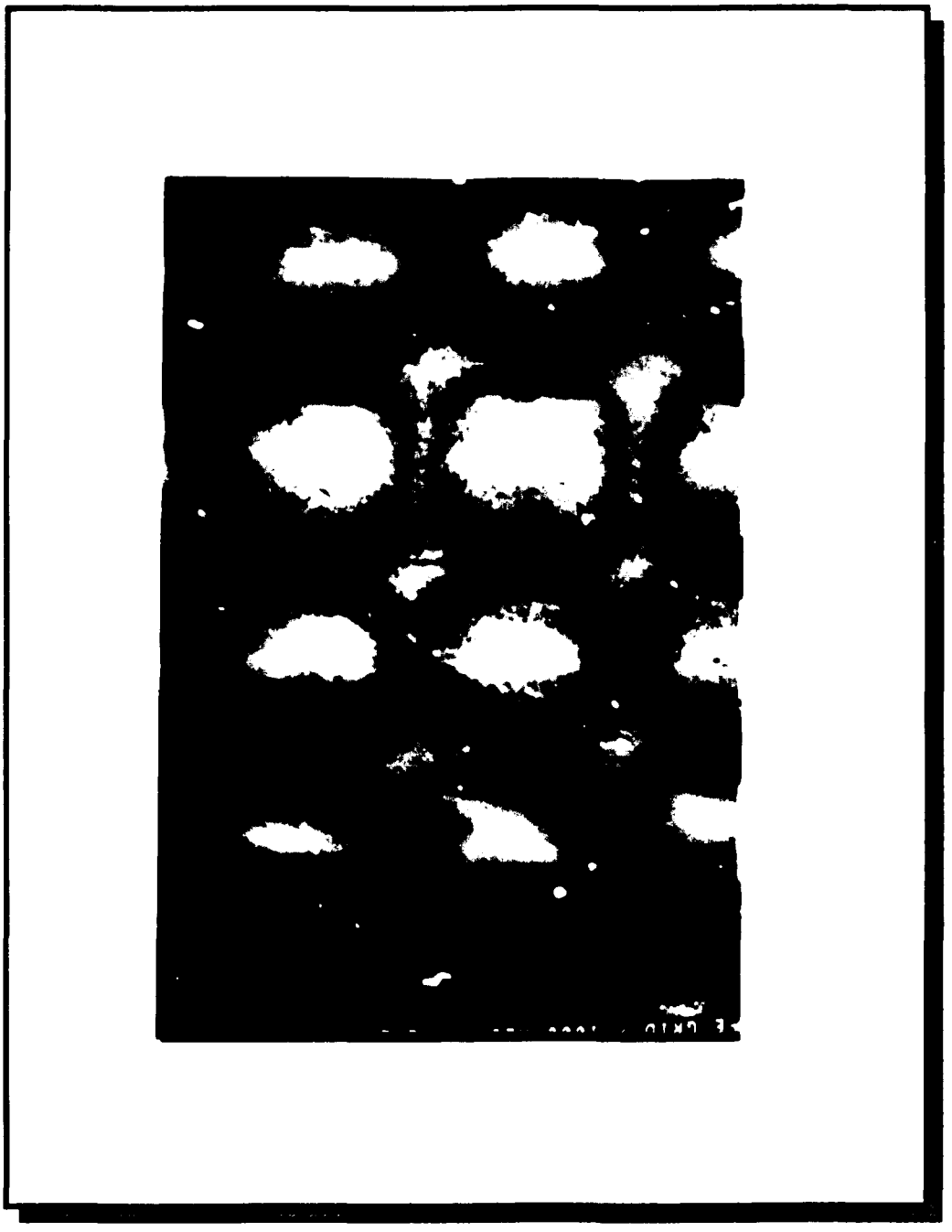

Figure 7.22 - Fresnel lens pattern made by the photodeposition of SnO_2 onto PVG.

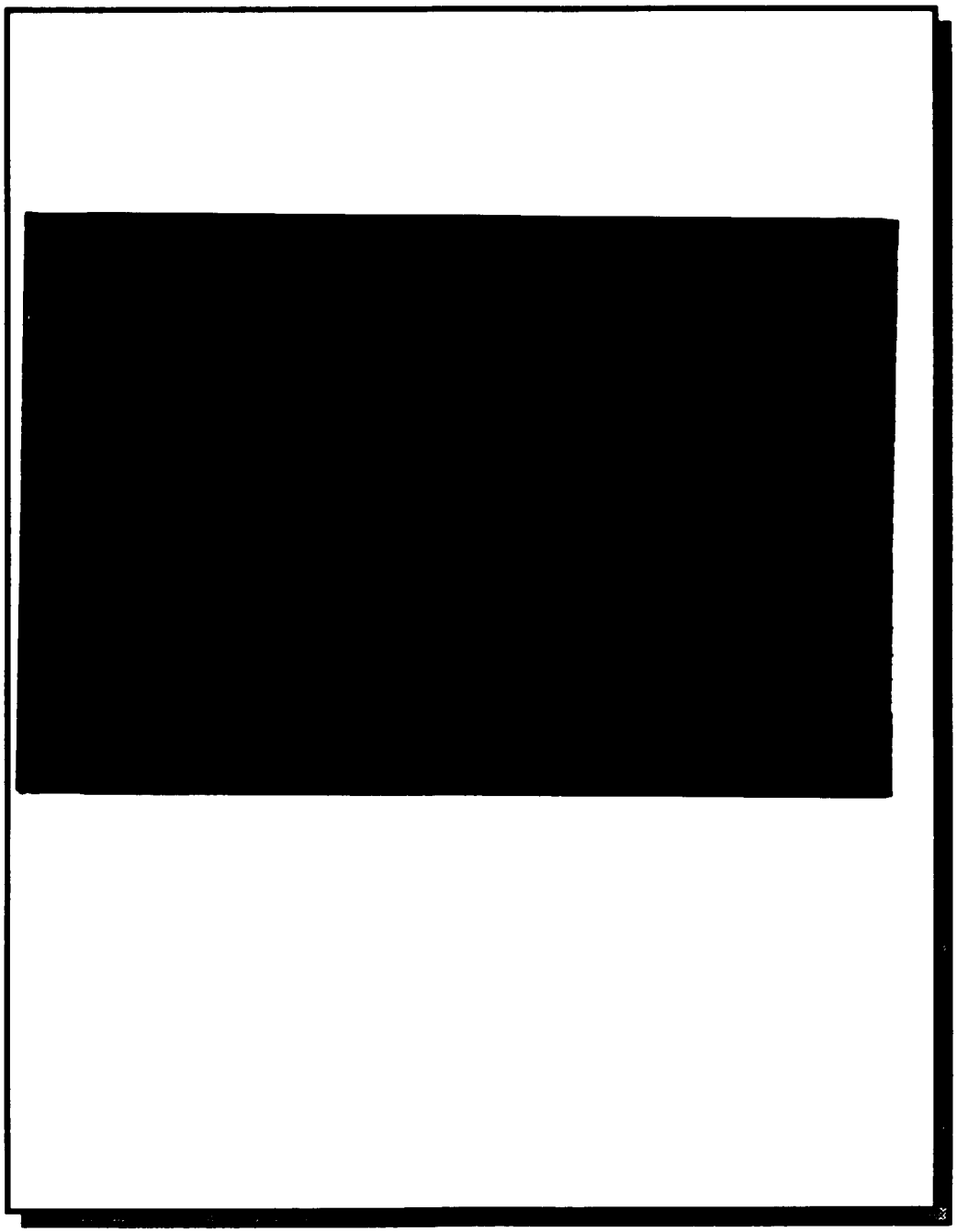

Figure 7.23 - Optical micrograph of a 5.0 μm^2 square array of photodeposited SnO_2 microlenses onto PVG.

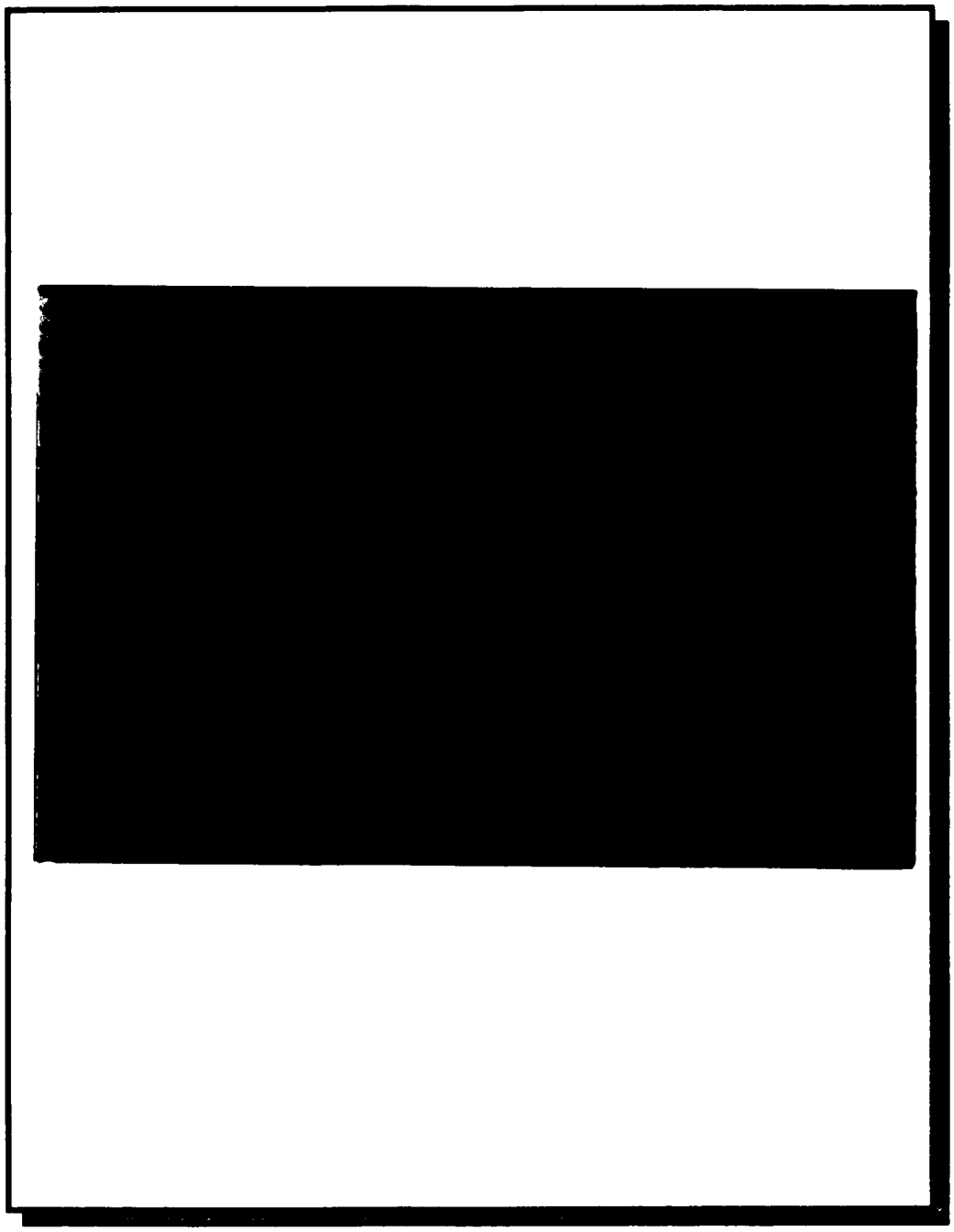

Figure 7.24 - Optical micrograph of a 5.0 μm^2 hexagonal array of photodeposited SnO_2 microlenses onto PVG.

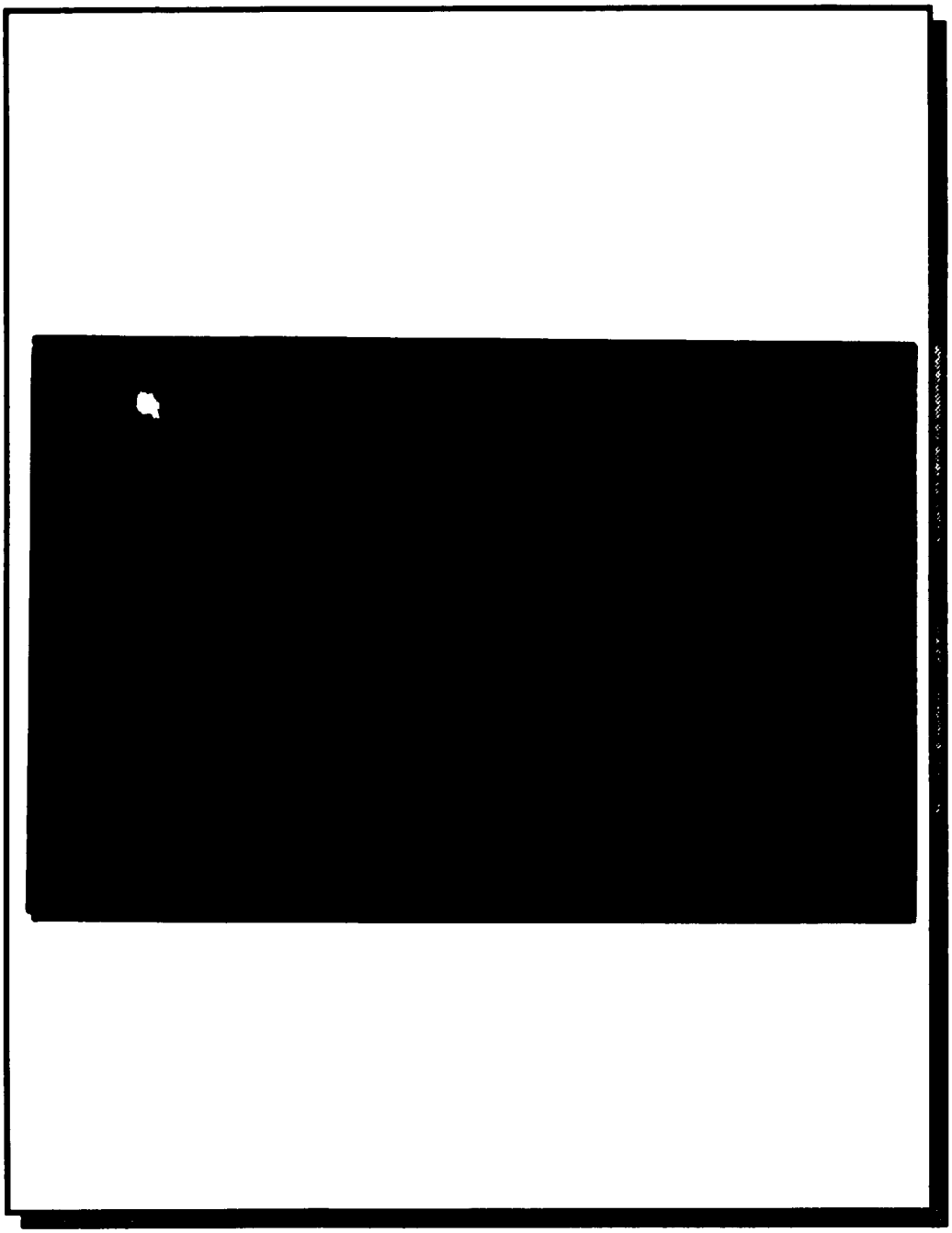

offer the unique advantage of multiplexing several interconnections in thin, lightweight recording materials. The requirements in the fabrication of BPG's are: a) high optical efficiency thereby reducing optical input power; b) lightweight and compact; c) a reasonable misalignment tolerance; and d) a reasonable wavelength tolerance. Achieving the combination of recording materials and recording techniques to achieve the desire properties is a challenge.

BPG's capable of generating equal beam intensities were made by the photodeposition of SnO_2 and Fe_2O_3 oxide microlenses on PVG or TMOS xerogels, Figure 7.25. The characteristics of the 2-dimensional array depends in the choice of a suitable phase grating, which in this case depends in the configuration of the photomask. The approach taken here was to use a commercially available diffraction program (DAFRAC from Drexel Inc.) to generate the desire diffraction array, the program then produced the required graphic element for the photomask, Figure 7.26.

Although the BPG's designed can be used to generate multiple equal beams, their diffraction efficiencies are limited to the existence of undesired high diffraction orders, Figure 7.27-28. To prevent this error, the BPG is designed so no two adjacent spots interfere with each other. Assuming that the BPG has diffraction limited performance and is illuminated by a uniform, normal, incident beam, the grating equation

$$d \sin\theta_1 = \lambda \qquad 7.1$$

shows that the relationship between the grating period d and the diameter D of the incident beam is

Figure 7.25 - 6 x 6 hexagonal spot array diffraction pattern produce by cascading a BPG made by the photodeposition of SnO_2 microlenses onto PVG.

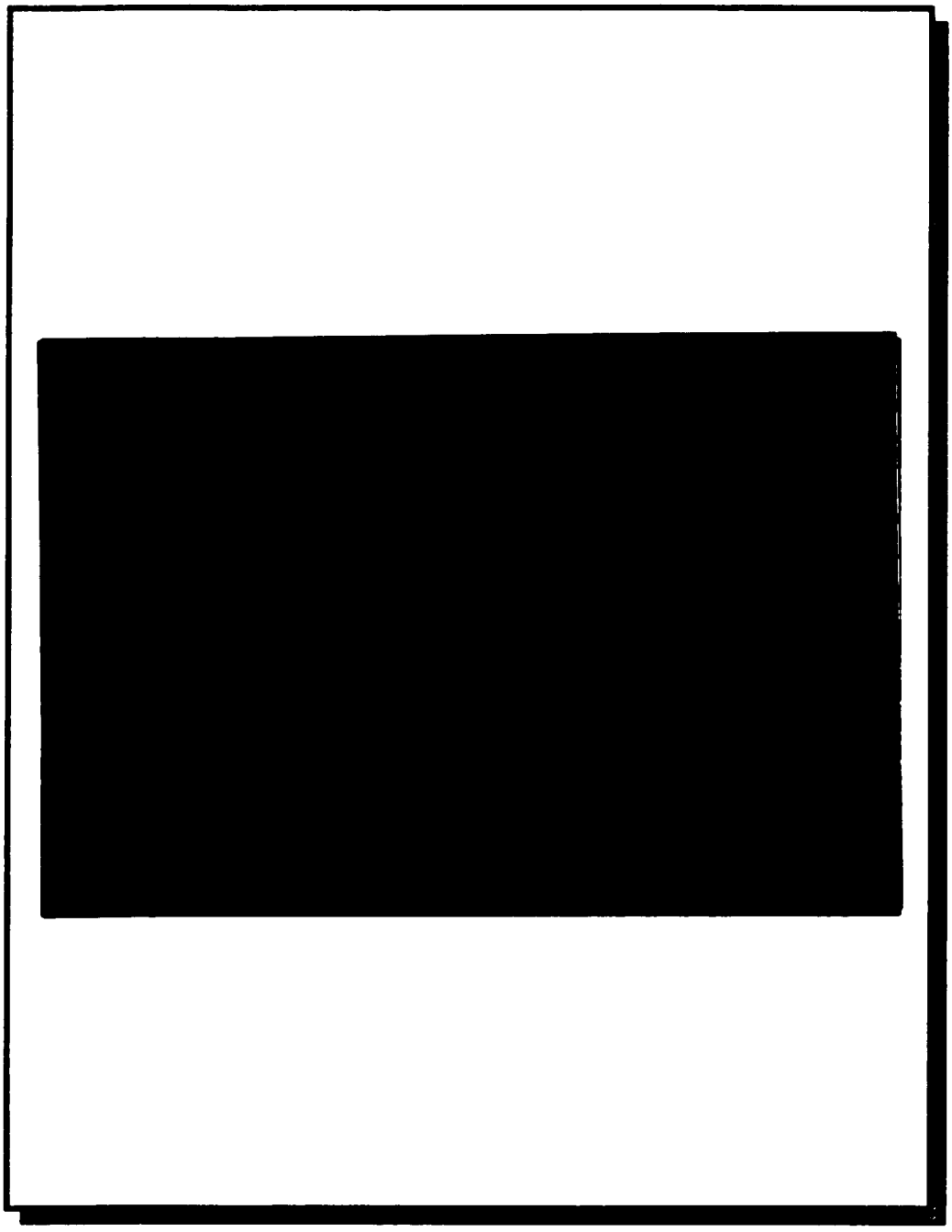

Figure 7.26 - Mask of a post-cript generated distribution of Fresnel zone plates.

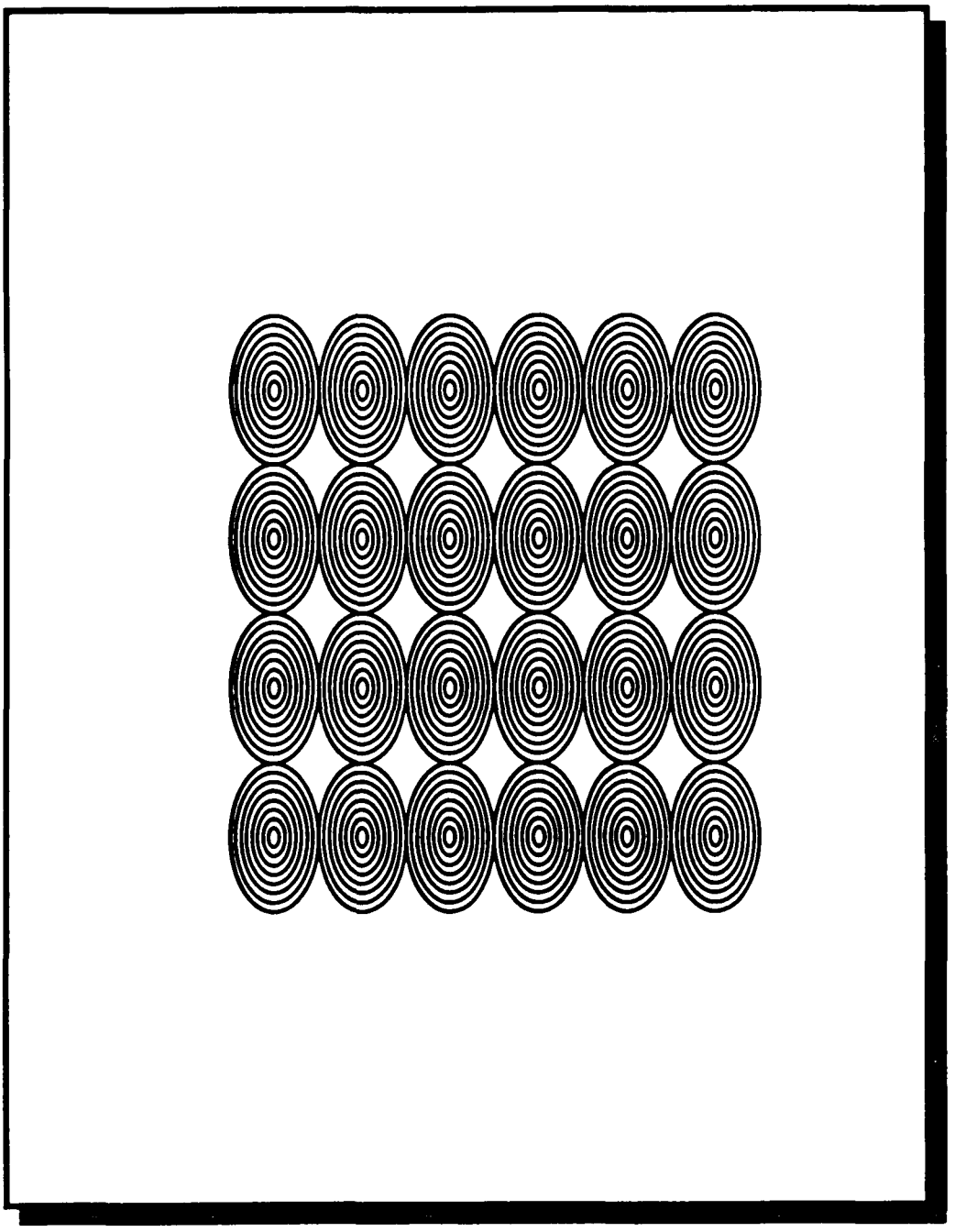

Figure 7.27 - Schematic diagram showing the 1 x m equal intensity beams generated by a BPG.

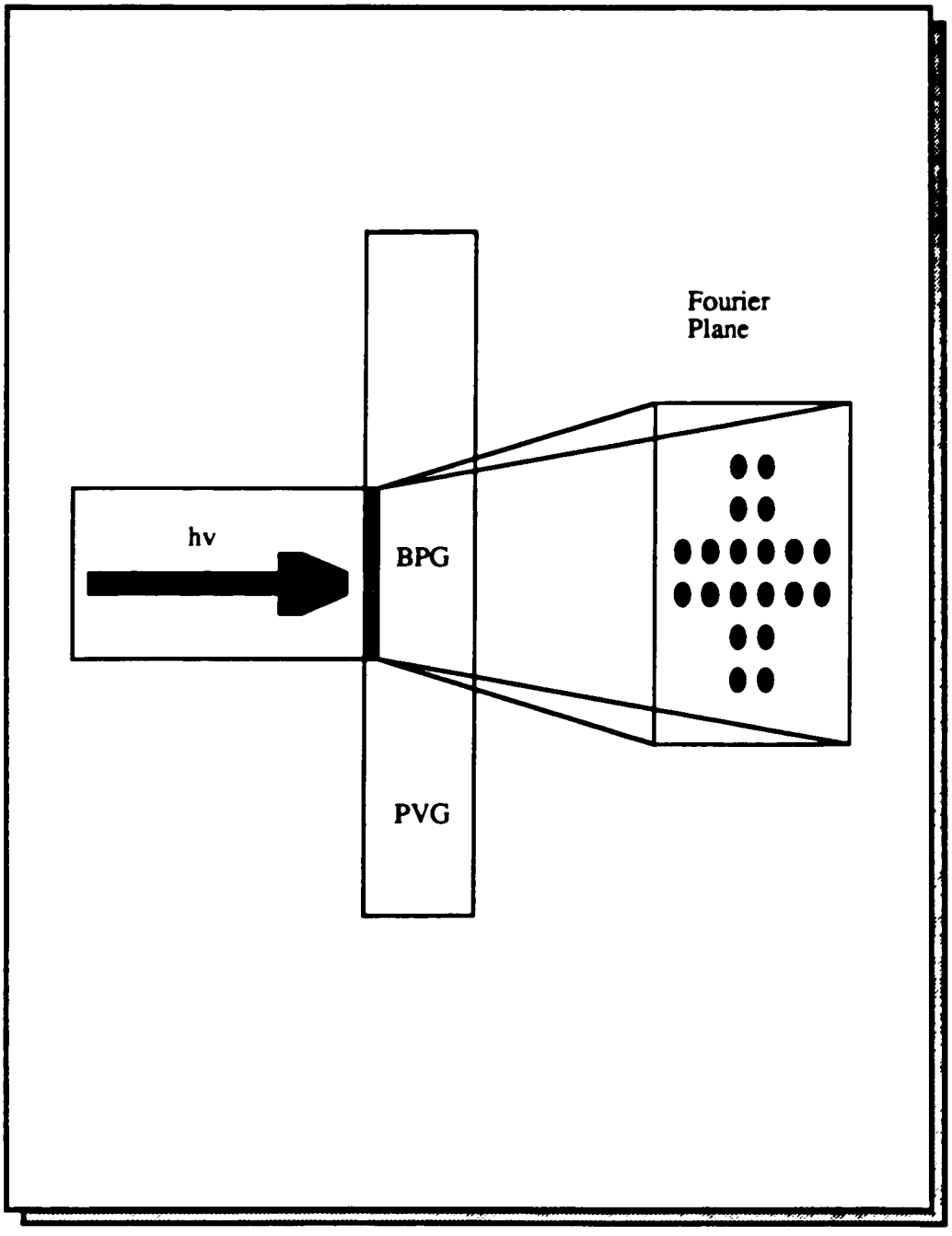

Figure 7.28 - Higher order diffraction beams observed from a 3 x 3 BPG diffraction pattern made by photodeposition of SnO_2 onto PVG.

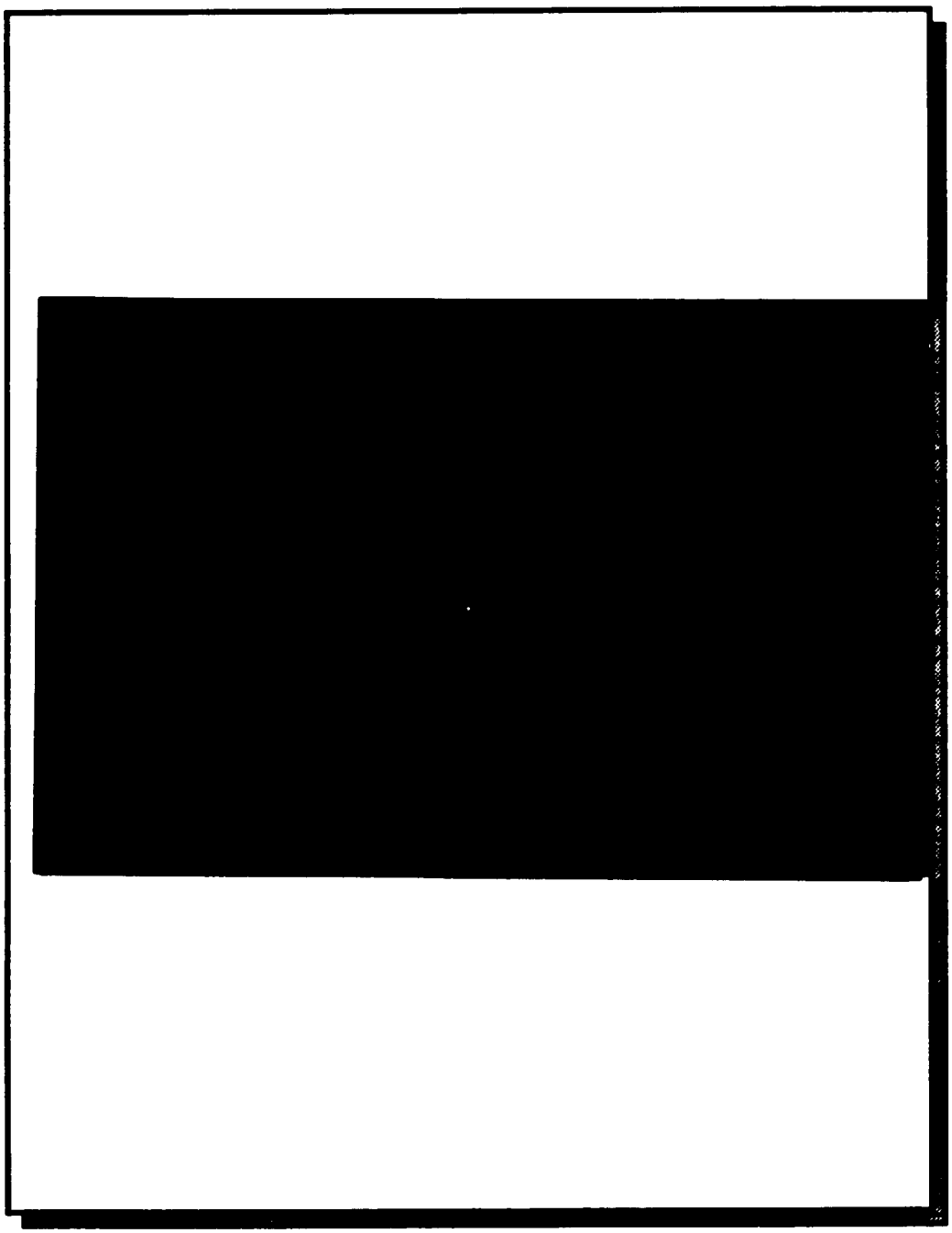

$$d \leq \left[\left(\frac{D}{2.44}\right)^2 + \lambda\right]^{1/2} \approx \left(\frac{D}{2.44}\right) \qquad 7.2$$

where λ is the illumination wavelength. In other words cross-talk is prevented when the diameter of an incident beam is at least 2.5 times greater than the grating period. In these experiments, the diameter of the incident beam was 100 μm, while the grating space range from 50 to 1.0 μm.

The results presented clearly demonstrate the capability to construct BPG's in porous glasses. The efficiency of the BPG's is being evaluated for maximum spatial performance.

7.3 Passive integrated optic devices.

Passive waveguides in glasses are considered to be prime candidates for integrated optic (IO) device applications such as star couplers, access couplers, wavefront sensors, multiplexers, demultiplexers, and in sensors such as gyroscopes. The importance of the glass waveguide-base IO components is borne out by their compatibility with optical fibers, potential low cost, and propagation losses. However, strict tolerance requirements are placed on passive components as the glass index cannot be varied by an applied external field. Fabrication of devices such as multiplexers calls for reproducibility in the propagation of the guided mode of the order of 10^{-4}. In order to fabricate glass waveguide devices with such reproducible

characteristics, it is necessary that the role of the processing parameters of the waveguide structure be well understood.

7.3.1 Waveguide processing :

An illustration of the formation of a planar waveguide using the photolithographic deposition of tin (~$1.0x10^{-4}$ mol ads./g) and iron (~$1.0x10^{-7}$ mol ads./g) oxides on PVG and/or TMOS xerogels is shown in Figure 7.29. Planar waveguides, ranging from 1-100 μm in width were made using this technique. The technique involves the photodeposition of a metal oxide into the glass substrate. The deposited metal oxide then adds as a gradient index modifier upon consolidation of the porous glass.

The characterization of the optical waveguides, which is obviously important, is not easy, because of the extreme thinness of the layers. The parameters to be measure are the width, the thickness, the refractive index, the shape of the index gradient, and the losses.

7.3.2 Width and thickness of waveguides.

The width of the planar waveguide is controlled by the resolution of the photomask used. The width of the deposited waveguide is readily measure by optical microscopy techniques. The thickness of the waveguides range from 10- to 500-μm. The parameters that controlled the thickness of the waveguide are : (a) the concentration of the organometallic precursor, and (b) the exposure time to the excitation source. The thickness profile can be measure from the cross-sectional cut of the waveguide by optical microscopy, (Figure 7.7). However, more accurate measurements are

Figure 7.29 - Optical micrograph of a 50 μm (width) planar waveguide photodeposited onto PVG.

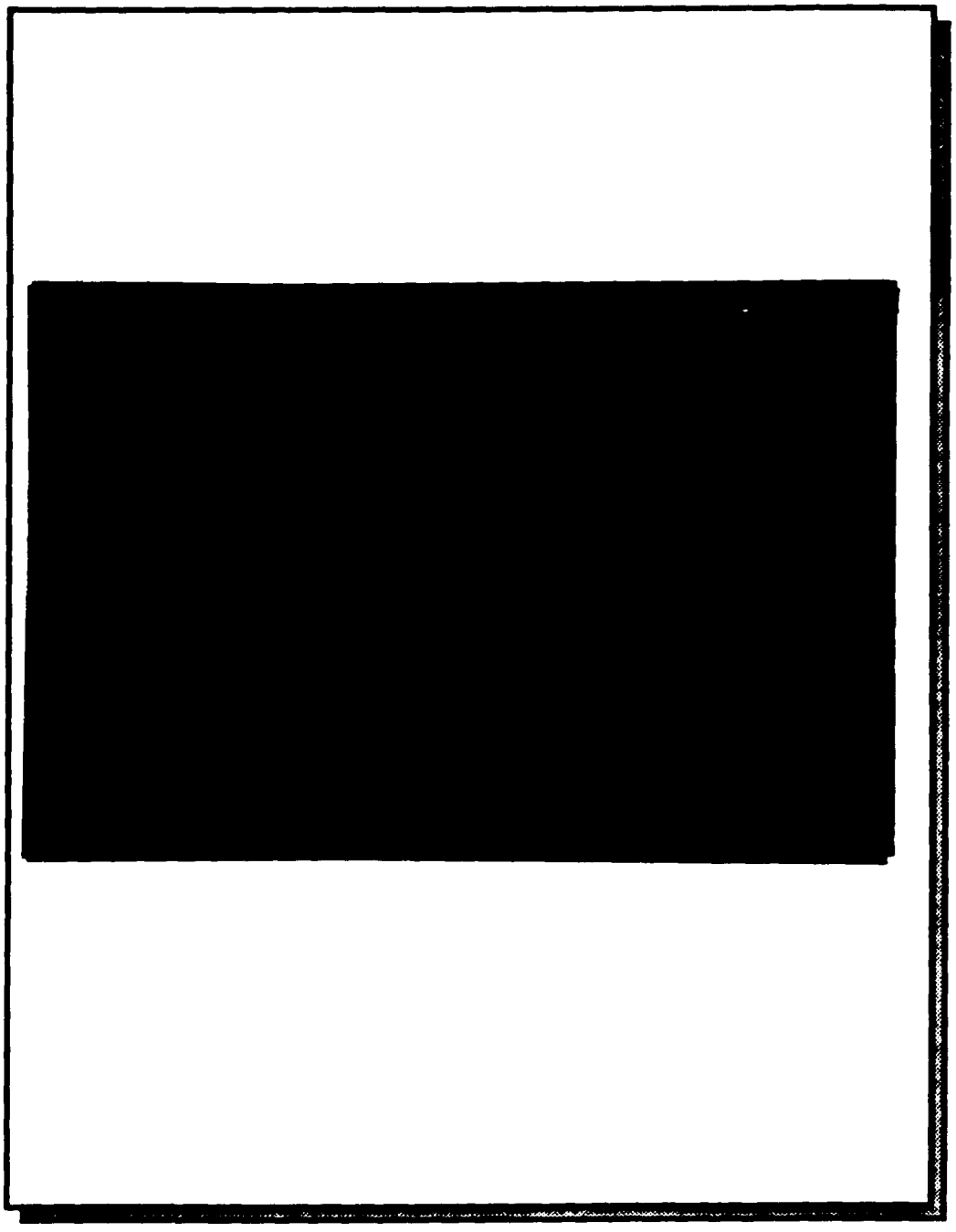

made from x-ray profiles obtained from SEM, TEM or TXRF, (Figures 7.25-27).

7.3.3 Index of refraction.

The index of refraction in the waveguide was calculated from direct measurements of the angle (α_c) at which total internal reflection occurs (Figure 2.17). A standard 10 μm waveguide was fabricated by the impregnation of (CH3)3SnI (10^{-4} mol/g) onto PVG, followed by exposure for 5 minutes with a 400W Hg flash lamp, and heat treated to 1200 °C. The calculated index of refraction for the standard waveguide varied from 1.551 to 1.601 ± 0.050, using an index of refraction value of 1.500 for PVG. The index of refraction in the tin oxide impregnated PVG agrees with a previous measurement made by the Corning laboratories using Mach-Zhender interferometry (Δn = 0.1 to 0.001). [51]

7.3.4 Gradient index profile.

The gradient index profile of the buried waveguides depends on various parameters in an intricate manner. The purity of the host glass, the nature and concentration of the metal oxide deposited, the diffusion of the metal oxide onto the glass, and the time and power of the excitation source, all affect the index profile. There are several techniques for directly measuring the gradient index profile in waveguides. These include interferometry, [52] reflectivity measurements, [53] and the inverse WKB method which relies on mode indices data. [54] By far interferometry is the most accurate technique.

The gradient index profile can also be obtained by indirect methods,

such as, the measurement of the metal oxide concentration. It has been previously demonstrated that the concentration profile gives the gradient index profile. [55, 56] In all the cases a good agreement between the chemical concentration and the gradient index profiles has been reported. Figure 7.30 shows the predicted gradient index profile for a tin and iron oxide waveguides. base on concentration data. The concentration profiles for the tin and iron oxide waveguides on PVG were obtained from x-ray data obtained from TXRF measurements, as discussed in chapter 6.

7.3.5 Loss measurements.

The use of low loss devices in optical communication systems is an important requirement for success. Therefore, it is important to be able to measure accurately the losses of individual modes, as well as the mode conversion of optical waveguides. The most widely used method for measuring the attenuation in a waveguide is to measure the transmitted power as a function of the waveguide length. In this method, all the energy flowing through the waveguide must be collected by a detector. The fundamental method is to introduce a known optical power into one end of the waveguide and measure the power emerging from the other end. However, there are many problems and inaccuracies inherent in using such a simple approach. For example, coupling losses at the input and output are not known, and can largely obscure the true waveguide loss per cm. Also, if the waveguide is multimode, losses attributed to individual modes cannot be separately determined.

Figure 7.30 - Predicted gradient index profile of metal oxide planar waveguides buried onto porous glasses.

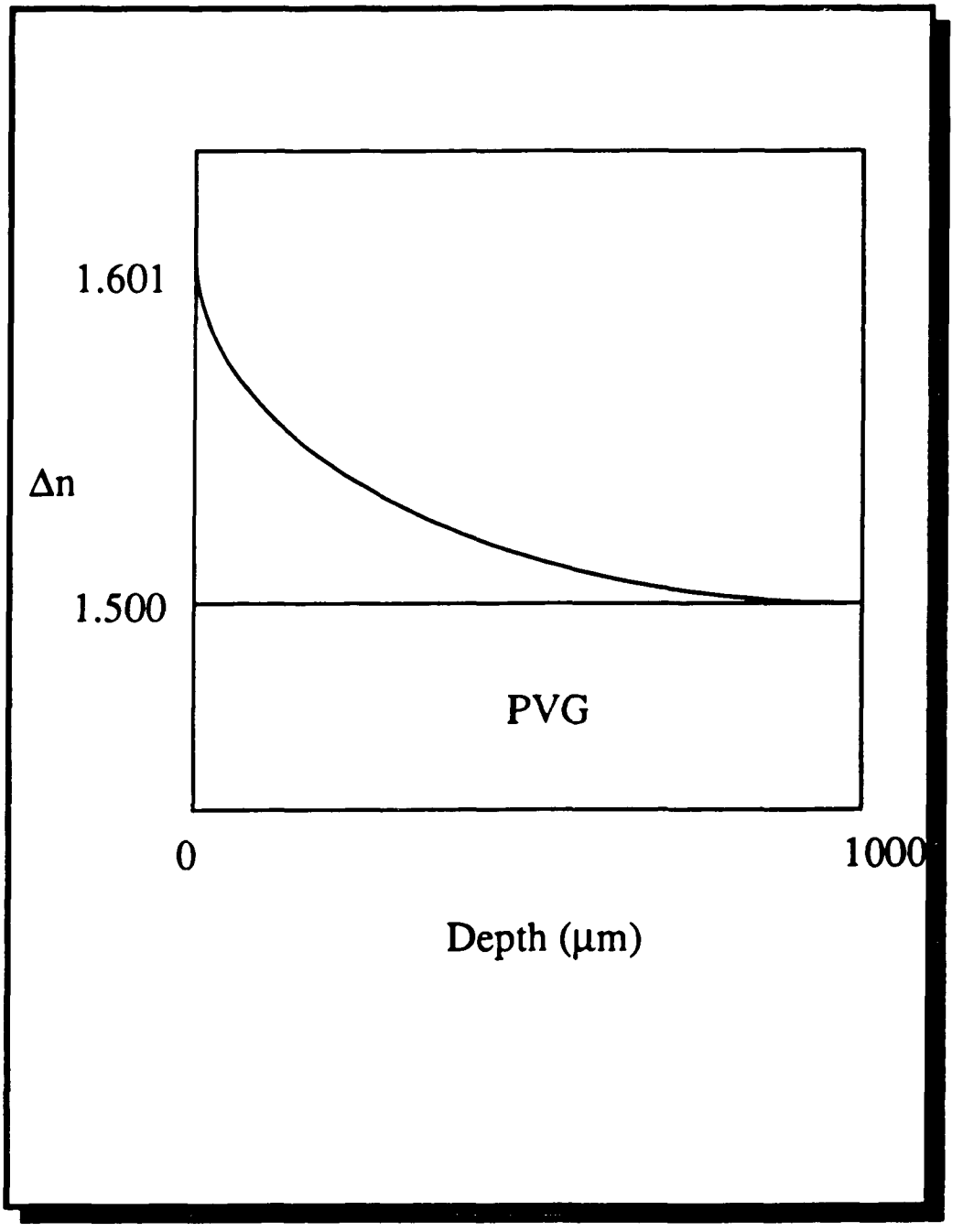

The method used to measure the waveguide loss in the standard SnO_2 waveguide was to focus a Ar^+ ion laser beam directly onto a polish input face of the waveguide as shown in Figure 2. 18, and then measure the total power transmitted. The measurement was repeated for a number of waveguide samples of different length, but otherwise identical. Care was taken to align the laser beam and the sample for maximum coupling power before each measurement. The resulting loss data falls in a straight line when the log of the transmitted power vs. the waveguide length is plotted as shown in Figure 7.31. The loss coefficient is obtained from the slope of the line. From the graph it was determine that the loss of the SnO_2 waveguide is ~0.6 dB/cm. The extent of the scatter of the data points is a measure of the consistency of the sample input/output coupling loss, which depends on face preparation, and on sample alignment. Any departure of the data from a straight line is an indication of experimental error. For example, the increasing differential loss in Figure 7.31 for samples with length greater than 20 mm is cause by the aperturing of the output beam, which spreads laterally to an extent that cannot be collected completely by the output lens.

Since waveguide bends are a necessary part of all but the simplest IOC's the radiation losses from a curve waveguide must be considered in circuit design. The minimum allowable radius of curvature of a waveguide is generally limited by the radiation losses rather than by fabrication techniques. There are two broad categories of loss mechanisms due to waveguide bends. The first is a power loss due to the curvature of the waveguide developed by Marcatilly [57] and Marcuse. [58] The second is the power scattered from the fundamental mode when incident on a junction between two nonidentical waveguides. [59] In order to calculate the curvature

Figure 7.31- Attenuation measuarement for SnO_2 planar waveguide buried onto PVG.

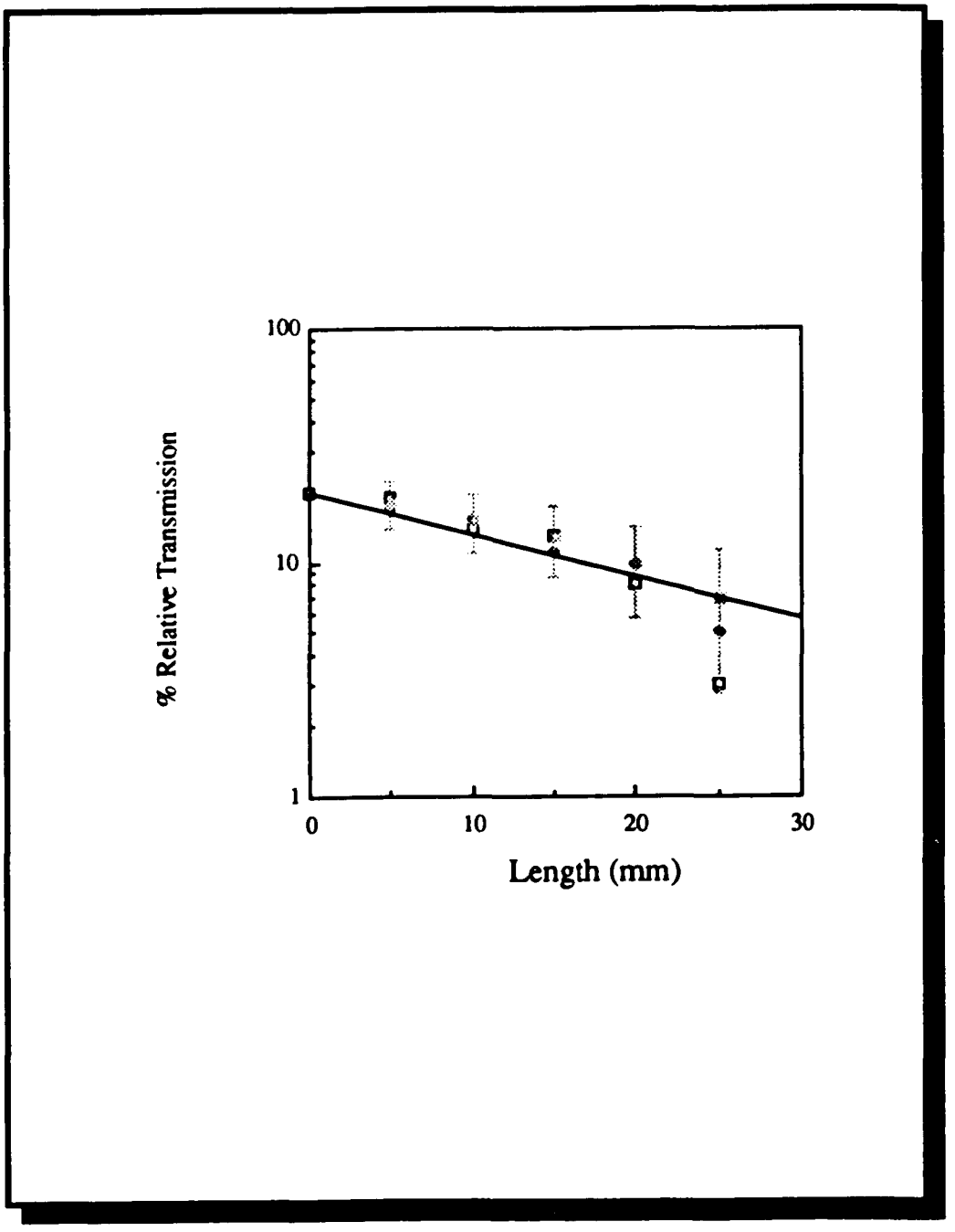

loss an accurate determination of the waveguide parameters and its associate mode parameters is required.

Figure 7. 32 shows a He-Ne laser beam launched into a planar SnO_2 waveguide with a 2.54 cm radius of curvature. The configuration of the bend waveguide is shown in Figure 7.33. In this case, the losses are due to the junction of the straight to curve waveguide, and the radiation loss due to the curvature of the waveguide. The waveguide losses were obtained, as previously described, by measuring the input and the output powers of a series of waveguides having a different radius of curvature. Results for the straight to curve junction are shown in Figure 7.34.

7.3.6 Waveguide couplers.

Multimode fiber-optic systems currently use couplers for data distribution to several user terminals. Couplers are made by fiber optic (fussing, tapering, lapping, and gluing), micro-optic components (microlenses, and beam splitters) and planar waveguide technologies. The cost of mass produced couplers is severely affected by the reproducibility of the fabrication technique. In the fiber optic and micro-optic technologies, the problem of reproducibility is quite severe.

The planar waveguide fabrication approach previously describe directly attacks the problems of reproducibility, one-by-one fabrication, and precise placement of components, which are controlled by using photolithographic technology. The basic processing steps are : (a) mask deposition, (b) pattern definition, (c) and metal oxide diffusion.

The first devices studied were planar waveguide splitters. Figure 7.32 and 7.33 shows the top view of a PVG plate where a He-Ne laser beam has

Figure 7.32 - He-Ne laser beam launched into a SnO_2 waveguide with a 2.54 cm radius of curvature.

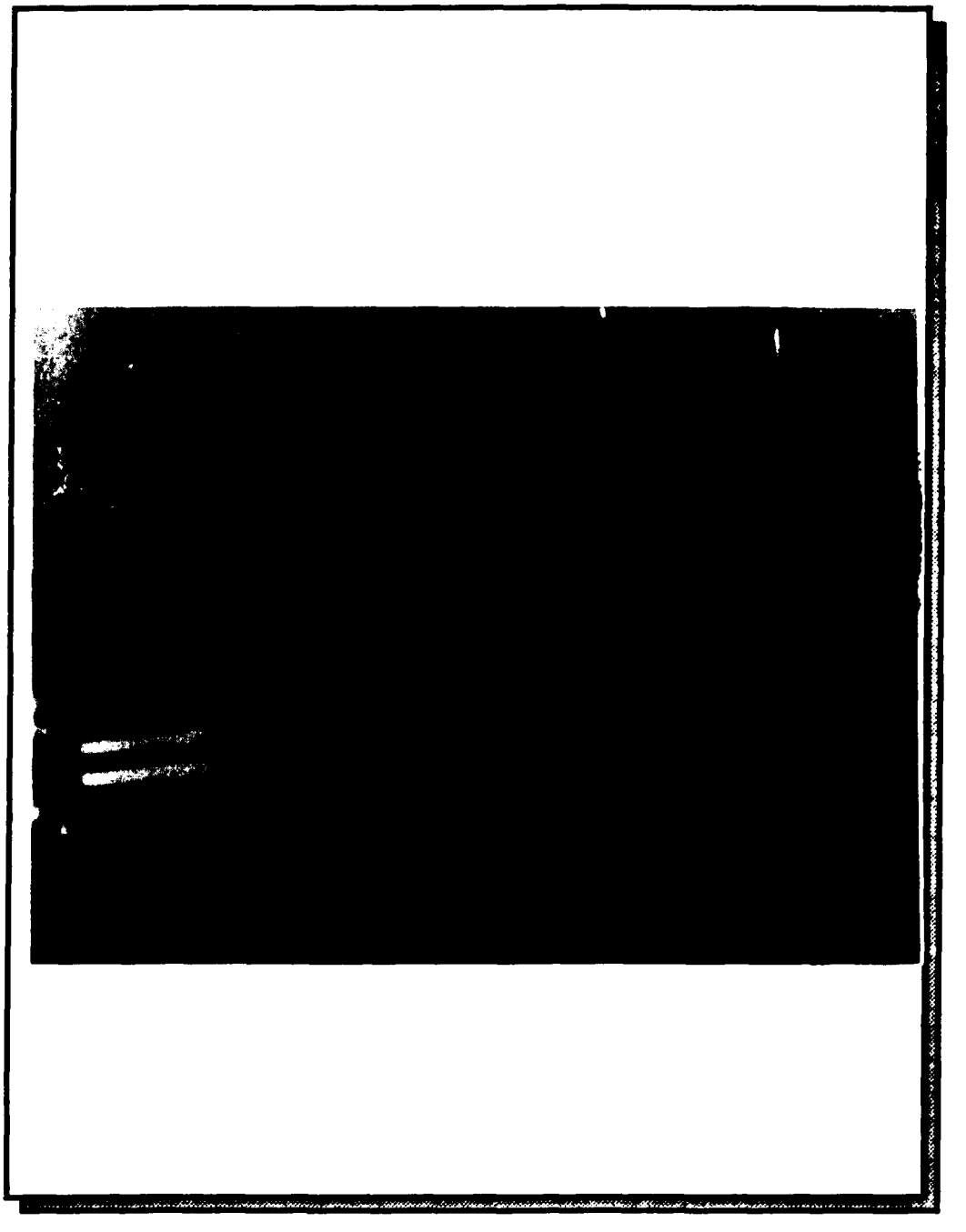

Figure 7.33 - Schematic diagram for a curve planar waveguide.

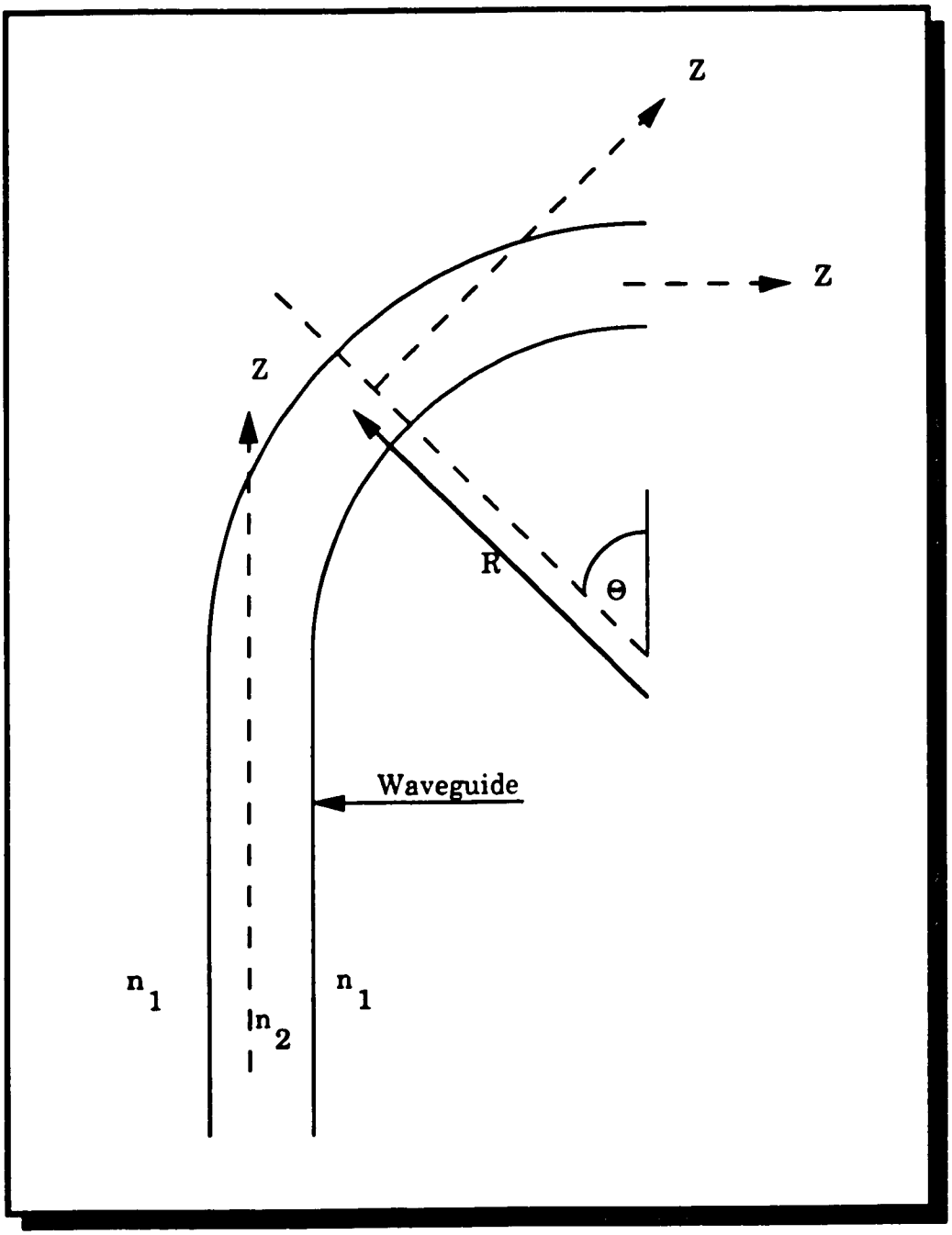

Figure 7.34 - Bending losses in SnO_2 curve waveguides photodeposited onto PVG.

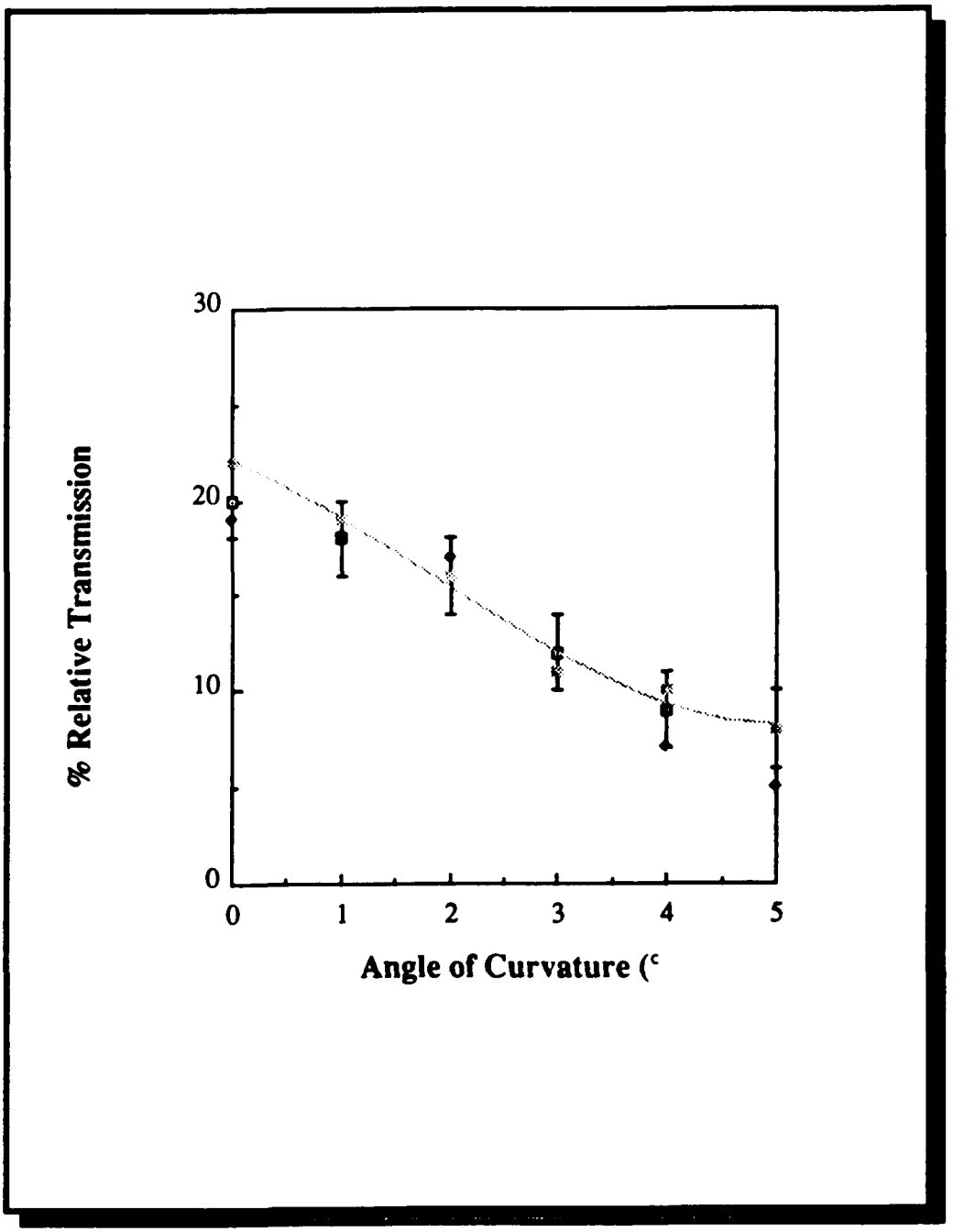

Figure 7.35 - He-Ne laser beam launched into a 10 μm photoinduced tin oxide curved signal splitter waveguide onto PVG.

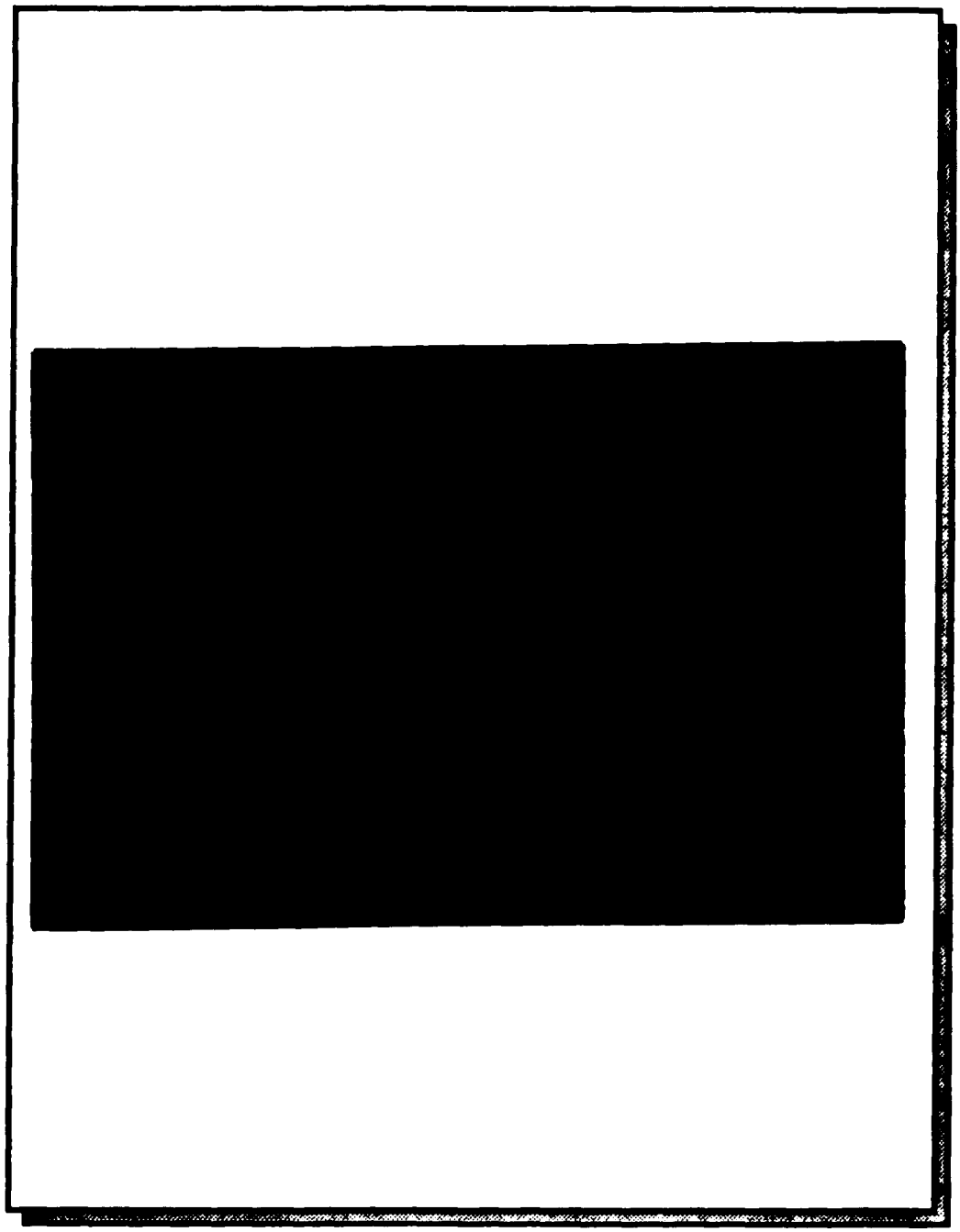

Figure 7.36 - He-Ne laser beam launched into a 10 μm photoinduced tin oxide combined - staright and curved - signal splitter waveguide onto PVG.

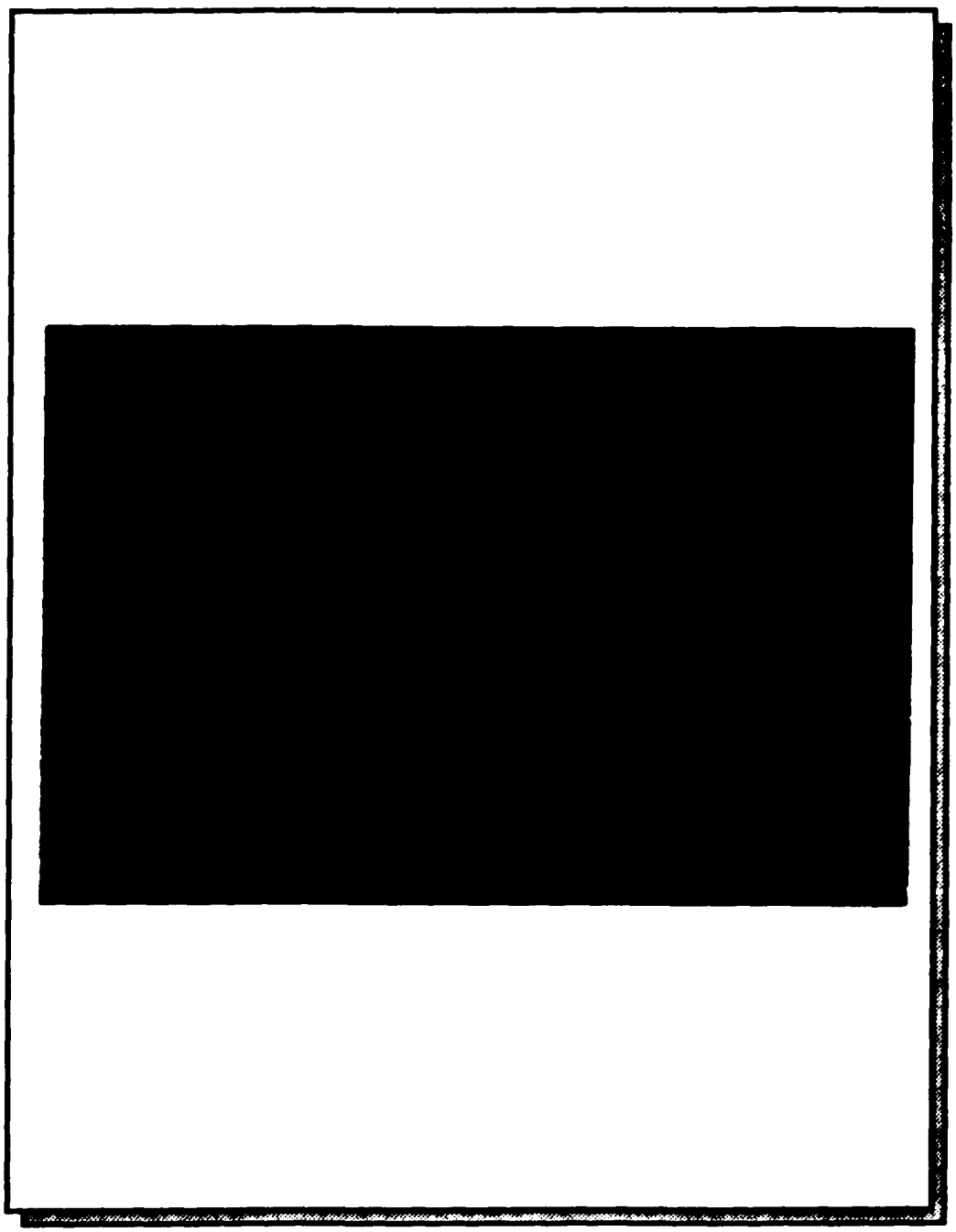

been launched into a SnO_2 waveguide coupling structure. In Figure 7.32 the splitter is formed from a straight waveguide into two curve waveguides having a 1.25 cm radius of curvature, while Figure 7.33 shows a junction of a straight waveguide into a curve one. The coupling efficiency of waveguide splitters formed using 2°, 4°, 6°, 8°, and 10° branches is shown in Figure 7.34. The coupling ratio $[P_R/(P_R + P_L)]$ was measured for the two outputs P_R and P_L, where P_R is the output in the right branch and P_L is the output in the left branch. A clear trend of decreasing coupling efficiency with increasing branching angle is observed. The error bars are due to experimental errors involving the coupling of the laser beam with the waveguide, and the fanning of the output beam.

Another coupling configuration is the "Y" comfiguration, where two waveguides are connected to a third straight waveguide (Figure 7.35). In this case, the losses are due to the scattering at the junction. Structures like this are commonly used in the fabrication of star couplers, optical modulators, and Mack-Zenhder interferometers. Figure 7.36 shows a 2-3 star coupler and a combination of a coupler with a Mack-Zenhder interferometer, which are in the process of being evaluated for their optical efficiency.

To conclude, it has been demonstrated that the photolithographic impregnation of metal oxides onto porous glasses allows the fabrication of passive integrated optic devices with low optical losses. It's potential applications in the field of optics and integrated optics devices are numerous. However, further advancement of this technique needed for the fabrication of all optical integrated devices in glasses requires the ability to incorporate metal oxides onto the glass network capable of producing nonlinear optical changes under the influence of an external stimulus.

Figure 7.37 - Coupling efficiency in branch waveguides with different angles of branching.

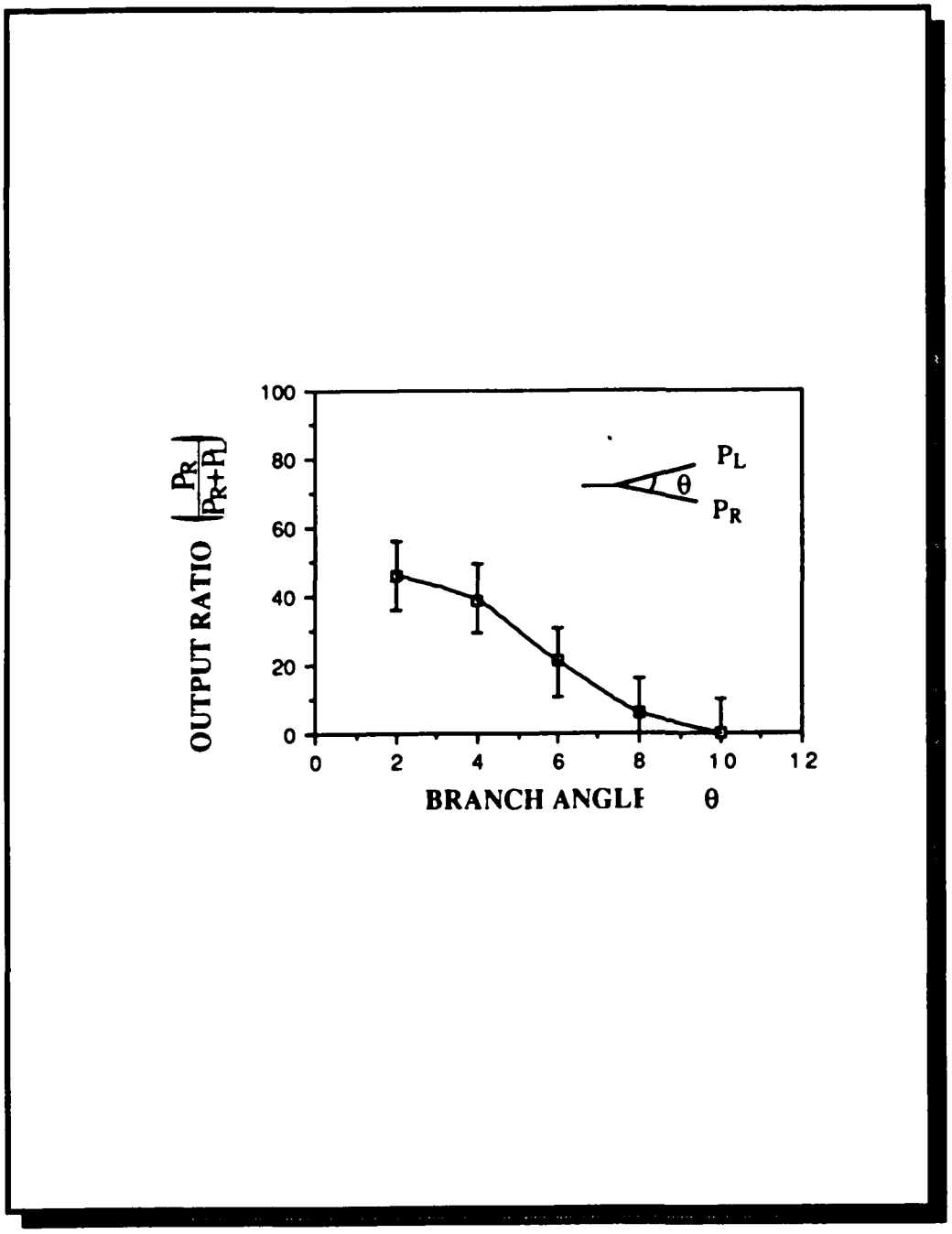

Figure 7.38 - Schematic diagram of waveguide coupling comfigurations.

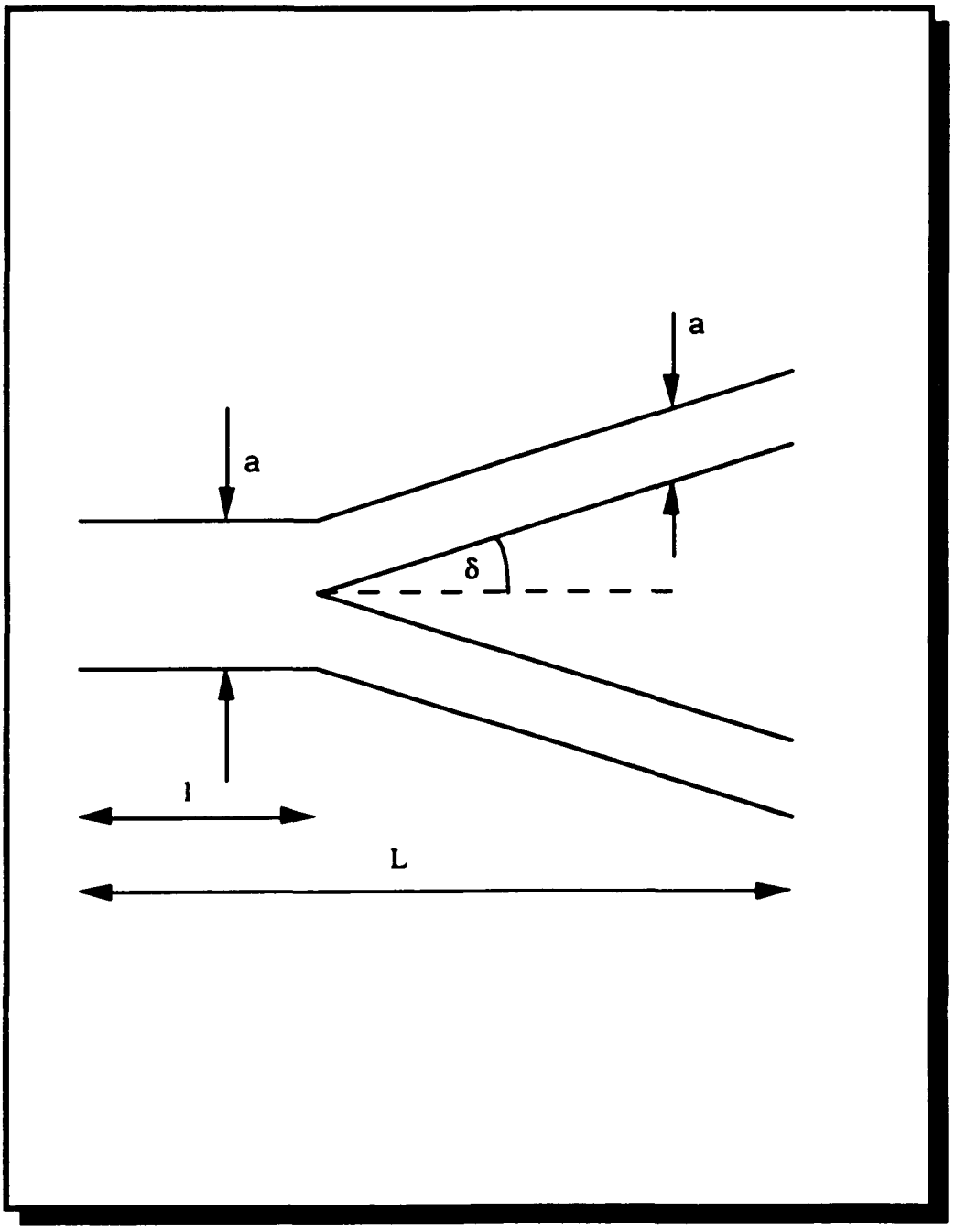

Figure 7.39 - Mach-Zehnder waveguide comfiguration made by the photodeposition of SnO_2 onto PVG.

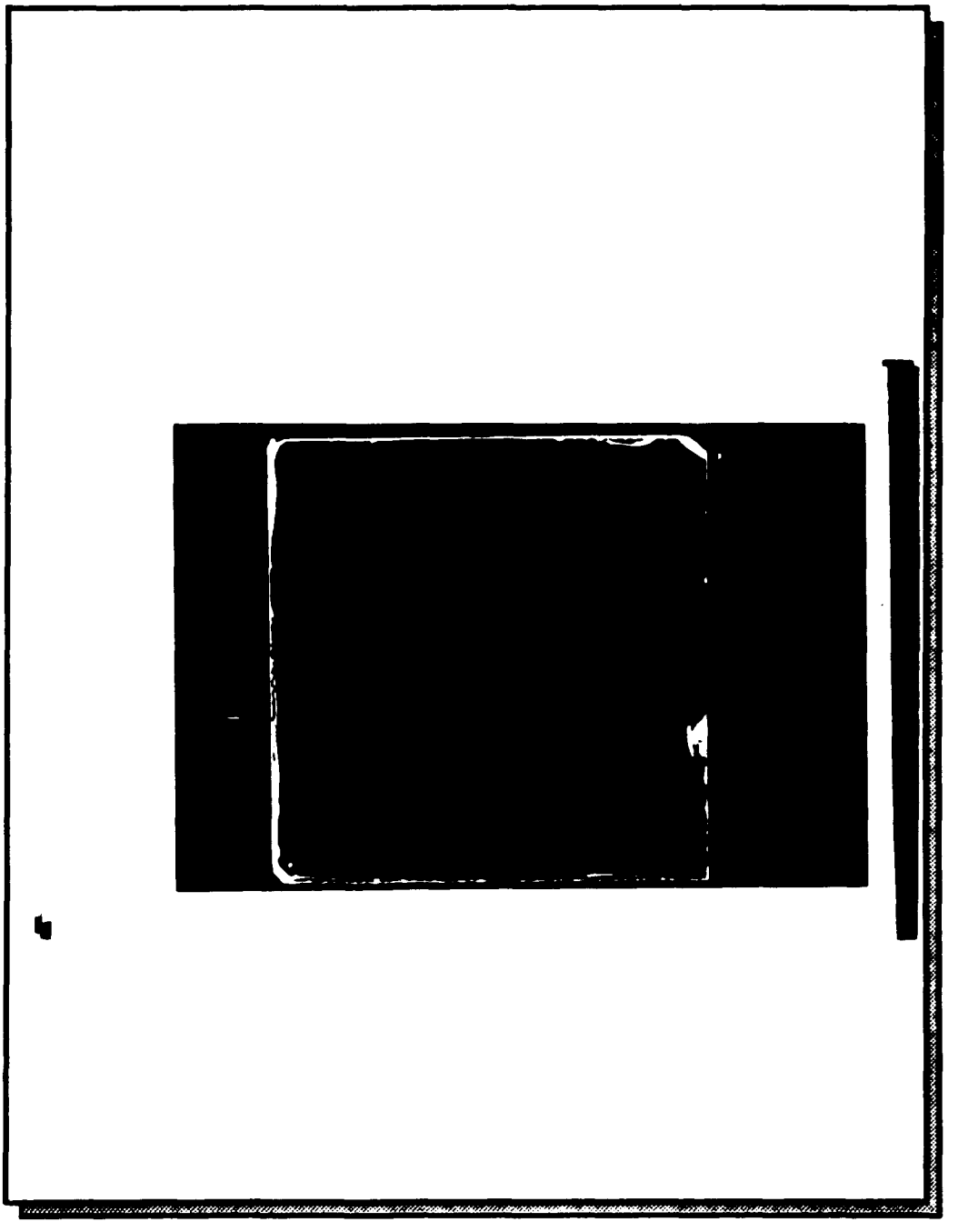

Part IV

Discussion.

1. Adsorption of Organotin Compounds onto Porous Glass Matrices.

1.1 Porous Silica Glasses.

The micro-structure of porous silicate glasses such as PVG and TMOS xerogels consist of interconnecting voids distributed through out the entire body of the glass. Scanning electron microscopy reveals a structure composed of glass nodules with a fractal morphology in which the larger nodules are composed of smaller nodules. Transmission electron microscopy on a length scale of 0-1.0 nm shows a fine porous structure composed of smaller uniform diameter particles.

Comparing PVG and the TMOS xerogels reveals a tenuous assemblage of clusters that bond together to form interstitial cavities in PVG. A similar structure occurs in the xerogels, although in these glasses two levels of porosity exist; a microporosity within clusters and a mesoporosity between clusters. Because adsorption characteristics change with pores size, it is convenient to classify porosity in the terms proposed by Dubinim, i.e., [1]

	Pore Diameter (Å)	Surface Area [2] (m^2/g)
Micropores	10-12 to 26-28	>500
Mesopores	30-32 to 100-2000	500-10
Macropores	2000-4000	<10

Although electron microscopy gives a subjective representation of the surface morphology, quantitative comparisons of different systems are difficult. Cohan and Watson [3] described a technique for measuring the particle diameter for carbon black. However, it measures only those particles whose silhouettes are more than a semicircle of the cross-section. This method requires the measurement of several hundred samples in order to meet the statistical requirements. SEM studies of fracture and polished surfaces of porous glasses have been reported on the literature. [4] Nevertheless, interpretation of the images furnished by fracture surfaces, where the pore size scales with the fracture features, is ambiguous because of the inability to distinguish between surface topology and true pores. Also, sample pullout during fine polishing may obscure the true morphology.

It is desirable to describe a porous glass in such a way that it can be analytically compared to those prepared by other investigators, or produced by different methods. Key indicators are surface area, pore size, and glass transition temperature, T_g. In fact, a more quantitative description of the

surface morphology arises from BET adsorption-desorption nitrogen isotherm determinations of surface area, and pore size, than from electron microscopy. The main feature observed from the BET measurements is that porous silicate glasses have very large surface areas in the order of 100 to 1000 m^2/g. PVG has a surface area of 170 ± 30 m^2/g, while TMOS xerogel has a much larger surface area of 600 ± 50 m^2/g. Surface area remains constant from room temperature up to about the glass transition temperature (Tg) where a rapid decline is observed. Tg occurs at 550 °C in PVG, and at 790 °C in TMOS xerogels. The decline corresponds to the sintering transition of the porous structure to a nonporous structure. Pore size varies in the same manner as surface area; pore size remains constant to the glass transition temperature, and decreases above T_g to a nonporous structure at the sintering temperature. The decrease in pore size and surface area above T_g occurs with a relaxation of the microstructure and the conversion of the silanols to pure silica.

The properties of porous silicate glasses depend largely on the chemistry of its surface, which is entirely covered by dangling OH groups. Consequently, its adsorption behavior and its surface reactivity depend directly on the behavior of these OH groups. [5] According to Lagmuir, [6] when the surface is covered by one layer of adsorbed molecules, a second layer is not adsorbed. Further adsorption of a second layer can occur only through the interaction of weaker secondary forces extending from the surface beyond the first adsorbed layer. Formation of the first layer is termed "chemisorption", whereas formation of the second layer, which involve weaker forces, is termed "physisorption".

Siloxane (Si-O-Si) surfaces of silicate glasses also react with water to form silanol groups (SiOH). The hydroxyl groups formed can either

covalently or ionically bond to the surface Si atoms. Hydrogen bonding also occurs occurs between oxygen atoms of adjacent silanol groups. The various types of hydroxyl groups that exist on the silicate surface are shown in Scheme I. Surface hydroxyl groups are sites where physical adsorption of water, and other polar molecules, occurs. At room temperature, the physically adsorbed water covers all accessible Si-OH sites forming a multiple hydrogen bonded layer.

Other types of functional groups also present on the surface of TMOS xerogels are esters, produced by esterification of the silanol layer by adventitious alcohols, that remain after incomplete hydrolysis of TMOS during the gelation process. According to Mertens and Fripiat, [7] who studied ester formation at 150-190°C, the process involves the reaction of SiOH with the releasing MEOH to form $SiOCH_3$. Abayashi [8] reports that thermal decomposition of $SiOCH_3$ is an exothermic process that occurs at about 500 °C. However, a similar process is not observed in the DTA measurement of the TMOS xerogels prepared in these experiments. Instead, an exothermic peak with an onset a 250 °C occurs, which is assigned to the desorption of unpolymerized TMOS, and residual solvent. Esterification of the silanol surface can also occur at higher temperatures, ~400 °C, by chemisorbed alcohols. [9] To prevent esterification of the silanol surface, complete hydrolysis must be promoted by using larger amounts of water during the hydrolysis of TMOS. The various types of surface functional groups, as well as their changes during dehydroxylation, are readily identify by infrared spectroscopy, their characteristic frequencies are listed in Table 3.2.

Heat treatment of silicate glasses results in desorption of the physically adsorbed water at temperatures between 25-180 °C. Lange [10]

Scheme I[11]

(A) Vicinal hydrated; (B) Vicinal anhydrous; (C) Hydroxylated; (D) Isolated; (E) Siloxane-dehydrated; (F) Germinal; (G) Vicinal-hydrogen bonded.

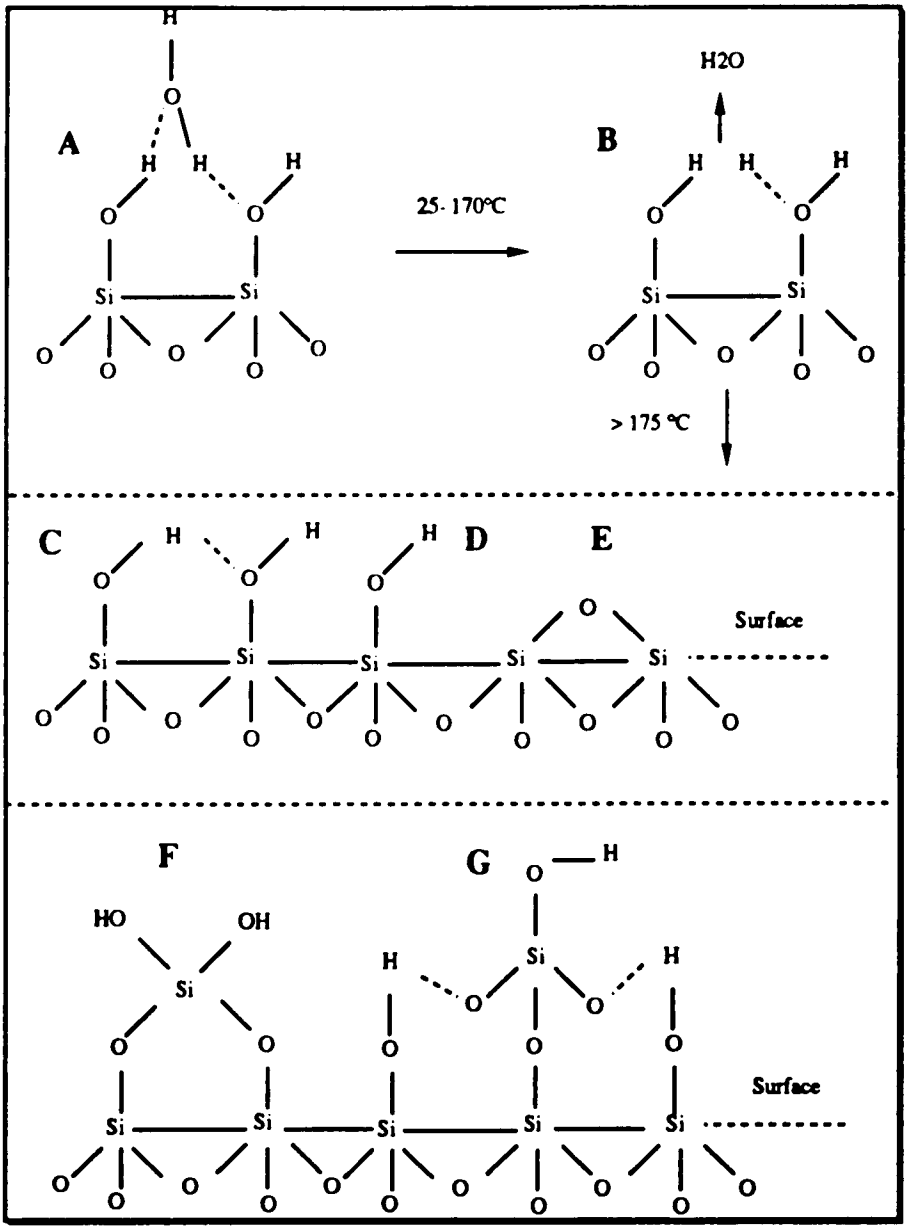

claims that there are two kind of physical adsorbed water on hydroxylated silica. The one that desorbes from 25-105 °C is called " physically adsorbed ", while the other, which desorbes from 105-180 °C is called " hydrogen bonded ". Above 170 °C, dehydration occurs at a much slower rate. The silanol groups start to condense and evolved water extensively, but at 400 °C, less than half of the hydroxyl groups have been removed. Most of the remaining hydroxyl groups are still adjacent to one another, and these can further adsorbed water so that the surface readily rehydrates. [12] Above 600 °C, only free, unpaired SiOH are present. In the higher temperature range, the concentration of residual SiOH groups was measured by Curthoys [13] as follows:

Temperature °C	OH nm^{-2}
25	5.0
700	1.2
800	0.9
900	0.6
1000	0.4

The presence of even a small number of OH groups can induce bloating during viscous sintering of the glass, which occurs at ≥ 700 °C. This can be a severe problem during the sintering of glass gels, but more so for multicomponent glasses, like PVG, that sinter at lower temperatures.

To achieve extensive thermal dehydroxylation requires optimizing both the glass microstructure and the thermal processing. Microstructural

variables include pore size, surface area, and particle curvature. For any system, the most beneficial microstructural improvement is an increase in pore size. Larger pores enhance the diffusion of water and allow more complete dehydroxylation to occur prior the pore closure during the final stages of sintering. Curvature is directly proportional to the OH content; the larger the radius of curvature the higher the OH content. [14] Therefore, it is desirable to have glass particles of small curvature to reduce the total OH content. Smaller particles are beneficial from the stand point of curvature, but smaller particles have a larger surface area which increases necking formation, and in turn, the OH concentration. Presumably, an optimum particle size exists that will have a minimum OH content during sintering conditions. To our knowledge, however, the relationship between particle size, OH content, and sintering behaviour have yet to be deliniated. Nevertheless, small particles should be avoided in order to reduced the total OH content of the glass surface.

The thermal processing cycle for PVG and sol-gels is shown in Figure 4.2 (Part II). In general, heat treatment procedures are designed to minimize the water content prior to sintering by maintaining the sample at the highest possible temperatures prior to the onset of sintering. Gallo [15] and coworkers recommend prolonged isothermal heating at the onset of the glass transition followed by quenching to room temperature. Dehydroxylation that occurs during the isothermal hold increases the sintering temperature so that a second higher isothermal heat treatment can be employed. Repeating this procedure several times results in more complete dehydroxylation.

In summary, the chemistry and structure of porous silicate glasses is dominated by their large surface area. High surface areas are

problematic when preparing high purity glasses for optics, since the surface is terminated by hydroxyl groups that can induced bloating during the sintering process. For example, a TMOS glass-gel with a surface area of 600 m^2/gr, a typical high surface area glass, may contain over 8 wt % water. Complete dehydroxylation can be accomplished by controlled sintering, but glasses with large pores are also advantageous. It is clear from a comparison of the microstructures of PVG and the TMOS xerogels that compromises are needed to obtain a surface that meet all the requirements. PVG possesses mesopores in the 70-130 Å diameter range, a moderatly large surface area, 160 m^2/gr, and moderate OH content. TMOS xerogel possesses micropores in the 10-30Å diameter range, and mesopores in the 30-50Å diameter range, very large surface areas, 600 m^2/gr, and an extremely high OH content. Although large pores and surface areas present problems with respect to consolidation, they are advantageous for chemical modification, since large pores and surface areas offers accessibility into the bulk.

1.2 Spectral Properties of Adsorbed Compounds.

Although there is considerable interest in Group IVA organometallic compounds, particularly in the interaction between the metal and the ligand, [16] little attention has been paid to the electronic spectra of molecules such as $(CH_3)_{(4-n)}MX_n$. Only the spectrum of $(CH_3)_3SiN_3$ has been reported, [17] and in this case, the spectrum is interpreted in terms of a LMCT transition from the electron pair localized on the nitrogen to the

metal. Similar charge transfer transitions are expected in the $(CH_3)_3SnX$ compounds since the halogens have unpaired p-electrons. The absorptions of $(CH_3)_3SnX$ compounds have not been assigned, and the nature of the excited states is clouded by extensive electron delocalization and covalent bonding. [18]

In the 200 to 800 nm region, the electronic spectra of the trimethyltin halides consist of a single absorption. Although of little interest in these experiments, because of its high energy, a second absorption assigned to a methyl locallyzed $\sigma \rightarrow \sigma^*$ transition occurs at ~ 180 nm. If the lower energy transition, which is photochemically accessible, possess charge transfer character, then the transition possesses LMCT character since the band shift to lower energy as the ionization potential of the ligand declines. It should be noted, however, that in molecules possessing a high degree of covalency, such as $(CH_3)_3SnX$ compounds, the assignment of distinct charge transfer transitions is questionable.

The electronic spectra of trimethyltinhalides are also dependent on the solvent medium. A bathochromic shift, which increases with increasing solvent dielectric, is assigned to the formation of a charge transfer adduct between the tin atom and the solvent. [19] . Job's plots, Figure 2.4 Part III, indicate the formation of a 1:1 $(CH_3)_3(I)Sn–OHC_6H_{13}$ adduct. A linear relationship between the spectral shift and the degree of adduct formation is observed. Although the limited solubility of ethanol in n-hexane precluded equivalent experiments with ethanol, the spectral changes found on addition of 1-hexanol closely resemble the shift from 234 nm in n-hexane to 218 nm in ethanol. Trimethyltinhalides exhibit a marked tendency to form 1:1 and 1:2 addition complexes with Lewis bases. These adducts appear to be approximately trigonal bypiramidal in solution

[20] as well as in the solid state. [21] Clearly, formation of the adduct results in rehybridization of the central tin atom.

When $(CH_3)_3SnX$ compounds are adsorbed onto PVG, the absorption maxima shift to higher energy. For example the absorption maximum of $(CH_3)_3SnI$ is 234 nm in n-hexane, but shifts to 220 nm when adsorbed onto the glass. In view of the polarity of the glass surface, the tendency of these complexes to react with Lewis bases, and the DRIFT spectra, the shift is attributed to the reaction with the glass surface (Scheme II).

1.3 Adsorption of Trimethyltinhalides onto Porous Glasses.

Trimethyltinhalides reversibly adsorb onto the surface of porous silicate glasses. The spectroscopic properties of the desorbed compound remain equivalent to those prior to adsorption. This would suggest a relatively weak interaction between the adsorbate and adsorbent, i.e., trimethyltinhalides physisorb onto the glass surface. However, DRIFT spectra (Figure 5... Part III) reveal changes in the coordination sphere of the adsorbed complex.

Adsorption of trimethyltiniodide onto the surface of PVG occurs with a decline in the intensities of the free and hydrogen bonded silanol bands at 3744 cm^{-1} and 3660 cm^{-1}. Concurrent with these changes are increases in the intensities of the 2993 cm^{-1} and 2917 cm^{-1} C-H streches of the methyl groups, and the growth of a broad band at 3550 cm^{-1}. The growth of the 3550 cm^{-1} band concurrent with the decline of the 3744 cm^{-1} and 3660 cm^{-1} silanol bands implies that adsorption weakens the Si-OH bond. This suggest that adsorption occurs by a concerted mechanism in which the

incoming tin atom begins to interact with a silanol oxygen. It was not possible to unambiguously define the strength of these interaction since the Si-O-Sn region is masked by the strong adsorptions of the silica network. However, the relative ease of desorption of the intact complex suggest a relatively weak interaction. Nevertheless, the interaction is sufficient to reduce the SiO–H bond strength as evidence by the appearance of the broad 3550 cm^{-1} band. Depending on the electronegativity of the coordinated halogen, there may also be some hydrogen bonding with a second silanol group as shown in Scheme II.

Scheme II

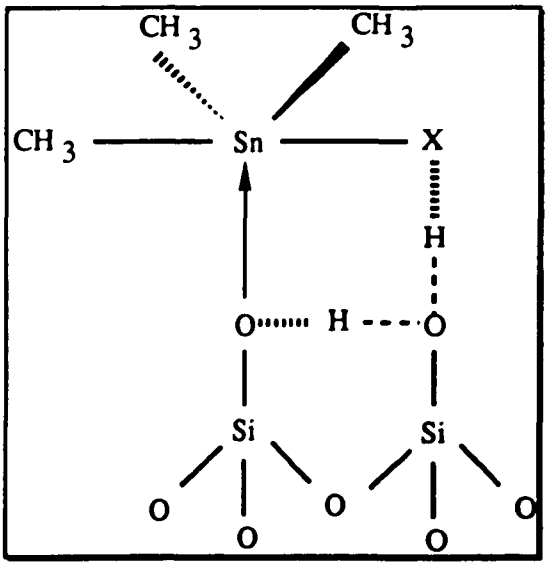

From the preceding discussion it is clear that the different types, and concentrations of silanol groups present on the surface of the glass play a key role in the adsorption of trimethyltinhalide compounds. Similar studies have been reported on the adsorption reactions of organosilicates, such as $(CH_3)_{(4-n)}SiCl_n$, onto silica surfaces as a function of the concentration of the silanol groups; the latter being varied by sintering the glass at different temperatures.[22] As the sintering temperature increases, the number of silanol groups decreases, and therefore the adsorption reactions decrease and become stereoselective. Accordingly to Snyder and Ward, [23] this type of concerted adsorption behavior is dependent on the pore size and the curvature of the glass particle. In small pores, $\leq$ 100 Å in diameter, curvature brings the silanol groups closer together so there can be more mutual interaction between the silanol groups and the incoming reactant. In pores with diameters from 100-50 Å, the reactive fraction increases from about 0.05 to 0.8. In general, the pore size decreases, the silanol groups are closer together, and the adsorption reactivity increases.

Porous glasses can be impregnated with trimethyltinhalides by either vapor or solution deposition techniques. Both techniques yield a uniform distribution of the complex on the outer most surfaces of the glass, but neither yield a uniform cross sectional distribution. Total x-ray fluorescence analyses show that the distribution of the adsorbed tin compound decreases exponentially through the cross-section of the glass upto depths of 1000 μm depending on the time of exposure of the vapors, or its concentration in the liquid phase.

Typically, impregnation depths are of the order of 10^3 μm. This can be varied by either changing the time the sample is exposed to the vapor, or the concentration of the compound in the impregnating solution.

Unfortunately, the variation is not linear, i.e., doubling the time or the concentration increases, but not doubles the depth of impregnation. Although penetration depths are dependent on the nature of the impregnate, this result suggest that the principal determinant is the tortuosity of the glass itself.

The rate of adsorption of the different trimethyltinhalides onto the surface of PVG decreases in the order $(CH_3)_3SiI > (CH_3)_3SiBr > (CH_3)_3SiCl$. This is primarly due to the differences in the enthalpies of sublimation of the three halide compounds. However, the lack of sufficient thermodynamic data for the trimethyltinhalides precludes a quantitative analysis. Nevertheless, a semiqualitative interpretation of the rates of adsorption can be put forth. The rates of adsorption of trimethyltinhalides onto PVG (Figure 5.4 Part III) exhibit three distinct regions. Region I shows a slow initial rate of adsorption that can be associated with the sublimation enthalpy of the compound. The greater the enthalpy of sublimation, the slower the vaporization rate, and the smaller the number of molecules available for adsorption. Hence, the initial rate of adsorption declines with time. Once the compound has been completly vaporized, however, the rate of adsorption is independent of the phase transformation of the compound. A steady state adsorption develops where the rate is direclty proportional to the number of molecules in the gas phase. This occurs in region II, where the slope of the curve increases linearly as a function of time. However, other effects, can also influence the rate of adsorption in this region. Specifically, if adsorption involves a concerted mechanism similar to that in Scheme II, the role of the molecular parameters of the adsorbate may become more evident. For example, saturation effects may be evident with the iodine analog. Iodine is larger

than chlorine, and the Sn-I bond length (2.72 Å) is longer than the Sn-Cl bond (2.3 Å). Consequently, surface coverage will require less $(CH_3)_3SnI$ than $(CH_3)_3SnCl$, and if the rates of diffusion onto the surface are similar, the time required for saturation will also be less. On the other hand, if the electronegativity of the halogen is important - for example, the halogen may hydrogen bond to the surface - then the relative rates of adsroption will be different, i.e., $(CH_3)_3SnCl > (CH_3)_3SnBr > (CH_3)_3SnI$. Since the observed order is $(CH_3)_3SnI > (CH_3)_3SnBr > (CH_3)_3SnCl$, hydrogen bonding to the halogen appears to be of little importance.

Region III in Figure 5.4 Part III corresponds to a saturation region where no further adsorption occurs. Here the accessible adsorption sites are filled and the rate of adsorption equals the rate of desorption. For $(CH_3)_3SnI$ saturation occurs at 3.0×10^{-5} mol ads/gr. of PVG, whereas $(CH_3)_3SnBr$ and $(CH_3)_3SnCl$ require 4.0×10^{-5} and $> 8.0 \times 10^{-5}$ mol ads/gr. of PVG respectively. Since $(CH_3)_3SnI$ is larger, apparently fewer molecules are needed to saturate the surface.

2. Photochemistry of Trimethyltin Halides in Solution.

It is generally assumed that UV photolysis of $(CH_3)_3SnX$ complexes in solution results in homolytic cleavage of the Sn–X bond. However, the experiment carried out during this study reveal a marked solvent dependence.

2.1 Nonpolar Solvents.

2.1.1 Photochemistry of trimethyltiniodide.

In nonpolar solvents, such as n-hexane, the photolytic results, as well as the stoichiometry of the reaction, 1 mol of I_2 or $(CH_3)_6Sn_2$ formed per 2 mole of $(CH_3)_3SnI$ reacted are consistent with the homolytic cleavage of the Sn–I bond. The radical products combine to form I_2 and $(CH_3)_6Sn_2$.

Evidence for the radical mechanism derives from the spectroscopic studies. UV-visible spectra, Figure 2.7 Part III, recorded during photolysis shows the disappearance of the $(CH_3)_3SnI$ absorption band (234 nm) accompanied by the appearance of the I_2 and $(CH_3)_6Sn_2$ absorption bands at 520 and 211-nm respectively. Raman spectra recorded during photolysis, Figure 2.8 Part III, shows the dissapearance of the 167-, 512-, and 546 cm^{-1}

bands of $(CH_3)_3SnI$ concurrent with the appearance of the 186 cm^{-1} of $(CH_3)_6Sn_2$. Similarly, FTIR recorded during photolysis, Figure 2.9 Part III, shows the growth in the Sn-CH_3 band at 508 cm^{-1} correponding to the formation of $(CH_3)_6Sn_2$. The spectroscopic observations clearly indicate that the disappearance of $(CH_3)_3SnI$ occurs simultaneously with the appearance of I_2 and $(CH_3)_6Sn_2$.

The radical mechanism was further confirmed with isoamylnitrite which is known to scavange I atoms. [24] 254 nm photolysis of a solution of $(CH_3)_3SnI$ containing isoamylnitrite prevents the formation of I_2 and increases the rate of dissapearance of $(CH_3)_3SnI$, and appearance of $(CH_3)_6Sn_2$.

2.1.2 Kinetics of the photochemical reaction of trimethyltiniodide.

To obtain the mechanism of the primary and secondary events occuring during photolysis of alkyltin halides, reaction efficiencies were obtained under different conditions. Efficiency is given by the quantum yield, and in these experiments, the quantum yield of reactant dissapearance and product appearance were determined as a function of solvent, concentration, and excitation wavelengthand intensity.

The quantum yield of $(CH_3)_3SnI$ dissappearance is independent of its initial concentration, or the O_2 concentration, and declines rapidly as the excitation wavelength shifts from 254 nm to 355 nm (Table 2.9 Part III). Similarly, the 370 nm emission band of $(CH_3)_3SnI$ is also independent of the O_2 concentration. The wavelength dependence as well as the fact that the efficciency is independent of the O_2 concentration indicate that the primary photochemical event occurs in the excited singlet populated on absorption.

The ratio of the quantum yield of $(CH_3)_3SnI$ dissapearance relative to the quantum yields of I_2 and $(CH_3)_6Sn_2$ appearance, Figure 2.12 Part III, extrapolate to a limiting value of 2.06. Consequently, the overall reaction is

$$2\ (CH_3)_3SnI \xrightarrow{Ia} I_2 + (CH_3)_6Sn_2 \qquad 2.1$$

With 254 nm excitation, the rate of $(CH_3)_3SnI$ dissapearance is given by

$$-\frac{d[(CH_3)_3SnI]}{dt} = \Phi Ia \qquad 2.2$$

where

$$I_a = I_0\left(1 - 10^{-\varepsilon^{254}_{(CH_3)_3SnI}[(CH_3)_3SnI]\,l}\right) \qquad 2.3$$

For optically dilute solutions, the rate law reduces to

$$-\frac{d[(CH_3)_3SnI]}{dt} = 2.30\,\Phi\,\varepsilon^{254}_{(CH_3)_3SnI}[(CH_3)_3SnI]\,l \qquad 2.4$$

and is consistent with the experimental results during the initial stages of the reaction. However, as the fraction of $(CH_3)_3SnI$ photolyzed increases, the thermal back reaction

$$I_2 + (CH_3)_6Sn_2 \xrightarrow{k_t} 2\,(CH_3)_3SnI \qquad 2.5$$

occurs. Consequently, the overall rate law is

$$-\frac{d[(CH_3)_3SnI]}{dt} = \Phi I_a - 2\,k_t\,[(CH_3)_6Sn_2][I_2] \qquad 2.6$$

The stoichiometry and kinetics of reaction 2.1 show that absorption of 254 nm photons by $(CH_3)_3SnI$ results in the population of the singlet excited state where homolytic cleavage of the Sn–I bond occurs as the primary photochemical event, followed by the combination of the radical products to form I_2 and $(CH_3)_6Sn_2$ as a secondary chemical event, as postulated in scheme III.

Scheme III

$$(CH_3)_3SnI \xrightarrow{I_a} (CH_3)_3SnI^* \qquad 2.7$$

$$(CH_3)_3SnI^* \xrightarrow{k_1} (CH_3)_3Sn\cdot + I\cdot \qquad 2.8$$

$$(CH_3)_3SnI^* \xrightarrow{k_2} (CH_3)_3SnI + \text{heat} \qquad 2.9$$

$$I\cdot + I\cdot \xrightarrow{k_3} I_2 \qquad 2.10$$

$$2(CH_3)_3Sn\cdot \xrightarrow{k_4} (CH_3)_6Sn_2 \qquad 2.11$$

$$(CH_3)_6Sn_2 + I_2 \xrightarrow{k_5} 2(CH_3)_3SnI \qquad 2.12$$

In this mechanism the rate of $(CH_3)_3SnI$ dissapearance, assuming a steady state approximation for the reactive intermediates, is given by (see Appendix IV for complete derivation of the rate law)

$$-\frac{d[(CH_3)_3SnI]}{dt} = I_a\left[1 - \left(\frac{k_2}{k_2 + k_1}\right)\right] - 2\,k_5\,[(CH_3)_6Sn_2][I_2] \qquad 2.14$$

Where the constant (k_5), for the thermal reaction of $(CH_3)_6Sn_2$ with I_2 to produce $(CH_3)_3SnI$ in hexane, was determined spectrophotometrically to be 226 ± 0.5 M^{-1}-sec^{-1}. A value of 740 M^{-1}-sec^{-1} is given by Tagliavini, et.al. [25] At all times the concetrations of the products is small, consequently, the second term, $2\,k_5\,[(CH_3)_6Sn_2][I_2]$, is negligable as compared to the first term, i.e.,

$$I_a\left[1 - \left(\frac{k_2}{k_2 + k_1}\right)\right] >> 2\,k_5\,[(CH_3)_6Sn_2][I_2] \qquad 2.15$$

consequently, the rate law reduces to

$$-\frac{d[(CH_3)_3SnI]}{dt} = I_a\left[1 - \left(\frac{k_2}{k_2 + k_1}\right)\right] \qquad 2.16$$

and agrees with the kinetic results, since k_1 and k_2 are related to the quantum yield F by

$$\Phi = \left[1 - \left(\frac{k_2}{k_2 + k_1}\right)\right] \qquad 2.16$$

In the limit where the quantum yield approaches one k_1 is much larger than k_2, consequently reaction 2.9 becomes the rate determining On the other hand, in the limit where the quantum yield approaches zero, k_2 is much larger than k_1, and reaction 2.8 becomes the rate determining step.

The kinetic results indicate that the quantum yield of dissapearance of $(CH_3)_3SnI$ is linear with respect to the excitation intensity, and approaches a value of one at excitation intensities exceeding ca. $\geq 5.0 \times 10^{-7}$ (Einstein/L-sec). Consequently, the thermal relaxation of $(CH_3)_3SnI^*$ to the ground state, reaction 2.9, is the rate determining step. Under these conditions, the rate constant k_1 is

$$k_1 >> k_2 \qquad 2.16$$

Similarly, Marshall and Davidson measured the rate constant (k_3), at room temperature, for the recombination of iodine radicals in several nonpolar solvents by flash photolysis techniques. [26] An average value of $1.4 \times 10^{10} M^{-1} sec^{-1}$ was calculated accordingly to reaction 2.10. A similar value, $1.1 \times 10^{10} M^{-1} sec^{-1}$, was measured by Rabinovitch and Wood. [27] Since the radical recombination itself presumably has no activation energy, the overall recombination process is diffusion controlled. Furthermore, since the rate of appearance of I_2 and $(CH_3)_6Sn_2$ is equal and maintained through 50% of the reaction, the rate constant (k_4) for the recombination of $(CH_3)_3Sn\cdot$ radicals to form $(CH_3)_6Sn_2$ is also diffusion control. Consequently, the rate constant (k_4) is estimated to be of approximately the same magnitude as (k_3), $\sim 1.0 \times 10^{10} M^{-1} sec^{-1}$.

To conclude, the primary photochemical process of $(CH_3)_3SnI$ in

nonpolar solvents is the homolytic cleavage of the Sn–I bond. The radical products combine to form I_2 and $(CH_3)_6Sn_2$. The rate determining step is the thermal decay of $(CH_3)_3SnI$ from the reactive singlet excited state, which is populated directly on absorption.

2.1.3 Photochemistry of trimethyltinbromide and trimethyltinchloride.

The photochemistry of $(CH_3)_3SnBr$ and $(CH_3)_3SnCl$ were also studied in nonpolar solvents for the purpose of comparing the mechanism and efficiencies of the photochemical reaction with those of $(CH_3)_3SnI$. However, it was inmediately apparent that it would not be possible to examine these reagents at the same level of detail as was done for $(CH_3)_3SnI$. The principal limitation encountered was that the absorption maxima of these compounds occur beyond the transmittance of the solvent, and beyond the UV range of the spectrometer. Nevertheless, experiments were carried out, although in most cases, the results and their discussion are base on the appearance of the respective halogen or halide product.

As in the case of $(CH_3)_3SnI$, the photochemical reaction of $(CH_3)_3SnBr$ involves the homolytic cleavage of the Sn-Br bond. The radical products combine to form Br_2 and $(CH_3)_6Sn_2$. Evidence for this behaviour is given by the photolytic and stoichiometric results; one mol of Br_2 formed per 2 moles of $(CH_3)_3SnBr$ reacted. UV-vis spectra show that the decrease of the absorption band of $(CH_3)_3SnBr$ (212nm) upon UV exposure is accompanied by the simultaneous growth of the Br_2 absorption band (420nm), and a nondescriptive increase in absorbance at 210 nm assigned to $(CH_3)_6Sn_2$ formation. Other spectroscopic techniques, such as infrared and Raman, show no changes in the spectra during UV exposure, due to the

poor efficiency of the reaction, and/or the poor sensitivity of this techniques to detect small concentrations, usually in the ppm range.

The quantum yield of $(CH3)3SnBr$ dissapearance is independent of its initial concentration, or the O_2 concentration, and shows no reaction at 310- and 355-nm. The ratio of the quantum yield of $(CH_3)_3SnBr$ dissapearance and the quantum yield of Br_2 appearance extrapolate to a limiting value of 2.3, consequently the overall reaction is

$$2\,(CH_3)_3SnBr \xrightarrow{Ia} Br_2 + (CH_3)_6Sn_2 \qquad 2.17$$

Quite different results are obtained in the case of $(CH_3)_3SnCl$. UV photolysis of $(CH_3)_3SnCl$ does not induced a photochemical reaction. This result is associated with the low efficiency of $(CH_3)_3SnCl$ to absorb the excitation energy (254-, 310-, and 355-nm), since the absorption maxima of $(CH_3)_3SnCl$ occurs at 195 nm. It was not possible in theses experiments to determine wheter $(CH_3)_3SnCl$ is photoreactive. With 254-nm excitation, however, no reaction was found to occur. Therefore it is conclude that $(CH_3)_3SnCl$ is not photoactive.

The quantum yield results shows that the photochemical reaction of of $(CH3)3SnI$ is approximately 100 times more efficient than that for $(CH_3)_3SnBr$, and at least 1000 times more efficient than that of $(CH_3)_3SnCl$. The efficiency of the photoreaction is explained in terms of the absorption efficiency at the excitation wavelength, and the dissociation energy of the

Sn-X bond.

Emission spectra shows that the intensity of the emission band at 330-nm decreases as the halogen atom is substituted from I to Br and Cl, indicating that less energy is absorbed at the particular wavelength by the corresponding trimethyltinhalide. Since the reactive state is the emisive state, the photo reactivity should also decrease. Furthermore, the dissociation energies of the Sn-X bond increases by almost 30 Kcal/mol from I to Br and Cl, hence more energy is require to dissociate the Sn-X bond within the series.

2.2 Polar Solvents.

The primary photochemical event that occurs upon uv photolysis of $(CH_3)_3SnI$ in nonpolar solvents is the homolytic cleavage of the Sn–I bond. The resulting radicals then combine to form the observed products I_2 and $(CH_3)_6Sn_2$. However, quite different behavior occurs in polar solvents. Spectroscopic data recorded during photolysis of $(CH_3)_3SnI$ in polar solvents, such as ethanol and acetonitrile, reveal a fundamentally different behaviour. In ethanol or acetonitrile, for example, absorption spectra, Figure 2.21 Part III, reveal the inmediate formation HI, while I_2 or $(CH_3)_6Sn_2$ are not detected, and stoichiometric measurements indicate the formation of one mole of HI per mole of $(CH_3)_3SnI$ reacted.

Since alcohols in particular, are effective radical scavengers, the change in reactivity is not due to a change in the secondary reactions. Rather, the primary process has change from a homolytic cleavage to a

heterolytic cleavage of the Sn–I bond. This change in the primary process is attributed to the charge redistribution on formation of 1:1 solvent adduct as shown in scheme IV.

Scheme IV [28]

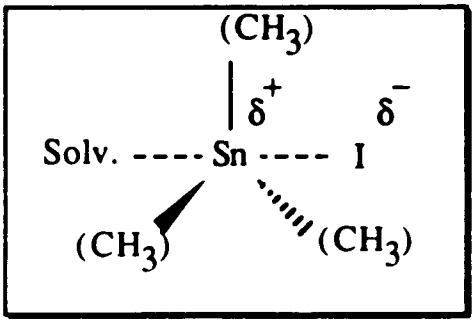

Formation of the solvent adduct shifts the absorption from 234 nm to ca. 218 nm. However, Raman spectra shows that the Sn–I band at 167 cm^{-1} does not change uppon addition of hexanol to an n-hexane solution of $(CH_3)_3SnI$. Either, relatively little change in the polarity of the Sn–I bond on formation of the 1:1 adduct, or an increased polarity of the Sn–I bond offsets the charge redistribution that may occur on formation of the solvent adduct. In either case, UV excitation of the adduct results in heterolytic cleavage of the Sn–I bond. Conductivity measurements reveal an inmediate formation of ions when $(CH_3)_3SnI$ is irradiated in ethanol or acetonitrile. Consequently, the photochemical behaviour is not that of the complex per se, but rather that of the solvent adduct. In this sense, it is not suprising that a fundamental change in reactivity occurs.

Evidence for the photochemical mechanism in polar solvents is obtained from spectral changes in the uv-vis region, as well as from cyclic

voltammetry, and titration meaurements. The dissapearance of the $(CH_3)_3SnI$ absorption band (226 nm in acetonitrile and at 218 nm in ethanol) is followed by the appearance of two photoproduct peaks at 290- and 360 nm. The latter are assigned to the formation of HI, since the uv-vis spectra of HI is identical to the one observed in the photolytic reaction. Stoichiometric measurements yield 0.97 mol of HI per mol of $(CH_3)_3SnI$ reacted. Electrochemical analyses of the photolyte exhibit a reduction wave with a half wave potential equivalent to that of HI, and treating the photolyte with excess $AgNO_3$ yield AgI.

In ethanol the quantum yield of dissapearance of $(CH_3)_3SnI$ is independent of its initial concentration, or the O_2 concentration, and delines as the excitation wavelength shifts from 254- to 310- and 355-nm.

The data gathered in polar solvents preclude homolytic cleavage of the Sn–I bond. Instead, $(CH_3)_3SnI$ reacts with the polar solvent to form a 1:1 adduct, and excitation of the adduct results in the inmediate formation of ionic species. Consequently, the primary photochemical event of the solvent adduct is heterolytic cleavage of the Sn–I bond.

Ia

$$(CH_3)_3SnI \longrightarrow I^- + (CH_3)_3Sn^+$$

2.18

The reaction is written as a straight forward heterolytic cleavage of the Sn–I bond, and the inonic dissociation of organotin halides in electron rich solvents has been reported. This appears to occur in polar solvents such as acetonitrile which are unable to act as a proton donor. [29] However,

in a polar protic solvent such as ethanol, it is also possible that excitation results in a concerted process in which a partially dissociated I^- abstracts a proton from the alcohol, i.e.,

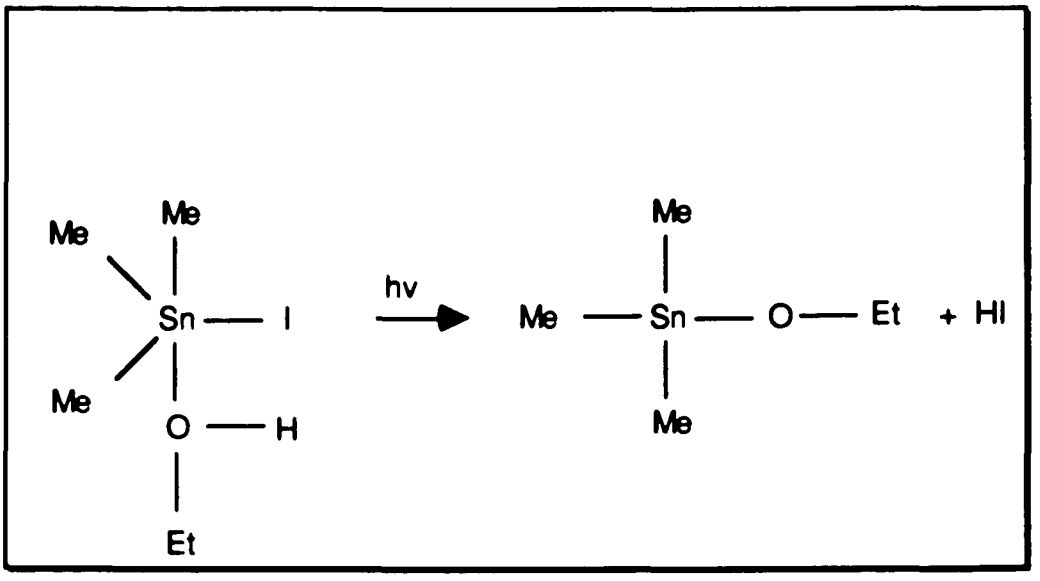

In this case, the increase conductivity that occurs during photolysis may reflect the dissociation of HI.

In either case, the primary photoprocess in the solvent adduct appears to involve principally heterolytic cleavage of the Sn–I bond, whereas that in the individual molecule, which exists in nonpolar solvents, is homolytic cleavage. This change in reactivity is thought to arise from the rehybridization that occurs with the organotin halide on formation of the solvent adduct.

3. Photochemistry of Phenyltin Halides and Phenyltin Azides in Solution.

The low energy absorptions of $(C_6H_5)_{(4-n)}SnCl_n$ and $(C_6H_5)_{(4-n)}Sn(N_3)_n$ (n= 1,2,3) compounds (A_{max} ~ 260nm) makes them better compounds for the study of photochemical reactions on glass surfaces, as compared to the $(CH_3)_3SnX$ compounds ($A_{max} \leq 230$ nm), where the absorptions occur beyond the transmittance of the glass (50% at 250nm).

The absorption spectra of $(C_6H_5)_{(4-n)}SnCl_n$ and $(C_6H_5)_{(4-n)}Sn(N_3)_n$ (n= 1,2,3) compounds consists of a series of vibronic bands centered at approximately 260 nm. This bands are assigned to the $\pi \rightarrow \pi^*$ transitions of the phenyl rings, and resemble the B bands observed in the benzene absorption spectrum. The intensity of the absorption bands is proportional to the number of phenyl rings present, and it is independent of the number of halide or pseudohalide ligands present. There is no evidence of a bathochromic shift in the position of the absorption bands when the samples are dissolved in polar or nonpolar solvents. Consequently, the tetrahedral structure of this compounds remains unaffected in solution.

3.1 Photochemistry of Phenyltinchlorides in Solution.

The photochemical results as well as the stoichiometry of the reaction, 1 mol of Cl_2 per 2 mole of $(C_6H_5)_{(4-n)}SnCl_n$ (n= 1,2,3) reacted, are consistent with the homolytic cleavage of the Sn-Cl bond. The radical products combine to form Cl_2, or $(C_6H_5)_{(8-2n)}Sn_2$ (n= 1,2,3). However, as the number of Cl ligands increases multiple radical reactions that lead to a undetermined products become predominant. Consequently, an indepth study of the mechanism of the photochemical reaction was not possible, because of the lack of knowlege of most of the reactive species present during the photochemical event. Nevertheless, kinetic experiments were carried out, and in most cases the results and their discussion are base on the appearance of Cl_2.

Evidence for the mechanism is obtained from the spectroscopic studies. Since, excitation with 254 nm light induces the decrease of the $(C_6H_5)_{(4-n)}SnCl_n$ (n= 1,2,3) absorption band at ~ 260-nm, accompanied by the simultaneous growth of the Cl_2 absorption band at 330 nm. With $(C_6H_5)_3SnCl$, prolonged photolysis induces the reappearance of the 260-nm band which is assigned to the formation of $(C_6H_5)_6Sn_2$. However, the 260 nm band does not reappear upon prolonged photolysis of $(C_6H_5)_2SnCl_2$ and $(C_6H_5)SnCl_3$.

Other evidence for the mechanism occurs from FTIR spectroscopy, which shows that the Sn-(C_6H_5) bond does not dissociates upon UV excitation, since there is no change in the IR spectra. The Sn-Cl streching vibration occurs at 300 cm^{-1}, and can not be observed with spectrometers equipped with KBr optics. Raman spectra which allows the measurement

of the Sn-Cl streching vibration was not possible due to the low solubility of these compound. Similarly, NMR spectroscopy also shows no changes in the spectra upon UV excitation, indicating again no change in the Sn-(C_6H_5) coordination sphere.

In the case of $(C_6H_5)_3SnCl$ in ethanol, prolonged UV exposure induces the appearance of two absorption bands at 1658-, and 1579 cm^{-1} in the IR spectra. These bands are assigned to the formation of a $(C_6H_5)_3Sn$-O-(C_2H_5), since similar absorption bands are observed in Sn-O-R compounds. [30] Also, prolonged UV exposure of $(C_6H_5)_3SnCl$ in hexane does not show the appearance of the 1658-, and 1579 cm^{-1} absorption bands.

The formation of the $(C_6H_5)_3Sn$-O-(C_2H_5) suggest homolytic cleavage of the Sn-Cl bond. The Cl· radical abstracts H· from ethanol to form HCl, while the $(C_6H_5)_3Sn$· radical combines with the ethoxide radical to form $(C_6H_5)_3Sn$-O-(C_2H_5). In the case of $(C_6H_5)_2SnCl_2$ and $(C_6H_5)SnCl_3$ compounds there are no changes in the FTIR spectra upon prologed UV excitation.

The quantum yield of dissapearance of $(C_6H_5)_{(4-n)}SnCl_n$ (n= 1,2,3) compounds is independent of their initial concentration, or the oxygen concentration, and shows no reaction with 310-, or 355-nm excitation. The ratio of the quantum yield of $(C_6H_5)_{(4-n)}SnCl_n$ (n= 1,2,3) dissapearance and the quantum yield of Cl_2 appearance extrapolate to a limiting value consistent with the following reaction

Ia

$$(C_6H_5)_{(4-n)}SnCl_n \text{ (n= 1,2,3)} \longrightarrow (n/2)\ Cl_2 + \text{other products} \qquad 3.1$$

Quantum yield data shows that the photodecomposition of $(C_6H_5)_{(4-n)}SnCl_n$ (n= 1,2,3) compounds occurs with low efficiency, since the value of the quantum yields of $(C_6H_5)_{(4-n)}SnCl_n$ (n= 1,2,3) disappearance range from 0.02 to 0.009. Furthermore the efficiency depends in the number of chlorine ligands present, since the quantum yield of $(C_6H_5)_{(4-n)}SnCl_n$ (n= 1,2,3) disappearance and the quantum yield of Cl_2 appearance increases as the number of Cl ligands increases from one to three. This tends to indicate that the rate determining step is the dissociation of the Sn-Cl bond. Also, the ratio of the quantum yield of $(C_6H_5)_{(4-n)}SnCl_n$ (n= 1,2,3) disappearance and the quantum yield of Cl_2 appearance decreases from 1.8 to 0.7 as the number of Cl ligands increases from one to three, indicating that there are multiple Sn-Cl bond dissociations when there are more than one Cl ligands, as expected.

To sumarize, UV excitation of $(C_6H_5)_{(4-n)}SnCl_n$ (n= 1,2,3) compounds induces the homolytic dissociation of the Sn-Cl bond. The formation of Cl_2 is readily observed, but there is no clear evidence as to the fate of the $(C_6H_5)_{(4-n)}Sn\cdot$ radicals. The uv-vis results in hexane indicate a $(C_6H_5)_{(4-n)}Sn\cdot$ radical recombination to form $(C_6H_5)_6Sn_2$, while other results, specifically those obtained in ethanol, indicate the formation of $(C_6H_5)_3Sn\text{-}O\text{-}(C_2H_5)$.

3.2 Photochemistry of Phenyltinazides in Solution.

The photochemistry of $(C_6H_5)_{(4-n)}Sn(N_3)_n$ (n= 1,2,3) compounds was also studied for the purpose of comparing the mechanism and efficiencies of the

photochemical reaction with those of the $(C_6H_5)_{(4-n)}SnCl_n$ (n= 1,2,3) compounds. UV excitation of $(C_6H_5)_{(4-n)}Sn(N3)_n$ (n= 1,2,3) compounds leads to N_2 evolution and a photoproduct that absorbs at 350-nm. The latter is tentatively assigned to $(C_6H_5)_{(4-n)}Sn\text{-}N{=}N\text{-}Sn(C_6H_5)_{(4-n)}$. However, as in the case of $(C_6H_5)_{(4-n)}SnCl_n$ (n= 1,2,3) compounds, a complete identification of the photoproducts was not possible. Nevertheless, the mechanistic ideas arising from the study of $(C_6H_5)_3Sn(N3)$ are presented below.

The photochemical reaction appears to involve the dissociation of the $Sn\text{-}N_3$ moiety involving radical intermediates. This dissociation can occur via two reactive intermediates. One involves the homolytic dissociation of the Sn-N bond, the other involves the formation of a nitrene radical intermediate as shown in Scheme I.

Scheme I

$$(C_6H_5)_3Sn\text{-}N_3 \xrightarrow{hv} (C_6H_5)_3Sn\cdot + N_3\cdot \qquad 3.1$$

$$(C_6H_5)_3Sn\text{-}N_3 \xrightarrow{hv} (C_6H_5)_3Sn\text{-}N\text{:} + N_2 \qquad 3.2$$

The radical intermediates react to form a diversity of photoproducts. As the number of azide substituents increases from one to three the photochemical reaction becomes extremely complex due to the multiple side reactions.

Evidence for the dissociation of the Sn-N bond arises from spectroscopic data. UV excitation of $(C_6H_5)_3Sn\text{-}N_3$ in ethanol causes a

decrease in the 260 nm absorption band, and a simultaneous growth of two new bands at 275- and 364nm. The 275nm band is assigned to the phenyl chromophores of the dimer, while the 364 nm band is assigned to the formation of the azo chromophore (-N=N-), which has a characteristic absorption in this region of the spectrum (360-340 nm). [31] Both bands are assigned to a single species since exciting the photoproduct with 350 nm light causes a simultaneous dissapearance of these bands. FTIR spectra shows that UV excitation induces the dissapearance of the azide (N_3) chromophore band at 2073 cm^{-1}, followed by the simultaneous growth of two new bands at 1732- and 1665 cm^{-1}. The latter are tentatively assigned to the formation $(C_6H_5)_3Sn\text{-}N\text{-}O\text{-}(C_2H_5)$, since the (-N-O-R) functionality has a characteristic absoroption in this region. [32] However, the strong azo (-N=N-) band at 2200 cm^{-1} does not appear until prolonged photolysis ($\geq$ 2.0 hr.). Although G.C. analysis comfirmed N_2 formation, the amount is constant and independent of the $(C_6H_5)_3Sn\text{-}N_3$ concentration, the excitation intensity, and exposure time. Also, it never exceeded more than 5 % from the total amount of $(C_6H_5)_3Sn\text{-}N_3$ photolyzed.

The available data is not sufficicent to propose a detailed mechanism, but it must be kept in mind that many of the initial photochemical experiments were of a survey nature, i.e., to determine which organotin compound might be used as a precursor for the photodeposition of tin in glass. However, the complexity of reaction mechanism and relatively low quantum efficiency of decomposition of $(C_6H_5)_3Sn\text{-}N_3$, 0.001 with 254-nm ligth, suggested that organotin azides were not as viable as the originally studied $(CH_3)_3SnX$ compounds.

In summary, UV excitation of $(C_6H_5)_{(4-n)}SnCl_n$ (n= 1,2,3) compounds induces the homolytic cleavage of the Sn-Cl bond, and the

radicals produced combine to form Cl_2 and $(C_6H_5)_{(4-n)}Sn\text{-}Sn(C_6H_5)_{(4-n)}$. The photochemistry is similar to that found for $(CH_3)_3SnX$ compounds. UV excitation of $(C_6H_5)_{(4-n)}Sn(N_3)_n$ (n= 1,2,3) compounds appears to induce the cleavage of the azide (N_3) functionality, but subsequent chemistry leads to a number of photoproducts, and the apparent quantum efficiency of precursor decomposition is supprisingly low.

4. Photochemistry of Trimethyltin Halides Adsorbed onto Porous Glasses.

The photochemistry of $(CH_3)_3SnX$ (X= I, Br, Cl) in solution depends on the solvent polarity. In nonpolar solvents, such as hexane, the primary photochemical event is the homolytic cleavage of the Sn–X bond, while in polar solvents, such as ethanol, uv excitation results in the heterolytic cleavage of the Sn-X bond. Similarly, photolysis of $(CH_3)_3SnX$ (X= I, Br,) adsorbed onto porous glasses results in the heterolytic cleavage of the Sn-X bond, and the inmediate formation of HX in a 1:1 stoichiometric ratio.

4.1 Photochemistry of $(CH_3)_3SnI$ Adsorbed onto PVG.

When $(CH_3)_3SnI$ is adsorbed onto PVG, electronic difference spectra show that the absorption maximum shifts to ≤ 220 nm. Irradiation of the sample in vacuo ($p \leq 10^{-4}$ torr) with 254 nm light causes spectral changes equivalent to those in ethanol, and HI is detected immediately in a 1:1 stoichiometric ratio. [33]

$(CH_3)_3SnI$ reacts with polar solvents to form 1:1 complex adduct, as the solvents polarity increases the absorption maxima shift to higher energies, and FTIR spectra of the complex in ethanol reveals a five

coordinate species. [34] When $(CH_3)_3SnI$ is adsorbed onto PVG, the absorptium maximum shifts to ≤ 220 nm. DRIFT spectra show a decline in intensity of the silanol band, 3775 cm^{-1}, and a concurrent growth of a broad O–H band centered at 3500 cm^{-1}. Although, all PVG samples are calcined at 550 °C prior to use, thermal gravimetric analysis and DRIFT spectra indicate the presence of chemisorbed water. [35] Both chemisorbed water and silanol groups are Lewis bases, and in principal, potential reaction sites. Since the spectral changes are independent of the extent of calcination, however, the dominant reaction appears to be with a silanol group to form a surface-bound five coordinated adduct. The growth of the broad O–H band without the addition of water suggests that the complex does not formally displace the silanol hydrogen. Instead, the complex binds to the silanol oxigen, i.e.,

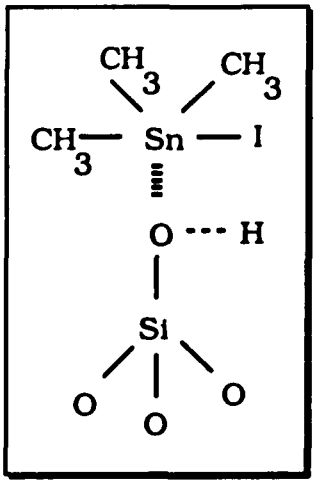

The interaction with the oxygen reduces the SiO–H bond strength and shifts the SiO–H band to lower frequency.

Addition of the silanol group not only increases the coordination number but also changes the electron distribution within the molecule. The specific nature of the electronic change is by no means clear, but the adduct is not a charge transfer complex per se.[36] The shift in the electronic absorption to higher energy, without a concurrent change in the 167 cm^{-1} Sn–I vibration, suggests that the major change in polarization occurs in the excited state. The addition of the Lewis base polarizes the Sn–I bond. Photolysis releases I^- which then abstracts a proton to form HI, i.e.,

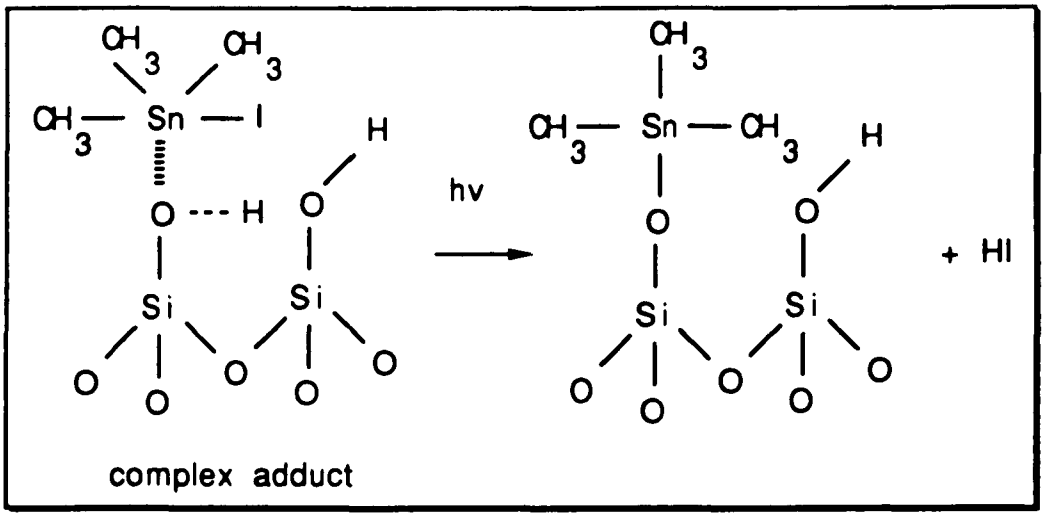

The quantum yield of the photochemical reaction in ethanol is 0.63 ± 0.05 with 254 nm light but reduces to 0.24 ± 0.03 on the glass surface. The wavelength dependence as well as the absence of an O_2 dependence suggest that the photoreaction in both media continues to occur from the high energy state populated upon absorption. The smaller yield on the glass appears to be a consequence of the topology and rigidity of the glass surface.

The reaction occurs within the creavices in the glass surface, and these irregularities enhance recombination by curtailing product separation. During consolidation, the surface-bound photoproduct is converted to SnO_2.

4.2 Photochemistry of $(CH_3)_3SnBr$ and $(CH_3)_3SnCl$ Adsorbed onto PVG.

The photochemistry of $(CH_3)_3SnBr$ and $CH_3)_3SnCl$ adsorbed onto PVG was also studied with the purpose of comparing the mechanism of the reaction with that of $(CH_3)_3SnI$ adsorbed onto PVG. However, it was immediately apparent that a detailed characterization would be hampered by the fact that only the edge of the high energy absorption band of $(CH_3)_3SnBr$ and $(CH_3)_3SnCl$ is observed in PVG.

Irradiation of $(CH_3)_3SnBr$ and/or $(CH_3)_3SnCl$, adsorbed onto PVG, with 254 nm light shows very small spectral changes. Prolonged exposure of upto 72 hours of adsorbed $(CH_3)_3SnBr$ results in the appearance of a small absorption band at 420 nm. The latter is assigned to Br_2 formation, since the absorption spectrum of Br_2 adsorbed onto PVG appears at 450 nm. However, prolonged exposure of $(CH_3)_3SnCl$ to 254-nm light results in no change in the absorption spectra.

Establishing the reactive state points out the major draw back of $(CH_3)_3SnI$ and related analogs. The reactive excited state lies at high energy, and the optical absorption populating the state occur beyond the UV-transmittance of the glass (50% at 250 nm). Consequently, the reactions and the resulting gradient index structures are limited to the outer glass

surfaces. This is not to say that they are monolayer structures on a flat surface. The glass is initially pororus and the surface topology allows some access into the bulk material. Cross-sectional x-ray micrographs show that, after consolidation, the SnO_2 gradient index structures have depths of the order of hunderds of microns.

4.3 Photochemistry of $(CH_3)_3SnI$ Adsorbed onto TMOS Xerogels.

Adsorption of $(CH_3)_3SnI$ onto TMOS xerogels,occurs via a five coordinate surface-adduct, since the absorption spectra shifts in a simmilar fashion to $\leq$ 220 nm as observed in PVG. Although irradiation of the sample in vacuo with 254 nm light produces spectral changes similar to those observed in PVG, the position of the HI absorption bands, 290-, and 360-nm in ethanol and in PVG, shifts to 270- and 330-nm in the sol-gel glass. However, the intensities of the 270 and 330 bands, as well as their ratio, $A^{270}/A^{330} \sim 1.9$, remains constant as a function of irradiation time, and has the same value as found in ethanol and/or on PVG. The shift in the HI bands is believe to occur due to an increase in the surface polarity of the gel, since sol-gel glasses have greater OH content, ~ 20 % OH, than PVG, ~ 5% OH. However, further evidence needs to be obtained for this argument to be conclusive. Furthermore, The quantum yield of dissapearance of $(CH_3)_3SnI$ asorbed onto the TMOS sol-gel glass is of the same magnitude, within experimental error, to that of PVG, $\Phi = 0.25$.

The photochemical and quantum yield results indicate that photolysis of $(CH_3)_3SnI$ adsorbed onto porous silica glasses proceed via the heterolytic cleavage of the Sn–I bond, as observed in polar solvents such as ethanol. Adsorption of $(CH_3)_3SnI$ onto the polar surface forms a five coordinated surface-adduct. Photolysis releases I^- which then abstracts a proton to form HI.

5. Photodeposition of Metal Oxides onto Porous Glass Matrices.

Tin and iron oxide have been photodeposited in porous Vycor glass and TMOS sol-gels and examined before and after consolidation of the glass. Scanning electron microscopy reveals that the iron oxide particles are larger than the tin oxide particles. However, small angle x-ray scattering and Rutherford backscattering show that the glass consolidates about the iron oxide, but not about the tin oxide. Photodeposition of tin oxide, which appears to chemically modify the glass surface and to prevent its consolidation, which offers a means of producing highly resolved regions of porosity in the otherwise consolidated glass.

5.1 Effect of the Photodeposited Tin and Iron Oxide on the Consolidation of Porous Vycor Glass.

Future developments of optical circuitry hinge on the development of new photonic materials. The results presented in this study show that highly resolved gradient index patterns, or patterns of electrically and magnetically addresable adsorbates, can be produced by photochemically deposition of metal oxides onto porous Vycor glass (PVG).

To gain some insight into the relationship between glass morphology and the distribution of metal oxide, i.e., the factors that ultimately control pattern resolution, tin and iron oxide were examined by surface analysis techniques. Small angle x-ray scattering (SAXS) and scanning electron microscopy (SEM) were used to examine the microstructure of the metal oxide impregnated glass, while Rutherford backscattering spectroscopy (RBS) was used to determine sample stoichiometry and near-surface sample concentration. The results consistently show dramatic differences in the effect of tin and iron oxide on the consolidation of the glass.

SAXS's from four samples were measured: unconsolidated and consolidated PVG (Figure 6.4 Part III), and tin and iron oxide on consolidated PVG (Figure 6.5 Part III). The SAXS curves show an interference peak at Q = 0.018 $Å^{-1}$, where Q is the scattering vector. The presence of the SAXS peak and the absence of higher order peaks suggest that the sample microstructure can be modeled by a bicontinuous spinodal structure as shown by Berk. [37] Results from the consolidated PVG and the iron oxide consolidated PVG show the absence of the SAXS peak indicating that the porous network has consolidated to a noporous glass. In theory, heating a PVG sample to 1200 °C consolidates the sample and consequently causes the scattering peak to dissapear as the spinodal order is lost. This is indeed what is observed to occur with the iron oxide impregnated sample consolidated to 1200 °C; the scattering peak is almost entirely eliminated in the SAXS curve. The suppresion of the peak suggest that the spinodal structural ordering has diminished and the iron oxide becomes a distributed component within the glass matrix.

SAXS from the tin oxide impregnated sample heated at the consolidation temperature of 1200 °C is quite different from that of the

consolidated sample impregnated with iron oxide. The broad peak Q = 0.018 $Å^{-1}$ persists despite the heat treatment and the measured correlation length of l = 230 Å is the same as that for unconsolidated PVG. Thus the glass impregnated with tin oxide apparently retains its original ordered spinodal structure.

The lack of consolidation of the glass in the presence of tin oxide is further comfirmed by Rutherford backscattering. The scattering data from impregnated tin and iron samples heated to 1200 °C (Figures 6.7 and 6.6 Part III respectively) are compared with calculated spectra for scattering from a smooth $SiO_2M_{0.01}$, [38] where M= Sn or Fe. The consolidated iron oxides agree with the model, but the tin oxide impregnated samples show an nonstoichiometric excess of oxygen and deviations from the calculated step-like profile. The poor fit to the model in the tin oxide case indicates that the metal oxide exists in a nonuniform, granular or porous material.

The behaviour of these metal oxides on consolidation is not simply a size phenomenon, where the larger metal oxide particle prevents the PVG from consolidating about it and the smaller metal oxide particle does not. SEM analysis indicate that the iron oxide particles (Figure 6.3 Part III) are larger than the photodeposited tin oxide particles (Figure 6.2 Part III). Yet at 1200 °C, the glass apparently consolidates about the larger iron oxide particles, but resists consolidation about the smaller tin oxide particles.

The ability of tin oxide to inhibit consolidation of the glass appears to be a chemical effect. Luong, et. al. [39] have shown that photodeposited $(CH_3)_3Sn–O–Si$ or tin oxide reacts with the glass surface, and this may prevent consolidation to a nonporous nonunifiorm glass. Recent experiments using secondary-ion mass spectroscopy and x-ray fluorescence micrography [40] show that the majority of the deposited tin,

following consolidation is in the outermost surface of the glass, consistent with this idea. Further experiments to elucidate the nature of the chemistry and that of the metal oxides at different stages of the reaction are in progress.

5.2 Diffusion of Metal Oxides onto Porous Glasses.

The photolithographic deposition of metal oxide refractive index gradients in porous glass is based on photochemically binding the reagent to the glass surface, converting the photoproduct to a metal oxide during thermal consolidation, and volatalizing the unreacted adsorbate from the glass. Therefore, pattern contrast depends on the relative amounts of metal oxide in the photolysed and unphotolyzed regions.

In samples initially containing 10^{-4} mol $(CH_3)_3SnI$/g, photolyzed with 254 nm light and heated to 1200 °C to remove the unreacted adsorbate, the amount of tin near the surface of the photolyzed region (Figure 6.9 Part III), is approximately three times larger than in the unphotolyzed region. Nevertheless, a significant amount of Sn remains in the unphotolyzed region, thereby reducing pattern contrast. On the other hand, in an iron oxide image (Figure 6.13 Part III), very little iron is found in the unphotolyzed regions of samples prepared under equivalent conditions, i.e., 10^{-4} mol $Fe(CO)_5$/g, photolyzed with 254 nm light and heated to 1200 °C to remove the unreacted adsorbate. With both complexes the amount of metal oxides in the photolyzed region relative to that of the unphotolyzed region increases with increasing initial loading, but at all loadings the difference obtained with $Fe(CO)_5$ is significantly better than that obtained with

$(CH_3)_3SnI$. This appears to be due to two factors. First, the larger fraction of the exciting light absorbed and the higher quantum efficiency of reaction of $Fe(CO)_5$(ads). The latter yields a higher iron oxide content in the photolyzed regions relative to that obtained with $(CH_3)_3SnI$(ads). Second, $Fe(CO)_5$ physisorbs onto the glass, and this relatively weak interaction is readily overcome during subsequent heating. $(CH_3)_3SnI$ reacts with the glass surface to form a five-coordinated species. Apparently, coordination to the glass surface curtails desorption so that a larger fraction of $(CH_3)_3SnI$(ads) undergoes thermal oxidation during heating, thereby reducing pattern contrast.

Particle size is related to, but is not simply a fucntion of, initial loadings. With sample containing ~10^{-4} mol of $(CH_3)_3SnI$(ads),/g, image formation is visually apparent during photolysis as a darkening in the exposed region. SEM analysis of the consolidated samples show that the tin oxide image (Figure6.1 Part III) is composed of distinct microscopic particles of the order of 10- to 50-nm in diameter, and secondary-ion mass spectra (SIMS) (Figure 6.8 Part III) shows that the concentration of tin oxide is maximum at the outermost surface and decreases exponentially. At a depth of ~1000 Å, the amount of tin oxide present reaches a steady plateau and remains essentially constant to a depth of 4000 Å.

Similarly, SEM analysis (Figure 6.2 Part III) of a consolidated PVG sample impreganted with ~10^{-4} mol of $Fe(CO)_5$(ads)/g shows that the image formed is composed of iron oxide particles that are of the order of 10- to 50-nm. The particles form large clusters of aggregate particles that extend from 1 to 5 μm in length. Mossbauer spectra indicates that the majority of the iron oxide is magnetite, Fe_3O_4. SIMS spectra (Figure 6.11 Part III) shows that relatively little iron oxide is on the outermost surfaces of the

consolidated glass. Instead, there is an overlaying layer of glass ~50 Å thick that contains little or no iron. At a depth of 50 Å there is a sharp increase in iron content and the amount present remains essentially constant to a depth of at least 4000 Å.

5.3 Comparison of Iron Oxide Photodeposited in Porous Vycor Glass and TMOS sol-gel glasses.

The iron oxides obtained by photolysis of $Fe(CO)_5$ physisorbed onto porous Vycor glass are compared to those obtained in TMOS xerogels. Mossbauer and X-ray absorption fine structure, extended, data indicate the formation of surface-bound, octahedrally coordinated Fe^{3+} species in both materials. Although photoimaging experiments show that iron oxide images of equivalent resolution can be photodeposited in both glasses, consolidation of the PVG samples, but not the xerogel samples, yields magnetically ordered materials exhibiting magnetic hyperfine fields of 370 and 425 kG, respectively. Formation of a magnetically ordered material depends on initial $Fe(CO)_5$ loadings, and its occurence in one glass, but not the other, is thought to reflect differences in the morphologies of the two materials.

Mosbauer spectra recorded after photolysis of 10^{-4} mol of $Fe(CO)_5$(ads)/g (Figure 6.16a Part III) adsorbed onto PVG, at 650°C, exhibit two quadrupole doublets with splittings of 0.98 and 0.93 mm/s, consistent with the formation of octahedrally coordinated Fe^{3+}. Similarly, near edge EXAFS spectra also indicates the formation of octahedrally coordinated Fe^{3+}. However, the Fe–O bond distance in the photodeposited iron oxide

(1.5 ±0.5 Å), agrees with the formation of Fe_2SiO_4, where the Fe–O bond distance is 1.3 ±0.5 Å, rather that the formation of iron oxides where the bond distances are approximately 2.0 ± 0.5 Å.

Under equivalent loadings and photolysis similar results occur in the xerogel. After heating to 650 °C, however, the Mosbauer spectra (Figure 6.16b Part III) consist of a single quadrupole doublet with a splitting at 0.91 mm/s. Apparently, the majority of the iron in the xerogel exist in a unique site. Nevertheless, the isomer shift is consistent with octahedrally coordinated Fe^{3+}. [41]

Pott and McNichol report that when Fe^{3+} is absorbed onto silica and then heated to > 400 °C, Fe^{3+} assumes a tetrahedral coordination, and at 800 °C, crystallyzes to a-Fe_2O_3. [42] However, in these glasses, Mossbauer and EXAFS data indicate that photolysis leads to surface-bound, octahedrally coordinated Fe^{3+} species, which shows no detectable change on heating to 650 °C. The isomer shifts suggest, that two different sites exist in PVG, and these differ from those in the xerogel. Both substrates posses Si–OH surface functionalities, [43, 44] but differ with respect to the other species present. PVG is an acid leached glass and posseses B_2O_3 Lewis acid sites, [45] whereas the xerogel does not. On the other hand, DRIFT spectra reveal the presence of Si-OCH_3 functionalities in the xerogel, which are not present ion PVG.

Attributing the different sites to the involvement of these groups, however, is neither chemically nor physically consistent with the available data. Chemically , it is unlikely that Fe^{3+}, itself a Lewis acid, would bind to an electron-defficient site in the glass matrix. Physically, x-ray photoelectron spectroscopy (XPS) indicates that the amount of B present in the first 50 Å of these PVG samples is 2.6 ± 0.1%. If B were involved in one

of the sites, the amount present implies doublets of quite different intensities. Yet, in all samples, the relative intensities of the two quadrupole dopublets are similar, and differ by no more than 30%. Invoking the Si–OCH_3 functionalities would suggest two sites in the xerogel, and one in PVG, whereas the opposite is observed. Most likely, the observed differences arise from structural variations rather than different coordinating atoms.

Heating the samples to 1200 °C consolidates the glass matrix. Consolidation occur with a 40% volume reduction in both substrates, and as a result, the image is also reduced by 40%. However, it occurs with no detectable loss of image resolution in either glass. Consolidation entraps the iron species, but it occurs without further chemical change. Mossbauer spectra of the iron in the consolidated xerogel remains equivalent to those at 650 °C (Figure 6.18 Part III). And consolidation of a PVG sample with initial $Fe(CO)_5$ loading of $\leq 10^{-5}$ mol(ads)/g yields equivalent results. In both glasses consolidation entraps a nonmagnetic, octahedrally coordinated Fe^{3+}species. However, consolidation of a PVG sample with initial $Fe(CO)_5$ loading of $\geq 10^{-4}$ mol(ads)/g results in the loss of the quadrupole doublets and the appearance of two six line spectra (Figure 6.19 Part III) characteristic of two hyperfine magnetic fields. The isomer shifts correspond to Fe^{3+} and EXAFS spectra yields an iron-nearest neighbor distance of 1.5±0.15 Å. These data suggest that the same species is formed in all samples, i.e., an octahedrally coordinated Fe^{3+} species. Yet, magnetically hyperfine splittings appear only in the consolidated PVG samples prepared with high loadings.

The appearance of magnetically ordered material in consolidated PVG samples, but not in consolidated xerogels prepared under equivalent

conditions, is surprising. Chemically and physically, the two materials are similar, equivalent Fe^{3+} species are formed in both glasses. One possible explanation, however, arises from the different surface area of the two materials. The surface area of the calcined xerogels, 600 ± 30 m^2/g, is significantly larger than that of calcined PVG, 183 ± 15 m^2/g. Electronic spectra, recorded at different locations on the same sample, show that $Fe(CO)_5$ uniformly distributes as individual molecular entities on both surfaces. Assuming that the Fe^{3+} species are also uniformly distributed in the porous glasses, since neither PVG or the xerogel exhibit magnetic hyperfine splittings when heated to 650 °C, then the average spacing between the species in the xerogel is ca. 3 times that in PVG. Consolidation reduces the spacing, but with these equivalent initial loadings, the spacing between the Fe^{3+} species in the xerogel may be beyond magnetic coupling distances. Of course, aggregation could occur, although the appearance of hyperfine splittings suggests that this is limited to the formation of small, fine particles.

In either case, the formation of magnetically ordered material, whether it derives from the aligment of individual Fe^{3+} species or the formation of small aggregates, depends on the spacing of the Fe^{3+} species in the porous glass. In turn, this depends on the initial loading of the porous glass. To date, magnetically hyperfine splittings have been observed only in consolidated PVG samples prepared with $Fe(CO)^5$ loadings of $\geq 10^{-4}$ mol/g.

In conclusion, it has been demostrated that photodepositing tin in PVG yields highly resolved regions of porosity in an otherwise consolidated glass. These regions offer an opportunity of incorporating a variety of reagents into the glass at ambient temperatures that were previously

excluded because of the inability of the active reagents to withstand the consolidation conditions. In addition, it has also been demostrated that highly resolved patterns of magnetically order Fe^{3+} species can be deposited onto consolidated PVG. By using well-established microlithographic technologies these results can be used in the processing of active integrated optical components.

6. Photolithography of Integrated Optic Devices in Porous Glasses.

The success of photonic switching depends on the development of materials capable of processing light signals without the interweaving conversion to electronic signals. The photodeposition of metal oxides onto porous Vycor glass and silica glass sol-gels produces changes in the index of refraction of the glass of the order of 0.1 to 0.001. Nonlinearities in transmission and refractive index allow the deposition of 0.1- to 10.0-μm width planar waveguides with attenuations of 0.6 dB/cm. This technique is being evaluated for the optical performance of couplers, dividers, and interferometers.

6.1 Introduction.

The starting point in the fabrication of many types of integrated optic devices is a substrate on which a planar waveguide can be formed. The planar optical waveguide is the fundamental element that interconnects the various devices of an optical integrated circuit, just as a metallic strip does in an electrical integrated circuit. Optical waveguiding depends in the

ability to create a change in the index of refraction between the waveguiding region and the surrounding media. Many techniques have been developed that produce that required index difference. The choice of the specific technique for waveguide fabrication depends on the application, and on the facilities available. Thin-film combined with microlithograpy technologies, such as those used in the fabrication of electrical integrated circuits, are commonly used in the processing of planar waveguides on a variety of substrates. [46]

Ideally one would dream of a single material where the various functions required by optical systems could be made, since this would yield totally integrated systems. The only possible materials, at the moment, belong to the III-V semiconductor family, and mainly to the GaAs family. Although many functions for optical circuitry can be made in GaAs, this medium is not the best for each function; and it can be reasonably be assumed that for a long time, if not forever, integrated optics will have to be hybrids. Many materials have been used for making optical waveguides; and many of them have been proposed principally because they were easy to be elavorated but they will definitely not have industrial importance. Currently, the most important materials for integrated optics are GaAs, $LiNbO_3$, glass, and silicon.

Planar optical waveguides made by the photolithographic deposition of metal oxides onto porous silicate glasses are ideal for the fabrication of low loss integrated optic devices. [47] Both passive and active devices can be fabricated by the deposition of a suitable metal oxide. The deposition of SnO_2 onto porous silicate glasses produces changes in the index of refraction of the glass of the order of 0.1 to 0.001 that allows a He-Ne laser beam to be guided through a 1.0 μm (width) waveguide with a 1.0 in radius

of curvature. Similarly, opto-magnetic strip waveguides can be made by the deposition of magnetic Fe_2O_3.[48] The advantage of the photodeposition technique for waveguide processing is that it offers the possibility of integrating a variety of devices at the submicron scale in one single substrate at a low cost and with a relatively little effort.

6.2 Fabrication of Planar Optical Waveguides in Porous Glasses.

Optical waveguides of the dielectric type are made of a medium having a higher refractive index than the surrounding media. As they must be very thin (on the order of micrometers) one cannot think of making them in the shape of a sheet floating in the air. Therefore, optical waveguides necessarly lie on a substrate. Fabrication technologies that are used for making optical waveguides can be roughly classified into two types: in the first one, a thin transparent layer is grown on a less refringent substrate; in the second, a transparent substrate is submitted to some physical process which increases the refractive index starting from the surface.

The problem is to increase the refractive index of the transparent substrate in the region of its surface. Consequently, one has to intervene from the outside, through the surface. Since, a modification of the substrate is needed, starting from its surface, diffussion is a well adapted method. The physical reason for diffusion is the existence of a concentration gradient .

Porous silica glasses impregnated with photosensitive organometallic compounds exhibits optical changes when exposed to light.

Optical changes in transmission and refractive index can be induced and are permanent after consolidation of the glass to a nonporous matrix. [49] For example, highly resolved patterns of gradient indices are obtained by photochemically binding $(CH_3)_3SnI$ to the glass matrix followed by thermal consolidation. [50] Similarly, photolysis of $Fe(CO)_5$ followed by thermal consolidation leads to equally well resolved patterns of iron oxide. [51] With both compounds, photolysis binds the reagent to the glass matrix. Binding prevents migration and maintains pattern resolution during the thermal consolidation. Thermal consolidation, which requires temperatures of ≥ 1000 °C, volatilizes the unreacted adsorbate from the glass and converts the photoproduct to a metal oxide.

The criteria in selecting the proper organometallic compound are : (a) photoactivity, (b) volatility, and (c) thermal stability. The organometallic compound must be photoactive in the visible or near UV, since a key step in forming an image pattern on the glass surface involves the photochemical reaction of the organometallic compound with the dangling silanol groups of the glass. Volatility is essential for a homogeneous adsorption of the organometallic compound onto the glass surface, and also for the complete removal of the unreacted compound from the glass surface prior to the thermal treatment. And finally thermal stability is required since the unreacted precursor must be disorved from the substrate, and the photoproduct must withstand the temperatures required to consolidated the porous glass to a nonporous glass without decomposition or loss of image resolution.

The planar waveguides are photolithographed by contact printing using a photomask, laser writing, and/or holography. The wavelength of the light source depends on the absorption characteristics of the

organometallic compound, and the glass substrate. Typical light sources include Hg, and Xe flash lamps, and Nd:YAG laser. The thermal treatment involves heating the glass from room temperature to the consolidation temperature of the glass (~ 1200 °C) at several stages. The first stage is carried out at a low heating rate ~ 2°C/min to the temperature of vaporization of the organometallic compound. Once the unreacted compound has been removed, the heating rate is increased to 5 °C/min and brought up to 1200 °C. SnO_2 and Fe_2O_3 planar waveguides have been made by this method from the photolysis of $(CH_3)_3SnI$ and $Fe(CO)_5$ respectively.

6.3 Characterization of Planar Waveguides.

Besides the fabrication technique, the characterization of the optical properties of the planar waveguides is essential for a complete description of the performance of the waveguides. The parameters to be considered are the width, thickness, the wavelength transparency, magnitude and shape of the refractive index profile, and the scattering losses.

Both single and multimode planar waveguides were fabricated by the photolithographic deposition of tin and iron oxides onto porous Vycor glass. The thickness of the waveguides depends on the resolution of the photomask, and the processing conditions, i.e., concentration of organometallic precursor adsorbed onto the glass, excitation wavelength and exposure time.

Two refractive indices have to be considered: the index of the substrate and the index of the layer. The refractive index of PVG is 1.500,

and that of the waveguide layer varied from 1.551- to 1.601 ± 0.050. A very small difference (Dn) in the refractive indices of the substrate and the layer is enough to observe lightwave guiding (Figure 7.29 PartIII). The change in the index of refraction is directly proportional to the concentration of organometallic precursor on the glass, and the excitation intensity. The obtained refractive index profile is a gradient index profile, as observed in the concentration profiles, (Figure 6.13) and it follows a gaussian distribution.

The transparency of the waveguides is about the same as that of the substrate from the ultraviolet (50% transparency at 250nm) to the infrared (20% transparency at 1.0 μm). The losses are of the order of 0.6 dB/cm (at 514 nm), and are mainly due to coupling losses, and the scattering losses at the interfaces. Also there are some losses due to the absorption of the waveguiding material. From this point of view, graded index waveguides are preferable as well as waveguides buried below the surface of the substrate.

6.4 Planar Tees and Couplers.

Multimode fiber optic systems currently use couplers and splitters for data distribution to several user terminals. Couplers are made by modifying optical fibers (fusing, tapering, lapping, and gluing) or with micro-optic components (such as microlenses and beam splitters), and by the planar approach, which is the subject of this program. The success of mass produced couplers depends in the reproducibility of the technique. In the

case of fusing optical fibers reproducibility is a major concern, and component placement and packaging in current micro-optic devices requires considerable attention during coupler assembly. The planar fabrication approach attacks directly the problems of reproducibility, one-by-one fabrication, and precise placement of components which are encountered in the two conventional approaches by emphasizing the photolithographic control of the coupling structure and the batch processing capabilities inherent in the planar approach.

The photolithographic approach was used to produce Y-junctions of different splitting ratios depending on the angle of separation. The results clearly demostrate the batch processing potential of planar couplers. The results are shown in Figure 7.34 Part III where, for two outputs P_L and P_R, the coupling efficiency decreases with increased branching angle. However, at small branching angles (~ 2°) the coupling efficiency approaches 50:50 in each arm.

The photolithographic deposition of metal oxides on PVG and silica glasses produces changes in the index of refraction of the glass of the order of 0.1 to 0.001. Changes in the index of refraction of the glass allows the fabrication of planar waveguides with losses in the range of 0.6 dB/cm ± 0.5. The technique is currently being used for the fabrication of more complicated integrated optical components such as star coupler and Mack-Zenhder interferometers.

Part V

Conclusion

Highly resolved photolitographic patterns and passive integrated optics devices have been demonstrated by making use of photoinduced metal oxide deposition onto the surface of porous Vycor glass. The ability to produce changes in the refractive index of the glass of the order of 0.1 to 0.001 has allowed guidance of a He-Ne laser beam through a photolitographed optical waveguide. Coupling of the laser beam was achieved by placing two optical waveguides in close proximity to each other, and splittings and junctions were made of different varieties. The results obtained with the photolitographic technique have shown the possibility of making a wide variety of integrated optics components without the expense and technological effort that is usually required.

The mechanism and kinetics of the photochemical reaction of trimethyltiniodide in solution, and in PVG have been investigated. Characterization of the photoproducts by spectroscopic techniques have established that the primary photochemical event is dependent on the environment that surrounds the organotin molecule. In nonpolar media, the primary event is the homolytic cleavage of the Sn--X bond. On the other hand, in polar media, the molecule undergoes a structural rearrangement, from tetrahedral to essentially trigonal bypyramidal by forming a 1:1 adduct between the tin atom and the electron donor surroundings. Therefore, in polar media the tin-halide bond is weaken by the interaction of the surroundings, and the primary photochemical event takes place as a heterolytic cleavage of the already weaken Sn--X bond. The same reactions observed in polar solvents were observed on the PVG matrix. This result was expected since the surface of PVG, which consist of silanol groups, is polar in nature.

The secondary events in nonpolar solvents were established as the

combination of the photoproduced radicals to form the corresponding diatomic halogen and the hexamethylditin dimer. In polar media, the charged species photoproduced remain as ionic species, or combined with the adventitious solvent to form the corresponding photoproducts.

From the kinetic studies, it was established that the photoreaction is independent of the concentration of the reactants, but due to secondary photolysis, on the concentration of the products. However, under the conditions used during the kinetic studies, the product concentration effect could be ignored. As a result, the overall reaction is first order with respect to the light intensity, and the rate determining step is the cleavage of the Sn-X bond.

The photochemical reaction of phenyltin halides and pseudohalides was partially investigated. The motive behind these experiments was to find compounds that will facilitate the study of the photochemical reactions on PVG in the near UV-VIS region, in order to obtain higher quantum yields. From the compounds investigated, phenyltinchlorides and phenyltin azides, it was concluded that the mechanism of the photochemical reaction proceeded through a radical mechanism as found in the photochemical reaction of trimethyltiniodide. Unfortunately, the quantum yields of the photoreactions was found to be less than 0.1 in all cases.

The photochemical reaction of trimethyltiniodide in PVG follows the same mechanism as in polar media. The trimethyltiniodide forms an adduct between the dangling hydroxides form the silanol groups of PVG. On photolysis, the partially polarized bond breakes heterolytically releasing the iodine ion and forming a partially covalent bond between tin and oxygen from the silanol groups. This bond is further stabilized through oxidation during the low temperature heat treatment stages. As the temperature is

increased under high vacuum conditions, the remaining attached methyl groups volatilized leaving behind a covalently tin oxide molecule. This tin oxide molecule was found to act as a modifier of the glass matrix preventing its consolidation at 1200 °C. Possibly higher temperatures are required to fully consolidated the tin oxide impregnated glass. This result, on the other hand, opens the possibility of having highly resolved and specific regions of porosity in an already consolidated glass. This regions could be used trough further etching of the tin oxide layer for the deposition of nonlinear optic materials in a consolidated glass. From diffusion studies, it was found that the tin oxide molecules do not diffuse laterally on the surface of the glass, but inward into the bulk of the glass. The depth of diffusion of trimethyltiniodide was in the 100 to 1000 μm range depending on concentration and photolysis time. As a result, these photolitographic techniques offer a means of patterning materials on the surface and at least partially into the bulk of the glass, which offers the possibility of three dimensional arrays of integrated optic structures.

The quantum yield of the photochemical reaction of trimethyltiniodide makes it an ideal compound for the photolitographic generation of highly resolved gradient refractive indices in PVG, and Si-based xerogels. By using modern laser photolitographic techniques, capable of reducing the laser tip down to the submicron level, schematic diagrams of complicated integrated optics circuits can be deposites. Eventually, these techniques may be useful in designing the optical analogs that will constitute the optical computer. Advances in this field of integrated optics is taking place in many laboratories world wide.

The large variety of molecular and material structures, which are currently under investigation, will without any doubt lead to new insights and device concepts towards an all integrated optical computer. The photolithography of planar waveguides in glasses has the potential for exploration on basic components for switching and interconnections, however for a complete integrated system the following parameters have to be investigated: mode field dimensions for low loss waveguide coupling, and electro-optic coefficients.

Appendix .

1. Quantum Yield Calculation Program.

```
DIM x(200),y(200),calcy(200),dif(200)
INPUT "Enter Volume of Actinometer Irradiated in ml";v1
INPUT "Enter Volume of V1 Analyzed in ml";v2
INPUT"Enter Volume V2 is diluted to in ml";v3
avogadro=6.023E+20
REM Ferrioxalate is 1.11E4
INPUT "Enter epsilon of actinometer";epsilon
INPUT "Enter length of cell in cm";length
INPUT"Number of Absorbance Readings for Actinometer";number
FOR counter=1 TO number
READ absorb(counter)
NEXT counter
REM Data for the actinometer goes here
DATA 0.0001,0.160,0.308,0.401,0.512,0.637,0.646,0.704,0.694,0.720
CLS
FOR counter=1 TO number
NumMoleculesAct(counter)=(avogadro*v3*v1*absorb(counter))/(epsilon*v2*
length)
PRINT "Number of Fe2+ molecules after irradiation
is";NumMoleculesAct(counter)
LPRINT "Number of Fe2+ molecules after irradiation
is";NumMoleculesAct(counter)
NEXT counter
```

```
LPRINT
REM Ferrioxalate irradiated at 254 nm and measured at 510nm is 1.25
INPUT"Enter Quantum Yield of the Actinometer";QuantYieldAct
CLS
FOR counter=1 TO number
READ times(counter)
REM Enter times here in seconds
DATA 0.0001,5,10,15,20,25,30,35,40,50
IntensityAct(counter)=NumMoleculesAct(counter)/(QuantYieldAct*times(
counter))
PRINT "The Number of photons emitted at time t="IntensityAct(counter)
LPRINT "The Number of photons emitted at time t="IntensityAct(counter)
NEXT counter
WHILE MOUSE(0)<>1:WEND
begin:MENU RESET:CLS
FOR counter=1 TO number
x(counter)=times(counter)
y(counter)=IntensityAct(counter)
NEXT counter
sumx=0
sumy=0
sumxy=0
sumxx=0
sumdif=0
FOR j=1 TO number
sumx=sumx+x(j)
sumy=sumy+y(j)
```

```
sumxx=sumxx+x(j)^2
sumxy=sumxy+x(j)*y(j)
NEXT j
g=number
denom=sumx^2-g*sumxx
slope=(sumx*sumy-g*sumxy)/denom
b=(sumx*sumxy-sumy*sumxx)/denom
FOR j=1 TO number
calcy(j)=slope*x(j)+b
dif(j)=y(j)-calcy(j)
sumdif=sumdif+dif(j)^2
NEXT j
s=SQR(sumdif/(g-2))
denom=SQR(sumxx-sumx^2/g)
errors=t*s/denom
xmean=sumx/g
errint=t*SQR((sumdif)*(1/g+xmean^2/(sumxx-g*xmean^2)))
PRINT:PRINT:PRINT:PRINT:PRINT:PRINT TAB(5)"The equation for this
line is  y = "slope;"x  +";b
LPRINT:PRINT:PRINT:PRINT:PRINT:LPRINT TAB(5)"The equation for
this line is  y = "slope;"x  +";b
WHILE MOUSE(0)<>1:WEND

Intensity00=b

PRINT:PRINT:PRINT:PRINT "                This is the Intensity at t=0-
"Intensity00
```

```
LPRINT:PRINT:PRINT:LPRINT "                This is the Intensity at t=0-
"Intensity00
WHILE MOUSE(0)<>1:WEND
PRINT:PRINT:PRINT:PRINT "                  This is the end of the
Actinometer Calculation
PRINT:PRINT:PRINT:LPRINT "                 This is the end of the
Actinometer Calculation
WHILE MOUSE(0)<>1:WEND:CLS
REM End of Actinometer Calculation

INPUT"Enter volume for Sample Irradiated in ml";v1samp
INPUT"Enter Volume of V1 Sample taken for analysis in ml";v2samp
INPUT"Enter Volume V2 is diluted to in ml";v3samp
REM Epsilonsamp=5630 for  (CH3)3SnI
INPUT "Enter epsilon of Reactant";epsilonReac
INPUT "Enter epsilon of Product";epsilonProd
REM We used 4
INPUT "Enter Number ofAbsorbance Readings";numbersamp
FOR counter= 1 TO numbersamp
READ AbsorbReac(counter)
REM Absorbance Data For REACTANT Goes Here
DATA 1.3539,1.1263,1.1395,1.1365,1.1256,1.110,1.110,1.222,1.2152,1.2071
NEXT counter
FOR counter= 1 TO numbersamp
READ AbsorbProd(counter)
REM Absorbance Data For PRODUCT Goes Here
DATA 0.0001,-0.013,-0.026,-0.04,-0.055,0.0669,0.089,0.2452,0.2535,0.2863
```

```
NEXT counter

FOR counter= 1 TO numbersamp
NumMoleculesProd(counter)=(avogadro*v3samp*v1samp*AbsorbProd(cou
nter))/(epsilonProd*length*v2samp)
PRINT "Number of Molecules of Product";NumMoleculesProd(counter)
LPRINT "Number of Molecules of Product";NumMoleculesProd(counter)
NEXT counter
WHILE MOUSE(0)<>1:WEND
FOR counter= 1 TO numbersamp
NumMoleculesReac(counter)=(avogadro*v3samp*v1samp*AbsorbReac(cou
nter))/(epsilonReac*length*v2samp)
PRINT "Number of Molecules of Reactant";NumMoleculesReac(counter)
LPRINT "Number of Molecules of Reactant";NumMoleculesReac(counter)
NEXT counter
WHILE MOUSE(0)<>1:WEND

PRINT
LPRINT
REM Calulate Ia for sample
PRINT:PRINT
PRINT:LPRINT
PRINT "Intensity00=";Intensity00
LPRINT "Intensity00=";Intensity00
FOR counter= 1 TO numbersamp
IntensityAReac(counter)=Intensity00*(1-(1/10^AbsorbReac(counter)))
PRINT "Intensity Reac AA=";IntensityAReac(counter)
```

```
LPRINT "Intensity Reac AA=";IntensityAReac(counter)
NEXT counter
WHILE MOUSE(0)<>1:WEND
PRINT
LPRINT
FOR counter=1 TO numbersamp
READ timessamp(counter)
NEXT counter
DATA 0.0001,5,10,15,20,25,30,35,40,50
PRINT "Time","Num. Molecules in Reac","Num. Molecules in Prod"
LPRINT "Time","Num. Molecules in Reac","Num. Molecules in Prod"
FOR counter=1 TO numbersamp
P R I N T
timessamp(counter),NumMoleculesReac(counter),NumMoleculesProd(cou
nter)
L P R I N T
timessamp(counter),NumMoleculesReac(counter),NumMoleculesProd(cou
nter)
NEXT counter
WHILE MOUSE(0)<>1:WEND
PRINT
LPRINT
PRINT"ΔA","Δt"
LPRINT"ΔA","Δt"
FOR counter =1 TO numbersamp
ConcentrationDifferenceReac(counter)=NumMoleculesReac(counter)-
NumMoleculesReac(1)
```

```
ConcentrationDifferenceReac(counter)=ABS(ConcentrationDifferenceReac(
counter))
timessampDifference(counter)=timessamp(counter)-timessamp(1)
P R I N T
ConcentrationDifferenceReac(counter),timessampDifference(counter)
L P R I N T
ConcentrationDifferenceReac(counter),timessampDifference(counter)
NEXT counter
FOR counter =1 TO numbersamp
ConcentrationDifferenceProd(counter)=NumMoleculesProd(counter)-
NumMoleculesProd(1)
ConcentrationDifferenceProd(counter)=ABS(ConcentrationDifferenceProd(
counter))
timessampDifference(counter)=timessamp(counter)-timessamp(1)
P R I N T
ConcentrationDifferenceProd(counter),timessampDifference(counter)
L P R I N T
ConcentrationDifferenceProd(counter),timessampDifference(counter)
NEXT counter

WHILE MOUSE(0)<>1:WEND
PRINT
LPRINT
FOR counter =2 TO numbersamp
Changeconcoverchangetime Reac(counter)=ConcentrationDifferenceReac(c
ounter)/timessampDifference(counter)
PRINT "d[A]/dt";ChangeconcoverchangetimeReac(counter)
```

```
LPRINT "d[A]/dt";ChangeconcoverchangetimeReac(counter)
NEXT counter
WHILE MOUSE(0)<>1:WEND
FOR counter =2 TO numbersamp
ChangeconcoverchangetimeProd(counter)=ConcentrationDifferenceProd(c
ounter)/timessampDifference(counter)
PRINT "d[B]/dt";ChangeconcoverchangetimeProd(counter)
LPRINT "d[B]/dt";ChangeconcoverchangetimeProd(counter)
NEXT counter
WHILE MOUSE(0)<>1:WEND

PRINT
LPRINT
FOR counter =2 TO numbersamp
Quantum Yield A Reac(counter) =
ChangeconcoverchangetimeReac(counter)/IntensityAReac(counter)
PRINT "Quantum Yield A";QuantumYieldAReac(counter)
LPRINT "Quantum Yield A";QuantumYieldAReac(counter)
NEXT counter
WHILE MOUSE(0)<>1:WEND

FOR counter =2 TO numbersamp
Quantum Yield A Prod(counter) =
ChangeconcoverchangetimeProd(counter)/IntensityAReac(counter)
PRINT "Quantum Yield B";QuantumYieldAProd(counter)
LPRINT "Quantum Yield B";QuantumYieldAProd(counter)
NEXT counter
```

```
WHILE MOUSE(0)<>1:WEND

PRINT
LPRINT
begin2:CLS
FOR counter=1 TO 100
x(counter)=0
y(counter)=0
calcy(counter)=0
dif(counter)=0
NEXT counter
PRINT
LPRINT
PRINT"Time","Quantum  Yield at time=t"
LPRINT"Time","Quantum  Yield at time=t"
PRINT:PRINT
PRINT:LPRINT
OPEN "CLIP:"FOR OUTPUT AS 1
FOR counter=2 TO numbersamp
x(counter)=timessamp(counter)
y(counter)=QuantumYieldAReac(counter)
PRINT x(counter),y(counter)
LPRINT x(counter),y(counter)
WRITE #1,x(counter),y(counter)
NEXT counter
CLOSE 1
slope=0
```

```
b=0
sumx=0
sumy=0
sumxy=0
sumxx=0
sumdif=0
denom=0
FOR j=2 TO numbersamp
sumx=sumx+x(j)
sumy=sumy+y(j)
sumxx=sumxx+x(j)^2
sumxy=sumxy+x(j)*y(j)
NEXT j
g=numbersamp-1
denom=sumx^2-g*sumxx
slope=(sumx*sumy-g*sumxy)/denom
b=(sumx*sumxy-sumy*sumxx)/denom
FOR j=2 TO numbersamp
calcy(j)=slope*x(j)+b
dif(j)=y(j)-calcy(j)
sumdif=sumdif+dif(j)^2
NEXT j
s=SQR(sumdif/(g-2))
denom=SQR(sumxx-sumx^2/g)
errors=t*s/denom
xmean=sumx/g
errint=t*SQR((sumdif)*(1/g+xmean^2/(sumxx-g*xmean^2)))
```

```
PRINT:PRINT:PRINT:PRINT:PRINT:PRINT TAB(5)"The equation for this
line is  y = "slope;"x  +";b
PRINT:PRINT:PRINT:PRINT:PRINT:LPRINT  TAB(5)"The equation for
this line is  y = "slope;"x  +";b
QuantYieldReac=b
PRINT:PRINT:PRINT:PRINT "              Quantum Yield of Reac (finally!!!)
is";QuantYieldReac
PRINT:PRINT:PRINT:LPRINT "             Quantum Yield of Reac (finally!!!)
is";QuantYieldReac
WHILE MOUSE(0)<>1:WEND

FOR counter=1 TO 100
x(counter)=0
y(counter)=0
calcy(counter)=0
dif(counter)=0
NEXT counter
PRINT
LPRINT
PRINT"Time","Quantum  Yield at time=t"
LPRINT"Time","Quantum  Yield at time=t"
PRINT:PRINT
PRINT:LPRINT
OPEN "CLIP:"FOR OUTPUT AS 1
FOR counter=2 TO numbersamp
x(counter)=timessamp(counter)
y(counter)=QuantumYieldAProd(counter)
```

```
PRINT x(counter),y(counter)
LPRINT x(counter),y(counter)
WRITE #1,x(counter),y(counter)
NEXT counter
CLOSE 1
slope=0
b=0
sumx=0
sumy=0
sumxy=0
sumxx=0
sumdif=0
denom=0
FOR j=2 TO numbersamp
sumx=sumx+x(j)
sumy=sumy+y(j)
sumxx=sumxx+x(j)^2
sumxy=sumxy+x(j)*y(j)
NEXT j
g=numbersamp-1
denom=sumx^2-g*sumxx
slope=(sumx*sumy-g*sumxy)/denom
b=(sumx*sumxy-sumy*sumxx)/denom
FOR j=2 TO numbersamp
calcy(j)=slope*x(j)+b
dif(j)=y(j)-calcy(j)
sumdif=sumdif+dif(j)^2
```

```
NEXT j
s=SQR(sumdif/(g-2))
denom=SQR(sumxx-sumx^2/g)
errors=t*s/denom
xmean=sumx/g
errint=t*SQR((sumdif)*(1/g+xmean^2/(sumxx-g*xmean^2)))
PRINT:PRINT:PRINT:PRINT:PRINT:PRINT TAB(5)"The equation for this
line is  y = "slope;"x  +";b
PRINT:PRINT:PRINT:PRINT:PRINT:LPRINT  TAB(5)"The  equation  for
this line is  y = "slope;"x  +";b
QuantYieldProd=b
PRINT:PRINT:PRINT:PRINT "              Quantum Yield of Prod (finally!!!)
is";QuantYieldProd
PRINT:PRINT:PRINT:LPRINT "             Quantum Yield of Prod (finally!!!)
is";QuantYieldProd
WHILE MOUSE(0)<>1:WEND
LOAD "HD 20:APPLICATIONS:Ed's Launcher",r
```

2. Quantum Yield Calculation Result.

Volume of Actinometer Irradiated =	5.0 ml
Volume of V1 Analyzed =	5.0 ml
Volume of V2 Analyzed =	5.0 ml
Epsilon of Actinometer =	1.11e4
Lenght of cell in cm =	1.0
Number of Absorbance Readings Actinometer	10

Actinometer Absorbance Data at 510 nm

Time (sec)	Absorbance
0.0001	0.0001
5.0	0.160
10.0	0.308
15.0	0.401
20.0	0.512
25.0	0.637
30.0	0.646
35.0	0.704
40.0	0.694
50.0	0.720
60.0	0.760

First Calculation :

Number of Fe2+ molecules after irradiation is 2.713063E+13
Number of Fe2+ molecules after irradiation is 4.340902E+16
Number of Fe2+ molecules after irradiation is 8.356235E+16
Number of Fe2+ molecules after irradiation is 1.087938E+17
Number of Fe2+ molecules after irradiation is 1.389089E+17
Number of Fe2+ molecules after irradiation is 1.728221E+17
Number of Fe2+ molecules after irradiation is 1.752639E+17
Number of Fe2+ molecules after irradiation is 1.909997E+17
Number of Fe2+ molecules after irradiation is 1.882866E+17
Number of Fe2+ molecules after irradiation is 1.953406E+17

Second Calculation :

The Number of photons emitted at time t= 2.170451E+17
The Number of photons emitted at time t= 6.945443E+15
The Number of photons emitted at time t= 6.684988E+15
The Number of photons emitted at time t= 5.802338E+15
The Number of photons emitted at time t= 5.556354E+15

The Number of photons emitted at time t= 5.530309E+15
The Number of photons emitted at time t= 4.673704E+15
The Number of photons emitted at time t= 4.365707E+15
The Number of photons emitted at time t= 3.765732E+15
The Number of photons emitted at time t= 3.125449E+15

Third Calculation :

The equation for this line is y = -2.174228E+15 x + 7.635679E+16

This is the Intensity at (t = 0) = - 7.635679 E+16

This is the end of the Actinometer Calculation

Volume for Sample Irradiated=	5.0ml
Volume of V1 Sample taken for analysis =	5.0ml
Volume V2 is diluted to =	5.0ml
Epsilon of Reactant =	3450
Epsilon of Product =	917
Number ofAbsorbance Readings =	10

Reactant Absorbance Data :

Time (sec)	Absorbance
0.0001	1.3539
5.0	1.1263
10.0	1.1395
15.0	1.1365
20.0	1.1256
25.0	1.1100
30.0	1.1100
35.0	1.2220
40.0	1.2152
50.0	1.2071
60.0	1.2035

Product Absorbance Data :

Time (sec)	Absorbance
0.0001	0.0001
5.0	0.0130
10.0	0.0266
15.0	0.0405
20.0	0.0556
25.0	0.0661
30.0	0.0897
35.0	0.1245

40.0	0.1253
50.0	0.1286
60.0	0.1320

Fourth Calculation :

Number of Molecules of Product 3.284079E+14
Number of Molecules of Product-4.269303E+16
Number of Molecules of Product-8.538605E+16
Number of Molecules of Product-1.313632E+17
Number of Molecules of Product-1.806243E+17
Number of Molecules of Product 2.197049E+17
Number of Molecules of Product 2.92283E+17
Number of Molecules of Product 8.052561E+17
Number of Molecules of Product 8.325141E+17
Number of Molecules of Product 9.402318E+17

Number of Molecules of Reactant 1.181817E+18
Number of Molecules of Reactant 9.831457E+17
Number of Molecules of Reactant 9.94668E+17
Number of Molecules of Reactant 9.920493E+17
Number of Molecules of Reactant 9.825347E+17
Number of Molecules of Reactant 9.689175E+17
Number of Molecules of Reactant 9.689175E+17
Number of Molecules of Reactant 1.066682E+18
Number of Molecules of Reactant 1.060746E+18
Number of Molecules of Reactant 1.053676E+18

Fifth Calculation :

IntensityI_0	= 7.635679E+16
Intensity Reac I_a	= 7.297655E+16
Intensity Reac I_a	= 7.064795E+16
Intensity Reac I_a	= 7.081886E+16
Intensity Reac I_a	= 7.078047E+16
Intensity Reac I_a	= 7.063874E+16
Intensity Reac I_a	= 7.042962E+16
Intensity Reac I_a	= 7.042962E+16
Intensity Reac I_a	= 7.177698E+16

Intensity Reac I_a = 7.170470E+16
Intensity Reac I_a = 7.161712E+16

Sixth Calculation :

Time	Num. Molecules in Reac	Num. Molecules in Prod
.0001	1.181817E+18	3.2840791E+14
5	9.831457E+17	-4.269303E+16
10	9.946688E+17	-8.538605E+16
15	9.920493E+17	-1.313632E+17
20	9.825347E+17	-1.806243E+17
25	9.689175E+17	2.1970499E+17
30	9.689175E+17	2.9228333E+17
35	1.066682E+18	8.0525613E+17
40	1.060746E+18	8.3251411E+17
50	1.053676E+18	9.4023181E+17

Seventh Calculation :

Δ[R]	Δt
0.000000	0.00000
1.986716E+17	4.99999
1.871493E+17	9.99999
1.897680E+17	14.9999
1.992827E+17	19.9999
2.128999E+17	24.9999
2.128999E+17	29.9999
1.151352E+17	34.9999
1.210709E+17	39.9999
1.281413E+17	49.9999

Δ[P]	Δt
0.000000	0.000000
4.302143E+16	4.9999
8.571446E+16	9.9999
1.316916E+17	14.9999

1.809527E+17	19.9999
2.193765E+17	24.9999
2.919546E+17	29.9999
8.049277E+17	34.9999
8.321856E+17	39.9999
9.399034E+17	49.9999

Eighth Calculation :

d[R]/dt 3.973513E+16
d[R]/dt 1.871512E+16
d[R]/dt 1.265128E+16
d[R]/dt 9.964185E+15
d[R]/dt 8.516029E+15
d[R]/dt 7.096686E+15
d[R]/dt 3.289587E+15
d[R]/dt 3.026781E+15
d[R]/dt 2.562832E+15

d[P]/dt 8.604459E+15
d[P]/dt 8.571532E+15
d[P]/dt 8.779496E+15
d[P]/dt 9.047683E+15
d[P]/dt 8.775093E+15
d[P]/dt 9.731853E+15
d[P]/dt 2.2998E+16
d[P]/dt 2.080469E+16
d[P]/dt 1.879811E+16

Nineth Calculation :

Quantum Yield R .5624385
Quantum Yield R .2642674
Quantum Yield R .1787398
Quantum Yield R .1410584
Quantum Yield R .1209155
Quantum Yield R .1007628
Quantum Yield R 4.583067E-02
Quantum Yield R 4.221175E-02
Quantum Yield R 3.578519E-02

Quantum Yield P .1217935

Quantum Yield P .1210346
Quantum Yield P .1240384
Quantum Yield P .1280839
Quantum Yield P .1245938
Quantum Yield P .1381784
Quantum Yield P .3204091
Quantum Yield P .2901441
Quantum Yield P .2624806

Tenth Calculation :

Time	Quantum Yield of R at time=t
5	.5624385
10	.2642674
15	.1787398
20	.1410584
25	.1209155
30	.1007628
35	4.583067E-02
40	4.221175E-02
50	3.578519E-02

The equation for this line is y = -9.316126E-03 x + .4038577

Quantum Yield of Reac (finally!!!) is .4038577

Time	Quantum Yield of P at time=t
5	.1217935
10	.1210346
15	.1240384
20	.1280839
25	.1245938
30	.1381784
35	.3204091
40	.2901441
50	.2624806

The equation for this line is y = 4.512188E-03 x + 6.588363E-02

Quantum Yield of Prod (finally!!!) is 6.588363E-02

3. FTIR Kinetic Macro.

```
" FTIR Kinetics Macro Program "
INTEGER TEM
STRING NAME
STRING TITLE
STRING TGFILE

CRT KINETICS
" Program to monitor a photochemical reaction; stop spectral adquisition
when a threshold is exceeded "
LEDS = 0
DCLX
CR " YOUR SPECTRAL REGION OF INTEREST EXTENDS FROM "XSP
CR "                                    TO "XEP
CT " WHAT IS THE LOCATION (CM-1) OF THE PEAK TO BE MONITOR?
" XCUR
CR "ENTER ABSORBANCE VALUE OF PEAK WHICH WILL END
EXPERIMENT?" THR
CR " ENTER NUMBER OF SCANS FOR THE SAMPLE" NSS
CR " HOW MANY BACKGROUND SCANS" NSB
CR " ENTER TIME BETWEEN SCANS (IN SEC)?" BDL
CR " INSERT FORMATTED DATA DISK IN DRIVE 1" PAU
MNTD "-F1"
CR " ENTER GENERIC FILE NAME (8 CHAR.MAX.)" NAME
```

```
CR " ENTER TITLE (FOR PLOTTED SAMPLES)" TIT
CR " CLEAR BEAM PATH" PAU
CR " SCANNING BACKGROUND" SCB
CR " INSERT SAMPLE" PAU
CR " ENTER DISPLAY MAXIMUM" YEP
CR " ENTER DISPLAY MINIMUM" YSP
CR " SCANNING SAMPLE" SCS
EXT=1
    SCS RAS ABS DSS
    DRAW ROLL
    TGFILE= NAME+EXT   (Calculate file name)
    PDS TGFILE              (Store spectrum)
    EXT=EXT+1               (Increment file name)
    VALS                    (Find value of peak of interest)
    YCUR = YCUR-THR    (See if it has exceeded threshold)
    UNTIL YCUR GEZ          (If it has quit)
    END.
```

4. $(CH_3)_3SnI$ Rate Law Derivation.

$$(CH_3)_3SnI \xrightarrow{I_a} (CH_3)_3SnI^* \quad 4.1$$

$$(CH_3)_3SnI^* \xrightarrow{k_1} (CH_3)_3Sn\cdot + I\cdot \quad 4.2$$

$$(CH_3)_3SnI^* \xrightarrow{k_2} (CH_3)_3SnI + \text{heat} \quad 4.3$$

$$I\cdot + I\cdot \xrightarrow{k_3} I_2 \quad 4.4$$

$$2\,(CH_3)_3Sn\cdot \xrightarrow{k_4} (CH_3)_6Sn_2 \quad 4.5$$

$$(CH_3)_6Sn_2 + I_2 \xrightarrow{k_5} (CH_3)_3Sn\cdot + I\cdot \quad 4.6$$

$$-\frac{d[(CH_3)_3SnI]}{dt} = I_a - k_2[(CH_3)_3SnI^*] - 2k_5[(CH_3)_6Sn_2][I_2] \quad 4.7$$

$$\frac{d[(CH_3)_3SnI^*]}{dt} = I_a - k_1[(CH_3)_3SnI^*] - k_2[(CH_3)_3SnI^*] \quad 4.8$$

$$\frac{d[(CH_3)_3Sn\bullet]}{dt} = k_1[(CH_3)_3SnI^*] - 2k_4[(CH_3)_3Sn\cdot]^2 \quad 4.9$$

$$\frac{d[I\bullet]}{dt} = k_1[(CH_3)_3SnI^*] - 2k_3[I\bullet] \quad 4.10$$

$$\frac{d[I_2]}{dt} = -k_5[(CH_3)_3Sn_2][I_2] - 2k_3[I\bullet]^2 \qquad 4.11$$

$$\frac{d[(CH_3)_3Sn_2]}{dt} = -k_5[(CH_3)_3Sn_2][I_2] - 2k_4[(CH_3)_3Sn\bullet]^2 \qquad 4.12$$

$$[(CH_3)_3SnI^*] = \left[\frac{I_a}{k_1 + k_2}\right] \qquad 4.13$$

$$[(CH_3)_3Sn\bullet] = \left[\frac{I_a\left\{\left[\frac{k_1}{k_1 + k_2}\right]\right\}}{2k_4}\right]^{1/2} \qquad 4.14$$

$$[I\bullet] = \left[\frac{I_a\left\{\left[\frac{k_1}{k_1 + k_2}\right]\right\}}{2k_3}\right]^{1/2} \qquad 4.15$$

$$\boxed{-\frac{d[(CH_3)_3SnI]}{dt} = I_a\left[1-\left(\frac{k_2}{k_2 + k_1}\right)\right] - 2k_5[(CH_3)_6Sn_2][I_2]} \qquad 4.16$$

References.

Part I. Introduction.

1 Miller, S. E., *Bell System Technical Journal*, **48**, 2059-2069, (1969)

2 Borrelli, N. F.; Morse, D. L., *U. S. Pattent #4,403,031*

3 Borrelli, N. F.; Morse, D. L., *O. S. A. Gradient Index Meeting*, Kobe, Japan, 983; Monterrey, CA., 1984

4 Mendoza, E. A.; Morse, D. L.; Gafney, H. D., *Comference on Optoelectronic Materials*, Harvard University, Cambridge, Mass., 1987; *Symposium on Imaging*, White Bear Lake, Mn., 1988

5 Geoffroy, G. L.; Wrighton, M. S., " *Organometallic Photochemistry* ", Academic Press, New York, 1979

6 (a) Akio, B., *Bull. Chem. Soc. Japan*, **60**, 1552-1554, 1987
(b) Girbasova, N. V., *Zh. Obshch. Khim.*, **56**, 2753-2760, 1986
(c) De Ryck, P. H., et al., *Bull. Chem. Soc. Belg.*, **95**, 217-227, 1986; **94**, 621-629, 1885; *International Journal of Chemical Kinetics*, **17**, 95-108, 1985
(d) Kashin, A. N., *J. Organometal. Chem.*, **292**, 205-215, 1985

7 Maiman, T. H., *Nature*, **187**, 493, (1960)

8 Gambling, W. A., *Radio and Electronic Eng.*, **45**, 537, (1975)

9 Hall, R. N.; Fenner, G. E.; Kingsley, J. D.; Soltys, T. J., Carlson, R. D., *Phys. Rev. Lett.*, **9**, 366, (1962)

10 Bradley, D. J., *Contemp. Phys.*, **16**, 263, (1975)

11 Hayashi, I., Panish, M. B., Foy, P. W., Sumski, S., *Appl. Phys. Lett.*, **17**, 109, (1970)

12 Chen, D.; Zook, J. D., *Proc. IEEE*, **63**, 1207, (1975)

13 Krumme, J. P.; Hill, B.; Kruger, J.; Witter, K., *J. Appl. Phys.*, **46**, 2733, (1975)

14 Collin, R. E., " *Field Theory of Guided Waves*", McGraw-Hill, New York, (1960)

15 Miller, S. E., *Bell Syst. Tech. J.*, **48**, 2059, (1969)

16 (a) Tien, P. K., *Appl Opt.*, **10**, 2395, (1971)
(b) Taylor, H. F., Yariv, A.; *Procc. IEEE*, **62**, 1044, (1974)
(c) Cheo, P. K., *Appl. Phys.*, **6**, 1, (1975)
(d) Kogelnik, H., *IEEE Trans.*, **MTT-23**, 2, (1975)

17 (a) Kapani, N. S.; Burke, J. J., " *Optical Waveguides* ", Academic Press, New York, 1972
(b) Marcusse, D.," *Light Transmission Optics* ", Van Norstrand Reinhold,

Princeton, 1972

(c) Marcusse, D.," *Theory of Dilelectric Optical Waveguides* ", Academic Press, New York, 1972

18 (a) Marcusse, D.," *Integrated Optics* ", IEEE Press, New York, 1973

(b) Tamir, T., " *Integrated Optics* " Topics in Applied Physics, **6**, Spinger-Verlag, Berlin, 1975

19 (a) Goell, J. E., *Bell System Technical Journal*, **48**, 2133-2160, (1969)

(b) Marcateli, E. A. J., *Bell System Technical Journal*, **48**, 2071-2102, (1969)

20 A. W. Snyder, J. D. Love, " Optical Waveguide Theory " Chapman & Hall , New York, pp-599, 1983

21 Kawachi, M.; Yamada, Y.; Yasu, M.; Kobayashi, M., *Electron. Lett.*, **21**, 314-315, (1985)

22 (a) Valette, S.; et al., *Electron. Lett.*, **19**, 883-885, (1983)

(b) Valette, S.; Lizet, J.; Mottier, P., *Opt. Eng.*, **24**, 235, (1985)

(c) Valette, S.; Gidon, P.; Jadot, J. P., *Proc. 4th European Conf. on Integrated Optics*, Glasgow, (1987)

23 Paul, P. H.; Kychakoff, G., *Appl. Phys. Lett.* , **51**, 12-14, (1987)

24 Nishizawa, K.; Sudo, E.; Maeda, M. Yamasaki, T., *Proc. European Comf. on Optical Comm.* , Barcelona, Spain, 99-102, (1987)

25 Pavalth, G. A., Suman, M. C , *J. Inst. Navig.*, **31**, 70-83, (1984)

26 Kist, R.; Sohler, W., *J. Lightwave Tech.*, **1**, 105-110, (1983)

27 Nishihara, H. et al, *Appl. Opt.* , **21**, 1785-1790, (1982)

28 Frankland, E., Liebigs Ann. Chem., 71, 171, esp. 212 (1849)

29 Frankland, E., *J. Chem. Soc.*, **2**, 267, (1850)

30 Frankland, E., *Liebigs Ann. Chem.*, **85**, 329, (1853)

31 Cahours, A.; Riche, A., *Compt. Rend.*, **35**, 91, (1852)

32 Lowig, C., *Liebigs Ann. Chem.*, **84**, 308, (1852)

33 Kekule, A., *Liebigs Ann. Chem.*, **109**, 190, (1861)

34 Krause, E.; Von Groose, A, *Die Chemie der Metallorganischem Verdindungen*, Verlag Borntraeger, Berlin, 1937; Reprint, Verlag sandig, Wiesbaden 1965

35 Ingham, R. K.; Rosenberg, S. D.; Gilman, H.,*Chem . Rev.*, **60**, 459, (1960)

36 Dub M., *Organometallic Compounds.*,Vol **II**, Springer, Berlin, 1961

37 Seyferth, D.; King, R. B., *Annual Surveys of Organometallic Chemistry*, **1**, (1964).; **2**, (1965).; **3**, (1966).; From 1967, continued as Section B of *Organometallic*

Chemistry Reviews.

38 Neumman, W. P., " *The Organic Chemistry of Tin* ", Wiley, New York, (1970)

39 Poller, R. C., " *The Chemistry of Organotin Compounds* ", Logos, London, (1970)

40 awyer, A. K. (Ed.), " *Organotin Compounds* " Vols 1, 2, 3, Decker, New York, (1971)

41 Davies, A. G., Smith, P. J., *Adv. Inorg. Chem. Radiochem.*, **23**, 1, (1980)

42 Aylett, B. J., " *Organometallic Compounds* ", 4th Ed., Vol 1, part 2, groups IV and V, Chapman and Hall, London, (1979)

43 Poller, R. C., in " *Comprehensive Organic Chemistry . The Synthesis and Reactions of Organic Compounds*" , Ed. Baron, D.; Ollis, W. D., Vol. 3, Pergamon Press, Oxford, (1979)

44 Davies, A. G., Smith, P. J., " *Comprehensive Organometallic Chemistry . The Synthesis Reactions and Structures of Organometallic Compounds*" , Ed. Wilkinson, G.; Stone, F. G. A., Abel, E. W., Vol. 2, chap 11, Pergamon Press, Oxford, (1982)

45 (a) Luitjen, J. G. A., *Chemy Ind.*, 103, (1973

(b) Bloodworth, A. J.; Davies, A. G., *Chemy Ind.*, 490, (1972)

(c) Pereyre, M., Pommier, J. C., *J. Organometal. Chem. Library*, **1**, 161, (1976)

(d) Smith, P. J., *Chemy. Ind.*, 1025, (1976)

(e) NeguishiE. I., " *Organometallic in Organic Synthesis* ", Vol. 1, " *General Discussions and Organometallics of Main Group Metals in Organic Synthesis* ", Wiley, New York, (1980)

46 Lehn, W. L., *Inorg. Chem.*, **6**, 1061-1063, (1966)

47 Borrell, P.; Platt, A. E., *Trans. Faraday Soc.*, **66**, 2279-2285, 2285-2296, (1970)

48 (a) DeRyck, P. H.; Verdonck, L.; Van der Kelen, *Int. J. Chem. Kinet.*, **17**, 95-108, (1985)

(b) Verdonck, L.; DeRyck, P. H.; Hoste, S.; Van der Kelen, *J. Organometall. Chem.*, **288**, 289-294, (1985)

(c) DeRyck, P. H.; Verdonck, L.; Van der Kelen, *Bull. Soc. Chim. Belg.*, **94**, 621-629, (1985)

(d) DeRyck, P. H.; Hoste, S.; Van der Kelen, *Bull. Soc. Chim. Belg.*, **95**, 217-227, (1985)

49 Fukuzumi, S.; Kochi, J. K., *J. Phys.Chem.*, **84**, 617-624, (1980); *J. Org. Chem.*, **45**, 2654-2662, (1980)

50 Wheatley, P.J., *J. Chem. Soc.*, 5027, (1961)

51 Skinner, H. A.; Sutton, L. E., *Trans. Faraday Soc.*, **40**, 164, (1944)

83 See for Example :
(a) Avnir, D.; Bruise, R.; Ottolenghi, M ; Wellner, E.; Zachariasse, K. A., *J. Phys. Chem.*, **89**, 3521, (1985)
(b) Lochmuller, C. H.; Colborn, A. S.; Hunnicutt, M. L.; Harris, J. M., *J. Am. Chem. Soc.*, **106**, 4077, (1984)
(c) Francis, C.; Lin, J.; Singer, L. A., *Chem. Phys. Lett.*, **94**, 162, (1983)
(d) Furlong, D. N.; Sasse, W. H. F., *Colloids Surf.*, **7**, 29, (1983)
(e) Kajiwara, T.; Hasimoto, K.; Kawal, T.; Sakata, T., *J. Phys.Chem.*, **86**, 4516, (1982)
(f) Hara, K.; De Mayo, P.; Ware, W. R.; Weedon, A. C.; Wong, G. S. R.; Wu, K. C., *Chem. Phys. Lett.*, **69**, 105, (1980)
84 Kalyansundaran, K., "*Photochemistry in Microheterogeneous Systems*"; Academic Press, Inc.: New York, 1987; pp 183-193, 317-324, 336-360.
85 See for Example :
(a) De Mayo, P., *Pure Appl. Chem.*, **54**, 1623, (1984)
(b) Thomas, J. K., *J. Phys.Chem.*, **91**, 267, (1987)
(c) "*Phototransformations in Nonhomogeneous Media*", Fox, M. A., Ed.; ACS Symposyum Series 278, American Chemical Society: Washington, DC, 1985
86 Thomas, J. K., "*Chemistry of Excitation at Interfaces*"; ACS Monograph 191; American Chemical Society: Washington, DC, 1983
87 ibid 12
88 ibid 11
89 DeGlass, W. N.; Haller, G. L.; Kellerman, R.; Lunsford ,J. H., "*Spectroscopy in Heterogeneous Catalysis*", Academic Press: New York, (1979)
90 Ernsberger, F. M., *Annual Review of Materials Science* , **2**, 529, (1972)
91 McDonald, R. S., *J. Phys. Chem.*, **62**, 1168, (1958)
92 Young, G. J., *J. Colloid Sci.*, **13**, 67, (1958)
93 M. L. Hair, *Infrared Spectroscopy in Surface Chemistry*, Marcel Deckker, New York, (1967)
94 R. S. McDonald, *J. Phys. Chem.*, **62**, 1168, (1958)
95 R. S. McDonald, *J. Phys. Chem.*, **62**, 1168, (1958)
96 R. H. Doremus,*J. Phys. Chem.*, **75**, 3147, (1971)
97 F. H. Hambleton, J. A. Hockey, and J. A. G. Taylor ,*Trans. Far. Soc.*, **62**, 801, (1966)
98 Taylor, A. J.; Hambleton, F. H.; Hockey, J. A.,*J. Catal.*, **13**, 35, (1969)
99 V. R. Deitz; Turner ,N. H.,*J. Phys. Chem.*, **74**, 3823, (1970)

52 Herber, R. H.; Stockler, H. A., *Trans. N.Y. Acad Sci., Ser. II*, **26**, 929, (1964)
53 Olson, D.H.; Rundle, R. E., *Inorg.Chem.*, **2**, 1310, (1963)
54 Schick, R., Dissertation Thesis, Univ. Giessen, (1965)
55 Kraus, C. A.; Callis, C. C., *J. Am. Chem. Soc.*, **45**, 2624, (1923)
56 J. Katomzeff, *Compt. Rend.*, **230**, 536, (1950)
57 P. F. Oesper; Smyth, C. P., *J. Am. Chem. Soc.*, **64**, 173, (1942)
58 (a) C. P. Smyth, *J. Org. Chem.*, **6**, 421, (1941)
59 C. P. Smyth, *J. Am. Chem. Soc.*, **63**, 57, (1941)
60 Tobias, R.S., *Organometal. Chem Rev.*, **1**, 93, (1966)
61 Beattie, I. R.; McQillan , G. P., *J. Chem. Soc.*, 1519, (1963)
62 Van der Berghe, E. V.; Van der Kelen, G. P., *J. Organometal. Chem.*, **11**, 479, (1968)
63 Van der Berghe, E. V.; Verndock, L.; Van der Kelen, G. P., *J. Organometal. Chem.*, **16**, 497, (1969)
64 Matwiyoff, N. A; Drago, R. S., *Inorg. Chem.*, **3**, 337, (1964)
65 Van der Berghe, E. V.; Van der Kelen, G. P, *J. Organometal. Chem.*,**11**, 479, (1968)
66 Yergey, A. L.; Lampe, F. W., *J. Am. Chem. Soc.*, **87**, 4204, (1965)
67 Bolles, T. F; Drago, R. S., *J. Am. Chem. Soc.*, **87**, 5015, (1965)
68 Bolles, T. F; Drago, R. S., *J. Am. Chem. Soc.*, **88**, 392, (1966)
69 Bolles, T. F; Drago, R. S., *J. Am. Chem. Soc.*, **88**, 5730, (1966)
70 Frank, J.; Rabinowitch, E., *Trans. Faraday Soc.*, **30**, 120, (1934)
71 Creemers, H. M. H. C.; Noltes, J. C., *J. Organometal. Chem.*, **7**, 237-245, (1967)
72 Griffiths, V. S.; Derwish, G. A. W., *J. Chem. Soc. (A)*, 1679, (1967)
73 Mendelsohn, J.; Marchand, A.; Valade, J., *J. Organometal. Chem.*, **6**, 25-32, (1966)
74 **Infrared spectra of organometallic compounds**
75 Simons, P. B.; Graham, W. A. G., *J. Organometal. Chem.*, **8**, 479, (1968)
76 Clark, R J.; Davies, A. G.; Puddephatt, R., *J. Chem. Soc. (C)*, 1828, (1968)
77 Poller, R. C.; Toley, D. L. B., *J. Chem. Soc. (A)*, 1578, (1967)
78 Thayer, J. S.; Strommen, D. P., *J. Organometal. Chem.*, **5**, 383, (1966)
79 Poller, R. C., *J. Inorg. Nucl. Chem.*, **24**, 593, (1962)
80 Tobias, R. S.; Freidline, C. E., *Inorg. Chem.*, **4**, 215, (1966)
81 Maddox, M. L.; Stafford, S. L.; Kaesz, H. D., "*Advances in Organometallic Chemistry* ", Academic Press, New York, 1965
82 Van der Kelen, *Nature*, **193**, 1069, (1962)

83 See for Example :
(a) Avnir, D.; Bruise, R.; Ottolenghi, M., Wellner, E., Zachariasse, K. A., *J. Phys. Chem.*, **89**, 3521, (1985)
(b) Lochmuller, C. H.; Colborn, A. S.; Hunnicutt, M. L.; Harris, J. M., *J. Am. Chem. Soc.*, **106**, 4077, (1984)
(c) Francis, C.; Lin, J.; Singer, L. A., *Chem. Phys. Lett.*, **94**, 162, (1983)
(d) Furlong, D. N.; Sasse, W. H. F., *Colloids Surf.*, **7**, 29, (1983)
(e) Kajiwara, T.; Hasimoto, K.; Kawai, T., Sakata, T., *J. Phys.Chem.*, **86**, 4516, (1982)
(f) Hara, K.; De Mayo, P.; Ware, W. R.; Weedon, A. C.; Wong, G. S. R.; Wu, K C., *Chem. Phys. Lett.*, **69**, 105, (1980)
84 Kalyansundaran, K., "*Photochemistry in Microheterogeneous Systems*"; Academic Press, Inc. New York, 1987; pp 183-193, 317-324, 336-360
85 See for Example
(a) De Mayo, P., *Pure Appl. Chem.*, **54**, 1623, (1984)
(b) Thomas, J. K., *J. Phys. Chem.*, **91**, 267, (1987)
(c) "*Phototransformations in Nonhomogeneous Media*", Fox, M. A., Ed.; ACS Symposyum Series 278, American Chemical Society, Washington, DC, 1985
86 Thomas, J. K., "*Chemistry of Excitation at Interfaces*", ACS Monograph 191; American Chemical Society, Washington, DC, 1983
87 ibid 12
88 ibid 11
89 DeGlass, W. N.; Haller, G. L.; Kellerman, R.; Lunsford, J. H., "*Spectroscopy in Heterogeneous Catalysis*", Academic Press, New York, (1979)
90 Ernsberger, F. M., *Annual Review of Materials Science*, **2**, 529, (1972)
91 McDonald, R. S., *J. Phys. Chem.*, **62**, 1168, (1958)
92 Young, G. J., *J. Colloid Sci.*, **13**, 67, (1958)
93 M. L. Hair, *Infrared Spectroscopy in Surface Chemistry*, Marcel Deckker, New York, (1967)
94 R. S. McDonald, *J. Phys. Chem.*, **62**, 1168, (1958)
95 R. S. McDonald, *J. Phys. Chem.*, **62**, 1168, (1958)
96 R. H. Doremus,*J. Phys. Chem.*, **75**, 3147, (1971)
97 F. H. Hambleton, J. A. Hockey, and J. A. G. Taylor ,*Trans. Far. Soc.*, **62**, 801, (1966)
98 Taylor, A. J.; Hambleton, F. H.; Hockey, J. A *J. Catal.*, **13**, 35, (1969)
99 V. R. Deitz; Turner ,N. H *J. Phys. Chem.*, **74**, 3823, (1970)

100 Brinker, C. J.; Scherer, G. W., Roth, E. P., *J. Non-Cryst. Solids*, **72**, 345-368, (1985).

101 (a) Iler, R. K., "*The Chemistry of Silica*", Wiley, New York, 1979
(b) Dent-Glasser, L. S., Lachowski, E. E., *J. Chem. Soc. Dalton Trans.*, **393**, 399-413, (1980).

102 Iler, R. K., "*The Chemistry of Silica*", pp. 629, Wiley, New York, 1979.

103 Klein, L. C.; Garvey, G. J., "*Ultrastructure Processing of Ceramics, Glasses and Composites*", pp. 88, J. Wiley & Sons, Inc., 1984.

104 Susa, K.; et. al., "*Method for Producing Silica Glass*", U.S. Patent 4,317,668, Filed Jan 21, 1981.

105 Kamiya, K.; Sakka, S.; Yamanaka, T., *Proc. 10th Intern. Cong. in Glass*, **13**, 44, (1974).

106 Henning, S.; Svensson, L., *Physica Scripta*, **23**, 697, (1981).

107 Brinker, C. J., Scherer, G. W., Roth, E. P., *J. Non-Cryst. Solids*, **72**, 345-368, (1985).

108 Iler, R. K., *The Chemistry of Silica*, pp. 637, Wiley, New York, 1979.

109 Iler, R. K., "*The Chemistry of Silica*", pp. 645, Wiley, New York, 1979.

110 Caturan, G.; Gottardi, V.; Graziani, M., *J. Non-Cryst. Solids*, **29**, 41-48, 1978).

111 Kiselev, A. V., *J. Col. and Inter. Sci.*, **69**, 1979.

112 Iler, R. K., *The Chemistry of Silica*, pp. 295, Wiley, New York, 1979.

113 Gonzales-Oliver, C. J. R.; James, P. F.; Rawson, H., *Proc. International Congress on Glass*, July 6-11, 1980

114 Zarzycki, J., "*Crystallization of Gel-Produced Glasses*", Symposium on Nucleation and Crystallization in Glasses, Am. Cerm. Soc., Columbus, OH, pp 104, (1982)

115 Iler, R. K., "*The Chemistry of Silica*", pp. 625, Wiley, New York, 1979.

116 Elmer, T. H., *J. Am. Cerm. Soc.*, Oct-Nov, (1979).

117 Yamane, M.; Aso, S.; Okano, S.; Sakaino, T., *J. Mat. Sci.*, **14**, 607-609, (1979)

118 Iler, R. K., "*The Chemistry of Silica*", pp. 638, Wiley, New York, 1979.

119 Nogami, M.; Moriya, Y., *Yogio-Kyokai-Shi*, **89**, (1981).

120 Brimker, C. J.; Scherer, G. W., *J. Am. Cerm. Soc.*, **69**, C-12, (1986).

123 Krol, D. M.; van Lierop, J. C., *J. Non-Cryst. Solids*, **63**, 131-136, (1984).

122 Hair, M. L., *J. Non-Cryst. Solids*, **19**, 299-306, (1975).

123 Hair, M. L., *J. Non-Cryst. Solids*, **19**, 299-306, (1975).

124 Brunauer, S.; Kantro, D. L.; Weise, C. H., *Can. J. Chem.*, **34**, 171, (1956).

125 Brinker, C. J.; Scherer, G. W.; Roth, E. P., *J. Non-Cryst. Solids*, **71**, 171-178, (1985).

126 Iler, R. K., "*The Chemistry of Silica*", pp. 640, Wiley, New York, 1979.

127 Krol, D. M.; van Lierop, J. C., *J. Non-Cryst. Solids*, **63**, 131-136, (1984).

128 Brinker, C. J.; Scherer, G. W.; Roth, E. P., *J. Non-Cryst. Solids*, **72**, 345-368, 1985).

129 Brukner, R., *J. Non-Cryst. Solids*, **5**, 123, (1970).

130 Scherer, G. W., *Surface and Colloidal Science*, Vol 14, Ed. E. Matyevic, Plenum Publ.

131 Brinker, C. J.; Scherer, G. W.; Roth, E. P., *J. Non-Cryst. Solids*, **72**, 345-368, (1985).

132 Brunauer, S.; Kantro, D. L.; Weise, C. H., *Can. J. Chem.*, **34**, 171, (1956).

133 Yamane, M.; Okano, S., *Yogio-Kyokai-Shi*, **87**,56, (1979).

134 Iler, R. K., "*The Chemistry of Silica*", pp.545, Wiley, New York, 1979.

135 Brinker, C. J.; Scherer, G. W.; Roth, E. P., *J. Non-Cryst. Solids*, **72**, 345-368, (1985).

136 Strawbridge, I.; Craievich, A. F.; James, P. F., *J. Non-Cryst. Solids*, **72**, 139-142, (1985).

137 Brukner, R., *J. Non-Cryst. Solids*, **5**, 123, (1970).

138 Iler, R. K., "*The Chemistry of Silica*", pp 467, Wiley, New York, 1979.

139 Iler, R. K., "*The Chemistry of Silica*", pp 550, Wiley, New York, 1979.

140 Klein, L. C.; Gallo, T. A.; Garvey, G. J., *J. Non-Cryst. Solids*, **63**, 23, (1984).

141 Iler, R. K., "*The Chemistry of Silica*", pp.545, Wiley, New York, 1979.

142 Iler, R. K., "*The Chemistry of Silica*", pp.546, Wiley, New York, 1979.

143 Nogami, M.; Moriya, Y., *J. Non-Cryst. Solids*, **37**, 191, (1980).

144 Brinker, C. J.; Scherer, G. W.; Roth, E. P., *J. Non-Cryst. Solids*, **72**, 345-368, (1985).

145 Klein, L. C.; Gallo, T. A.; Garvey, G. J., *J. Non-Cryst. Solids*, **63**, 23, (1984).

146 Nogami, M.; Moriya, Y., *J. Non-Cryst. Solids*, **37**, 191, (1980).

147 Brinker, C. J.; Scherer, G. W.; Roth, E. P., *J. Non-Cryst. Solids*, **72**, 345-368, (1985).

Part II. Experimental Section.

1 (a) Maslowsky Jr, E., "*Vibrational Spectra of Organometallic Compounds*," Wiley Interscience Publication, New York, 1976; pp
(b) Sadtler UV-VIS Spectra.

2 (a) Aldrich Co., FTIR Library Book II, Organometallics Section, 1988
(b) Poller, R. C., *J. Inorg. Nucl. Lett.*, **24**, 593-600, (1962)

3 Sadtler UV-VIS Spectra

4 Thayer, J. S.; West, R., *Inorg Chem*., **3**, 889-893, (1964)

5 Hatchard, C. G., Parker, C. A., *Proc R Soc London A*, **235**, 518, (1956)

6 Bowman, W. D.; Demas, J. N., *J Phys Chem*., **80**, 2434, (1976)

7 Calvert, J.G., Pitts J. N., *Photochemistry*, Interscience Publication, New York, 1971; pp 780-788

8 Zarzycki, J., "*Ultrastructure Processing of Ceramics, Glasses and Composites*", Eds., Hench, L. L., Ulrich, D. R., Wiley, New York, 1884, pp 43

9 Orr, C., Dalla Valle J. M., "Fine Particle Measurement", pp 175, MacMillan, New York, 1959

10 A. J. Lecloux, "Texture of Catalysts", pp 172-230 in *Catalyst Science and Technology*, Vol 2, J. R. Anderson and M. Boudart (Eds.), Springer-Verlag, West Berlin, 1981

11 Bonse, U., Hart, M. Z., *Physic*, **189**, 151, (1966)

12 Lake, J. A., *Acta Cryst*., **23**, 191, (1967)

Part III. Results.

1 McDonald R. S., *J. Phys Chem*., **62**, 1168, (1958)

2 Prassas M., PhD Thesis (1981), France

3 Prassas M.; Phalippou, J., Zarzycki J., *XIII Int. Comf. on Glasses*, Hamburgh, Germany, July 1985

4 a) Woignier, T.; Phalippou, J., *Ric. Staz. Sper. Vetro*., **5**, 47, (1984)
b) McDonald R. S., *J. Phys Chem*., **62**, 1168, (1958)
c) Benesi, J. B.; Jones, A. C., *J. Phys Chem*., **63**, 179, (1959)
d)Wu, C. K.; *J. Non-Cryst. Solids*, **70**, 2837, (1964)
e) Pouchert, C. J., *The Aldrich Library of Infrared Spectra*, ed. III, Aldrich Chemical Co., (1981)

5 Borrell, P.; Platt, A. E., *Trans. Faraday. Soc*., **66**, 2279-2285, (1970)

6 Petrosyan, V.S.; Yashina, N.S.; Reutov, O.A., *Advances in Photochemistry*, **11**, 512, (1971)

7 Vogler, A.; Paukner, A.; Kunkely, H., "*Coord. Chem. Rev.*", in press

8 Petrosyan, V.S.; Yashina, N.S.; Reutov, O.A., *Advances in Photochemistry*, **11**, 512, (1971)

9 Sutsui, T., "*Characterization of Organometallic Compounds*", Wiley Interscience, New York, 1970, pp467

10 Maslowsky, E., J., "*Vibrational Spectra of Organometallic Compounds*", Wiley-Interscience, New York, 1977, pp 69

11 Calvert, G. C., Pitts, J. N., *Photochemistry*, John Wiley & Sons, New York, 1966, pp 587-588

12 Frost A. A.; Pearson R. G., "Kinetics and Mechanism", 2nd Ed.,John Wiley & Sons, pp13-15, 1961

13 Davies, A. G.,"*J. Organometallic Chem.*", **39**, C55, (1972)

0 Voguel, Arthur I., *A Textbook of Quantitative Inorganic Analysis Including Elementary Instrumental Analysis*, 4th Edition, Longman, London, new York, 1979, pp372-373

14 Scriven, J., *Azides and Nitrenes, Reactivity and Utility*., Academic Press, New York, (1984)

15 Calvert, G. C., Pitts, J. N., *Photochemistry*", John Wiley & Sons, New York, 1966, pp 332-334

16 Avram, M.; Mateescu, G. H.," *Infrared Spectroscopy*", Wiley-Interscience, New York, 1966, pp. 216-218

17 Poller, R. C., *J. Inorg. Nucl. Chem*., **24**, 593-600, (1962)

18 Maslowsky, E., J., "*Vibrational Spectra of Organometallic Compounds*", Wiley-Interscience, New York, 1977

19 Calvert, G. C.; Pitts, J. N., "*Photochemistry*", John Wiley & Sons, New York, 1966, pp 452-453

20 Avram, M.; Mateescu, G. H.," *Infrared Spectroscopy*", Wiley-Interscience, New

York, 1966, Apendix 1

21 Clark, A. J.; Davies, A. G.; Puddephat, R. J., *J. Chem. Soc. C*, 1828, (1968)

22 Poller, R. C.; Toley, D. L. B., *J. Chem. Soc. A*, 1578, (1967)

23 Gafney, H. D., *J. Imag. Sci.*, **33**, 37-4, (1989)

24 Borrely, N. F.; Cotter M. D; Luong, J. C., *IEEE J. of Quantum Electronics* , **QE-22**, 896, (1986)

25 Darsillo, M. S.; Gafney, E. A.; PAquete, M. S ," *J. Am. Chem. Soc.*", **109**, 3275, (1987).

26 Yukawa, Y. " *Handbook of Organic Structural Analysis* ", Benjamin, New York, pp 544-545, (1965)

27 Darsillo, M., *The Photochemistry and Photocatalytic Reactions of Iron Carbonyls Adsorbed onto Porous Vycor Glass*, Ph.D. Thesis, City University of New York, 1986

28 Gafney, H. D., " *J. Macromol. Sci. Chem* ", **A27 [9-11]**, 1187, (1990)

29 Mendoza, E. A.; Wolkow, E.; Sunil, D.; Wong, P.; Sokolov, J.; Rafailovich, M.; Boer, M.; Gafney, H. D., *Lagmuir* , **7**, 3046-3051, (1991)

30 Mendoza, E. A.; Gafney, H. D., D. L. Morse, Proccedings of the International Symposium on Non-Linear Optical Materials, Center for Materials Excellence, University of Texas at El Paso, El Paso, TX, Octover 1990

31 Mendoza, E. A.; et.al, *Appl. Phys. Lett.*, **57**, 209, (1990)

32 Wiltzius, P.; Bates, F. S.; Dierker, S. B.; Wignall, G. D., *Phys. Rev. A*, **36**, 2991-2994, (1987)

33 Cahn, J. W., *Acta Metall.*, **9**, 795, (1961)

34 Tamaki, J.; Nagaishi, M.; Teraoka, Y.; Miura, N.; Yamazoe, N., *Surface Science*, **21**, 183-196, (1989)

35 Mendoza, E. A.; Wolkow, E.; Sunil, D.; Wong, P.; Sokolov, J.; Rafailovich, M.; Boer, M.; Gafney, H. D., *Lagmuir* , **7**, 3046-3051, (1991)

36 (a) Bancroft, G. M., *Mossbauer Spectroscopy An Introduction for Inorganic Chemist and Geochemist.*; Wiley-Interscience: New York, (1973), pp 157. (b) Bancroft, G. M.; Maddock, A. G.; Burns, R. G., *Geochim. Cosmochim. Acta*, **31**, 2219, (1967).

37 Waychunas, G. A.; Brown, G. E.; Jackson, W. E.; Pondar, P. W., *Physica B (Amsterdan)*, **158**, 67, (1989)

38 Slater, J. C., *Symmetry and Energy Bands in Crystals*; Dover: New York, (1972), pp.318

39 Kistner, O. C.; Sunyar, A. W., *Phys. Rev. Lett.*, **4**, 412, (1960)

40 Bauminger, R., Cohen, S. G., Marinov, A., Ofer, S.; Segal, S., *Phys. Rev.*, **122**, 1447, (1960)

41 Gafney, H. G.; *J. Macromol. Sci.-Chem.*, **A27**, 1187-1202, (1990)

42 Mendoza, E. A.;Morse, D. L., Gafney, H. D., *SPIE Proc.*, Symposium in Integrated Optics, OE/ Boston, 1990

43 Borreli, N. F.; Morse, D. L.; Scheurs, J. H., *J. Appl. Phys.*, **54**, 6, (1983); (c) Borreli, N. F.; Morse, D. L., *J. Appl. Phys.*, **43**, 992, (1983)

44 Mendoza, E. A.; Gafney, H. D., *SPIE Proc.*, Symposium in Integrated Optical Circuits, OE/ Boston, 1991

45 Halliday, D.; Resnick, R., " *Fundamentals of Physics* ". John Wiley & Sons, New York, 1974, pp-672

46 Halliday, D.; Resnick, R., " *Fundamentals of Physics* ". John Wiley & Sons. New York, 1974, pp-741

47 Streibl, N., *J. Mod. Opt.*, **36**, 1559-1573, (1989)

48 Goodman, J. W.; Loemberger, F., Kung, S. Y.; Athale, R *Proc. IEEE*, **72**,850, (1984)

49 Jenkins, B. K., et.al., *Appl. Opt.*, **23**, 3465, (1984)

50 Morse, D.L., private communications

51 Martin, W. L., *Appl Opt.*, **15**, 2112, (1976)

52 Heibi, J.; Vogues, E., *IEEE Journ. Quant. Elec.*, **QE 14**, 501, (1978)

53 White, J.; Heidrich, P., *Appl. Opt*, **15**, 151, (1976)

54 Gladstone, D.; Dale, T., *Phil Trans. Roy. Soc. London*, **153**, 1893.

55 Chartier, G.; Jaussaud, A., Laybourn, P.; Parriaux, O., *Electron. Lett.*, **14.5**, 134, (1978)

56 Marcatilly, E. A. J., *Bell Syst. Tech. J.*, **48**, 2013, (1969)

57 Marcuse, D., *Bell Syst. Tech. J.*, **50**, 2551, (1971)

58 Miller, S. E., *Bell Syst. Tech. J.*, **43**, 1727, (1964)

Part IV. Discussion.

1 Dubinim, M. M., *Adv. Collid. Interface. Sci*, **2**, 217, (1968)

2 Unger, K., *Angew. Chem. Int. Ed.*, **11**, 267, (1972)

3 Cohan, L.H.; Watson, J. H. L., *Rubber Age*, **68**, 687, (1951)

4 (a) Mukherjee, S. P.; Cordaro, J. F.; Debsikdar, *Adv. Cerm. Mater.*, **3**, 463-467, (1973)

(b) Tomanova, D.; Zbuzek, B.; Jerabek, K.; Schenider, P., *Collect. Czech. Chem. Commun.*, **46**, 2060-2067, (1981)

(c) Ministri, Z., *Proc. Int. Symp. Pore Struct. Mater.*, **Part I**, C155-C171, (1973)

5 (a) Iler, R. K., *The Chemistry of Silica*, Wiley, New York, (1979)

(b) Kiselev, A.V., *Trans. Faraday Soc. Disc.*, **52**, 14, (1971)

(c) Barby, D., " Silicas " in *Characterization of Powder Surfaces*, Eds. Parfitt, G. D.; Sing, K. S. W., Academic Press, New York, Ch 8, (1976)

6 Lagmuir. I., *J. Am. Chem. Soc.*,**40**, 1361, (1918)

7 Mertens, G.; Fripiat, J. J., *J. Colloid. Interface. Sci.*, **42**, 169, (1973)

8 Abayashi, H.; Yoshida. A., *J. Chem. Soc. of Jap. Ind. Chem. Sec.*, **70**, 156, (1967)

9 Lambert, R.; Singer, N., *J. Colloid. Interface. Sci.*, **45**, 440, (1973)

10 Lange, K. R., *J. Colloid. Sci.*, **20**, 231, (1965)

11 Iler, R. K., *The Chemistry of Silica*, Wiley, New York, (1979)

12 Armistead, C. G.; Hockey, J. A., *Trans. Faraday Soc.*, **63**, 2549, (1967)

13 Curthoys, V. Y.; Davydov, A. V., *J. Colloid. Interface. Sci.*, **48**, 58, (1974)

14 Brinker, C. J.; Scherer, G. W., *Sol-Gel Science*, Academic Press, New York, (1989), pp. 623

15 Gallo, T. A.; Brinker, C. J. .; Klein, L. C.; Scherer, G. W., " *Better Ceramics Through Chemistry* ", Eds. Brinker, C. J.; Clark, D. E.; Ulrich, D.R., Elsevier, New York, (1984), pp.85-90

16 Bulten, E. J., *Organometal. Chem. Rev.*, **B5**, 663, (1969)

17 Thayer, J. S.; West, R., *Inorg. Chem.*, **3**, 889-893, (1964)

18 Vogler, A.; Paukner, A.; Kunkely, H., *Coord. Chem. Rev.*, in press

19 Mendoza, E.A.; Gafney, H. D., *Inorg. Chem.*, **29**,4853-4854, (1990)

20 Matwiyoff, N. A.; Drago, R. S., *Inorg. Chem.*, **3**, 337-341, (1964)

(b) Poller, R. C., *J. Organometall. Chem.(London)*, **3**, 321, (1965)

21 (a) Hulme, R., *J. Chem. Soc.*, 1524, (1963)

(b) Beattie, I. R.; McQuillan, G. P.; Hulme, R., *Chem. Ind.(London)*, 1429, (1962)

22 (a) Hair, M. L., *J. Colloid. Interface. Sci.*, **60**, 154, (1977)

(b) Frazier, S. E.; Bedford, J. A.; Hower, J.; Kenney, M. E., *Inorg. Chem.*, **6**,

1693, (1967)

(c) Armistead, C. G.; Hockey, J. A., *Trans. Faraday Soc.*, **63**, 2549, (1967)

23 Snyder, L. R.; Ward, J. W., *J. Phys Chem.*, **70**, 394-399, (1966)

24 Insert isoamylnitrite reference from results

25 Tagliavini, G.; Faleshini, S.; Pilloni, G., *J. Organometal. Chem.*, **5**, 136-146, (1966)

26 a) Marshall, R.; Davidson, N., *J. Chem. Phys.*, **21**, 2086, (1953)

b) Rosman, H.; Noyes, R. M., *J. Am. Chem. Soc.*, **80**, 2410, (1958)

27 Rabinovitch, E.; Wood, W. C., *Trans Faraday Soc.*, **32**, 547,(1936)

28 (a) Bone, S.; Gielen, M.; Nasielski, J., *Bull. Soc. Chim. Belges*, **73**, 864-870, (1964)

(b) Tagliavini, G.; Faleschini, S.; Pilloni, G.; Plazzogna, G., *J. Organometall. Chem.*, **5**, 136, (1966)

29 (a) Prince, R. H., *J. Chem. Soc.*, 1783, (1959)

(b) Thomas, A. B.; Rochow, E. G., *J. Inorg. & Nucl. Chem.*, **4**, 205, (1957)

(c)Kraus, C. A., *J. Am. Chem Soc.*, **46**, 2196, (1924)

30 Aldrich, FTIR spectra Books 1, 2

31 Calvert, J. G.; Pits, J. N., *"Photochemistry"*, Wiley & Sons, New York, (1966), pp452-453.

32 Aldrich, FTIR spectra Books 1, 2

33 E. A. Mendoza; D. L. MOrse; H. D. Gafney, Conference on Inorganic Chemistry, Harvard University, Cambridge, Ma, (1987); Manuscript in preparation

34 H. D. Gafney, *J. Macromol. Sci*, **A27**, pp.1187-1202, (1990)

35 M. S. Darsillo; M. S. Paquette; H. D. Gafney, *J. Am. Chem. Soc.*, **109**, pp.3275, (1987)

36 S. Hoste; G. G. Herman, F. F. Roclant, W. Lippeus, and L. Verndock, *Spectrochim. Acta*, **39(A)**, pp.959, (1983); **40(A)**, pp.215, (1984)

37 Berk, N. R., *Phys. Rev. Lett.*, **58**, 2718, (1987)

38 Doolitlle, L. R., *Nucl. Instrum. Methods*, **218**, 11, (1983)

39 Luong, J. C.; Borreli, N. F.; Scheurs, W. H.; Morse, D. L., *MRS Symp. Proceed.*, **75**, 671, (1987)

40 Sunil, D.; Wolkow, E.; Mendoza, E. A.; Sokolov, J.; Rafailovitch, M.; Long, G.; Jemian, P. R.; Gafney, H. D.; Hansen, A., *MRS Symp. Proceed.*, in press

41 Bancroft, G. M., *Mossbauer Spectroscopy an Introduction for Inorganic Chemists and Geochemist*, Wiley-Intersience: New York, (1973), pp157

42 Pott, G. T.; McNichol, B. D., *Disc. Faraday Soc.*,**52**, 121, (1971)

43 Darsillo, M. S.; Gafney, H. D.; Packette, M. S., *J. Am. Chem. Soc.*, **109**, 3275, (1987)

44 Brinker, C. J.; Sherer, G. W., *Sol-Gel Science; The Physics and Chemistry of Sol-Gel Processing*, Academic Press: New York, 1972, Ch. 9

45 Kiselev, A. V., *The Structure and Properties of Porous Materials*, Everett, D. H.; Stone F. S., Eds., Butterworth: London, (1958), pp.195

46 Hunsperger, R. G., *Integrated Optics: Theory and Technology*, Springer-Verlag: New York, pp. 47, (1985)

47 E.A. Mendoza, D.L. Morse, and H.D. Gafney, "*The Photochemical Deposition of Non-Linear Optical Materials into Porous Glass* ", International Symposium on Non-Linear Optical Materials, University of Texas at el Paso, El Paso, Texas, CRC Press (1990)

48 E. A. Mendoza, E. G. Wolkow, D. Sunil, J. Sokolov, M. H. Rafailovich, M. den Boer; and H.D. Gafney, "*Photoimaging on Porous Vycor Glass and TMOS Xerogels* ", Langmuir, (1991), Accepted

49 E. A. Mendoza; D. L. Morse; H. D. Gafney, *Comference on Optoelectronic Materials*, Harvard University, Cambridge, MA, 1987; *Symposium on Imaging* , White Bear Lake, Mn, 1988.

50 E. A. Mendoza; D. L. Morse; H. D. Gafney, *Proceedings SPIE Society* , OE/Boston 90, Symposium on Laser Science and Optics Applications, Boston, MA, 1990

51 H. D. Gafney, *J. Imaging Sci* , **33**, 37, (1989)